



PhD-FSTC-2013-33
The Faculty of Sciences, Technology and Communication

DISSERTATION

Defense held on 08/11/2013 in Luxembourg

to obtain the degree of

DOCTEUR DE L'UNIVERSITÉ DU LUXEMBOURG EN SCIENCES DE L'INGÉNIEUR

by

Vincent DIAS

Born on 28th October 1986 in Thionville (France)

DEVELOPMENT OF ADHESIVES CONSTITUTIVE MATERIAL LAWS FOR THE ASSESSMENT OF BONDED STEEL TO GLASS PARTIAL COMPOSITE BEAMS

Dissertation defense committee

Dr Christoph Odenbreit, dissertation supervisor

Professor, Université du Luxembourg, Faculté des Sciences, de la Technologie et de la Communication

Dr Oliver Hechler

Université du Luxembourg, ArcelorMittal Chair of Steel and Façade Engineering

Dr Frank Scholzen, Chairman

Professor, Université du Luxembourg, Faculté des Sciences, de la Technologie et de la Communication

Dr Albert Giraud

Professor, Université de Lorraine, Georessources

Dr Tarak Ben Zineb, Vice Chairman

Professor, Université de Lorraine, ESSTIN - LEMTA

Abstract

Glass products are widely employed in transparent facade and roof structures as tertiary non-structural elements despite their large in-plane compressive resistances. To structurally implement them in building, tensile stresses must be consequently reduced or avoided. The later requirements would be fulfilled by realizing composite steel to glass connection, whose principal difficulty would arose from the connection mean which should be sufficiently rigid to transfer shear forces and sufficiently soft to not alter the glazing. Two possible jointing methods were envisaged and investigated to accomplish this assembly and overcome this problem, i.e. a linear adhesive bonding of the steel and glass parts and a mixed mechanical-adhesive connection. In consequence, two potential adhesives were selected, a silicone elastomer and a UV-curing acrylic thermoset. A lack of knowledge with regards to their mechanical properties implied the conduction of several series of quasi-static, cyclic and long-term relaxation tests. The possible influence of external parameters, such as temperature, humidity or UV-radiation, on their uniaxial tension/compression and shear behaviours was evaluated with the help of statistical methods applied on the results of Taguchi design of experiments tables. With the invariance of the silicone properties, a new hyperelastic quasi-incompressible constitutive material law accounting for the quasi-static and post Mullins effect behaviour was developed and validated with finite element analyzes of the small-scale experimental tests. The UV-acrylic was however found strongly dependent on the loading rate and one-dimensional models were suggested to describe the quasi-static tension and shear behaviour under specific rates. In reason of the poor long-term properties of the UV-acrylic, only the silicone was regarded for the construction of the two types of composite beams. Pre-evaluations issued from numerical simulations including the developed material law accommodated perfectly with theoretical data and approached the large-scale tests results by considering the manufacturing operations conducted on the steel beam.

Keywords: Steel-Glass assembly, adhesive connection, mechanical connection, partial composite beam, hyperelastic quasi-incompressible constitutive material law, Mullins' effect, thermoset rate-dependency, finite element design

Résumé

Les produits verriers sont de nos jours utilisés pour la réalisation de façades ou toitures transparentes comme éléments tertiaires non-structurels malgré leur importante résistance aux efforts de compression plane. Pour pleinement développer les capacités structurelles du verre en construction, les contraintes de traction doivent être réduites au maximum, voire éliminées. Ce dernier critère est rempli par la mise en œuvre de poutres mixtes verre-acier, dont la principale difficulté provient de la connexion qui doit être suffisamment rigide pour transférer les efforts de cisaillement et suffisamment souple pour n'introduire aucun dégât dans le verre. Deux méthodes ont été envisagées pour construire un tel assemblage et s'affranchir de cette dernière difficulté, i.e. par l'intermédiaire d'une connexion linéaire purement adhésive et avec une connexion hybride à la fois mécanique et adhésive. Ainsi, deux adhésifs potentiels ont été sélectionnés, un élastomère silicone et un acrylique durcissant sous rayons UV. Comme leurs propriétés mécaniques n'étaient pas proprement établies, plusieurs séries de tests quasi-statiques, cycliques et de relaxation à long-terme ont été effectuées. Les possibles influences de paramètres extérieurs, comme la température, l'humidité ou le rayonnement UV, sur le comportement en traction/compression uni-axiale et en cisaillement ont été identifiées à l'aide de méthodes statistiques appliquées sur les résultats des tests entrepris conformément aux plans d'expériences de Taguchi. L'invariance des propriétés du silicone a permis d'établir une unique loi matérielle hyperélastique et incompressible décrivant les comportements quasi-statique et post-effet Mullins. Cette loi a été validée par simulations numériques des tests à petite échelle. A l'opposé, l'acrylique a été identifié fortement dépendant de la vitesse de chargement et seuls des modèles

unidimensionnels ont pu être proposés pour caractériser le comportement quasi-statique en traction et cisaillement. En raison de la faible résistance face aux actions à long-terme de l'acrylique, seul le silicone a été conservé pour la production des deux types de poutres composites verre-acier. Plusieurs pré-dimensionnements ont été réalisés à partir de simulations numériques incluant la loi matérielle développée. Ces évaluations correspondaient parfaitement aux données issues de la théorie et n'étaient que peu éloignées des résultats obtenus avec les tests à large échelle en considérant toutefois les opérations faites lors de la fabrication des poutres en acier.

Mots-clés: Assemblage verre-acier, connexion par adhésifs, connexion mécanique, poutre mixte à connexion partielle, loi matérielle hyperélastique quasi-incompressible, effet de Mullins, adhésif dépendant de la vitesse de chargement, éléments finis et analyses numériques

Remerciements

Ce travail de thèse a été réalisé au sein du « Laboratoire Acier et Construction Mixte » sous la direction de M. Christoph Odenbreit, Professeur à l'Université du Luxembourg. Je tiens à le remercier très chaleureusement et lui témoigne toute ma reconnaissance et toute ma considération, d'une part pour m'avoir offert la possibilité d'entreprendre cette étude sur un sujet original et d'autre part pour l'intérêt et le temps qu'il m'a consacrés tout au long de ces quatre enrichissantes années.

Je tiens également à remercier les membres de mon comité d'encadrement de thèse, M. Frank Scholzen, Professeur à l'Université du Luxembourg et M. Tarak Ben Zineb, Professeur à l'Université de Lorraine, pour leurs conseils et commentaires expérimentés, distillés au cours des différentes étapes de ce projet. Mes remerciements s'adressent aussi à M. Oliver Hechler, collaborateur scientifique à l'Université du Luxembourg et membre de « ArcelorMittal Chair of Steel and Façade Engineering », pour l'intérêt qu'il m'a porté et son aide continue. Je suis très reconnaissant envers M. Albert Giraud, Professeur à l'Université de Lorraine, pour avoir accepté de participer à l'évaluation de ce travail.

Les parties expérimentales de cette recherche, comprenant la fabrication des divers échantillons à petite ou grande échelle, les mises en place mécaniques et informatiques des différents tests, ont entièrement été réalisées au sein du laboratoire de l'Université du Luxembourg et n'auraient pu aboutir sans les précieuses aides de nombreux techniciens. Je tiens donc à témoigner toute ma gratitude à la formidable équipe « mécanique » composée de Claude Collé, Ed Weyer, Vicente Adonis et Logan Freitas et également à l'ingénieuse équipe « acquisition », constituée de Marc Seil, Gilbert Klein, Ralf Reiter, Raphaël Hinger, grâce auxquelles j'ai pu apprendre de nombreuses techniques et passer de très bons moments.

Je remercie l'ensemble des doctorants de l'Université avec lesquels j'ai pu étudier, échanger, découvrir... et plus particulièrement mes proches collègues, David Rodrigues, Paulo Osorio, Anh Tuan Tran, Mike Tibolt, Sébastien Nellinger et Andreas May, pour leur soutien, leur complicité, voire leur amitié. Enfin je suis reconnaissant à l'égard de l'ensemble du personnel de l'Université qui, de près ou de loin, a rendu possible l'aboutissement de ce projet.

Je tiens à exprimer ma gratitude à ArcelorMittal, Guardian Luxembourg et VitrumLux pour leurs supports et leurs donations de matériel en acier et verre, mais encore Dow Corning et Kömmerling-Chemie pour leurs approvisionnements en silicone structurel et leur coopération.

TABLE OF CONTENTS

1. INTRODUCTION

1.1 Background and problems	1
1.2 Objectives	2
1.3 Organization of the thesis	3

PART I: SELECTION OF COMPOSITE SYSTEMS AND MATERIALS

2. LITERATURE REVIEW AND STATE OF THE ART

2.1 Introduction	5
2.2 Glass for structural applications	6
2.2.1 Monolithic glass	6
2.2.2 Glass assemblies	11
2.2.3 Design methods	14
2.3 Connecting steel to glass	18
2.3.1 Considerations for connections	18
2.3.2 Mechanical connections	19
2.3.3 Adhesive connections	25
2.3.4 Summary	30
2.4 Adhesive material properties	31
2.4.1 General review	31
2.4.2 Elastomer material laws	33
2.4.3 Thermoset material laws	44
2.4.4 Summary	49
3. STRUCTURAL CONNECTIONS	
3.1 Introduction	51
3.2 Composite steel-glass beam	52
3.2.1 System description	52
3.2.2 Domain of validity and advantages	52
3.2.3 Employed products	53
3.2.4 Actions on composite beams	53
3.2.5 Additional application conditions	56
3.3 Linear adhesive connection	57
3.4 Mechanical-adhesive connection	59

3.5 Summary and conclusions	61
 PART II: DEVELOPMENT OF CONSTITUTIVE MATERIAL LAWS FOR ADHESIVES	
 4. EXPERIMENTAL INVESTIGATIONS	
4.1 Introduction	63
4.2 Silicone Dow Corning DC993	64
4.2.1 Tension	64
4.2.2 Compression	86
4.2.3 Push-out shear tests	103
4.2.4 Oedometric	120
4.3 UV-Acrylic Bohle MV-760	124
4.3.1 Tension	124
4.3.2 Modified shear	137
4.3.3 Push-out shear tests	150
4.4 Summary and conclusion	155
 5. DERIVATION OF ADHESIVE MATERIAL LAWS	
5.1 Introduction	163
5.2 Silicone material law	164
5.2.1 Formulation of the isochoric part of the strain energy potential	166
5.2.2 Formulation of the volumetric part of the strain energy potential	180
5.2.3 Final proposed model	184
5.3 Acrylic material law	186
5.3.1 Tension characterization	186
5.3.2 Modified shear characterization	192
5.4 Summary and conclusion	198
 6. VALIDATION OF THE LAWS WITH NUMERICAL SIMULATIONS	
6.1 Introduction	199
6.2 Silicone material law	200
6.2.1 Implementation in the finite element software Abaqus®	200
6.2.2 Uniaxial numerical simulations	202
6.2.3 Shear numerical simulations	213
6.2.4 Oedometric simulations	230

6.3 Acrylic material law	237
6.3.1 Implementation in the finite element software Abaqus®	237
6.3.2 Modified shear simulations	237
6.4 Summary and conclusion	242
 PART III: EVALUATION OF STEEL-GLASS COMPOSITE ACTIONS	
7. LINEAR ADHESIVE CONNECTION EVALUATION	
7.1 Introduction	243
7.2 Description and evaluation of the system	244
7.2.1 Description of the composite beam	244
7.2.2 Theoretical and numerical analysis	245
7.3 Experimental investigations	250
7.3.1 Manufacturing of the beam	251
7.3.2 Description of the tests	253
7.3.3 Tests results	255
7.3.4 Discussion of the results	259
7.4 Summary and conclusion	262
 8. MECHANICAL-ADHESIVE CONNECTION EVALUATION	
8.1 Introduction.....	263
8.2 Description and requirements of the system	264
8.2.1 Description of the composite beam	264
8.2.2 Theory requirements	265
8.3 Small-scale investigations	265
8.3.1 Numerical simulations	265
8.3.2 Experiments	276
8.3.3 Discussion of the results	282
8.4 Large-scale investigations	283
8.4.1 Numerical simulations	283
8.4.2 Experiments	287
8.5 Summary and conclusion	294

9. CONCLUSION AND OUTLOOK

9.1 Conclusion	295
-----------------------------	------------

9.2 Outlook	297
--------------------------	------------

REFERENCES	299
-------------------------	------------

LIST OF FIGURES	a
------------------------------	----------

NOMENCLATURE	g
---------------------------	----------

APPENDICES

APPENDIX A – Quality control of the adhesive samples	A1
--	----

APPENDIX B – Choice of the Taguchi table	B1
--	----

APPENDIX C – ANAVAR method	C1
----------------------------------	----

APPENDIX D – Evaluation of the distribution	D1
---	----

APPENDIX E – Finite element procedures and subroutines	E1
--	----

APPENDIX F – Theoretical background of composite beams	F1
--	----

APPENDIX G – Control quality of the large-scale beam tests	G1
--	----

1. INTRODUCTION

1.1 BACKGROUND AND PROBLEMS

Glass in façade or roofing structures is extensively used in modern constructions in reason of the large transparency offered by this material and of the recent improvements of its thermal capacities with specific coatings or with the manufacture of triple glazing units. The actual use of glass consequently responds in priority to an architectural demand. To characterize the contribution of each element of a building to its stability, a hierarchy was created according to the different load bearing capacities. The primary level is constituted of only structural elements, which have to fulfill the safety and serviceability requirements. The failure of one of these parts would lead to the complete collapsing of the whole structure. The secondary level concerns elements fixed to the primary structure and of local structural importance. The failure of one of these parts does not affect the principal stability of the building, but generates a local failure of the components of the same level. Finally, the third level regroups the elements, which are not structurally contributing to the resistance of the building. The breakage of one of these parts has no repercussion on the elements of the upper level. In the actual façade construction field, the glass belongs to the third level and rarely to the second. It simply acts as a physical barrier between indoor and outdoor conditions.

However, the intrinsic properties of glass would allow increasing its level in this last hierarchy. Indeed, the compressive strength of glass is very high in reason of its amorphous structure, up to 500MPa according to recent investigations. To reach such values the forces introduced in the glass have to be in-plane loads uniformly distributed over the cross-section. This, with regards to the glass plate length and to the employed connection, could lead to buckling instabilities. To prevent these instabilities and use the compressive resistance of the glass, the greenhouses created during the 19th century, as the Kew gardens palm house or the Bicton gardens of Fig. 1.1, presented small pieces of glass firmly fixed on all the edges in cast iron profiles. In these constructions, the level of the glass was equivalent to the one of the cast iron, i.e. of the primary level. With the large number of profiles, the failure of one glass plate would lead to a redistribution of the loads in the surrounding elements. In consequence, the size of the glass plates and the types of connections were vital part for the general stability.



Figure 1.1- Greenhouses of (a) the Kew gardens palm house in London and (b) the Bicton gardens dating from the 19th century

To use the compressive properties of the glass, composite systems, as existing for the steel-concrete composite beams, were investigated in the following chapters. In these assemblies, the tensile stress-sensitive material was disposed on top of the more ductile steel material. The transfer of the load between the upper and lower elements had to be achieved with a sufficiently rigid jointing to associate it to a perfectly rigid connection with almost no displacement at the interface. The dimensions of the different components should be designed to have a neutral axis in the steel part, such that the upper glass plate would simply be subjected to non-decisive uniaxial compression only. The development of a steel glass composite assembly for façade would allow increasing the rigidity of the structure and consequently decreasing the out-of-plane displacements. Under equivalent loading, compared to an

unconnected system, the size of the steel element could be decreased or the total span length increased to end with larger and more transparent connections.

The real difficulty results however from the connecting system, which has to be sufficiently rigid to transfer the load without inducing crucial stress concentrations in the glass. Hence, steel to glass contact must be totally prevented. Further, by achieving a perfectly rigid connection, problems induced by the different thermal coefficients of the two materials could arise, as large in-plane loading would be generated at the interface. This effect should also be regarded for the design of the connection. In the consequence, the aim of this work was to find innovative connection methods to build steel-glass composite beam sufficiently rigid to activate a load transfer between these two elements using the compression properties of glass. One way, principally investigated, relied on employing adhesive materials which were able to transfer the load uniformly over large surfaces without inducing stress peaks, as it is generally the case for mechanical connections. Even if the adhesives were extensively used in several fields, such as in the aeronautics, their full properties were not well-known and their behaviours could not be represented with simple constitutive laws.

1.2 OBJECTIVES

With the aim to realize steel-glass composite beams, involving generally adhesive materials as connector, the principal objectives of this thesis are divided in two distinct categories.

From a local point of view and for the adhesives, the following steps are needed:

- Investigation on the current adhesives in use. A complete list of the products employed on existing glass façades has to be set to select the most suitable ones for the planned beams. Their invariances towards environmental conditions and the different types of action, i.e. short- or long-term, constitute important criterions.
- Development of a test program adapted to each adhesive. In composite beams, the adhesives are subjected to different tension/compression or shear actions. Hence, the most important properties should be assessed depending on these solicitations and on the specific adhesive family, i.e. elastomer, thermoset or thermoplastic. A review of the constructed tests set-up used by other researchers is also fundamental.
- Conduction of the different tests to acquire the adhesive material properties accounting for the possible influence of preselected parameters, such as temperature, humidity or UV-radiation.
- Determination of adapted material laws. Based on the tests results, adapted constitutive laws should be proposed for the selected adhesives. The procedures leading to the determination of the coefficients should be included.
- Implementation of the material law in finite element software and numerical simulations of the carried out tests for validation. With the numerical approval, further numerical calculations should be performed for prior assessment of the envisaged composite beam behaviour.
- Recommendations for adhesive joint design. Manufacturing procedures and limitations should be detailed for the selected adhesives.

From a general point of view and for the chosen composite beams, the following objectives have to be fulfilled:

- Investigation on the existing theories for fully composite beams, unconnected beams and also for beams with partial connection. Their domains of validity should be recorded, as well as the operated mathematical modifications to properly represent the envisaged beam behaviour.
- Small-scale tests should be performed on reduced connections in order to prove the validity of numerical results.
- Pre-design with finite element modeling. With the adhesive properties and small-scale tests results, pre-designs of the beams should be undertaken with numerical simulations. A first comparison to the foreseen theories could also be made.

- Large-scale tests. To prove the correctness of the selected theories or to enhance them by bringing some modifications, large-scale tests should be conducted.
- Practical recommendations for systems. The manufacturing of long beams can be subjected to possible limitations, which have to be defined. Further, several parametric studies should be performed to note the evolution of the rigidity according to the dimensions of the different constituents.

1.3 ORGANIZATION OF THE THESIS

This thesis is divided in 8 central chapters, whose contents are shortly summarized in the following paragraphs and organization chart.

Chapter 2 presents the principal properties and design methods of glass material employed in the construction of buildings. The recent researches on its in-plane resistance and stability are described. The current adhesive and mechanical glass to steel fixation methods are gathered and discussed.

Chapter 3 describes the principle of the glass-steel beam by analogy to the well-known concrete-steel beam. The different types of actions are detailed according to the application field of the beam. Based on these actions, the geometries and involved materials of two connections are outlined, i.e. the linear adhesive connection and the mechanical-adhesive connection.

Chapter 4 contains the experiments conducted on selected silicone and UV-acrylic adhesives. The manufacture, the tests conductions and the obtained results in function of the possible influent factors are detailed for each type of action. For the silicone, uniaxial tension, compression, shear and oedometric tests were performed to assess the quasi-static, cyclic and long-term properties. For the UV-acrylic, uniaxial tension and two shear configurations were investigated under quasi-static and long-term actions. The whole results are summarized in the conclusion of this chapter.

Chapter 5 is centered on the development of material laws for the two adhesives. A hyperelastic constitutive law, accounting for the slight compressibility of the material, is proposed for the silicone. For the acrylic, two one-dimensional models, describing respectively the rate-dependent tension and the shear behaviours are proposed. The determinations of all the coefficients are explained and the laws summarized in the conclusion.

Chapter 6 evokes the implementation of the developed material laws via user-subroutines. Depending on the solving methods, two subroutines were written for the silicone elastomer. The latters were used to model the tests carried out in chapter 4 in order to fully validate them. For the UV-acrylic, due to the extraction of its shear behaviour from the silicone law, some modifications were brought to the implicit subroutine of the silicone. The shear behaviour of the modified system was modeled for approval.

Chapter 7 accounts for the evaluation of the linear adhesive composite beam. Partial connection theories and numerical simulations, including the non-linear behaviour of the silicone adhesive, are first compared. Large-scale tests were conducted and the obtained results compared to the latter. The variations observed were explained by the modifications operated on the steel beams.

Chapter 8 concerns the mechanical-adhesive composite beam. First numerical simulations were made in order to evaluate the rigidity of one holed connection. The obtained results were compared to small-scale experiments on the same configuration. The rigidity, acquired with the last method, was inserted in the partial connection theory and in numerical simulations via the use of springs. The obtained global rigidity of the beam was compared to the one issued from large-scale tests on the final assembly. With the experiments, lower degrees of connection were achieved compared to the theory and to the linear numerical calculations. This effect was attributed to the modifications done on the steel beams.

Chapter 9 regroups all the principal results of this thesis and proposes new steps to be conducted to increase the range of application of the composite beams.

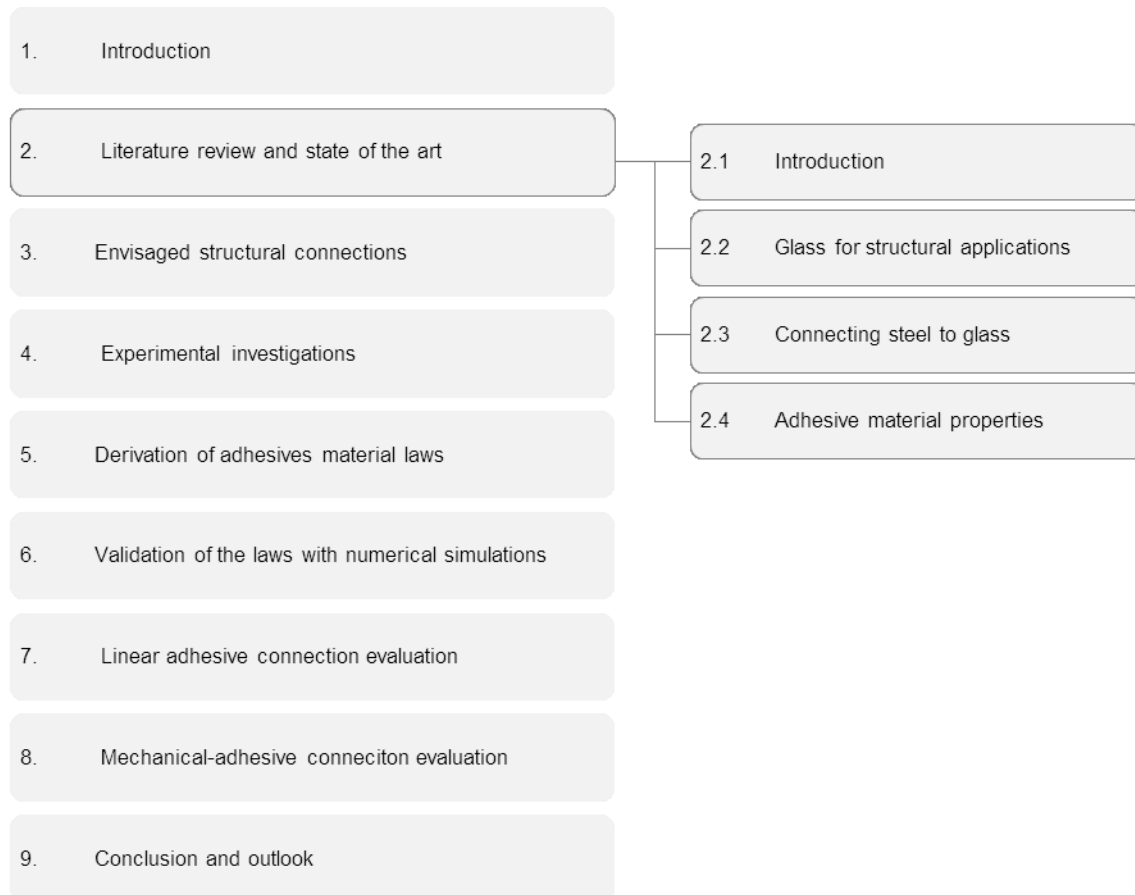
-
- ```
graph TD; 1[1. Introduction] --> 2[2. Literature review and state of the art]; 2 --> 3[3. Envisaged structural connections]; 3 --> 4[4. Experimental investigations]; 4 --> 5[5. Derivation of adhesives material laws]; 5 --> 6[6. Validation of the laws with numerical simulations]; 6 --> 7[7. Linear adhesive connection evaluation]; 7 --> 8[8. Mechanical-adhesive connection evaluation]; 8 --> 9[9. Conclusion and outlook];
```
1. Introduction
  2. Literature review and state of the art
  3. Envisaged structural connections
  4. Experimental investigations
  5. Derivation of adhesives material laws
  6. Validation of the laws with numerical simulations
  7. Linear adhesive connection evaluation
  8. Mechanical-adhesive connection evaluation
  9. Conclusion and outlook

**Figure 1.2-** Organization diagram of the thesis

## 2. LITERATURE REVIEW AND STATE OF THE ART

### 2.1 INTRODUCTION

The principal aims of the first part of this chapter are to summarize the different glass products used in the building construction and to list the current designing methods. The most employed steel to glass connections, either adhesive or mechanical, are described and discussed. In the second part of this chapter, the properties of the different adhesive families used to achieve these connections are exposed. The organization chart of this chapter is detailed on Fig. 2.0.



**Figure 2.0-** Organization chart of Chapter 2

**Glass for structural applications.** In this section are presented the composition, the mechanical and physical properties of monolithic glass plate. The different glass products composed by two or several monolithic plates, such as laminated or insulating glazing, are also detailed. For all these products, the current design methods are exposed.

**Connecting steel to glass.** The most important considerations for the steel to glass connections are evoked. A distinction is made according to the type of fixation, i.e. the mechanical continuous local or point fixations, separated from the adhesive connections. The advantages and drawbacks of each are also discussed.

**Adhesive material properties.** The majority of the actual steel-glass jointing is based on the use of several adhesives, whose properties depend on their families. The characteristics of elastomers and thermosets, as well as the existing material laws, are described and summarized.

## 2.2 GLASS FOR STRUCTURAL APPLICATIONS

### 2.2.1 Monolithic glass

A comparison between the atomistic states of glass and steel, widely employed for the construction of buildings, allows apprehending and understanding the behaviour of glass materials. In contrary to steel, in which the atoms are spatially organized on a crystalline network, glass presents a muddled configuration similar to the one observed in liquids. This irregular arrangement of silicon and oxygen atoms is characteristic of amorphous solid and depends mainly on the production process. The realization of glass material is achieved by rapidly cooling down a blend of melted raw minerals. The change of phase, from the liquid state to the solid state, that occurs at a certain temperature, referred as glass transition temperature, is accompanied by a considerable increasing of viscosity. Thus, glass was defined by Zarzycki [2.1] as “a non-crystallized solid presenting a glassy transition”.

The amorphous state of glass gives him also stability and chemical resistance to a large variety of solvents and acids.

#### 2.2.1.1 Types and constituents

The manufacture of glass depends mainly on the composition of the raw minerals which possess different melting points and also imply different cooling rates. Two large families distinguish themselves regarding this criterion, i.e. the soda-lime-silica glass (SLSG) and the borosilicate glass (BG). Both names comprise the elements that constitute more than 5% of the composition of the blend. The full chemical compositions of SLGS and BS, described respectively in the European standards EN 572-1 [2.2] and EN 1748-1-1 [2.3], are presented in Table 2.1.

| Constituent     | Chemical formula               | Soda-Lime-Silicate | Borosilicate |
|-----------------|--------------------------------|--------------------|--------------|
| Silica          | SiO <sub>2</sub>               | 69-74%             | 70-87%       |
| Lime            | CaO                            | 5-12%              | -            |
| Soda            | Na <sub>2</sub> O              | 12-16%             | 0-8%         |
| Boron oxide     | B <sub>2</sub> O <sub>3</sub>  | -                  | 7-15%        |
| Potassium oxide | K <sub>2</sub> O               | -                  | 0-8%         |
| Magnesium oxide | MgO                            | 0-6%               | -            |
| Aluminium oxide | Al <sub>2</sub> O <sub>3</sub> | 0-3%               | 0-8%         |
| Other           |                                | 0-5%               | 0-8%         |

**Table 2.1-** Chemical composition of mineral glass

The major difference between the compositions of these two families lies in the presence of boron oxides, which enhance the thermal resistance of the glass. Therefore, borosilicate glasses are preferably used as fire protective barrier. However, in reason of the difficult preparation of boron elements, this glass type is less implemented in building.

As the minerals employed for the manufacture of glass are not pure, some trace of iron oxides (Fe<sup>2+</sup> and Fe<sup>3+</sup>) can be found in the finished product. These small quantities of iron are responsible for the standard green tint of the glass. The reduction of these oxides allows obtaining white-clear glass almost colorless, generally named low iron glass.

#### 2.2.1.2 Manufacture

Regardless of the glass families, i.e. the soda-lime-silicate or the borosilicate family, the manufacturing method remains identic. The float glass (FG) process, developed by the Pilkington Brothers at the beginning of the sixties, represents actually 90% of the world production of flat glass. And, with the last improvements in mechanical engineering, the production lines deliver each and in continuous several tons (~700t) of flat glass per day. In these lines, the raw materials are continuously inserted in an oven

at about 1600°C-1800°C, where they melt and become liquid. Then, the upper part of the liquid glass overflows and goes to the next bath, where it floats on a denser tin bath. At the exit of the tin bath the glass is at 600°C (glass transition temperature) and gains in viscosity before entering in the last cooling section. At this transition step, the thickness is given to the glass by adjusting the speed of the conveying rollers. To ensure no imperfection, the glass is finally inspected with special video equipment and cut to standard dimensions of 6m x 3,2m. The thicknesses of flat glass vary from 2mm to 19mm (25mm being the maximum thickness).

In spite of the parallel smooth surfaces of glass panes, researches showed that the two sides of glass are not identic [2.4]. Indeed, the lower side of the glass faces first the tin bath, where a diffusion of tin atoms occurs and then encounters the conveying rollers, which induce some flaws and reduce its strength.

### 2.2.1.3 Properties

Glass material properties depend on the glass family and can be separated in two main categories, i.e. the mechanical properties indispensable to design glass assemblies and façades, and the physical properties necessary to the low energy consumption of the building and the occupants' comfort.

#### Mechanical properties

As glass is an amorphous solid, no dislocation is permitted as for metallic materials, such as steel or aluminum. Thus, glass materials exhibit purely elastic behaviour without ductility. This lack of yielding implies that this material is strongly sensitive to stress peaks, which are generally located on the surfaces or edges, where micro-flaws or -scratches, created by the manufacturing and cutting processes, are numerous. In consequence, the behaviour of glass is considered as stochastic, meaning that bigger will be the size of the glass pane, bigger will be the probability to find flaws.

|                                                   | Notation             | Unit                              | Soda lime silicate glass (SLSG) | Borosilicate glass (BSG)                                 |
|---------------------------------------------------|----------------------|-----------------------------------|---------------------------------|----------------------------------------------------------|
| Density                                           | $\rho$               | kg/m <sup>3</sup>                 | 2 500                           | 2 200 – 25 000                                           |
| Modulus of elasticity                             | E                    | MPa                               | 70 000                          | 60 000 – 70 000                                          |
| Poisson's ratio                                   | $\nu$                | -                                 | 0,23                            | 0,2                                                      |
| Knoop hardness                                    | HK <sub>0,1/20</sub> | GPa                               | 6                               | 4,5 - 6                                                  |
| Thermal expansion coefficient                     | $\alpha_T$           | 10 <sup>-6</sup> K <sup>-1</sup>  | 9                               | Class 1: 3.1 – 4<br>Class 2: 4.1 – 5<br>Class 3: 5.1 – 6 |
| Thermal conductivity                              | $\lambda$            | Wm <sup>-1</sup> K <sup>-1</sup>  | 1                               | 1                                                        |
| Specific thermal capacity                         | C <sub>p</sub>       | Jkg <sup>-1</sup> K <sup>-1</sup> | 720                             | 800                                                      |
| Emissivity                                        | $\epsilon$           | -                                 | 0,837                           | 0,837                                                    |
| Average refractive index for the visible spectrum | n                    | -                                 | 1,52                            | 1,5                                                      |

**Table 2.2-** Standard glass properties according to [2.5]

The basic elastic properties of glass materials are referenced in the upper part of the Table 2.2. The theoretical value of glass strength was first given by Orowan stress formula (2.1), which characterizes the stress needed to break an interatomic bond.

$$\sigma = \sqrt{\frac{E\gamma}{r_0}} \quad (2.1)$$

Where  $\gamma$  is the fracture surface energy ( $\sim 3 \text{ Jm}^{-2}$ ),  
 E is the young modulus ( $= 70 \text{ 000 MPa}$  for SLSG),  
 $r_0$  represents the equilibrium distance between two atoms ( $\sim 0,2 \text{ nm}$ ).

This formulation implies a theoretical resistance of about 32000 MPa, which does not reflect the reality because of the material strong dependency to surface flaws (Griffith), water “corrosion” and load duration. Hence, several experiments are undertaken, according to two European Standards, to evaluate the bending strength of glass in prescribed conditions. The first standard EN 1288-5 [2.6] details a coaxial double ring test allowing calculating the bending strength of a small square (100mm x 100mm) glass sample, without considering the influence of the edge flaws, see Fig 2.1. The second standard EN 1288-3 [2.7] envisages to test, under a four point bending configuration, larger glass plates (1100mm x 360 mm) including the edge effect, see Fig 2.2. The recommended characteristic bending strength (5% fractile) of float glass is of 45MPa [2.8] and its design value depends on the application of the glazing, either vertical ( $\theta \leq 10^\circ$ ) or overhead [2.9].

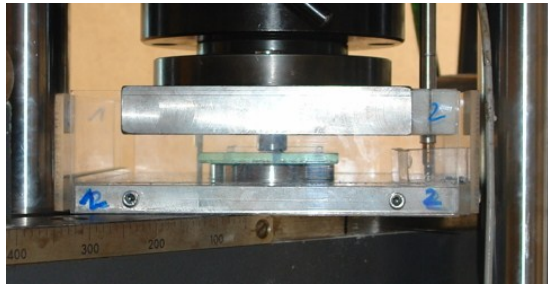


Figure 2.1- Coaxial double ring tests - EN 1288-5



Figure 2.2- Four point bending test - EN 1288-3

The uniaxial compressive strength was first determined on glass cylinders of 10mm of diameter and height under a loading rate of 3 to 4kN/s according to DIN 1249-10 [2.10]. The compressive strength, provided by this standard, should lie in a range of 700MPa to 900MPa, but further tests [2.11], in which different loading rates were applied, demonstrated a much lower mean value of about 500MPa. However, the pure compressive strength of glass remains more than ten times higher than the bending strength.

This large amount of compression is rarely attained due to the thin dimensions of glass panes, for which normal in-plane compressive forces generate instabilities, such as column and plate buckling, and large out-of plane deformations. Luible [2.12] experimentally investigated these two buckling modes on monolithic and laminated safety glass plates. For each case, analytical and numerical models were proposed taking into consideration several influent parameters, i.e. the thickness of the glass, the buckling length, the initial imperfections and load eccentricities. For column buckling of monolithic glass, an analytical method based on the same second order differential equation than steel showed good agreement with tests results, while for laminated glass plates, formulas derived from the elastic sandwich theory were adopted. For plate buckling, curves, resulting from tests and numerical simulations, were developed for the two glass types. Nevertheless, this study demonstrated the satisfying load carrying capacity of glass panels subjected to in-plane compressive force and also highlighted that the buckling strength is limited by the tensile stresses.

## Physical properties

### Thermal

The thermal expansion coefficient, which represents the change in size per unit length of the material under a temperature variation of 1K, represents a key factor to design a connection with glass and steel or aluminum elements. The thermal coefficient of glass  $\alpha_T$ , see Table 2.2 (middle part), is about 1,25 times lower than the one of steel and 2,4 times lower than the one of aluminum. Considering the brittle nature of glass, this could be fatal in case of a relatively rigid connection.

Three heat transfer modes, i.e. convection, conduction and radiation, characterize a material. Due to its nature, the thermal conductivity  $\lambda$  of glass is relatively high, meaning that the heat is easily transferred through this material. In addition, the standard DIN EN 673 [2.13] introduces the “U-value” defining the quantity of heat passing through  $1m^2$  of glass when a temperature difference of 1K exists between inside and outside. The lower is the U-value, the better is the isolation. For a simple monolithic glass of 6mm, the U-value obtained is about 5,7-5,8 W/m<sup>2</sup>K [2.14].

Transparency

The high degree of transparency of glass is an important challenge to ensure the comfort of the occupants. For a 4 mm glass, about 90% of the solar radiance is transmitted through the glass, while only 8% is reflected and 2% absorbed by the material. Thus, the short wavelengths of the visible spectrum are transmitted inside the building and are then transformed by the surrounding indoor materials into high wavelengths not transmitted by the glass, and so converted in heat by convection and radiation. This phenomenon, referred as greenhouse effect, is responsible of the high temperature increases. One method to reduce this effect consists in adding specific coatings to the glass elements.

Acoustic

Acoustic isolation is another factor to be considered for comfort. As for the propagation of light, a part of the sound waves is reflected while another is absorbed. A distinction between ambient noises, such as voices or transport noises, and impact noises, created for example by shoes hitting the floor, has to be made in reason of the different frequency domains. Higher are sound waves frequencies, higher is the reflection. Consequently, the noise reduction can be achieved by increasing the absorption of glass by selecting a larger glass thickness or using asymmetric laminated glass.

**2.2.1.4 Enhancement of glass mechanical properties**

As explained in section 2.2.1.3, glass material strength is strongly depends on the presence of flaws, appearing after the cutting process or during its transportation. Therefore, one way to reduce the number of defects consists in applying a mechanical treatment on the edge of the glass. This method ensures a better statistic of the strength, but does not improve significantly its value. Hence, other thermal or chemical treatments are frequently applied to generate a compressive state on the surface of the glass. These techniques affect the failure patterns of the glass and the size of the broken pieces, so that a classification of the glazing is made according the EN 12600 [2.15] with the help of a pendulum test. For certain applications, such as overhead or vertical glazing, a particular classification is imposed.

**Mechanical treatments**

After the cutting procedure with either water jet or diamond wheel, the glass edges are sharp and dangerous. Leaving the glass with no treatment is commonly not authorized. So glass edges are generally chamfered leaving some imperfections in the middle part or sanded producing a matt aspect. The optimum mechanical treatment corresponds to a polishing of the edges, which gives smooth finishing.

For specific connections in façades, drilled holes in the glass panes are indispensable. Manufacturing these kinds of products requires advanced and complex instruments, as machines drilling both side of the glass at the same time and avoiding the creation of high stresses. Nonetheless, these mechanical procedures must be undertaken before any thermal or chemical treatments.

**Thermal/chemical treatments**Fully tempered glass (FTG)

To enhance glass strength, a residual compression stress is created on its both surfaces. This state is obtained by heating, in a furnace, a standard float glass to about 640°C and then cooling it rapidly with cold air jets [2.16]-[2.17]. Under the temperature, the glass expands uniformly and as the surfaces are cooled first, they retract first. The balance of energy is reached by the material by compensating the compressive state on the outer surfaces by tensile stresses in the middle. This stress distribution is “frozen” permanently and the breakage of the glass occurs only when all the compressive reserve is reached. In consequence, the global strength of a fully tempered glass appears largely higher than the one of float glass, so as its resistance to large temperature variations. Typical values for the outer compressive stress in case of FTG are contained between 80 MPa and 170 MPa. These values

depend largely on the glass thickness and on the manufacturer, but the recommended characteristic (5% fractile) strength is of 120MPa [2.8].

During the fabrication of fully tempered glass plates, some Nickel Sulfide (NiS) inclusions can appear and lead to a spontaneous breakage of the glass after several years of service. The volumes of these particles increase rapidly with temperatures, reaching the inner tensile stress of the FTG. Thus, before installing FTG in façade, they undergo a heat-soak test [2.18], consisting in maintaining the glass at a high temperature for several hours.

Another important aspect of FTG, compared to float glass, concerns the fracture patterns. A broken float glass pane contains large fragments, which are very sharp and can easily harm, while the FTG fragments are very small and not dangerous. For that reason, fully tempered glass constitutes a security glass. However, the post breakage capacity of FTG is rather poor. That is why its application is regulated by standards [2.9], which prohibit, for example, its installation to a height superior to 4 meters as vertical glazing.

#### Heat strengthened glass (HSG)

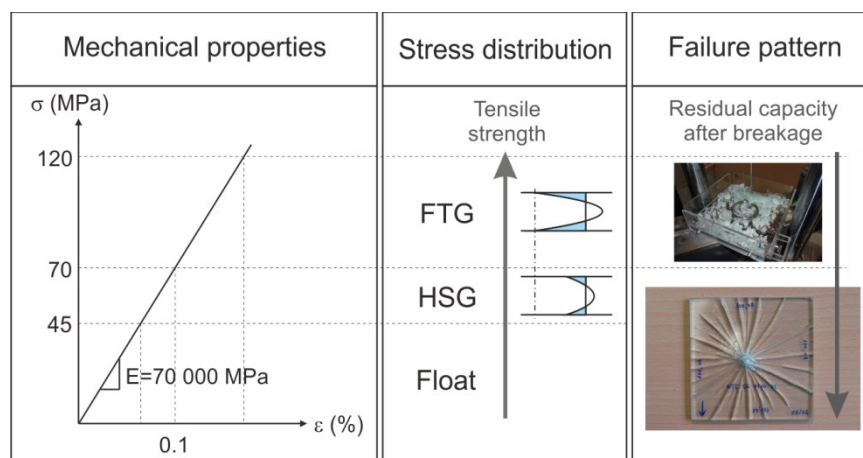
The method of production of heat strengthened glass is the same than the one of fully tempered glass [2.19]-[2.20]. The difference comes essentially from the cooling rate, which is slower for HSG, entailing a lower residual compression state. The recommended characteristic (5% fractile) strength of heat strengthened glass is of 70MPa [2.8]. The breakage pattern of this type of glass is similar to the one of float glass, with relatively large fragments. The high post breakage structural capacity of a HSG pane, well fixed along its circumference, allows maintaining these large fragments together, ensuring some resistance before total fracture.

Because the cooling rate of the HSG is very slow, the heat strengthening of thick glass, i.e. more than 12mm, represents a challenge. As for the FTG, all mechanical treatments must be done before the thermal treatment.

#### Chemical treatments

Chemical treatment of a float glass represents an alternative to the thermal tempering. This operation consists in immersing the glass in a potassium bath, where ions exchanges occur [2.21]-[2.22]. Potassium ions are larger than the glass sodium surface ions, so they have to tighten to accommodate to the glass structure. This results in a compression of the glass surfaces, whose depth depends on the immersion time (depth of several  $\mu\text{m}$ ). Because surface flaws can be deeper than the compression state, this method is generally avoided for structural applications. However, in contrary to thermally treated glass, mechanical treatment can be executed after the chemical process.

### 2.2.1.5 Summary



**Figure 2.3-** Summary of the principal properties of glass employed in structural applications



## 2.2.2 Glass assemblies

The section 2.2.1 inventories the mechanical and physical properties of monolithic glass. As detailed, this type of glass, either tempered or not, possesses an insufficient post breakage capacity limiting its application. The need to increase the mechanical capacities of glass as façade element has led to the development of new assemblies composed by several monolithic glass panes connected together, known as laminated glass. This mechanical improvement was accompanied by thermal properties amelioration, with the creation of insulating glass and vacuum glazing units, to meet the energetic requirements.

### 2.2.2.1 Laminated glass (LG)

Once the glass has undergone some mechanical or thermal treatments, its post breakage residual capacity can still be increased by realizing a laminated connection. This method consists in binding two or more glass panes, either FG or FTG or HSG, with a plastic and transparent interlayer, see Fig. 2.4.

#### Manufacture

The manufacture of a laminated glass unit is divided in three steps, i.e. the positioning of the defined number of interlayers between the glass panes, a pre-lamination under an assigned temperature and finally an autoclave process under 14 bars at 140°C to eliminate air bubbles.

Several films can be employed as interlayers, but only the Polyvinyl Butyral (PVB) is agreed to make safety laminated glass (SLG) [2.23]-[2.24]. PVB properties are temperature-dependent and decrease under high temperatures. At ambient temperature, a PVB foil, whose nominal thickness is 0,38 mm, is viscoelastic and soft and can deform greatly before breakage. For flat laminated glass, two (0,76 mm) to four (1,52 mm) foils are generally necessary, whereas six foils (2,28 mm) are common for curved glass. The other existing layers are:

- SentryGlas Plus (SGP) from DuPont Company, which presents a higher stiffness, a better resistance to large variations of temperatures and a good resistance to tearing. The lamination process is, however, more difficult to undertake.
- Ethylene Vinyl-Acetate (EVA), principally employed to insert photovoltaic cells between the glass panes.
- Cast in-place resin (CIR), introduced in a gap of 1 to 4 mm between the two glasses. In this resin the insertion of light emitting diodes LED is feasible.

Before the autoclave process, the PVB interlayer is opaque and seeing through is not possible, while after conditioning under high pressure, the layer is fully transparent and no difference between a monolithic glass and PVB is notable. This foil does not attenuate the optical properties of glass, but, considering its intrinsic properties, only acts as a barrier against UV-lights.

#### Mechanical properties

When a PVB interlayer is situated in the middle of two glass panes of the same thickness, i.e. in a symmetric way, the so formed LG subjected to bending (out-of-plane wind loads) does not exhibit any tensile or compressive stresses at the PVB foil, but only shear stresses. So higher is the shear stiffness of the interlayer, higher is the composite action of the assembly. This shear stiffness depends greatly on the load duration and the temperature. For short-duration loads at ambient temperature, the shear stiffness is maximal, while for high temperatures and for long-duration loads (dead loads, self-weight...), a sliding between the glass panes appears because of the loss in shear-resistance of the PVB foil.

Nevertheless, the PVB interlayer retains all fragments of a broken laminated glass. Thus, to increase the post breakage capacity, the use of float glass or heat strengthened glass is preferred. Indeed, these glass types break into large fragments, which are retained by the PVB interlayer and therefore less subjected to rotations.

## Physical properties

The soft layer of PVB presents also an acoustic advantage. The sound waves are better absorbed by the laminated glass decreasing the reflection significantly and providing the occupants comfort.

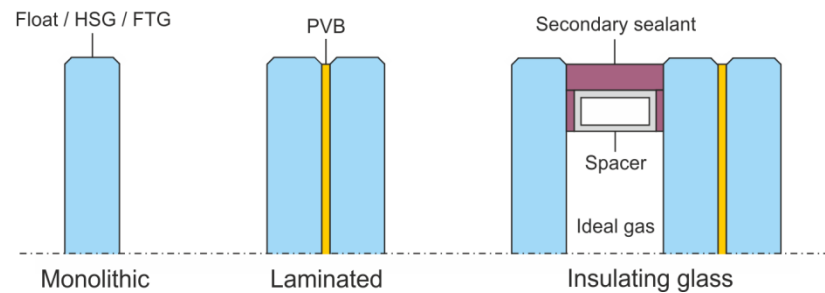


Figure 2.4- Examples and compositions of monolithic, laminated and insulating glass units

### 2.2.2.2 Insulating glass unit (IGU)

To reduce the U-value of a glazing and improve its thermal properties, insulating glass units (IGU) were created [2.25]-[2.26]. These systems involved two or more glass panes (monolithic or laminated), which are connected at their circumferences, either by an aluminum spacer containing desiccant elements and surrounded by a secondary sealant or by a thermoplastic spacer called TPS, see Fig. 2.4. The intermediate space, or cavity, situated between the glass elements is generally filled with dry air or with ideal gases such as Argon (Ag), Krypton (Kr) or Xenon (Xe). Inert gases are preferred regarding their lower thermal conductivities.

## Manufacture

To ensure a perfect bonding of the different surfaces, i.e. glass plates and aluminum spacer, a strict cleaning procedure involving solvents has to be effected. Then two methods exist to manufacture an IGU filled with gas. The traditional method consists in assembling the IGU and, then replacing the air trapped in the cavity by the ideal gas with the help of a vacuum pump and needles inserted at two diagonally opposed corners. The modern system corresponds to an automated production line, in which the assembly takes place in a chamber containing the inert gas. With this last procedure, no hole has to be drilled in the aluminum spacer and filled up.

Two types of sealant have to be applied in an insulating glass unit, i.e. a first protective barrier in butyl connecting the glass and the aluminum spacer and a secondary sealant, generally in silicone or polysulfide polymer. The first barrier is applied with a butyl extruder delivering the appropriate thickness of about 0,25 to 0,4mm with a height of about 0,48 to 0,61mm. This butyl joint aims to avert gas leakage. To ensure the structural stability of the IGU, the secondary sealant bonds all the elements together. The application of a continuous uninterrupted smooth sealant bead is frequently applied on the IGU edges with an automatic handgun. As for the first seal, the second joint must be checked to prevent voids or defects in the sealant. The size to be given to the secondary sealant (bite and depth) depends on the design of the insulating glass unit.

## Mechanical properties

In the difference to the monolithic glass or the laminated glass, the insulating glass units do not involve one or two materials, but at least four. With regards to the elevated number of materials, its design is complex and a simplification to the structural elements is commonly accepted [2.27]. Therefore, the design of an IGU is only based on the glass and the secondary seal. To apprehend its behaviour, the same assumption is envisaged with a special attention to the loads types:

- Thermal variations

The difference of temperature between the two glasses of an IGU induces dissimilar in-plane expansion. As the outside temperature fluctuates more than the internal temperature, the

outer glass plate tends to deform more than the inner glass. This induces considerable shear stresses in the secondary sealant, especially if the IGU is not retained by mechanical devices.

- Atmospheric pressure variations

The manufacture of an IGU takes place at constant temperature and atmospheric pressure. During its installation on façade, the change in altitude causes a pressure variation causing long-term out of plane loads. These loads bend the glass and create tension in the secondary sealant.

- Wind loads

Wind loads are short-term out of plane loads acting on the IGU surfaces and creating the same action, in the glass and in the sealant, than the atmospheric pressure variations in a more intense manner.

- Snow loads

These loads concerns mainly sloped glazing and acts permanently during a long or short period of time according to the considered latitudes. Different stress distributions can arise in the sealant depending on the installation.

- Self-weight of glass

The self-weight is a permanent in-plane load causing important shear in the sealant, if the IGU is not clamped in a structure or supported by mechanical devices, and compression in each glass pane.

Thus, the mechanical behaviour of an insulating glass unit varies strongly with the properties of the involved materials (glass and sealant), but also with its connection system. The complexity of an IGU assembly and the elevated loads, acting on it, limit its use as a structural element. However, as for monolithic glass pane, the post breakage capacity of an IGU can be increased by using heat strengthened glass combined to laminated glass.

## Physical properties

### Thermal

Heat propagates through three modes, i.e. radiation, conduction and convection. The radiation mode represents more than a half of the thermal transmission in an IGU, as air or gas are inapt to stop this propagation phenomenon. To reduce this thermal exchange, reflective silver coatings, also called transparent low-e coatings, are commonly applied on the inner glass pane surface.

The conduction takes place at the circumference of the IGU, where all the elements are in contact. These locations constitute privileged places for thermal bridges, which are so important that their influence must be taken into account for the calculation of the U-value according to EN 673 [2.13].

The thermal difference between the outer glass pane, directly subjected to temperature variations, and the inner glass induces some movements in the gas sealed in the IGU. These movements transport the heat from the hot outer glass to the ambient inner glass. This so generated convection must also be considered to measure the quality of an insulating glazing.

Compared to a standard monolithic glass of 4mm, the “U-value” of an insulating glass composed by two glass plates of 4mm with an argon filled cavity of 16mm, denoted (4/16/4), is divided by 5,2, i.e.  $U_{4/16/4} = 1,1 \text{ W/m}^2\text{K}$ , which definitely demonstrates the importance of IGU as façade element.

### Transparency

As for monolithic glass, 40 to 90% of the solar radiation is transmitted through the insulating glass unit. The wind and/or atmospheric pressure bend the glass plates of an IGU and are thus responsible for the deviations of light, creating visual effects and deformed shapes.

### Acoustic

The inert gas and the secondary sealant, closing the unit and presenting hyperelastic properties, act as absorbers. The reduction of the external noise is conceivable by increasing the space between the glass panes, by laminating one glass of the IGU or by changing the thickness of one glass creating an asymmetry.

### 2.2.2.3 Vacuum glazing

Recent researches, at the Fraunhofer Institute in Germany and at the Nippon Sheet Glass in Japan, to further increase the thermal properties of glass assemblies, led to the development of high vacuum glazing. This system consists of two glass sheets hermetically sealed together around the edges with the help of a stiff solder glass. A vacuum is created in the cavity with a special pump. The small space of 0,7mm between the two glass panes is achieved by disposing regularly at a distance of 30 to 40mm some transparent pillars possessing a low heat transfer coefficient. These pillars are sufficiently rigid to compensate for the vacuum, bending inwards the glass panes, and for the actions generated by atmospheric pressure changes.

Glass thickness is generally of 3 to 4mm, so that the total thickness of the whole unit is about 8-10 mm. Compared to a standard insulating glass units, the self-weight of a coated vacuum glazing is largely reduced and the U-value reached is about 2.5 times smaller, i.e.  $U_{\text{vacuum}}=0,45 \text{ W/m}^2\text{K}$  [2.28]. In reason of some problems arising at the solder of the edges, vacuum glazings are still in the state of the art and not yet installed on building.

### 2.2.3 Design methods

Actions on structures described by the EN 1991 [2.29] are valid for glass elements employed in façades. Static imposed loads, wind loads, snow loads, thermal stresses, impact due to fall or blast and the movements of the structure have to be regarded for the design of glazing units. In addition, as the glass properties are dependent on the loading rate, temperature and humidity, the complete load history must be examined too. These dependencies compared to standard materials, such as steel, are a characteristic of glass material, as well as the residual post breakage capacity.

According to the EN 1990 [2.30], the safety of the structure and of the people is ensured by the verification of ultimate limit states, while the normal functioning, the comfort and the appearance are guaranteed by verification of serviceability limit states. For glazing, the ultimate limit state generally consists in checking that the effects of the forces in terms of stresses do not exceed the resistance of the material. The serviceability state is based on controlling that the displacements, induced by the actions, are inferior to allowable displacements. Three different classes distinguish themselves to design with regard to these states:

- The deterministic procedure, also named level 0 by the Eurocode, is centered on the allowable stress design.
- The semi-probabilistic approach, called level I, concerns partial safety methods.
- The probabilistic concept, level II & III, includes the calculation of the probability of failure established with a normal or an exact distribution.

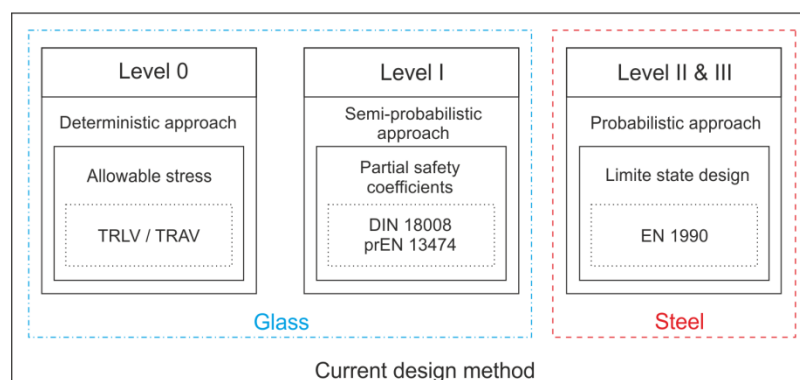


Figure 2.5- Summary of the current design methods for the glass elements

For glass design, the deterministic and semi-probabilistic classes were explored, mainly for their simplicity, and implemented in design guides, see Fig. 2.5. The following sections describe these two approaches by evaluating their limitations and citing the current standards composing them.

### 2.2.3.1 Allowable stress method (Level 0)

This approach represents the simplest conceivable method to design glazing elements and therefore constitutes more a rule of thumb than a real design tool. The ultimate state verification criterion consists in verifying that the maximum stress  $\sigma_{max}$ , obtained for the most unfavorable scenario of actions, is inferior to an allowable stress  $\sigma_{allowable}$ , found as the maximum experimental strength divided by a safety factor, accounting for uncertainties induced by actions, material or modeling (2.2).

$$\sigma_{max} \leq \sigma_{allowable} \quad (2.2)$$

The fixed allowable stress does not account for the load duration or history, although glass resistance precisely depends on these two parameters. The stochastic behaviour of glass, generating a size dependency, is also left aside by this formulation. So, this rule is preferably used to roughly pre-design a glazing unit.

Nevertheless, several glass companies, as Pilkington, employ the allowable stress scheme. It was also implemented in German technical guidelines for the proof of linearly supported glazing, TRLV 2006 [2.31], and for fall-protecting glazing, TRAV [2.32]. In these codes, the allowable stresses are based on the type of glass, either tempered or not, and on its application, either vertical ( $\theta \leq 10^\circ$ ) or horizontal ( $\theta \geq 10^\circ$ ). To obtain these values, for vertical glazing, an elevated security factor of about 2.4 is used. The allowable displacements are chosen regarding the boundary conditions of the glass pane and its application, Table 2.3.

| ULS              |            |                                        |                  | SLS                                    |                                                          |                        |
|------------------|------------|----------------------------------------|------------------|----------------------------------------|----------------------------------------------------------|------------------------|
| Verification     |            | $\sigma_{max} \leq \sigma_{allowable}$ |                  | $\omega_{max} \leq \omega_{allowable}$ |                                                          |                        |
|                  |            | $\sigma_{allowable}$                   |                  | $\omega_{allowable}$                   |                                                          |                        |
| Allowable values | Glass type | Overhead glazing                       | Vertical glazing | Boundary conditions                    | Overhead glazing                                         | Vertical glazing       |
|                  | FG         | 12                                     | 18               | 4 edges supported                      | 1/100 of the smallest supporting edge                    | No verification        |
|                  | HSG        | -                                      | -                | 2 or 3 edges supported                 | For monolithic:<br>1/100 of the smallest supporting edge | 1/100 of the free edge |
|                  | FTG        | 50                                     | 50               |                                        | For IGU:<br>1/100 of the free edge                       | 1/100 of the free edge |
|                  | LG(FG)     | 15 (25*)                               | 22.5             |                                        |                                                          |                        |

**Table 2.3-** Limit state concepts and maximum allowable values according to TRLV 2006 [2.31]

The load combinations have to be investigated according to current standards, i.e. the DIN 1055-100 [2.33], and the critical scenario will give the maximum stress and displacement. To calculate these maximum values for a laminated glass unit, an equivalent thickness, representing a loss of connection between the plates, has to be determined first. For insulating glass unit, the method developed by Feldmeier [2.34] is employed to redistribute the loads on both glazing and proceed to the estimation of the maximum values.

### 2.2.3.2 Semi-probabilistic approach (Level I)

Among the semi-probabilistic approaches, two standards are relevant at the European level, i.e. the German standard DIN 18008-1 [2.35] and the European draft standard prEN 13474-3 [2.36]. Strong similarities exist between these two design codes despite their formulation of combined actions, the design resistance of tempered glass and the calculation of a laminated glazing.

**DIN 18008**

This standard, actually in use in Germany, presents some general construction rules for glass elements and details the ultimate limit state and the serviceability state requirements.

For serviceability, the maximum displacement of the plate is evaluated and compared to a limit design displacement obtained by dividing the smallest supporting edge by 100. The combination of loads must be accomplished with the DIN 1055-100, as for the TRLV and TRAV, to then calculate the maximum displacement by considering the linear plate theory or the membrane effect, if appearing. In this code, no specific condition is provided to account for the membrane effect.

For the ultimate limit state, the limit design value is the stress, which has to be determined depending on the presence or not of a tempering process, Table 2.4. For a tempered glass, either fully tempered (FTG) or heat strengthened (HSG), the limit design stress is unrelated to the load duration, as the compressive pre-stress close the surface flaws. So, only a factor representing the construction type  $k_c$  (equal to 1) and a safety factor  $\gamma_M$  modify the characteristic strength. Float glass limit design stress is, however, corrected by a factor  $k_{mod}$ , including the glass properties decrease with the load duration. Longer is the load applied on glass and higher is the reduction of the glass design strength.

For laminated glass, the maximum stress must be calculated by employing the same effective thickness than the one described in the TRLV and for insulating glass unit, the method proposed by Feldmeier applies.

|                     | DIN 18008                                                                                                                                 | prEN 13474                                                                                                 |
|---------------------|-------------------------------------------------------------------------------------------------------------------------------------------|------------------------------------------------------------------------------------------------------------|
| Limit design values | FG $R_d = \frac{k_{mod} k_c f_k}{\gamma_{M,FG}}$                                                                                          | FG $R_d = \frac{k_{mod} k_{sp} f_{g,k}}{\gamma_{M,A}}$                                                     |
|                     | FTG/HSG $R_d = \frac{k_c f_k}{\gamma_M}$                                                                                                  | FTG/HSG $R_d = \frac{k_{mod} k_{sp} f_{g,k}}{\gamma_{M,A}} + \frac{k_v (f_{b,k} - f_{g,k})}{\gamma_{M,v}}$ |
| Coefficients        | $k_{mod} = \begin{cases} 0,25 \text{ for long term load} \\ 0,4 \text{ for mid term load} \\ 0,7 \text{ for short term load} \end{cases}$ | $k_{mod} = 0,663 \cdot t^{-1/16}$                                                                          |
|                     | $k_c = 1$                                                                                                                                 | $k_{sp} = 1 \text{ for float process}$                                                                     |
|                     | $f_k = \begin{cases} 45 \text{ MPa, for FG} \\ 70 \text{ MPa, for HSG} \\ 120 \text{ MPa, for FTG} \end{cases}$                           | $k_v = 1 \text{ for tempering process}$                                                                    |
|                     | $\gamma_{M,FG} = 1,8$                                                                                                                     | $f_{g,k} = 45 \text{ MPa}$                                                                                 |
|                     | $\gamma_M = 1,5$                                                                                                                          | $f_{b,k} = \begin{cases} 70 \text{ MPa, for HSG} \\ 120 \text{ MPa, for FTG} \end{cases}$                  |
|                     |                                                                                                                                           | $\gamma_{M,A} = 1,8$                                                                                       |
|                     |                                                                                                                                           | $\gamma_{M,v} = 1,2$                                                                                       |

**Table 2.4-** Expression of design values according to the DIN 18008 and prEN 13474

**prEN 13474**

Compared to the DIN, the limit design displacement is assimilated to the smallest value between a fixed deformation of 50mm and the span divided by 65. If the maximum deflection exceeds the half of the glass plate thickness, the membrane effect has to be regarded.

For float glass, the limit stress design value is equivalent between the two standards. Only the expressions of the factor  $k_{mod}$  differ, i.e. a quantification of the load duration must be established to calculate this factor according to the European Standard. This formulation allows to calculate very short duration load as explosion ( $t_{min} = 20ms$ ). Nevertheless, for both standards, the minimum  $k_{mod}$  is of 0,25 for long-term actions.

For tempered glass, a difference between the limit stress design values, proposed by these two standards, arises. While the resistance is obtained in the DIN by reducing the characteristic value of

the tempered glass with some factors, the European Standard envisages summing the resistance of float glass and the resistance created by the tempering. Thus, this last code tends to represent more closely the real phenomenon, for which the residual compression induced by the tempering has to be reached first before glass breaks normally.

While the method developed by Feldmeier remains valid to redistribute the external loads on each glass plates of an IGU, a new definition of the effective thickness is proposed to design laminated glass. In the DIN, two effective thicknesses are considered, i.e. one accounting for a perfect connection and another one for a loss in connection, but in the European Standard the definition of the equivalent thickness depends on the stiffness of the interlayer determined with the help of tests. Moreover, in comparison to the DIN, the European Standard envisages two different formulations of the thickness to either calculate the bending deflection or the bending stresses.

## 2.3 CONNECTING STEEL TO GLASS

The previous section detailed the properties of glass, exposing its brittle behaviour and some rules to design linearly supported glazing elements. In most buildings, even for fully transparent glass pavilions, the glazing elements are connected to the ground or to supporting structures made of steel or other alloys. Thus, the connecting methods are of high interest, especially to transfer the actions applied on glass to the substructure. Moreover, to design steel to glass assemblies, the resistance of the material has to be taken into account, as well as the resistance of the connection, which could fail first and independently of the glass or steel breakage.

The principal considerations to be regarded for the choice of a structural connection, implying steel and glass materials, will be presented in the following section, as well as, the most widely employed mechanical and adhesive connections.

### 2.3.1 Considerations for connections

#### Loading function of the application

A hierarchy, based on the load bearing action, was established to classify the degree of importance of each element constituting a building. The three levels of this hierarchy are as follows:

- The primary structure, the structural “heart” of a building, is composed by columns, beams, horizontal or vertical braced frames and shear walls. These parts carry all the loads, including their self-weight, and stabilize the edifice. A particular attention has to be devoted to their connections, which are subjected to considerable stresses. The failure of one of these elements entails the complete collapse of the construction.
- The secondary structure, such as façade frames fixed on the primary structure, also act in structural way. The elements of the secondary level transfer the loads to the primary structure by the connection means, which are places of possible breakage. The failure of these components does not affect the primary structure, but impact directly the tertiary structure.
- The tertiary structure, mainly the façade claddings, is the only one to not play a structural role. Components of a tertiary structure only and simply act as barrier between indoor and outdoor environmental conditions.

Glass, initially employed as tertiary constituent, started recently to climb in the hierarchy due to a better understanding of its behaviour. Evolving from the tertiary to the secondary level imply, on one hand, that the connection of the glass to the primary structure become essential in the design phase and, on other hand, that the intensity of the loads applied on it significantly increase. Therefore, depending on the application, the loads acting on the glass elements vary and the choice of the connection is of high consequence.

#### Soft versus rigid connection

As explained in the previous paragraph, loads acting on glass and transferred to the substructure impact directly the connection. Besides checking the resistance of the glass panes, special attention must be devoted to the resistance of the connections by controlling the tension, compression and shear stresses. Nowadays, various types of connection, either soft or rigid, exist. Soft connections easily deform without applying high loads and are, in consequence, able to compensate for the inability of glass to yield. However, in case of a too soft connection, the loads transfer from the glass to the steel structure is insufficient to develop a composite action. In a rigid assembly, the loads transfer appears greater, but stress concentrations can arise in the glass. For example, in case of façade use, loads are divided in two categories, i.e. the out-of-plane loads, such as wind/snow loads, and the in-plane loads, induced by the difference of thermal expansion of the jointed materials. With a rigid jointing method, the stresses in glass induce by the thermal loading cannot be redistributed via the connection resulting in glass failure. Thus, a compromise between a too soft and a too rigid assembly has to be found.



### **Direct steel to glass contact to be avoided**

Another consideration arises from the intrinsic properties of glass material, which exhibits fully elastic properties without any yielding, i.e. direct contact of glass to other stiff materials, such as steel or other alloys must be avoided. Indeed, for steel to glass connections, the hard contact between the rough surfaces of the materials creates damages. Additionally, some impurities, e.g. dust or sand particles, can lodge themselves between the surfaces in contact during the realization of the connection or in-use. These flaws strongly reduce the properties of glass, which could break instantly without any warning.

### **Manufacturing tolerance**

In order to enhance the interior use of natural light and the creation of light and transparent open spaces, connection means have to be less and less apparent. Consequently the recent mechanical connections consist in locally fixing the glass to the substructure with the help of bolts inserted in pre-drilled holes. Flaws on glass edges are generally induced by the realization of these holes. Therefore, precision in the manufacturing process, i.e. the finishing of the holes, their sizes and their distances to the edges or between themselves, constitutes a decisive factor.

In the same manner, adhesively jointing glass to steel requires applying uniformly a constant bead of adhesive to obtain a joint presenting the less air bubbles possible. The respect of the adhesive dimensions, determined according to design rules, is of importance for the stability of the structure and represents a challenge during the realization phase.

Eccentric loads, geometrical changes, material imperfections, manufacturing tolerances and stress induced in glass or in the connection must be considered carefully in the design step, to ensure the non-failure of the assembly.

### **Shop-glazing or on construction site**

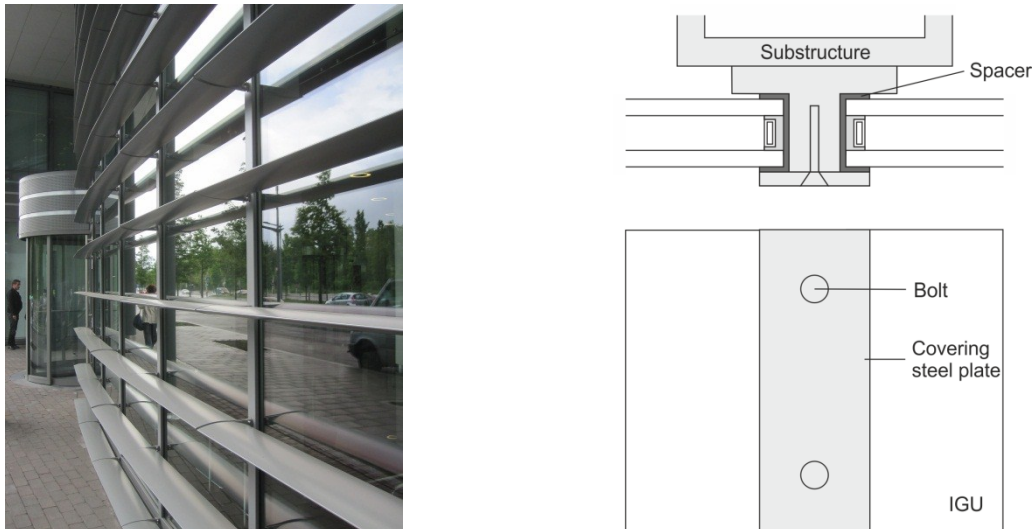
As for standard steel constructions, connections of steel to glass can be directly made on site. However the installation, i.e. the lifting process of the glazing and its fixation on the steel substructure, is time consuming. Moreover, the curing time of adhesive connection, i.e. the time necessary to obtain a perfectly dry seal, is usually longer in outdoor conditions than indoor, where the humidity and temperature can be controlled. So shop-glazing is advised, when possible.

## **2.3.2 Mechanical connections**

The research of transparency in architecture led to an evolution of the mechanical connection means, for which the glazing units were first supported linearly and are nowadays supported locally, either at the edge with clamping devices or through glass with point fixations. Within these classes, several methods of fixation exist and will be presented in the following paragraphs.

### **2.3.2.1 Supported linearly**

Linearly supported glazings are widely employed for the construction of glass façades and individual houses, mainly due to their simple implementations. Monolithic, laminated or insulating glazing units (IGU) composed by either float glass, fully tempered glass or heat strengthened glass can constitute these systems. These rectangular glazings are placed in a metallic frame and lay down on setting blocks of Neoprene or EPDM rubber, which are sufficiently soft and elastic to absorb in-plane deformation caused, for example, by thermal loadings or by the self-weight of the glazing. Moreover, the direct contact between glass edges and the metallic frame is prevented by these setting blocks. The out-of-plane loads, wind/snow loads and pressure variations, are transferred to the supporting frame by an elastic material, identical or presenting similar properties to the setting blocks, installed directly in contact with the glass surfaces.



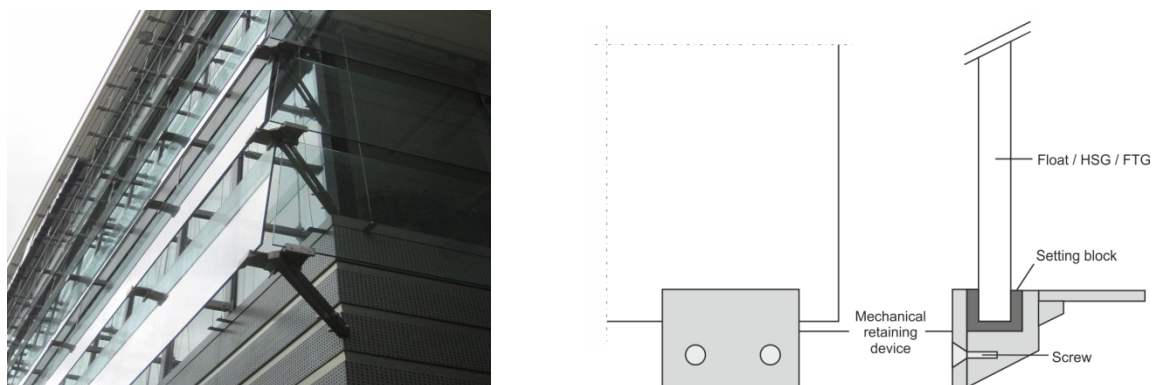
**Figure 2.6-** Mechanically and linearly supported glass façade – General and detailed view

The manufacture of such assembly, i.e. the installation of the glazing inside the metallic frame, is preferably realized in-shop, if it can be fixed onto the primary structure afterwards. However, when the glass pane is linearly clamped all around its edges, between the primary structure on one side and a pressure plate on the other an on-site installation cannot be avoided, see Fig. 2.6. The soft behaviour of the setting supports can compensate for geometry imperfections, e.g. glass edge imperfections or small offset between the positions of both glass edges of an IGU. The dimensions (6 to 15mm) and the elastic behaviour of the supports, providing a sufficient degree of rotation of the glass, allow considering the glazing as simply supported element and allow therefore applying the design methods presented in section 2.2.3.

### 2.3.2.2 Supported locally on the edge

#### Clamped fixation

A high resemblance between the clamp fixations and the linearly supported glazing method exist. The layout of the elements is the same for both connections (Fig. 2.7), but the size of the clamped areas and so the repartitions of the loads are different, local versus global. Further, with clamp fixings, the structure appears lighter and more transparent, because the visual impact of the assembly is greatly reduced compared to a linear connection. In addition, the water does not stagnate in the channel of the linear fixation and is therefore better drained, preventing moisture of the setting blocks.



**Figure 2.7-** Mechanically and locally clamped fixation – General and detailed view

All the glass products, presented in section 2.2, i.e. monolithic, laminated or insulating glazing units made from float glass, fully tempered glass or heat strengthened glass, can be used. Almost frictionless materials, e.g. Teflon, are used as interlayer between the glass pane and the steel support.

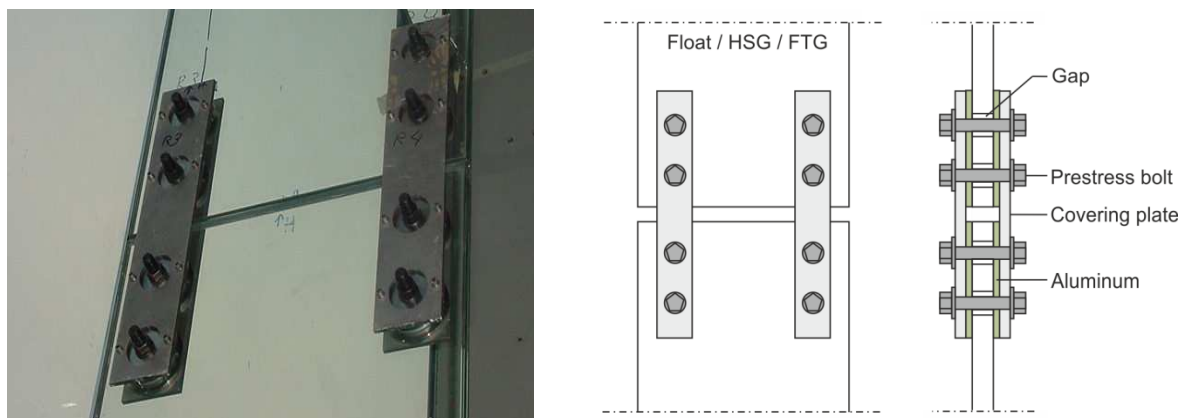
Thus, the clamp fixings cannot only be installed along the vertical edges, but also on the horizontal edges to bear the weight of the whole glazing. Clamping glass at the four corners represents another fastening way. Nevertheless, and as for the linear supported glazing, setting blocks of Neoprene or EPDM rubber are placed at the bottom of the clamps. In consequence, glass to steel contact is prevented and the in-plane and out-of-plane loads acting on the glass pane are correctly transmitted to the substructure.

The installation of locally clamped glass panes takes place on the construction site and is similar to the one of linearly supported glass. The setting blocks compensate for the imperfections of the glass edges or of the clamping devices. Because of the local fixations and the complexity of the assembly glass stress concentrations cannot be checked by hand calculations and have to be evaluated with Finite Element Analysis (FEA).

### Friction fixation

Even if the layout of friction assemblies is similar to the one of clamping, the maintaining of the glass differs, i.e. tangential forces at the surfaces for the friction fixation versus local in-plane force for the clamping fixation. The friction connection can necessitate, especially for large “contact” area, the drilling of holes in the glass to ensure a better repartition of the frictional force. This kind of fixation is composed by several layers symmetrically disposed around the glass pane. The central glass plate is covered locally and at both side by a gasket, which is in its turn covered by the steel plates. A normal force is inserted in this configuration with the help of one or several prestressed bolts, see Fig. 2.8. In case of in-plane loading, the microscopic frictions, originating from the imperfections of the surfaces in contact, i.e. imperfections, on one hand, between the steel and the gaskets and, on the other hand, between the gasket and the glass, are responsible of the stability of the assembly.

The standard glass product, monolithic and laminated glass, can be employed, except for insulating glass units due to their edges weaknesses. Moreover, for laminated glass, the PVB or SentryGlas® interlayer has to be replaced locally at the connection, by a stiffer material to avoid creep deformations, e.g. aluminum alloys. The gasket, introduced between the glass and steel elements and preventing their direct contact, has to be used in his purely elastic range to avoid permanent deformation loosen the connection. Therefore, the most common employed materials for gaskets are soft metals, e.g. almost “pure” aluminum and fibers reinforced plastics.



**Figure 2.8-** Assembly by friction in glass fins [2.37] – General and detailed view

The choice of the gasket and its thickness are responsible for the rigidity of the connection. For a very stiff or a thin gasket, the rotations of the glass around its fixations, induced by out-of-plane loads, will be restricted. This will entail local high stress concentrations in glass panes. A too high prestress in the bolts can also affect the glass in the same way. Self-weight and especially thermal loads, undertaken by the friction arising in the fixation, may lead to failure of the glass initiating at its edges.

In contrary, if the connection is too soft or if the prestress in the bolt is insufficient, the transfer of the loads by friction will not be effective and glass may slide between the fixation devices. Thus, a balance must be found to prevent the introduction of too high stresses in the glazing and to ensure enough

friction to maintain it. Moreover, other problems from the environmental conditions, in case of an outdoor use, can reduce the friction, e.g. a poor circulation of water.

Friction assemblies are mostly realized on construction sites and require a perfect knowledge of the involved materials. Oversized holes are frequently drilled in the glass in order to avoid the contact with the prestressed bolts. In consequence, the installation of such system does not constitute a simple task. Additionally, in cold environmental conditions, materials retract, while it is the opposite in hot conditions. Therefore, the implementation under one of these environmental conditions necessitates a perfect control of the bolt prestress to not induce too elevated stress in the glass or too less friction.

Panaît [2.37] investigated experimentally and numerically friction-jointed assemblies and more particularly the frictional contact between aluminum gaskets and glass elements. A tribometer was realized to evaluate the friction coefficient corresponding to the limit between adherence and sliding. Surfaces of contact were relatively small, i.e.  $30 \times 30 \text{ mm}^2$ , and several possible influent factors were tested. From this experimental study, the contact time and the normal loading path were found as the most significant influent factors. The mean value of the friction coefficient was of 0,17. This value remained constant under the both tested temperatures ( $10^\circ\text{C}$  and  $25^\circ\text{C}$ ) and independent on the glass type (FTG or HSG). However, an increase of the contact time on an already realized assembly before the application of the tangential load was followed by an increase of the friction coefficient up to 65-70%. This was interpreted as creep of the surfaces asperities with the help of a model developed by Greenwood-Williamson. Besides, two different normal loading paths were applied with tribometer in another series of tests, i.e. a direct application of the load and an indirect application presenting a plateau at constant force. Results showed that the friction coefficient obtained with the indirect loading was about 60% higher than the one acquired with the direct loading. This other phenomenon was interpreted as a destruction of the oxide layer present on the aluminum during the plateau phase.

With these experimental results, Panaît proposed a model based on the characterization of the surfaces state by several internal variables. This model was implemented in FEA programs and numerical results were close to the experimental ones.

### **2.3.2.3 Supported locally by point fixations**

#### **Through glass**

A wide variety of bolted connections were created in order to fulfill transparency and aesthetic demands. Nevertheless, they all have in common that, compared to clamping devices, holes have to be drilled in glass to later insert bolts. Thus, as glass cannot yield, high stress concentrations appear at the hole. The sizes of the boreholes are always larger than the diameter of the bolts to inject or insert, in the gap, soft materials, presenting lower elastic modulus. This detail allows avoiding direct steel to glass contact and redistributing the loads more uniformly and on a larger area. These inserted soft materials are usually aluminum alloys, plastics (EPDM, POM, and polyamide), cast-resins or mortars. As they are part of the façade, they are subjected to environmental conditions and must therefore possess good resistance to water, UV and temperature variations. A good cyclic behaviour is also required as a creep resistance to prevent oozing out of the joint. In-plane loads, i.e. self-weight of the glass or thermal loads, induce compressive and tensile stresses in the glass and in the bushing material. So, the in-plane rigidity of the connection is directly related to the uniaxial rigidity of the involved components. Monolithic glazings employed in these assemblies are preferably tempered glass, either FTG or HSG, as they possess a residual prestress. For laminated glazing, misalignments between the holes of the two glass plates are frequent, but the bushing materials compensate for these imperfections.

Point fitted fixations through glass are generally split in two categories regarding the cylindrical or conical shape of the drilled hole:

- For cylindrical holes, the out-of plane loads bend the glazing inwards or outwards and have to be undertaken by additional mechanical devices. Therefore two steel plates are disposed on both sides of the glass pane with another interlayer in between. In this case, this connection mean visually looks like a punctual clamping device. The transparency of the construction is

thereby reduced and the added steel plates on the outer face of the façade are locations of dust and water accumulation making its cleaning more difficult.

- For conical holes, the out-of-plane loads are undertaken by the conical bolts. The outer surface of the façade appears smoother with no risk of water or dust accumulation. However, the disadvantage of this kind of fixations resides in the small contact area between the bolt and the glass plate, introducing high stress concentrations and reducing to zero its post breakage capacity. Furthermore, the realization of conical fixations is less simple, as the shape of the bolt has to fit closely the shape of the hole. The bushing material being not able to compensate this difficulty during the manufacturing. Therefore, special solutions, such as slotted holes, have to be realized.

With the aim to reduce the stress concentrations for the both configurations, hinged point fixations were developed. These hinged connections allow rotation of the glass plate of about  $10^\circ$  to  $20^\circ$  and represent a major asset when the glazing is subjected to elevated out-of-plane loads. The hinge is commonly realized with the help spherical joint, either positioned at the glass level or in the bolt, introducing an additional bending moment.



**Figure 2.9-** Through glass point fixations for cylindrical and conical holes (Source: Glasströsch)

The manufacturing of the holes in the glazing is made with special diamond saw in indoor controlled conditions, but its implementation on the main structure is done on construction site in outdoor environmental conditions. Thermal expansions of materials can be responsible for non-coincidence between glass holes and steel bolts. So manufacturing tolerances must be included in the design and fabrication steps.

To design a point fixation assembly, a correct evaluation of the stress peak at the hole has to be done. Due to the large variety of the fixation and the involved materials, no empirical rules exist and numerical simulations have to be carried out. The validation of a FEA model is only possible with the help of intensive experiments. In the consequence, several procedures were developed to design point fittings:

- Brendler's method [2.38], only valid for conical holes, can be divided in two parts, i.e. the determination of the stiffness of the point fixation and then the verification of the glass plate. The stiffness of the point fixation is considered as directly related to the stiffnesses of the bushing/interlayer materials and of the steel covering plates. Thus, pre-defined series of small scale tests, in which the glass plate is replaced by a rigid steel plate, have to be carried out. Tension, compression and shear have to be applied, as the system can be composed of dissimilar material, and the resulting displacements have to be measured. Knowing the displacements in each configuration, a FEA model can be calibrated by varying the properties of the materials. An additional flexibility, introduced by the presence of a hinged connection, can be introduced in the finite element model by adding linear springs, whose resistances are experimentally determined. The simulation of the complete system is then possible and the peak stresses in the hole of the glazing unit can be evaluated. This procedure was integrated in a German Technical Approval [2.39].
- Siebert's method [2.40] is also based on a series of tests followed by numerical simulations. The first step of this procedure consists in modeling a simple rectangular glass plate subjected to tensile forces and presenting a central hole. The validity of the model is checked with the

help of analytical formulas (e.g. stress concentration factors), ensuring the correct calibration of the latter. The second step is to evaluate and define the contact with the help of small scale tests, in which the strains are measured along certain path. Pilot tests with aluminum interlayers have to be executed before testing the final configuration with the correct materials. The implementation of the material properties in the finite element model is, as for the Brendler's method, a succession of trials on the Young's modulus to reach the measured strains. The model is calibrated by comparing both numerical and experimental results. The peak stresses at the hole can finally be assessed.

- Kasper's method [2.41] is, as the previous ones, based on several tests followed by numerical simulations. Complete series of tests are realized with different load application angles, i.e. at  $0^\circ$ ,  $22,5^\circ$ ,  $45^\circ$  and  $90^\circ$ , equivalent to pure tension, combined tension and shear and pure shear. Tests are carried out with the final materials and the results (strains on pre-defined paths and load intensity) constitute important data. The finite element model is then calibrated by varying the Young's modulus until reaching the strains of the experimental data sheets. The so obtained model is used to evaluate the stress peaks at the hole.

For all the presented models, the unilateral contact and the friction between the interlayer material and the glass were not considered. Therefore, these procedures are each time employed from the start for new connections, even if they involve the same constituents but with other geometries.

### Undercut ties

Smoother and lighter glass surfaces can be produced by employing undercut ties, see Fig. 2.10. For this kind of fixation, the bolts do not penetrate through the whole glass thickness but only a part. Thus, air- and water-tightness are achieved with this connection mean. By limiting the entrance depth of the bolt, no additional outer steel plate can maintain a glazing unit subjected to out-of-plane loads. Therefore, conical countersunk bolts must be used to hold the glass in vertical position. A bushing material has to be inserted between the edge of the glass hole and the steel conical bolt to prevent steel to glass contact and lessened the stress peaks. The bushing materials are generally made of rigid plastics, such as polyamide PA6. Monolithic or laminated glass composed of thermally tempered glass, either partially or fully tempered, can be employed.

The Fischer FZP-G-Z undercut ties are actually regulated in German by a technical approval [2.42]. Its manufacture takes place in indoor conditions. First, the conical hole is realized in the glass with a special drill, able to rotate. Then, the glass is tempered and the Fischer FZP-G-Z is finally mounted with a special setting tool controlling the torque. The final assembly is made on construction site with the difficulties generated by climatic fluctuations and temperature changes.



**Figure 2.10-** Undercut point fitting (Fisher FZP-G-Z) – General and detailed view

The design method, for the Fisher FZP-G-Z, was developed by Beyer [2.43]. It is based on the superposition principle, which allows decoupling the local effect at the borehole to the overall global behaviour of the glass plate. Regarding solely the local effects, small scale tests were carried out with the aim to evaluate the stiffness of the point fixation. Thus, for predefined Fisher connections (glass plate thicknesses and bolt geometries), the translational and rotational stiffnesses were recorded in special data sheets. A formula was also established to calculate equivalent stiffnesses accounting for



the rigidity of the substructure and the rigidity of the Fisher fixation. With these last values, the user can model the glazing with a 2D shell supported by linear springs representing the connection. The complete assemblies of the countersunk bolts and the holes do not need to be model in details, saving calculation time. The maximum tensile stress in the center of the glass plate and its maximum displacement, obtained with the numerical simulation, can be compared to allowable values ensuring the global safety of the plate without considering the peak stresses arising near the holes. The limit of the local area was defined as three time the diameter of the hole. Along a circular path defined at the border between local and global area, the maximum stresses have to be extracted from the finite element simulation and multiplied by a stress concentration factor to derivate the stress peak at the borehole. Finally, the verification of the connection is done with the help of an equation established by Beyer and based on the internal forces and the peak stress.

### 2.3.3 Adhesive connections

The previously detailed mechanical connections of section 2.3.2 do not guarantee uniform distribution of the loads due, on one hand, to local fixations and, on the other hand, to the applied rigid or semi-rigid materials, generating crucial stress peaks in glass components. Therefore, new connections using adhesives, similar to the one developed in the aeronautic field, were introduced for façades. The advantages of adhesive connections are:

- The distribution of the stress along the jointed parts is nearly uniform and without inducing stress concentration peaks;
- Adherents with dissimilar mechanical and thermal properties can be bonded;
- Some adhesives have the capacity to transfer high loads between the jointed elements.

As for the mechanical connections, several topologies exist to adhesively fix the glass to the steel substructure, i.e. linearly or locally by points. Furthermore, other adhesive assemblies, involving glass and steel, will also be presented within the next paragraphs.

#### 2.3.3.1 Supported linearly

Structural sealant glazing systems (SSGS), regulated by the technical guide ETAG 002 [2.44] and released by the European Organization for Technical Approvals, represent the majority of the built linear adhesive connections. These systems are generally composed by a glazing structurally glued to a secondary frame which will be mechanically fixed to the main structure of the building. Glazing can be monolithic (annealed glass, FTG or HSG), laminated glass or insulating glass. But IGUs are preferred and widely employed, due to their better thermal properties.

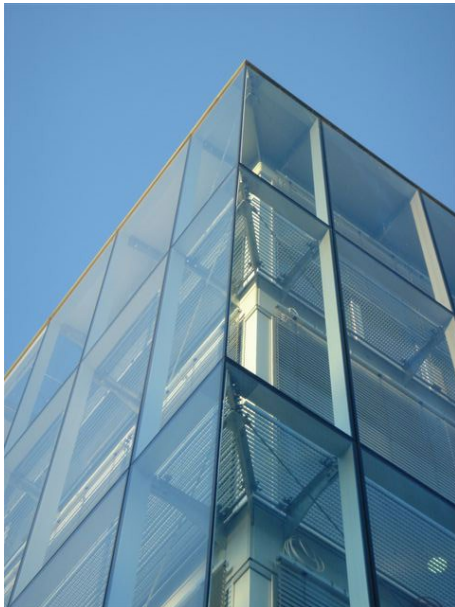
Four different layouts were envisaged by the European Approval:

- Type I: The weight of the glazing element is supported by mechanical devices and retaining devices are added to maintain the glass in case of sealant failure.
- Type II: The weight of the glazing element is supported by mechanical devices and no retaining devices are added.
- Type III: The weight of the glazing element is only supported by the structural sealant, but retaining devices are added to maintain the glass in case of sealant failure.
- Type IV: The weight of the glazing element is supported by the structural sealant and no retaining devices are added.

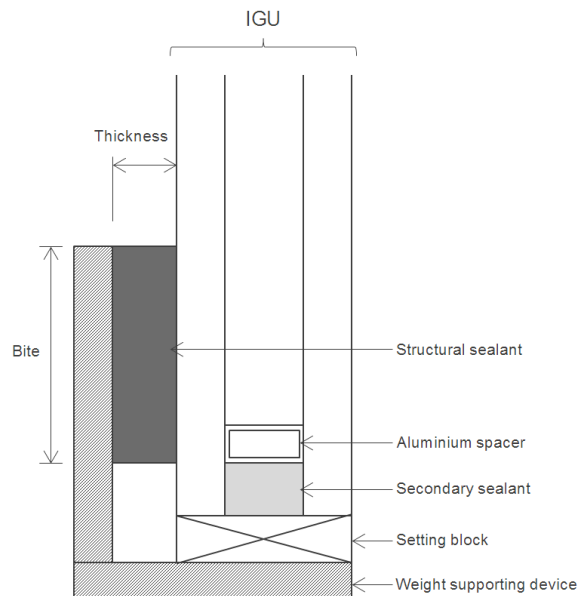
This distinction takes into consideration the resistance of the structural sealant and the dangerousness of the connection. Thus, the connection type I represents a less risky assembly than the connection type IV, in which loads of greater intensity and of long-duration act on the adhesive. Hence, monolithic glazings are the only possibilities for connections types III and IV, according to ETAG 002.

The structural sealant glazing system of the Zeppelin University, exposed on Fig. 2.11, corresponds to a connection type II with a laminated glazing, whose weight is supported mechanically. This building, constituted by 4-storey, reaches a height of about 16m. As for the SSGS with IGU of Figure 2.12, the structural sealant, mainly silicone, is inserted vertically between the glass pane and the secondary

frame, commonly in aluminum or stainless steel. Elastic setting blocks, installed horizontally on the mechanical support, bear the weight of the glazing. Additional gaskets or adhesive foams can also be installed above the structural sealant, as a finishing seal, to provide better air- and water-tightness.



**Figure 2.11-** SSGS of the Zeppelin University, Germany



**Figure 2.12-** SSGS layout (with IGU)

In SSGS types I and II, setting blocks support the weight of the whole glazing units and compensate for the different thermal expansions of the involved materials. Therefore, in case of vertical façade, these elements are essentially subjected to high compressive loads. For connections types III and IV, the weight of the glazing and the thermal loads are only supported by the structural sealant, which is subjected to a superposition of long- and mid-term high shearing stresses. Thus, to design the structural sealant, regarding the in-plane loads, the weight of the glazing can only be neglected for the two first connections types. Nevertheless, the out-of-plane loads, such as wind, snow and pressure variations, act on the same way on the structural sealant whatever the connection type. Tension and compression stresses appear along the bite of the structural sealant and manifest more or less intensely according to the location around the glass edges. Positive wind pressure, bending the glass inwards, generate compression stresses in the sealant along the edges but also up-lifting forces in the corners and so tensile stresses in the joint. In consequence, complex combinations of tension, compression and shear are introduced in the sealant and a perfect knowledge of its static and dynamic properties are imperative.

The installation and the bonding process of the glazing (monolithic, laminated, IGU) on a secondary frame takes place in indoor conditions, while the mechanical assembly of the so-formed element to the primary substructure is realized on construction site. The first step, after the realization of the glazing, consists in injecting the structural sealant by respecting the dimensions, e.g. bite and thickness, calculated in the design phase. This procedure is relatively complex and necessitates a good know-how. Then, the prefabricated element is installed on the façade and several checks have to be performed to ensure the durability of the adhesive connection. In case of sealant failure or glazing failure, quick and easy reparations can directly be made on construction site, which represents a non-negligible advantage. Moreover, the softness of the materials compensate for the manufacturing defaults, as for examples, the non-alignment of the two edges of a laminated glass pane or the edges imperfections of the glazing unit.

The ETAG 002 specifies limitations and proposes design rules for structural sealant glazing systems. This guideline is only applicable for vertical SSGS or inclined roof glazing, whose angle to the horizontal is superior to 7°. No inclination outwards, i.e. overhanging the street, is authorized. The adhesive employed must have a certified technical approval or be conform to the specifications given



in the guideline. Thus, complete series of tests are generally carried out on new adhesives to properly understand their behaviours under several environmental conditions. Knowing the allowable stresses of the adhesive, some simple design rules can be applied. The bite of the structural sealant of SSGS types I and II is determined by considering the out-of plane loads, such as negative wind pressure, generating critical tensile stresses in the joint. The deformed shape of a structural sealant glazing is then assimilated to a trapeze, obtained by bisecting the 4 angles of the rectangular plate, see Fig. 2.13. The maximum tensile stresses are found in the middle of the smallest edges and along the central part of the largest edges. Only regarding these zones, the maximum out-of plane force applied on a small section (delimited by  $Y$  and  $a/2$ ) must be equal to the maximum tensile force allowable by the sealant. This equation allows calculating the bite of the structural adhesive. For connections types III and IV, the weight of the glazing, inducing shear stresses in the sealant, represents also a criterion to be analysed for the calculation of the bite. Thus, the bite corresponds to the maximum amount between the value calculated by the out-of-plane loads based on the trapezoidal method and the value found due to the self-weight of the glazing.

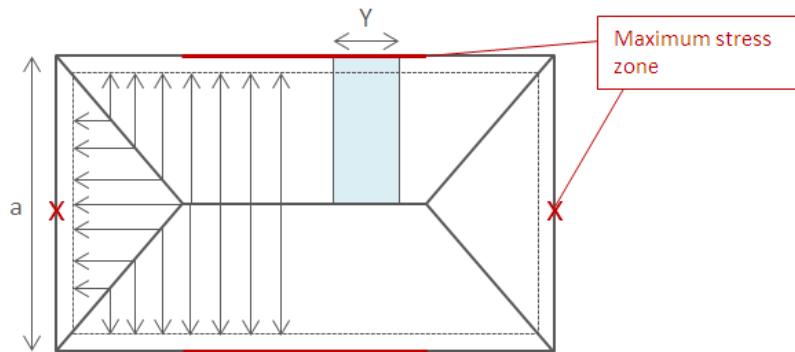


Figure 2.13- Trapezoidal deformations in SSGS

The thickness of the structural sealant is determined from the climatic loads and depends again on the connection type. Thermal loads create shear stresses in the joint, not activated for a supported glazing. The thickness is simply calculated by multiplying the shear modulus of the adhesive by the in-plane displacements divided by the allowable shear stress.

Minimal and maximal values for the bite and thickness are given by the ETAG 002, see Equation (2.3).

$$6 \text{ mm} \leq \text{thickness} \leq \text{bite} \leq 20 \text{ mm} \quad (2.3)$$

The American Standard ASTM C1401 [2.45], "Standard guide for Structural Sealant Glazing", and the French technical approval CSTB 3488 [2.27] provide also the same calculation methods. In addition to the joint dimensions, the maximal deflection of the glass pane must not exceed 1/100 of the size of the smallest edge.

### 2.3.3.2 Supported locally by point fixations

This adhesive fixing method is largely inspired by the mechanically point supported, presented in section 2.3.2.3. Their visual aspects are very close, making the structure lighter. Circular steel plates are directly glued to the glass surface with transparent structural adhesive, avoiding thereby the manufacture of holes generating stress peaks. Indeed, in contrary to the mechanical point fixing, the forces transferred to the glass are not localized but distributed all over the glued area. On one hand, the stresses in glass are consequently lessened but, on the other hand, the stresses in the adhesive become quite high. To hold the glazing element, stiff adhesives, such as acrylic or epoxy resin, are frequently employed. New transparent structural silicone adhesive (TSSA), developed by Dow Corning [2.46], are also very popular for point supported adhesive fixing, see Fig. 2.14 and 2.15. This last material presents enhanced properties compared to the existing structural silicones with a tensile strength about 8 times higher and the same invariance towards UV, temperature and humidity

variations. As TSSA is delivered as a film of a constant thickness of 1mm, the rigidity in shear is also better. Its application heat- and pressure-activated constitute an advantage too.

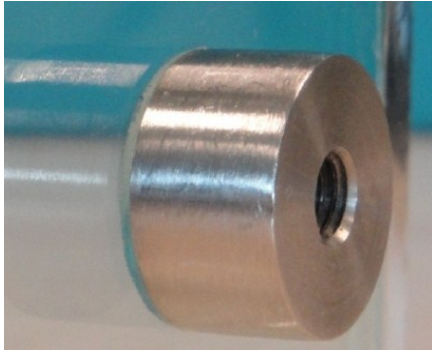


Figure 2.14- Adhesive point fixing (TSSA)



Figure 2.15- TSSA transparency (front view)

While the relative small thickness of TSSA is able to compensate for the local rotation of the glass plate under out-of-plane loading, it remains important to insert a hinged to allow these rotations for stiff thermoset adhesive. Nevertheless, these adhesive point fixings are still at the state of the art.

### 2.3.3.3 Hybrid components

Hybrid connections refer generally to systems in which two components, presenting dissimilar properties, are structurally jointed to optimally cooperate. As glass is brittle and fails in tension, a ductile material possessing a good tensile behaviour, e.g. steel, constitutes the second component. Steel-glass beams, studied within the INNOGLAST [2.47], represent good examples of hybrid connections. In these assemblies, an I-shaped beam is composed by steel flanges and a glass web, all connected with the help of adhesives. The ideal aim is to transfer sufficiently shear forces to activate a composite action, in which only the bottom steel flange would be subjected in tension or in which the glass would undergo minimized tension due to the presence of the steel plate. Such hybrid beams could be applied vertically, as façade element, or horizontally, as roof supporting beams. However, outdoor installation, i.e. subjected to varying environmental conditions, is not recommended because adhesives lose their structural properties. The maximum length of the beam should be 6 meters to avoid any glass overlap joints.

Several tests were carried out on four different joint geometries to find the one transferring the maximum shear forces without introducing to high stress peaks. Butt splice bonding and channel bonding were directly performed on the steel flange, while additional U- and L-profiles were added to realize the bonding, see Fig. 2.16.

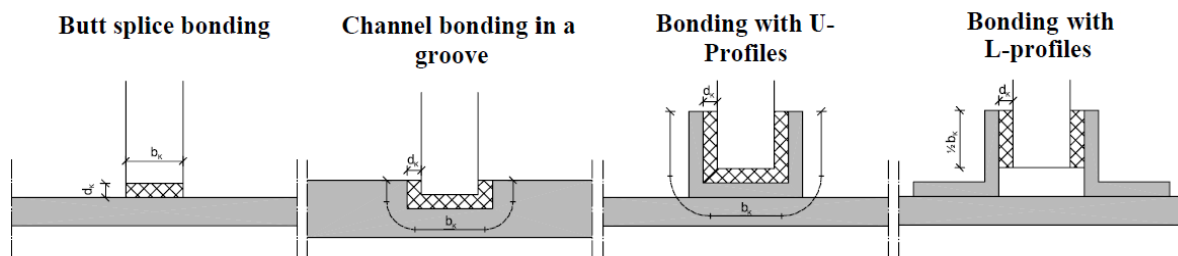


Figure 2.16- Jointing details of hybrid steel-glass beams [2.47]

In addition to the experimental investigations on the joints geometries, several adhesive types, either silicone rubbers or thermosets, were also tested. Too stiff adhesives, such as epoxy resins, generated failure of the glass plate, while too soft, such as the silicones, were not able to transfer enough shear forces. A correct compromise, in terms of rigidity, was found with polyurethanes. However, these last adhesives are known to be strongly UV-dependent, making their use in façade more delicate.

From this research, it was demonstrated that the butt-joint or U-profiles, combined with correct surfaces treatments of steel (sand blasting and degreasing) and glass (degreasing), represent the better connection means with large bonding areas. Nevertheless, the manufacturing of a jointing with U-profiles appears more complicated, because the shaped has to be completely filled by respecting the determined dimensions of the adhesive. Partial connection theories developed by Pischl and Möhler, combined with numerical simulations, successfully described the behaviour of the hybrid beams and are therefore recommended for design.

#### 2.3.3.4 Laminated connections

In hybrid steel-glass components, the quantity of steel is almost equivalent to the quantity of glass with the aim to manufacture an independent system that could be used as column. However lighter system can be achieved by inserting a steel bars at the bottom of laminated glass plates to increase its strength and its post breakage capacity. These kinds of assemblies are mostly employed as glass fins for large transparent façades.

Louter [2.48] investigated experimentally and numerically the resistance of stainless steel/ fibers reinforced laminated glass beams. For the stainless steel reinforced laminated beams, the sum of the heights of the inner glass plate and the inner lower steel profile was equivalent to the height of the two outer glass plates. The whole was laminated together obtaining a proper global cross section see Fig. 2.17. This system was compared to an equivalent one, manufactured with a transparent UV-curing acrylate only. Four point bending tests were carried out on both beam configurations under several temperatures. Results showed the better strength and post breakage capacity of the laminated system, even under negative ( $-20^{\circ}\text{C}$ ) and elevated temperatures ( $60^{\circ}\text{C}$ ).

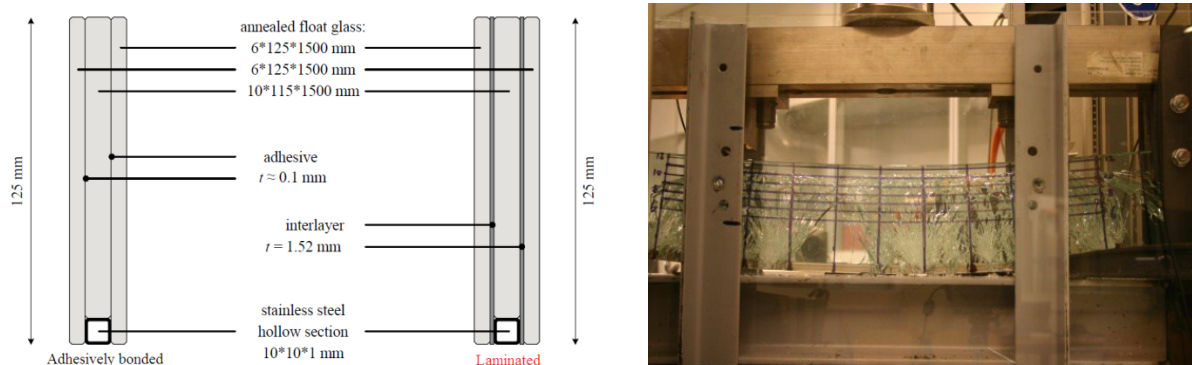


Figure 2.17- Details of the adhesively bonded and laminated reinforced glass beams investigated by Louter [2.47]

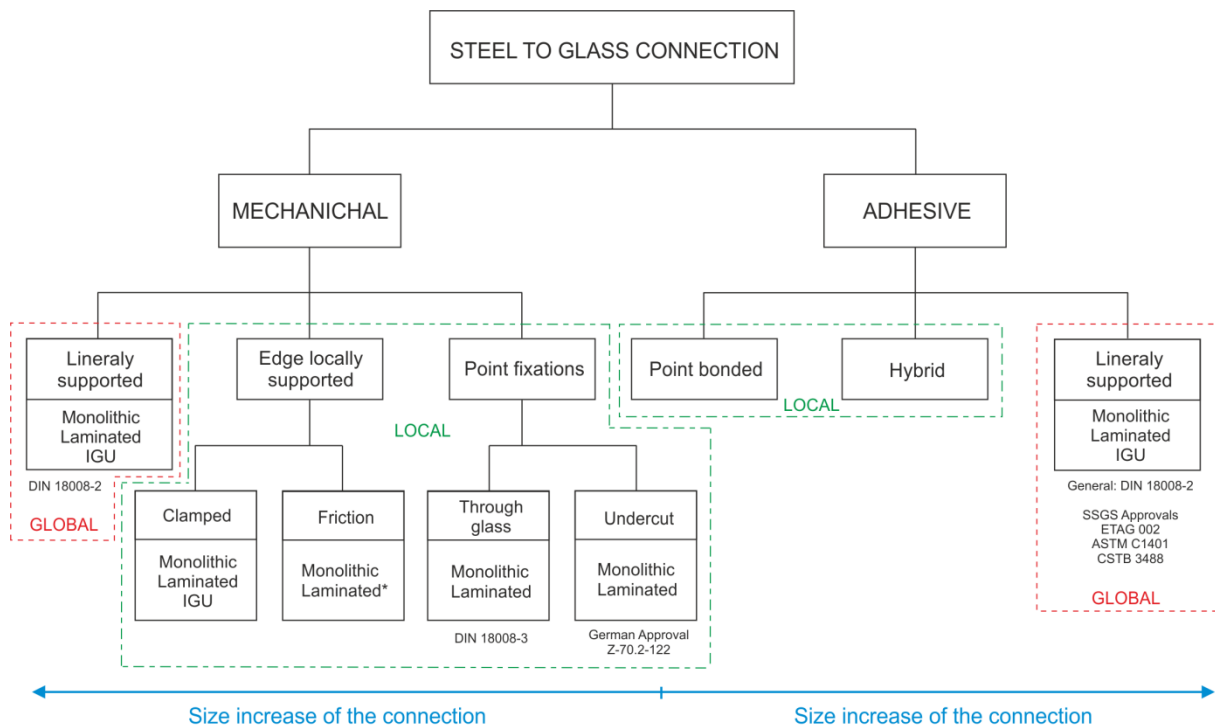
Further experimental investigations to evaluate the influence of the length of the beam and the percentage of steel reinforcement were conducted. While the length of the beam had only a negligible effect on the post breakage behaviour, the percentage of reinforcement was important. A rectangular stainless steel hollow profile was compared to a stainless steel solid section presenting the same external dimensions in order to keep the same bonding area. With the solid and heavier steel section, the neutral axis of the beam goes down, decreasing the tensile zone in the glass. This phenomenon stops the propagation of cracks, the latter remaining confined in the tensile zone. Thus, the post breakage behaviour of a beam presenting a high percentage of reinforcement appears clearly better.

Other experimental investigations were carried out on laminated glass plates with stainless steel perforated plates of 1mm thickness in the tensile zone by Carvalho [2.49]. To not affect the lamination of the glass plates, a large numbers of perforations were realized in the stainless steel plates. The first idea was to increase the residual capacity in case of glass breakage, but these perforated steel plates could also be extended outside the glass to envisage a connection between two identical elements. As the steel plates are very thin (1mm) and present many holes, their resistance towards tensile forces is rather poor. Therefore, only connections subjected to bending were investigated. These connections were composed by two symmetric parts, in which a perforated stainless steel plate was laminated

(with SGP interlayer) halfway between two glass plates. The two elements were assembled at the non-embedded side of the steel plates with the help of several bolts. Four types of jointing systems were considered, i.e. one simply bolted, one with bolts and thick covering steel plates, another one with bolts and aluminum L-profiles in the compressive zone and the last one with nylon bars. For the three first methods, buckling occurred in the perforated steel plates in spite of the added reinforcement in the tensile zone and/or stress peaks appeared in the glass due to contact with other materials. Thus, only the connection with the nylon bar showed interesting results with no instabilities, even if steel yielded under non-elevated loads.

### 2.3.4 Summary

The most employed steel-to-glass connections for façades are summarized in the following Fig. 2.18. The glazing products, actual standards and current approvals are also exposed for each assembly type. While, the mechanical connections were mainly investigated, a lack of knowledge exists for the adhesive ones, especially with the rapid development of new adhesives. Further, with regards to the aforementioned considerations, the latter appear as suitable candidates for steel-to-glass connections.



**Figure 2.18-** Summary of the actual steel-to-glass connections

## 2.4 ADHESIVE MATERIAL PROPERTIES

### 2.4.1 General review

To optimize the transfer of loads between two bonded parts, avoiding stress peaks, several types of adhesives were created. All these adhesives are polymers, i.e. large macromolecules chemically or mechanically linked together and composed by a repetition of atoms chemically fixed on them. A classification of the polymers was therefore established according to the spatial arrangements of these macromolecules. Their lengths and degrees of connection are essentially responsible for their thermomechanical behaviour. Regarding these criterion, three principal groups are listed:

- **Thermoplastics**, linear or branched chains are relatively weak and largely temperature-dependent. Heat softens these materials, but not definitely, as they are able to recover their shape after cooling. PVB foils, employed in laminated glass, belong to the thermoplastic category. However, as they do not present a sufficient rigidity to activate a correct load transfer between connected parts, they will not be detailed in the following sections.
- **Elastomers**, called rubber polymers, are long cross-linked chains, which can reorientate and largely elongate. Even if they possess a low degree of cross-linking, once the applied stress is removed, they return to their initial form. The most widespread elastomers in the construction field are silicones and polyurethanes.
- **Thermosets** consist of high cross-linked chains highly temperature-dependent. Once heated to a certain point, they cannot regain their initial shape. The chains movements are notably restrained by the high density of cross-linking, generating a strong rigidity of the thermosets at the macroscale. Epoxy resins and acrylics represent good examples of thermosets employed in building.

### Mechanical properties

For the three afore mentioned groups, the behaviour of the adhesives are directly in relation with the spatial configuration of the polymers networks. Thus, in terms of pure mechanical rigidity, it becomes possible to sort them in ascending order, i.e. thermoplastic being the weakest, followed by elastomer and finally thermoset.

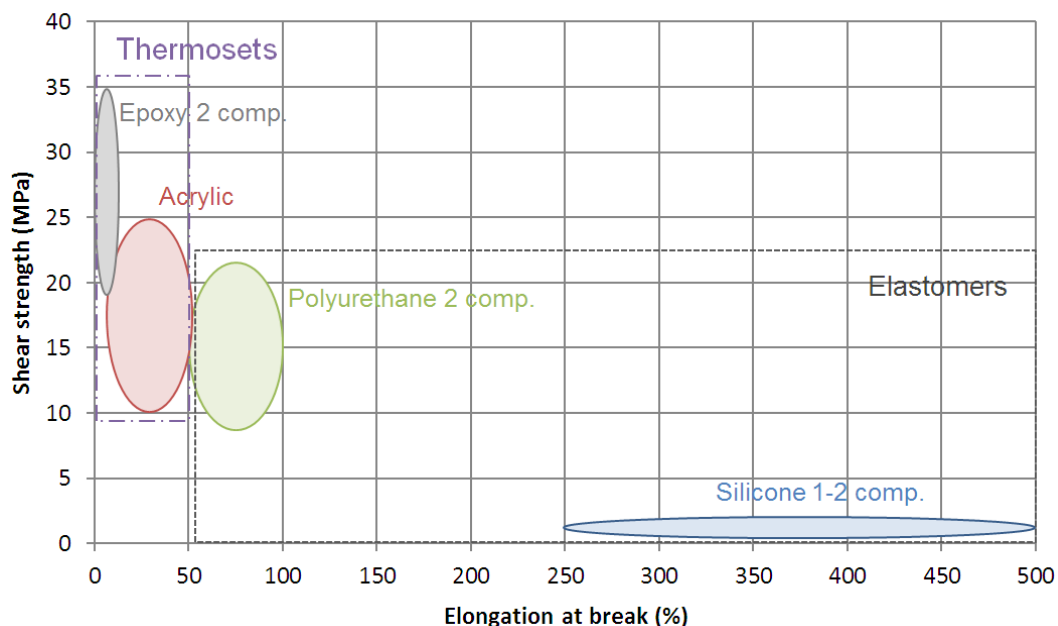


Figure 2.19- Shear strength (issued from tensile lap-joint shear tests) versus elongation at break [2.50]

According to the previous Fig. 2.19, the range of shear deformation at break of standard one- or two-component silicones varies from 250% to 500% for a maximum strength of approximately 2,5MPa. Polyurethanes exhibit fewer deformations, usually 50 to 100%, for a higher strength of 8 to 22MPa. Hence, elastomers cover large shear deformations for rather low to medium strengths, in opposite to thermosets. Indeed, acrylics undertake smaller elongations at break, 10 to 50%, for shear strengths slightly superior to the ones of polyurethanes. And epoxies are assimilated to the stiffest adhesive, possessing the highest strength, up to 35MPa, with the lower deformations range, i.e. less than 10%. The data presented in Figure 2.19 were obtained with the help of shear short-term experiments and do not account for long-term loads applications. Therefore, the resistance to creep/relaxation and fatigue loading must also be regarded to predict the lifetime of the adhesive. However, these characteristics are not automatically given by the adhesives manufactures, due to a lack of researches in these domains.

### Durability

In façades, adhesives are subjected to environmental conditions variations, which modify their mechanical behaviour. As they are long polymer chains, their lifetime in service depends greatly on their cross-linking degrees and their chemical compositions. Thus, each adhesive possesses a thermomechanical behaviour influenced by specific factors. The agents deteriorating the properties of silicone elastomers are different from the ones influencing the properties of polyurethane elastomers, which also differ from the ones of acrylic or epoxy thermosets. Nevertheless, the most regarded factors impacting the adhesives properties are the hot/cold temperatures, the water under liquid or vapor form, the UV-radiations and the cleaning solvents.

Table 2.5 summarizes qualitatively the resistance of four common adhesives, divided in two families, to various parameters. Generally, elastomers present a better behaviour towards hot and cold temperatures than thermosets, even if both categories are equivalent and relatively stable regarding water and acids. Although the mechanical properties of polyurethane adhesives are higher than the ones of the silicones, they are more sensitive to UV-light, which constitutes an important drawback for façade use.

| Class      | Adhesive     | Shear | Peel | Heat | Cold | Water | Acids | Light | Solvents |
|------------|--------------|-------|------|------|------|-------|-------|-------|----------|
| Elastomers | Silicone     | 3     | 5    | 1    | 1    | 2     | 3     | 2     | 3        |
|            | Polyurethane | 2     | 3    | 3    | 2    | 2     | 3     | 6     | 5        |
| Thermosets | Acrylic      | 2     | 6    | 5    | 3    | 1     | 2     | -     | 2        |
|            | Epoxy        | 2     | 5    | 3    | 5    | 2     | 2     | -     | -        |

**Table 2.5-** Qualitative resistance of adhesive to environmental conditions [2.51]  
(1: Excellent, 2: Good, 3: Fair, 4: Poor, 5: Very poor, 6: Extremely poor)

### Failure mode

To connect two dissimilar materials together, the only thermomechanical properties of the adhesive are insufficient. In the consequence, other factors, such as the possible adhesive or cohesive mode of failure of the assembly, have to be considered. Adhesive failure corresponds to a bond breakage between the adhesive and adherent interface, while a cohesive failure coincide with a breakage of the adhesive itself. Following an adhesive failure, the adherent surface is completely free of adhesive, as if the bonding has never been done. This last configuration must be avoided as the full material properties cannot be reached. The failure mode depends on the involved substrates (e.g. glass, steel, aluminum), i.e. on the surface state, either treated or not with sand blasting or degreasing. The poor wettability of the adhesive can also be a decisive aspect leading to an adhesive failure.

## 2.4.2 Elastomer material laws

### 2.4.2.1 Thermomechanical behaviour

As shortly and qualitatively mentioned in the previous paragraph 2.4.1, elastomers possess a relatively invariant behaviour at hot and cold temperatures, which is closely related to their chains cross-linking. The quantitative determination of the maximal and minimal temperatures, for which changes in material properties are recorded, is of high importance. Indeed, in façade, temperatures can rise up to 65°C and decrease to -20°C and the adhesive materials have to withstand this large range.

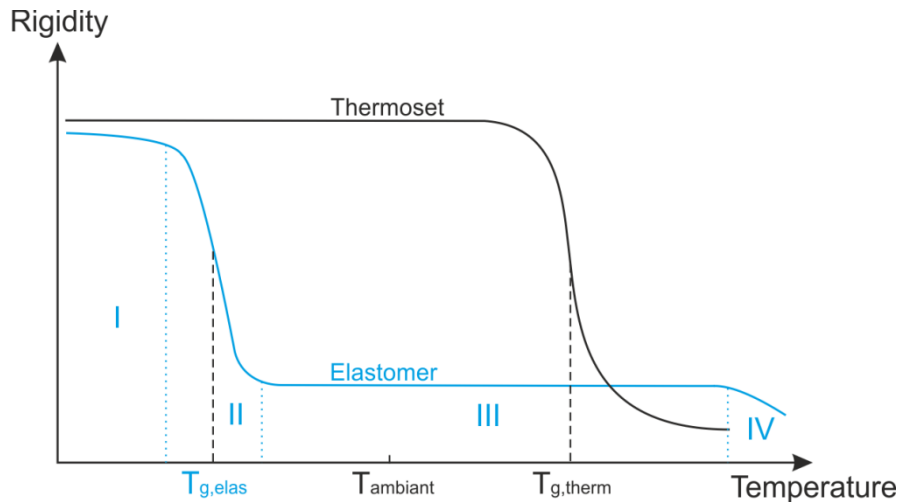


Figure 2.20- Rigidity of the adhesives versus temperatures

To evaluate the “transition” temperatures for one elastomer, the rigidity, e.g. the Young’s modulus, is plotted versus the temperature (Fig. 2.20). This kind of diagram highlights four distinct material states:

- Zone I, a glassy state at low temperatures and for a small range. In this state, the movements of the polymer chains are restricted and the elastomer is therefore very stiff and brittle.
- Zone II, a transition state, during which a significant degree of rigidity is lost with the increase of the temperatures.  $T_g$  corresponds to the glass transition temperature, i.e. the temperature delimiting the glassy and rubbery states.
- Zone III, a rubbery state, characterized by very large deformations under moderate rigidity. Once this state is reached, the rigidity of the material does not evolve with the increase of the temperatures. For elastomers, this plateau is quite wide.
- Zone IV, a flow state at high temperatures. The material behaves as a non-Newtonian incompressible and viscous fluid, having no rigidity.

With regards to the large variety of elastomers existing, the glass transition temperature is always negative, comprised between -10°C and -120°C, and thus inferior to the ambient temperature. For silicone, this value lies in a smaller range, i.e. -70° and -120°C. Consequently, only the mechanical behaviour in the rubbery state is of interest for façade use.

In the rubbery state, the macromolecules form a disorderly 3D network, whose polymer chains are oriented randomly. Hence, the elastomer does not exhibit a higher resistance in a privileged direction. The isotropy of the material, at the macroscale, is then assumed. In addition, all the elastomers present an identic mechanical behaviour in the rubbery state, despite their different chemical compositions. The characteristic stress-strain diagram obtained with tensile tests on high damping rubber (HDR) by Amin [2.52] is presented in Figure 2.21. The behaviour of rubber polymer appears clearly non-linear with changes in curvature. Three domains can be identified on this diagram, i.e. a first part (zone I) with small deformations and in which the behaviour can be considered as linear; a second part (zone II) with a slight increase of the stresses under large deformations; and the last part



(zone III) where the stresses rise drastically with small deformations. Even after been subjected to high deformations of the zone III, the elastomers are able to recover their initial dimensions. Thus, they are described as isotropic non-linear hyperelastic rubber materials.

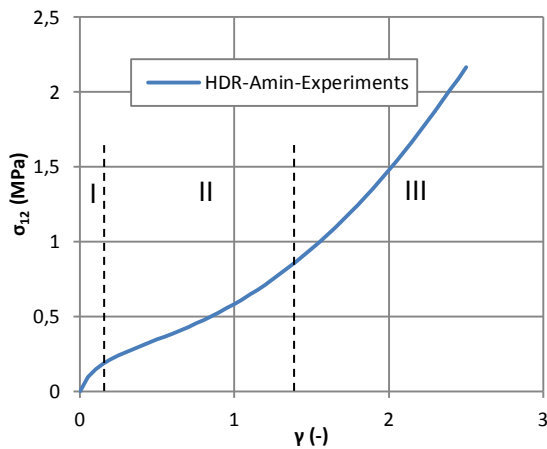


Figure 2.21- Characteristic tensile stress-strain curve [2.52]

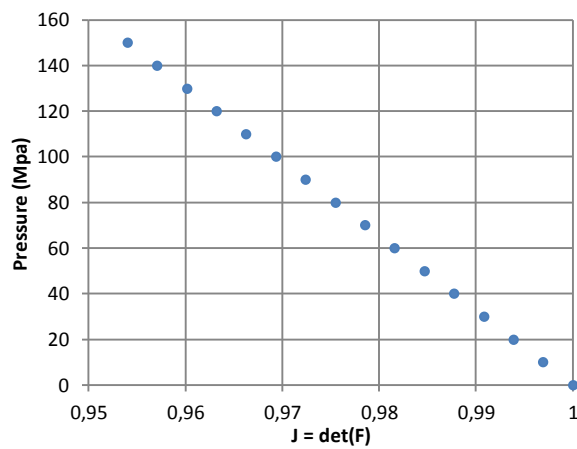


Figure 2.22- Volumetric compression test results [2.53]

With these properties, elastomers are widely employed as damping materials, shock absorber bushings (bearings for earthquake resistant structures) and seals (O-ring). For these applications, they are highly confined and subjected to elevated compressive forces. However, even if the Poisson's ratio of elastomers is very close to 0.5, the assumption of incompressibility is not valid. Indeed, some experiments were carried out by Bradley [2.53] with an oedometric system, which showed a linear variation of the elastomer's volume under pressure increases, see Fig.2.22. Consequently, the quasi-incompressible behaviour has to be regarded, especially for confined applications.

The quasi-static properties of elastomers are insufficient to determine their lifetime in use, in spite of their astonishing recovery. Therefore, cyclic tests are needed to apprehend their lifetime behaviour and to evaluate any stress softening. Miehe [2.54] conducted cyclic tests at fixed maximum displacements and suggested to explain the stress softening by the combination of two types of damages:

- A discontinuous damage, commonly referred as Mullins' effect, depending essentially on the maximum displacement encountered by the material. The Figure 2.23 represents the typical behaviour of an elastomer subjected to cyclic loadings, from its virgin state up to three imposed displacements. The material is loaded to a first strain, path "0a1", and then unloaded,

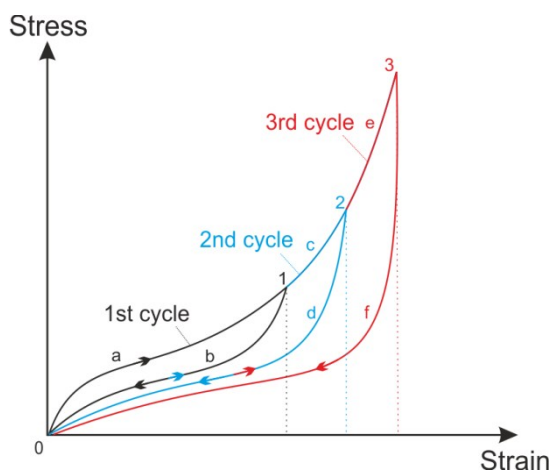


Figure 2.23- Discontinuous damage (Mullins)

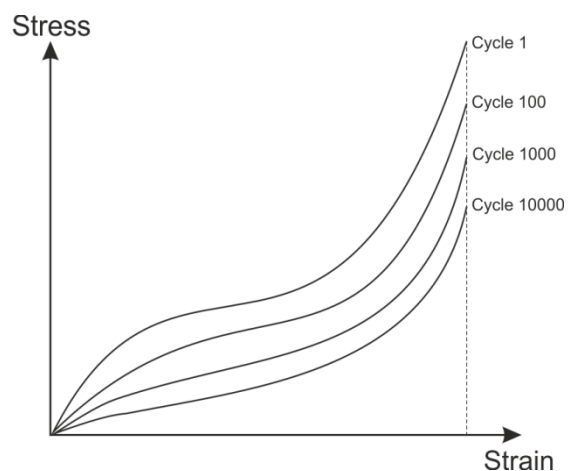


Figure 2.24- Continuous damage (unloading only)



path “1b0”. During this 1<sup>st</sup> cycle, the loading and unloading paths are different, i.e. the stress in the unloading is less than the one in the initial loading. Several theories were proposed to describe this phenomenon, such as a rupture of the chains of the molecular network [2.54] or as the sliding of the chains at the connecting nodes. During the second cycle to a higher strain “2”, the loading path does not correspond to “0a1c2”, but to “0b1c2”, demonstrating the irreversible nature of this damage. The unloading “2d0” presents a greater stress softening than the unloading of the first cycle. Finally, the third cycle, to the strain “3”, is composed by a loading “0d2e3” and an unloading “3f0”. However, this representation of the Mullins’ effect could not completely reflect the reality, as it is based on the assumption that, for an imposed strain, the stress softening will only affect the two first cycles. For example, it implies that, by limiting to the strain “1”, the loading and unloading paths should always coincide, even after numerous cycles.

- A continuous damage, also referred as progressive or cumulative damage. This stress softening, only related to the unloading path, is schematically represented on Fig. 2.24. For this kind of damage, at imposed displacement, the stress softening accumulates with the increase in cycles. This damage at larger cycle numbers should be added to the Mullins’ effect to correctly represent the material behaviour. Nevertheless, this effect can be neglected for some elastomers.

*To conclude, elastomers are isotropic and quasi-incompressible hyperelastic materials, subjected to damages affecting their long-term behaviour.*

#### 2.4.2.2 Existing material laws

##### Assumption of incompressibility

The most widespread hyperelastic models, describing the behaviour of elastomers, were based on the assumption of incompressibility, whose validity could only be justified for non-confined applications subjected to large deformations. With this postulate, two different approaches, both depending on the first and second laws of the thermodynamics, were suggested to represent the mechanical properties of elastomers, i.e. the phenomenological approach, based on the continuum mechanic and on tests at the macroscale, and the probabilistic approach, based on the formulation of the entropy, making a link between the micro- and macroscale.

##### a. Phenomenological models

With regard to the considerable strains (up to 700%) exhibited by elastomers, the large deformation theory has to be regarded to establish the fundamental equations describing the material behaviour. Therefore, the principal concepts and notations of this theory are summarized in Table 2.6.

| Designation                               | Definition                                                | Specifications                                                                                                              |
|-------------------------------------------|-----------------------------------------------------------|-----------------------------------------------------------------------------------------------------------------------------|
| $\bar{\bar{F}}$ deformation tensor        | $\overrightarrow{dx} = \bar{\bar{F}} \overrightarrow{dX}$ | $\bar{\bar{F}} = \bar{\bar{I}} + \overline{\text{Grad}}(\bar{\bar{U}})$<br>With $\bar{\bar{U}}$ displacement vector         |
| $\bar{\bar{U}}$ right deformation tensor  | $\bar{\bar{U}} = \bar{\bar{C}}^{1/2}$                     | $\bar{\bar{F}} = \bar{\bar{R}}\bar{\bar{U}}$<br>With $\bar{\bar{R}}$ rotation tensor ( $\bar{\bar{R}}\bar{\bar{R}}^T = 1$ ) |
| $\bar{\bar{V}}$ left deformation tensor   | $\bar{\bar{V}} = \bar{\bar{B}}^{1/2}$                     | $\bar{\bar{F}} = \bar{\bar{V}}\bar{\bar{R}}$<br>With $\bar{\bar{R}}$ rotation tensor ( $\bar{\bar{R}}\bar{\bar{R}}^T = 1$ ) |
| $J$ third invariant of $\bar{\bar{F}}$    | $J = \det(\bar{\bar{F}})$                                 | For incompressibility $J = 1$                                                                                               |
| $\bar{\bar{C}}$ right Cauchy-Green tensor | $\bar{\bar{C}} = \bar{\bar{F}}^T \bar{\bar{F}}$           | Symmetric<br>Lagrangian tensor                                                                                              |

|                                         |                                                      |                                          |
|-----------------------------------------|------------------------------------------------------|------------------------------------------|
| $\bar{B}$ left Cauchy-Green tensor      | $\bar{B} = \bar{F} \bar{F}^T$                        | Symmetric Eulerian tensor                |
| $\bar{E}$ Green-Lagrange tensor         | $\bar{E} = \frac{1}{2}(\bar{C} - \bar{I})$           | Symmetric Lagrangian tensor              |
| $\bar{A}$ Almansi-Euler tensor          | $\bar{A} = \frac{1}{2}(\bar{I} - \bar{B}^{-1})$      | Symmetric Eulerian tensor                |
| $\bar{L}$ spatial velocity gradient     | $\bar{L} = \dot{\bar{F}} \bar{F}^{-1}$               | Non-symmetric Eulerian tensor            |
| $\bar{D}$ rate deformation tensor       | $\bar{D} = \frac{1}{2}(\bar{L} + \bar{L}^T)$         | Symmetric Eulerian tensor                |
| $\bar{\sigma}$ Cauchy tensor            | $\bar{\sigma}$                                       | Symmetric Eulerian tensor                |
| $\bar{P}$ first Piola-Kirchhoff tensor  | $\bar{P} = J \bar{\sigma} \bar{F}^{-T}$              | Non-symmetric Eulerian/Lagrangian tensor |
| $\bar{S}$ second Piola-Kirchhoff tensor | $\bar{S} = J \bar{F}^{-1} \bar{\sigma} \bar{F}^{-T}$ | Symmetric Lagrangian tensor              |

**Table 2.6-** Principal concepts employed in the large deformation theory

Moreover, as previously mentioned, the behaviour of an elastomer has to conform to the two fundamental principles of the thermodynamics, presented in Table 2.7, and more precisely to a combination of both, called the inequality of Clausius-Duhem.

| Principle                    | Equations                                                                                                   | Symbol and designation                                                                                                                                                                                                      |
|------------------------------|-------------------------------------------------------------------------------------------------------------|-----------------------------------------------------------------------------------------------------------------------------------------------------------------------------------------------------------------------------|
| Conservation of mass         | $\frac{D\rho}{Dt} + \rho \operatorname{div}(\vec{V}) = 0$                                                   | $\rho$ density (kg/m <sup>3</sup> )<br>$\vec{V}$ velocity vector (m/s)                                                                                                                                                      |
| Equilibrium equations        | $\operatorname{div}(\bar{\sigma}) + \rho \vec{f}_m = \rho \vec{\gamma}$<br>$\vec{T} = \bar{\sigma} \vec{n}$ | $\vec{f}_m$ volume force per mass unit<br>$\vec{\gamma}$ acceleration vector (m/s <sup>2</sup> )<br>$\vec{T}$ Stress vector of normal $\vec{n}$                                                                             |
| First law of thermodynamics  | $\rho \frac{Du}{Dt} = \bar{\sigma} : \bar{D} - \operatorname{div}(\vec{q}) + r$                             | <u>Internal energy:</u><br>$U = \int \rho u \, dv$<br><u>Thermal power:</u><br>$P_{cal} = - \int \vec{q} \vec{n} \, ds + \int r \, dv$<br>$\vec{q}$ heat fluxes (W/m <sup>2</sup> )<br>$r$ heat sources (W/m <sup>3</sup> ) |
| Second law of thermodynamics | $\rho \frac{Ds}{Dt} = \frac{r}{T} - \operatorname{div}\left(\frac{\vec{q}}{T}\right) + \frac{\phi}{T}$      | <u>Entropy:</u><br>$S = \int \rho s \, dv$<br><u>Internal production of entropy:</u><br>$\frac{\phi}{T}$                                                                                                                    |

**Table 2.7-** Fundamental mechanic and thermodynamic equations

The Clausius-Duhem's inequality is obtained, in its Eulerian form, by injecting the first principle in the second principle, with the aim to suppress the heat sources  $r$ , as shown in equation (2.4).

$$\frac{\phi}{T} = \rho \frac{Ds}{Dt} + \operatorname{div}\left(\frac{\vec{q}}{T}\right) + \frac{1}{T} \left( -\rho \frac{Du}{Dt} + \bar{\sigma} : \bar{D} - \operatorname{div}(\vec{q}) \right) \quad (2.4)$$

This last equation can be rewritten by using the relations existing between the divergence and the gradient as:

$$\phi = \rho \left( T \frac{Ds}{Dt} - \frac{Du}{Dt} \right) + \bar{\sigma} : \bar{D} - \vec{q} \overrightarrow{\operatorname{grad}}(T) \quad (2.5)$$

Then, by considering that the internal production of entropy is always positive, i.e.  $\phi \geq 0$ , and introducing the Helmholtz free energy function  $\psi = u - Ts$ , the inequality of Clausius-Duhem in the Eulerian formulation can be established:

$$\phi = -\rho \left( \frac{D\psi}{Dt} + s \frac{DT}{Dt} \right) + \bar{\sigma} : \bar{D} - \frac{\bar{q}}{T} \overrightarrow{\text{grad}}(T) \geq 0 \quad (2.6)$$

However, within the framework of the solid continuum mechanics, the Lagrangian or the mixed formulations are more commonly employed. Hence, regarding the large deformations of the elastomers, only the mixed form will be conserved in the following paragraphs, see Eq. (2.7):

$$-\rho_0 \left( \frac{D\psi}{Dt} + s \frac{DT}{Dt} \right) + \bar{P} : \dot{\bar{F}} - \frac{\bar{Q}}{T} \overrightarrow{\text{grad}}(T) \geq 0 \quad (2.7)$$

With  $\rho_0$  the density in the initial configuration,  $\rho_0 = J\rho$ ,  
 $\bar{Q}$  the heat fluxes in the initial configuration,  $\bar{Q} = J\bar{F}^{-1}\vec{q}$ .

At this step, the physical definition of a hyperelastic material has to be set properly. Thus, several assumptions are made on the material behaviour:

- The elastomer should possess an initial configuration free of any stress.
- The spatial distribution of the macromolecule should be homogeneous. The material can therefore be regarded as a uniform and continuous solid.
- No dissipation of energy, i.e. all the transformations are reversible and consequently the inequality of Clausius-Duhem Eq. (2.7) becomes equality. This induces that the damages, continuous or discontinuous, have to be neglected.
- In the rubbery state, the material is independent on the temperature variations. Hence, the free-Helmholtz free-energy function, describing the elastomer behaviour, only depends on the deformations, i.e.  $\psi = \psi(\bar{F})$ .

With regards to the aforementioned hypotheses, the equation Eq. (2.7) can be reduced to:

$$\left( -\rho_0 \frac{D\psi(\bar{F})}{D\bar{F}} + \bar{P} \right) : \dot{\bar{F}} = 0 \quad (2.8)$$

The last notion to be inserted to the equation Eq. (2.8) corresponds to the strain energy function  $W(\bar{F}) = \rho_0 \psi(\bar{F})$ . The fundamental material law, linking the stresses to the deformations, is finally set up:

$$\bar{P} = \frac{DW(\bar{F})}{D\bar{F}} \quad (2.9)$$

Thus, to completely characterize the material behaviour of elastomers, only the mathematical definition of the strain energy function  $W$  is of importance. This principle constitutes the basis of the existing phenomenological models. In this context, a large number of tests under different uniaxial or multiaxial actions have to be performed to generate the strain energy function fitting the best the experimental results. Nevertheless, this last function has to obey some rules:

- The normalization condition, for which, at zero deformation, the strain energy potential should be nil, i.e.  $W(\bar{I}) = 0$  with  $\bar{I}$  the identity tensor.
- The positive condition, for which the strain energy function should increase with the deformation, i.e.  $W(\bar{F}) \geq 0$ .
- The objectivity principle, for which the material law should be frame indifferent, i.e. invariant regardless of the observer.
- For isotropic elastomer, the compatibility regarding the material symmetries. The material law should be unchanged regardless of the selected orientation, in other words unchanged by any rotation, i.e.  $W(\bar{F}) = W(\bar{F}\bar{Q}^T)$  with  $\bar{Q}$  an orthogonal tensor.

In addition, with the definitions of the strain tensors given in Table 2.6, determining the form of the strain energy function in terms of the deformation gradient tensor  $\bar{\bar{F}}$  is equivalent to determining the strain energy function in terms of the left Cauchy-Green tensor  $\bar{\bar{B}}$ . This last definition is preferably employed in finite element codes because of the symmetry of the left Cauchy-Green tensor. And, considering the isotropy of the material, the strain energy potential can directly be expressed in function of the invariants of  $\bar{\bar{B}}$ :

$$W(\bar{\bar{B}}) = W(I_1(\bar{\bar{B}}), I_2(\bar{\bar{B}}), I_3(\bar{\bar{B}})) \quad (2.10)$$

$$\text{With} \quad \left\{ \begin{array}{l} I_1(\bar{\bar{B}}) = \text{Tr}(\bar{\bar{B}}) \\ I_2(\bar{\bar{B}}) = \frac{1}{2} [\text{Tr}(\bar{\bar{B}})^2 - \text{Tr}(\bar{\bar{B}}^2)] \\ I_3(\bar{\bar{B}}) = \det(\bar{\bar{B}}) = \det(\bar{\bar{F}} \bar{\bar{F}}^T) = J^2 = 1 \end{array} \right. \quad \begin{array}{l} (2.11a) \\ (2.11b) \\ (2.11c) \end{array}$$

The assumption of incompressibility allows to set the third invariant equal to 1 and to reduce the definition of the strain energy potential of equation Eq. (2.10) to the first two invariants.

Within this framework, several experiments in uniaxial/biaxial tension, compression and shear were carried out on elastomers to obtain a mathematical form for the strain energy potential. The most well-know and widely used forms are the following ones:

i. Polynomial form

$$W = \sum_{i+j=1}^N C_{ij} (I_1 - 3)^i (I_2 - 3)^j \quad (\text{PF})$$

ii. Mooney-Rivlin form

$$W = C_{10}(I_1 - 3) + C_{01}(I_2 - 3) \quad (\text{MR})$$

iii. Reduced polynomial form

$$W = \sum_{i=1}^N C_{ij} (I_1 - 3)^i \quad (\text{RPF})$$

iv. Yeoh form

$$W = C_{10}(I_1 - 3) + C_{20}(I_1 - 3)^2 + C_{30}(I_1 - 3)^3 \quad (\text{Y})$$

v. Neo-Hookean form

$$W = C_{10}(I_1 - 3) \quad (\text{NH})$$

In all the evoked models,  $C_{ij}$  and  $N$  are material parameters. While the  $C_{ij}$  can be real numbers,  $N$  is always an integer. The most general form of the strain energy potential corresponds to the polynomial form, from which derivate the other models. For example, the Mooney-Rivlin law can be obtained from the polynomial form by setting  $N = 1$ , while the reduced polynomial form is achieved by simply choosing  $j = 0$ . Simple linear least square methods can be employed to fit the experimental stress-strain results and calculate the  $C_{ij}$  coefficients. Consequently, these models encounter a large popularity in behalf of the easy determination of the material constants.

Even if, the previous models are able to describe the material behaviour for strains up to 100%, they do not possess sufficient accuracy to model the behaviour at low deformations. Therefore, one

method developed by Amin [2.52], to properly model high-damping rubber in compression and shear on all their deformations range consisted in considering the exponents of the polynomial terms as real numbers.

vi. Amin form

$$W = C_5(I_1 - 3) + \frac{C_3}{N+1}(I_1 - 3)^{N+1} + \frac{C_4}{M+1}(I_1 - 3)^{M+1} + C_2(I_2 - 3) \quad (A)$$

With  $C_i$ ,  $N$  and  $M$  material parameters, which are all real numbers. These coefficients are evaluated with the help of a non-linear least square method. Nevertheless, in spite of the relative good fitting of the experimental results, this form is only valid for uniaxial tests in tension or compression and shear. Indeed, if the non-integer exponents are inferior to 1, the strain-energy function does not respect the normalization condition.

In addition, other forms of the strain energy potential were developed to compensate for the lack of precision at very large deformations up to 200% of the “simple” models, i.e. from i. to v., such as:

vii. Gent-Thomas form

$$W = A(I_1 - 3) + B \ln\left(\frac{I_2}{3}\right) \quad (GT)$$

With  $A$  and  $B$  material parameters (real numbers). As for the Amin model and due to the presence of a logarithmic function, a non-linear least square method has to be applied to determine the coefficients  $A$  and  $B$ .

viii. Ogden form

$$W = \sum_{i=1}^N \frac{2\mu_i}{\alpha_i^2} (\lambda_1^{\alpha_i} + \lambda_2^{\alpha_i} + \lambda_3^{\alpha_i} - 3) \quad (O)$$

With  $\lambda_i$  the principal stretches and  $N$ ,  $\mu_i$ ,  $\alpha_i$  material parameters to be evaluated from testing. While  $\mu_i$  and  $\alpha_i$  are real numbers,  $N$  is an integer. In this equation, Ogden [2.56] postulates, that the strain energy potential could directly be expressed in function of the principal stretches. This law fits well the behaviour of the material under large deformations, but requires a large amount of data with at least uniaxial and equibiaxial experiments due to the existence of multiple optimum sets of material coefficients. Moreover, a non-linear least square method has to be employed to evaluate the material parameters.

### b. Probabilistic models

As shown on Figure (Fig. 2.17), elastomers exhibit a stiffening third zone. Therefore, the idea behind the probabilistic models consists in assuming that the entropy diminishes importantly in this zone. This decrease of entropy is interpreted as an orientation of the macromolecules in the direction of the applied force. The determination of the entropy variation is first realized on a simple polymer chain, before being extended to a network of chains, i.e. to the whole material. A chain is supposed to be constituted of  $n$  sections of identic length  $l$  with no restrictions on the angles between the sections. At this step, two theories were developed considering or not the limit of extensibility of the chain, i.e. the Gaussian models, for which the chain is free to indefinitely extend and the non-Gaussian models, accounting for the finite elongation of the chain.

Nevertheless, these both theories are based on the first and second laws of the thermodynamics. The assumption of reversibility is conserved and it is conceded that the transformation takes place under constant temperature. Thus, the second law of the thermodynamics can be reformulated as:

$$\Delta U = \Delta W + T\Delta S \quad (2.12)$$

$\Delta U$  the variation of internal energy,  
 With  $\Delta S$  the variation of entropy,  
 $\Delta W$  the variation of strain energy.

In addition, as the transformation is reversible and cyclic, meaning that the material recovers its initial dimensions, the variation of internal energy is nil, i.e.  $\Delta U = 0$ . Thus, the following equation, linking the strain energy to the entropy can be obtained:

$$\Delta W = -T\Delta S \quad (2.13)$$

An expression of the entropy was proposed by Boltzmann to account for all the possible configurations of the polymer chain, see Eq. (2.14).

$$S = k \ln(\Omega(\vec{r})) \quad (2.14)$$

$k$  the Boltzmann's constant ( $k = 1.381 \times 10^{-23} \text{ JK}^{-1}$ ),  
 With  $\Omega(\vec{r})$  the number of possible configurations,  
 $\vec{r}$  the end-to-end chain vector.

Hence, to characterize the entropy, the number of possible configurations had to be evaluated and statistical theories had to be introduced. When one end of the chain is fixed, the probability  $P$  that the second end of the chain is within a small volume  $dxdydz$  is of high interest, as this probability is directly proportional to the number of possible configurations.

$$\Omega(\vec{r}) = A \cdot P(\vec{r}) \quad (2.15)$$

Finally, the both Gaussian and non-Gaussian theories distinguish themselves by the different assumptions leading to different forms of the probability  $P(\vec{r})$ .

#### i. Gaussian model

For the Gaussian models, the elongation of the chain is not limited and the junctions between the sections are supposed to move with the deformations. The probability that the one end of the chain is within a small volume  $dxdydz$ , while the other end is fixed on an orthonormal basis, is described by a Gaussian probability function:

$$P(x, y, z)dxdydz = \frac{b^3}{\pi^{3/2}} \exp(-b^2(x^2 + y^2 + z^2)) dxdydz \quad (2.16)$$

With  $b^2 = 3/(2nl^2)$  and  $n$  the number of sections of length  $l$ . By setting  $r^2 = x^2 + y^2 + z^2$ , the probability becomes:

$$P(r) = \frac{b^3}{\pi^{3/2}} \exp(-b^2r^2) \quad (2.17)$$

Then re-injecting this last equation in equation Eq. (2.14) allows obtaining a general expression of the entropy for one chain:

$$S = c - kb^2r^2 \quad (2.18)$$

With  $c$  a constant. By writing the variation of entropy for one chain and considering that the total entropy of the elastomer is equivalent to the sum of the entropy of all constituting chains, it is then possible to arrive at the following equation:

$$\Delta S = -\frac{1}{2}nk(\lambda_1^2 + \lambda_2^2 + \lambda_3^2 - 3) \quad (2.19)$$

With  $\lambda_i$  the elongation of the materials in the  $i$  direction. So the final form of the strain energy variation is achieved by inserting Eq. (2.18) into Eq. (2.13).

$$\Delta W = \frac{1}{2}nkT(I_1(\bar{\bar{B}}) - 3) \quad (\text{GM})$$

With  $I_1(\bar{\bar{B}}) = \text{Tr}(\bar{\bar{B}}) = \lambda_1^2 + \lambda_2^2 + \lambda_3^2$ . A comparison of this law to the phenomenological models allows establishing the similitude with the Neo-Hookean model. The only difference arises from the temperature dependency of the probabilistic model, even if this last was considered constant to find this material law. Nevertheless, as for the Neo-Hookean law, this formulation characterizes correctly the material for deformations up to 100%, which is lower than the total elongation at break. This limitation is explained by the non-finite deformation of the chains, without increase of stiffness, as they are free to extend.

## ii. Non-Gaussian models

To compensate for the inaptitude of the Gaussian models to represent the behaviour at large strains, especially for the stiffening appearing, another formulation of the probability function was proposed. This approach supposes that the chains possess a finite elongation. Therefore, when the maximum elongations of the sections of a polymer chain are reached, the force is transmitted through the junction points. This concept was postulated by Wang and Guth [2.57], who defined the tensile force acting on a chain as:

$$f = \left(\frac{kT}{l}\right)L^{-1}\left(\frac{r}{nl}\right) \quad (2.20)$$

With  $L$  the Langevin function defined by  $L(x) = \coth(x) - 1/x$ . With regards to the complexity of this function, a Taylor expansion is generally applied and the expression of the tensile force evolves into:

$$f = \left(\frac{kT}{l}\right)\left[3\left(\frac{r}{nl}\right) + \frac{9}{5}\left(\frac{r}{nl}\right)^3 + \frac{297}{175}\left(\frac{r}{nl}\right)^5 + \frac{1539}{875}\left(\frac{r}{nl}\right)^7 + \dots\right] \quad (2.21)$$

Consequently, the chain acts as a finite non-linear spring in reason of the polynomial terms. The probability function is also described by this Langevin function, so as the configurational entropy of the chain. By using the Boltzmann's equation Eq. (2.14) with the expression of the probability function  $P$ , the entropy becomes:

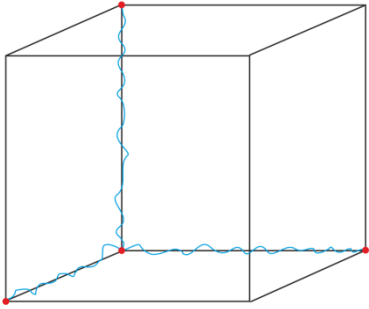
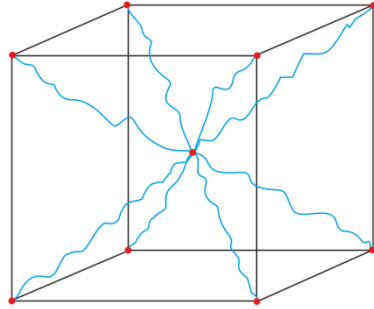
$$S = c - kn\left[\frac{r}{nl}\beta + \ln\left(\frac{\beta}{\sinh(\beta)}\right)\right] \quad (2.22)$$

With  $\beta = L^{-1}(r/nl)$ .

At this step, several spatial configurations of the chains, depending on their number, were employed to characterize the behaviour of elastomers:

- 3-chain model of Wang and Guth [2.57]. In this model, one vertex of a parallelepiped constitutes the fixed point of three chains, whose directions corresponds to the ones of the adjacent edges.
- 8-chain model of Arruda-Boyce [2.58]. This fixed point of the 8 chains is assimilated to the centre of the parallelepiped and the diagonals give the orientation of the chains.

These models and the expression of the strain energy potential are summarized in Table 2.8.

| 3-chain model [2.57]                                                                                                                                                        | 8-chain model                                                                                                                                                                                                                    |
|-----------------------------------------------------------------------------------------------------------------------------------------------------------------------------|----------------------------------------------------------------------------------------------------------------------------------------------------------------------------------------------------------------------------------|
|                                                                                            |                                                                                                                                                |
| $W_{3-chain} = nkT \left[ b_1 \frac{I_1}{3} + \frac{b_2}{5} \left( I_1^2 - \frac{4}{3} I_2 \right) + \frac{b_3}{7} \left( I_1^3 - \frac{12}{5} I_1 I_2 \right) + c \right]$ | $W_{8-chain} = C_1 \left[ \frac{1}{2} (I_1 - 3) + \frac{1}{20\lambda_m^2} (I_1^2 - 9) + \frac{11}{1050\lambda_m^4} (I_1^3 - 27) + \frac{19}{7000\lambda_m^6} (I_1^4 - 81) + \frac{519}{673750\lambda_m^8} (I_1^5 - 243) \right]$ |
| With $b_i$ material parameters and $c$ a constant                                                                                                                           | With $C_1$ material parameter and $\lambda_m$ locking stretch                                                                                                                                                                    |

**Table 2.8-** Strain-energy potential of non-Gaussian hyperelastic models

The 8-chain model presents the advantage of a smaller number of coefficients compared to the 3-chain model. But, a nonlinear least square method has to be employed to determine its coefficients, while a linear least-square method can be used for the 3-chain coefficients. Nevertheless, in spite of the physical interpretation of these theories, the coefficients in the aforementioned models have to be determined with the help of intensive tests, as for the phenomenological models.

### Extension to compressibility

As explained in paragraph 2.4.2.1, the hypothesis of incompressibility is not valid for confined elastomers. Therefore, when the material can undergo some volume changes, a new definition of the strain energy potential  $W(\bar{\mathbf{F}})$  has to be formulated. The idea proposed by Flory [2.59], consisting in the decomposition of deformation into a volumetric part and an isochoric part, has to be adopted. The deformation gradient tensor  $\bar{\mathbf{F}}$  is written as follows:

$$\bar{\mathbf{F}} = J^{1/3} \bar{\mathbb{F}} \quad (2.23)$$

Where  $J^{1/3}$  account for the volume-changing deformations,  $J$  being the Jacobian of the deformation tensor  $\bar{\mathbf{F}}$  ( $J = \det(\bar{\mathbf{F}})$ ) and  $\bar{\mathbb{F}}$  corresponding to the volume-preserving deformation tensor. The decoupled form of the strain energy function  $W$  based on the kinematic assumption of Eq. (2.23) becomes:

$$W(\bar{\mathbf{F}}) = W_{iso}(\bar{\mathbb{F}}) + W_{vol}(J) \quad (2.24)$$

With  $W_{iso}(\bar{\mathbb{F}})$  the isochoric part of the strain energy tensor (identic to incompressible case),  
 $W_{vol}(J)$  the volumetric part of the strain energy tensor.

In addition, as for the incompressible case, it is equivalent to write the strain energy function in terms of the deformation tensor and in terms of the left Cauchy-Green tensor. Thus the deviatoric stretch tensor  $\bar{\mathbb{B}}$  can be defined, in a similar way to the left Cauchy-Green strain tensor, as  $\bar{\mathbb{B}} = \bar{\mathbf{F}}\bar{\mathbf{F}}^T$ . And with



the isotropy of the material, the function  $W(\bar{\mathbb{B}})$  can be described in terms of the deviatoric strain invariants  $\bar{I}_1$  and  $\bar{I}_2$  ( $\bar{I}_3 = 1$ ) as:

$$W(\bar{\mathbb{B}}) = W_{iso}(\bar{\mathbb{B}}) + W_{vol}(J) = W_{iso}(\bar{I}_1(\bar{\mathbb{B}}), \bar{I}_2(\bar{\mathbb{B}})) + W_{vol}(J) \quad (2.25)$$

With respect to the fundamental rules imposed on the strain energy potential, i.e. the normalization condition, the positive condition, the objectivity principle and the material symmetries, several laws for the volumetric part were proposed, see Table 2.9.

| Designation                        | $W_{vol}(J)$                                       |
|------------------------------------|----------------------------------------------------|
| Sussman and Bathe (Abaqus®) [2.60] | $\frac{K}{2}(J-1)^2$                               |
| Simo, Taylor and Pister [2.61]     | $\frac{K}{2}(\ln(J))^2$                            |
| Ogden [2.62]                       | $\frac{K}{\beta^2}(\beta \ln(J) + J^{-\beta} - 1)$ |
| Simo and Miehe [2.63]              | $\frac{K}{2}(J^2 - 1 - 2 \ln(J))$                  |

**Table 2.9-** Volumetric part of the strain energy potential

### Consideration of cyclic effects

To account for the damages induced by cyclic loadings, more particularly for the discontinuous Mullins' effect, Ogden and Roxburgh [2.64] proposed to include in the definition of the strain energy potential of Eq. (2.25) a scalar variable  $\eta$ , also referred as damage variable such as  $0 \leq \eta \leq 1$ . This factor does not affect the volumetric strain energy function, as the volume variations are very small. Only the isochoric strain energy function is affected by the damage variable. For the first loading,  $\eta = 1$  to conserve the original form of the strain energy function. The new constitutive material law is given as follows:

$$W(\bar{\mathbb{B}}, \eta) = \eta W_{iso}(\bar{I}_1(\bar{\mathbb{B}}), \bar{I}_2(\bar{\mathbb{B}})) + \Phi(\eta) + W_{vol}(J) \quad (2.26)$$

Where  $\Phi(\eta)$  corresponds to a damage function, with  $\Phi(1) = 0$ . This function can be interpreted as a measure of the energy required to damage the elastomer. The material behaviour in the unloading following the first loading depends clearly on the maximum reached deformation or in an equivalent way on the maximum reached strain energy. Thus, both the damage parameter and the damage function have to be written in terms of the actual strain energy function and the previously maximum energy encountered  $W_m$ . Continuously checking the difference between these two values allows "activating" or "deactivating" the damage parameter during the further loadings and unloadings. The final expressions for  $\eta$  and  $\Phi(\eta)$ , established by Ogden and Roxburgh are:

$$\eta = 1 - \frac{1}{r} \operatorname{erf} \left[ \frac{1}{m} \left( W_m - W_{iso}(\bar{I}_1(\bar{\mathbb{B}}), \bar{I}_2(\bar{\mathbb{B}})) \right) \right] \quad (2.27)$$

With  $m$  and  $r$  material constants,  
 $\operatorname{erf}$  the error function defined by  $\operatorname{erf}(x) = \frac{2}{\sqrt{\pi}} \int_0^x \exp(-w^2) dw$ .

$$-\Phi'(\eta) = m \operatorname{erf}^{-1}[r(\eta - 1)] + W_m \quad (2.28)$$

With  $\operatorname{erf}^{-1}$  the inverse of the error function.

## 2.4.3 Thermoset material laws

### 2.4.3.1 Thermomechanical behaviour

The glass transition temperature of thermosets is generally superior to the ambient temperature, in contrary to elastomers. Thus, for façade application, thermosets are in their glassy state and often not so far from the transition state, see Fig. 2.20. Consequently, these materials are, most of the time, temperature-dependent. Regarding the types of adhesive, the influences of the temperatures and of the loading rates, four types of behaviour, see Fig. 2.25, can be envisaged:

- A brittle behaviour associated to curve (I). This behaviour is observed for thermosets at high loading rate or low temperature. Epoxy resins present mainly this kind of behaviour, for which elevated forces are achieved under very small deformations. The most important data for design are the strength, the strain at breakage and the Young's modulus.
- A ductile behaviour with yield point, represented by curve (II), which is the most common behaviour for thermosets. The stress-strain diagram can be divided in three main parts, i.e. a first linear or non-linear viscoelastic part from zero deformation to the yield point, a second softening part between the yield point and the minimum threshold and finally a last hardening part until breakage. At the yield point, the necking of the sample starts at the center of the sample and extends to the extremities. Therefore, measuring the changes in the section of the sample becomes impossible without the use of video-controlled equipment. Hence, the most useful values for design are the stress and strain at the yield point and the elastic modulus. When the minimum threshold is attained, large molecular reorientations lead to a hardening of the material before rupture. For some thermosets, the elongation at break can occur at very large strains up to 1000%.
- A ductile behaviour without yielding, corresponding to curve (III). This behaviour is typical of resilient crystalline polymer. Stress and strain at breakage are the most common values, but a conventional yield point is determined, either according to the ASTM D638 [2.65] or the EN ISO 527 [2.66]. The ASTM standard defines this point as the intersection of the parallel of the tangent at the origin at a defined strain (0,1 to 1%) and the curve. In the ISO standard, this yield point corresponds to the intersection of the curve with a determined deformation.
- A soft behaviour, curve (IV), which can be found at high temperatures (over the glass transition temperature). This curve possesses a high degree of similarity with the one of an elastomer. The strength, the strain at failure and the Young's modulus, chosen as a secant modulus at 100% or 200% of deformation, constitute essential information.

In the following paragraphs, a particular attention will be paid on material law describing the curve (II), as the latter is the most recurrent.

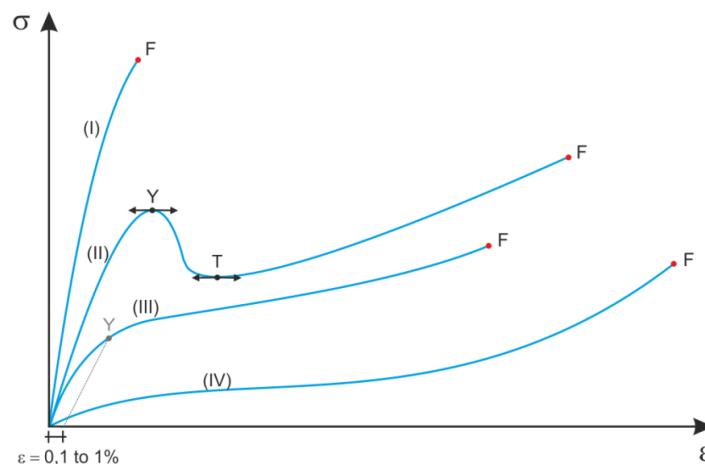


Figure 2.25- Typical stress-strain diagrams of thermosets

As briefly mentioned, the mechanical behaviour of thermosets varies also with the applied loading rates, see Fig. 2.26. Higher is the loading rate and higher are the yield point and the strength. The applied velocity is such that the microscopic rearrangements of the chains are not feasible. This phenomenon is observable for the three main modes of deformation.

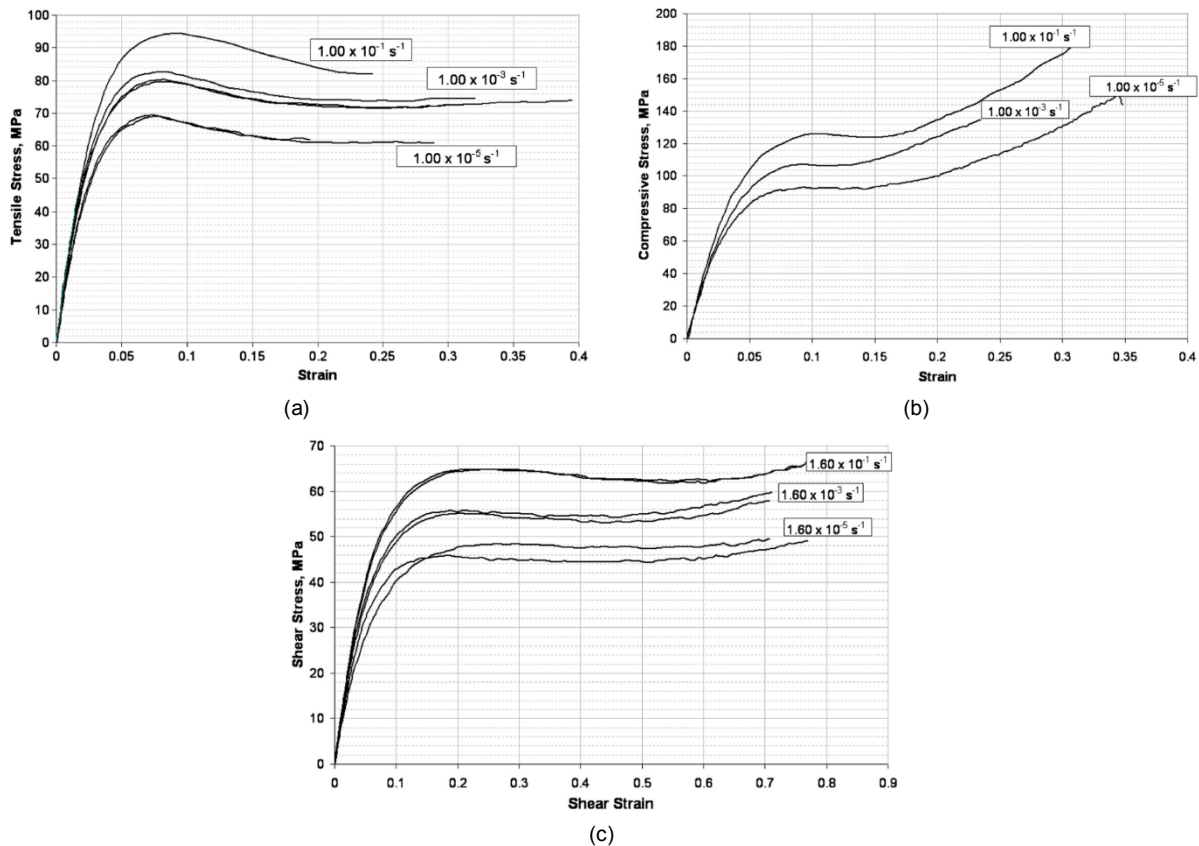


Figure 2.26- Tensile (a), Compressive (b) and Shear (c) stress-strain diagrams for Epoxy E862 [2.67]

Form the previous Fig. 2.22, it can also be noted that the behaviour in tension of thermosets differs to the behaviour in compression, which implies that pressure-dependent criterion are often employed.

Another crucial property for the design of an adhesive connection corresponds to the long-term behaviour, obtained with creep, relaxation or fatigue experiments. These data are important to characterize the lost in rigidity of the adhesive during its time in use, which is a consequence of the molecular relaxations at the micro-scale. On Fig. 2.27 is represented a relaxation test conducted by Chiu on a stiff epoxy resin. As it can be noted, a consequent loss of stiffness, of about 25%, occurs after the first ten seconds. Then the decrease is progressive and can extend over a long period.

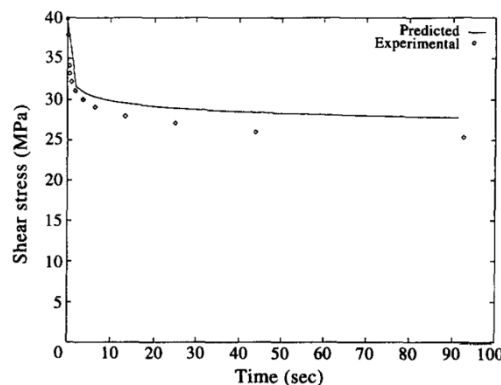


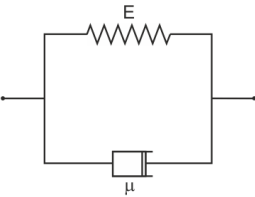
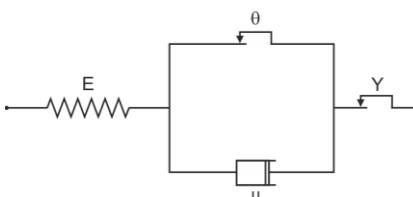
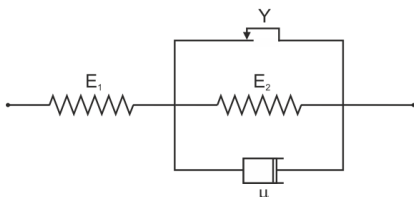
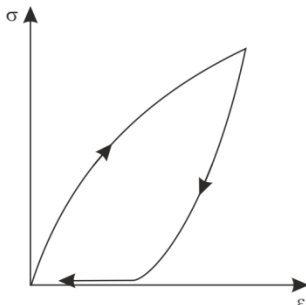
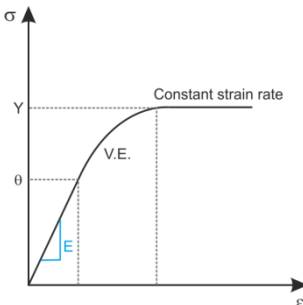
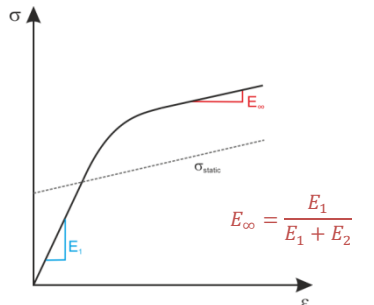
Figure 2.27- Relaxation test on thermoset adhesive FM73 [2.68]

Carrying long-term tests on time equivalent to the reality is rarely done, as some adhesive connection can last for 50 years. Therefore some principles are used to extrapolate test results, during 6 months to 1 year, to real lifetime. The most employed method is based on the time-temperature superposition criteria [2.69] established by Williams, Landel and Ferry (WLF). Tests are carried out at different selected temperatures, frequently higher than the maximum in-use temperature to create an accelerated damage, and during a predefined duration. Then a sliding on the time axis of the curves representing the elevated temperatures is realized to obtain one single and principal curve describing the behaviour at long-term. Nevertheless, this procedure is limited to a small temperature range (100K) near the glass transition temperature.

### 2.4.3.2 Existing material laws

#### One-dimension models

As mentioned previously, only the behaviour corresponding to the curve (II) will be explored. Moreover, as it is relatively difficult to record the correct stress after the yield point, due to the necking of the sample, the majority of the simple models are centered on the first part of the curve, i.e. up to the yield point. The one-dimension behaviour of thermosets, obtained with the help of uniaxial experiments such as tension or compression, can be correctly modeled with some 1D rheological models. In the first portion of the stress-strain curve, the material is characterized by linear or non-linear viscoelastic behaviour. Thus, three corresponding models were found in the literature and are presented in Table 2.10.

| Kelvin Model (KM)                                                                   | Bingham Model (BM)                                                                                                                                                                                              | Chase-Goldsmith Model (CGM)                                                                                                                                                                                                                                                                                                                                   |
|-------------------------------------------------------------------------------------|-----------------------------------------------------------------------------------------------------------------------------------------------------------------------------------------------------------------|---------------------------------------------------------------------------------------------------------------------------------------------------------------------------------------------------------------------------------------------------------------------------------------------------------------------------------------------------------------|
|  |                                                                                                                              |                                                                                                                                                                                                                                                                           |
| $\dot{\epsilon} + \frac{E}{\mu} \epsilon = \frac{\sigma}{\mu}$                      | $\sigma = E\epsilon \quad \text{for } \sigma \leq \theta$ $\dot{\epsilon} = \dot{\sigma} + \frac{(\sigma - \theta)}{\mu} \quad \text{for } \theta < \sigma \leq Y$ $\sigma = Y \quad \text{for } \sigma \geq Y$ | $\sigma = E\epsilon \quad \text{for } \sigma \leq \sigma_{static}$ $\dot{\epsilon} = \frac{\dot{\sigma}}{E_1} + \frac{(\sigma - \sigma_{static})}{\mu'} \quad \text{for } \sigma \geq \sigma_{static}$ $\text{With } \sigma_{static} = \left[ \frac{E_1}{E_1 + E_2} \right] (Y + E_2 \epsilon)$ $\text{and } \mu' = \left[ \frac{E_1}{E_1 + E_2} \right] \mu$ |
|  |                                                                                                                              |                                                                                                                                                                                                                                                                          |

**Table 2.10-** One-Dimension rheological models for thermosets characterization

The first rheological model (KM) corresponds to the model of Kelvin, which is the most well-known model for viscoelastic solid. A linear spring is placed in parallel to a linear dashpot leading to a delayed elasticity and a delayed reversibility. With this model, a relaxation test results in an immediate decrease in stress, which will then remain at a fixed value. To account for damage of the polymer, other models based on the overstress concept were developed. The two last models exposed in Table

2.10 follow this idea. The Bingham model (BM) possess two “termination points”  $\theta$  and  $Y$  allowing defining three distinctive zones, i.e. a first fully linear part from zero stress to first termination point  $\theta$ , a second zone viscoelastic until  $Y$  and a last part at fixed stress. When the stress is superior to  $\theta$ , sliding element activated, the behaviour is similar to the one of the Maxwell model. However the plateau at constant stress does not reflect the reality for all polymers. Therefore a three parameters model was proposed by Chase and Goldsmith (CGM) to compensate this point. Adding in the parallel branch another linear spring allowed them to introduce a limit  $\sigma_{static}$  evolving linearly with the deformation. In consequence, the last portion of the curve evolves with this limit.

Another simple equation allowing describing the stress-strain curve of uniaxial test was established by Ramberg-Osgood [2.70]. For this model, only three parameters are needed, i.e. the Young's modulus and two secant yield strengths. The total strain is expressed as the sum of the elastic strain and an inelastic strain, see Eq. (2.26).

$$\varepsilon = \frac{\sigma}{E} + K \left( \frac{\sigma}{E} \right)^n \quad (2.26)$$

With  $E$  the Young's modulus,  $K$  and  $n$  material constants. This equation was first proposed to model the behaviour of soft alloys, such as aluminium, but also proved useful to describe the behaviour of polymers. In its original form, the previous equation is inapt to account for the loading-rate dependency presented in paragraph 2.4.3.1. Hence, McLellan [2.71] proposed to modify the equation of Ramberg-Osgood and more particularly the expression of the parameters  $K$  and  $E$ , see Eq. (2.27). Tests on several materials demonstrated the invariance of the factor  $n$  and the rate-dependency of the two other factors.

$$K(\dot{\varepsilon}) = a\dot{\varepsilon}^b \quad (2.27a)$$

$$E(\dot{\varepsilon}) = c\dot{\varepsilon}^d \quad (2.27b)$$

With  $a, b, c$  and  $d$  material constants. The modified form consists in simply injecting the Eq. (2.27) in the initial form of the Ramberg-Osgood Eq. (2.26):

$$\varepsilon = \frac{\sigma}{c\dot{\varepsilon}^d} + a'\dot{\varepsilon}^{b'}\sigma^n \quad (2.28)$$

With  $a'$  and  $b'$  material constants. This last equation was successfully used by Renieri [2.72] to model the rate- and time-dependent behaviour of two structural adhesives Metlbond 1113 and 1113-2, which were employed in composite materials.

### Unified constitutive models

Facing the difficulties to characterize properly the different characteristics of the polymer's behaviour, i.e. the elastic, viscoelastic and yield point, and their evolutions with the loading rates and the temperatures, unified constitutive models, first developed for alloys, were envisaged. After the yield point, the material properties are not recoverable, so this point can be considered as a limit of elasticity and, as for metals, as the beginning of “plasticity”. In the classical theory, the total strain corresponds to the sum of the elastic, viscoelastic, plastic, creep and thermal strains, see Eq. (2.29). Within the plasticity theory, the postulated criterions, e.g. Von Mises or Tresca criterions, are independent of loading rate. The time-dependency is only introduced with creep models. Thus the creep and plasticity terms are assumed independent, which does not reflect the reality and the coupling existing between them.

$$\varepsilon_{total} = \varepsilon_{elastic} + \varepsilon_{viscoelastic} + \varepsilon_{plastic} + \varepsilon_{creep} + \varepsilon_{thermal} \quad (2.29)$$

Consequently, the idea behind the unified constitutive theories is to regroup the viscoelastic, plastic and creep strains to form an inelastic strain accounting for these effects, see Eq. (2.30). This

formulation allow, on one hand, considering that the inelastic strain occurs at stresses below the yield point, but, on the other hand, the definition of yield surfaces is lost.

$$\varepsilon_{total} = \varepsilon_{elastic} + \varepsilon_{inelastic} + \varepsilon_{thermal} \quad (2.30)$$

In the following paragraph, the thermal expansions of the material are neglected, as the temperature variations acts preferentially on the properties of the polymers. Hence, only the elastic and inelastic strains have to be formulated. One of the more complete unified constitutive models, based on the overstress concept, was introduced by Ramaswamy [2.73]. For this model, the inelastic strain rate is described by:

$$\dot{\varepsilon}_{inelastic} = \dot{\varepsilon}_{ij}^I = D \exp \left[ -\frac{A}{2} \left( \frac{Z^2}{1.5 |\tilde{\sigma}_{ij}|^2} \right)^n \right] \frac{\tilde{\sigma}_{ij}}{|\sigma_{ij}|} \quad (2.31)$$

With  $A$ ,  $D$ ,  $n$  material constants evaluated with test results. The deviatoric stress is denoted by  $\sigma_{ij}$  and the overstress vector by  $\tilde{\sigma}_{ij} = \sigma_{ij} - \Omega_{ij}$ , where  $\Omega_{ij}$ , called the back stress vector, is defined by:

$$\dot{\Omega}_{ij} = f_1 \dot{\varepsilon}_{ij}^I - f_1 \frac{\Omega_{ij}}{\Omega_{sat}} \dot{\varepsilon}_{ij}^I + f_2 \dot{\sigma}_{ij} \quad (2.32)$$

With  $f_1$  and  $f_2$  material constants and  $\Omega_{sat}$  the maximum saturated back stress evaluated with test results. The scalar  $Z$  of Eq. (2.31), named drag stress vector, depends essentially on the accumulated inelastic work  $W^I$ .

$$\dot{Z} = m |Z - Z_{max}| \dot{W}^I \quad (2.33)$$

With  $m$  and  $Z_{max}$  material constants evaluated with test results. As it can be remarked, the determination of all the constants implies a large number of tests, uniaxial quasi-static tests under different loading rates, relaxation tests but also cyclic tests. In addition, at least two non-linear optimizations have to be performed to obtain on the one hand the back stress and on the other hand the drag stress. Thus, even if this model was successfully employed by Chiu [2.68] to characterize the behaviour of the thermoset FM73, its implementation requires too much tests.

### 3-dimension models

The previous evoked laws are able to characterize the one-dimensional behaviour of polymers, but are insufficient to evaluate shear from bulk tensile tests or to represent the complex stress distribution arising in the adhesive joint of a glass façade. Moreover, the behaviour of the thermoset could not be completely modeled, especially after the yield point. Consequently, other models were developed to account for the three-dimensional behaviour at large strains. The main concept behind these models consists in a decomposition of the non-linear stress  $\sigma^{NL}$  into an activation stress  $\sigma^A$  and a hardening stress  $\sigma^H$ .

$$\sigma^{NL} = \sigma^A + \sigma^H \quad (2.34)$$

The activation stress allows characterizing the behaviour of the material until the minimum threshold and including the yield point, while the hardening stress aims to essentially define the hardening at large strains. The superposition of the stress can be schematized with a simple rheological form, see Fig. 2.28, obtaining, for the uniaxial case, the behaviour of Fig. 2.29. The hardening stress is often assimilated to a non-linear spring, e.g. a Langevin spring or even the 3-chain model detailed for hyperelastic materials, and the major difficulty is to find a suitable form for the activation stress. Arruda [2.58] choose to use the theory from Argon to represent the activation stress by a viscous element, while Haward [2.74] employed an Eyring dashpot.

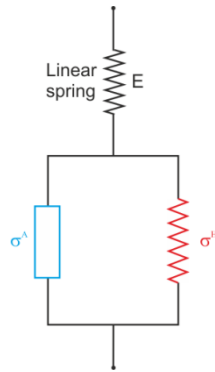


Figure 2.28- 3D rheological model

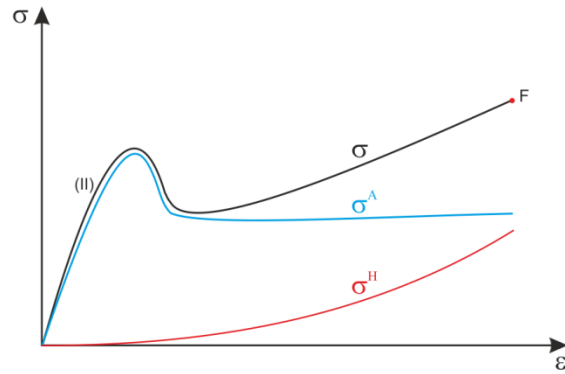


Figure 2.29- Uniaxial behaviour from the stress superposition

Other rheological models were created by Bergström, [2.75] to [2.78], to better fit the behaviour of thermosets, including strain rate and temperature effects, i.e. the dual network, the three network and the parallel network models, which extensively used the eight-chain non-Gaussian theory suggested by Arruda and Boyce. Nevertheless, all these models required a consequent number of parameters to be determined with test results.

## 2.4.4 Summary

All the essential properties, characterizing the elastomers and the thermosets, and the corresponding material laws are summarized in Fig. 2.30.

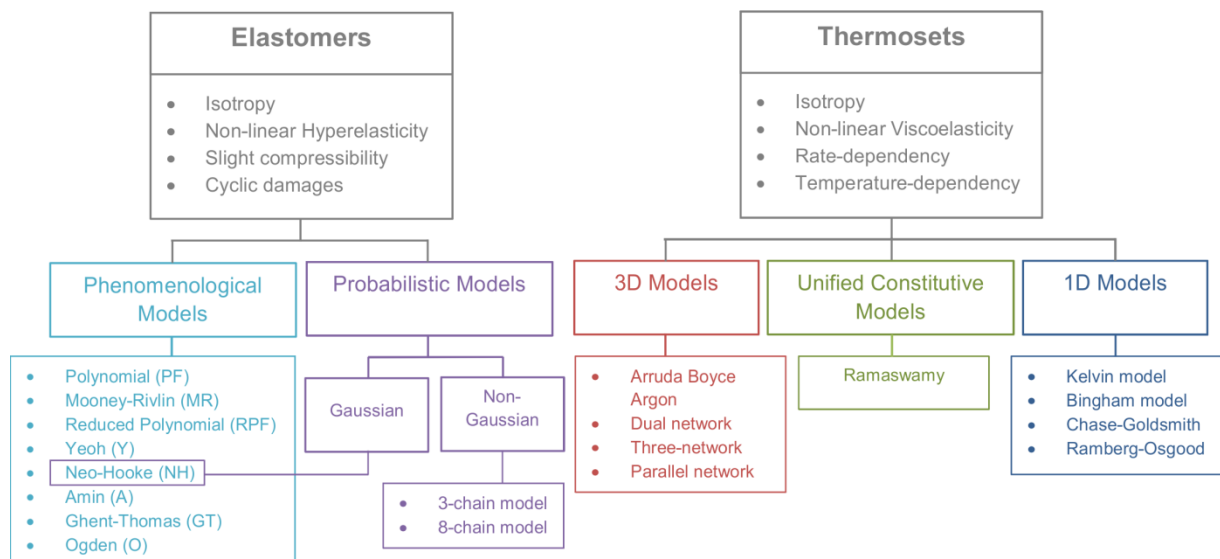


Figure 2.30- Materials laws summary





### 3. ENVISAGED STRUCTURAL CONNECTIONS

#### 3.1 INTRODUCTION

In this chapter, the steel to glass beam connections that will be studied experimentally and numerically are presented. Two approaches are foreseen, i.e. a fully adhesive approach and a hybrid mechanical adhesive approach. The employed products and possible domain of use of these two beams are introduced.

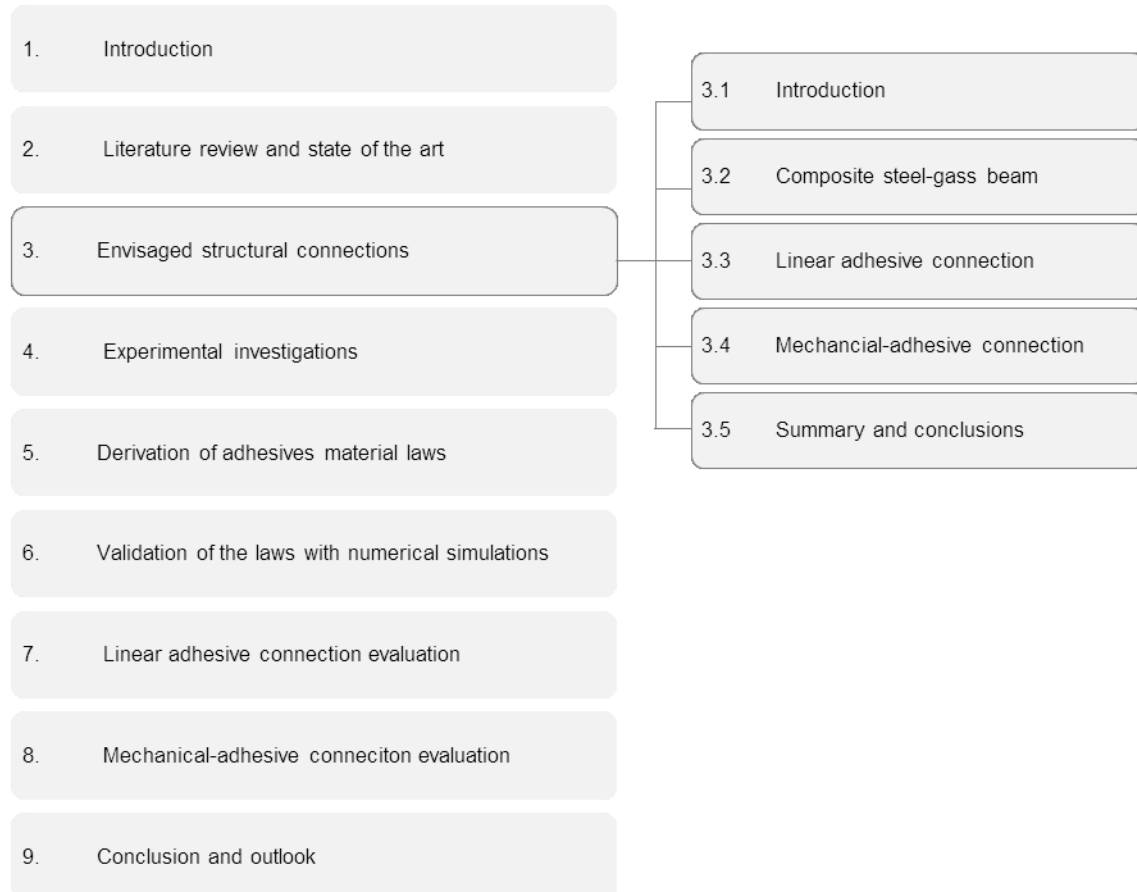


Figure 3.0- Organization chart of chapter 3

**Composite steel-glass beam.** The global studied system and principle are evoked in this section. Its domain of validity and the employed components are regrouped. The actions acting on each domain of use are summarized in Table 3.2.

**Linear adhesive connection.** The details of this fully adhesive connection are outlined, as well as its advantages. The possible adhesive candidates are chosen according to the previous chapter and the recent researches in this field.

**Mechanical-adhesive connection.** As for the linear adhesive connection, the mechanical-adhesive one is fully described in this section. A short comparison between these two systems is also realized. Due to the geometry, the choice of the adhesive is more restrictive and the reasons leading to its selection are explained.

**Summary and conclusions.** A general review of the two envisaged connection, as well as of the corresponding adhesives, is provided in the conclusion.

## 3.2 COMPOSITE STEEL-GLASS BEAMS

In the steel to glass connections detailed in section 2.3, the glazing elements are limited to the tertiary level, i.e. as a non-structural element only acting as a physical barrier between the inside and the outside. However, recent researches on glass panels, [2.12] and [3.1], demonstrated their promising in-plane compressive properties. Therefore, the main idea is to utilize the intrinsic behaviour of the glass in combination with steel beams to realize composite beams.

### 3.2.1 System description

A composite beam is fabricated with two dissimilar materials, whose properties are complementary. The most well-known and wide spread composite assemblies in civil engineering field correspond to the steel-concrete beams, see Fig. 3.1. Steel materials possess a good resistance against tension and shear, while the more brittle concrete materials are exclusively able to undertake compression. Thus, in order to efficiently use both, the concrete should only be subjected to compression and the steel to shear and tension, non-supported by the concrete. This distribution of the stresses can be achieved for a certain degree of connection by adjusting the geometries and dimensions of the materials cross sections. As concrete does not stick directly to steel, the connection means constitute a crucial aspect of these composite beams. Indeed, the degree of connection is precisely controlled by the jointing methods, as their behaviour is responsible for the possible sliding at the materials interface. A connection is considered as “perfect”, when there is no discontinuity in the deformations at the end of the beam, and “partial”, when a sliding at the interface is measured. For steel-concrete composite beams, the connectors generally are bolts welded on the top flange of the steel beam.

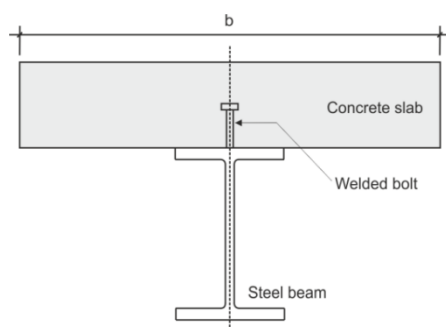


Figure 3.1- Steel-concrete composite beam

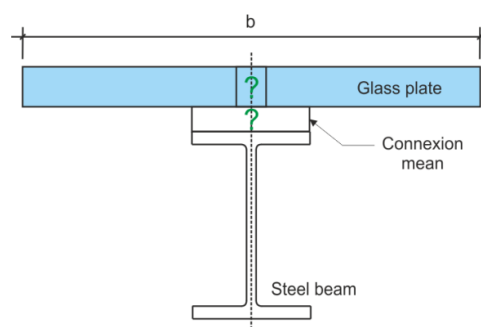


Figure 3.2- Steel-glass composite beam

A similar assembly could be produced by replacing the concrete by a glass plate, see Fig. 3.2. These two materials are brittle and present very high strengths in compression, but poor properties in tension leading to their breakage. Hence, the connection means play decisive roles, as they have to transfer high loads to activate the composite action and to not introduce too much local damage or stress peaks respectively in the concrete and in the glass. Consequently, several connection types should be investigated to find the optimal one for the prescribed conditions.

### 3.2.2 Domain of validity and advantages

As for linearly supported glazing detailed in the DIN 18008-2 [3.2], two positions can be envisaged for the application of a composite beam, i.e. vertically or horizontally. The distinction between these two orientations is defined by the angle formed between the glass plate and the vertical. While for structural sealant glazing systems, an angle less than  $15^\circ$  is required to consider the glass as a vertical element according to the ASTM C1401 [2.45], this angle is fixed at  $10^\circ$  according to the DIN 18008-2. For the following sections, the more restrictive angle of  $10^\circ$  will be taken as the limit between vertical and horizontal systems. However, the case of reversed slope mentioned in the ASTM, i.e. the glazing positioned over the street, have to be envisaged too. With regards to this definition and by simply considering the horizontal cases, another important factor determining the loads acting on the

structure has to be carefully checked, i.e. the accessibility of the glazing. As examples, for horizontal roofs, cleaning operations may have to be realized and could include additional loadings, and for footbridges, pedestrians' traffic could induce specific vibrations. Thus, three important classes can be found:

- i. Vertical non-accessible glazing (angle  $\leq 10^\circ$ ).
- ii. Horizontal (angle  $> 10^\circ$ ) non-accessible glazing, except for maintenance operations.
- iii. Horizontal (angle  $> 10^\circ$ ) accessible glazing.

Consequently, a composite steel-glass beam could be employed as façade element (i), for roofs (ii) or footbridges/floors (iii). The link between two adjacent glass panes could be realized with the help of soft infill air- and water-tight elastomer. For these applications, some improvements, compared to the classical non-composite systems, could be achieved:

- A higher rigidity of the assembly, compared to a non-composite beam. This improvement allows supporting higher loads, diminishing the maximum displacements or increasing the length between supports.
- For the same system, i.e. length and loads, it becomes possible to reduce the size of the steel profile and thus the total height and weight of the structure.
- No loss in transparency with regards to other linearly fixed glass system.
- The possibility to pre-assemble the elements in-shop and proceed to the installation on-site with more facility and more rapidly.

### 3.2.3 Employed products

Regardless of the evoked class of the composite system, the metallic beam can be made of construction steel (S235, S355, etc.), stainless steel or aluminum. Classical "H", "T" or rectangular hollow sections can constitute this element.

However, the choice of the glazing unit and its maximum dimensions depend clearly, for safety reasons, on the class of the composite beam. For horizontal applications, an important post-breakage residual capacity should ensure the stability of the element to avoid injuring the persons walking over or under it. Therefore, the glazings that could be employed for each class are:

- For class (i), simple annealed or heat-strengthened monolithic glass plates. The application of a monolithic fully tempered glass should be limited to specific applications due to the absence of residual capacity after breakage. Safety laminated annealed or heat-strengthened glazings with PVB or SentryGlas (SG) interlayers could also be used.
- For class (ii), only annealed or heat-strengthened laminated glass with PVB or SG interlayers can be employed. The numbers of glass plates and their thickness have to be determined with regard to the loads acting on the composite beam.
- For class (iii), annealed or heat-strengthened laminated glass with PVB or SG. As for others standards, e.g. the German TRLV [2.31], a minimum number of glass plates should be determined, considering that the upper panel should not be accounted for the design of the composite beam. In addition, an anti-slip system should be implemented on the upper plate to prevent persons falling.

Nevertheless, curved glass or steel beam will not be regarded for the realization of composite steel-glass assemblies. Finally, as several types of connections necessitate to be investigated, the products employed to achieve the complete beam are detailed in sections 3.3 and 3.4.

### 3.2.4 Actions on composite beams

Eurocode EN 1990 [2.30] proposes a classification of the external loads acting on a structure and, therefore, on the studied composite steel-glass beams. The duration of the actions and their nature, either static or dynamic, are summarized in Table 3.1.

| Action                                        | Origin   | Variation in time   | Nature         |
|-----------------------------------------------|----------|---------------------|----------------|
| Self-weight                                   | Direct   | Permanent           | Static         |
| Wind loads                                    | Direct   | Variable/accidental | Dynamic        |
| Snow loads                                    | Direct   | Variable/accidental | Static/dynamic |
| Thermal actions                               | Indirect | Variable            | Static         |
| Imposed loads<br>(persons, objects, vehicles) | Direct   | Variable/accidental | Static/dynamic |
| Seismic                                       | Direct   | Variable/accidental | Dynamic        |

**Table 3.1-** Loads acting on composite beams

As detailed in section 3.2.1, a steel-glass composite beam is constituted of three components, i.e. a steel beam, a glass plate and the connection mean, with the aim to act as only one system. However, depending on the configuration of the composite beam, either for vertical façade, horizontal roof, footbridge or floor, the loads of Table 2.1 can act preferentially on one of these components. For example, the self-weight of the glazing only creates a constant shear stress in the connection mean for a fully vertical system and a possible combination of constant compression and shear stresses for a horizontal system. Thus, with regard to the application scopes, making the distinction between the loads contributing to the bending of the global composite and the loads acting on isolated parts appears important for a correct design. This concept is equivalent to distinguish the out-of-plane loads from the in-plane loads. Moreover, this principle has to be applied for each class, as the loads can be or not present, e.g. imposed loads must be taken into account for composite beams class (iii), but not considered for class (i) because these last configurations are inaccessible to normal building users.

### **Actions on system class (i)**

Fully composite steel-glass beams, employed as vertical façade elements, are subjected to the following forces:

- Wind loads, normal to the glass panel, contribute to the bending of the global system. The intensity of these out-of-plane actions has to be evaluated with the help of the Eurocode EN 1991-1-4 [3.3]. Wind loads can be either positive, displacements towards the inside of the building, or negative, causing suction towards the outside. Out-of-plane wind loads induce short-term shear stresses in the connection, but can also generate additional short-term compression stresses in case of positive wind pressure or short-term tensile stresses in case of negative wind pressure.
- Self-weight of the composite beam, for a non-nil inclination angle, also contributes to the bending of the beam. Additionally, regardless of the inclination angle, the self-weight of the glazing unit is transferred to the steel beam via the connection method. Long-term pure shear stresses are generated in the connection for no inclination and either a combination of shear and tension or shear and compression for respectively a reversed slope (outwards) or an inclined inwards vertical glazing.
- Thermal actions generate in-plane differential movements due to the different thermal expansion coefficient of steel and glass, leading to the introduction of pure shear in the connection.

Regarding the small inclination angle ( $\alpha \leq 10^\circ$ ), the snow loads do not have to be accounted for design according to the Eurocode EN 1991-1-3 [3.4].

### **Actions on system class (ii)**

The principal loads acting on non-accessible (except for maintenance) horizontal composite steel-glass beams are the following ones:

- Wind loads, according to EN 1991-1-4, even for fully horizontal plates, as they can generate positive or negative pressure. Thus, combinations of shear and tension or shear and compression can occur in the connection.
- Snow loads are only responsible for a positive pressure on the global system. The intensity of these loads is determined with the EN 1991-1-3 standard. They only cause a combination of shear and compression stresses in the connection.
- Self-weight of the system, also responsible for the bending of the composite beam. And constant long-term shear and compressive stresses are created in the connection by the self-weight of the glazing.
- Imposed loads, generated by the maintenance operations. According to the Eurocode EN 1991-1-1 [3.5], maintenance loads have to be split in two, i.e. uniform and concentrated loads; the latter could be applied anywhere on the glass plate of the composite beam.
- Thermal actions, inducing, as for system class (i), pure shear in the connection mean.

### **Actions on system class (iii)**

The biggest difference with system class (ii) comes from the intensity of the imposed loads generated by the traffic of pedestrian. Thus, the loads of class (iii) appear similar to the previous class:

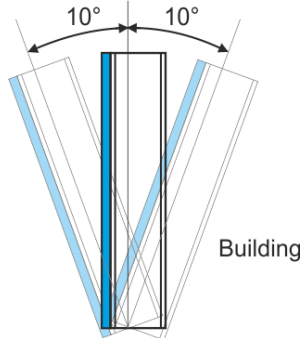
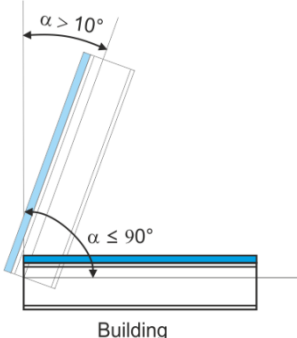
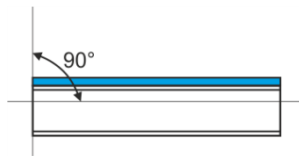
- Wind loads positive or negative evaluated with the EN 1991-1-4. Tension and shear or compression and shear stresses can arise in the connection.
- Snow loads, positive constant pressure determined with the EN 1991-1-3. From these loads compression and tension stresses originate in the means of fixation.
- Self-weight of the global system participating of the bending of the composite beam. The connection is then subjected to the same type of stresses than for the snow loads, i.e. a combination of compression and shear.
- Imposed loads, generated by the pedestrian actions. Uniform and concentrated loads are necessary to represent these live loads. The EN 1991-1-1 defines their intensities for different types of application, e.g. floor used in individual houses or in offices would not be subjected to the same loads magnitudes.
- Thermal loads, which are the only in-plane actions, produce constant shear stresses in the connection.

If the composite beam is employed in a building as a floor or a footbridge, the wind and snow loads no longer need to be investigated.

### **Summary of the actions**

All the evoked actions, depending on each configuration, are summarized in the Table 3.2. The mixed actions refer to loads, which could be decomposed in two directions, i.e. a direction perpendicular to the glazing (out-of-plane) and another along the length of the beam (in-plane). As a composite beam is constituted by three elements, three possible material failures can occur, i.e. in the glass, in the steel or in the connection. However, without the connection, the assembly of a steel beam and a glass plate cannot be realized and therefore this element necessitates a particular attention. While the in-plane loads only introduce shear stresses in the connection, the out-of-plane or mixed loads generate combination of shear and either tension or compression stresses. The intensity and the variation in time of these stresses are directly related to the configuration of the system. The impact on the connection of the self-weight of the glazing for a fully vertical system is greater than the one of the same action for a fully horizontal system. Indeed, for the vertical system, the connection has to withstand permanently all the weight of the glazing unit, while for the horizontal system the weight of the glazing unit is transmitted to the supporting steel beam. Hence, knowing the loads acting on the connection and their variations in time constitute one of the main aspects to properly design the jointing method of a composite beam.

In addition, for a given connection type, the combinations of all the listed loads allow evaluating the resistance of the composite beam under the most unfavorable case.

| Class                | (i) Vertical non-accessible glazing                                                                                           | (ii) Horizontal non-accessible glazing (except for maintenance)                                                                                                           | (iii) Horizontal accessible glazing                                                                                                                          |
|----------------------|-------------------------------------------------------------------------------------------------------------------------------|---------------------------------------------------------------------------------------------------------------------------------------------------------------------------|--------------------------------------------------------------------------------------------------------------------------------------------------------------|
| Application          | Façades                                                                                                                       | Roofs                                                                                                                                                                     | Footbridges/Floors                                                                                                                                           |
| Domain of validity   |                                              |                                                                                         |                                                                           |
| Glass products       | <ul style="list-style-type: none"> <li>• Monolithic (annealed/HSG)</li> <li>• Laminated with PVB/SG (annealed/HSG)</li> </ul> | <ul style="list-style-type: none"> <li>• Laminated with PVB/SG (annealed/HSG)</li> </ul>                                                                                  | <ul style="list-style-type: none"> <li>• Laminated with PVB/SG (annealed/HSG)</li> </ul>                                                                     |
| Out-of-plane actions | <ul style="list-style-type: none"> <li>• Wind loads</li> </ul>                                                                | <ul style="list-style-type: none"> <li>• Wind loads</li> <li>• Snow loads</li> <li>• Maintenance loads</li> <li>• Self-weight (<math>\alpha = 90^\circ</math>)</li> </ul> | <ul style="list-style-type: none"> <li>• Self-weight of the assembly</li> <li>• Wind loads</li> <li>• Snow loads</li> <li>• Traffic imposed loads</li> </ul> |
| In-plane actions     | <ul style="list-style-type: none"> <li>• Thermal actions</li> <li>• Self-weight (<math>\alpha = 0^\circ</math>)</li> </ul>    | <ul style="list-style-type: none"> <li>• Thermal actions</li> </ul>                                                                                                       | <ul style="list-style-type: none"> <li>• Thermal actions</li> </ul>                                                                                          |
| Mixed actions        | <ul style="list-style-type: none"> <li>• Self-weight (<math>\alpha \neq 0^\circ</math>)</li> </ul>                            | <ul style="list-style-type: none"> <li>• Self-weight (<math>\alpha \neq 90^\circ</math>)</li> </ul>                                                                       | -                                                                                                                                                            |

**Table 3.2-** Specifications of composite steel-glass beams

### 3.2.5 Additional application conditions

The choice of the glazing types constitute, for each system, a first important requirement to ensure the non-failure of the whole composite beam. Indeed, the glazing unit, possessing a good post-breakage carrying capacity, is combined with a connection method to ensure the stability of the structure. However, some additional requirements have to be imposed in case of failure of the connection or of both the connection and the glazing unit. Hence, the installation of the composite beam for vertical configuration should be limited to a certain height, in case of a non-supported by mechanical devices glazing, to retain the glass and to not harm the persons nearby.

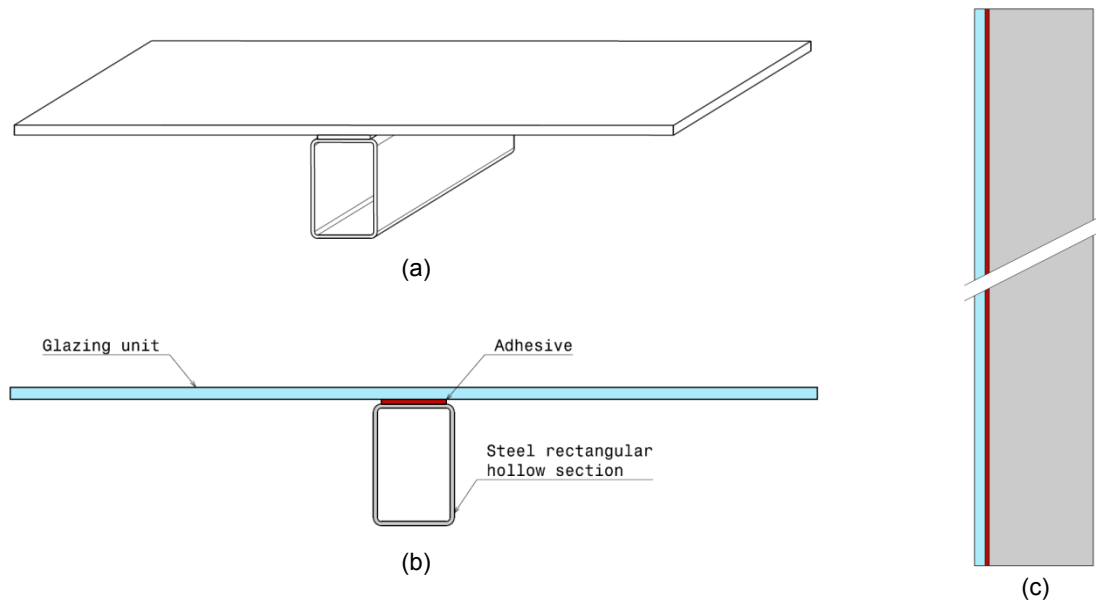
Additionally, employed in outdoor conditions, a composite beam is not only subjected to the aforementioned external loads, which can either be static or dynamic, but also to climatic variations, related to humidity and UV-radiation. While the glass remains unaffected by the UV and quasi non-affected by the humidity (neglecting the water corrosion), the connection, either mechanical or adhesive, may undergo important changes of properties. Consequently, the durability of a composite beam is closely affiliated to the durability of the connection, which has to be investigated in detail. Moreover, for horizontal systems class (ii) and (iii), the accumulation of water can arise at the junction of the different glass plates. Therefore, the joints should not be inwardly incurved or should present a water-tight covering device.

For building used, acoustic and thermal insulation should be evaluated to guarantee the comfort of the occupants and fire resistance should also be appraised for safety.

### 3.3 LINEAR ADHESIVE CONNECTION

#### 3.3.1 System description

The first envisaged connection type for the realization of composite steel-glass beam is an adhesive connection. The detail of this linear adhesive connection is shown on Fig. 3.3. For the present system, a rectangular hollow section was chosen for the steel beam in order to avoid lateral buckling. In addition, to only study the influence of the connection, a thick monolithic glass was first considered, especially for the large-scale tests, to then envisage the use of laminated glass plate. The glazing unit must always be supported, for stability reasons, in its middle and along the largest dimension. The adhesive material is inserted between the surfaces of “contact” of the steel flange and the glass to form the composite beam. Thus, the width of the adhesive is directly proportional to the flange of the selected steel beam, as well as the length of the adhesive, which is related to the length of the total beam.



**Figure 3.3-** Detail of the linear adhesive connection – (a) Isometric view – (b) Cross section – (c) Side view

As it was evoked in section 2.3 with the presentation of several connections, adhesive jointing methods possess several advantages compared to mechanical fixations:

- The distribution of the stress along the jointed parts is nearly uniform over the entire bonded area, without inducing stress peaks as it is generally the case for local mechanical fixings.
- No additional material, e.g. Teflon or Neoprene, is necessary to prevent the fatal contact between the brittle glass plate and the steel beam.
- Adherents with dissimilar mechanical and thermal properties can be bonded. The joint may, in some cases, compensate for the different thermal expansions coefficients the materials.
- With the recent researches lead in the adhesive fields, elevated loads can be transmitted through these elements.

Furthermore, special manufacturing of the glass plate, such as holes, are not necessary for this kind of connection, which prevents unwanted stress peaks in the glazing unit. Besides, with regards to the different configurations mentioned previously, the outer surface of the composite beam appears totally flat and smooth, as no mechanical connections cover the glazing. Hence, from the aesthetic point of view, a façade or roof can seem lighter.

Nevertheless, in spite of these advantages, some limitations have to be established concerning the size of the different elements, as the width of the adhesive depends on the flange of the steel beam. Hence, smaller is the beam and smaller will be the width of the adhesive and therefore the maximum force allowed by the connection. Consequently, a minimum ratio, the width of the flange over the width of the glass plate, could be imposed.

## Selection of adhesives

As mentioned in section 2.4.1, the various adhesives on the market are essentially classified in three categories, i.e. the elastomers, the thermosets and the thermoplastics. While the elastomers were presented as softer and exhibiting a larger range of deformations up to 500% under little shear forces, the thermosets were introduced as stiffer materials and reaching higher shearing stress with minor deformations. Moreover, in practice, the structural bonding of steel-glass constructions is commonly achieved with elastomer adhesives, e.g. silicone, and thermosets, e.g. acrylic or epoxide resin.

For this linear connection, the choice of the adhesive is directly dependent of the different loads acting on it. For vertical façade, the self-weight of the glazing induces permanent shear stresses in the connection, to which the adhesives are strongly sensitive, especially thermosets as presented in section 2.4.31. Therefore, for this type of application, an adhesive material able to withstand these long-term shear stresses has to be chosen. To these stresses, additional static shear stresses are provided by the thermal expansions of steel and glass and by the out-of-plane loads. Hence, the quasi-static and long-term maximum allowable shear stresses constitute decisive criterions. Moreover, some quasi-static tension stresses can also appear in the connection due to the wind suction of the glazing and have therefore to be taken into account. The compression stresses do not represent a crucial failure criterion for most of the adhesive material. For the other configurations classes (ii) and (iii), the critical stresses acting in the bonding are the same but varying in intensity, except for the long-term shear generated by the self-weight of the glazing unit which are almost inexistent for fully horizontal applications.

Consequently, for these structural applications, the adhesive should both, incorporate a high bearing capacity in short- and long-term shear and tension, but also possess a certain ductility to compensate for differential thermal expansion of the adherents, which could lead to the failure of the glass panel. In addition, a good durability and invariance of properties towards environmental conditions, such as humidity and UV-radiation, are imperative too.

With regard to these requirements, a representative elastomer and thermoset have been selected for the linear adhesive steel-glass composite beam:

- The two-component silicone elastomer DC993 from the Dow Corning company, meeting the requirements according to the ETAG 002 [2.44] for the realization of structural sealant glazing systems. As elastomer, its behaviour should be invariant under environmental conditions and temperature variation. With this kind of adhesive, a correct control of the joint thickness and a relatively quick curing (2<sup>nd</sup> component helping) could be achieved.
- The Bohle UV-acrylic MV760, which has, compared to other acrylics, the highest tensile and shear strength with almost no changes after immersion in façade cleaning product (solvents) under elevated temperatures [3.6], see Fig. 3.4. In addition to these properties, this adhesive cures with the help of an UV-lamp in few minutes.

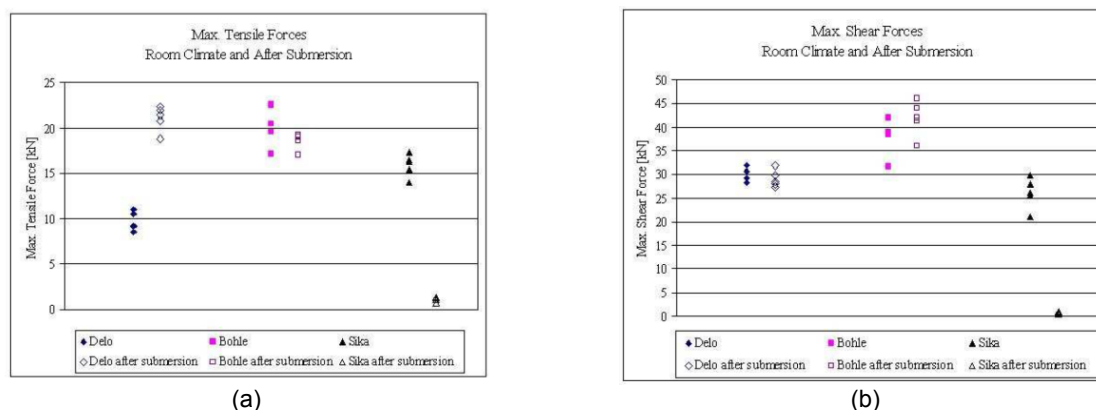


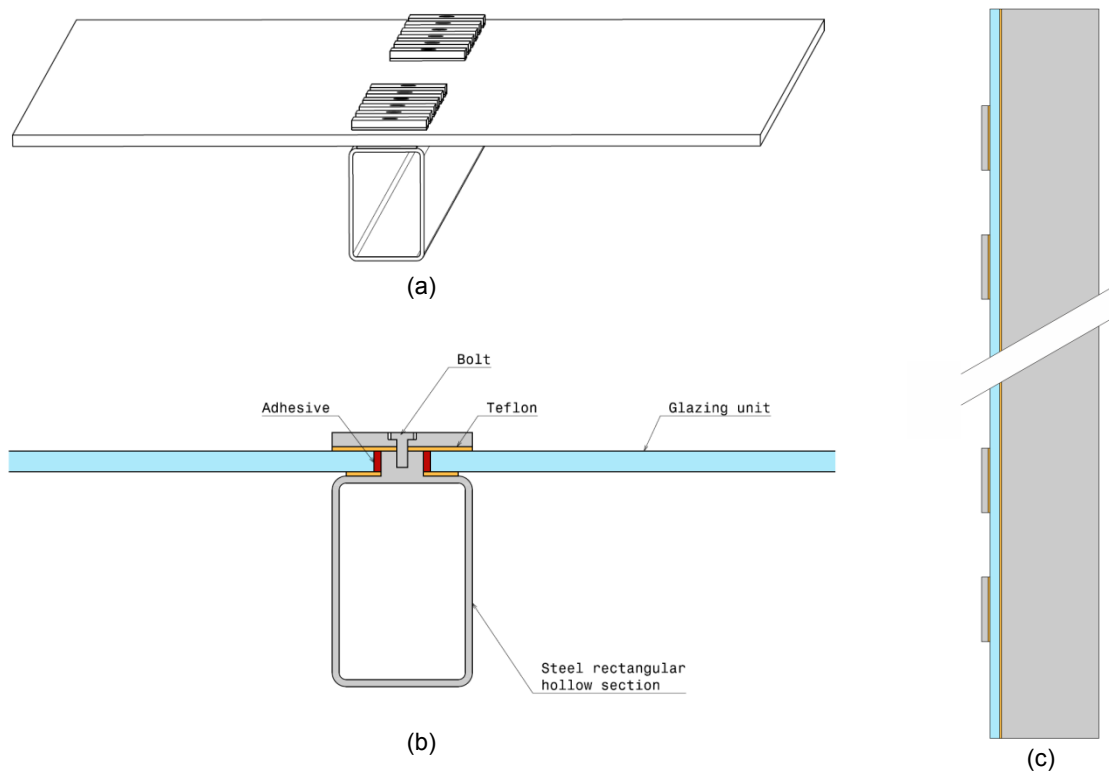
Figure 3.4- Comparison between the tensile (a) and shear (b) properties of acrylic adhesives [3.6]



### 3.4 MECHANICAL-ADHESIVE CONNECTION

#### 3.4.1 System description

The second connection envisaged to manufacture a composite steel-glass beam is a combination of a local mechanical connection and an adhesive, see Fig. 3.5. As for the simple linear adhesive bonding, the steel profile employed is a rectangular hollow section to avoid the lateral buckling, and the glass corresponds to a thick monolithic glass to simply concentrate on the fixation between steel and glass. The glazing is again supported at its middle along the largest dimension but, in contrary to the previous connection, necessitates the realization of several cylindrical holes. These holes fit around steel stops welded on the top flange of the steel beam. The remaining gaps between the holes of the glazing unit and the steel stops are filled with an elastic adhesive material, which prevents steel to glass contact and must be able to undergo deformations. In addition, to avoid squeezing out of this elastic material and to enhance its resistance, covering steel plates have to be added locally. Hence, the connection is composed by several layers, i.e. starting from the flange of the beam, a Teflon layer to avoid steel to glass surfaces contacts, then the glazing unit fitting around the steel stops with the elastic material, another Teflon layer and finally a covering steel plate. To fix all these layers together, a bolt should be screwed in each steel stop.



**Figure 3.5-** Detail of the mechanical-adhesive connection – (a) Isometric view – (b) Cross section – (c) Side view

The difference with the linear adhesive connection, for which the main stresses acting on the joint were the shear stresses, is that, with this mixed assembly, the adhesive will mainly be subjected to compression stresses. Hence, the probability to encounter an adhesive failure is lowered. However, due to the manufacturing of the glass plate, stress peaks are induced in this brittle material, increasing its probability of breakage. Consequently, a careful mechanical treatment of the edges of the boreholes, such as chamfer and polishing, should automatically be done. Thus, even if the connection requires less adhesive than the previous one, a larger number of operations on the adherends, i.e. glass and steel (welding of the steel stops), must be carried.

Nevertheless, this mixed mechanical-adhesive connection present several advantages compared to the standard mechanical connection presented in section 2.3:

- The peak stress in the glass can be reduced by distributing the loads more uniformly over the hole. And a better distribution of the total load, transferred from the glass to the beam, between all the local fixations can be achieved.
- The adhesive allows avoiding steel to glass direct contact for the horizontal displacement and provided sufficient elasticity to compensate for the thermal expansions of the adherends.
- The covering steel plates prevent any vertical separation between the glazing unit and the beam and prevent the squeezing out of the in-fill adhesive material.

The composite beam appears less light, from an aesthetical point of view, than the linear adhesive connection, in reason of the covering steel plates making the surface less smooth. For vertical applications, these discontinuous steel covering plates could be replaced by a single and continuous steel bar, in order to avoid water and later moisture accumulations. And for horizontal accessible configurations, an upper glass plate, whose thickness corresponds to the sum of the thicknesses of the steel covering plate and the upper Teflon layer, could be used to flatten and equalize the surface, see the following Fig. 3.6.

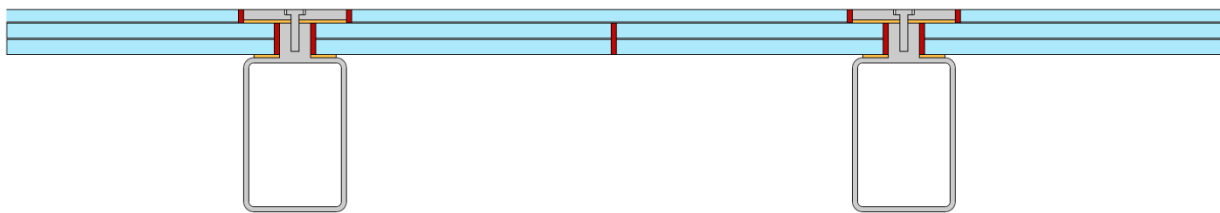


Figure 3.6- Possible mechanical-adhesive connection for system class (iii)

### 3.4.2 Selection of adhesives

The local mechanical connections presented in section 2.3.2.3 were first created to simply support a glazing unit locally with the help of point fixations. In these systems, plastics or mortars were employed as in-fill materials to transfer the load and avoid steel to glass contact. However, these materials possess generally thermal coefficient expansion largely greater than the one of glass, e.g. for POM C the thermal coefficient is about 8 times higher and for Hilti HIT-HY 70 about 4 times higher. This lead to the introduction of stress peaks in the glass, which could be decisive. Therefore, inserting an elastomer, whose properties are constant in the in-use temperatures range, represents an advantage.

As mentioned previously, all the tangential forces, generated by the out-of-plane and in-plane actions and transferred from the glass plate to the steel beam, induce in the adhesive compression and minor tension stresses. In addition, the Teflon plates, covering the glazing unit to avoid contact with steel, possess a friction coefficient quasi nil. Thus, the integrality of the tangential loads is transmitted through the adhesive. Consequently, the strength of the adhesive in short-term and long-term compression and tension constitute the most important characteristics. Furthermore, as for the previous connection, the adhesive should be stable towards humidity, temperature and UV-radiation.

As the majority of thermosets present temperature-dependent behaviour, only elastomers were envisaged for this connection. Moreover, to manufacture easily the composite beam a material, whose thickness could be controlled, had to be chosen. Thus, the adhesive should possess a medium viscosity to inject it properly in the gaps between the glass holes and the steel stops. In these confined areas, the curing process is difficult to control as the air cannot fully reach the bottom part of the adhesive. Therefore, to avoid a partial curing only on the upper surface, a two-component silicone was selected. As for the previous connection, the silicone elastomer DC993 for Dow Corning, well known in glass façade, appeared as the best choice.

### 3.5 SUMMARY AND CONCLUSIONS

The construction of a steel-glass composite beam was largely inspired from the existing composite steel-concrete beams, i.e. with an upper plate acting in compression and a steel beam undertaking the tensile stresses. For both connections, even if the materials differ, the connection constituted one of the most decisive points to be designed. For the steel-glass beam, the applications possibilities were described, as well as the respective types of forces acting on it. For all the configurations, the loadings coming from the out-of-plane actions were more intense than the one of the in-plane actions, which were principally induced by the different thermal expansion coefficients. Hence, the behaviour of a steel-glass composite beam subjected to bending was more fundamental. If the beams are able to withstand these actions, its behaviour towards the in-plane force could be investigated.

Two different types of connections were planned for the construction of steel-glass composite beams, i.e. a linear adhesive connection and a mechanical-adhesive connection. For the linear adhesive one, the force is transmitted from the glass plate to the steel beam by shear in the adhesive. Consequently, the adhesive shear strength is primordial, as well as the total bonding area. This connection relies essentially on the size of the adherents and its rigidity could be increased by reducing the adhesive thickness to the minimum. Therefore, the UV-acrylic could be preferred than the silicone in this case. For the mechanical-adhesive connection, the shear forces at the interface are transmitted via the infill adhesive in tension and essentially compression. The UV-acrylic could not be used for this type of connection due to its viscosity and to the incapacity to control its thickness via the curing process. Thus, only the silicone was considered for the mechanical-adhesive beam manufacturing. Further, to increase the rigidity, the silicone was completely restrained by adding covering plate. These two types of connections will be investigated after complete determination of the adhesive properties.



## 4. EXPERIMENTAL INVESTIGATIONS

### 4.1 INTRODUCTION

In this chapter are presented the different testing procedures and tests results associated to the two selected adhesive, i.e. a silicone elastomer and an acrylic thermoset. The conducted experiments should provide sufficient data to identify appropriate material laws implementable in finite element software.

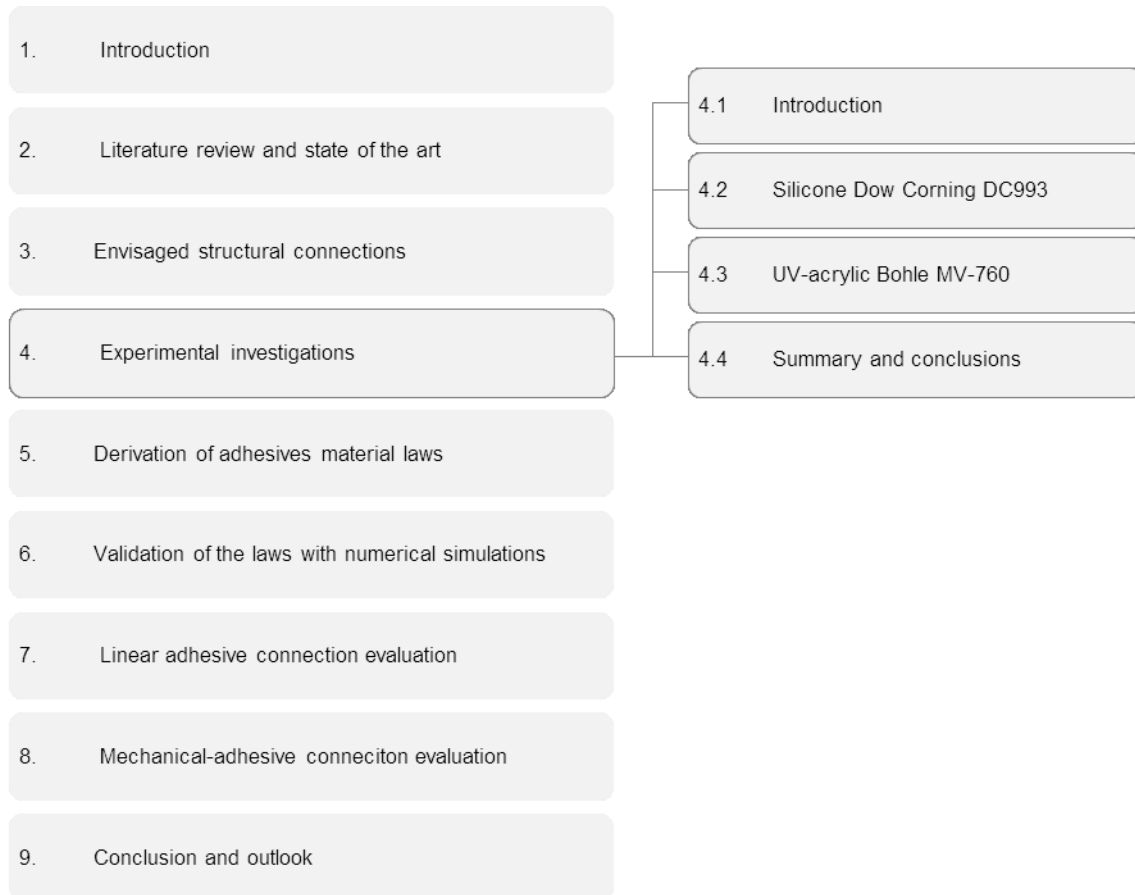


Figure 4.0- Organization chart of chapter 4

**Silicone Dow Corning DC993.** Three isochoric tests, i.e. tension, compression and shear, conducted on the silicone, are made to evaluate its principal properties in quasi-static, cyclic and long-term relaxation. Their dependencies to environmental factors are also regarded. To these standard tests is added a volumetric oedometric experiments characterizing the quasi-incompressible behaviour. All the manufacturing, testing procedures and results are detailed in this section.

**UV-acrylic Bohle MV-760.** Uniaxial tensions tests are performed on the acrylic adhesive to assess its dependency to the loading rate under quasi-static actions. Long-term tension relaxation tests are also conducted to appraise the stress decrease. In addition to these uniaxial experiments, shear tests are carried out with two different test layouts, due the difficulty to control this adhesive thickness. The shear long-term behaviour is investigated too. The steps leading to the analyses of the results are presented.

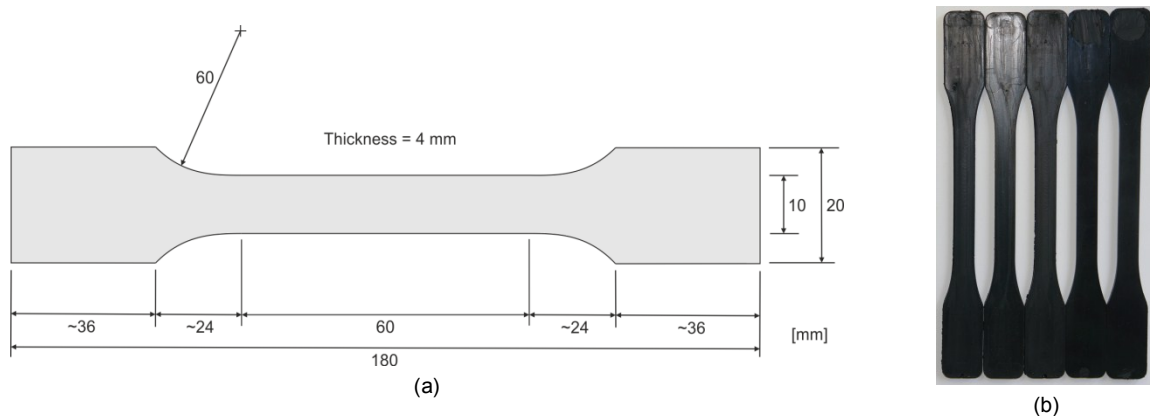
**Summary and conclusions.** All the data recorded for the different types of actions are summarized for the two selected adhesives.

## 4.2 SILICONE DOW CORNING DC993

### 4.2.1 Tension

#### 4.2.1.1 Manufacturing of the samples

For this test campaign, the main objective is to determine the tensile properties of silicone material with no consideration to glass or steel adherents. This choice was motivated by the mode of failure of this kind of adhesive for the H specimens described in the ETAG 002 [2.44], which corresponds to a cohesive failure [4.1]. In addition, pure tensile tests provide the elementary data to select the most suited hyperelastic material law for silicone elastomers. Hence, the dimensions “type 1B”, provided by the ISO 527-2 standard [4.2], were employed for the dog-bone samples, see Fig. 4.1.

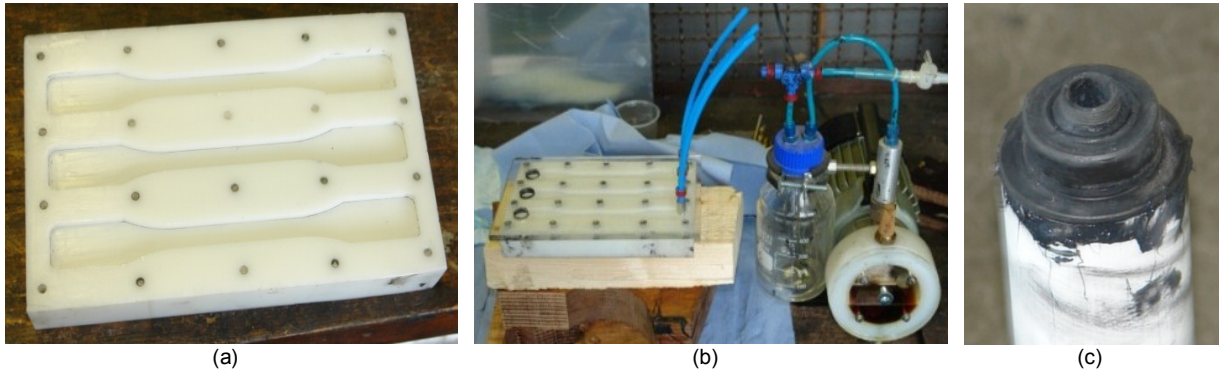


**Figure 4.1-** (a) Dimensions of the silicone dog-bone samples according to ISO 527-2 and (b) Manufactured samples

Three main procedures can be used to produce these dog-bone samples, i.e. molding, cutting and manufacturing. The manufacturing process, consisting in the rectification of a parallelepiped piece of silicone to the milling machine, is quasi-impossible with regards to the softness of this material. Additionally, the cutting method, based on cutting dies and defined in the ISO 23529 [4.3], necessitates the fabrication of a silicone plate of constant thickness, which is difficult to achieve. Furthermore, with this last technique, the produced dog-bone samples could present edge flaws, air bubbles and dispersions in dimensions. Consequently, two molding procedures were investigated to make the “dog-bone” samples:

- i. A pouring procedure, for which the shapes of a POM C self-manufactured mold were simply filled with silicone, see Fig. 4.2 (a). A Teflon plate was then pressed against the mold to evacuate the excess of adhesive and to obtain a smooth surface. The resulting specimens were full of defects, such as small holes on the edges but also on the surface. Therefore, this method was rejected.
- ii. An injection procedure, making use of a vacuum pump (Kälte Fischer Klima type DB 1, 130W, 50Hz) at ambient temperature and humidity. The POM C mold was covered by a screwed transparent 8mm thick Plexiglas plate. Before each injection, the Plexiglas plate was degreased with acetone and a spray containing Teflon was pulverized. Twenty screws were distributed evenly to perfectly close these two parts and avoided air infiltration, see Fig. 4.2 (b). Injection and suction holes were crucial points for the success of this method considering the viscosity of this adhesive. While the suction holes were relatively small with a diameter of 5mm, the injection holes were larger with a diameter of 15mm. The connections between the vacuum pump and the suction holes were done with quick push-in fittings and 6 mm plastic tubing PUN (polyurethane). At the end of the silicone cartridge another plastic piece was fabricated to properly adapt to the injecting holes of the Plexiglas plate, see Fig. 4.2 (c). An O-ring was inserted on this part to ensure air tightness between the cartridge and the mold. After injection, the curing process of the two component silicone started in the mold in spite of its

air-tightness. The specimens were unmolded 24 hours after the injection and then stored for a period of one month at ambient temperature and humidity shielded from light. No visible flaws at the surface or at edges were visible with this procedure. After the first visual inspection of the surfaces, several specimens were cut in half to confirm the absence of air bubbles inside.



**Figure 4.2-** (a) POM C mold for dog-bone samples production and (b) Vacuum pump installation and (c) Injection part

Consequently, the vacuum injection procedure was adopted to produce all the 33 dog-bone samples. The control of their dimensions in the tested zone was realized with a caliper and is listed in Appendix A.2. The position of the samples in the mold was also recorded to evaluate if dispersion in dimensions could be due to some imperfections of one specific shape. From this analysis, it was demonstrated that dimensions of the dog-bone samples were independent of the position and presented negligible dispersion, which definitely proved the good reproducibility of the carried manufacturing procedure.

#### 4.2.1.2 Quasi-static tests

To evaluate the dependencies of the silicone instantaneous mechanical properties towards external conditions, the design of experiments method proposed by Taguchi was envisaged. In contrary to the conventional analysis methods, in which the possible influent factors were isolated and separately tested, the Taguchi design of experiments method offered the possibility to order and combine these lasts with the aim to appraise, with the help of statistical approaches, their effective impacts on the acquired values. With this methodology, the effects generated by a combination of factors were also measurable. Thus, the Taguchi procedure was used to maximize the information issued from the tests and conserve a low number of tests. The different sub-parts of the present section constitute the fundamental steps leading to a proper implementation of this method.

#### Definition of the objectives

The first step in the design of experiments consists in defining precisely the expected outcomes and the indispensable data. As detailed in section 2.4.2.1, a non-linear behaviour under large deformations is expected for this two-component silicone. Thus, to completely characterize this behaviour, stress-strain diagrams until breakage have to be established. These curves allow, on one hand, to determine the constitutive material law that fits the best the experimental results and, on the other, to settle the maximum authorized limits in terms of strength and deformation. In addition, the environmental conditions acting on a glass façade, can likely change and soften the non-linear behaviour of silicone. Therefore, a preliminary identification of the possible influent factors has to be made and their effects on the stress-strain diagrams evaluated.

Consequently, the properties to be measured with these quasi-static tests are the following one:

- Stress-strain diagrams of several tests in order to obtain an averaged and exploitable curve for the selection of the constitutive material law able to properly model this silicone in finite element analysis (FEA).

- The evolution of the material behaviour under various environmental conditions to include these outcomes in the constitutive material law.
- Stress-strain values at breakage and also the total energy at failure to define limits for design.
- As described by the ETAG 002 [2.44], an analysis on the initial stiffness of the material could also be undertaken to characterize the behaviour at small deformations.

### Selection of the influent factors

The factors influencing the expected results are established with the help of an Ishikawa diagram, also called fish-bone diagram. This approach consists in listing all the possible causes of these changes around six main criteria, i.e. material, manpower, methods, measuring methods, machining and environment. In the case of quasi-static tensile tests, the Ishikawa diagram is given in Fig. 4.3.

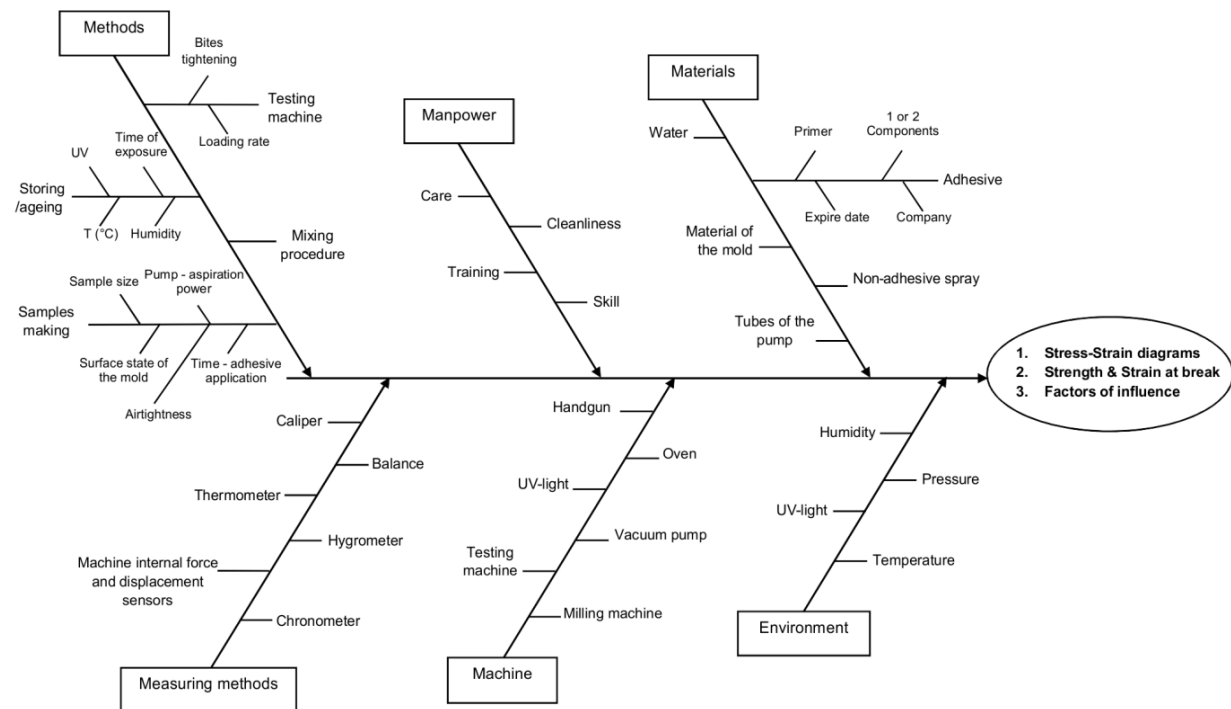


Figure 4.3- Ishikawa diagram for dog-bone quasi-static tests

With this diagram, the most influent factors can be easily selected to set up the complete planning of the tests. Two main classes were chosen considering the final use of this silicone:

- The “environment” criterion, comprising the temperature, humidity and UV-light factors.
- The “method” criterion, with special attention to the loading rate.

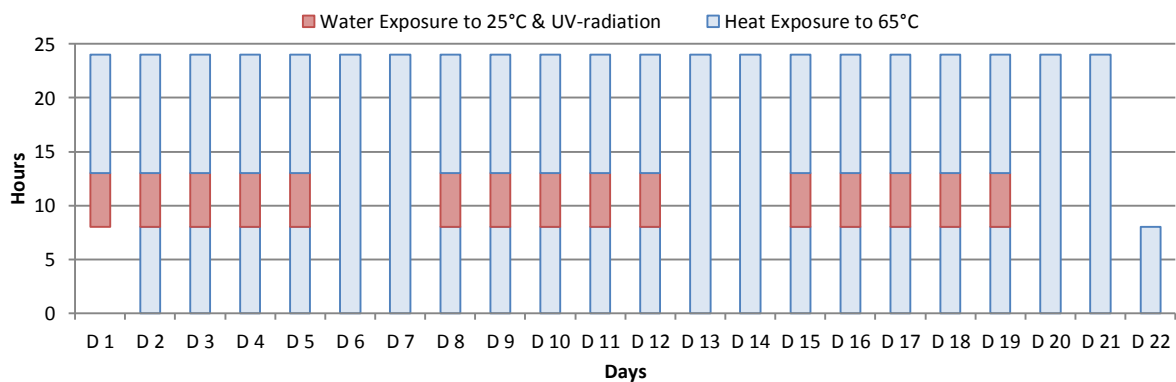
Thus, with no regards to the class, four distinct parameters can be varied in total.

To account for the environment parameters, two different approaches are feasible, i.e. installing the adhesive in real conditions for long duration, also referred as natural ageing, or employing an accelerated ageing procedure under a reduced period. With both methods, the ageing has to be applied before the testing during a prescribed period. Thus, the so-determined properties reflect the state of the adhesive after a certain time. As it is senseless to conduct a natural ageing on a long period of about 25 years (lifetime of SSGS according to [2.44]), an artificial ageing procedure was envisaged. In addition, as in-use silicone adhesive can be subjected to elevated or negative temperatures, to a high or low relative humidity, depending on the geographical position or on the seasons, and to a strong or low level of UV-radiation, a grouping of factors was also considered. Indeed, these aforementioned factors are not strictly independent, especially the humidity and the temperature, i.e. for an elevated temperature, the relative humidity is different than the one for a low temperature. However, all the existing ageing procedures do not regard low temperatures and



concentrate only on high temperatures. Therefore, in order to use an artificial ageing procedure, it was decided to divide the consideration of the environment factors in two parts regarding the temperature:

- For elevated temperatures, it was possible to group the three environmental factors according to the accelerated ageing procedure proposed in the EN ISO 11431 [4.4]. This procedure is indicated in the ETAG 002 and recommended by the latter to test adhesive of SSGS. The described method presents the advantage of regrouping and combining the exposure to heat, UV-light and water and so avoiding testing each factors separately. Unfortunately, as for the other existing artificial ageing, no time correspondence between the artificial ageing process and the natural ageing was established. A manual cyclic exposure during 504 hours (3 weeks) is foreseen by this standard. Three cycles of 108 hours (1 week) are divided in a period of 5 days consisting of 5 hours of water immersion at  $25\pm 3^\circ\text{C}$  and 19 hours of exposure to heat at  $65\pm 5^\circ\text{C}$  and UV-light, and a period of 2 days to only heat and UV-radiation. The heating to  $65^\circ\text{C}$  was realized in an oven with a regulation system and the UV-radiation with an UV-Lamp from Bohle Company (UVA-Star “Long Light XL” - 90W). The complete ageing planning is presented in Fig. 4.4.



**Figure 4.4-** Detail of the artificial ageing procedure for elevated temperatures



**Figure 4.5-** Water and UV- exposure



**Figure 4.6-** Heat exposure in oven

- For low/negative temperatures, the chosen artificial ageing procedure simply consists in putting the dog-bone samples in a cooling device at  $-20^\circ\text{C}$  during three weeks. Thus, the humidity and UV-radiation were not examined in this case.

The “method” factor corresponds to the loading rate. This, in contrary to the artificial ageing procedure, has to be taken into account during the testing phase. With regards to the high deformations of the silicone and to the tested length of 60mm, two different loading rates were envisaged: 50mm/min (relatively slow) and 500mm/min (high).

### Choice of the Taguchi table

By regrouping the elevated temperature, humidity and UV-radiation into a single “environmental” class, only two distinctive factors have to be studied:

- A. Ageing, a qualitative Boolean factor taking only two values, i.e. with ageing or without.  
 B. Loading rate, a quantitative continuous factor with two levels, i.e. 50mm/min and 500mm/min.

| Standard Test n° | Factors  |           | Samples to be tested |               |               |
|------------------|----------|-----------|----------------------|---------------|---------------|
|                  | A        | B         | Test series 1        | Test series 2 | Test series 3 |
| 1                | 1        | 1         | S-04                 | S-05          | S-19          |
| 2                | 1        | 2         | S-01                 | S-16          | -             |
| 3                | 2        | 1         | S-02                 | S-12          | S-13          |
| 4                | 2        | 2         | S-06                 | S-08          | -             |
| Level 1          | Not Aged | 50mm/min  |                      |               |               |
| Level 2          | Aged     | 500mm/min |                      |               |               |

**Table 4.1-** Design of experiments for silicone dog-bone samples under quasi-static tension

The choice of a Taguchi table for two factors at two levels is described in Appendix B. In this context, the possible interaction between the two factors can be integrated in the design of experiments (DOE) presented in Table 4.1, even if it does not appear directly. Furthermore, as the ANAVAR [4.5] method is employed to analyze the variance of the coefficients of the model, a repetition of the complete test planning is at least necessary. Thus, the minimal number of experiments to be carried out is 8, i.e. 2 per each type of test. But for the present study, 10 samples were randomly selected and distributed in each category, see Table 4.1. The random distribution was effected in order to overcome any influence of size or curing of the dog-bone samples, as they could not all produced at the same time and with the same cartridge.

Additionally, to account for the possible influence of negative or very low temperatures, occurring generally in winter over long periods, a parallel test planning has to be established. Indeed, as the current ageing procedure according to the ISO 11431 standard contains a grouping of factors, it becomes too stiff to be modified and to only consider low temperatures without control of humidity or UV-radiation. Therefore, another independent series of tests is added to only concentrate on low temperatures. The chosen artificial ageing procedure is detailed in the previous paragraph and was conducted in parallel to the artificial ageing at elevated temperature. Thus, the design of experiments (DOE) containing only one factor, i.e. the loading rate, and the random repartition of the samples for low temperature are the following one:

| Standard Test n° | Factors          | Samples to be tested |               |               |
|------------------|------------------|----------------------|---------------|---------------|
|                  | B = loading rate | Test series 1        | Test series 2 | Test series 3 |
| 1                | 1                | S-09                 | S-14          | S-15          |
| 2                | 2                | S-07                 | S-10          | -             |
| Level 1          | 50mm/min         |                      |               |               |
| Level 2          | 500mm/min        |                      |               |               |

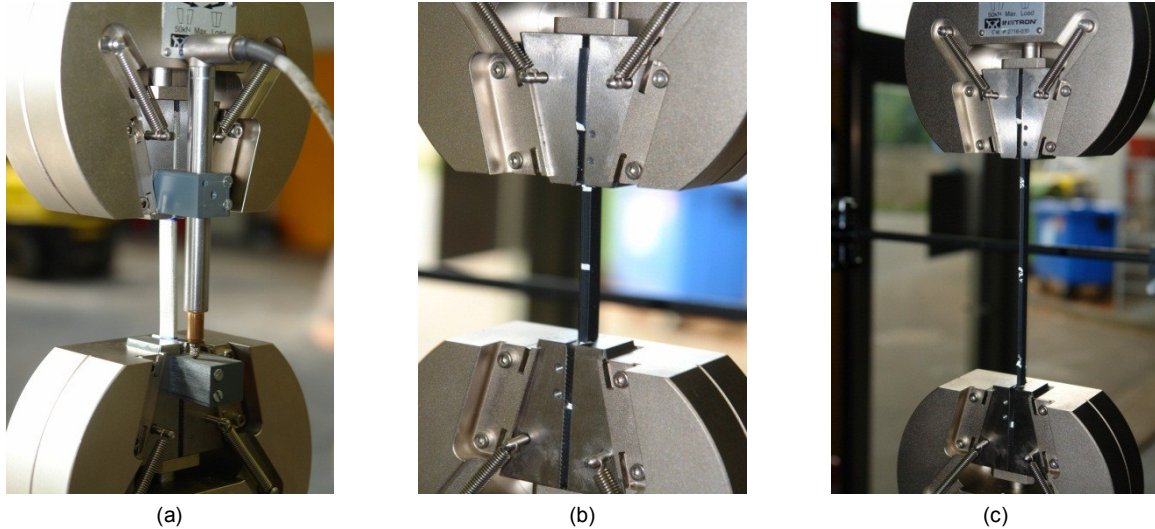
**Table 4.2-** Additional design of experiments for low-temperature influence on silicone dog-bone samples

### Description of the tests

The tensile tests were realized on a 10kN INSTRON mobile hydraulic press equipped with self-closing wedge clamps having a large number of teeth at their surface to avoid any sliding, see Fig. 4.7. A 10kN force sensor was installed to measure the applied load, while the total displacement measured was the displacement between the grips. Thus, the positioning of samples was of a crucial importance and only the tested zone of 60mm was free of any fixation.

Pilot tests were first carried out on aluminum sample of lower cross-section ( $10 \times 3 \text{ mm}^2$ ) to ensure the accuracy of the force and displacement sensors with very low loading rate. Then, four other pilot tests were conducted at the envisaged loading rates on manufactured silicone dog-bone samples, i.e. [S-03

/ S-11 / S-18 / S-23]. In addition to the measurement of the total force and displacement, the possible sliding of the dog-bone sample was also checked for each pilot test by measuring the remaining vertical space existing between the extremities of the “heads” (top and bottom) of the specimens and the lower part of the grips. With this verification, it could have been concluded that no sliding happened for the two loading rates.



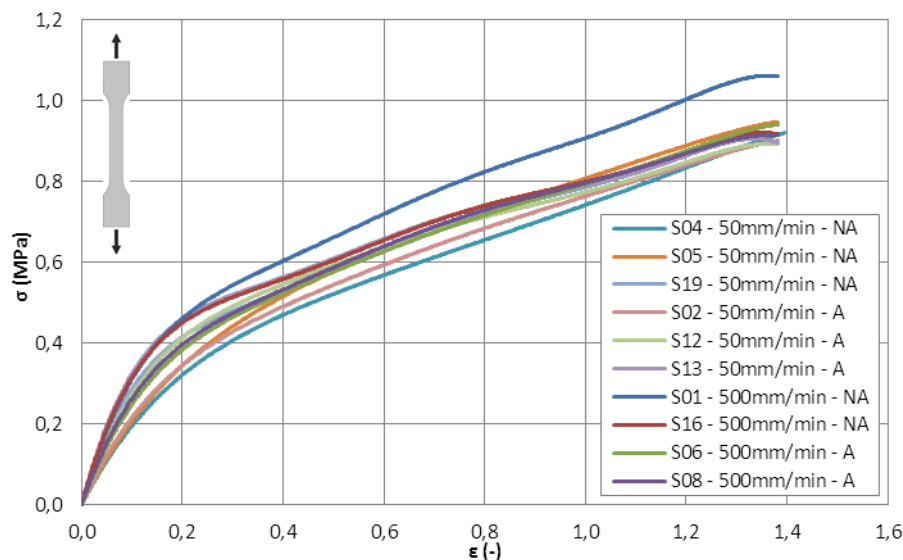
**Figure 4.7-** (a) Pilot tests on aluminum, (b) Installation of a silicone dog-bone sample and (c) Deformed silicone sample

Finally, all the fifteen experiments detailed in Tables 4.1 & 4.2 were performed following rigorously the same protocol, for which the samples were marked beforehand and then installed in the clamps of the machine preset to automatically have the gap of 60mm.

### Tests results

For all the tested specimens, with no regard to the design of experiments, the measured force-displacement data were converted in stress-strain curves by dividing the force by the tested section area (dimensions of Appendix A.2) and the displacement by the initial tested length of 60mm. To analyse the results and apply the ANAVAR method, the two designs of experiments will at first be regarded separately.

#### i. First DOE with grouping of factors (Table 4.1)



**Figure 4.8-** Stress-strain diagram corresponding to the design of experiments of Table 4.1 (NA=non-aged, A=aged)

The obtained tensile stress-strain diagrams for the first design of experiment, Table 4.1, are exposed in Fig. 4.8. Only one dog-bone sample failed under the maximum imposed deformation of 140% (about 85mm), i.e. sample S-02. This imposed deformation was well above the elongation at break provided by the adhesive manufacturer, i.e. of 130% corresponding to a strength of 0,95MPa. All the other 14 specimens were unloaded after reaching the maximum displacement and measured. From this analysis, it was found that the samples recovered totally their initial dimensions after being unloaded. Hence, the obtained curves confirm the strong non-linear behaviour with a full-recovery of the dimensions after unloading as expected for hyperelastic silicone material.

All the curves are visually in the same range, relatively well superposed, and making a distinction between the aged or non-aged samples and between the one subjected to low or elevated loading rates appears difficult. Nevertheless, it was decided to investigate in detail, with the ANAVAR method, the influence of the two factors, i.e. ageing and loading rate, on the stress for the maximum deformation and on the stiffness at the origin calculated in accordance with the ETAG 002.

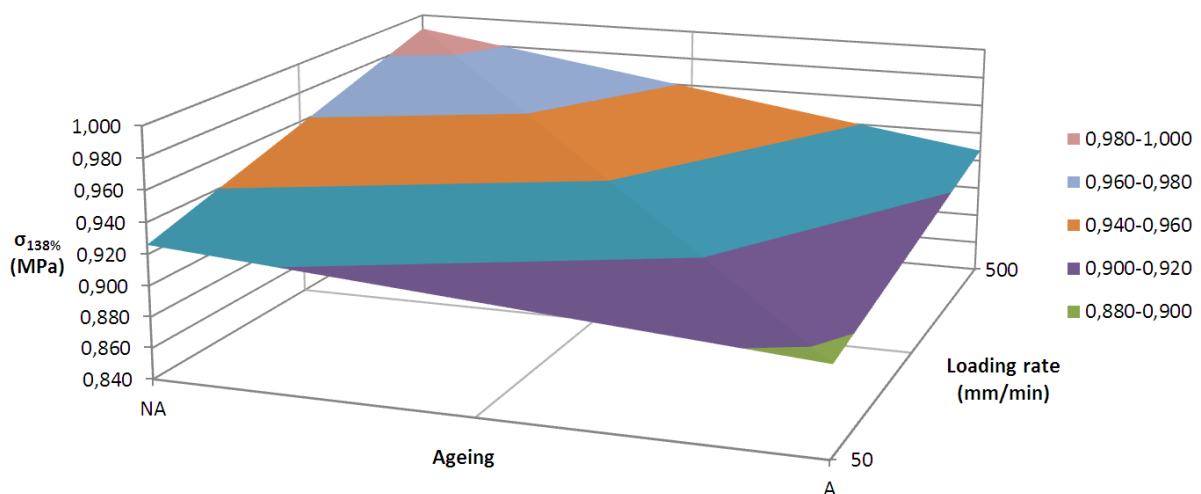
- Influence of the factors on the stresses

The elongation of the only sample, which failed in tension, is taken as the reference for the evaluation of the stresses. Thus, for each specimen of the first design of experiments, the stress at an elongation of 138% was determined and recorded in Table 4.1.

| Test n° | A      | B            | $\sigma_{138\%}$ (MPa) |                |               |
|---------|--------|--------------|------------------------|----------------|---------------|
|         | Ageing | Loading rate | Test series 1          | Tests series 2 | Test series 3 |
| 1       | No     | 50mm/min     | 0,915                  | 0,948          | 0,916         |
| 2       | No     | 500mm/min    | 1,062                  | 0,918          | -             |
| 3       | Yes    | 50mm/min     | 0,901                  | 0,892          | 0,896         |
| 4       | Yes    | 500mm/min    | 0,941                  | 0,914          | -             |

**Table 4.3-** Stress results of the design of experiments for silicone dog-bone samples of Table 4.1

By taking the averaged values of the test series for each test number, it is possible to generate a surface plot allowing concluding on the effect of the factors. This type of diagram is represented in Fig. 4.9. As it can be observed, an axis of symmetry, corresponding to a diagonal, separates the surface in two equal parts generating a roof shape. While the lowest value of stress is reached for aged samples at low loading rate, the maximum is achieved for non-aged samples under elevated loading rate. In addition, non-aged specimens tested at 50mm/min presents the same stress at an elongation of 138% than aged specimens tested at 500mm/min.



**Figure 4.9-** Surface plot of the defined stress versus the ageing and loading rate for silicone dog-bone samples of Table 4.1

Consequently, to draw conclusions from this only graph is not an easy task. Therefore, the ANAVAR method was conducted based on Table 4.1. The complete procedure is detailed in Appendix C. This approach allows determining the effect of each factor and of the interaction of the factor on the recorded values, by comparing the real standard deviations of the coefficients to ideal standard deviations for which the factors have no effect. The realization of this analysis on the data showed that the ageing and loading rate have no influence on the so-defined stress. This could be schematically observed through the two opposite slopes of the diagrams presenting the total effect of a factor, see Appendix C.

To evaluate the probability distribution followed by the stress, the normality test proposed by Lilliefors [4.6] and based on the empirical distribution function was employed, as it necessitates a smaller amount of data than the chi-squared method. From this analysis, presented in Appendix D, the null hypothesis agreeing with the normal distribution was rejected. Therefore, the Lilliefors test adapted to evaluate the null hypothesis of the log-normal distribution was then carried-out and it was found a correct concordance to this distribution. Knowing that the stress complies with the log-normal distribution, the calculation of the 5% fractile was undertaken according to the simplified method suggested in EN 1990 [2.30]. The characteristic stress value obtained for the tensile dog-bone tests of the first design of experiment was of 0,843MPa.

- Influence of the factors on the initial stiffnesses

In Fig. 4.8 were presented the stress-strain diagrams of the tensile tests carried out according to the first design of experiment and it can be noted that dispersions exist at the origin of the curves. To evaluate if a factor affect the material behavior at small deformations, the linear stiffness at the origin was determined with the help of the method detailed in the ETAG 002. It consists in a first linearization of the tension curves, which is only approved for materials with a Poisson's ratio close to 0,5, such as the studied silicone. While the stresses remain unchanged, the linearization is effected on the deformations with the following equation Eq. (4.1):

$$\frac{u_c}{L_0} = \frac{(a - \frac{1}{a^2})}{3} \quad (4.1)$$

With  $u_c/L_0$  the linearized deformation,  
 $L_0$  the initial length of the dog-bone sample,  
 $a = L/L_0$  and  $L$  the length of the loaded piece.

The above equation allows plotting the new stress-linearized strain curves on which will be evaluated the tangent stiffness at the origin. An example of a linearized stress-strain curve is shown on Fig. 4.10.

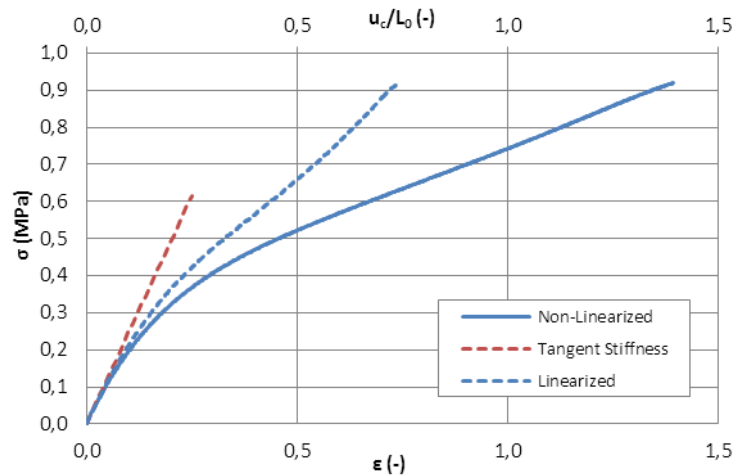


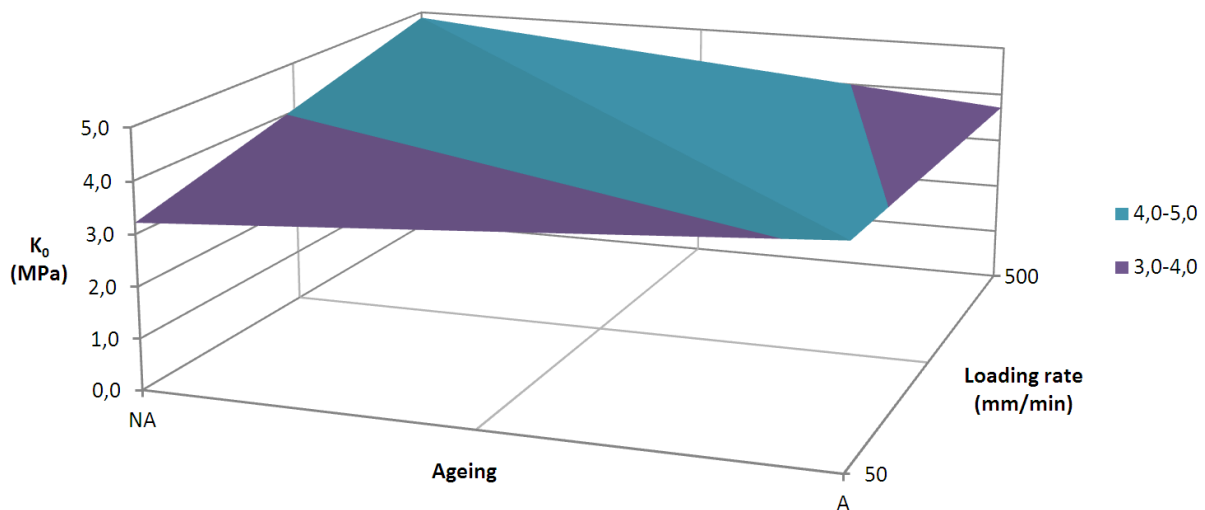
Figure 4.10- Example of linearized curve – sample S-04-50mm/min-NA (Top x axis only for dashed lines)

The complete operation was performed for all the ten samples of Table 4.1 and the corresponding stiffnesses at origin were recorded in Table 4.4.

| Test n° | A      | B            | Initial stiffness $K_0$ (MPa) |                |               |
|---------|--------|--------------|-------------------------------|----------------|---------------|
|         | Ageing | Loading rate | Test series 1                 | Tests series 2 | Test series 3 |
| 1       | No     | 50mm/min     | 2,457                         | 2,599          | 4,592         |
| 2       | No     | 500mm/min    | 4,727                         | 5,027          | -             |
| 3       | Yes    | 50mm/min     | 2,863                         | 4,015          | 5,345         |
| 4       | Yes    | 500mm/min    | 3,516                         | 3,913          | -             |

**Table 4.4-** Initial stiffness results of the design of experiments for silicone dog-bone samples of Table 4.1

As for the study concerning the influence of the factors on the defined stress, the averaged values of the stiffnesses at the origin were averaged over the test series for each test number in order to plot the surface curve of the results, see Fig 4.10. The global shape of the curve is similar to a roof with a maximum diagonal. For non-aged specimens, the stiffness at the origin increases with the loading rate, while for aged specimens, the opposite effect occurs with a decreasing of the stiffness with increase of the loading rate. Hence, with this only graph, no conclusion could be drawn. Consequently, the ANAVAR method was again carried out to evaluate the influence of each factor.



**Figure 4.11-** Surface plot of the initial stiffness versus the ageing and loading rate for silicone dog-bone samples of Table 4.1

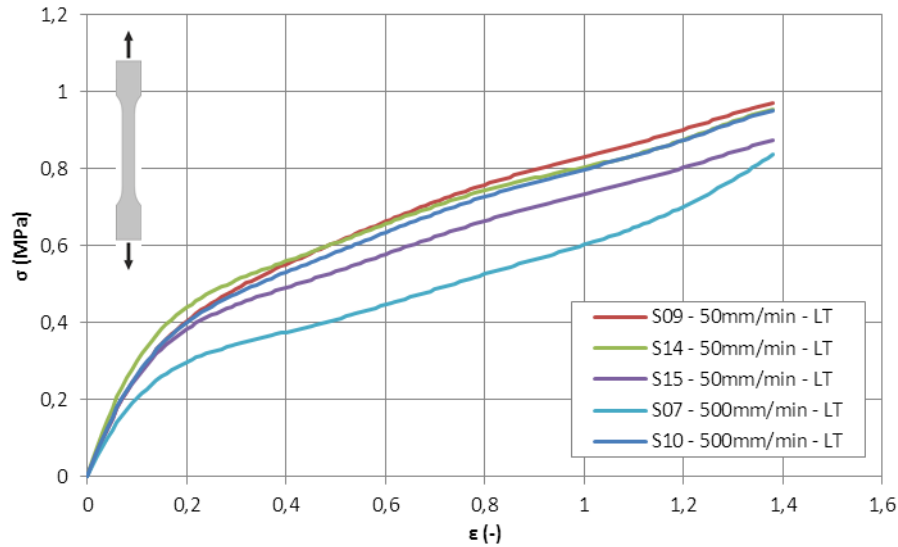
The complete procedure is detailed in Appendix C and it could be stated that none of the ageing and loading rate factors or the interaction influence the properties of the silicone at low deformations.

ii. Second DOE concerning only low temperature (Table 4.2)

In this section, only the additional design of experiments concerning the influence of the loading rate after an artificial ageing at low temperature, see Table 4.2, is of interest. The corresponding stress-strain diagrams of the five experiments are given in Fig. 4.12. Under the maximum imposed elongation of about 140% no sample broke. In addition, and as for the previous design of experiments, the behaviour of the dog-bone samples was clearly non-linear and once unloaded they instantly recovered their original dimensions.

After the ageing at low temperature, one curve differed from the other by smaller stresses at given deformations. Hence, to evaluate if this behaviour was due to the impact of the loading rate, a first analysis of the stress at the maximum deformation was performed followed by a second one concerning the initial stiffness in accordance to the ETAG 002. Finally, to evaluate the effect of the low temperature on the silicone, a comparison with the first design of experiments was realized.





**Figure 4.12-** Stress-strain diagram corresponding to the design of experiments of Table 4.2 (LT=Low Temperature)

- Influence of the loading rate on the stresses

As for the previous design of experiment, the stress at an elongation of 138% was evaluated for all the five specimens and recorded in Table 4.5. This enables to have an element of comparison between the two DOE.

| Standard Test<br>n° | Factors          | $\sigma_{138\%}$ (MPa) |               |               | Average (MPa) |
|---------------------|------------------|------------------------|---------------|---------------|---------------|
|                     | B = loading rate | Test series 1          | Test series 2 | Test series 3 |               |
| 1                   | 50mm/min         | 0,971                  | 0,954         | 0,873         | 0,933         |
| 2                   | 500mm/min        | 0,836                  | 0,951         | -             | 0,894         |

**Table 4.5-** Stress results of the additional design of experiments for silicone dog-bone samples of Table 4.2

The calculation of the average results over the test series for each test number allows determining a relative difference of 4,4% between the two imposed loading rates, which can be neglected, especially with regards to the same value calculated for the first design of experiments and equal to 5,2%. The simple diagram concerning the total effect of the loading rate, presented in Fig. 4.13 (a), corroborates the fact that this factor has no effect on the maximum stresses.

- Influence of the loading rate on the initial stiffnesses

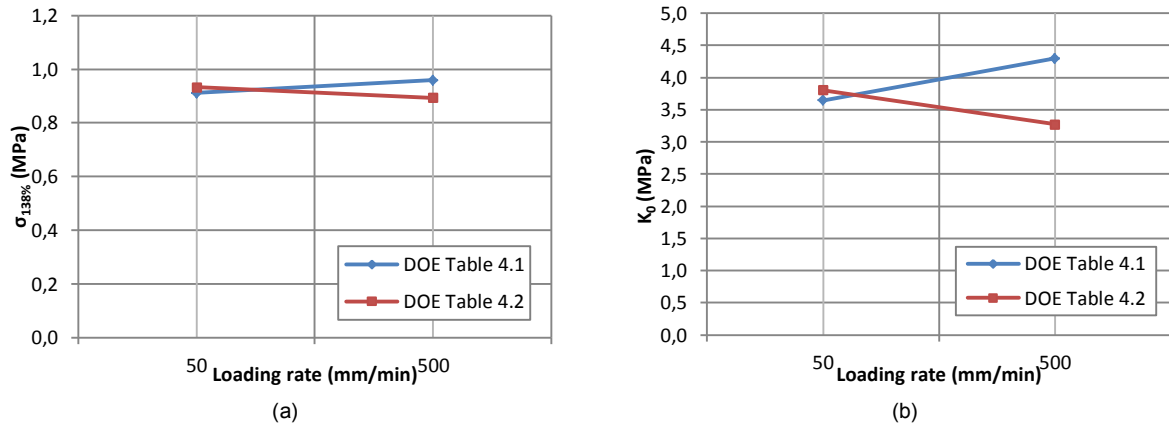
To ensure that the loading rate has no influence on the first portion of the stress-strain diagram, i.e. at low deformations, the stiffness at the origin was determined for the five dog-bone samples with the method of the ETAG 002. The tangent stiffness results are recorded in Table 4.6.

| Standard Test<br>n° | Factors          | Initial stiffness $K_0$ (MPa) |               |               | Average (MPa) |
|---------------------|------------------|-------------------------------|---------------|---------------|---------------|
|                     | B = loading rate | Test series 1                 | Test series 2 | Test series 3 |               |
| 1                   | 50mm/min         | 3,544                         | 4,252         | 3,618         | 3,805         |
| 2                   | 500mm/min        | 2,890                         | 3,652         | -             | 3,271         |

**Table 4.6-** Initial stiffness results of the additional design of experiments for silicone dog-bone samples of Table 4.2

The relative difference between the averaged initial stiffnesses of the two loading rates is of 16,3%, which is quite close to the one of the first design of experiment of 15,1%. With this large gap, it is difficult to conclude on the invariance of the initial stiffness towards the loading rate. Therefore, the

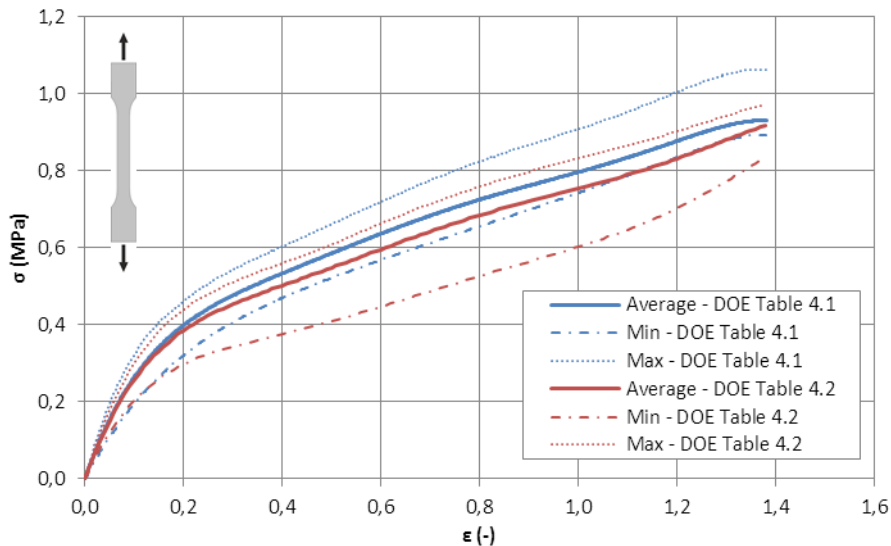
total effect of the loading rate is plotted for the both design of experiments, see Fig. 4.13 (b). From this diagram, it can be noted that the two design of experiments present opposite slopes with relatively close values. Consequently, as for the maximum stress, the loading rate does not seem to affect the initial stiffness.



**Figure 4.13-** Total effect of the loading rate on (a) the maximum stress and (b) the initial stiffness for DOE Table 4.2

- Comparison between first and second DOE

With the first design of experiments, the invariance of the silicone properties towards the ageing, regrouping the elevated temperature, the humidity and the UV-radiation, and the loading rate over the full deformation range was assessed. The second design of experiment on aged specimens at low temperature demonstrated the stability of the silicone properties facing different loading rates. Then, to appraise the influence of the ageing at low temperature, the average curves of the first and second design of experiments can be compared, see Fig 4.14.



**Figure 4.14-** Stress-strain diagram comparing the first and second DOE

By simply analyzing the average curves of the both design of experiments, it is possible to remark that they are relatively well superposed over all the deformations, which suggests that the ageing at low temperature does not influence the behaviour. To validate this observation, a comparison in terms of average and standard deviation was executed for the two measured specifications, i.e. the stress at an elongation of 138% and the initial stiffness. For the so-defined maximum stress, the average value of the first design of experiments is of 0,930Mpa with a standard deviation is of 0,049Mpa, while the average is of 0,926Mpa with a standard deviation of 0,051Mpa for the overall tests including the ones under low temperature ageing. The difference between the two maximum stresses is less than 0,5%.



For the initial stiffness, the average value of the first design of experiments is of 3,905Mpa with a standard deviation of 1,029Mpa, while the average value for all the tests, low-temperature ageing included, is of 3,801Mpa with a standard deviation of 0,878Mpa. Thus, by comparing the two averaged initial stiffnesses, a relative difference of 2,7% is observed. Consequently, for the two measured data, it can be concluded that none of the possible influent factors has an impact on the tensile properties of silicone adhesive.

All the data concerning the maximum stress were regrouped to evaluate with the Lilliefors test if the null hypothesis of the log-normal distribution was still valid. The complete analysis is presented in Appendix D. From this analysis, it was found a good concordance with the log-normal distribution. Therefore, the characteristic stress, corresponding to the 5% fractile, was again calculated with the EN 1990 [2.30]. The estimated stress characteristic value of 0,837Mpa could later be employed for the design of DC993 silicone subjected to tension.

#### 4.2.1.3 Cyclic tests

In addition to these quasi-static tests, a second test series of five dog-bone samples was subjected to cyclic loadings with the aim to appraise the stress softening occurring, i.e. the Mullin's effect and the cumulative damage. The same procedure than the one employed for the quasi-static tests, leading to the analysis of the results, was applied.

#### Definition of the objectives

The main objective of these tests is to characterize the tensile behaviour, i.e. non-linear stress-strain diagrams, for the Dow Corning silicone DC 933 after a finite number of load cycles. The complete list of objectives to meet is the following one:

- Cyclic stress-strain diagrams on sufficient dog-bone samples to apprehend the stress softening arising in this material.
- Evaluate the number of cycles during which the Mullins' effect is really effective. This allows, on one hand, making the distinction between discontinuous and continuous damage and, on the other hand, including this phenomenon in the material law. However the full representation of this effect, with the dependency on the maximum deformation attained previously, as presented in Fig 2.19, is not of interest and of crucial importance for the design with FEA. The principal aim is to determine at which cycle the dissipated energy, i.e. the area of the hysteresis, becomes constant for a given deformation, larger than the maximum allowable deformation. The loading curve of this cycle is then conserved for numerical simulations. This method is made possible because the maximum allowable stress and corresponding deformation were evaluated in the case of quasi-static tests (1<sup>st</sup> loading) and because the unloading path is lower for higher attained deformations. If the silicone is subjected to a higher deformation than the maximum allowable deformation, the unloading curve, superposed for the loading curve of the second cycle, is always lower and more conservative than the first unloading curve obtained for a deformation equivalent to the maximum allowable deformation.
- The prediction of the stress softening related to the continuous damage is also of high interest to foresee the in-use behaviour of silicone under cyclic tension.
- A result of the quasi-static tests is the invariance of the silicone properties towards environmental conditions, such as the ageing and the loading rate. This invariance should also be assessed for similar criteria in the case of cyclic tests.

#### Selection of the influent factors

The selection of the influent factors was mainly based on the results obtained from the previous analysis on the quasi-static tests. Indeed, it was demonstrated that the silicone properties in tension do not vary with the application of an artificial ageing procedure and with the applied loading rate.

However, to fully reject these two factors, a comprehension of the two types of damage is essential. As evoked in section 2.4.2.1, the stress softening undergone by silicone materials under cyclic tests are irreversible and could be due to either a rupture of the chains of the molecular network, or to a sliding of the chains at the connecting nodes. Therefore, even if the influence of the artificial ageing on the two types of damage seems unlikely, the loading rate could impact the properties. Elevated loading rates could generate more damage, such as more chain failures or more sliding. Hence, the applied frequency constitutes a probable influent factor.

In addition, with the expected results for the Mullins' effect, the maximum encountered deformations do not fall in the category of influent factors, but a correct definition of the amplitude of the deformations is of importance for the cyclic tests. Indeed, in order to be conservative for the definition of the Mullins' effect, the imposed displacement should be higher than the maximum allowable displacement found for the first cycle, i.e. the maximum allowable displacement of the quasi-static test of 70mm (at a stress of 0,837Mpa). Thus, within the scope of this study, the selected maximum displacement to be imposed on the dog-bone samples was of 80mm, corresponding to an amplitude of 40mm.

Consequently, only one possible influence factor was selected for these cyclic tests, i.e. the frequency. Two values were envisaged, a low frequency of 0,1Hz and an elevated of 1Hz equivalent to one cycle per second, for an imposed displacement of 80mm in total (strain of about 1,3).

### Choice of the Taguchi table

As the imposed deformation is fixed, only one factor, the frequency, with two levels will be evaluated. The design of experiments, presenting a repetition of the tests and containing the repartitions of the five dog-bone specimens tested, is exposed in Table 4.7.

| Standard Test n° | Factors       | Samples to be tested |               |               |
|------------------|---------------|----------------------|---------------|---------------|
|                  | A = frequency | Test series 1        | Test series 2 | Test series 3 |
| 1                | 1             | S-33                 | S-32          | S-31          |
| 2                | 2             | S-30                 | S-28          | -             |
| Level 1          | 0,1Hz         |                      |               |               |
| Level 2          | 1Hz           |                      |               |               |

**Table 4.7-** Design of experiments for frequency influence on silicone dog-bone samples under cyclic loading

### Description of the tests

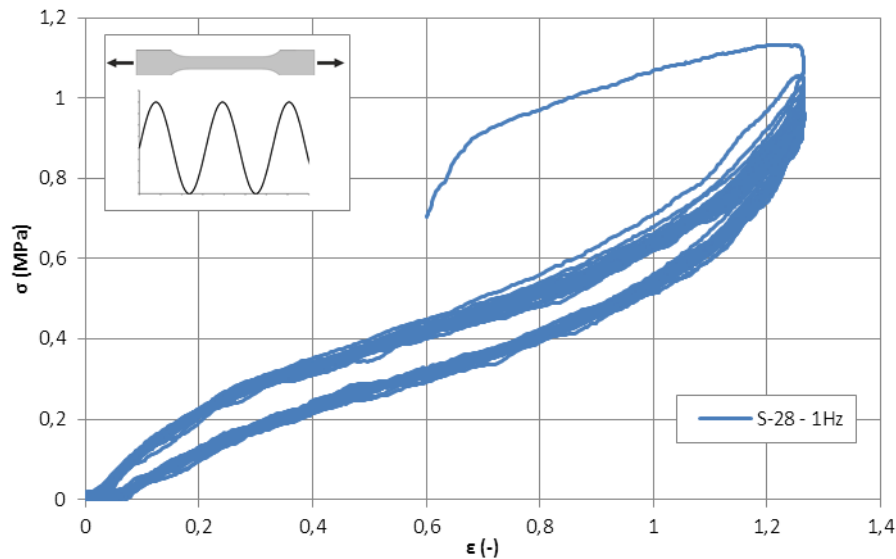
The cyclic tests in tension were conducted on the 10kN INSTRON mobile hydraulic press employed for the quasi-static tests. The layout of the system remained identical with the same self-closing wedge clamps, see Fig. 4.7. Pilot tests were carried out with unbroken samples from the quasi-static tests to validate the non-sliding of the specimens between the grips even at high frequencies. The force was measured with the help of an external force sensor of 10kN and the imposed displacement was evaluated between the grips. Before installing the sample, the distance between the grips was automatically preset to 60mm to always ensure of the tested length.

All the five tests were conducted in two steps, i.e. they were initially elongated to 40mm (equivalent to a strain of 0,65) and then subjected to sinusoidal loading of 40mm of amplitude and under the desired frequency. For the specimens subjected to low frequency, a minimum of 25 cycles were realized while for the specimens under high frequency, 60 cycles were performed.

### Tests results

As for the quasi-static tests, the stress-strain diagrams were obtained by dividing the force by the tested cross section (dimensions of Appendix A.2) and the displacement by the initial testing length of

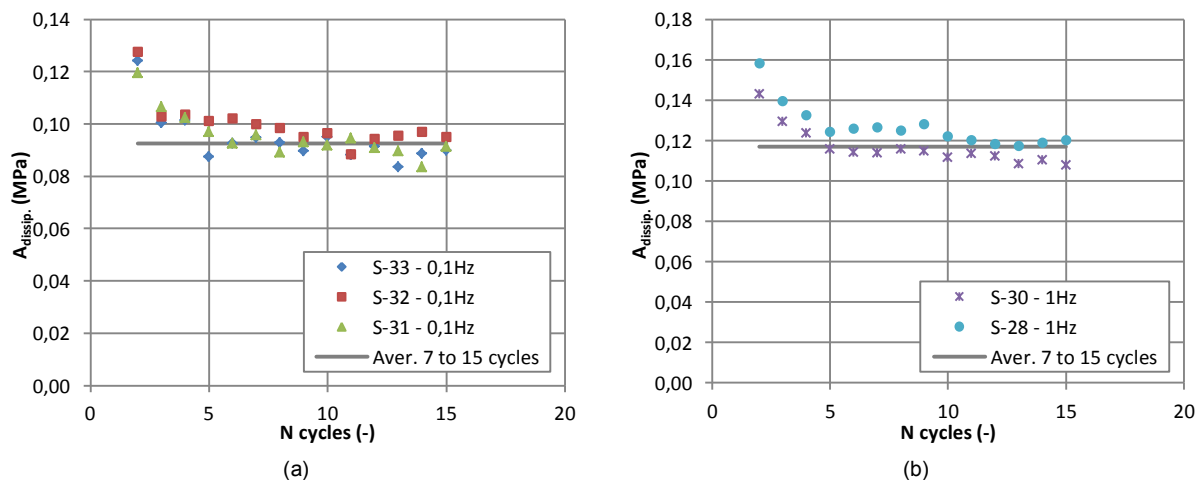
60mm. A typical resulting cyclic curve is introduced in Fig. 4.15 for the dog-bone S-28 tested at a frequency of 1Hz. The behaviour appears clearly non-linear and after the first cycle, the stress shows an important softening over all the strain range. Nevertheless this stress softening becomes less important with increasing of the number of cycles.



**Figure 4.15-** Cyclic tension stress-strain diagram for silicone sample under a frequency of 1Hz

- Mullins' effect characterization

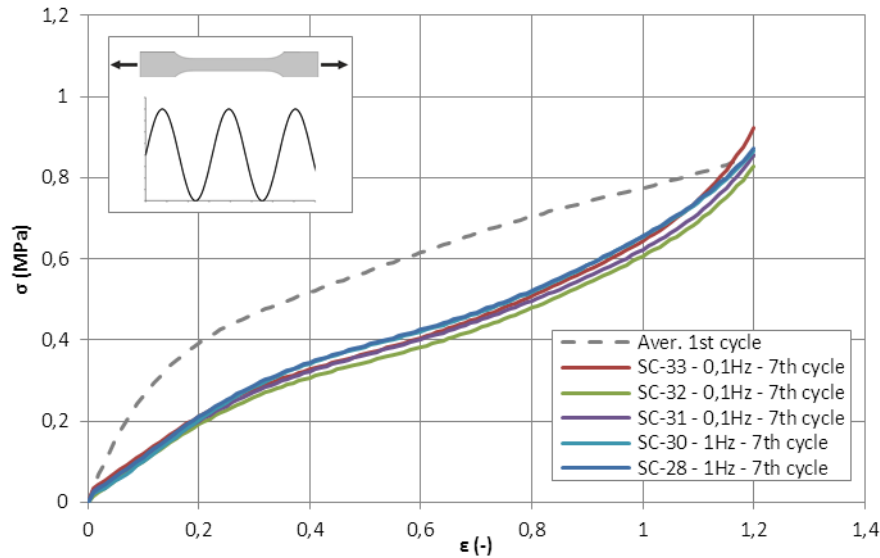
As mentioned in the definition of the objectives, to make a proper distinction between the continuous damage and discontinuous Mullins' effect, an analysis of the dissipated energy has to be effected for each tested samples. The dissipated energy corresponds to the area comprised in the hysteresis. For the first incomplete cycle of Fig. 4.15, the dissipation appears larger than for the other cycles and determining at which cycle this energy becomes constant is essential to characterize the duration of the Mullins' effect. Thus, the area within the hysteresis was calculated for each specimen starting from the 2<sup>nd</sup> cycle to the 15<sup>th</sup> cycle and these values were recorded and plotted on Fig 4.16.



**Figure 4.16-** Evaluation of the dissipated energy for samples (a) at low frequency and (b) at high frequency

As it can be noted, for all the cycles, a small difference between the samples tested at low frequency and the samples at elevated frequency existed, i.e. at 0,1Hz the area of the hysteresis was about 20% lower than the one measured at 1Hz. The origin of this difference was not attributed to the frequency only, as the hydraulic press also influenced these results with slight differences in displacement amplitudes between the two imposed frequencies. Indeed, a control of the amplitudes versus time exposed that the maximum displacement was lower for the low imposed frequency. Nevertheless, the

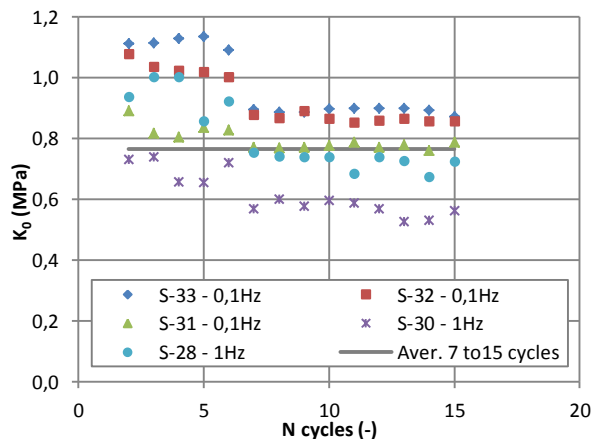
dissipated area decreased for both cases in the same manner with a drop of about 0,2MPa over the seven first cycles. Beyond this cycle, almost no variation of the dissipated energy was observable. For the two diagrams, the averages of the dissipated area from the 7<sup>th</sup> to the 15<sup>th</sup> cycles were drawn on Fig. 4.16 to appraise this behaviour and detect a plateau. It can be conclude, that the Mullins' effect only disappears after the seven cycles. Theoretically, this effect is commonly regarded as acting on the first cycle, which is explained by the energy loss of about 70% between the first cycle exposing a dissipated area of 0,45MPa and the averaged value of the second cycle of 0,135MPa. Nevertheless, considering the 7<sup>th</sup> cycle as the limit of the Mullins' effect is more conservative. The loading path of this cycle was then compared, for each specimen, to the averaged loading path of the first loading, i.e. from the quasi-static tests, see Fig.4.17.



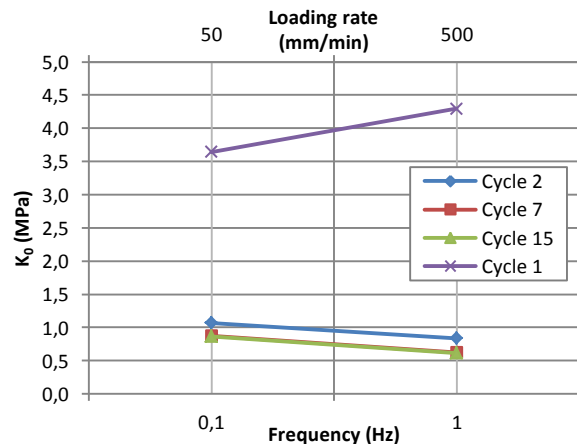
**Figure 4.17-** Comparison between the averaged 1<sup>st</sup> cycle and the limiting 7<sup>th</sup> cycle of the Mullins' effect

All the 7<sup>th</sup> loading curves, at low or high frequencies, are in the same range without major deviation for the studied deformations. Therefore, the influence of the frequency on the evolution of the behaviour after several cycles does not seem to be important. In addition, the stress softening between the first loading and the 7<sup>th</sup> is consequent, e.g. for a deformation of 0,8, the stress decreases from 0,7MPa for the first cycle to 0,5MPa for the 7<sup>th</sup> cycle.

In complement to the analysis on the dissipated energy, the evaluation of the frequency influence over the cycles was assessed with an analysis of the stiffness at the origin  $K_0$ . The linearization method of the ETAG 002 to calculate the tangent stiffness was again employed for the first 15 cycles, see Fig. 4.18. For the most relevant cycles, the total effects of the frequency were plotted on Fig. 4.19.



**Figure 4.18-** Initial stiffness versus the cycle number



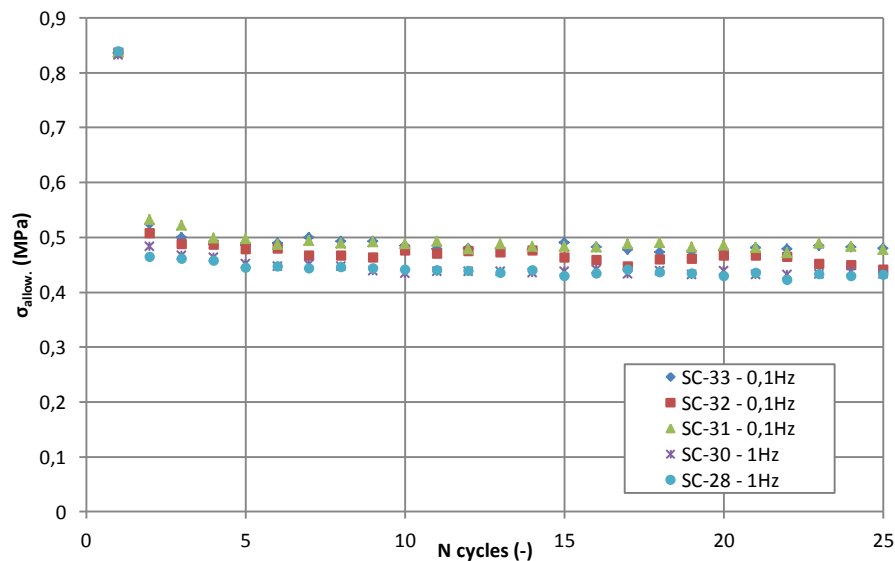
**Figure 4.19-** Total effect of loading rate on the initial stiffness (Top x axis only for cycle 1)

As for the dissipated energy, the 7<sup>th</sup> cycle appears as the limit of some change in behaviour. Concerning the initial stiffness study, an important loss, for all the specimens, is remarked at this cycle number and then a plateau is reached. This can easily be remarked on Fig. 4.19, in which the total effect of the frequency for the cycle 7 and 15 are completely superposed. Moreover, if the initial stiffness obtained for the quasi-static tests (3,97MPa) is compared to the in averaged stiffness from the 7<sup>th</sup> to the 15<sup>th</sup> cycles (0,765MPa), a difference of about 80% is found, which, with regards to the large gap between the first cycle and the other cycles, allows to prove the conservative criterion for the limit of the Mullins' effect.

In addition, the slope representing the evolution of the initial stiffness in function of the frequency is similar for each cycle, i.e. a decrease of tangent stiffness with the increase of the frequency, see Fig. 4.19. However, by concentrating, on the first loading, representing the quasi-static results, the opposite phenomenon occurs with an increase of the initial stiffness with the increase of the loading rate. Consequently, even if the loading rates compared are different, no influence of the frequency could be postulated. This could also be confirmed by looking independently the tested samples of Fig. 4.18, e.g. for a small number of cycle the tangent stiffness determined for the dog-bone specimen S-28 under a frequency of 1Hz is clearly higher than the one of the sample S-31 subjected to 0,1Hz. Thus, it can be assumed that the frequency do not impact the behaviour of silicone elastomer subjected to uniaxial cyclic tension.

- Prediction of the continuous damage

The evaluation of the maximum allowable stress and deformation for the case of quasi-static tests constituted the reference for the prediction of the stress softening under cyclic loadings. Indeed, the evolution of the stress was analyzed at a fixed deformation, corresponding to the maximum allowable deformation. All the samples were tested at least on 25 cycles, for which the loss in stress was recorded and plotted according to the cycle number, see Fig. 4.20.



**Figure 4.20-** Evolution of the maximum allowable stress with the increase of cycles

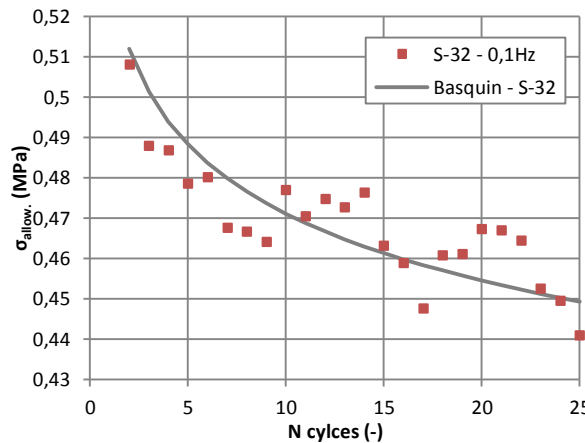
For the first cycle, the maximum allowable stress was of 0,837MPa, as obtained during the quasi-static tests. Then, for the second cycle, an important loss was remarked and finally a more homogenous decrease was observed for the following loadings. The considerable drop of stress between the two first cycles could be explained by the testing method, as the samples were subjected to a higher deformation than the maximum allowable deformation. The unloading of the first cycle, very close to the loading of the 2<sup>nd</sup> cycle, was lower than one under the exact allowable deformation. For the prediction after a large number of cycles, the stress for the first cycle was consequently let aside.

For fatigue tests, Wöhler curves or SN curves are commonly employed to assess the lifetime of a material, in terms of load cycles, under an applied stress. For the presented cyclic tests on silicone

samples, the determination of similar curves, not based on the complete failure but on the maximum allowable displacement, had to be established. In order to fulfill this objective, several mathematical formulations representing the Wöhler curve were envisaged, i.e. the simple Wöhler formulation necessitating expressing the stress as a linear function of the logarithm of the cycle and the Basquin formulation, see Eq. (Bas), relying solely on logarithmic functions.

$$\log(N) = \log(a) + b \log(\sigma) \quad (\text{Bas})$$

With  $a$  and  $b$  material constants. These two parameters are generally determined with the help of a linear regression for each test. The axes of Fig. 4.20 were transformed into logarithmic values and a good concordance with the Basquin formulation was found, see Fig. 4.21 for a typical example and Table 4.8 for the material constants and correlation coefficients  $R$ .



| Samples    | Basquin coefficients |       | Correlation coefficient |
|------------|----------------------|-------|-------------------------|
|            | a                    | b     |                         |
| S-33-0,1Hz | 1,5E-07              | -25,1 | 0,802                   |
| S-32-0,1Hz | 4,6E-06              | -19,4 | 0,853                   |
| S-31-0,1Hz | 1,1E-06              | -22,6 | 0,851                   |
| S-30-1Hz   | 1,2E-07              | -22,5 | 0,915                   |
| S-28-1Hz   | 1,2E-09              | -28,0 | 0,933                   |

Table 4.8- Basquin coefficients for the tensile samples

Figure 4.21- Wöhler curve representation with Basquin form

Over the 25 cycles and for each sample, the estimation of the Wöhler curve with the Basquin formulation showed good results with correlation coefficient close to 1. Therefore, an averaged curve was calculated based on all these curves, see Fig. 4.22. For this mean curve, the material coefficients were equal to ( $a = 2,2\text{E-}07$ ;  $b = -23,2$ ).

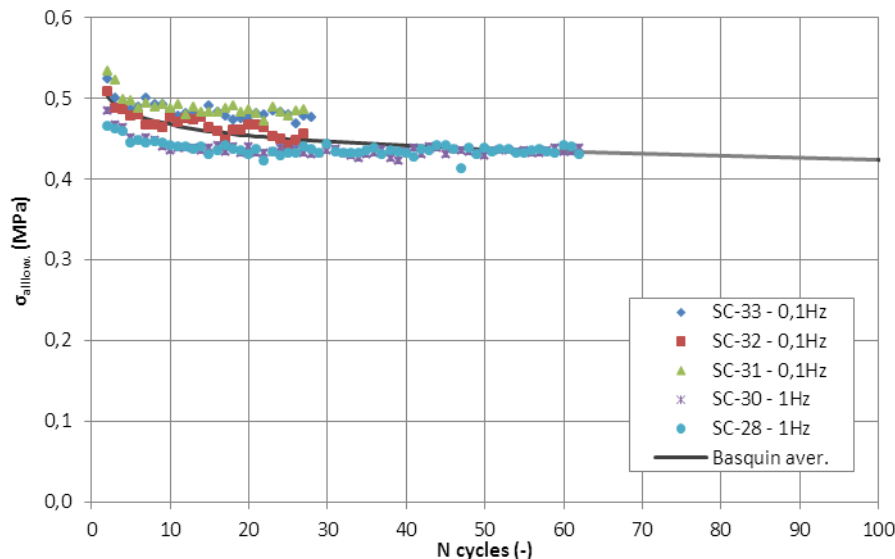


Figure 4.22- Comparison between the averaged Basquin formulation and the tensile tests results

A comparison at the 60<sup>th</sup> cycle, between the predicted stress (0,433MPa) and the effective stress results for specimens subjected to a frequency of 1Hz (0,437MPa), was realized and showed a difference less than 1%. This validated the envisaged model for a small number of cycles. In addition,

at this cycle, the maximum allowable stress of the first loading of 0,837MPa was divided by about 2. For a larger number of cycles, the prediction of the allowable stress decreased more importantly, i.e. for 1000 cycles the stress was equal to 0,383MPa, for 10000 cycles equal to 0,347MPa and for one million of cycles equal to 0,285MPa.

#### 4.2.1.4 Long-term tests

The last type of tensile action, arising in the case of vertical non-accessible façade inclined towards the outside, corresponds to long-term. To appraise the influence of these long duration actions on the chosen silicone elastomer, eight samples were tested in relaxation according to the Taguchi design of experiments.

#### Definition of the objectives

The main objectives of these relaxation long-term tests are to characterize the loss of stress under constant imposed displacements and to determine if, after a certain time, a plateau is reached. The complete list of objectives to meet is the following one:

- Quantify the decrease of the stress for a given time and under an imposed displacement. The minimal time during which were carried out these relaxation tests is of 1200s (20min), equivalent to the minimal value found in literature [4.7] for similar elastomer. According to this reference, the variation in stress was found quasi-nil largely before this time.
- As the effective time of tests of 1200s is low compared to the lifetime expected for a glass façade (~25 years for SSGS), a prediction of the loss in stress, expressed with the help of reduction factors, may be necessary.
- Different imposed displacements could be applied to evaluate if the decrease of the stress depends on the maximum imposed displacement.
- Ensure that the tensile properties under relaxation long-term actions are, as for the quasi-static and cyclic tests, independent of environmental conditions. This would allow to definitely considering silicone material subjected to tension as stable.

#### Selection of the influent factors

With the above definition of the objectives, two factors had to be analyzed, i.e. the ageing and the maximum imposed displacement. Concerning the ageing, the influence of low temperatures on the silicone properties was not investigated. Thus, as for the quasi-static tests, the artificial ageing procedure, described in the EN 11431 [4.4] and regrouping the elevated temperature, the humidity and the UV-radiation, was employed. This artificial ageing method allowed reducing the total number of experiments. For the imposed displacement, two values were retained corresponding to the half of the tested dog-bone sample length, i.e. 30mm (equivalent to a deformation of 0,5), and to a displacement of 72mm (deformation of 1,2), which was slightly higher and consequently more conservative than the maximum allowable displacement of 70mm found for the quasi-static tests.

#### Choice of the Taguchi table

Hence, with the grouping of the environmental parameters, two factors at two levels were selected for this design of experiment:

- A. Ageing, a qualitative Boolean factor taking only two values, i.e. with ageing or without.
- B. Imposed displacement, a quantitative continuous factor with two levels, i.e. 30mm and 72mm.

Therefore, with regards to Appendix B, the chosen Taguchi table, presenting a repetition of the tests in order to have a better analysis of the variance (ANAVAR), is the  $L_4(2)^3$  table, see Table 4.9. Again, the repartition of the dog-bone samples in this table was done randomly to eliminate the possible influence of the manufacturing process, i.e. the difference in size due to the mold shapes or the mixing.

| Standard Test n° | Factors  |                           | Samples to be tested |               |
|------------------|----------|---------------------------|----------------------|---------------|
|                  | A        | B                         | Test series 1        | Test series 2 |
| 1                | 1        | 1                         | S-25                 | S-27          |
| 2                | 1        | 2                         | S-17                 | S-21          |
| 3                | 2        | 1                         | S-20                 | S-26          |
| 4                | 2        | 2                         | S-22                 | S-24          |
| Level 1          | Not Aged | 30mm ( $\epsilon = 0,5$ ) |                      |               |
| Level 2          | Aged     | 72mm ( $\epsilon = 1,2$ ) |                      |               |

**Table 4.9-** Design of experiments for silicone dog-bone samples under long-term tension

### Description of the tests

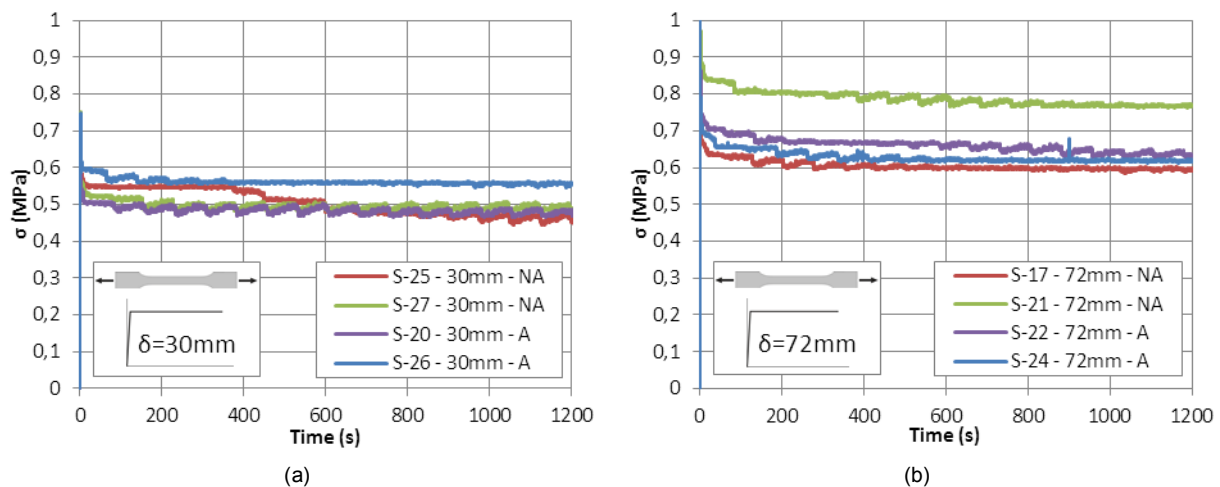
As for all the experiments on dog-bone samples, the 10kN INSTRON mobile hydraulic press equipped with self-closing wedge clamps was used, see Fig. 4.7. The force was measured with the help of an external force sensor and the displacement was recorded between the grips. To always start the test with the same length, the press was automatically preset to have a gap of 60mm between the grips.

For the realization of relaxation tests, a fixed displacement should be imposed quickly and keep constant to note the evolution of the stress. Thus, setting the imposed displacement could lead to some difficulties, such as oscillations, damaging the properties of the dog-bone specimen, especially with regards to the large envisaged imposed deformations. To avoid these effects, the desired displacement was applied in one second and then maintained constant during the total test duration of 1200s. With this procedure, generally applied for creep tests, the first measure of the result should be done 60s after reaching the imposed plateau.

Pilot tests to make sure of the non-sliding of the dog-bone and of the correct measurement of the force were carried out on specimens S-03 and S-11. With these two first tests, the procedure was validated and the experiments on the eight samples of the Taguchi table were realized.

### Tests results

As mentioned for the other tensile tests, the imposed displacement was checked and the measured force was converted in stress by simply dividing by the tested cross section (dimensions in Appendix A.2). For long-term tests, standard stress-time diagrams were drawn for the 2 imposed displacements, see Fig. 4.23.



**Figure 4.23-** Stress-time diagrams for an imposed displacement of (a) 30mm and (b) 72mm

For the two imposed displacements, the stresses decreased rapidly during the first 200s and then the variations became smaller. The final stresses at 1200s were naturally different for the two series, which meant that the final values depended on the imposed deformation. In addition, some dispersion



was found within each series, i.e. one curve being above the other during the whole test duration. Hence, to properly set conclusions with these diagrams and to study the influence of the possible influent parameters, a variance analysis was first performed on the presented data and then a comparison with the corresponding quasi-static stresses was made.

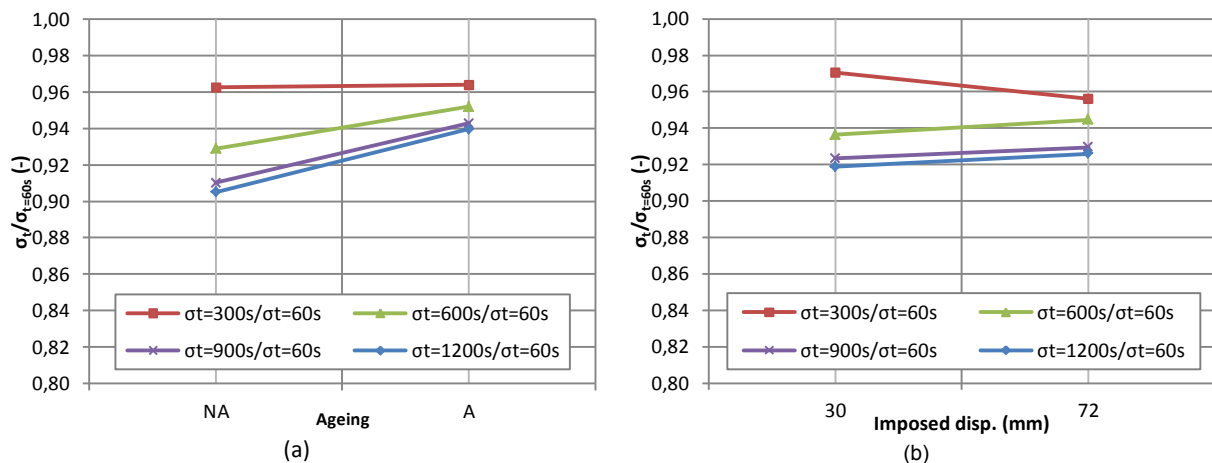
- Analysis of the stress ratio decrease

As evoked in the description of the test method, the first measure of the stress had to be effected after the first 60s following the final imposed displacement in order to avoid the influence of the quick loading. Therefore, this value was determined for each result and was assimilated to a reference value. Other characteristic stress values at 300s, 600s, 900s and 1200s were evaluate too. For each dog-bone specimen, the ratio of the stress at one instant over the reference stress at 60s was calculated to appraise the softening during the loading time. This operation allowed checking if the silicone properties in long-term tension after a time of 60s depended on the influent factors, i.e. the ageing and the imposed displacement. An example of this ratio concerning the maximum tested duration is given in Table 4.10.

| Standard Test n° | A      | B             | $\sigma_{t=1200s}/\sigma_{t=60s}$ (-) |               |
|------------------|--------|---------------|---------------------------------------|---------------|
|                  | Ageing | Imposed disp. | Test series 1                         | Test series 2 |
| 1                | No     | 30mm          | 0,829                                 | 0,933         |
| 2                | No     | 72mm          | 0,940                                 | 0,918         |
| 3                | Yes    | 30mm          | 0,965                                 | 0,948         |
| 4                | Yes    | 72mm          | 0,902                                 | 0,944         |

**Table 4.10-** Maximum stress ratio of the design of experiments for long-term silicone dog-bone tests in tension (Table 4.9)

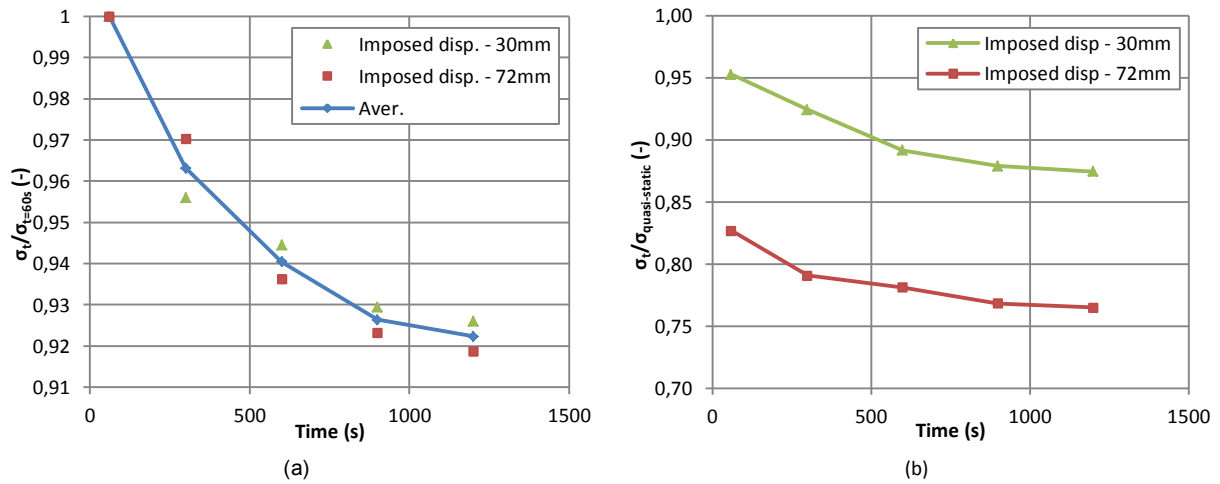
This procedure was done for the four stress ratios and the total effect of the ageing and loading rate factors were plotted for each case, see Fig 4.24.



**Figure 4.24-** Total effect of (a) the ageing and (b) the imposed displacement for long-term dog-bone tests in tension (Table 4.9)

While the influence of the ageing factor after 300s was neglected considering the quasi-nil slope, some variation could be observed after 600s. Indeed the non-aged samples exhibited a lower stress ratio than the aged ones and so a larger stress reduction factor. Nevertheless, these variations were relatively small. In addition, with no regard to the time, the stress ratios of the two imposed displacements were surprisingly close. Thus, the stress reduction after the first 60s of long-term tension seemed to decrease identically for aged and non-aged specimens and for large or small imposed deformations. To confirm this postulate, an ANAVAR analysis was carried out with the ratio of the stress at 1200s over the reference stress at 60s i.e. the smallest resulting ratio, see Appendix C.3. For both representations of the total effects of the ageing and of the imposed displacement, it could also be remarked that the gap between two consecutive lines diminished with the load duration. As the

last two lines were not superposed, it implied that the plateau was not reached during the first 1200s, but their closeness also indicated that this last could have been attained after few additional seconds. To assess this observation, the averaged stress reduction factor of all the tested samples (no influence of the ageing and imposed displacement) was drawn versus time, see Fig. 4.25 (a).

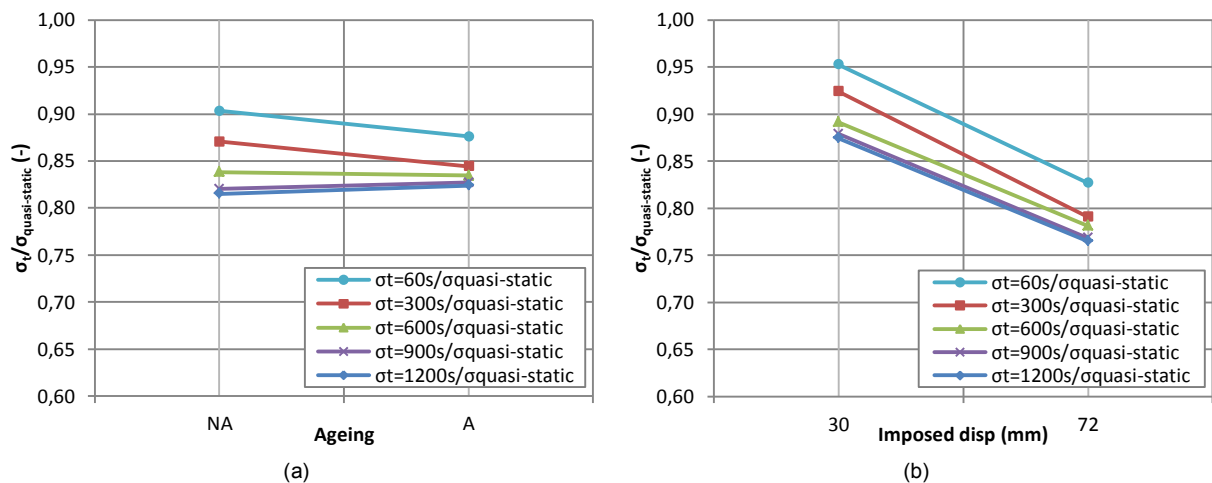


**Figure 4.25-** Reduction stress factor with comparison to (a) the reference stress at 60s and (b) to the quasi-static stress

To conclude, it could be argued that the loss in stress following the first 60s of long-term relaxation loading was independent of the ageing and of the imposed displacement.

- Comparison to quasi-static stresses

However, the reference stresses at 60s of these long-term relaxation tests were studied for only two displacements, i.e. 30mm and 72mm, and therefore could not constitute exploitable and fundamental characteristic values. The complete behaviour in tension was determined with the help of quasi-static tests, i.e. for any selected deformations in the allowable range only corresponded a single stress. Consequently, the useful comparative stress should be the quasi-static stress for a given displacement. By keeping the discretization of the loading time evoked previously, i.e. 60s, 300s, 600s, 900s, 1200s, the new stress ratios were calculated to plot the total effect of ageing and imposed displacement diagrams, see Fig. 4.26.



**Figure 4.26-** Total effect of (a) the ageing and (b) the imposed disp. on the stress reduction compared to quasi-static results

While the effect of the ageing was not relevant with almost no variation of the stress ratio, the effect of the imposed displacement was consequent. Indeed, all the curves decreased in the same way showing an important loss, e.g. the stress reduction was about 87,5% for an imposed deformation of 30mm and of about 76% for 72mm. Hence, the imposed deformation was considered as an influent

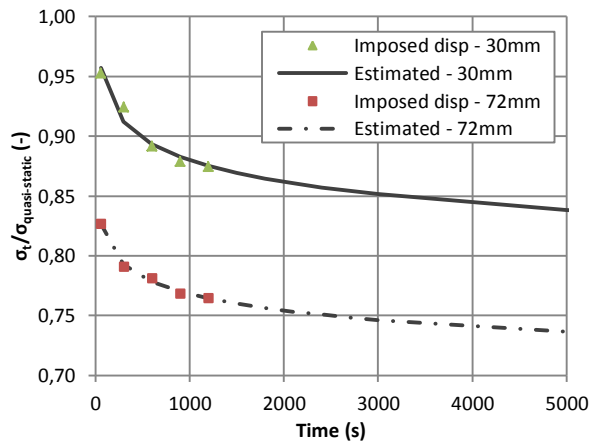
factor and separated analyses concerning the evolution of the stress towards this factor were envisaged.

The averaged stress ratios of the four samples tested under a deformation of 30mm were evaluated independently of the presence of an ageing, as well as the averaged results of the other four specimens tested under a deformation of 72mm. With these data were drawn the variations of the stress ratios in function of the time for the two imposed deformations, see Fig. 4.25 (b). As expected, the two curves were clearly distinct but showed the same evolution between 60s and 1200s. This allowed concluding that the main loss in stress occurred between 0s and 60s and depended on the maximum imposed deformation, but also that after the first 60s the loss was identical.

As for the long-term tests, the established curves of Fig. 4.25 (b) could be represented by a simple mathematical equation, in order to evaluate the variations in stress over a large period. One effective way to achieve this goal was to employ a power function expressed as follows:

$$\sigma_t / \sigma_{quasi-static} = a t^b \quad (\text{Pow})$$

With  $a$  and  $b$  material constants. The determination of these two coefficients was done with the help of a linear regression effected on the curves plotted in logarithmic axes. With the material constants given in Table 4.11, the estimated curves based on the power law were established and compared to the tests results, see Fig. 4.27.



| Imposed disp. | Power coefficients |        | Correlation coefficient |
|---------------|--------------------|--------|-------------------------|
|               | a                  | b      |                         |
| 30mm          | 1,082              | -0,030 | 0,959                   |
| 72mm          | 0,920              | -0,026 | 0,993                   |

**Table 4.11-** Power law coefficients for the 2 imposed disp.

**Figure 4.27-** Estimation of the stress loss – 2 imposed disp.

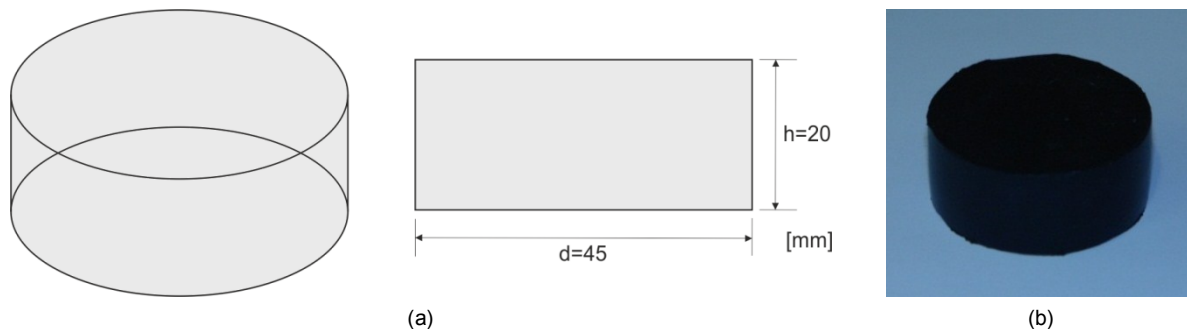
For the both estimated curves, the coefficients of correlation were close to 1, indicating a good fitting to the experimental results. The extension of the stress ratio to longer time was then possible. For in-use duration of 25 years, equivalent to the advised lifetime of structural sealant glazing units, the stress ratio was equal to 0,586 for an imposed displacement of 30mm and 0,539 for 72mm, meaning that the real long-term stress corresponds to the quasi-static stress divided by approximately 2. Nevertheless, this reduction constitutes an estimated value and does not replace the value found for tests on very long period.

## 4.2.2 Compression

The choice and determination of the material parameters of a constitutive law for hyperelastic silicone can be done with the curve fitting of experimental results in uniaxial tension only. In some finite element codes, such as Abaqus®, the definition of stress-strain data in tension is judged as sufficient to test standard hyperelastic models, such as Neo-Hooke, Money-Rivlin and other polynomial forms. However this method, only based on the tension results, is not reliable to simulate a complex stress distribution involving compression, as it is the case in adhesive glass façade, e.g. in SSGS. Only the modeling of silicone joints subjected to pure tensile loading could be correctly represented. Hence, to include the compressive behaviour of the DC 993 silicone in the constitutive material law, tests have to be carried out to provide sufficient information to realize a curve fitting over both tension and compressive uniaxial loadings.

### 4.2.2.1 Manufacturing of the samples

The compressive test specimens were manufactured in a Teflon mold of 45mm of diameter and 20mm of height cut out of a circular standard silicone cartridge. Taking the large dimensions into account, the silicone was simply poured inside the mold and the surplus was evacuated by closing the free extremities with Teflon plates and applying a constant pressure. The samples were let for 24 hours in the mold to achieve a complete curing, then unmolded and finally stored for a period of one month shielded from the light at ambient temperature and humidity. No visible flaws were detected on the surfaces or the edges of the specimens. To ensure the absence of too large air bubbles trapped inside, some samples were cut in half and inspected.



**Figure 4.28-** (a) Dimensions of the silicone compressive samples and (b) Manufactured sample

In addition to the visual inspection, an analysis of the dimensions, i.e. diameter and height, was done for all the specimens, to evaluate the reproducibility of the fabrication method, see Appendix A.3. The dispersion concerning the weight was also investigated to strengthen the observation about the absence of large air bubbles. From these two studies, it was demonstrated that all the 35 produced compressive samples possessed negligible variations in dimensions and weight, validating the manufacturing procedure.

### 4.2.2.2 Quasi-static tests

The Taguchi design of experiments, successfully applied in the case of tension quasi-static tests, was reused for the compressive tests. The complete procedure, leading to the analysis of the results and to the evaluation of the influent factors, is detailed below.

#### Definition of the objectives

The expected objectives for the compression quasi-static tests were relatively close to the ones desired for the tension tests, i.e. the characterization of the non-linear behaviour of the selected silicone, the definition of limits (strength and maximum strain) and the evaluation of the influence of

some environmental parameters. Thus the complete list of objectives to fulfill and the resulting aims, for these experiments in compression, are the following one:

- Establish exploitable stress-strain diagrams in order to obtain sufficient data to propose a coherent and proper constitutive material law based on tension and compression uniaxial tests and to model more complex stress distributions similar to the ones appearing in glass façade.
- Evaluate the influence of environmental factors under compressive actions and compare the results of this study to the tensions results.
- Define the maximum allowable stress and associated strain for design of adhesive joint.
- Analyze the initial stiffness of the silicone with the linearization method proposed by the ETAG 002 to describe the behaviour under small strains.

### Selection of the influent factors

An Ishikawa diagram could be realized to determine all the possible causes of the changes occurring in silicone properties under quasi-static compression actions. However, this diagram would be identical to the one of Fig. 4.3, as the objectives are the same than for quasi-static tension. Only the fabrication of the sample, in the “methods” criterion would differ as a simple pouring was employed instead of an injecting procedure. Nevertheless, this possible influence was already examined by the analysis of the dimensions and weights of the manufactured samples. Thus, the two main classes retained for this design of experiments were the “environment” criterion, i.e. temperature, humidity and UV-radiation, and the “method” criterion, as for the tension tests.

To account for the “environment” factor, a separation was made between the possible influence of low and elevated temperatures. This allowed comparing the final results of this tests campaign with the results of quasi-static tension tests. Therefore, for the consideration of elevated temperature, the manual artificial ageing procedure detailed in the EN ISO 11431 [4.4] was applied, as it possesses the advantage of regrouping and combining the exposure to heat, UV-radiation and humidity. The complete procedure, explained in section 4.2.1.2, was carried out at the same time on the tensile and compressive specimens, see Fig. 4.5 and Fig. 4.6. For low temperatures, the ageing consisted in cooling down the samples to -20°C during a period of three weeks, without UV-radiation and humidity.

The “method” factor, assimilated to the loading rate, was taken into account in the testing phase. With regard to the height of the sample was of 20mm, a low and an elevated loading rate were selected, i.e. respectively 5mm/min and 50mm/min.

### Choice of the Taguchi table

With the separation of the low and high temperatures, two designs of experiments were created. For the elevated temperatures, the two studied influent parameters, possessing each two levels, were:

- Ageing, a qualitative Boolean factor with two values, i.e. non-aged and aged.
- Loading rate, a quantitative continuous factor with two investigated values, i.e. 5mm/min and 50mm/min.

| Standard Test n° | Factors  |          | Samples to be tested |               |
|------------------|----------|----------|----------------------|---------------|
|                  | A        | B        | Test series 1        | Test series 2 |
| 1                | 1        | 1        | SC-05                | SC-20         |
| 2                | 1        | 2        | SC-15                | SC-18         |
| 3                | 2        | 1        | SC-02                | SC-06         |
| 4                | 2        | 2        | SC-10                | SC-01         |
| Level 1          | Not Aged | 5mm/min  |                      |               |
| Level 2          | Aged     | 50mm/min |                      |               |

**Table 4.12-** Design of experiments for silicone samples under quasi-static compression

Hence, the chosen Taguchi table corresponded to the table  $L_4(2)^3$ , see Appendix B. The complete resulting design of experiments, presented in Table 4.12, shows the random repartition of all the specimens, to overcome the different curing durations or mixing differences, and the repetition of the whole test series, to realize a better analysis of the variance.

For the second design of experiments, essentially centered on low temperature ageing, the only evolving factor, at two levels, was the loading rate. The design of experiments, containing the number and the repartition of the sample, is the following one.

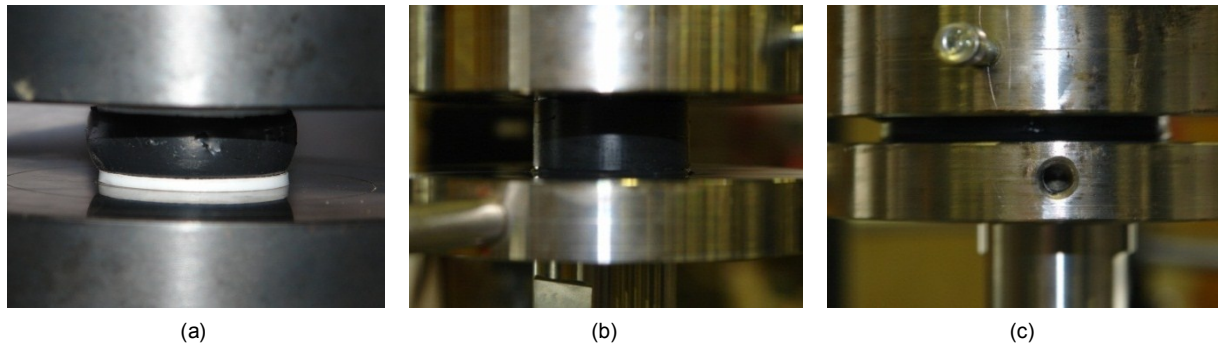
| Standard Test n° | Factors          | Samples to be tested |
|------------------|------------------|----------------------|
|                  | A = loading rate | Test series          |
| 1                | 1                | SC-13                |
| 2                | 2                | SC-16                |
| Level 1          | 5mm/min          |                      |
| Level 2          | 50mm/min         |                      |

**Table 4.13-** Additional design of experiments for low-temperature influence – silicone quasi-static compressive tests

### Description of the tests

The 10kN INSTRON mobile hydraulic press, employed for the tensile tests, was reused for the compressive tests. The self-closing wedge clamps were removed and a system composed of two parallel steel plates was adapted to the press. The total force, applied to the sample, was measured with the help of an external force sensor of 10kN, while the displacements were measured by the internal sensor of the machine, and so equivalent to the displacements between the parallel plates.

Pilot tests were first carried out with 3mm thick Teflon plates disposed at the extremities of the samples to avoid the friction between the silicone and the steel. This method has proved to be insufficient restricting the lateral expansion of the specimen. Thus a Teflon spray was pulverized on the steel plates before proceeding to each test, see Fig. 4.29.



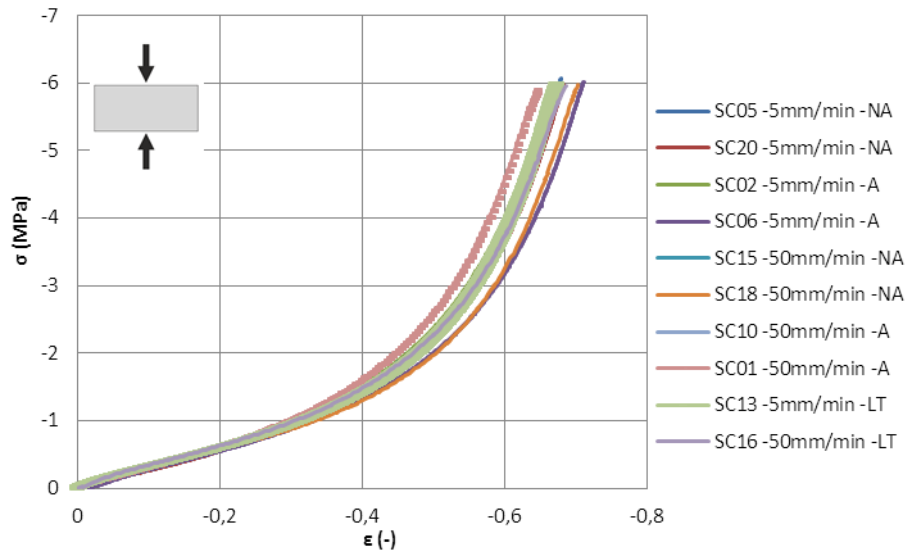
**Figure 4.29-** Pilot compression tests with (a) Teflon plates, (b) with pulverized Teflon spray and (c) deformed shape

Finally, all the ten compressive experiments, detailed in Tables 4.12 and 4.13, were carried out with this last method. A particular attention had been paid on the positioning and centering of the specimens as they were covered by a thin non-adhesive film of liquid Teflon.

### Tests results

Stress-strain diagrams were achieved for all the samples by simply dividing the force by the tested area and the displacement by the initial tested height, both initial values referenced in Appendix A.3. As the number of compressive specimens subjected to low temperature ageing was small, all the stress-strain curves were regrouped into one diagram for a first visual comparison, see Fig. 4.30. For all the experiments, no failures were recorded under the maximum force of 10kN, equivalent to a

stress of about 6MPa. Once unloaded, the specimens were measured again and it was found that they recovered their initial dimensions.



**Figure 4.30-** Stress-strain diagram –silicone under quasi-static compression (NA=non-aged, A=aged, LT=low temperature)

As for the tensile tests, the compressive behaviour of the chosen silicone appeared clearly non-linear at high deformations, typical of hyperelastic behaviour. Additionally, all the curves, aged or non-aged and subjected to low or elevated loading rates, were in the same range without major dispersions, letting envisage that the factors were not influent. To corroborate this observation, variance analyses, based on the ANAVAR method, were conducted on two portions of the curve, i.e. the first part at low deformations with the study of the initial stiffness and the last portion at elevated strains with the evaluation of the deformation at a fixed maximum stress.

- Influence of the factors on the initial stiffness

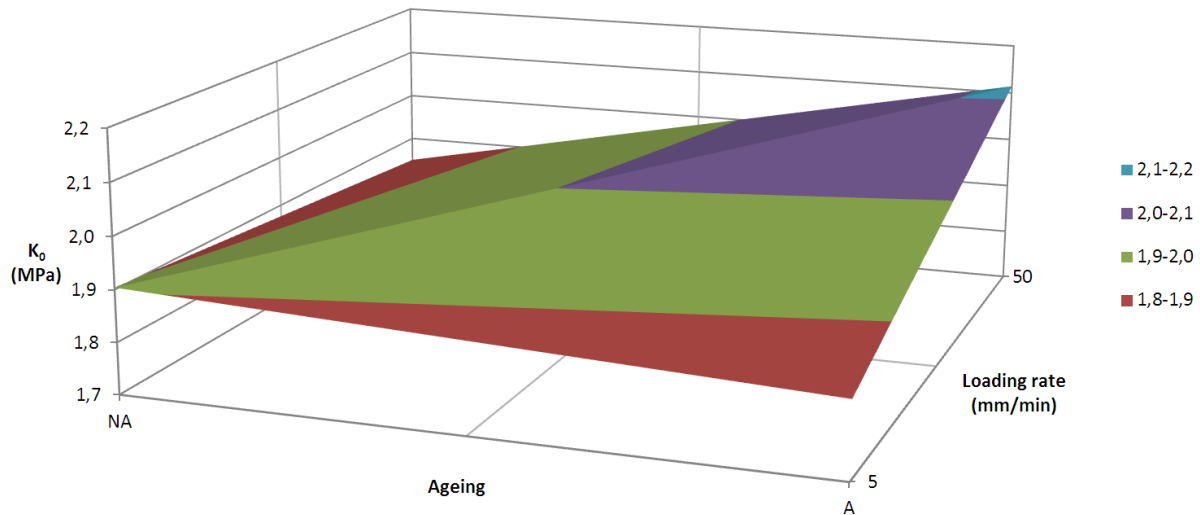
To evaluate the influence of the ageing, the loading rate or a combination of both on the initial stiffness, the linearization of the curve in terms of strain, followed by a determination of the tangent at the origin, was realized for each sample according to the ETAG 002, see Eq. (4.1). The corresponding results of the design of experiments accounting for elevated temperatures were stored in Table 4.14.

| Test n° | A      | B            | Initial stiffness $K_0$ (MPa) |               |
|---------|--------|--------------|-------------------------------|---------------|
|         | Ageing | Loading rate | Test series 1                 | Test series 2 |
| 1       | No     | 5mm/min      | 1,932                         | 1,876         |
| 2       | No     | 50mm/min     | 2,025                         | 1,674         |
| 3       | Yes    | 5mm/min      | 2,067                         | 1,622         |
| 4       | Yes    | 50mm/min     | 1,912                         | 2,317         |

**Table 4.14-** Initial stiffness results – DOE of Table 4.12 – silicone quasi-static compressive tests

The averages over the test series were calculated for each tests number, to generate the surface plot presented in Fig. 4.31. A maximum diagonal separates the surface in two symmetrical parts, given a global roof shape. For non-aged specimens, the initial stiffness decreases with the increase of the loading rate and the opposite occurs for the aged specimens, for which the initial stiffness increases with the loading rate. A similar phenomenon is observable by locking on the loading rate and studying the evolution of the results with the presence of ageing. Thus, as for the initial stiffness under quasi-static tension, the factors selected do not seem to be influent. However to conclude on this first investigation, the ANAVAR method was carried out, see Appendix C.4. This analysis confirmed the stability of silicone under quasi-static compression and for small strains.





**Figure 4.31-** Surface plot of the initial stiffness versus ageing and loading rate - silicone quasi-static compressive tests

With the verification of the invariance of silicone properties towards an artificial ageing procedure including elevated temperature, a mean value of all the resulting initial stiffnesses of Table 4.14 could be calculated. The average stiffness at the origin found was of 1,928MPa with a standard deviation of 0,221MPa. This value could be then compared to the average value of the second design of experiments accounting for low temperatures only. The initial stiffnesses of the additional DOE of Table 4.13 were recorded in the following table.

| Standard Test n° | Factors      | Initial stiffness $K_0$ (MPa) |         |
|------------------|--------------|-------------------------------|---------|
|                  | Loading rate | Test series                   | Average |
| 1                | 5mm/min      | 1,956                         | 1,932   |
| 2                | 50mm/min     | 1,909                         |         |

**Table 4.15-** Initial stiffness results – DOE Table of Table 4.13 – silicone quasi-static compressive tests

Hence, the average value of the initial stiffness for the first design of experiments 1,928MPa appeared close to the average of the second design of experiments 1,932MPa, which implied that the influence of the low temperatures on the behaviour of the silicone at small strain was nil. Consequently, all the results could be regrouped into one large class with no regards to the presence of an ageing or the tested loading rate.

- Influence of the factors on the strains at a fixed stress

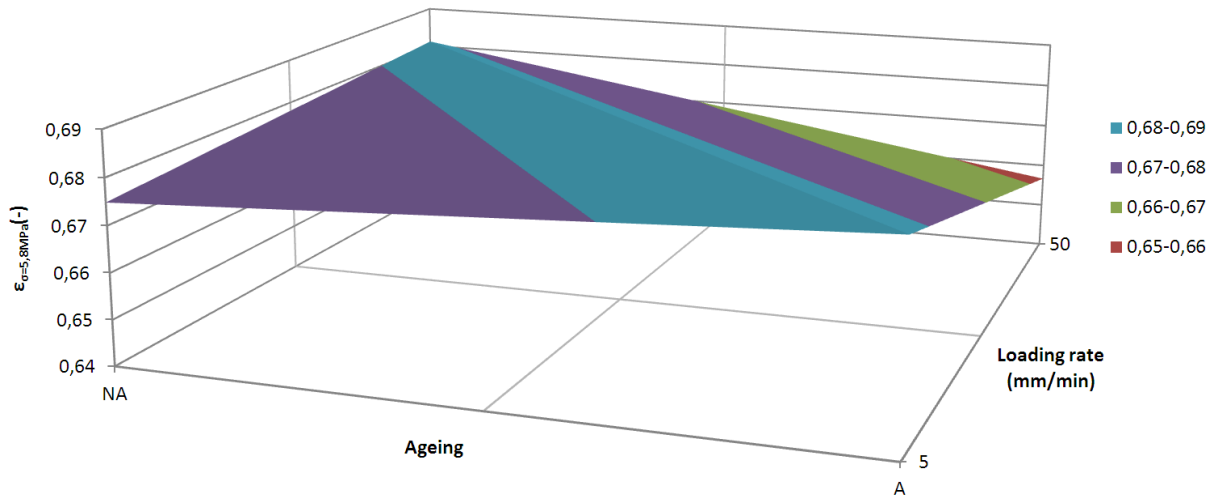
To appraise the possible influence of the selected environmental and method factors on the behaviour of the silicone at large strains, it was decided to select a fixed stress and to estimate the strains for each specimen. This choice was motivated by the non-failure at the maximum force of 10kN and by the fact that at a given large deformation, the dispersion in the stresses was consequent. For example, at a given strain of 0,6, the maximum stress was of 4,4MPa and the minimum of 3,1MPa. A stress of 5,8MPa, equivalent to a force of 9,5kN, was fixed as the limit, for which were determined the strains. All these strains  $\epsilon_{\sigma=5.8\text{MPa}}$  of the first design of experiments were recorded in Table 4.16.

The surface of the results for the studied domain was plotted with the averages of the strains over the test series and for each test numbers, see Fig. 4.32. The obtained curve presented a roof shape with a maximum diagonal and opposite variations of strains for a given factor, e.g. for non-aged specimens the stress increased with the loading rate, while for aged specimens a decrease of the strains with the loading rate was observed. Thus, an ANAVAR was carried out to ensure the non-influence of the studied factors on the silicone behaviour at large strains, see Appendix C.5. From this study, it had been concluded that none the ageing or the loading rate influenced the behaviour at large strains.



| Test n° | A      | B            | $\epsilon_{\sigma=5.8\text{MPa}} (-)$ |               |
|---------|--------|--------------|---------------------------------------|---------------|
|         | Ageing | Loading rate | Test series 1                         | Test series 2 |
| 1       | No     | 5mm/min      | 0,672                                 | 0,678         |
| 2       | No     | 50mm/min     | 0,666                                 | 0,697         |
| 3       | Yes    | 5mm/min      | 0,661                                 | 0,705         |
| 4       | Yes    | 50mm/min     | 0,673                                 | 0,640         |

**Table 4.16-** Strains at a stress of 5.8MPa results – DOE Table of Table 4.12 – silicone quasi-static compressive tests



**Figure 4.32-** Surface plot of the strains versus ageing and loading rate - silicone quasi-static compressive tests

The estimation of the strains at a stress of 5.8MPa was also undertaken for the second design of experiments, concentrating only on the possible influence of the loading rate for aged specimens at low temperatures. The values were gathered in Table 4.17 and their total average was calculated. This last value of 0,673 was equivalent to the average value of 0,674 of the first design of experiments of Table 4.12, which allowed making sure that after being subjected to low-temperatures the loading rates did not change the silicone properties at large strains.

| Standard Test n° | Factors      | $\epsilon_{\sigma=5.8\text{MPa}} (-)$ |         |
|------------------|--------------|---------------------------------------|---------|
|                  | Loading rate | Test series                           | Average |
| 1                | 5mm/min      | 0,668                                 | 0,673   |
| 2                | 50mm/min     | 0,679                                 |         |

**Table 4.17-** Strains at a stress of 5.8MPa results – DOE Table of Table 4.13 – silicone quasi-static compressive tests

All the results, independently of the ageing or the loading rate, were regrouped into one large class, whose statistical distribution was evaluated with the Lilliefors test [4.6]. The complete analysis, detailed in Appendix D.3, was employed to evaluate the null hypotheses of the normal distribution and then the log-normal distribution. Both distributions could have been supposed, but, in order to stay coherent with the tensile results, the log-normal distribution was retained. With this statistical distribution, the 5% fractile was estimated in compliance with the simplified method proposed by the EN 1990 [2.30]. The 5% fractile strain at a stress of 5.8MPa was found equal to 0,64. Nevertheless, as no sample broke at a force of 9,5kN, this value could only be viewed as a conservative allowable strain for design.

#### 4.2.2.3 Cyclic tests

The quasi-static compression tests were followed by a series of five cyclic tests to consider the continuous and discontinuous damages occurring for compressive actions in the silicone DC 993. The

Taguchi procedure, leading to the design of experiments and to the evaluation of the results was applied again.

### Definition of the objectives

The principal objective of this test campaign is to assess the non-linear softened stress-strain behaviour of the Dow Corning silicone after a finite number of cycles, to later include this in numerical simulations. However, as for the cyclic tension tests, the complete characterization of the Mullins' effect, depending on the maximum attained strain during the previous cycles as presented in Fig. 2.19, is not of interest for design. This phenomenon, disappearing after a certain number of cycles for a fixed strain, can simply be represented by the last loading path during which it is still effective. Indeed, after reaching the loading path ending this effect, the next cycles are superposed. Then the cumulative damage takes over and has to be estimated. Thus, the complete list of the objectives to meet is:

- Cyclic stress-strain diagrams on sufficient compressive samples to characterize the stress softening arising in the material.
- Appraise the number of cycles during which the Mullins' effect is really active, to be able to distinguish the continuous damage from the discontinuous damage. This objective should be realized by analyzing the dissipated energy, i.e. the area of the hysteresis. When these values become constant after some consecutive cycles, the last loading path should be recorded.
- The continuous damage, corresponding to the stress softening after a large number of cycles and so decisive to apprehend the behaviour of silicone subjected to cyclic compression actions during a long period, equivalent to the foreseen lifetime of adhesive façade joints, should be predicted.
- As for the cyclic tension tests, the influence of environmental conditions, such as ageing and loading rate should be assessed for cyclic compression too.

### Selection of the influent factors

Quasi-static compression tests demonstrated the invariance of the silicone properties towards the artificial ageing and the loading rate. Hence, these two factors could be theoretically excluded for this design of experiments. Nevertheless, with respect to the origin of the damage, it would be wise to not ignore the possible influence of the loading rate. Two types of frequencies were consequently investigated, i.e. a low frequency of 0,1Hz and an elevated to 1Hz.

As the full characterization of the Mullins' effect with the evolution of the stress-strain cycles was not of interest for this study, the maximum previously encountered displacement was not chosen as an influent factor. The amplitude of the deformation associated to the cyclic tests was set to 6mm, equivalent to strain amplitude of 0,3. The allowable strain value of 0,64, found for quasi-static compression tests, could not be applied due to the limit of the 10kN press and force sensor and due to the evoked large variation of stresses for a given deformation, see Fig. 4.30.

In consequence, the only selected factor for these cyclic tests in compression was the frequency. Two frequencies had to be imposed, i.e. 0,1Hz and 1Hz, for a strain amplitude of about 0,3, implying a maximum attained strain of 0,6.

### Choice of the Taguchi table

| Standard Test n° | Factors       | Samples to be tested |               |               |
|------------------|---------------|----------------------|---------------|---------------|
|                  | A = frequency | Test series 1        | Test series 2 | Test series 3 |
| 1                | 1             | SC-32                | SC-31         | SC-30         |
| 2                | 2             | SC-33                | SC-34         | -             |
| Level 1          | 0,1Hz         |                      |               |               |
| Level 2          | 1Hz           |                      |               |               |

**Table 4.18-** Design of experiments for frequency influence - silicone cyclic compressive tests

The frequency factor, possessing two levels 0,1Hz and 1Hz, was the only one factor evaluated. Hence the design of experiments containing the repartition of the specimens and presenting a repetition of the test series is shown in Table 4.18.

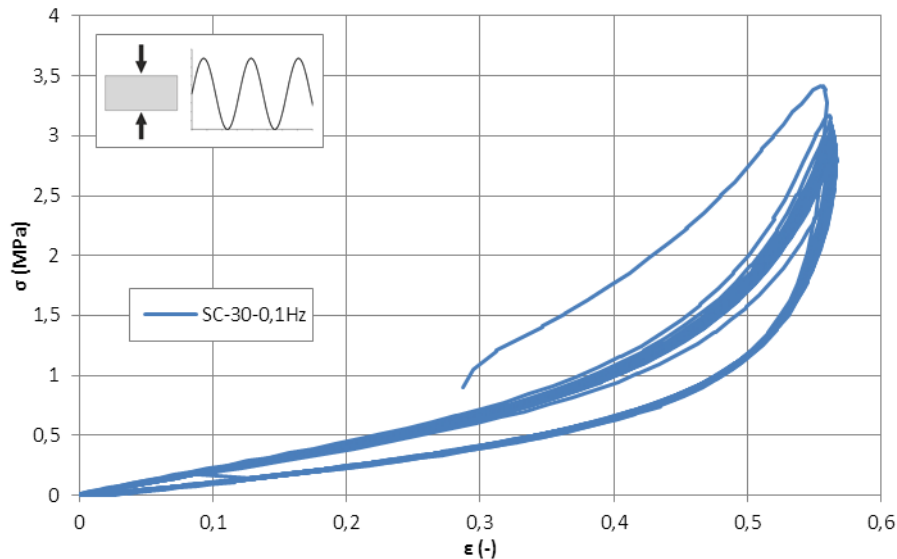
### Description of the tests

The cyclic tests in compression were carried out on the 10kN INSTRON mobile hydraulic press with the same set-up than for the quasi-static tests of section 4.2.2, i.e. composed of two rigid parallel steel plates, see Fig. 4.29. Pilot tests on unbroken specimens from the compression quasi-static tests were conducted to ensure that the pulverized thin layer of Teflon did not generate progressive sliding of the samples, changing the final results. The force was measured with an external 10kN force sensor and the displacement by the internal sensor of the machine, assimilated to the displacement between the two rigid steel plates.

The five cyclic tests were performed in two steps with a first compression of 6mm and then the application of the sinusoidal loading of 6mm of amplitude and under the desired frequency. For all the experiments, a minimum of 25 cycles were realized.

### Tests results

Stress-strain diagrams were achieved by dividing the force by the initial tested cross section and the displacement by the initial tested length, see Appendix A.3 for the dimensions. A typical resulting curve is introduced in Fig. 4.33 for the compressive sample SC-30 tested at a frequency of 0,1Hz. The strong non-linearity over a large strain range, characteristic of hyperelastic material, could once again be noted. The most import stress softening appeared between the first loading path and the following ones, as it was observed for the tension cyclic tests. Then this softening became less important with the increase of cycles.



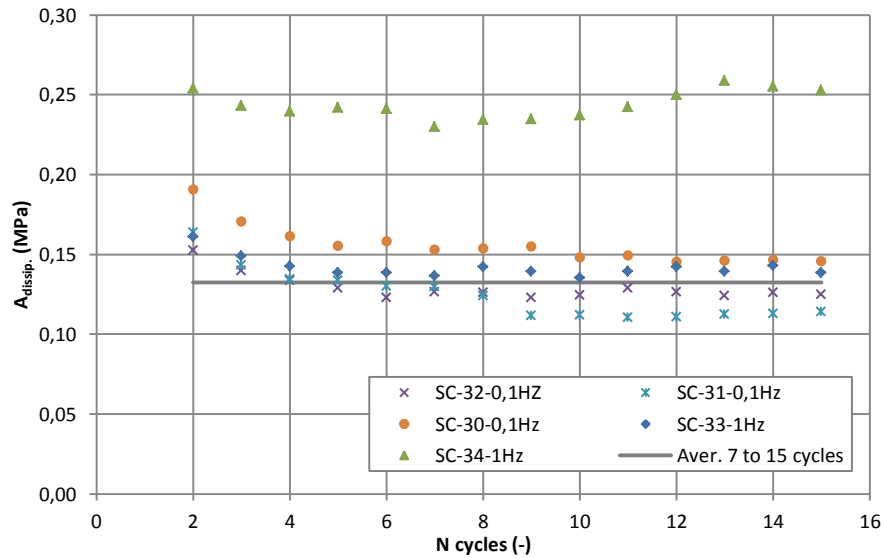
**Figure 4.33-** Cyclic compression stress-strain diagram for silicone sample under a frequency of 0,1Hz

- Mullins' effect characterization

To discern the Mullins' effect from the cumulative damage, the dissipated energy, corresponding to the area of the hysteresis, had to be compared for each cycle. The last cycle for which the evolution of this value could be acknowledged as nil served as limit. Hence, with regard to the theory and the number of cycles ending the Mullins' effect for the cyclic tension experiments, the dissipated energy was determined and recorded for the 15 first cycles, see Fig.4.34.

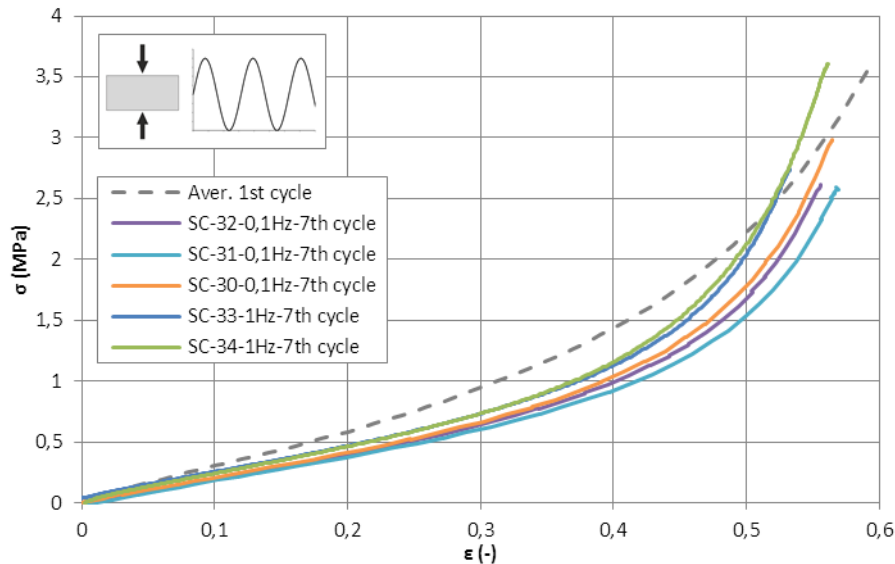
As it can be remarked, one specimen gave overestimated results compared to the other, i.e. SC-34-1Hz. In addition, while for all the samples the energy dissipated decreased, for this last one almost no

uniform variations were seen, the final value after 15 cycles being the same than at the first cycle. This could be due to the mixing process, as this sample was manufactured independently of the others, or due to a too small quantity of Teflon pulverized on both surfaces generating friction. Moreover, no conclusion on the influence of the frequency could be drawn out from this observation.



**Figure 4.34-** Evaluation of the dissipated energy for samples under cyclic compression

Nevertheless, in spite of the dispersion for this sample, the other curves decreased lightly from the second to the 7<sup>th</sup> cycle before reaching a plateau. The average value calculated after the 7<sup>th</sup> cycle was plotted to better notice this conjecture. Hence, as for the tensile cyclic tests, the Mullins' effect could be recognized as affecting the first seven cycles, which is more conservative than the commonly adopted first cycle. The loading path of this 7<sup>th</sup> cycle was retrieved for all the tested samples and compared to the initial loading issued from the average curve of quasi-static compressive tests, see Fig. 4.35.



**Figure 4.35-** Comparison between the averaged 1<sup>st</sup> cycle and the limiting 7<sup>th</sup> cycle of the Mullins' effect – cyclic compression

All the stress-strain curves after the 7<sup>th</sup> cycles were approximately in the same range until a strain of 0,4 and then some stress dispersions, inherent to compressive tests involving elevated forces, were remarked. The comparison of these diagrams to the average quasi-static results allowed quantifying the importance of the Mullins' effect, which appeared less considerable than for the cyclic tension. For example, at a strain of 0,4, the stress softening was below 0,5MPa.

To confirm the limit, in terms of cycle, of the Mullins' effect even at small strain, a complementary analysis on the initial stiffness was conducted. For each specimen, the linearization method of the ETAG 002 was used to determine tangent stiffness for each cycle until the 15<sup>th</sup>, see Fig. 4.36. For the most relevant cycles, the total effects of the frequency were plotted on Fig. 4.37.

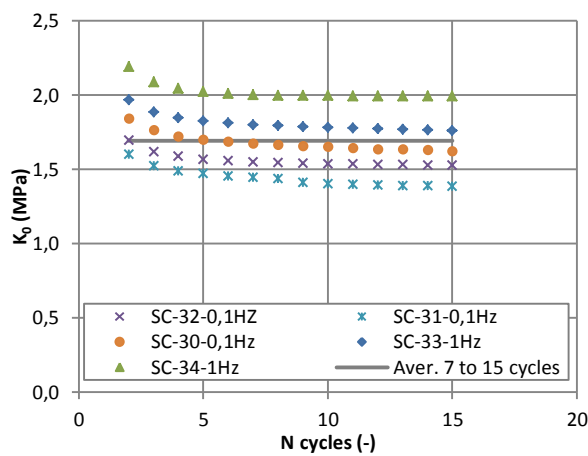


Figure 4.36- Initial stiffness versus the cycle number

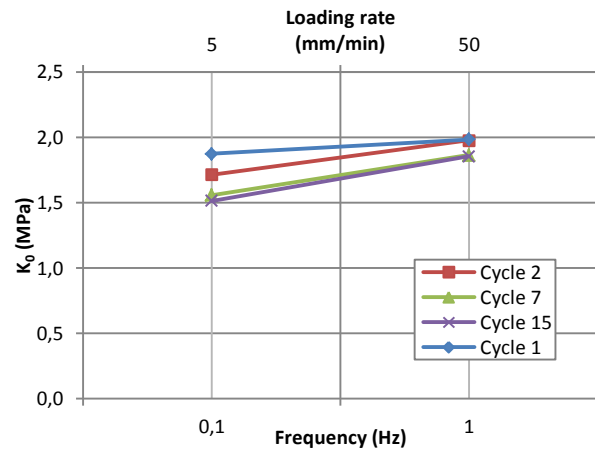


Figure 4.37- Total effect of loading rate on the initial stiffness (Top x axis only for cycle 1)

The initial stiffness diminished slightly for the first 5 cycles before reaching a plateau after the 7<sup>th</sup> cycle, as for the dissipated energy. This phenomenon was visible for both diagrams but more evident on Fig. 4.37, in which the curves of the 7<sup>th</sup> and 15<sup>th</sup> cycle, representing the total effects of the frequency, were superposed. The mean initial stiffness of 1,694MPa, obtained by averaging all the tangents at the origin over all the cycles between the 7<sup>th</sup> and the 15<sup>th</sup>, showed a gap of 12% with the average stiffness of the quasi-static compression tests equal to 1,928MPa.

The slope of the total effect of the frequency was identical for each specific cycle 2, 7 and 15 as well as the slope only accounting for the first cycle, i.e. quasi-static compression for 5mm/min and 50mm/min. Moreover, it was demonstrated in the previous section that the loading rate did not impact the silicone properties for the first loading. Thus, as the slope and consequently the variations were small between the two imposed frequencies, it was also envisaged that this factor did not change the properties of silicone after several cyclic compression.

- Prediction of the continuous damage

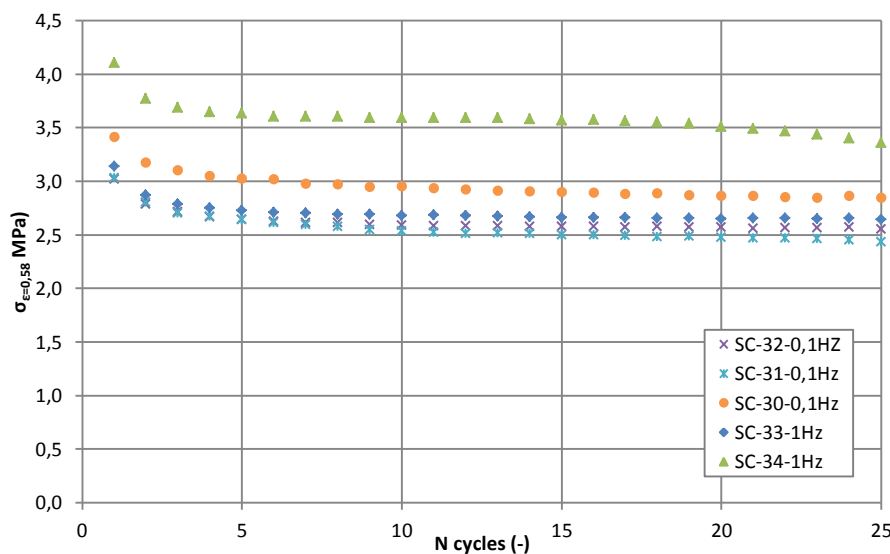
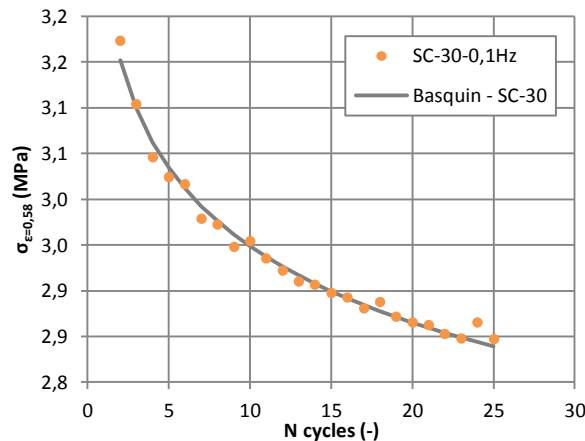


Figure 4.38- Evolution of the maximum stress at a given strain of 0,58 with the increase of cycles

For the maximum displacements imposed during a cycle, i.e. 12mm, equivalent to a strain of 0,58, the

stresses were evaluated for each specimen on 25 cycles. All these data were collected to draw the diagram of Fig. 4.38, allowing appraising the stress softening in function of the cycle number.

The decrease of the maximum stress was more important for the first portion of the curve, i.e. for a number of cycles inferior to 7. Then the softening became more uniform and linear. In contrary to the cyclic tension tests, no discontinuous drop of stress was found due to the selection of the recorded values corresponding to the stresses at the maximum displacement attained during the different cycles. Thus the mathematical formulation of Basquin, see Eq. (Bas), could be used to model the Wöhler curves, based on the maximum stress at a strain of 0,58, over all the 25 cycles. The parameters  $a$  and  $b$  of this model were obtained by expressing each curve of Fig. 4.38 in logarithmic axes to applied a simple linear regression. Once these coefficients determined, each curve issued from the tests was compared to the prediction of Basquin, see Fig. 4.39 for a typical example. The coefficient of correlation, indicating the closeness of the estimated curve to the test data, was almost equal to one in each case, see Table 4.19.



| Samples     | Basquin coefficients |         | Correlation coefficient |
|-------------|----------------------|---------|-------------------------|
|             | a                    | b       | R                       |
| SC-32-0,1Hz | 1,837E+14            | -31,850 | 0,937                   |
| SC-31-0,1Hz | 1,200E+09            | -19,854 | 0,988                   |
| SC-30-0,1Hz | 2,217E+12            | -24,159 | 0,994                   |
| SC-33-1Hz   | 7,770E+15            | -34,581 | 0,945                   |
| SC-34-1Hz   | 2,622E+14            | -24,224 | 0,879                   |

Table 4.19- Basquin coefficients for the compressive samples

Figure 4.39- Wöhler curve representation with Basquin form

As the estimated curves fitted relatively well the experimental maximum stresses over the 25 first cycles, except for specimen SC-34, two averages curves were calculated including or excluding this sample, see Fig. 4.40.

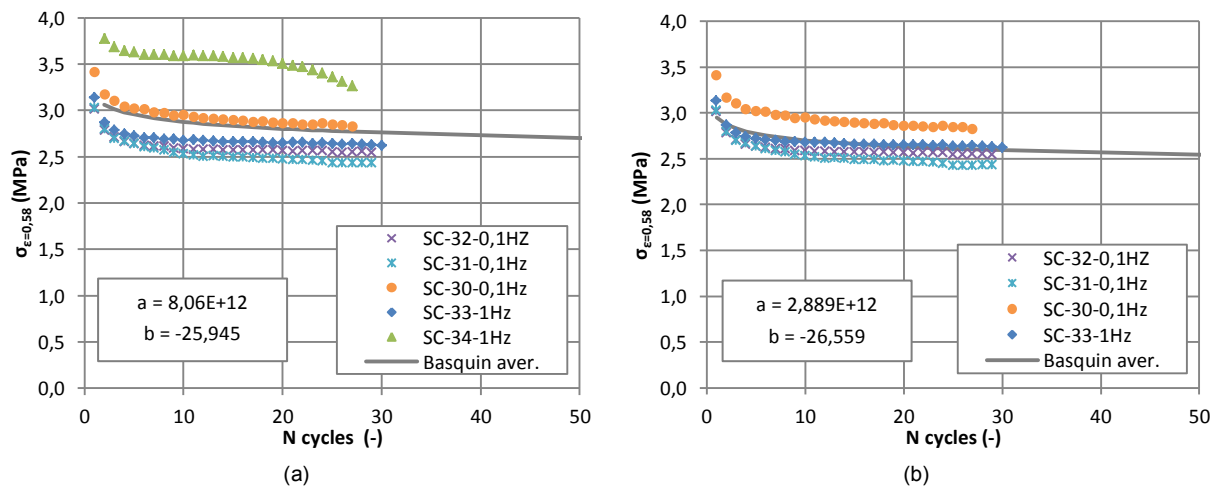


Figure 4.40- Comparison between the tests results and the averaged Basquin for (a) all the samples (b) excepted SC-34

The coefficient  $b$  representing the slope of the curve in logarithmic axes was close in both estimations. Nevertheless, the most conservative estimated curve was the one excluding the sample SC-34, as the stress was lower for a given cycle number, e.g. for 100 cycles, the stress was of 2,632MPa in case (a) and of 2,476MPa in case (b). This was also confirmed at very large cycle, as the Basquin estimation (a) provided a stress of 1,847MPa for  $10^6$  cycles and a stress of 1,752MPa for estimation (b), i.e. about 6% of difference. Therefore, the Basquin formulation with the coefficients of the conservative

case (b) could be employed for design. The averaged stress of the first cycle of all the sample of case (b) was equal to 2,49MPa, which represented a loss of about 41% compared to the value at  $10^6$  cycles. This drop in stress was similar to the decrease of about 43% found in the case of cyclic tension between the first and this elevated number of cycles.

#### 4.2.2.4 Long-term tests

In adhesively bonded façade, long-term compression could arise in the joint for vertical non-accessible glazings inclined inwards. Therefore this type of action was induced in eight compressive samples to apprehend the evolution of the stress under some imposed displacements.

#### Definition of the objectives

Relaxation tests in compression are necessary to apprehend the variations of the stress under long periods, i.e. the initial loss after several seconds and also if a plateau is reached. The objectives to meet are the following ones:

- As for the tension long-term tension tests, the duration of the tests is of 1200s (20min). Thus the drop of the stress should be properly determined and quantified during this time.
- A prediction of the loss in stress for longer load duration of 25years, equivalent to the lifetime of the adhesive, should also be done with the help of reduction factors.
- The evaluation of the dependency of the stress decrease on the imposed displacement should be investigated too.
- It should also be verified that the environmental conditions, i.e. humidity, temperature and UV-radiation, do not impact the properties of silicone to conclude on its stability in compression towards all type of actions.

#### Selection of the influent factors

The definition of the objectives allowed extracting the two possible influent factors, i.e. the ageing and the imposed displacement. The artificial ageing procedure, detailed in the EN 11431 [4.4], was again considered, on one hand, to regroup the elevated temperature, the humidity and the UV-radiation and, on the other hand, to reduce the total number of tests. The low temperature ageing procedure was not envisaged, as found non-influent for the quasi-static compressive tests. Concerning the imposed displacement, three values were investigated, i.e. a displacement of 5mm corresponding to a strain of about 0,25, another one of 10mm equivalent to a strain of 0,5 and a last one of 14mm comparable to a strain of 0,7.

#### Choice of the Taguchi table

While three levels were selected for the imposed displacements, only two were regarded for the ageing. With this difference of level the Taguchi method could not be directly applied. Therefore, a separation of the imposed displacement was operated to establish a first design of experiment based on the Taguchi procedure and a second accounting for non-aged specimens under the three imposed displacements. Hence, the information of the influence of the ageing was only provided by the first design of experiments.

For the DOE relying on Taguchi table, the two investigated factors, possessing two levels, were:

- A. Ageing, a qualitative Boolean factor taking only two values, i.e. with ageing or without.
- B. Imposed displacement, a quantitative continuous factor with two levels, i.e. 5mm and 10mm.

According to Appendix B, the matching table was  $L_4(2)^3$ . A random repartition of the samples was realized, to overpass the possible influence of the manufacturing process, as the curing or the mixing, see Table 4.20.

| Standard Test n° | Factors  |                           | Samples to be tested |
|------------------|----------|---------------------------|----------------------|
|                  | A        | B                         | Taguchi series       |
| 1                | 1        | 1                         | SC-13                |
| 2                | 1        | 2                         | SC-04                |
| 3                | 2        | 1                         | SC-03                |
| 4                | 2        | 2                         | SC-07                |
| Level 1          | Not Aged | 5mm ( $\epsilon = 0,25$ ) |                      |
| Level 2          | Aged     | 10mm ( $\epsilon = 0,5$ ) |                      |

**Table 4.20-** First design of experiments for silicone samples under long-term compression

For the second design of experiments, concentrating on the influence of the imposed displacements, two levels were chosen, i.e. 10mm and 14mm. Larger strains were adopted for this analysis to cover the maximum range of deformations authorized by the 10kN press. The four non-aged specimens were distributed randomly in this design, see Table 4.21.

| Standard Test n° | Factors                   | Samples to be tested |               |
|------------------|---------------------------|----------------------|---------------|
|                  | A = frequency             | Test series 1        | Test series 2 |
| 1                | 1                         | SC-22                | SC-12         |
| 2                | 2                         | SC-21                | SC-24         |
| Level 1          | 10mm ( $\epsilon = 0,5$ ) |                      |               |
| Level 2          | 14mm ( $\epsilon = 0,7$ ) |                      |               |

**Table 4.21-** Design of experiments accounting for the imposed displacement - silicone samples under long-term compression

### Description of the tests

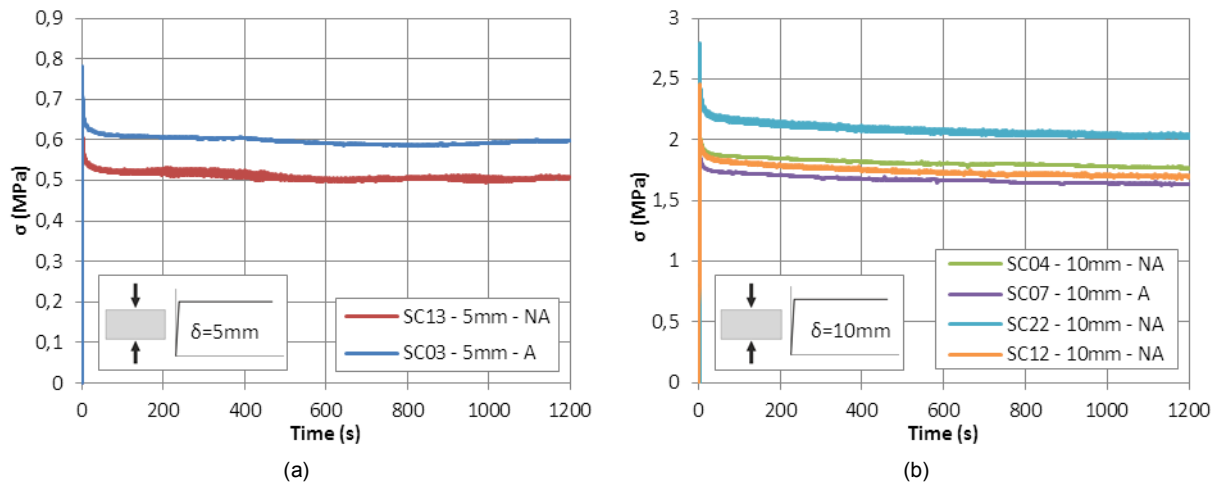
The 10kN INSTRON mobile hydraulic press, equipped with two parallel steel plates as exposed in Fig. 4.29, was reused to conduct the long-term relaxation tests in compression. The total force was recorded by an external 10kN force sensor and the displacements by the sensor of the machine. The required displacement was imposed to the sample in one second and maintain constant during the experiment. With this method, the first measure of the force was realized after 60s to not account for some slight oscillations which could occur. As for the other experiments in compression, Teflon was pulverized on the steel surfaces to avoid friction with the silicone, so that the tested sample was free to extend laterally. Pilot tests were carried out on unbroken specimens of the quasi-static compression series to ensure that they did not slide progressively due to small surface imperfections. Finally all the eight samples of the two designs of experiments were tested with this procedure.

### Tests results

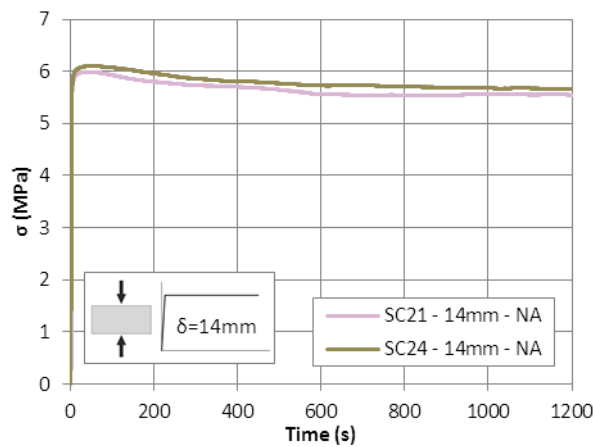
The constant displacement recorded by the machine was systematically checked for each experiment and the force obtained by the external sensor was divided by the cross section, whose dimensions are given in Appendix A.3, in order to determine the stress. With no regards to the ageing, the obtained long-term relaxation stress-time curves for the respective imposed displacements were plotted in Fig. 4.41 and Fig. 4.42.

As it can be observed, for a given imposed displacement, a progressive decrease of the stress occurred during the whole test duration without reaching a visible plateau. This was particularly visible for large imposed deformations, i.e. 10mm and especially 14mm. Nevertheless, the loss became smaller with the time increase. As expected, the final stresses at 1200s were different for each imposed deformation, suggesting that the final value of the stress depended on the intensity of the long-term action. However, conclusions could not be drawn by simply looking at the final stress value. A correct study of the stress evolution could only be achieved by comparing the stress at a certain time to a reference value.





**Figure 4.41-** Stress-time diagrams for an imposed displacement of (a) 5mm and (b) 10mm – silicone long-term compression



**Figure 4.42-** Stress-time diagrams for an imposed displacement of 14mm – silicone long-term compression

- Analysis of the stress ratio decrease

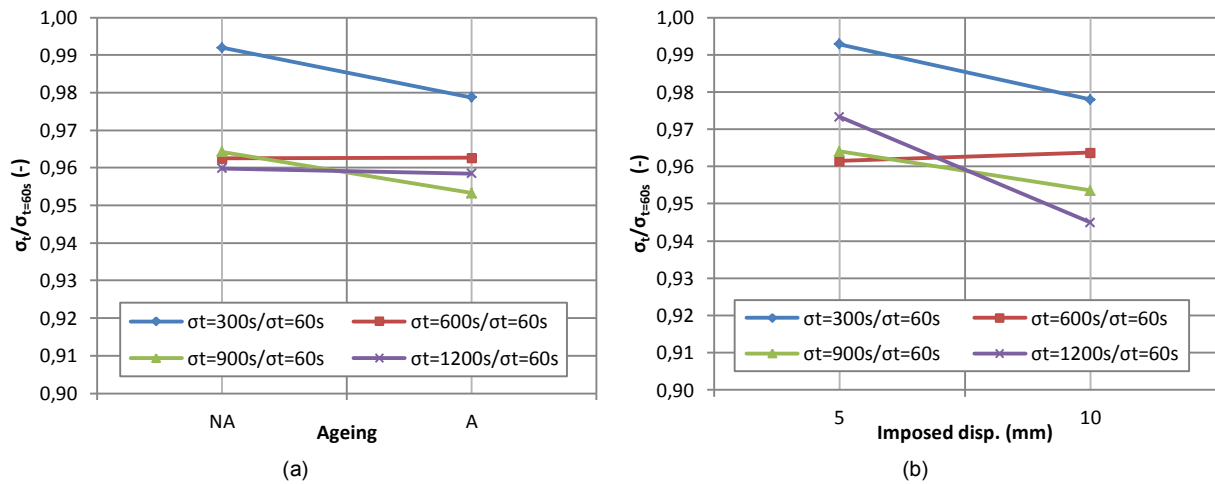
With the testing procedure, consisting in applying the desired deformation in only one second, the first measure of the stress could only be done after 60s. Thus, as for the tensile long-term tests, the value of the stress at this time was assimilated to the reference value. Then, a discretization of all the test duration was realized, i.e. the stress was recorded at 300s, 600s, 900s and 1200s. The decrease of the stress was symbolized by the ratio of the stress at a time “t” to the reference stress at 60s. Four ratios were consequently calculated for each sample. An example, corresponding to the stress ratio of the maximum duration, is given in Table 4.22, merging the results of the two designs of experiments.

| Standard Test<br>n° | A      | B             | $\sigma_{t=1200s}/\sigma_{t=60s}$ (-) |               |               |
|---------------------|--------|---------------|---------------------------------------|---------------|---------------|
|                     | Ageing | Imposed disp. | Taguchi series                        | Test series 1 | Test series 2 |
| 1                   | No     | 5mm           | 0,972                                 | -             | -             |
| 2                   | No     | 10mm          | 0,947                                 | 0,924         | 0,924         |
| 3                   | No     | 14mm          | -                                     | 0,927         | 0,928         |
| 4                   | Yes    | 5mm           | 0,974                                 | -             | -             |
| 5                   | Yes    | 10mm          | 0,943                                 | -             | -             |

**Table 4.22-** Maximum stress ratio regrouping the two designs of experiments – silicone long-term compression

Independently of the ageing, the stress ratio of the imposed displacement of 5mm was the same. This could also be observed for the imposed deformation of 10mm of the Taguchi series, letting envisaged

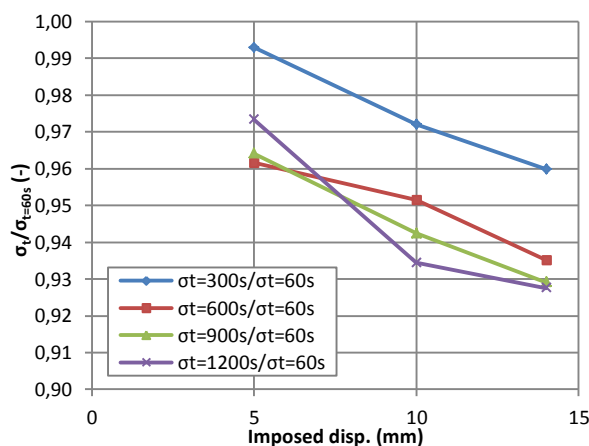
a non-influence of the ageing on the portion of the curve from 60s to 1200s. To confirm this, a complete variance analysis study was performed on the results of the first Taguchi DOE, limiting to an imposed range of displacement  $s$  between 5mm and 10mm. The total effect of the ageing and loading rate factors were plotted for the four stress ratios in Fig. 4.43.



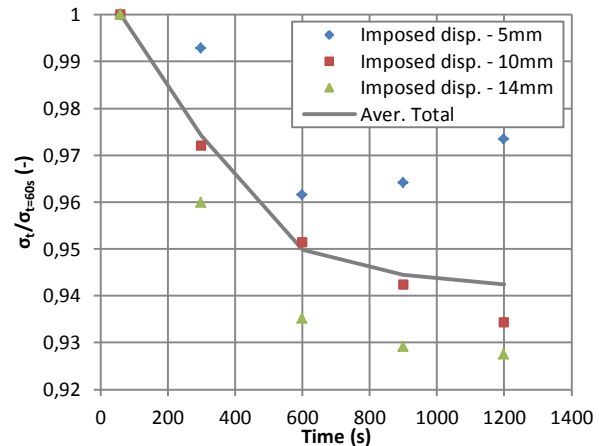
**Figure 4.43-** Total effect of (a) the ageing and (b) the imposed displacement – silicone long-term compression (Table 4.20)

Concerning the influence of the ageing, the only consequent variation was observed by comparing the stress at 300s to the reference stress at 60s for non-aged and aged specimens. Then, for stresses at longer duration, the slopes of the lines were quasi-negligible. In addition, while all the lines were superposed for the ratios of the stresses at and after 600s, the first line, equivalent to the ratio of the stress at 300s, was clearly superior. Thus, it could be supposed that after 600s, the decrease of the stress compared to the reference stress became minimal. For the imposed displacement, the first and last stress ratios showed the maximum variations between 5mm and 10mm. The other in-between ratios possessed a very small slopes and therefore no dependence on the imposed displacement. To properly assess the influence of this last factor on the stress decrease during time, an ANAVAR analysis was carried out with the ratio of the stress at 1200s to the reference stress at 60s, see Appendix C.3. From this study, the invariance of the stress ratio towards the ageing and the imposed deformation was demonstrated.

Hence, all the results from the first and second design of experiments could be regrouped into one large class, accounting for a larger range of imposed displacements. The total effect of the imposed deformation factor was once again plotted for all the samples, see Fig. 4.44.



**Figure 4.44-** Total effect of imposed disp. for all specimens



**Figure 4.45-** Reduction stress factor compared to  $\sigma_{t=60s}$

As it can be remarked for a large number of tests results, the decrease of the stress ratio for a given time was almost linear in function of the imposed displacement. Indeed, higher was the imposed

displacement and higher was the loss of stress. Nevertheless, the variations of the four stresses ratios between the 5mm and 14mm displacements represented less than 3%. This small difference also validated the non-influence of the imposed deformation on the loss of stiffness after a time of 60s.

In addition, as the three last lines were relatively close, the constant plateau could be almost reached after additional seconds. To assess this last hypothesis, the averaged stress reduction factor based on all the results was drawn versus time, see Fig. 4.45. Except for the smaller imposed displacement of 5mm, the ratio of the stresses became lower with the time and almost insignificant for 1200s.

In conclusion, the stress softening of silicone, after the first 60s, under long-term compression was independent of the presence of the ageing and of the imposed displacement, for which the variations were too small to be considered. These results were consistent with the ones found for the case of long-term tension.

- Comparison to quasi-static stresses

As the first 60s of the tests were not appropriate to evaluate the decrease of the stress, comparisons to the quasi-static stresses for the selected displacements were envisaged. The change of reference value was convenient, as the stress after 60s for a given deformation was a priori not known. The previous discretization of the time was conserved, i.e. 60s, 300s, 600s, 900s and 1200s and the new ratios were calculated to plot the total effect of the imposed displacement, see Fig. 4.46.

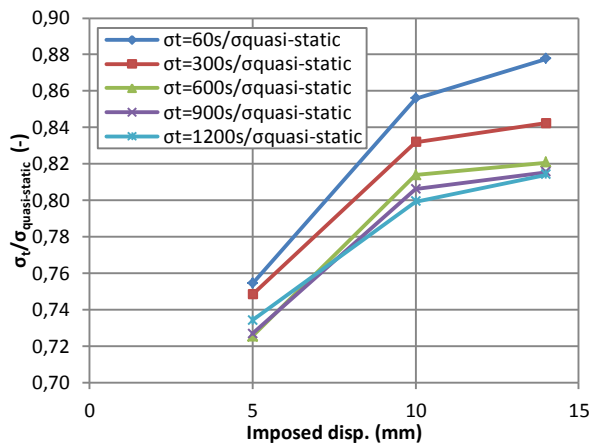


Figure 4.46- Total effect of imposed disp. for all specimens

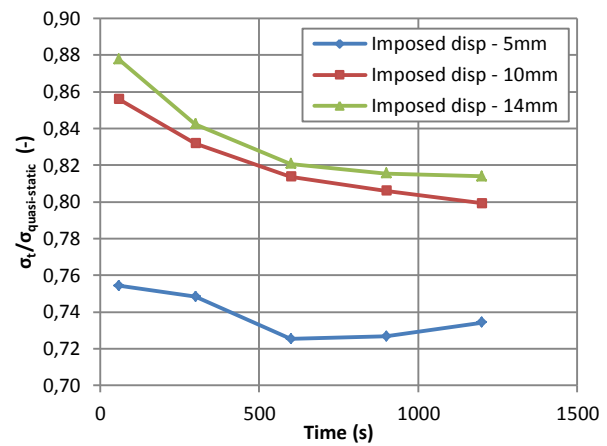


Figure 4.47- Reduction stress factor compared to  $\sigma_{quasi-static}$

The stress ratio was higher for higher imposed deformations with no regard to the selected time, meaning that the loss of stress was always lower for elevated imposed displacements. This evolution was contradictory with the one found for the reference stress of 60s. This could be explained by the fact that the decisive and bigger loss in stress occurred between the quasi-static stress and the stress at 60s for low imposed deformation. Furthermore, the gap between the stresses ratios for a displacement of 5mm and a one of 10mm was more than 10% in the present case, implying that the imposed deformation impacted the stress ratio before the first 60s. Consequently, a distinction had to be operated between the results under the different imposed displacements.

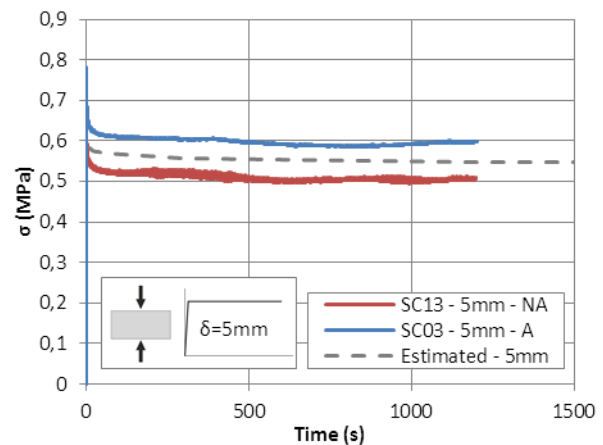
For each imposed deformation, the average curve of the stresses ratios was estimated, see Fig. 4.47. Two outcomes were extracted from this diagram, i.e. the most important loss of stress occurred for the minimum imposed displacement before the first 60s (minimum initial stress ratio) and the decreases of the curves after 60s became quasi-identical for the maximum imposed deformations.

To predict the evolution of the stress at very long-term, the power function, see section 4.2.1.4, could again be employed to fit the actual stress ratios over the tested 1200s. The coefficients of this mathematical equation were calculated with the help of linear regression applied on the curves of Fig. 4.47 drawn in logarithmic axes. The appraised material constants are recorded in Table 4.23 and the

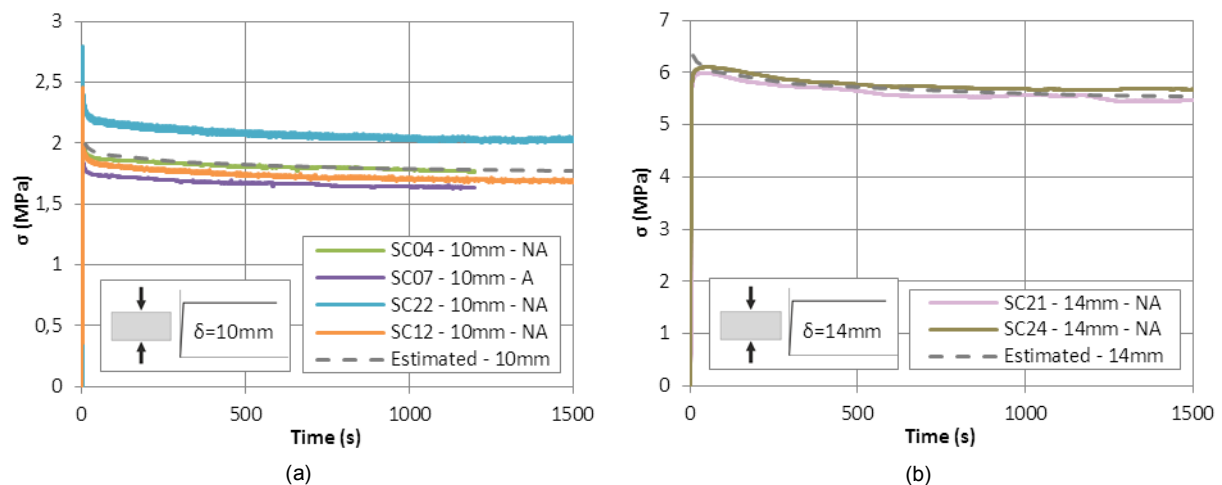
comparisons between the estimated curves and the experimental results are provided in the following figures Fig. 4.48 and 4.49.

| Imposed disp. | Power coefficients |        | Correlation coefficient |
|---------------|--------------------|--------|-------------------------|
|               | a                  | b      |                         |
| 5mm           | 0,795              | -0,012 | 0,708                   |
| 10mm          | 0,943              | -0,023 | 0,984                   |
| 14mm          | 0,978              | -0,026 | 0,986                   |

**Table 4.23-** Power law coefficients for the 3 imposed disp.



**Figure 4.48-** Estimated stress-time diagrams - disp. of 5mm



**Figure 4.49-** Estimated stress-time diagrams for an imposed disp. of (a) 5mm and (b) 10mm – silicone long-term compression

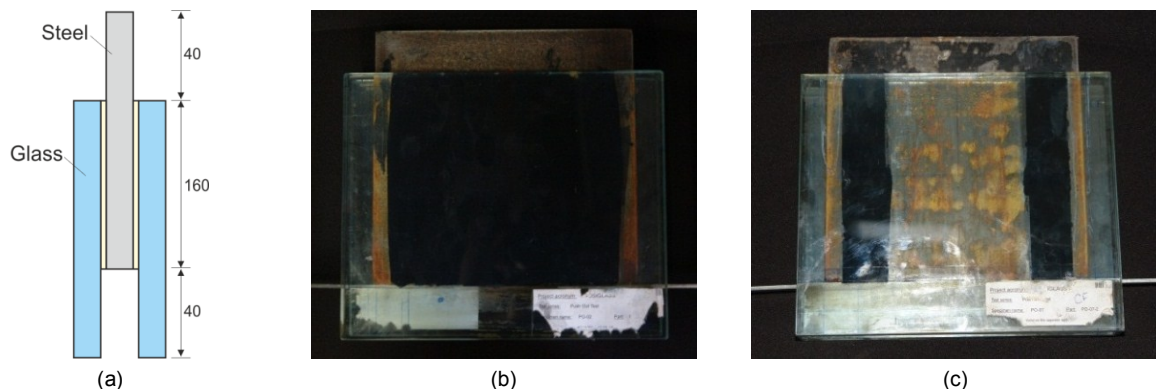
For the largest imposed deformation, the correlation coefficients were close to 1, indicating a good fitting of the experimental results. Based on these estimations, the long-term stresses for duration of 25 years were evaluated for each case. For the imposed displacement of 5mm, the final stress was equal to 0,465MPa, corresponding to the quasi-static stress divided by 1,62. For 10mm, the stress after 25 years was of 1,312MPa, which was the quasi-static stress divided by 1,7. Finally for 14mm, the quasi-static stress could have been divided by 1,76 to found the final stress of 3,911MPa. Nevertheless, these reduction factors were established with mathematical approximations depending on the first 20min and therefore could not replace tests on long period equivalent to the desired lifetime of the adhesive joints.

### 4.2.3 Push-out shear tests

To complete the series of uniaxial tests in tension and compression, the behaviour in shear of the structural silicone DC 993 was also investigated, as it constituted the main type of action arising in the adhesive joint of the systems presented in chapter 3. For façade use, the three mode of the load transfer through the silicone, i.e. quasi-static, cyclic and long-term, had to be studied. This provided fundamental information to, on one hand, evaluate the maximum authorized strength and, on the other hand, ensure of the established constitutive material law.

#### 4.2.3.1 Manufacturing of the samples

Shear tests found in literatures were essentially based on single lap-joint tests, constituted of two adherents bonded together with adhesive, e.g. the “H” geometry of the specimen described by the ETAG 002 [2.44]. In these unsymmetrical experiments, one adherent was generally fixed at one extremity, while either a force or a displacement was applied onto the extremity of the other adherent. An important drawback of this test arose from the peel stresses, interfering with the shear stresses and preventing the correct determination of the latter. Therefore, a symmetric geometry was selected for this study, i.e. the double-lap joint assembly investigated by Hart Smith [4.8]. Each sample was composed by two outer fully-tempered glass plates with dimensions of 240x200x12mm and an inner steel plate with dimensions of 200x200x12mm, see Fig. 4.50. An offset of 40mm between the two outer glass plates and the inner steel plates was foreseen to conduct the test in compression and avoid undesired tensile stresses in glass. In addition, the layering of the specimen was estimated more effective with two outer glass plates than with two outer steel plates, as the applied force was distributed in the most brittle element on a larger section.



**Figure 4.50-** (a) Double-lap joint geometry to test shear and (b) (c) Manufactured samples

The adhesive was disposed symmetrically on both sides at the steel-glass interfaces, see Fig. 4.50 (b) and (c). Two dimensions were envisaged to latter appraise the influence of this factor on the shear behaviour of the silicone. Consequently, with regards to the width of the adhesive, two different manufacturing procedures were considered:

- Procedure 1 consisted in a simple pouring process to realize samples fully glued at the steel-glass interfaces, 2x (160x170mm), independently of the joint thickness. With this method, the different parts were added horizontally step by step in a rigid frame in aluminum. A first glass plate was inserted in this frame and the silicone was applied on its surface delimited by calibrated Teflon spacers responsible for the thickness of the adhesive joint, see Fig. 4.51. Then the inner steel plate was positioned with other calibrated pieces to obtain the offset of 40mm at the bottom of the sample. Finally, silicone was poured on the second outer glass plate with identical calibrated Teflon spacers before being installed in the frame on the steel plate. The whole specimen was then subjected to compression to evacuate the surplus.
- Procedure 2 was based on an injection system to make four bands of silicone of (160x30mm) independently of the joint thickness. The main difficulty was to respect the symmetry of the

sample, i.e. the two front bands had to be identical in dimensions and at the same position than the two bands of the opposite side. To achieve these objectives, a self-designed injector adaptable to the cartridge, see Fig. 4.52, allowed the introduction of the adhesive in the pre-assembled element. The appropriate dimensions of the joint and of the offset at the bottom were obtained with the help of Teflon spacers.



**Figure 4.51-** Pouring process for large area



(a)



(b)

**Figure 4.52-** (a) Injector and (b) Injecting process for small area

Nevertheless, for both methods of fabrication, the specimens were removed from the aluminum frame after 24h of curing. The calibrated Teflon spacers were also taken out at the same moment. All the samples were stored during a period of one month at ambient temperature and humidity, shielded from light. The dimensions of the push-out assemblies were controlled with the help of caliper to, on one hand, check the parallelism of the extreme edges through which will be transferred the load and, on the other hand, evaluate the total thickness of silicone applied see Appendix A.4. For the largest joint thickness, almost no dispersion was found, while for small thickness, some imperfections in size were discovered for the pouring process concerning the large bonded area. However, these differences with the desired thickness did not impact the realization of the tests.

#### 4.2.3.2 Quasi-static tests

As for the tension and compression, the quasi-static tests constituted the basis for the establishment of a correct constitutive material law for silicone adhesive. The design of experiments, following the Taguchi procedure, was conserved and set up for these quasi-static shear tests.

#### Definition of the objectives

The non-linear behaviour of silicone elastomer in shear had to be determined, to complete the ones obtained for quasi-static tension and compression. Thus, stress-strain diagrams until breakage should be established for several samples. This would also allow fixing maximum authorized limits in terms of strength and strain for future design. Additionally, the possible influence of environmental parameters had to be assessed. Therefore the complete list of objectives to fulfill was the following one:

- Obtain sufficient exploitable information to plot stress-strain diagrams to implement a proper and complete material law in finite element software. By combining all the quasi-static data, numerical simulations under complex deformations, implying tension, compression and shear could then be conducted.
- As several adherents were considered, the mode of failure, either adhesive or cohesive, had to be controlled. The steel plates were not mechanically treated, e.g. sandblasting, but only cleaned and degreased with solvents. Hence, if an adhesive failure occurred on the steel side, some treatments and improvements could be brought to enhance the shear forces.
- From the tensile and compressive experiments, the stability of the silicone towards environmental conditions, i.e. ageing and loading rate, was demonstrated. However, in these both types of experiments, only the material properties were tested and not the adhesion. Consequently, as the envisaged quasi-static shear tests involved other constituents, such as



the steel and the glass, it could not be concluded on the invariance of the adhesive connection towards environmental factors. Therefore, the possible influence of these parameters had to be studied in detail.

- Defining limits in strengths and associated strains for design of the joint constituted also an important objective.
- A complementary analysis of the initial stiffness of the material could also be undertaken to characterize the behaviour at small strains.

### Selection of the influent factors

The classical “method factors”, extracted from the Ishikawa diagram for quasi-static tension presented in section 4.2.1.2, were conserved for the push-out shear tests. Thus the environmental criterion, accounting for the temperature, humidity and UV-light, and the method criterion, centered on the loading rate, were again studied. The influence of low temperature was neglected and only elevated ones were considered. The artificial accelerated ageing procedure described by the EN ISO 11431 [4.4] was used to regroup and combine the elevated temperature, humidity and UV-radiation factors into one large class. The manual cyclic exposure was the same than the one exposed in Fig. 4.4. Two loading rates were selected with regards to the dimensions of the bonded area and to the expected total displacements, i.e. a low loading rate at 3mm/min and a fast one at 90mm/min.

In addition to these two parameters were added the possible influences of two other method factors focusing on the geometries of the silicone, i.e. the size of the bonding area and of the thickness. As explained in the previous paragraph 4.2.3.1, two different areas were chosen, i.e. a large area 2x (170x160mm) assimilated to all the “contact area” between the outer glass plates and the inner steel plates and a smaller area divided in 4 sections of equal dimensions (160x30mm). Behind these two adhesive sections were hidden two different processes of fabrication. So the possible influence of the bonding area could be related to the influence of the manufacturing method. Furthermore, as the transmitted shear force depended on the thickness of the adhesive, two values were selected, i.e. a low one of 3mm and an elevated one of 6mm. This last value is prescribed by the ETAG 002 as the minimal authorized thickness for joints of structural sealant glazing units. Consequently, the dimension of one test followed the recommendation of European guidelines.

### Choice of the Taguchi table

The gathering of the environmental parameters, i.e. the elevated temperature, the humidity and the UV-radiation, into one large class allowed examining only four factors at two levels each:

- Ageing, a qualitative Boolean factor taking only two values, i.e. with ageing and without.
- Bonding area, a quantitative continuous factor of two distinct levels, i.e. 2x (170x160mm) and 4x (160x30mm).
- Bonding thickness, a quantitative continuous factor with two levels, i.e. 3mm and 6mm.
- Loading rate, quantitative continuous factor for which two levels were chosen, i.e. 3mm/min and 90mm/min.

| Standard Test n° | Factors |   |   |   | Samples to be tested |
|------------------|---------|---|---|---|----------------------|
|                  | A       | B | C | D | Taguchi series       |
| 1                | 1       | 1 | 1 | 1 | 15-1/14/15-2         |
| 2                | 1       | 1 | 1 | 2 | 13-1/11/13-2         |
| 3                | 1       | 1 | 2 | 1 | 23-1/09/23-2         |
| 4                | 1       | 1 | 2 | 2 | 24-1/10/24-2         |
| 5                | 1       | 2 | 1 | 1 | 16-1/13/16-2         |
| 6                | 1       | 2 | 1 | 2 | 14-1/12/14-2         |
| 7                | 1       | 2 | 2 | 1 | 18-1/15/18-2         |

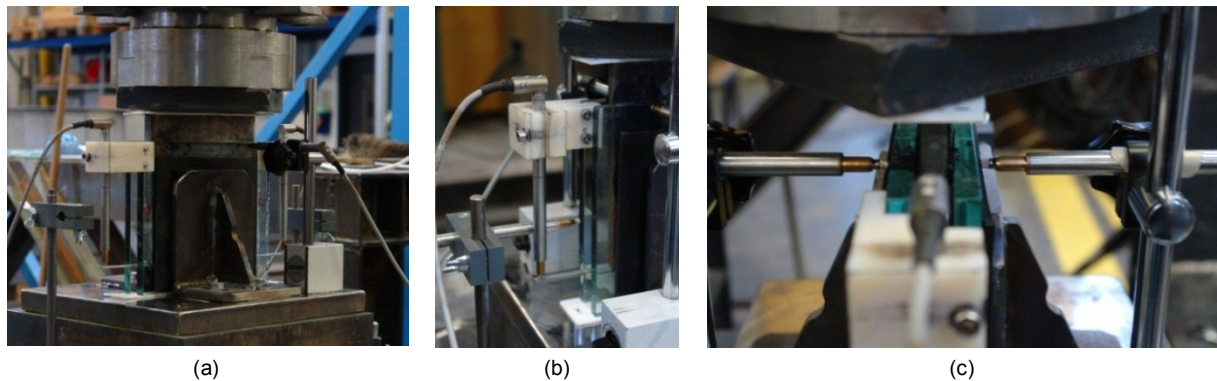
|         |          |               |     |          |              |
|---------|----------|---------------|-----|----------|--------------|
| 8       | 1        | 2             | 2   | 2        | 25-1/07/25-2 |
| 9       | 2        | 1             | 1   | 1        | 21-1/14/21-2 |
| 10      | 2        | 1             | 1   | 2        | 22-1/13/22-2 |
| 11      | 2        | 1             | 2   | 1        | 27-1/09/27-2 |
| 12      | 2        | 1             | 2   | 2        | 26-1/11/26-2 |
| 13      | 2        | 2             | 1   | 1        | 02-1/02/02-2 |
| 14      | 2        | 2             | 1   | 2        | 04-1/04/04-2 |
| 15      | 2        | 2             | 2   | 1        | 05-1/05/05-2 |
| 16      | 2        | 2             | 2   | 2        | 06-1/06/06-2 |
| Level 1 | Not Aged | 4x(160x30mm)  | 3mm | 3mm/min  |              |
| Level 2 | Aged     | 2x(170x160mm) | 6mm | 90mm/min |              |

**Table 4.24-** Design of experiments for silicone push-out quasi-static shear tests

With the help of Appendix B, the Taguchi table  $L_{16}(2)^{15}$ , containing four factors at two levels, was selected. As it can be noted, 16 experiments were required to complete this table and thus no repetition of the test series was envisaged. As for the other experiments, the constituents and samples were randomly distributed to overcome manufacturing problems arising from the mixing process or from the curing duration.

### Description of the tests

The push-out shear tests were all carried out displacement-controlled on a 630kN INSTRON mobile hydraulic piston. The test set-up was composed by a bottom steel support fully horizontal and two lateral supports in steel, see Fig. 4.53 (a). These last supports were installed to avoid the “opening” of the assembly, i.e. to ensure that the glass plates remained fully parallel during the tests to undertake only pure shear. Neoprene spacers 3mm thick were inserted between these steel supports and the glass plates to avoid steel to glass contact and possible stress concentrations leading to glass breakage before or during the test.



**Figure 4.53-** (a) Double lap-joint shear layout, (b) Relative displacement sensors and (c) Opening displacement sensors

To completely restrain the rotation of the glass plates around their supporting edges, a calibrated and rigid Polyamide spacer was placed between these two outer plates at the bottom in order to keep the silicone thickness constant. As already mentioned, the load was introduced through the upper steel part, where only non-crucial steel to steel contact occurred. A Teflon spacer of 3mm thickness was inserted at the bottom of the assembly under the glass plates to prevent steel to glass contact. The total applied force and displacement of the press were measured by the internal sensors of the machine and six additional external displacement sensors were positioned on the specimens. Two vertical 20mm displacement sensors, measuring the relative displacement between the steel plate and a glass plate, were equipped on each push-out specimen, see Fig. 4.53 (b). As they were positioned at the opposite edges of one glass plate, the in-plane rotation of the inner steel plate could also be

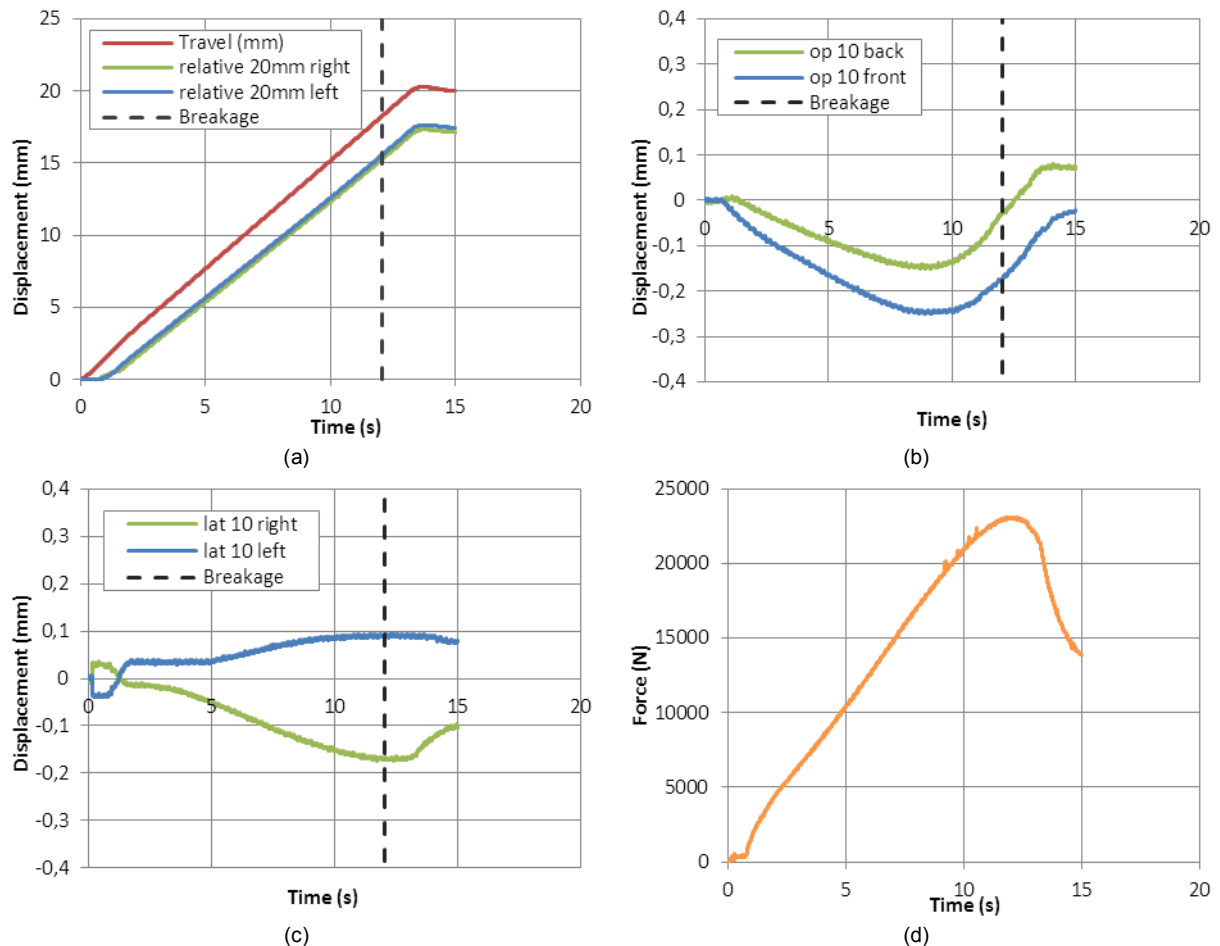


controlled. To check that no “opening” of the sample occurred, two 10 mm horizontal sensors were installed perpendicularly and at the top of the glass surfaces, see Fig. 4.53 (c). Two 10mm lateral sensors, placed perpendicularly to the edge of a glass plate, allowed measuring the expansion of this element.

Pilot tests were first carried out to make sure of the recorded force and displacements. From these tests, it was observed that the “openings” of the samples were negligible, implying that the glass plates remained parallel during all the test duration. Further, the two lateral displacement sensors recorded very small values, indicating that the lateral expansions of the glass were insignificant. Nevertheless, the whole system with all the sensors was conserved for all the 16 experiments of the Taguchi design table.

### Tests results

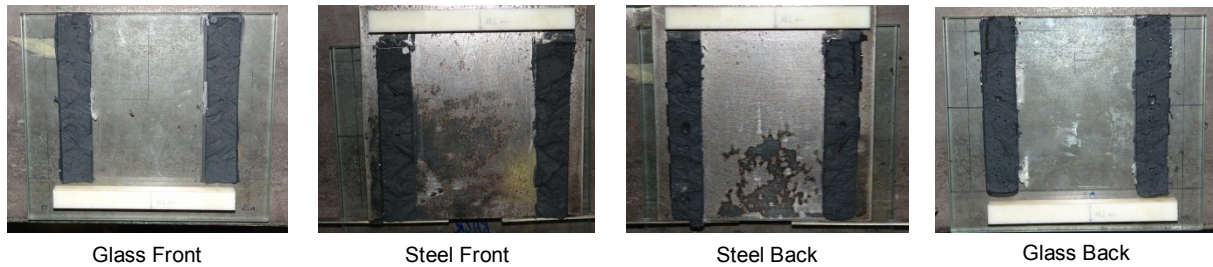
For each test result, the displacements recorded by the six external sensors were controlled and, as evoked previously, only the relative displacements between the inner steel plate and an outer glass plate were noteworthy. As example, the evolutions of all the displacements and of the force in function of the time were plotted for the test n°12 of the Taguchi Table 4.24, see Fig. 4.54.



**Figure 4.54-** (a) Relative disp. versus time; (b) Opening disp. versus time; (c) Lateral disp. versus time; (d) Force versus time

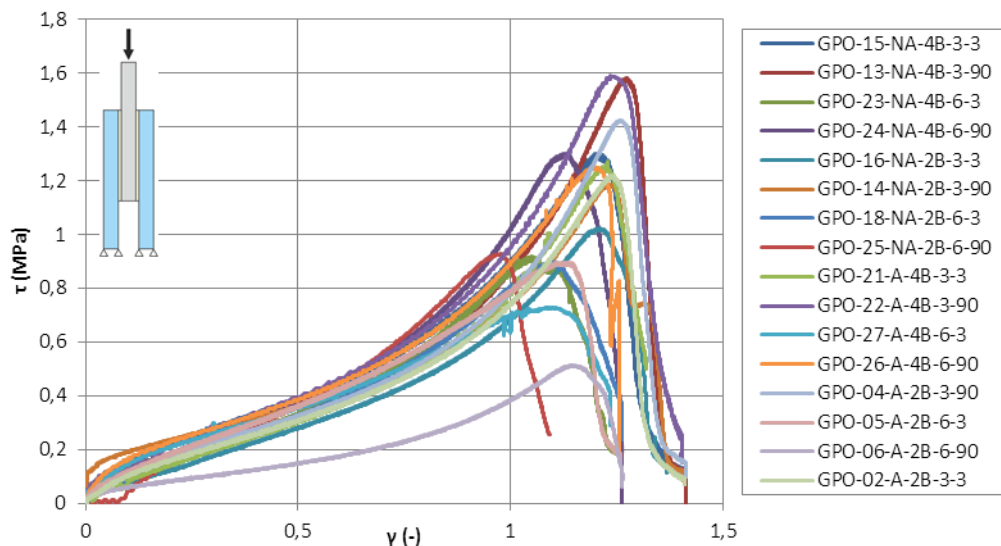
As it can be noted, the “opening” and lateral displacements were inferior to tenths of millimeters and consequently neglected. The total displacement of the hydraulic press did not coincide with the relative displacements, letting suppose that the initial compression of the Teflon was consequent. This was also confirmed by the diagram of the applied force versus time, in which a delay was perceived at the origin. Hence, for the 16 tests, the deformations in the silicone were assimilated to the measured relative displacements. The shear strains  $\gamma$  were then calculated by dividing the average of the relative displacements by the half of the total silicone thickness of the final assemblies see Appendix A.4.

As all the experiments were conducted until breakage, the mode of failure was analyzed. It was found that all the samples broke cohesively, i.e. in the core of the adhesive letting silicone on both steel and glass surfaces. The example of the test n°12 was conserved to expose the common obtained failure mode, see Fig. 4.55.



**Figure 4.55-** Mode of failure of the push-out silicone sample – Test n°12 of Table 4.24

After breakage and for each specimen, the net bonding area was measured at each side with an image-processing program. The air bubbles trapped inside the silicone were also removed from the measure, as non-participating to the transfer of the shear load. The shear stresses  $\tau$  were evaluated by simply dividing the total applied force by the net bonding area. This calculation was feasible with regards to the large length of the bonded area (160mm) and the soft properties of the elastomer. The corresponding shear stress-strain curves were then regrouped into one diagram, see Fig. 4.56.



**Figure 4.56-** Stress-strain diagrams- silicone under quasi-static shear  
(GPO=glass number, NA/A=non-aged/aged, 4B/2B=small/large area, 3/90=loading rate)

As under tension or compression actions, the shear behaviour of silicone appeared clearly non-linear, especially at large strains. Only one curve was lower in terms of stress than the others, which were relatively well matched until shear strains of about 1. Different strengths and strains at breakage were observed and no conclusion of the effects of the selected influent parameters could have been drawn. Furthermore, at small strains, the behaviour was not clear for all the samples. Consequently, two variances analysis, based on the ANAVAR method, were performed on two portions of the curve, i.e. at small strains and at breakage. The aims of these studies were to assess the impact of the possible influent factors on the shear properties of silicone.

- Influence of the factors on the initial stiffness

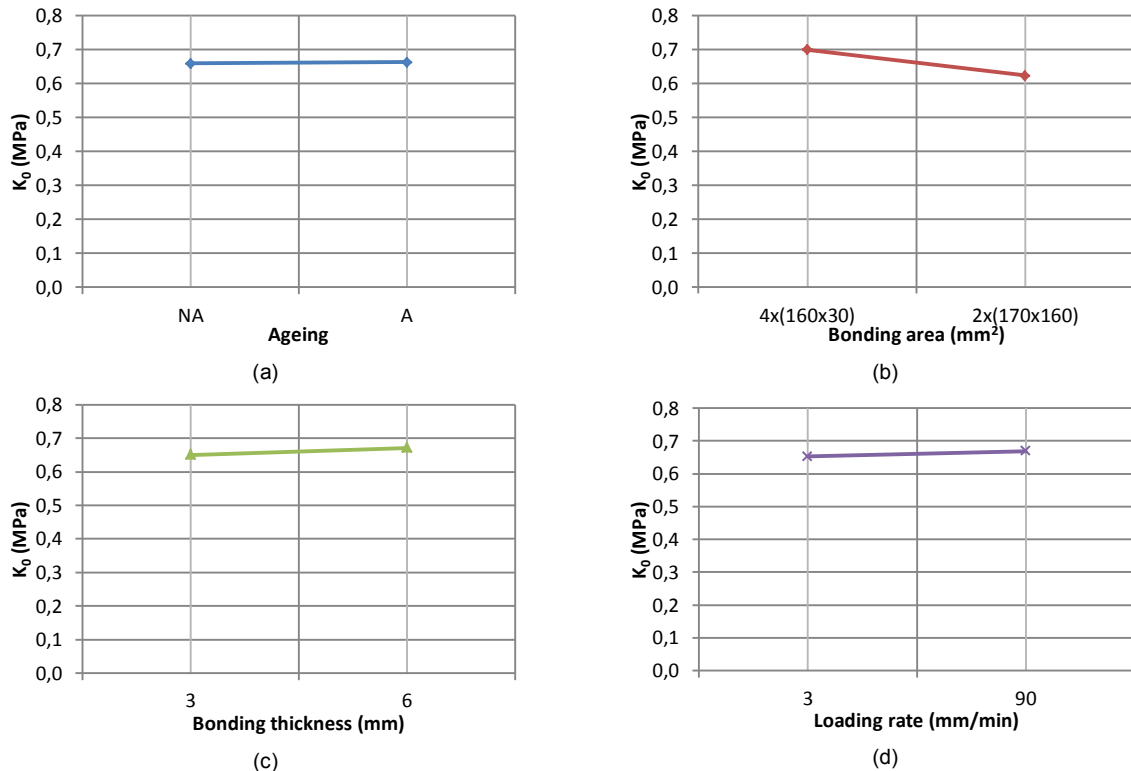
The method proposed by the ETAG 002 to determine the initial stiffness of stress-strain diagrams was only valid for uniaxial results in tension and compression and so not applicable for shear. Amongst the different existing possibilities to calculate the stiffness at the origin, e.g. tangent or secant, the most

conservative one was inspired from the chord modulus, which necessitated evaluating the slope of the curve between two defined strains. By proceeding in this way, the irregularities of the very first part of the behaviour were neglected. The two strains between which were determined the slope were  $\gamma=0,05$  and  $\gamma=0,2$ . All the slopes of the 16 tests were calculated and stored in Table 4.25.

| Test n° | A        | B             | C         | D            | Initial stiffness $K_0$ (MPa) |
|---------|----------|---------------|-----------|--------------|-------------------------------|
|         | Ageing   | Area          | Thickness | Loading rate |                               |
| 1       | Not Aged | 4x(160x30mm)  | 3mm       | 3mm/min      | 0,825                         |
| 2       | Not Aged | 4x(160x30mm)  | 3mm       | 90mm/min     | 0,555                         |
| 3       | Not Aged | 4x(160x30mm)  | 6mm       | 3mm/min      | 0,600                         |
| 4       | Not Aged | 4x(160x30mm)  | 6mm       | 90mm/min     | 0,653                         |
| 5       | Not Aged | 2x(170x160mm) | 3mm       | 3mm/min      | 0,489                         |
| 6       | Not Aged | 2x(170x160mm) | 3mm       | 90mm/min     | 0,495                         |
| 7       | Not Aged | 2x(170x160mm) | 6mm       | 3mm/min      | 0,710                         |
| 8       | Not Aged | 2x(170x160mm) | 6mm       | 90mm/min     | 0,945                         |
| 9       | Aged     | 4x(160x30mm)  | 3mm       | 3mm/min      | 0,604                         |
| 10      | Aged     | 4x(160x30mm)  | 3mm       | 90mm/min     | 0,859                         |
| 11      | Aged     | 4x(160x30mm)  | 6mm       | 3mm/min      | 0,755                         |
| 12      | Aged     | 4x(160x30mm)  | 6mm       | 90mm/min     | 0,744                         |
| 13      | Aged     | 2x(170x160mm) | 3mm       | 3mm/min      | 0,671                         |
| 14      | Aged     | 2x(170x160mm) | 3mm       | 90mm/min     | 0,704                         |
| 15      | Aged     | 2x(170x160mm) | 6mm       | 3mm/min      | 0,699                         |
| 16      | Aged     | 2x(170x160mm) | 6mm       | 90mm/min     | 0,267                         |

**Table 4.25-** Initial stiffness results – DOE of Table 4.24 – silicone quasi-static shear tests

Dispersions in the initial stiffness were found and a standard deviation of 0,163MPa was assessed. To properly evaluate the influence of the ageing, the bonding area, the joint thickness and the loading rate on these results, the total effects of each factor were plotted, see Fig. 4.57.



**Figure 4.57-** Total effect of (a) ageing, (b) bonding area, (c) bonding thickness and (d) loading rate on the initial stiffness

From this graphical examination, the invariance of the silicone shear properties towards the ageing, and the loading rate was appraised, as the slopes were quasi nil in these cases. To ensure that the bonding area and thickness did not influence the silicone behaviour at small strains, the ANAVAR method was employed, see Appendix C.7. From this study, it was demonstrated that none of the chosen parameters or of the interactions impacted the initial stiffnesses, which definitely concluded on the invariance of this material at small deformations towards quasi-static shear.

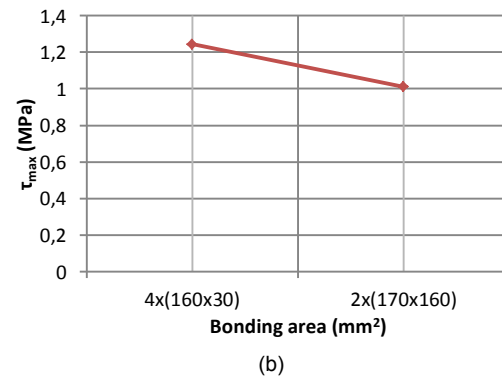
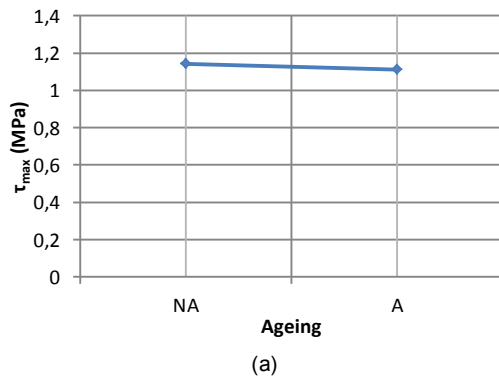
- Influence of the factors on the strength

For the 16 conducted experiments, large dispersions in strengths, assimilated to the maximum points of the curves, were observed, see Fig. 4.56. At these different values, the silicone started to break progressively, which, with the friction arising between the cohesively separated parts, explained the non-instantaneous losses of stresses. All the strengths were determined and recorded in Table 4.26.

| Test n° | A        | B             | C         | D            | Strength $\tau_{\max}$ (MPa) |
|---------|----------|---------------|-----------|--------------|------------------------------|
|         | Ageing   | Area          | Thickness | Loading rate |                              |
| 1       | Not Aged | 4x(160x30mm)  | 3mm       | 3mm/min      | 1,302                        |
| 2       | Not Aged | 4x(160x30mm)  | 3mm       | 90mm/min     | 1,583                        |
| 3       | Not Aged | 4x(160x30mm)  | 6mm       | 3mm/min      | 0,919                        |
| 4       | Not Aged | 4x(160x30mm)  | 6mm       | 90mm/min     | 1,302                        |
| 5       | Not Aged | 2x(170x160mm) | 3mm       | 3mm/min      | 1,024                        |
| 6       | Not Aged | 2x(170x160mm) | 3mm       | 90mm/min     | 1,185                        |
| 7       | Not Aged | 2x(170x160mm) | 6mm       | 3mm/min      | 0,898                        |
| 8       | Not Aged | 2x(170x160mm) | 6mm       | 90mm/min     | 0,931                        |
| 9       | Aged     | 4x(160x30mm)  | 3mm       | 3mm/min      | 1,270                        |
| 10      | Aged     | 4x(160x30mm)  | 3mm       | 90mm/min     | 1,591                        |
| 11      | Aged     | 4x(160x30mm)  | 6mm       | 3mm/min      | 0,729                        |
| 12      | Aged     | 4x(160x30mm)  | 6mm       | 90mm/min     | 1,252                        |
| 13      | Aged     | 2x(170x160mm) | 3mm       | 3mm/min      | 1,220                        |
| 14      | Aged     | 2x(170x160mm) | 3mm       | 90mm/min     | 1,425                        |
| 15      | Aged     | 2x(170x160mm) | 6mm       | 3mm/min      | 0,897                        |
| 16      | Aged     | 2x(170x160mm) | 6mm       | 90mm/min     | 0,514                        |

**Table 4.26-** Strengths results – DOE of Table 4.24 – silicone quasi-static shear tests

As for the initial stiffness analysis, large variations in the results were noticed with an average of 1,128MPa and a standard deviation of 0,3MPa. The raw data did not allow concluding on the influence of the selected factors, therefore the total effects of each parameter were again plotted, see Fig 4.58. The strength was not affected by the presence of ageing, as the slope was negligible. However, the bonding area, the thickness and the loading rate seemed to modify this final value. While the increase of the geometrical factors generated loss of strength, the loading rate had the opposite effect.



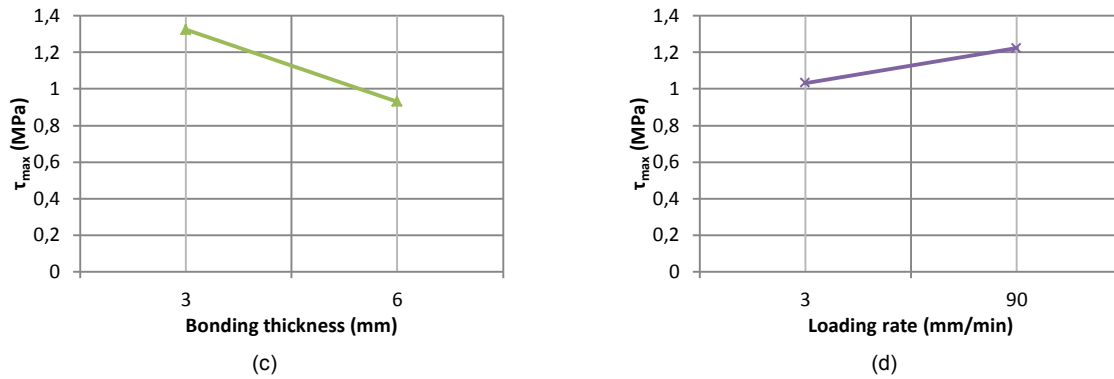


Figure 4.58- Total effect of (a) ageing, (b) bonding area, (c) bonding thickness and (d) loading rate on the strength

Nevertheless, the above diagrams did not indicate if the decreases of the maximum stress were due to a real decrease of the results for all the specimens presenting a certain level or if they were due to some local very small values accounted in the averages. Hence, the ANAVAR analysis was employed to accurately check the dependency to the four chosen factors, see Appendix C.8. With this study, it was proved that only two independent parameters were influent on the strengths, i.e. the bonding area and thickness. The variations of the maximum stress were identical for these two geometrical factors. A loss in strength was observed with the increase of glued area or the thickness.

The relation between strength and bonding area was explained by the process of fabrication, which was either based on an injection method for the small areas or on a pouring method for the large areas. With the obtained results, it could have been postulated, that the injecting procedure was more effective, giving stronger specimens. Furthermore, the relationship between the strength and the joint thickness could also be interpreted by some differences in the manufacturing procedure. Indeed, according to Appendix A.4, it was remarked that more deviations were encountered for the smaller thicknesses. The final thicknesses of the samples were always larger than the desired thickness of 3mm. For the large bonding area with minimal thickness, the surplus of the silicone was evacuated through large lateral compression of the assemblies and so all the silicone macromolecules were highly compressed for the curing. For the small glued area, the adhesive was injected with the same pressure in calibrated spaces possessing either a small or a large thickness. Thus, smaller was the gap and greater were the “density” of the silicone and the compression of the macromolecules.

To undertake the design of a silicone joint subjected to quasi-static shear, the characteristic value is of importance. Hence, the distribution followed by the shear strength was evaluated with the Lilliefors tests as only 16 experiments were carried out. In accordance to the previous distributions found for the quasi-static tension and compression, the null hypothesis of a log-normal distribution was investigated. The complete details of this study were gathered in Appendix D.4. From this analysis, it was found that the log-normal distribution could be assumed with good confidence. Therefore, the calculation of the 5% fractile was done with the method proposed by the EN 1990 [2.30]. The final characteristic strength obtained for the shear quasi-static tests was of 0,630MPa.

#### 4.2.3.3 Cyclic tests

The quasi-static test series in shear was followed by a second campaign centered on the cyclic shear behaviour of the silicone in order to assess the damage, continuous or discontinuous, sustained by this material. As a small number of specimens were manufactured, a standard analysis procedure was conducted.

#### Definition of the objectives

The non-linear behaviour of the selected elastomer DC 993 after several cycles and the stress softening constituted the main objectives of these experiments. The complete representation of the

Mullin's effect including the dependency on the previously maximum strain encountered was not of interest. Indeed, knowing the maximum authorized strain, corresponding to the allowable strength determined with the quasi-static shear tests, the application of an amplitude larger than this value allowed freeing oneself from this multi-steps characterization. At a same number of cycles, the loading path, superposed to the unloading path, of larger imposed deformation always presented a larger stress softening than the one of a smaller imposed deformation, see Fig. 2.19. Hence, higher was the imposed strain and lower was the stress-strain curve. The last loading path ending this effect for a high strain was then more conservative. Nevertheless, similar outcomes than the ones of the other cyclic experiments were expected:

- Cyclic shear stress-strain diagrams to properly account for the stress softening in finite element numerical simulations.
- The distinction between the Mullins' effect and the cumulative damage had to be appraised in terms of numbers of cycles by analyzing the dissipated energy. The last loading curve ending the discontinuous damage should be recorded.
- The second damage, i.e. continuous, under very long-term shear cyclic actions causing stress softening had also to be predicted.

The artificial ageing was not investigated for this study, as it was found non-influent on the quasi-static shear properties. Additionally, as the frequencies did not impact the cyclic behaviour in tension and compression, they were not considered. Consequently, only one constant frequency was applied, i.e. 0,1Hz, for a strain amplitude of 0,6 (equal to a displacement of 2mm).

### Description of the tests

Two specimens of identical bonding area 2x (170x160mm) and thickness (3mm) were prepared for the tests. These dimensions were chosen to approach an average value, as it was found, in the quasi-static shear tests, that the large bonding area tended to decrease the strength, while the small thickness generated an increase. It was also demonstrated that these changes were principally due to the manufacturing process. Therefore, a complete analysis of the silicone weight and thickness dispersions were operated, see Table 4.27.

| N° | Silicone weight (g) |       |           | 2 x Silicone thickness (mm) |     |     |     |         |       |           |
|----|---------------------|-------|-----------|-----------------------------|-----|-----|-----|---------|-------|-----------|
|    | Measured            | Ideal | Diff. (%) | t1                          | t2  | t3  | t4  | Average | Ideal | Diff. (%) |
| M1 | 240,1               | 208,7 | 15,0      | 6,2                         | 6,1 | 6,8 | 7,3 | 6,6     | 6     | 10,0      |
| M2 | 241,9               |       | 15,9      | 6,9                         | 6,4 | 6,1 | 6,7 | 6,5     |       | 8,7       |

**Table 4.27-** Silicone weight and thickness dispersions for the tested samples – silicone cyclic shear

It was noticed that the weight and thickness were each time higher than the expected values, meaning that the macromolecules were probably well compressed. This check allowed ensuring of the proper fabrication of the push-out samples.

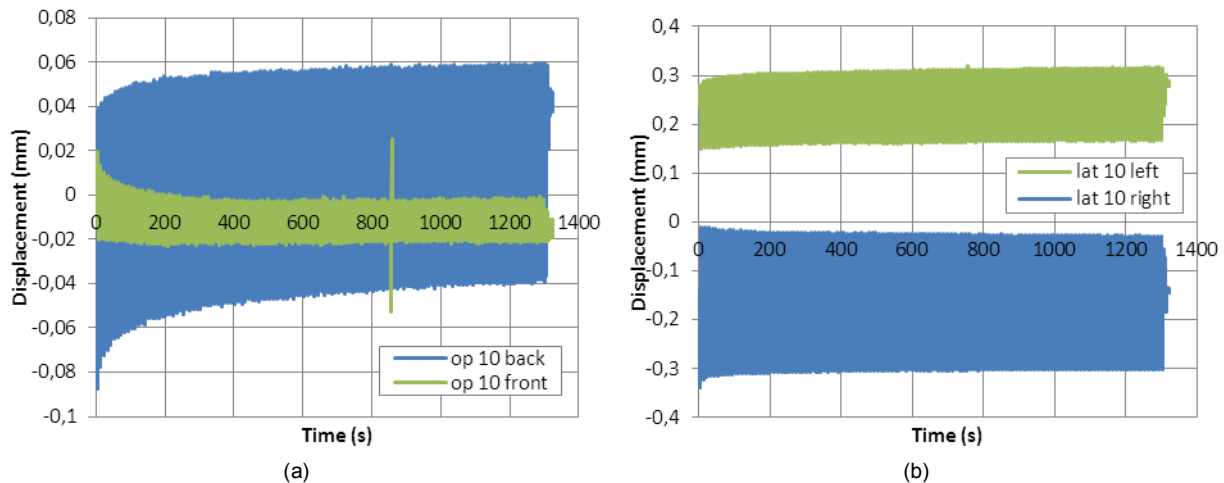
Cyclic shear tests were carried out on the same 630kN INSTRON mobile hydraulic press than the quasi-static tests. The complete test set-up and data acquisition system, composed by six external displacement sensors, were conserved for this tests campaign, see Fig. 4.53. A calibrated Polyamide spacer, inserted between the two outer glass plates at the bottom of the assembly, was combined to lateral steel supports, covered by 3mm Neoprene spacers, to ensure pure shear action. Under the specimen was disposed a 3mm thick Teflon spacer to avoid glass to steel contact. The load was introduced on the top inner steel plate and recorded by the machine, as the total displacement. The positions of all the six external displacement sensors remained identical, i.e. two vertical sensors measuring the relative displacement between the steel plate and a glass plate, two horizontal sensors for the opening and two for the lateral expansion of a glass plate.



Pilot tests on push-out specimens allowed approving the procedure, in which the samples were initially subjected to a relative displacement of 2mm (strain of about 0,58) and then subjected to a sinusoidal displacement of 2mm of amplitude under a frequency of 0,1Hz. At least 60 cycles were carried out to obtain sufficient information.

### Tests results

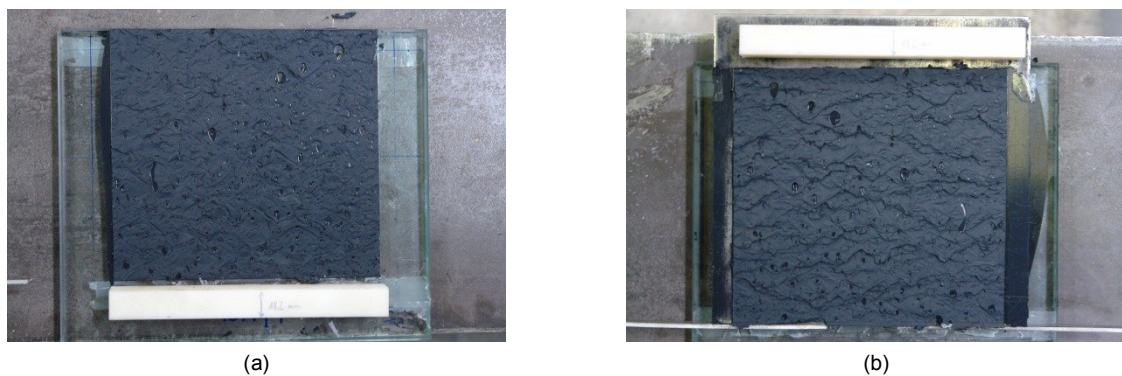
For the two experiments, the relative displacements assimilated to the silicone deformations were the only significant values. A control of the opening of the assembly and of the lateral expansion of the glass plate was realized to approve the tests, see Fig. 4.59 representative of test M1.



**Figure 4.59-** (a) Opening displacement versus time and (b) Lateral displacement versus time - silicone cyclic shear

The opening and lateral displacements were again inferior to tenths of millimeters during all the test duration, indicating respectively that the two outer glass plates stayed parallel and that no important expansion occurred in the glass. Hence, attention was only given to the relative displacements which were inferior to the total displacement of the machine. The averaged relative displacements were in each case divided by half of the total thickness of the silicone, Table 4.27, to obtain the tangent of the shear strain  $\gamma$ .

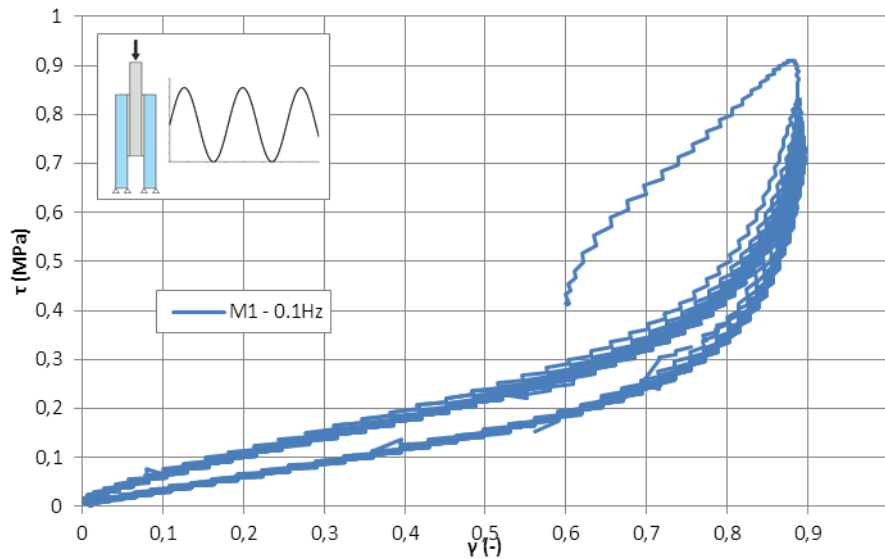
As none of the push-out specimens broke during the cyclic testing time, they were unloaded and then subjected to a quasi-static loading until breakage. The aim was to determine the mode of failure and the real bonded area. For both samples, cohesive failures, letting silicone parts on all the surfaces, were recorded, see M1 example on Fig. 4.60.



**Figure 4.60-** Mode of failure of the push-out silicone subjected to cyclic shear – (a) glass side and (b) steel side

The net bonding areas, excluding the air bubbles trapped inside, were measured on each side with an image-processing program. The total shear stresses  $\tau$  were simply evaluated by dividing the total applied force by the total net bonding area. Combining these last data with the shear strains, cyclic

stress-strain diagrams were plotted. A typical resulting curve is introduced in Fig. 4.61 for the shear sample M-1 tested at a frequency of 0,1Hz. The strong non-linearity, characteristic of the hyperelastic behaviour, was again observed with a first loading path exposing higher stresses than the following ones. Then, after the first cycle and as for the other cyclic experiments, the stress softening became less important with the cyclic repetitions.

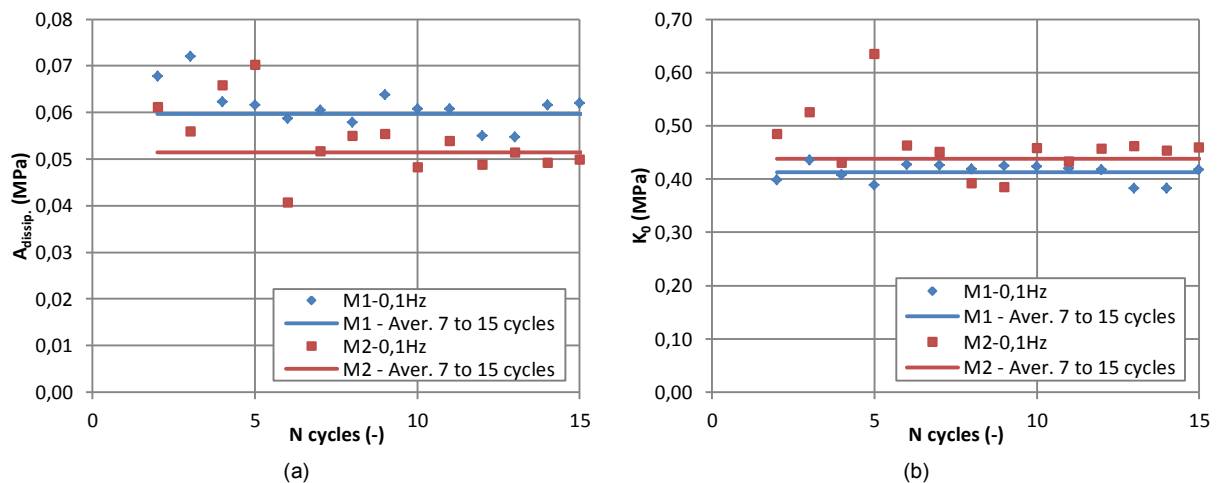


**Figure 4.61-** Cyclic shear stress-strain diagram for silicone push-out sample under a frequency of 0,1Hz

- Mullins' effect characterization

To assess the real number of cycles during which the Mullins' effect took place, two analyses were realized, i.e. a first one concerning the dissipated energy associated to the area of the hysteresis and a second one centered on the initial stiffness.

The areas of the hysteresis were calculated for both tested specimens over 15 cycles, as it was supposed that the discontinuous damage disappeared at the 7<sup>th</sup> cycle according to the results found with the cyclic tension and compression. The following Fig. 4.62 (a) gathered all these estimated results. As it can be remarked, the values of the dissipated area were higher for the first cycles and then seemed to reach a stable limit. To better apprehend this effect, the averaged area from the 7<sup>th</sup> to the 15<sup>th</sup> cycles were calculated for both experiments. The 7<sup>th</sup> cycle again appeared as the first cycle during which the Mullins' effect was absent.

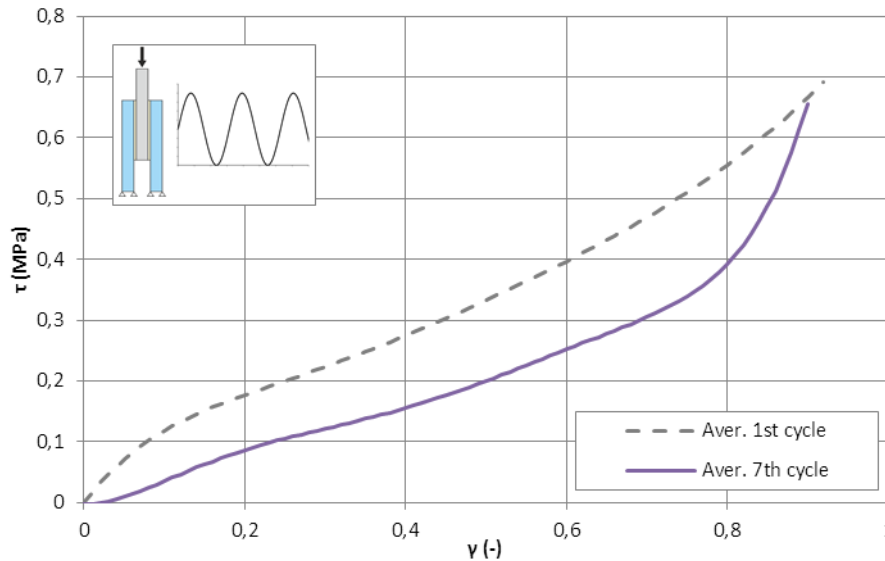


**Figure 4.62-** (a) Dissipated area versus cycle numbers and (b) Initial stiffness versus cycle numbers - silicone cyclic shear

To corroborate this result, the initial stiffnesses, corresponding to the chord modulus between  $\gamma=0,05$  and  $\gamma=0,2$ , were determined over the first 15 cycles for the both experiments, see Fig. 4.62 (b). While



for the first cyclic test M1, the initial stiffness was almost constant over the number of cycles, the second test M2 showed consequent dispersions until the 6<sup>th</sup> cycle. The average of the chord modulus from the 7<sup>th</sup> to the 15<sup>th</sup> cycles approximated relatively well the last recorded initial stiffnesses. Consequently, it confirmed that the 7<sup>th</sup> loading path ended the Mullins' effect. A comparison of this loading path with the averaged first quasi-static curve was then operated, see Fig. 4.63.

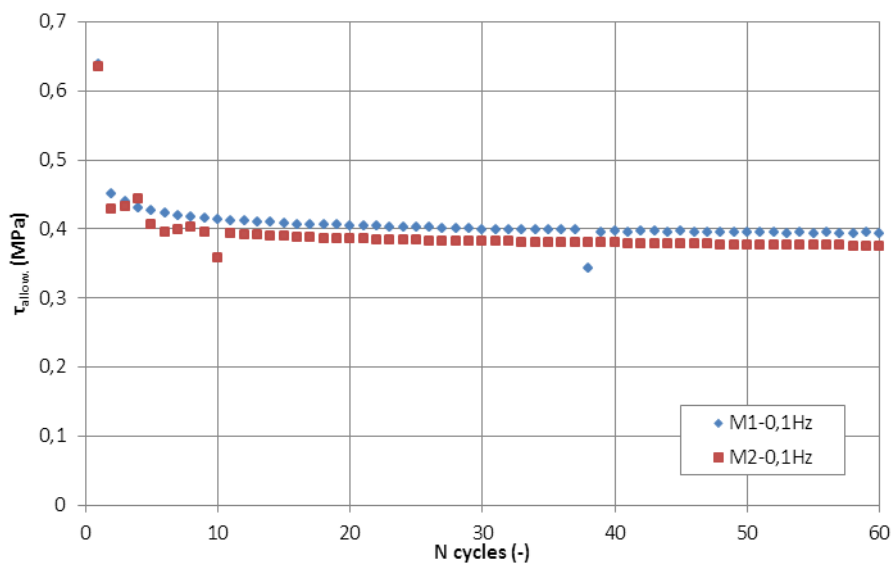


**Figure 4.63-** Comparison between the averaged 1<sup>st</sup> cycle and the limiting 7<sup>th</sup> cycle of the Mullins' effect - silicone cyclic shear

In contrary to the cyclic results in compression, an important softening occurred over all strains range, e.g. for a strain of 0,6 the loss of stress was about 0,15MPa which was consequent with regard to the total quasi-static stress of 0,4MPa. Therefore, the Mullins' effect must always be considered in numerical simulations of adhesively bonded façades.

- Prediction of the continuous damage

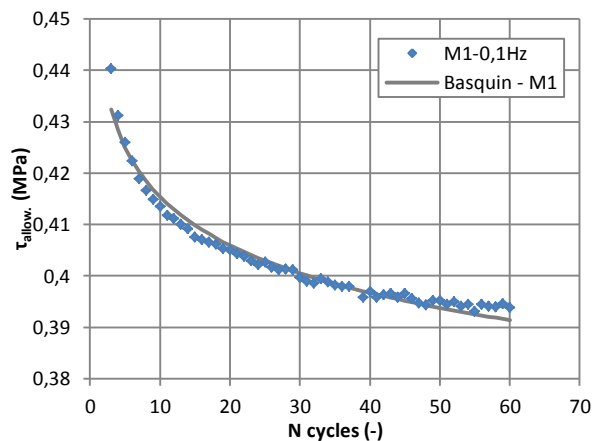
To predict the cumulative damage effect for very long continuous cyclic actions, the evolution of the stress at the maximum allowable strain was recorded. This last allowable strain coincided with the strain at the maximum allowable strength of 0,630MPa determined from the quasi-static shear tests. The two cyclic shear tests were conducted over 60 cycles for which the allowable strengths were archived, see Fig. 4.64.



**Figure 4.64-** Evolution of the maximum allowable stress with the increase of cycles - silicone cyclic shear

With the chosen definition, the stress value of the 1<sup>st</sup> cycle was equivalent to 0,630MPa for the two curves. The most significant drop of stress of about 0,2MPa took place between the 1<sup>st</sup> and 2<sup>nd</sup> cycle and then the decrease was clearly slower. The phenomenon appearing between the two first cycles came from the testing procedure, as the stresses were recorded at a lower strain than the maximum testing strain. Indeed, for a higher imposed strain, the unloading path, close to the following loading path, was more conservative, see Fig. 2.19. In consequence, the stress values of the two first cycles were let aside for the prediction at a larger number of cycles.

The mathematical formulation of Basquin (Bas) was employed over the 60 cycles to model the Wöhler curves, based on the maximum allowable strength. As already mentioned, the parameters  $a$  and  $b$  were calculated on the logarithmic representations of the curves of Fig. 4.64 with a simple linear regression. Each estimated curve was compared to the tests results, see Fig. 4.65 for an example, and the coefficients of correlation were estimated to ensure of the correct fitting, see Table 4.28.

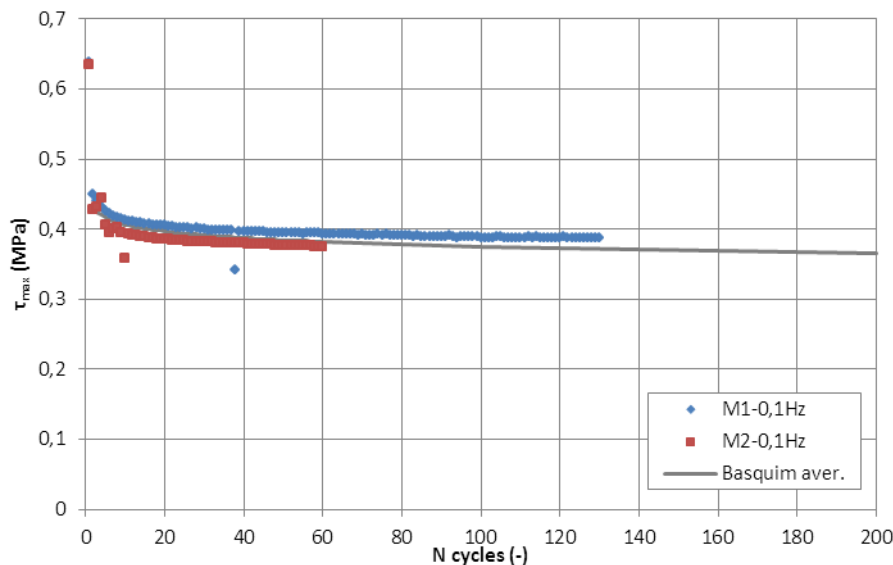


| Samples  | Basquin coefficients |         | Correlation coefficient |
|----------|----------------------|---------|-------------------------|
|          | a                    | b       |                         |
| M1-0,1Hz | 3,27E-11             | -30,105 | 0,986                   |
| M2-0,1Hz | 9,07E-11             | -27,573 | 0,948                   |

**Table 4.28-** Basquin coefficient for the shear samples

**Figure 4.65-** Wöhler curve representation with Basquin form

For these 60 cycles, the estimations of the Wöhler curves issued from the experiments were correctly represented by the Basquin formulation as the coefficients of correlation were close to 1. Hence, the average of the estimated curves was determined ( $a=5,46E-11$ ;  $b=-28,81$ ) and confronted to the complete testing Wöhler data, see Fig. 4.66.



**Figure 4.66-** Comparison between the averaged Basquin formulation and the tests results - silicone cyclic shear

For the first Mullins test, the total number of cycles applied was of 130. The maximum allowable stress at this cycle was compared to the Basquin result and a difference of 3,83% was found, which was acceptable and more conservative. The approximation made appeared therefore reasonable and

prediction at larger cycles possible. For 1000 cycles, the maximum allowable stress was of 0,346MPa, for 10000 cycles of 0,320MPa and for one million equal to 0,273MPa.

#### 4.2.3.4 Long-term tests

The long-term behaviour of silicone adhesive represents also vital information for design façade joints, especially for vertical glazing non-supported mechanically. Thus long-term relaxation shear tests were carried out on two samples to appraise the evolution of the stress.

#### Definition of the objectives

As for the tension and compression long-term tests, the main objective was to quantify the loss of stresses for long duration and to appraise if a constant value was reached after a certain time. The complete list of objectives to meet was the following one:

- To avoid extensive long-term tests, the total duration was set to 1200s, corresponding to 20min. During this time interval, the decrease of the stress had to be studied properly.
- With the previous data, the prediction on longer duration, e.g. 25 years for SSGS according to the ETAG 002, had to be realized with the help of reduction factors.

It was demonstrated with the shear quasi-static experiments, that the artificial ageing did not impact the properties of the silicone. For that reason, this factor was neglected in this analysis. Furthermore, with the previous long-term results, it was found that the loss in stress was independent of the imposed displacement after the first 60s, in contrary to the one occurring between the quasi-static stress and the stress at 60s. For tension, the biggest drop between these two last values appeared for the higher imposed deformation. Accordingly, it was decided to impose an elevated strain, larger than the maximum allowable strain of 0,87, to overcome the evaluation of the imposed displacement. The constant imposed strain, applied for both tests, was  $\gamma=1,05$ , equivalent to a relative displacement of about 5,75mm.

#### Description of the tests

The ideal silicone dimensions employed in this test series were identical to the ones of the cyclic shear samples, i.e. a large bonding area of 2x (170x160mm) and a small thickness of (3mm). These proportions were selected to acquire an average value, as it was found that the strength decreased with the bonding area and the thickness. The manufacturing process, influencing these results, was also investigated by examining the dispersions in weight and thickness, see Table 4.29. For the two specimens, the silicone weight and thickness were slightly larger than the ideal ones. The applied compression to evacuate the silicone surplus after the pouring was not enough to obtain the ideal thickness but sufficient to compress the macromolecules ensuring a correct fabrication.

| N°   | Silicone weight (g) |       |           | 2 x Silicone thickness (mm) |     |     |     |         |       |           |
|------|---------------------|-------|-----------|-----------------------------|-----|-----|-----|---------|-------|-----------|
|      | Measured            | Ideal | Diff. (%) | t1                          | t2  | t3  | t4  | Average | Ideal | Diff. (%) |
| LT-1 | 218,3               | 208,7 | 4,6       | 6,2                         | 6,2 | 6,2 | 6,1 | 6,2     | 6     | 3,0       |
| LT-2 | 222,5               |       | 6,6       | 6,4                         | 6,5 | 6,4 | 6,4 | 6,4     |       | 6,7       |

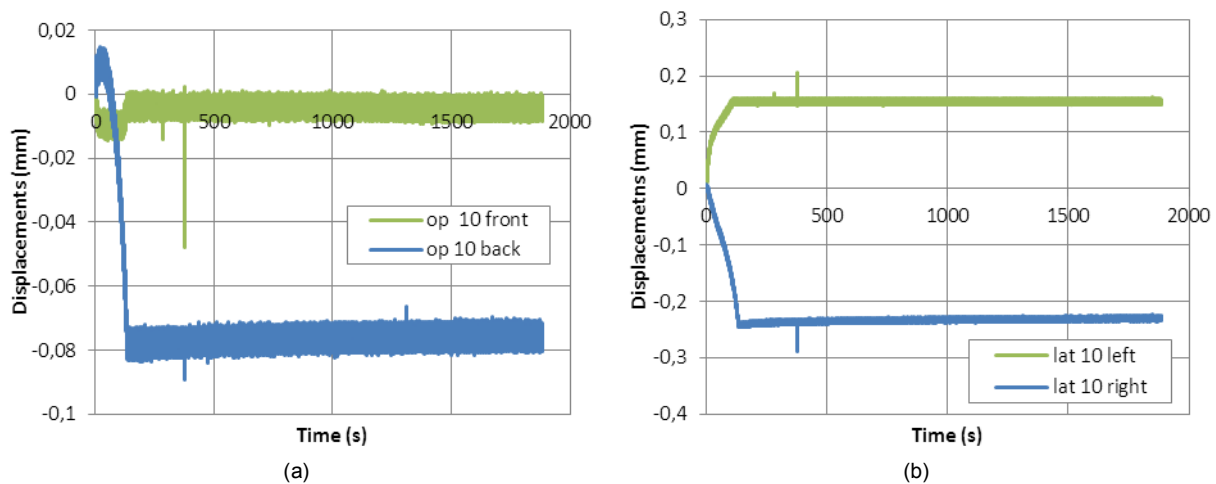
**Table 4.29-** Silicone weight and thickness dispersions for the tested samples – silicone long-term shear

The long-term relaxation tests were carried out on the same 630kN INSTRON mobile hydraulic press than the previous shear tests, with the same test set-up and data acquisition system, see Fig. 4.53. Pure shear actions in the adhesive were accomplished by the combination of two mechanical devices, i.e. the lateral steel plates and the inner calibrated Polyamide spacer. Steel to glass contacts were prevented by using laterally 3mm thick Neoprene and, at the bottom of the assembly, a 3mm thick Teflon plate, which also allowed the lateral expansion of the glass. The resulting force and total displacements were measured by the internal sensors of the press. Two external sensors recorded

the relative displacements between the inner steel plate and a glass plate, two others sensors evaluated the “opening” of the assembly and the last two registered the lateral expansion of the glass. With regards to the large relative displacements to be imposed of 5,75mm, the method employed for the tension and compression tests and consisting in applying the final strain in one second was not valid. To avoid oscillations or damage during the loading, the final deformation was applied under a constant loading rate of 3mm/min. Then, this reached relative displacement was kept constant during about 1200s. This procedure was validate by a pilot test for which the “opening” and lateral sensors displayed negligible values during the loading and constant parts.

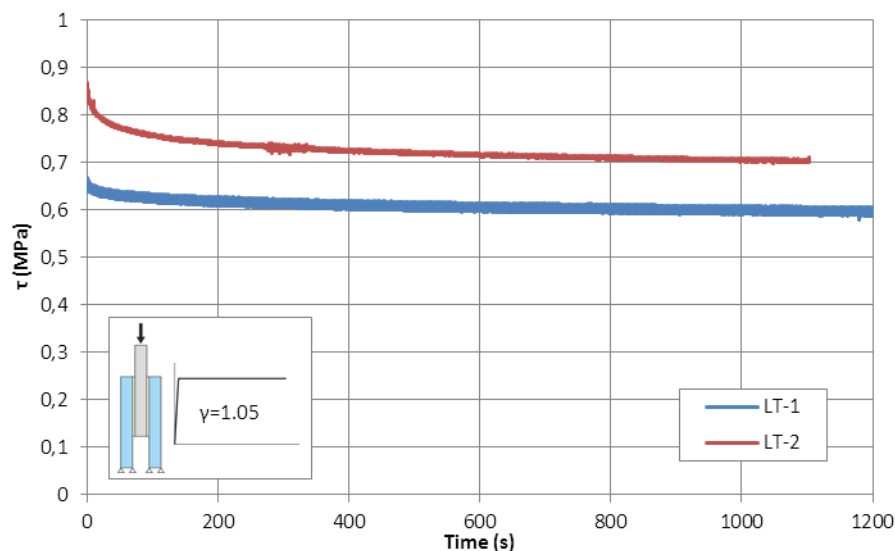
### Tests results

To reach the final imposed strain, the only relevant displacement values were given by the relative displacements sensors. The control of the opening and lateral sensors during the loading and the constant plateau exposed small displacements, see Fig. 4.67 for the curves concerning the first long-term test LT-1. Pure shear under relaxation long-term was so assumed.



**Figure 4.67-** (a) Opening displacement versus time and (b) Lateral displacement versus time - silicone long-term shear

As no specimen broke during the tested time, they were completely unloaded and then subjected to a quasi-static loading until breakage. This allowed, on one hand, confirming the cohesive mode of failure and, on the other hand, determining the net bonding area excluding trapped air bubbles. The total shear stresses  $\tau$  were simply calculated by dividing the total force by the total silicone net bonding area. Typical stress-time curves were then plotted for the two experiments, see Fig. 4.68.



**Figure 4.68-** Stress-time diagrams for an imposed strain of  $\gamma=1,05$  – silicone long-term shear

The dispersions observed between the two curves could be due to the large imposed strain, as it was located in the critical zone near breakage where large variations in strengths were noticed for the quasi-static action. To analyze properly the stress softening, a discretization of the time over the whole test duration was realized, i.e. at 60s, 300s, 600s, 900s and 1100s. Reductions factors, corresponding to the ratio of the stresses at these instant over the quasi-static stress, were calculated. The evolutions of these factors were plotted in function of the time, see Fig. 4.28.

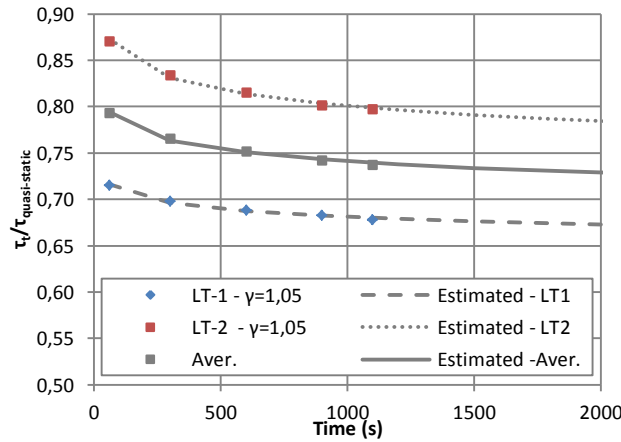


Figure 4.69- Reduction stress factors – tests and estimations

| N°                   | Power coefficients |        | Correlation coefficient |
|----------------------|--------------------|--------|-------------------------|
|                      | a                  | b      | R                       |
| LT-1 - $\gamma=1,05$ | 0,770              | -0,018 | 0,988                   |
| LT-1 - $\gamma=1,05$ | 0,989              | -0,030 | 0,994                   |
| Aver.                | 0,879              | -0,025 | 0,993                   |

Table 4.30- Power law coefficients – tests and average

The variations of the reduction factors following the first ratio were not consequent for both test results. The main loss in stress, with respect to the quasi-static stress, occurred before the first 60s, as the two ratios were directly low at the first point. The same conclusion was drawn out of the long-term tensile and compressive analyses.

The power function of section 4.2.1.4 was again employed to predict the evolution of the reduction factors at very long-term. For the two experiments and the average, the coefficients of this model were evaluated with a simple linear regression applied on the data of Fig. 4.69 expressed in logarithmic axes. All these constants were gathered in Table 4.30 and the resulting estimated curves were superposed to the ones of Fig. 4.69 for visual comparison. Good concordances were found in each case, which was also confirmed by the correlation coefficients close to 1.

The long-term stresses were then determined with the help of the reduction factors and confronted to the real curves, see Fig. 4.70. The stresses after 25 years of permanent shear at  $\gamma=1,05$  was of 0,471MPa for LT-1, 0,466MPa for LT-2 and the average. This was equivalent to the quasi-static stress divided by 1,9. By conserving this factor, the maximum allowable stress would drop to 0,333MPa.

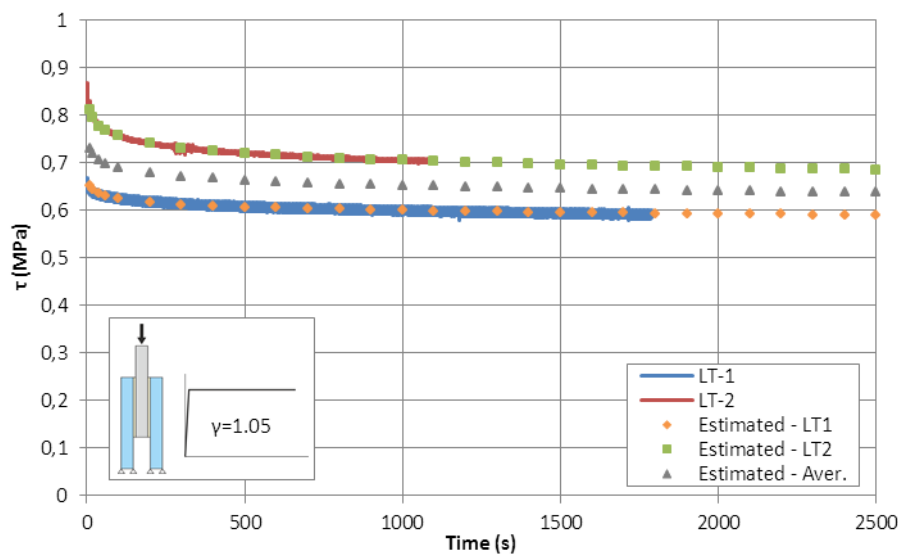


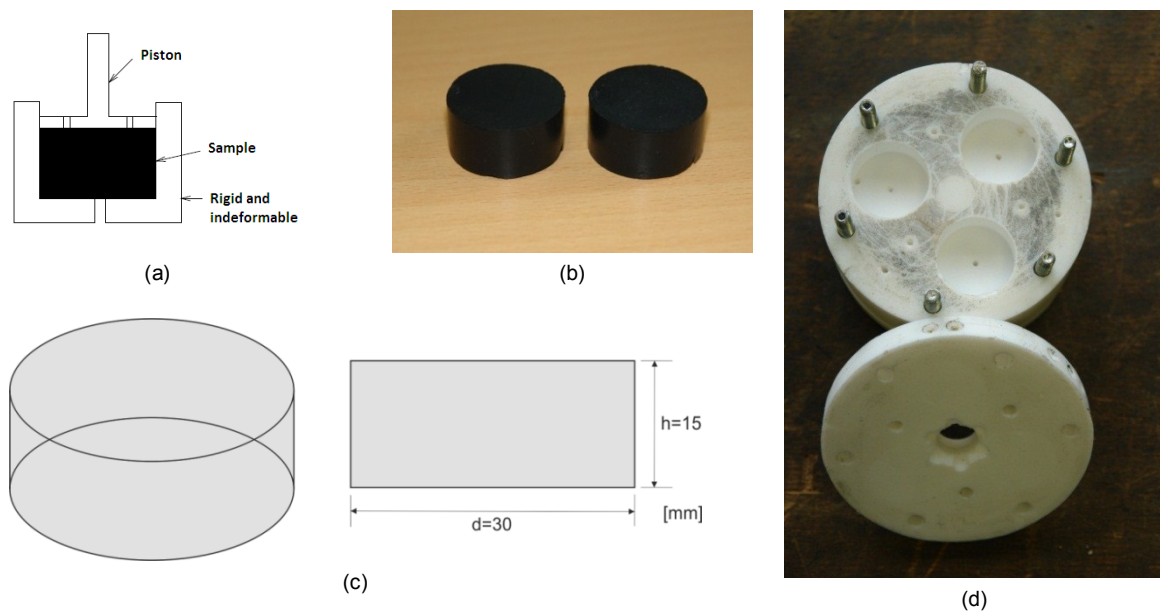
Figure 4.70- Estimated stress-time diagrams – silicone long-term shear

## 4.2.4 Oedometric

Elastomer materials were presented as quasi-incompressible in section 2.4.2.1, especially in confined environments in which minor variations of displacement induce large increases of forces. However, the previous tests series did not account for this property, as they did not imply volume changes. A new campaign of multiaxial tests, based on the layout of oedometric experiment, was therefore conducted. The obtained data would allow implementing the slight compressibility of the silicone material in the constitutive law for further numerical simulations. Modeling correctly this behaviour was particularly important for the mechanical-adhesive connection of section 3.4.

### 4.2.4.1 Manufacturing of the samples

An oedometric test consists in inserting a circular specimen in a steel rigid matrix of the same diameter to later apply a force through the last opened part, see Fig. 4.71 (a). The diameter of the tested silicone and of the matrix should be rigorously identic to fully restrain the lateral expansion of the sample from the start. The upper part composed by the piston should also be guided by the matrix to ensure the parallelism of the top and bottom surfaces. In addition to these external geometrical considerations, the samples had to be absolutely air bubble-free to always test in the same conditions. Thus, the manufacture of the oedometric specimens could not be done with a simple pouring process but with an injecting process.



**Figure 4.71-** (a) Oedometric test layout; (b) Manufactured samples and (c) dimensions; (d) Injecting mold in Teflon

Compared to the standard compressive sample exposed in section 4.2.2, the dimensions of the oedometric specimen were reduced to a diameter of 30mm and a high of 15mm to lessen the quantity of silicone to be injected and so the possibility of air-bubbles, see Fig. 4.71 (b) and (c). The mold composed in three pieces, i.e. a central part in which were drilled 6 cylindrical forms (3 above and 3 below), and a top and bottom covering parts, was entirely made of non-adhesive Teflon, see Fig. 4.71 (d). In each form of the central part were drilled two holes of 2mm of diameter, one in the center and another one at the opposite of the injection point, to evacuate the air during the shape filling. In the covering plates, these last holes were naturally extended and a central one was manufactured to adapt the thread of a standard cartridge. Regular small notches were done around this central hole to allow the injection of the three shapes at a time and to not affect the flatness of the final silicone surface. The whole system was simply closed with six screws and the elastomer injected with a standard handgun. The samples were let in the mold during 24hours to achieve a complete curing and were then unmolded with compressed air injected in one hole of 2mm of diameter. The residual

portions of silicone at the injection and evacuation holes were carefully cut. They were finally stored for a period of one month shielded from the light at ambient temperature and humidity. The external surfaces did not possess visible flaws and some pilot samples were cut in half to ensure of the absence of air bubble.

#### 4.2.4.2 Quasi-static tests

The multiaxial behaviour of silicone under quasi-static action constituted the only relevant information for the establishment of an accurate and complete constitutive material law. Indeed, with regards to the result acquired with the cyclic compression tests and the very small deformations involved for the oedometric experiments, no real damage affecting the properties could occur. Therefore, only six quasi-static oedometric tests were performed according to the Taguchi procedure.

#### Definition of the objectives

The principal objective of these oedometric tests was to obtain relevant stress-strain diagrams for the selection of the volumetric part of the strain energy potential, see Table 2.9. However, further aims had to be fulfilled concerning the maximum allowable stress-strain values and the stiffness. Thus the list of objectives to meet was the following one:

- Collect exploitable stress-strain diagrams to integrate multiaxial effect in the material law and undertake numerical simulations of restrained silicone system.
- Evaluate the possible influence of some factors on the elastomer behaviour and compare to the compression case.
- Define the maximum allowable stress and associated strain for the design of adhesive joint.

#### Selection of the influent factors

For all the type of actions studied, i.e. tension, compression or shear, and their natures, either quasi-static, cyclic or long-term, the artificial ageing was found as non-influent. Hence, it was not considered as an influent factor for this study. Only the loading rate was investigated with a low and a moderate speed, i.e. respectively 0,1mm/min and 1mm/min. These values were chosen considering the total height of the sample and the important predicted forces.

#### Choice of the Taguchi table

For this design of experiments, only one quantitative continuous factor, the loading rate, at two levels, 0,1mm/min and 1mm/min, was chosen. Consequently, the straightforward Taguchi table was set up, see Table 4.31. Three repetitions of the test series were planned to increase the confidence level in the results. On the 9 oedometric samples produced with the injecting method, the three first were used as pilot tests, while the six others were distributed in the design of experiments before being tested.

#### Description of the tests

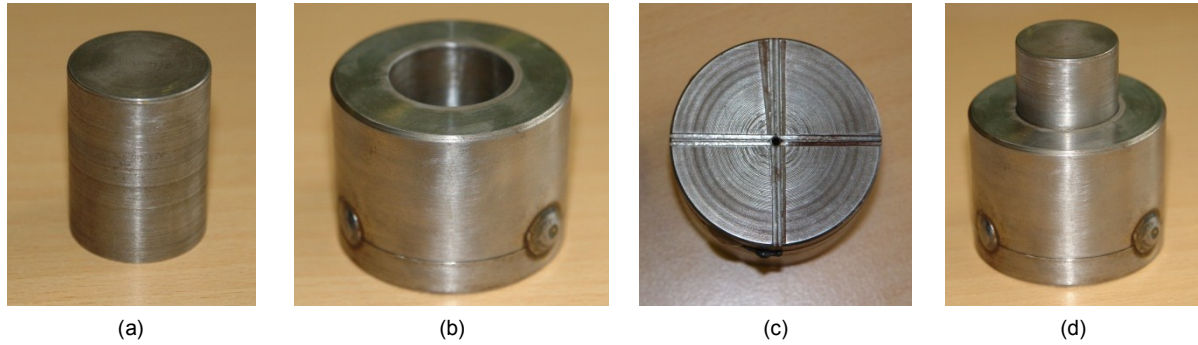
The 10kN INSTRON mobile hydraulic press, employed for the compression tests, was again used with the same set-up, i.e. the fully parallel steel plates. As shown on Fig. 4.71 (a) and 4.72 (c), a hole of 2mm of diameter was drilled in the central part of the matrix from side to side to avoid trapping air during the installation of the oedometric sample. In addition, four slots from this hole to the extremities were realized in the lower surface of the steel matrix to make sure than the air was free to escape even during the test. The final layout was thus composed by the matrix, in which was placed the sample, and the steel punch. This whole system was simply inserted between the two parallel steel plates of the press. The total applied force was measured with an external force sensor of 10kN and the displacement by the internal sensor of the hydraulic press. The weight of the punch was neglected compared to the expected large forces.

| Test n° | Factors        | Samples to be tested |               |               |
|---------|----------------|----------------------|---------------|---------------|
|         | A = Load. rate | Test series 1        | Test series 2 | Test series 3 |
| 1       | 1              | O-4                  | O-5           | O-6           |
| 2       | 2              | O-7                  | O-8           | O-9           |

|         |           |
|---------|-----------|
| Level 1 | 0,1mm/min |
| Level 2 | 1mm/min   |

**Table 4.31-** Design of experiments accounting for the loading rate - silicone oedometric samples

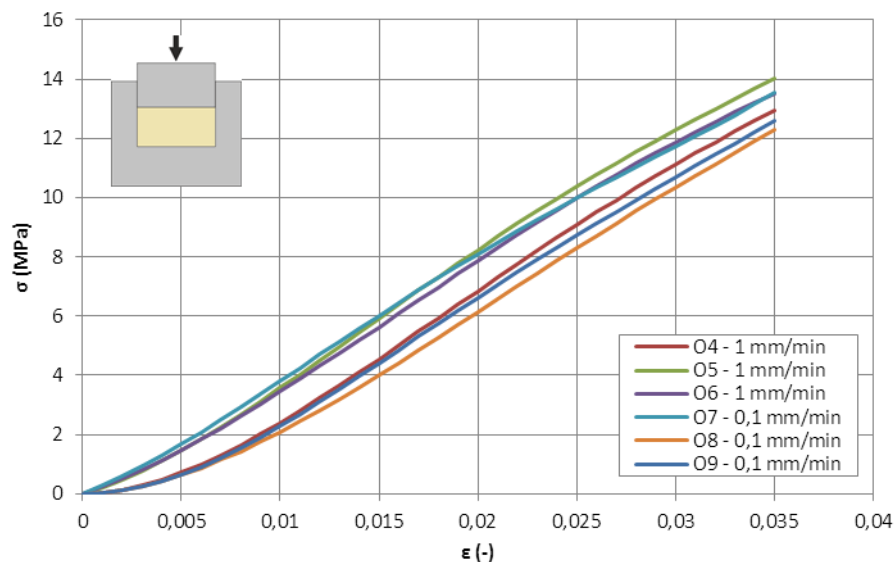


**Figure 4.72-** (a) Punch; Rigid steel matrix (b) side view and (C) bottom view; (d) Final oedometric assembly

The three first pilot tests were carried out to ensure that no major dispersion in the stress-strain diagrams occurred. As all these curves stayed in the same range, the testing procedure was validated and the six experiments of the Taguchi table were conducted.

### Tests results

For all the results, the force-displacement curves were converted in stress-strain diagrams by simply dividing the force by the constant tested area of 30mm and the displacement by the height of the sample of 15mm. All these data were regrouped into one diagram, Fig. 4.73, to apprehend the multiaxial behaviour of the silicone and to visually assess the influence of the loading rate.



**Figure 4.73-** Stress-strain diagram corresponding to the DOE of Table 4.31 – silicone oedometric quasi-static tests

As it could be observed, the obtained stress-strain curves were more “linear” than the ones of the other quasi-static tests and also presented very low dispersions, which could not be attributed to the loading rate. These differences could however be explained by non-visible imperfections at the upper or at the lateral surfaces of the oedometric sample. The linearity of the results was also demonstrated

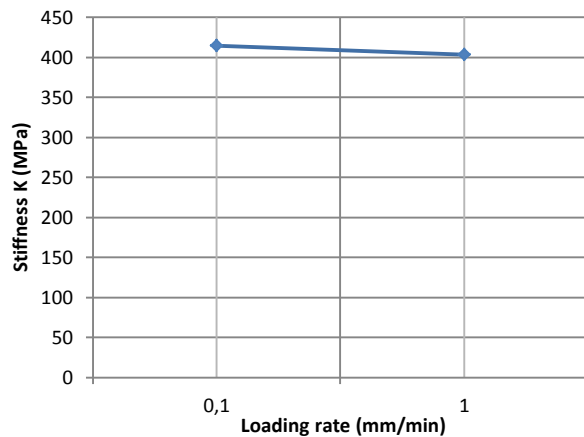


by other researchers on similar elastomers (Fig. 2.18), which tended to confirm the acquired data. All the curves were nearly in the same range, which allowed visually assessing the non-influence of the loading rate. Furthermore, under the maximum authorized load of 10kN no specimen broke and once unloaded no permanent change in dimensions was observed.

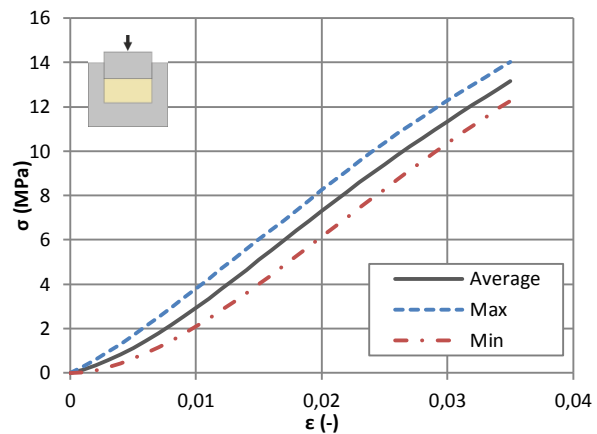
To confirm the independency of the multiaxial properties of the selected silicone, the stiffnesses of the curves between two strains, i.e. 0,01 and 0,035, were calculated. This choice was done to overcome the imperfections noticed at very small strains for three samples. All the stiffnesses  $K$  were recorded in Table 4.32, as well as the estimated averages for the two loading rates. The averaged stiffnesses were very close and presented a difference of 2,7%. This last result was visually discerned by drawing the total effect of the loading rate factor for which the slope was low, see Fig. 4.74.

| Test n° | Factors        | Stiffness K (MPa) |               |               | Average (MPa) |
|---------|----------------|-------------------|---------------|---------------|---------------|
|         | A = Load. rate | Test series 1     | Test series 2 | Test series 3 |               |
| 1       | 0,1mm/min      | 422,780           | 417,808       | 402,340       | 414,309       |
| 2       | 1mm/min        | 389,191           | 407,666       | 412,614       | 403,157       |

**Table 4.32-** Stiffness results - DOE Table of Table 4.31 – silicone oedometric quasi-static tests



**Figure 4.74-** Total effect of the loading rate on the stiffness



**Figure 4.75-** Average stress-strain diagram – oedometric test

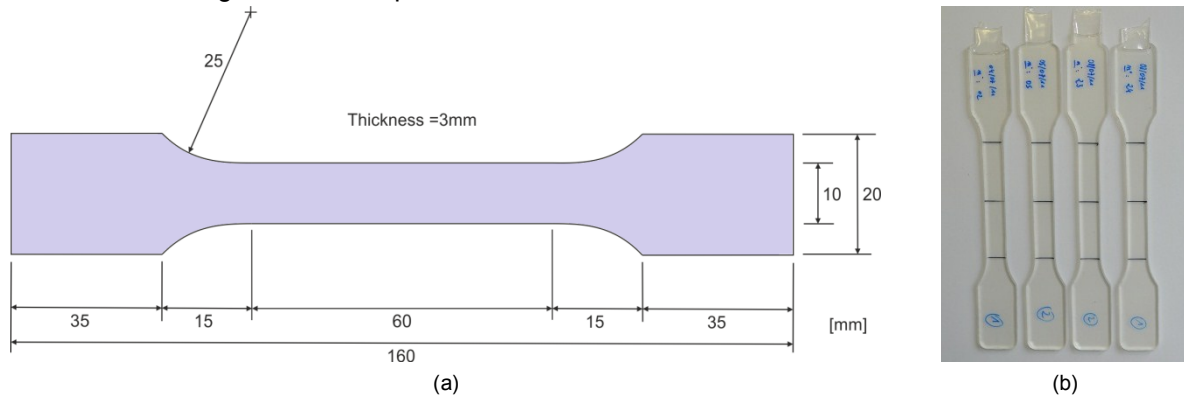
With the non-influence of the loading rate, all the curves were considered to determine an average, useful for the selection of the volumetric part of the strain energy potential. The stress distribution for a given strain of 0,035 was also analyzed with the Lilliefors test with the null hypothesis of a log-normal distribution. The details of this study are presented in Appendix D.5. A good concordance to this statistical distribution was found and the 5% fractile value was then evaluated with the method proposed by the EN 1990 [2.30]. The characteristic value at a strain of 0,035 was equal to  $\sigma_{\epsilon=0,035,k} = 11,792 \text{ MPa}$ .

### 4.3 UV-ACRYLIC BOHLE MV-760

#### 4.3.1 Tension

##### 4.3.1.1 Manufacturing of the samples

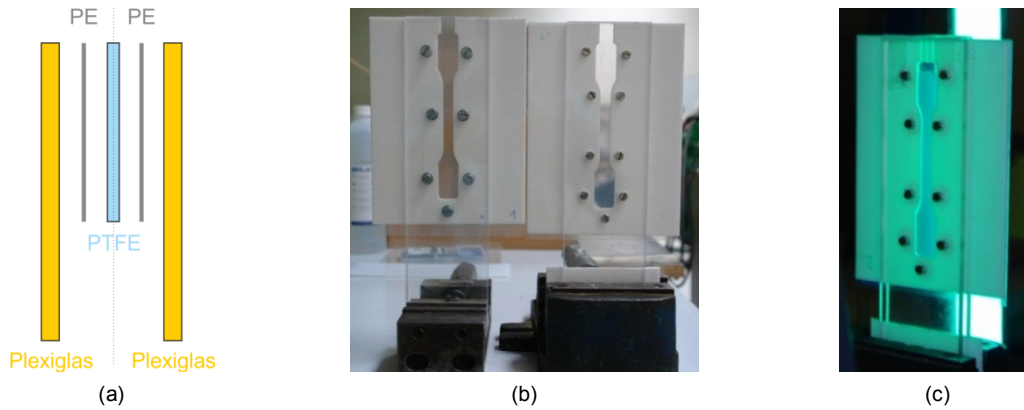
Tension tests on silicone elastomer aimed to the determination of the material properties without considering the adherents, either steel or glass. Hence, the same type of experiments was envisaged for the selected UV-acrylic MV-760 from the Bohle Company in order to obtain classical stress-strain diagrams for pure uniaxial action. Dog-bone samples were manufactured according to the dimensions “type 1B” of the ISO 527-2 standard [4.2] with two slight modifications, i.e. a radius of 25mm (similar to type “1A”) instead of 60mm and a thickness of 3mm replacing the recommended one of 4mm, see Fig. 4.76. These changes had to be operated with regards to two important characteristics of the adhesive, i.e. its medium viscosity and its curing procedure, which had to be realized with an UV-lamp applied at 90° of the surface to be bonded and as close as possible. In the technical data sheet provided by the manufacturer, the minimum and maximum advised thicknesses were respectively of 0,08mm and 0,5mm for a curing duration comprised between 60s to 5min.



**Figure 4.76-** (a) Dimensions of the acrylic dog-bone samples according to ISO 527.2 and (b) Manufactured samples

As for silicone, three methods were possible to realize the acrylic dog bone samples, i.e. molding, cutting and machining. However, with the curing conditions imposed, no large acrylic plate of constant thickness could have been realized as the lamp offered only a local zone of floodlighting. Furthermore, machining some piece of acrylic could have led to an important increase of temperature and to a change of state, see Fig. 2.16. For these reasons, only the molding procedure was conserved for the fabrication of the dog-bone specimens. This choice was also motivated by the medium viscosity of the acrylic easier to shape than the silicone. The self-manufactured mold was fully transparent to let the UV-light pierced through and composed by five symmetrically disposed layers. In the central part of 3mm thick Teflon was cut the shape of tensile sample. Two covering Polyethylene films of 0,1mm each covered this inner part and were at their turn surrounded by Plexiglas plates 5mm thick, see Fig. 4.77. Two identical systems were built and vertically hold in mechanical vices. The adhesive, simply injected through the upper hole of the assembly, flowed down slowly to the bottom of the shape under its self-weight. Bubbles of air were automatically rejected at the upper hole. Both systems containing the thermoset were then installed at a distance of 3cm to the UV-lamp during 2 hours in total, i.e. one hour on one side and the second hour on the other, to ensure a complete curing. As for the silicone samples, the acrylic dog-bone were stored during one month at ambient temperature and humidity, away from light radiation.

A first visual inspection allowed approving this manufacturing procedure as no air bubble was noticed in all the 34 produced samples. The edges were perfectly straight and did not present any defects. Nevertheless, a control of the dimensions of the tested zone was done to evaluate the exactness of the two molds and the reproducibility of the method, see Appendix A.5. From this analysis, it was demonstrated that the mold had no influence on the size of the tested zone and that the dispersions in the measured positions were negligible, indicating that the dog-bone specimens were properly made.



**Figure 4.77-** (a) Layering of the acrylic mold; (b) Self-manufactured mold pre-installed and (c) Curing of the adhesive

#### 4.3.1.2 Quasi-static tests

Quasi-static uniaxial stress-strain curves constitute vital information for the design of an adhesive connection. Depending on the glazing arrangement, the joint could be subjected to different types of environmental conditions. Therefore, it was decided to evaluate on one hand the behaviour of the material under quasi-static action and on the other hand the changes in properties induced by external conditions. The Taguchi design of experiments, applied for the silicone, was re-employed for these tensile tests. The complete procedure, leading to the determination of the influent factors, is detailed in the following paragraphs.

##### Definition of the objectives

Four distinctive types of stress-strain diagrams can describe thermoset material as detailed in section 2.4.3.1. Thus, the first objective corresponded to identify which one was the most appropriate for the selected UV-acrylic MV-760 under quasi-static uniaxial tension. Additionally, as this type of material is generally employed in its glassy state, its properties are susceptible to evolve rapidly with the environmental conditions. Consequently, assessing the factors of influence also represented essential information. The complete list of objectives to achieve is the following one:

- Establish classical stress-strain diagram to appraise the behaviour of this adhesive, either brittle, ductile with or without yielding, or soft, and to later propose an appropriate material law implementable in finite element analysis (FEA).
- As the acrylic is used in its glassy state dependencies to temperatures are expected. Hence, characterizing the evolution of the material behaviour under various environmental conditions, such as temperature, humidity, UV-radiation or loading rate is primordial.
- With the two previous objectives, it then becomes possible to define the maximum limits in terms of stress and strain for the design.

##### Selection of the influent factors

With the similar injecting method of fabrication of the dog-bone specimens and the similar objectives, the Ishikawa diagram detailed in section 4.2.1.2 for the dog-bones in silicone was identical for the acrylic. Two main categories of possible influent factors were extracted from this figure, i.e. the “environmental” criterion, accounting for the temperature, the humidity and the UV-radiation, and the “method” criterion centered on the loading rate. To deal with the environment parameters, an artificial ageing procedure conducted under a reduced period was once again envisaged with a distinction between low and high temperatures:

- For elevated temperatures, the ageing method proposed by the EN ISO 11431 [4.4] was employed as it possesses the advantage of regrouping and combining, as in real façade, the three environmental factors, i.e. temperature, humidity and UV-radiation. The manual cyclic exposure of Fig. 4.4 was performed during the recommended 3 weeks.

- For low temperatures, the ageing consisted in installing the dog-bone samples in a cooling device at -20°C during a period of 3 weeks, neglecting the UV-radiation and humidity.

In contrary to the ageing, the loading rate factor was accounted during the testing phase. As for the silicone, two loading rates were regarded, i.e. a low one of 50mm/min and an elevated one of 250mm/min. The highest loading rate for these acrylic tests was chosen lower than the one for the silicone in reason to the possible brittle behaviour of the present material.

### Choice of the Taguchi table

With the distinction of the temperatures, two Taguchi tables had to be drawn, one for the elevated temperature and another one for the low. For the high temperatures, with the regrouping of the three environmental parameters, only two factors had been to be studied:

- Ageing, a qualitative Boolean factor at two levels, i.e. aged or non-aged.
- Loading rate, a quantitative continuous factor with two levels, i.e. 50mm/min and 250mm/min.

| Standard Test n° | Factors  |           | Samples to be tested |               |               |
|------------------|----------|-----------|----------------------|---------------|---------------|
|                  | A        | B         | Test series 1        | Test series 2 | Test series 3 |
| 1                | 1        | 1         | A-05                 | A-24          | A-11          |
| 2                | 1        | 2         | A-02                 | A-23          | -             |
| 3                | 2        | 1         | A-06                 | A-21          | -             |
| 4                | 2        | 2         | A-08                 | A-19          | -             |
| Level 1          | Not Aged | 50mm/min  |                      |               |               |
| Level 2          | Aged     | 250mm/min |                      |               |               |

**Table 4.33-** Design of experiments for acrylic dog-bone samples under quasi-static tension

The choice of the  $L_4(2)^3$  Taguchi table was realized with the help of Appendix B. The possible influence of the interaction of ageing and loading rate was taken into consideration by this design of experiments. A minimum of two test series were performed to undertake a better analysis of the variance. The manufactured samples were randomly distributed in Table 4.33 in order to overcome any influence of the fabrication process, as they could not have been done at the same time and with the same mold.

No standard existed to operate an ageing at low temperatures and thus no regrouping of factor could have been made. The only evolving factor was the loading rate for which the testing speeds evoked previously were conserved, i.e. 50mm/min and 250mm/min. The complete corresponding design of experiments, containing the number and the repartition of the dog-bone samples to test, is presented in the following Table 4.34.

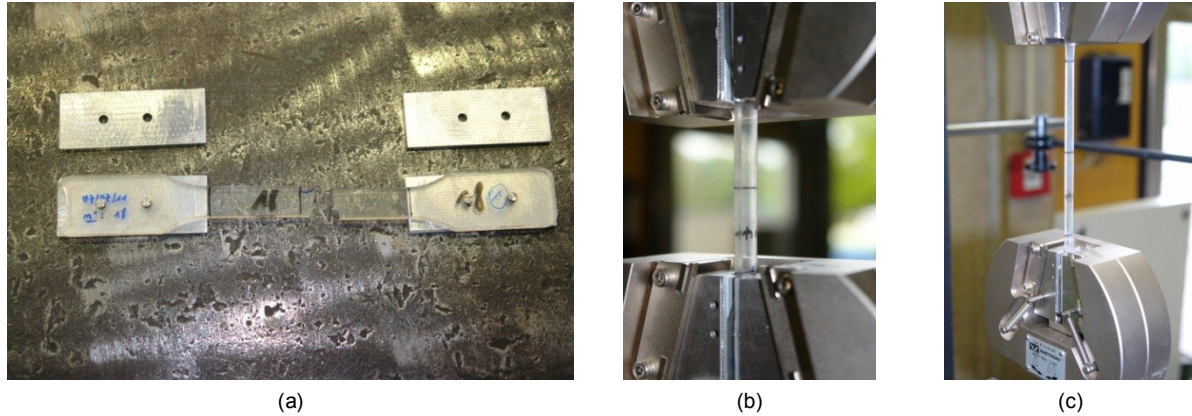
| Standard Test n° | Factors          | Samples to be tested |               |               |
|------------------|------------------|----------------------|---------------|---------------|
|                  | B = loading rate | Test series 1        | Test series 2 | Test series 3 |
| 1                | 1                | A-22                 | A-17          | A-20          |
| 2                | 2                | A-12                 | A-10          | -             |
| Level 1          | 50mm/min         |                      |               |               |
| Level 2          | 250mm/min        |                      |               |               |

**Table 4.34-** Additional design of experiments for low-temperature influence on acrylic dog-bone samples

### Description of the tests

Acrylic tensile tests were carried out with the 10kN INSTRON mobile hydraulic press equipped with self-closing wedge clamps having a large number of teeth at their surfaces to avoid any sliding, see

Fig. 4.78 (b). In spite of these devices, some sliding occurred during the first pilot tests due to the perfect mirroring surfaces of the dog-bone specimens. Therefore, in order to avoid these effects, influencing the final results, four covering plates in aluminum (50x20x2mm) and four steel centered pins were made. These aluminum plates were disposed around the “heads” of the specimens, letting only free the tested length of 60mm. The steel pins were installed at 15mm of the extremities and distant of the same value, Fig 4.78 (a). A 10kN force sensor was used to measure the applied load and the displacement recorded was the displacement between the grips. The installation of the specimens was consequently a determining factor and only the tested zone was let completely free.

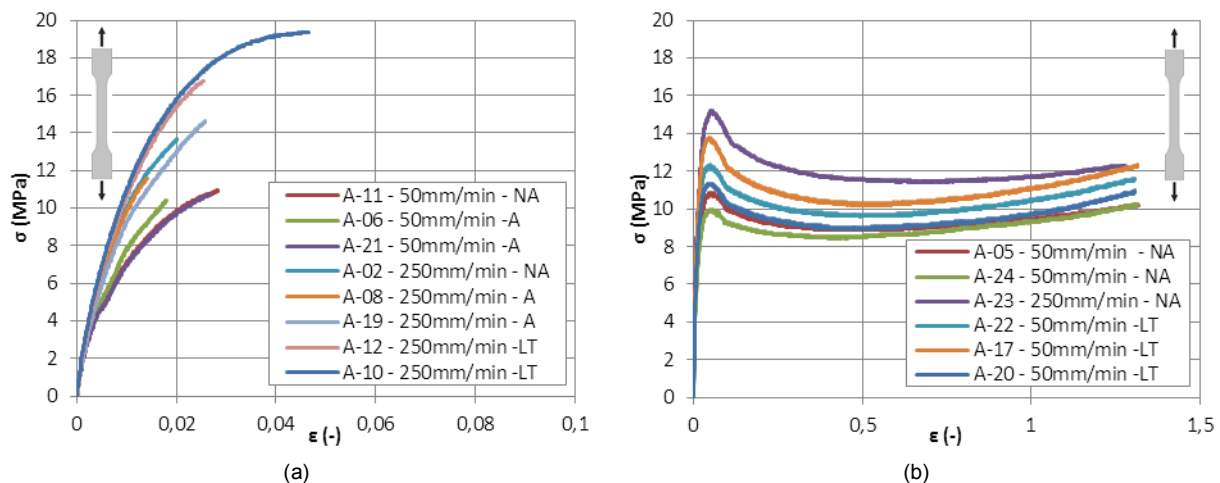


**Figure 4.78-** (a) Centering pins and covering aluminum plates; (b) Installed and (c) tested dog-bone sample

Pilot tests were conducted on three acrylic dog-bones equipped with the aluminum plates and the steel centering pins, i.e. [A-03 / A-07 / A-18]. The two loading rates of the design of experiments were investigated to on one hand verify the accuracy of the force and displacements sensors and the other hand ensure of the non-sliding. These first experiments allowed validating the testing procedure. Hence, the 14 tests of the Taguchi Tables 4.33 & 4.34 were carried out following the same protocol, for which the samples were marked beforehand, covered by the aluminum plates and then positioned in the clamps of the machine preset to automatically obtain the tested length of 60mm.

## Tests results

Independently of the design of experiments and for each test, the stresses were obtained by dividing the applied forces by the initial cross-section, whose dimensions were given in Appendix A.5, while the strains were calculated by dividing the total displacements by the initial tested length of 60mm. Stress-strain diagrams were then achieved and two types of curves were observed according to the influent parameters:



**Figure 4.79-** Stress-strain diagrams regrouping (a) the brittle type I curves and (b) the ductile with yielding type II curves (NA=non-aged, A=aged, LT=low temperature)

- A brittle behaviour, characterized by the curve type I of the Fig. 2.21, was globally recorded for artificial aged specimens of Table 4.33 under a low or a high loading rate and for samples of Table 4.34 subjected to a low temperature ageing tested at an elevated loading rate, see Fig. 4.79 (a). For all these brittle curves, a first linear part for very small strains was followed by non-linear stress-strain increases possibly dependent on the loading rate and on the type of ageing. Indeed, higher was the loading rate and higher was the stress for a given strain, the maximum being reached for the low temperature aged dog-bones tested at 250mm/min. The last ending points of the curves always corresponded to the failure of the dog-bone samples. Thus, strengths and strains at breakage constituted important measurable data. Except one sample, the common strain at breakage was about 0.02.
- A ductile behaviour with yielding, curve type II of Fig. 2.11, was only found for non-aged or aged under low temperature dog-bones subjected to a low loading rate, see Fig. 4.79 (b). No specimen broke during these experiments and the maximum attained strain was always assimilated to the allowable displacement of the hydraulic press. As mentioned in section 2.4.3.1, the necking of the sample occurred at the yield point and so the cross-section became inhomogeneous. Therefore, the only valuable and later studied part of these ductile curves was the first portion from zero to the maximum yielding stress. As for the brittle behaviour, higher stresses seemed to be attained for low temperature aged dog-bones, indicating a possible influence of the ageing.

To properly evaluate the influence of each factor on the total stress-strain curves, two analyses had to be performed with the ANAVAR method on the first portion with the evolution of the initial stiffness and on the last portion with the variation of the strengths/yield stresses.

- Influence of the factors on the initial stiffnesses

Among the existing possibilities allowing determining the Young's Modulus, the most often employed are the secant modulus recommended by the ASTM D638 [4.9] and the chord modulus proposed by the ISO 527-2 [4.2]. Both are within a very small range of strains, i.e. between 0 and 0,1% for the secant and between 0,05% and 0,25% for the chord. These two definitions of the Young's modulus were evaluated for each curves and the most conservative was the chord, which was consequently conserved for this study. The results of the first design of experiments, Table 4.33, were first regarded for an application of the ANAVAR method.

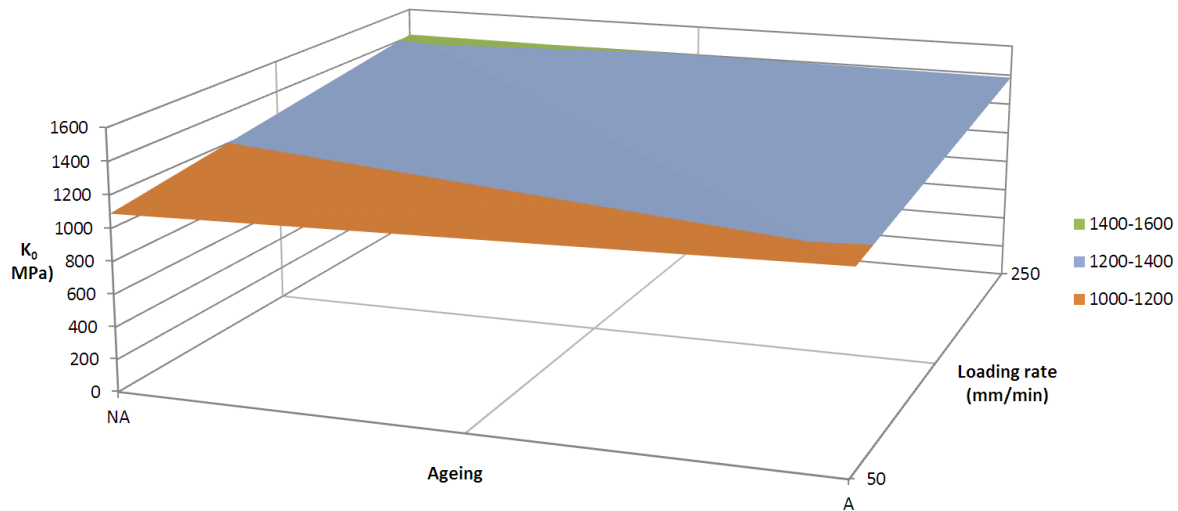
| Test n° | A      | B            | Chord modulus $K_0$ (MPa) |                |               |
|---------|--------|--------------|---------------------------|----------------|---------------|
|         | Ageing | Loading rate | Test series 1             | Tests series 2 | Test series 3 |
| 1       | No     | 50mm/min     | 1087,297                  | 980,461        | 1201,385      |
| 2       | No     | 250mm/min    | 1495,163                  | 1331,919       | -             |
| 3       | Yes    | 50mm/min     | 1209,374                  | 1154,144       | -             |
| 4       | Yes    | 250mm/min    | 1416,507                  | 1350,156       | -             |

**Table 4.35-** Initial stiffness results – DOE Table 4.33 – acrylic quasi-static dog-bone tests

For each configuration, i.e. presence or absence of artificial ageing and low or high loading rate, the mean values were calculated over the test series in order to plot the surface of the response as it was made for the previous results examinations, see Fig. 4.80. With this diagram, the influence of the loading rate on the Young's modulus was directly appraised. The lowest chord modulus data were obtained for 50mm/min, while the highest for 500mm/min. However, the possible influence of the ageing could not have been established with the only graphical analysis as no roof shape was found. Hence, the ANAVAR method was conducted based on Table 4.33. The complete procedure is exposed in Appendix C.9. From this investigation, it was demonstrated that only the loading rate modified the chord modulus with the aforementioned rule, meaning it was possible to regroup these results according to this factor alone. For 50mm/min and with no regards to the artificial ageing of the ISO 11431, the mean Young's modulus was of 1126,53MPa, while for 250mm/min, it was equal to



1398,44MPa. In the technical data sheet provided by the adhesive manufacturer a constant value of 1200MPa was suggested with no consideration to the loading rate.



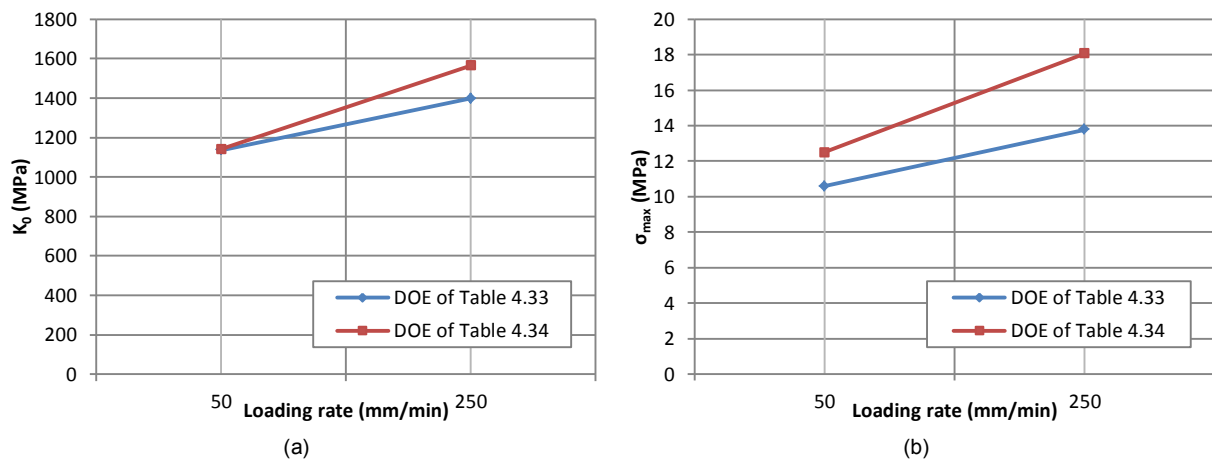
**Figure 4.80-** Surface plot of the initial stiffness versus ageing and loading rate – DOE Table 4.33 - acrylic quasi-static tension

The chord modulus of the second design of experiments only concerning five low-temperature aged specimens were also determined and stored in Table 4.36. As only the loading rate factor was investigated, the ANAVAR method could not have been performed but a comparison of the average values with the previous design of experiments was feasible.

| Standard Test<br>n° | Factors          | Chord modulus $K_0$ (MPa) |               |               | Average (MPa) |
|---------------------|------------------|---------------------------|---------------|---------------|---------------|
|                     | B = loading rate | Test series 1             | Test series 2 | Test series 3 |               |
| 1                   | 50mm/min         | 1123,135                  | 1200,429      | 1102,029      | 1141,864      |
| 2                   | 250mm/min        | 1514,253                  | 1614,774      | -             | 1564,514      |

**Table 4.36-** Initial stiffness results – DOE Table 4.34 – acrylic quasi-static dog-bone tests

With the evaluation of the mean chord modulus for these low-temperature aged dog-bones, a large difference of 37% was found between the two values, which confirmed the strong influence of the loading rate. These two values were then compared to the ones estimated with the previous design of experiments. While for 50mm/min, the two averaged Young's modulus were quasi equal with a difference of 1,4%, for the higher rate of 250mm/min, a larger difference of 11,9% was seen. This was effectively observed with the superposition of the total effect of the loading rate for the two designs of experiments, see Fig. 4.81 (a).



**Figure 4.81-** Total effect of the loading rate on (a) the initial stiffness and on (b) the strength for the two DOE

From this analysis on the stiffness at the origin for very small strains, it was concluded that the Young's modulus of acrylic adhesive increased with the loading rate regardless of the artificial ageing under ambient or elevated temperature, UV-radiation and humidity. However, this raise was slightly modified for a low-temperature ageing, i.e. the stiffness was more important especially for elevated loading rates. Consequently, the values at ambient or elevated temperatures were more conservative and only a distinction in terms of loading rate could have been operated.

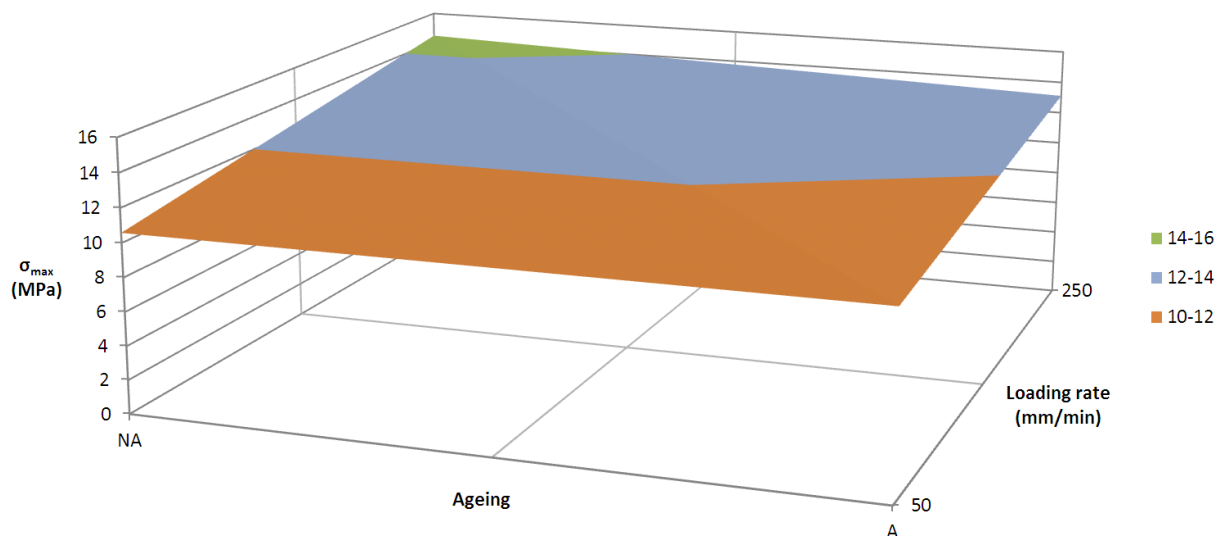
- Influence of the factors on the stresses

In spite of the two captured types of curve, only the maximum stresses were of interest. For the brittle diagrams, as all the samples broke at small strains, the strengths corresponding to the end point of the curves were conserved. For the ductile diagrams, only the yield points were regarded as the necking started at these limits. Hence, independently of the measured stress-strain, the strength/yield data were recorded in Table 4.37.

| Test n° | A      | B            | Strength/Yield $\sigma_{\max}$ (MPa) |                |               |
|---------|--------|--------------|--------------------------------------|----------------|---------------|
|         | Ageing | Loading rate | Test series 1                        | Tests series 2 | Test series 3 |
| 1       | No     | 50mm/min     | 10,849                               | 9,971          | 10,930        |
| 2       | No     | 250mm/min    | 13,672                               | 15,193         | -             |
| 3       | Yes    | 50mm/min     | 10,439                               | 10,742         | -             |
| 4       | Yes    | 250mm/min    | 11,603                               | 14,618         | -             |

**Table 4.37-** Maximum stress results – DOE Table 4.33 – acrylic quasi-static dog-bone tests

The average maximum stress values of each configuration were calculated over the test series to draw the surface of the response, see Fig. 4.82. An important geometrical similarity existed with the previous surface of the response concerning the initial stiffness as no roof shape was apparent. The minimum stresses were discerned for the lower loading rate and the maximum for the non-aged specimens under higher loading rate. Thus, from this graphical examination, it stood out that the loading rate impacted the strength/yield stresses. As the influence of the artificial ageing could not be assessed with this method, a complete ANAVAR was realized on the results of Table 4.37, see details in Appendix C.10. With this study, it was demonstrated that the loading rate affected the maximum stresses, while the artificial ageing and the interaction of the two parameters generated only negligible changes. The results were re-arranged to only account for the loading rate and the new mean values were evaluated. For 50mm/min, the averaged maximum stress was of 10,587MPa and for 250mm/min of 13,771MPa.



**Figure 4.82-** Surface plot of the stress versus ageing and loading rate – DOE Table 4.33 - acrylic quasi-static tension



The measurements of the maximum stresses for the second design experiments established for low-temperature aged dog-bones were also undertaken, see Table 4.38. The only evolving parameter was the loading rate, for which were determined the respective mean values.

| Standard Test<br>n° | Factors          | Strength/Yield $\sigma_{\max}$ (MPa) |               |               | Average (MPa) |
|---------------------|------------------|--------------------------------------|---------------|---------------|---------------|
|                     | B = loading rate | Test series 1                        | Test series 2 | Test series 3 |               |
| 1                   | 50mm/min         | 12,328                               | 13,793        | 11,366        | 12,496        |
| 2                   | 250mm/min        | 16,749                               | 19,388        |               | 18,069        |

**Table 4.38-** Maximum stress results – DOE Table 4.34 – acrylic quasi-static dog-bone tests

The averaged maximum stresses were clearly distinct for the two inspected loading rates with a difference of 44,6%. As for the previous case of Table 4.37, the strengths increased significantly with the loading rate. Additionally, by comparing the results of the two designs of experiments for a given rate, it was found that the low-temperature ageing was also responsible for a consequent increase of strengths, see Fig. 4.78 (b).

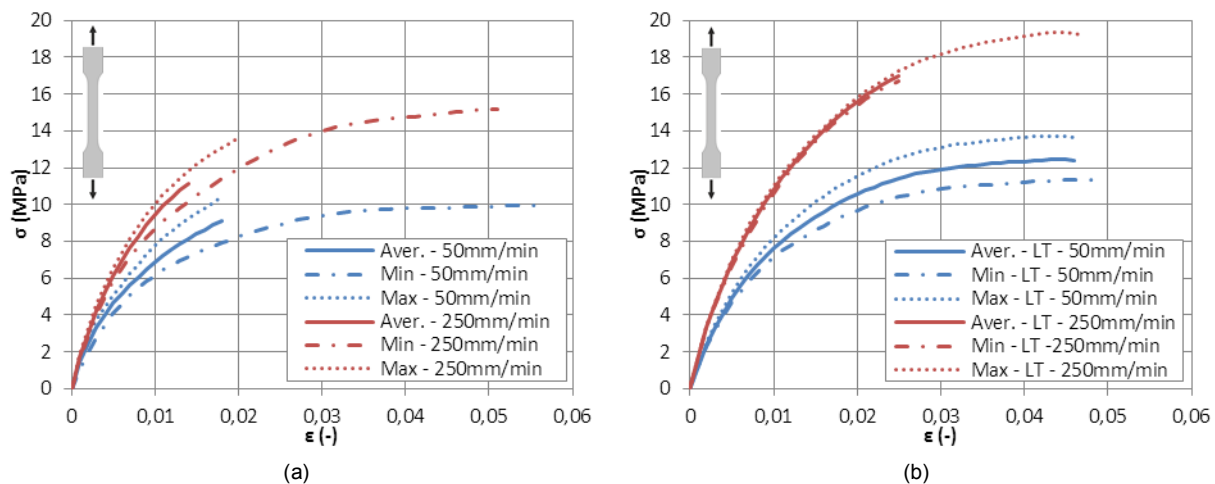
The analysis of the maximum stresses allowed concluding on the influence of the loading rate on the acrylic behaviour at break or at striction. While the combination of the elevated temperature, humidity and UV-radiation had no effect, the low-temperature ageing stiffened the acrylic which failed at higher stresses. This investigation therefore confirmed the results obtained from the initial stiffnesses study.

- Summary of the acrylic tensile properties

By considering the previous results on the influence of the studied factors, the characteristics points of the MV760 acrylic, i.e. Young's modulus, stress and strain at failure, were summarized in Table 4.39.

| Loading rate<br>(mm/min) | Ageing | Curve type | Chord modulus<br>$K_0$ (MPa) |      | Strength/Yield<br>$\sigma_{\max}$ (MPa) |      | Strain at break/yield $\epsilon_{\max}$ (-) |       |       |
|--------------------------|--------|------------|------------------------------|------|-----------------------------------------|------|---------------------------------------------|-------|-------|
|                          |        |            | Aver.                        | Std. | Aver.                                   | Std. | Aver.                                       | Min   | Max   |
| 50                       | LT     | II         | 1141,9                       | 51,8 | 12,5                                    | 1,2  | 0,048                                       | 0,046 | 0,050 |
|                          | NA     | II         | 1126,5                       | 95,0 | 10,6                                    | 0,4  | 0,056                                       | 0,054 | 0,057 |
|                          | A      | I          |                              |      |                                         |      | 0,024                                       | 0,018 | 0,028 |
| 250                      | LT     | I          | 1564,5                       | 71,1 | 18,1                                    | 1,9  | 0,036                                       | 0,025 | 0,047 |
|                          | NA     | I          | 1398,4                       | 74,0 | 13,8                                    | 1,6  | 0,028                                       | 0,014 | 0,051 |
|                          | A      | I          |                              |      |                                         |      |                                             |       |       |

**Table 4.39-** Characteristic points according to the factors of influence – acrylic quasi-static dog-bone tests



**Figure 4.83-** Stress-strain diagrams versus loading rate for (a) ambient/high temperatures and (b) for low-temperature ageing

Even if the non-dependencies of the Young's modulus and of the strength towards the ageing factor according to the ISO 11431 were proved, a distinction had to be made in terms of strain at break/yield. Indeed, for low loading-rate, the ductile curves type II always presented higher strains than the brittle curves type I. Hence, despite the same stresses at failure, a deviation of more than 50% existed in the mean strains. To be more conservative, the averaged curves of each configuration were evaluated until the minimum strain of Table 4.39, see Fig. 4.83.

#### **4.3.1.3 Long-term tests**

The minimal averaged strength of the acrylic adhesive under quasi-static uniaxial tension was found more than 10 times higher than the one of the silicone. This material constituted a real candidate for the realization of the adhesive connection of section 3.3. However, as evoked in section 2.4.31, the behaviour of these adhesive decreases seriously under constant action as molecular relaxations at the micro-scale occur. Relaxation long-term tests on dog-bones specimens were consequently envisaged to characterize the loss in stress. The applied Taguchi procedure, leading to the determination of the factors of influence, is detailed below.

##### **Definition of the objectives**

The objectives of this test campaign remained the same than for the previous long-term experiments with the stress decrease estimation over the tested time. The presence of a plateau had also to be examined. The complete list of objective was therefore:

- Quantify the drop of stress during the tested time of 1000s. This duration, lower than the one of the silicone tests, was chosen considering the first long-term pilot tests on acrylic.
- Predict the stress after 25 years of use with the help of reduction factors. This conjecture had to be based on the results obtained in the previous objective.
- The possible influence of factors, such as the imposed displacement and the environmental conditions, had to be analyzed.

##### **Selection of the influent factors**

In the above definition of the objectives were already cited the two parameters investigated, i.e. the artificial ageing and the imposed displacement. The previous quasi-static tensile tests on acrylic allowed assessing the stiffening of the material after a low-temperature ageing. Thus, to be more conservative, this last type of ageing was neglected. The specimens were only aged according to the ISO 11431 [4.4] regrouping and combining the elevated temperature, the humidity and the UV-radiation. The environmental factor possessed two levels, i.e. aged or non-aged.

For the imposed displacement, two values were selected to stay lower than the minimal recorded strain at break/yield found in the quasi-static analysis, which was of 0,018 for the 50mm/min loading rate. This strain value was regarded as the constant displacement was achieved after a loading at the speed of 50mm/min. The two imposed displacements were respectively equal to 0,6mm, assimilated to a strain of 0,01, and 1mm, comparable to a strain of 0,0167.

##### **Choice of the Taguchi table**

The grouping of the environmental parameters into one class allowed considering only two factors:

- A. Ageing, a qualitative Boolean factor at two levels, i.e. aged or non-aged.
- B. Imposed displacement, a quantitative continuous factor with two levels, i.e. 0,6mm or 1mm.

The choice of Taguchi table  $L_4(2)^3$  was made with the help of the Appendix B. A repetition of the test series was conceded in order to increase the degrees of liberties for the variance analysis. The repartition of the 7 manufactured samples was done randomly to eliminate parasite influencing parameters issued from the fabrication process, see Table 4.40.

| Standard Test n° | Factors |   | Samples to be tested |               |
|------------------|---------|---|----------------------|---------------|
|                  | A       | B | Test series 1        | Test series 2 |
| 1                | 1       | 1 | A-00                 | A-09          |
| 2                | 1       | 2 | A-14                 | A-25          |
| 3                | 2       | 1 | A-15                 | -             |
| 4                | 2       | 2 | A-01                 | A-13          |

|         |          |                             |
|---------|----------|-----------------------------|
| Level 1 | Not Aged | 0,6mm ( $\epsilon = 0,01$ ) |
| Level 2 | Aged     | 1mm ( $\epsilon = 0,0167$ ) |

**Table 4.40-** Design of experiments for acrylic dog-bone samples under long-term tension

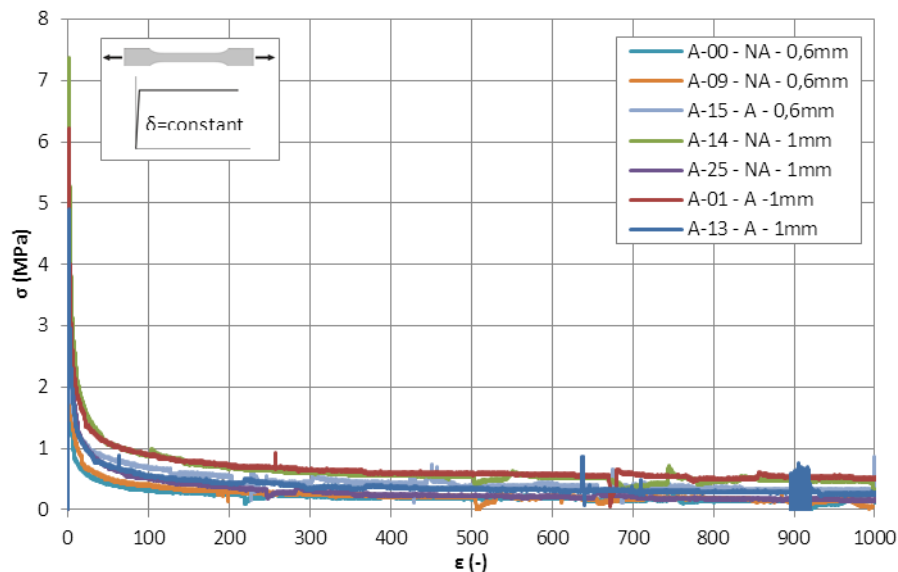
### Description of the tests

These long-term tensile tests were carried out on the 10kN INSTRON mobile hydraulic press already presented in Fig. 4.78. The self-closing clamping devices were employed with the aluminum covering plates and steel centering pins to avoid the sliding of the specimens. A 10kN force sensor measured the total applied load and the displacement recorded was the displacement between the grips. The press was automatically preset to have a gap between grips corresponding to the tested length of 60mm. A favorable reproducibility was accomplished with this testing method.

For these relaxation experiments, the final displacements were applied at a loading rate of 50mm/min and then kept constant for a minimum of 1000s. This operation was performed to avoid the possible oscillations or damage occurring for the other methods. Carried out pilot tests allowed verifying that no sliding arose during the test duration and ensuring of the proper measurements of the forces and displacements. Following these checks, the 7 dog-bone specimens of the design of experiments were conducted.

### Tests results

The imposed displacements for each test were controlled and the total applied forces were divided by the measured cross-section, whose dimensions are given in Appendix A.5. Regardless of the imposed displacements and of the aged/non-aged state, all the stress-time curves were plotted on the same diagram, see Fig. 4.84.



**Figure 4.84-** Stress-time diagram for the two imposed displacements – acrylic long-term tension

For all the presented curves, the most important drop of stress appeared during the first seconds after reaching the final constant displacement. Independently of the imposed displacement, all the curves

tended towards a stress value relatively close to zero. The stress at a certain time had to be compared to a reference value in order to properly appraise its evolution and evaluate the influent factors. Two different references were taken into account for this study, i.e. the stress at 60s and the averaged quasi-static stresses for 50mm/min.

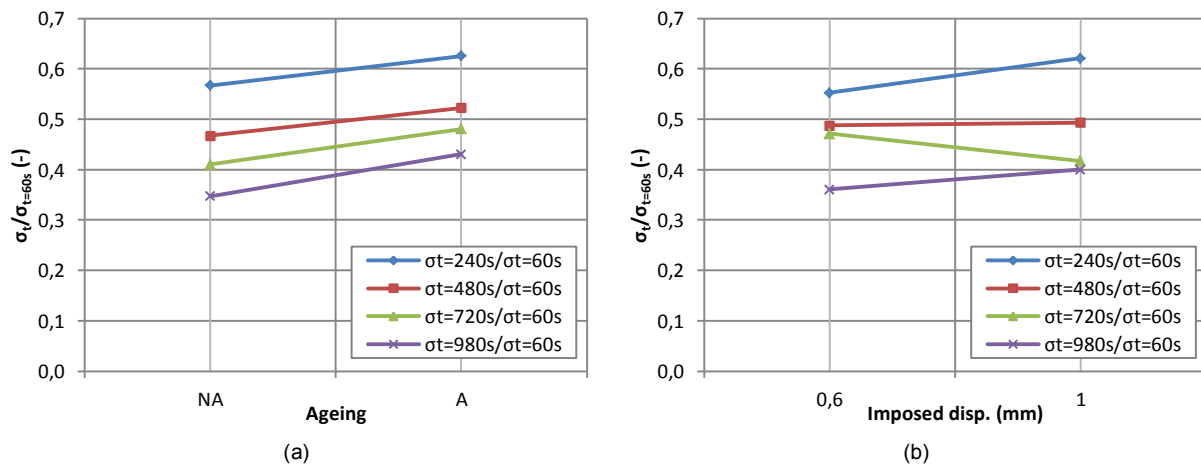
- Analysis of the stress ratio decrease

Even if the final constant displacement was not applied in one second, the first measure of the stress was managed at 60s after attaining the desired strain. For each curve, this stress was recorded and assimilated to the reference value. A discretization of the tests duration was realized to pick up the corresponding stresses, i.e. at 240s, 480s, 720s and 960s. Then the ratios of the stress at one of the aforementioned time over the curve reference stress at 60s were calculated. This enabled to quantify the loss after the reference time. An example of stress ratio for the maximal discretized time is exposed in Table 4.41.

| Standard Test n° | A      | B             | $\sigma_{t=960s}/\sigma_{t=60s} (-)$ |               |
|------------------|--------|---------------|--------------------------------------|---------------|
|                  | Ageing | Imposed disp. | Test series 1                        | Test series 2 |
| 1                | No     | 0,6mm         | 0,319                                | 0,370         |
| 2                | No     | 1mm           | 0,458                                | 0,243         |
| 3                | Yes    | 0,6mm         | 0,392                                | -             |
| 4                | Yes    | 1mm           | 0,514                                | 0,385         |

**Table 4.41-** Maximum stress ratio – DOE of Table 4.40 – acrylic long-term tension

As the raw data of the above table were not directly usable, the total effect diagrams of each factor were plotted. This operation was repeated for all the four stresses ratios and superposed in Fig. 4.85.



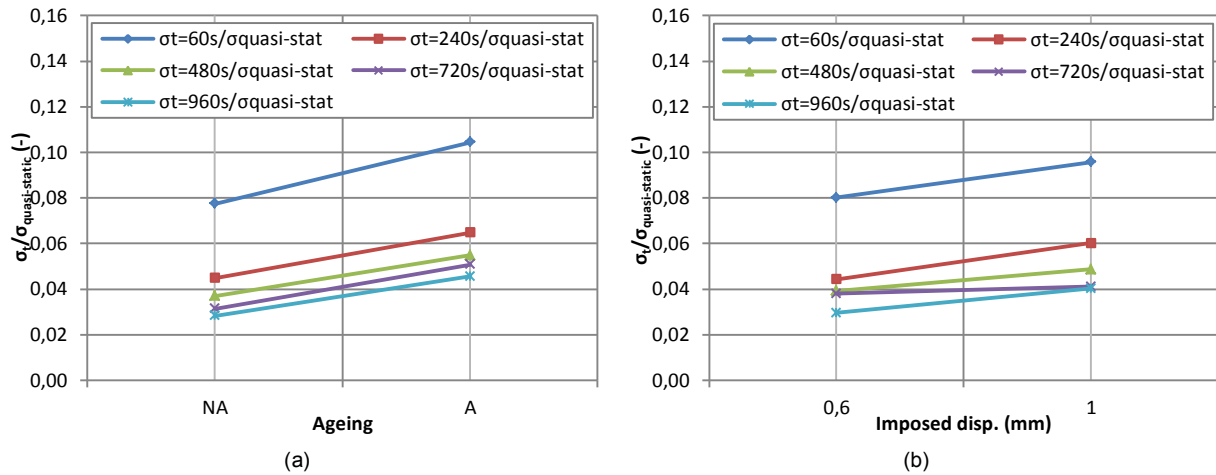
**Figure 4.85-** Total effect of (a) ageing and (b) imposed displacement on the stress ratio – acrylic long-term tension

After 240s, the global stress decrease was about 60% of the reference stress at 60s. This loss increased with the time and reached less than 40% of the reference stress at 960s. This phenomenon was observable in the both diagrams of Fig. 4.85.

Concerning the influence of the ageing, a small difference in favor of the aged dog-bone samples was remarked in each case. Indeed, the stress ratios were higher for aged specimens, indicating a less rapid loss. The influence of the imposed displacement was more confused as the slopes sometimes increased with the displacement, e.g. at 240s or at 960s, and sometimes decreased, e.g. at 720s. The ANAVAR method was performed with the highest time to ensure of the impact of each parameter, see Appendix C.11. The stress ratios with the reference stress at 60s were demonstrated invariant towards both the ageing and the imposed displacement, so as their interaction. With this study, it was therefore concluded that after the first 60s the loss in stress was independent of the studied factor and that no real plateau was reached during the total test duration of 1000s.

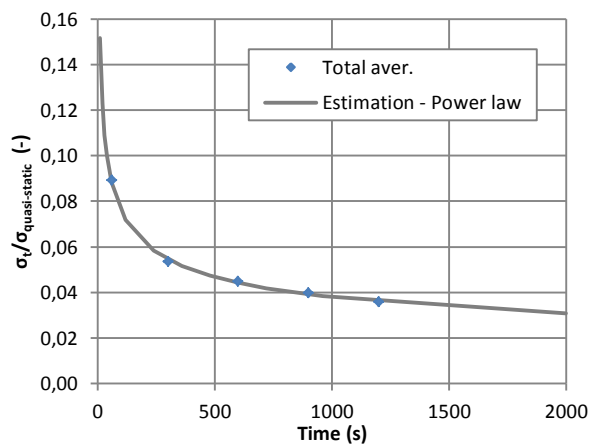
- Comparison to quasi-static stresses

The evolution of the stress after 60s did not vary in an important way compared to the peak attained at the very beginning. Thus, to appraise the real loss, the reference stress was chosen, for each imposed displacements 0,6mm and 1mm, as the averaged quasi-static stress for the loading rate of 50mm/min, see Fig. 4.83 (a), corresponding to the loading speed applied to reach the strain plateau. For the displacement of 0,6mm ( $\epsilon=0,01$ ), the quasi-static stress was of 6,878MPa and for 1mm ( $\epsilon=0,0167$ ) of 8,818MPa. The stress ratios were equal to the stress at a given discretized time, i.e. 60s, 240s, 480s, 720s and 960s, divided by the aforementioned reference stress. With these results, the total effect diagrams of each factor were drawn, see Fig. 4.86.



**Figure 4.86-** Total effect of (a) ageing and (b) imposed disp. on the stress ratio quasi-stat. reference – acrylic long-term tension

Without studying the influence of the parameters, the most consequent stress drop occurred between the quasi-static value and the value at 60s. Indeed the stress at 60s represented about 9% of the quasi-static stress and about 4% for a duration of 960s. For the two diagrams, the curves got closer with the time increase without superimposing, letting envisage that no stress plateau was reached during the whole experiments. The slopes were identical to the ones of the previous analysis with the reference stress of 60s. Hence the ANAVAR procedure was carried out with the aim to evaluate the influence of the two factors ageing and imposed displacement, see Appendix C.12. This procedure refuted the graphical observations and the stress ratios were not affected by the two factors or their interaction. In consequence, it was possible to regroup all the results to assess the evolution of the stress reduction factor relevant for the both imposed displacement. The averaged curve based on the stress ratios results and representing the evolution of the reduction factor during the time was drawn and then simply approximated with the power function (Pow) evoked in section 4.2.1.4, see Fig. 4.87 and Table 4.42.



**Figure 4.87-** Evolution of the stress reduction factor

| N°          | Power coefficients |        | Correlation coefficient |
|-------------|--------------------|--------|-------------------------|
|             | a                  | b      |                         |
| Total aver. | 0,303              | -0,301 | 0,999                   |

**Table 4.42-** Power law coefficients – stress reduction factor

The coefficient of correlation of the power law was relatively close to one, indicating a good fitting to the experimental data. The determination of the stress decrease after a certain time could be achieved by simply multiplying the quasi-static stress for any given strain by the reduction factor estimated with this mathematical model. For example, for 25 years of use under the maximum averaged strength of 10,6MPa, see Table 4.39, the estimated final stress would fall to:

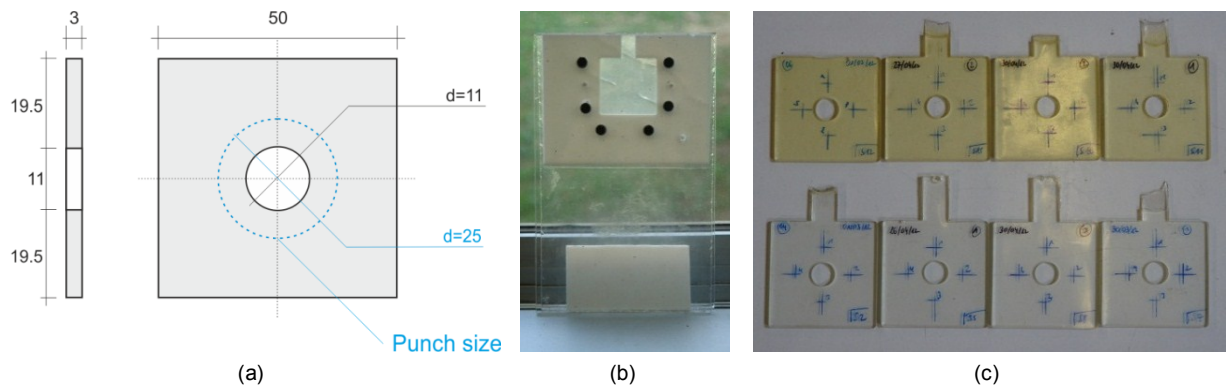
$$\sigma_{25y} = at_{25y}^b \times \sigma_{max} = 0,00064 \times 10,6 = 0,0067MPa \quad (4.2)$$

Compared to the silicone long-term allowable value of about 0,46MPa for the same lifetime of 25years, a factor of 70 existed. The UV-acrylic was therefore judged as inapt to carry long-term tensile action.

### 4.3.2 Modified shear

#### 4.3.2.1 Manufacturing of the samples

To appraise the intrinsic shear properties of UV-acrylic adhesive, the glass and steel adherents were at first neglected. The adhesive or cohesive modes of failure of an adhesively bonded joint were thus not regarded to only study the behaviour of the acrylic. To obtain exploitable stress-strain diagrams, the test set-up of the ASTM D732 [4.10] composed by a rigid steel fixing matrix and a steel punch was slightly modified to not only determine the stresses but also the strains. The employed system and measuring devices are detailed in the next section 4.3.2.2. The evoked standard imposed the shape and the dimensions of the samples, i.e. square specimens of 50mm length. The chosen thickness was equal to 3mm, within the thickness range authorized by the ASTM standard, i.e. 0,13mm to 13mm. A hole of 11mm had to be realized in the middle to fit the internal axis of the punch, see Fig. 4.88 (a).



**Figure 4.88-** (a) Dimension of the acrylic shear samples; (b) Manufactured mold and (c) aged and non-aged samples

The manufacturing process, based on an injecting method and used for the acrylic dog-bone samples, was conserved for these shear specimens. Two fully transparent molds of 5 layers were produced. The inner layer in 3mm thick Teflon was surrounded by Polyethylene films of 0,1mm, which were covered by 5mm thick Plexiglas plates. In the central part in Teflon was machined the square shape of the sample and a slot at the upper position for the injection, see Fig. 4.88 (b). The whole assembly was closed with the help of six screws tightened to prevent any leakage at the bottom and on the sides. The adhesive was simply injected from the upper part and flowed down slowly to the bottom to completely fill the shape. Air bubbles were naturally rejected through the opened slot. Once properly filled, one surface was first exposed during one hour to the UV-lamp disposed at 3cm and then the whole system was reversed to repeat the operation on the other side. This process allowed ensuring a proper curing of the adhesive even at the core of the specimen. All the produced samples were stored during one month shielded from light at ambient temperature and humidity. After this last step, the holes of 11mm of diameter were drilled in the center with a low rotation speed to not induce an increase of temperature changing locally the properties.

The dimensions of these bubble-free specimens were controlled to analyze the reproducibility of the fabrication process and the possible variations engendered by the two molds, see Appendix A.6. With this study, the influences of the mold and of the position of the thickness measurement were shown as negligible, which validated the production method.

#### 4.3.2.2 Quasi-static tests

The quasi-static shear properties of the selected UV-acrylic adhesive constituted basic information for the proper evaluation of a joint connection and vital information to evaluate the feasibility of the envisaged linear adhesive connection presented in section 3.3. The Taguchi procedure was applied to set a proper design of experiments by defining the objectives, the influent factors and the total number of tests to be carried out.

### Definition of the objectives

Two types of diagrams characterized the uniaxial tensile behaviour of the acrylic adhesive, i.e. a brittle behaviour for elevated loading rate and for aged specimens and a ductile behaviour with yielding for the low loading rate non-aged specimens. These two non-linear curves were expected for the quasi-static shear and a proper description was necessary. Hence, stress-strain diagrams until breakage had to be established for several specimens subjected to different loading rates. This would also allow fixing maximum authorized limits for design. The complete of objectives to meet was the following one:

- Set up classical stress-strain diagrams to determine the shear behaviour of acrylic material, either brittle or ductile, and to later combine it with the tension results for implementation in finite element software.
- Due to its nature, several parameters, such as the loading rate, the temperature, the humidity or the UV-radiation could influence the shear properties. Thus, the factors had to be studied to define the most influential.
- Evaluate the initial stiffness and the maximum authorized stress-strain data of the material in function of the parameters affecting the shear behaviour.

### Selection of the influent factors

The method of fabrication of these shear samples was identical to the one of the dog-bone specimens and so was the Ishikawa diagram. Two types of parameters were extracted, i.e. the “environmental” factors and the “method” factors. While the environmental regrouped the influence of the low or elevated temperature, the humidity and the UV-radiation, the method factor only accounted for the loading rate. To be more conservative, the stiffening of the sample noticed for the dog-bones after an artificial ageing at low temperatures was let aside for this quasi-static shear campaign. Accordingly, in the environmental parameters were only considered the elevated temperatures, the humidity and the UV-radiation which were treated with the 3 weeks artificial ageing procedure proposed by the EN ISO 11431 [4.4], see section 4.2.1.2 for details. The method factor, centered on the loading rate, was again examined during the testing phase. Two values were envisaged with regards to the dimensions of the samples and the test assembly, i.e. a low loading rate at 1mm/min and an elevated one of 15mm/min.

### Choice of the Taguchi table

By putting aside the low temperature ageing and regrouping the elevated temperatures, the humidity and the UV-radiation into one large class, only two factors were studied:

- Ageing, a qualitative Boolean factor with two distinct levels, i.e. with ageing or without.
- Loading rate, a quantitative continuous factor at two levels, i.e. 1mm/min and 15mm/min.

| Standard Test n° | Factors  |          | Samples to be tested |               |
|------------------|----------|----------|----------------------|---------------|
|                  | A        | B        | Test series 1        | Test series 2 |
| 1                | 1        | 1        | AS-02                | -             |
| 2                | 1        | 2        | AS-05                | AS-08         |
| 3                | 2        | 1        | AS-12                | AS-15         |
| 4                | 2        | 2        | AS-10                | AS-11         |
| Level 1          | Not Aged | 1mm/min  |                      |               |
| Level 2          | Aged     | 15mm/min |                      |               |

**Table 4.43-** Design of experiments for acrylic shear samples under quasi-static loading

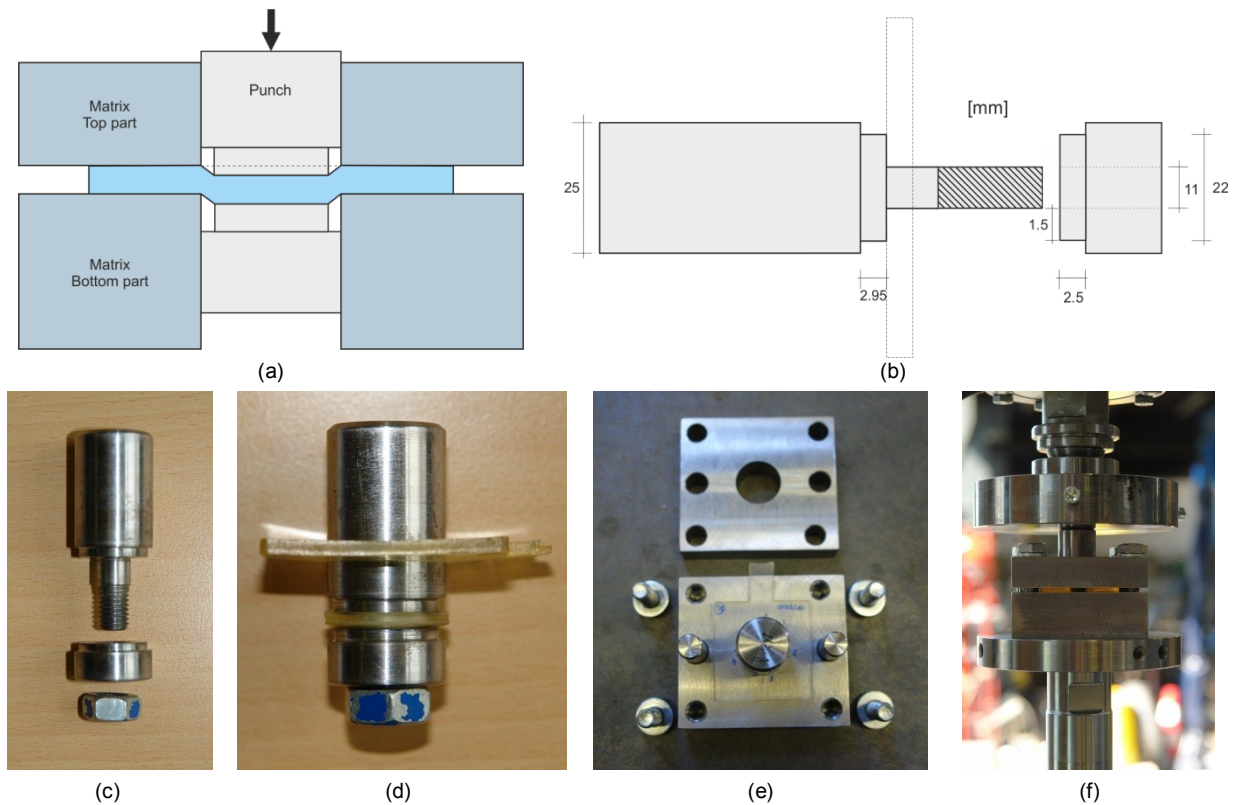
The Taguchi table  $L_4(2)^3$  was chosen with the help of the Appendix B. With the repetition of the test series sufficient degrees of liberties were provided to evaluate the impact of each factor but also the impact of their interaction. This repetition also allowed ensuring a better variance analysis with the



ANAVAR method. The seven specimens were distributed randomly within the Table 4.43 to overcome any influence arising from the manufacturing process, e.g. temperature variations during the curing.

### Description of the tests

Quasi-static shear tests on acrylic adhesive were performed on the 10kN INSTRON mobile hydraulic press equipped with the two parallel steel plates employed for the compression tests on silicone. The total applied force was measured by an external force sensor of 10kN and the applied displacement was assimilated to the displacement between the two steel plates. The main innovation came from the test set-up which was composed by two rigid main parts, i.e. a steel punch on which was installed the produced sample and whose principal dimensions are given in Fig. 4.89 (b) but also a rigid clamping matrix see Fig. 4.89 (e). This assembly was realized according to the ASTM D732 [4.10] with slight modifications. Indeed, as stated in the evoked standard, the two parts composing the steel punch had to present a constant circular cross section of 25mm. This dimension corresponded perfectly with the dimension of the rigid matrix hole to create shear stresses along this diameter. However, with this system, the displacements of the punch could not be converted in strains as the tested thickness was nil. Hence, a reduction of the circular cross section of the punch was locally made at both extremities clamping the specimen, i.e. the diameter of the punch around the sample was of 22mm, see Fig. 4.89 (c). The constant thickness subjected to shear was consequently of 1,5mm. Moreover, as the punch moved downwards, the maximum authorized displacement was of 2,95mm, almost equivalent to the tested thickness of the samples.

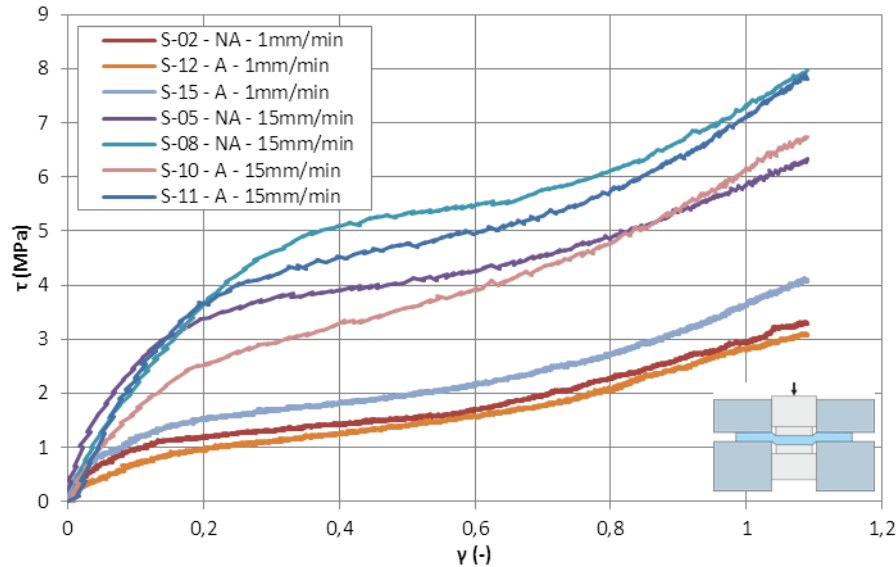


**Figure 4.89-** (a) Dimensions of the punch; (b) Details and (c) Position of the specimen; (d) Whole assembly; (d) Test set-up

Each specimen was first installed on the punch, i.e. fixed between the upper and lower parts with a nut. This assembly was then inserted in the bottom part of the matrix before being tightly closed with the remaining upper part by four screws. The whole system was placed between the two parallel steel plates positioned on the hydraulic press. Pilot tests under the two envisaged loading rates were carried out to ensure that no sliding occurred in the matrix. This verification allowed approving the testing method and the 7 tests of the design of experiments were finally conducted.

## Tests results

All the tests of Table 4.43 were conducted until breakage but as evoked in the test description only the first 2,95mm of displacement were of interest to plot stress-strain curves. The shearing strains were calculated by dividing the displacements by the constant tested thickness of 1,5mm and then taking the arctangent of these values. The stresses were obtained by dividing the applied force by the tested area equivalent to the lateral area of the cylinder delimited by the diameter of the matrix hole of 25mm. All the curves were superposed in Fig. 4.90 to observe the influence of the ageing and of the loading rate.



**Figure 4.90-** Shear stress-strain diagram – UV-acrylic under quasi-static shear (NA/A=non-aged/aged)

The three first curves representing non-aged or aged specimens tested at a loading rate of 1mm/min were relatively well superposed and exhibited the lowest shear stresses for a given deformation. The samples tested at a loading rate of 15mm/min showed some variations but were far enough from the others to assume the influence of the loading rate. To check the validity of this first observation, two variance analyses were performed on all the curves, i.e. one concerning the first portion at small strains with the study of the initial stiffness and another one at large strains for the maximum recorded stress.

- Influence of the factors on the initial stiffnesses

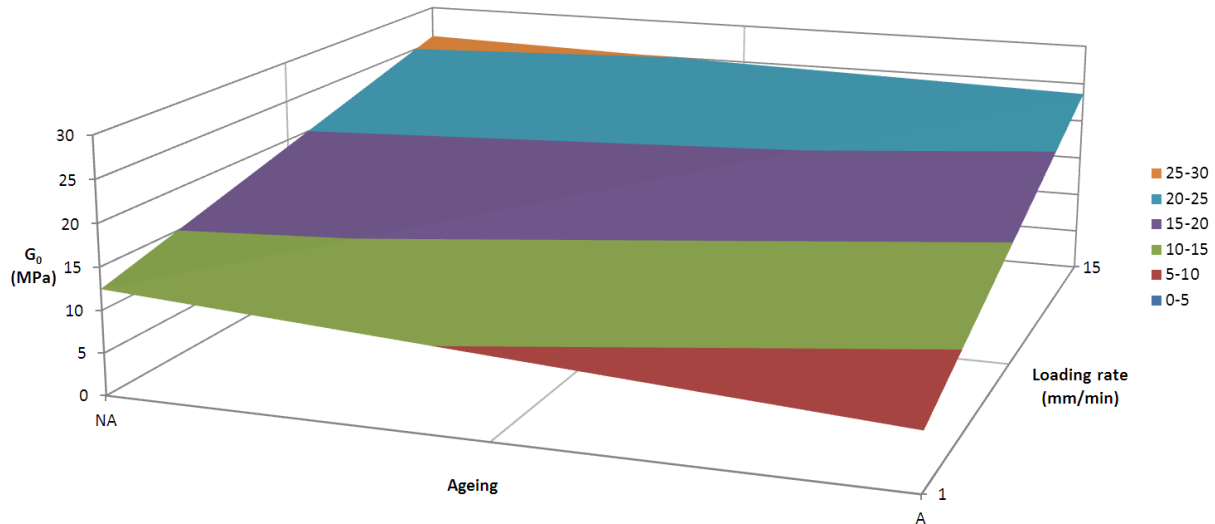
To eliminate the irregularities appearing at the very beginning of the curves, the initial stiffness was assimilated to a chord modulus delimited by two strains of  $\gamma=0,01$  and  $\gamma=0,05$ . For each curve this evaluation was realized and the final results were stored in Table 4.44.

| Standard Test n° | A      | B             | G <sub>0</sub> (MPa) |               |
|------------------|--------|---------------|----------------------|---------------|
|                  | Ageing | Imposed disp. | Test series 1        | Test series 2 |
| 1                | No     | 1mm/min       | 12,458               | -             |
| 2                | No     | 15mm/min      | 25,176               | 26,579        |
| 3                | Yes    | 1mm/min       | 4,616                | 8,869         |
| 4                | Yes    | 15mm/min      | 19,091               | 28,160        |

**Table 4.44-** Initial stiffness results – DOE of Table 4.43 – UV-acrylic quasi-static shear tests

The surface of the response, graphically exposing the influence of the ageing and loading rate factors, was drawn by calculating the average values of each test number over the test series, see Fig. 4.91. In contrary to the surfaces of response encountered for the silicone, no roof shape was remarked. The

minimal shear modulus was found for aged specimens at a low loading rate, while the maximum was noticed for non-aged specimens at an elevated loading rate, i.e. the extreme values were therefore diagonally opposed. Generally, the shear moduli observed at high loading rate were higher, inducing a probable influence of this factor on the results. To properly corroborate this assumption, the ANAVAR method was carried out on the results of Table 4.44, see Appendix C.13. The conclusion of this study allowed ensuring that, as for the tensile behaviour, only loading rate impacted the shear behaviour at small strains and that the results were completely invariant towards the ageing. The first observation was thus confirmed and higher initial stiffnesses were achieved with higher loading rates.



**Figure 4.91-** Surface plot of the initial stiffness versus ageing and loading rate – DOE Table 4.43 – acrylic quasi-static shear

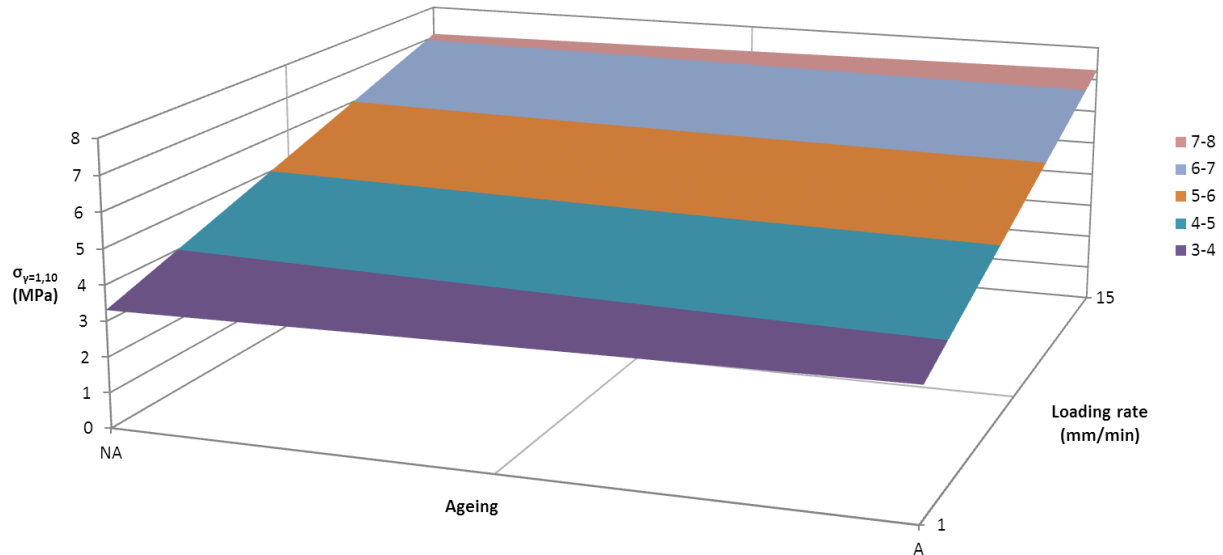
- Influence of the factors on the stresses

With the manufactured test set-up, the maximum displacement considered for all the experiments was constant, equal to 2,95mm, as the tested thickness of 1,5mm. Hence, the maximum stresses were regarded at the maximum strain of  $\gamma=1,10$ , which corresponded to the end point of the curves of Fig. 4.90. All these maximum stresses were evaluated and stored in Table 4.45.

| Standard Test n° | A      | B             | $\sigma_{\gamma=1,10}$ (MPa) |               |
|------------------|--------|---------------|------------------------------|---------------|
|                  | Ageing | Imposed disp. | Test series 1                | Test series 2 |
| 1                | No     | 1mm/min       | 3,311                        | -             |
| 2                | No     | 15mm/min      | 6,277                        | 7,923         |
| 3                | Yes    | 1mm/min       | 3,091                        | 4,064         |
| 4                | Yes    | 15mm/min      | 6,703                        | 7,903         |

**Table 4.45-** Maximum stress results – DOE of Table 4.43 – UV-acrylic quasi-static shear tests.

The results of the previous table could be sorted according to the loading rate, as lower maximum stresses were obtained at a lower loading rate. The surface of the response was plotted in order to graphically appraise this effect, see Fig. 4.92. As for the initial stiffness analysis, no roof shape was discovered but a uniform inclined plane. The minimal results were seen for the loading rate 1mm/min with no regards to the presence of the ageing, while the maximum were found for the highest loading rate of 15mm/min. To mathematical prove the influence of the loading rate on the maximum shear stresses, the ANAVAR method was applied to Table 4.45. The details of this study are exposed in Appendix C.14. Similar conclusions to the previous design of experiments concerning the shear modulus were extracted from this investigation, i.e. only the loading influenced the maximum stresses. Consequently, higher was the loading rate and stiffer was the behaviour of the acrylic.



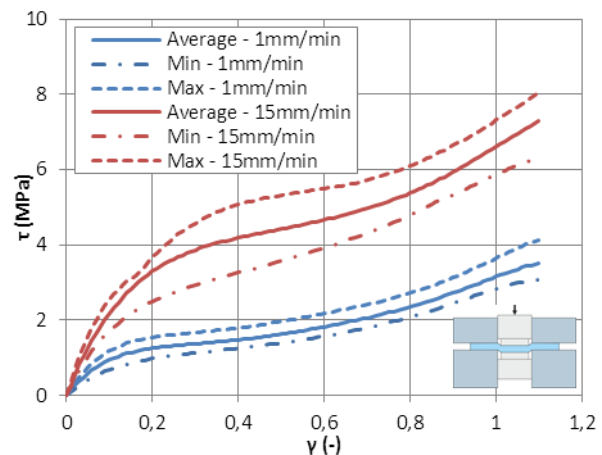
**Figure 4.92-** Surface plot of the maximum stress versus ageing and loading rate – DOE Table 4.43 – acrylic quasi-static shear

- Summary of the acrylic shear properties

By regrouping the results of the two previous analyses on the shear modulus and the maximum stress and distinguishing the loading rate, the characteristic points of the shear behaviour of the UV-acrylic adhesive were summarized in Table 4.46. The mean curves were also estimated with the same distinction towards the loading rate, see Fig. 4.93.

| Loading rate<br>(mm/min) | Shear modulus<br>$G_0$ (MPa) |       | Maximum stress<br>$\sigma_{V=1,10}$ (MPa) |       |
|--------------------------|------------------------------|-------|-------------------------------------------|-------|
|                          | Aver.                        | Std.  | Aver.                                     | Std.  |
| 1                        | 8,648                        | 3,926 | 3,488                                     | 0,511 |
| 15                       | 24,751                       | 3,966 | 7,202                                     | 0,840 |

**Table 4.46-** Characteristic points – acrylic quasi-static shear



**Figure 4.93-** Mean stress-strain diagrams – load. rate distinction

#### 4.3.2.3 Long-term

Relaxation long-term tests on the acrylic adhesive alone were conducted to apprehend its behaviour under permanent shear actions. The Taguchi procedure was employed to evaluate the number of specimens needed, to select some possible influent factors and to analyze the results.

#### Definition of the objectives

The quasi-static shear experiments allowed demonstrating the influence of the loading rate on the behaviour of the acrylic from small to large strains. Hence, for a giving imposed displacement, the final relaxed stresses of two samples tested under distinct loading rates could be different. A dependency of the stress decrease to the loading rate was then probable. Further, other factors, e.g. the imposed displacement, could lead to variations in stresses losses. The principal objective of this test series was to quantify the stresses decreases for several configurations and to assess if a plateau was reached during the whole test duration. The complete list gathering all the expected outputs was:

- Establish relaxation stress-time diagrams for duration of minimum 600s. This duration was chosen after carrying out pilot shear tests which exposed the most important decrease during the first seconds and minimal fluctuations in stresses after this time.
- Estimate, with the conducted experiments, the stresses differences induced by influent factors and propose a rule to predict the long-term behaviour of the acrylic under combinations of these factors.
- Evaluate, for each configuration, the stresses for lifetime duration of 25 years, as it was made for the long-term tension tests on this material.

### Selection of the influent factors

The possible influent factors studied for the long-term tension tests were conserved for these shear tests, i.e. the artificial ageing and the imposed displacement. However as evoked in the description of the objectives, the loading rate, exposed as influent for the quasi-static properties, was considered too. Indeed, this parameter could not have been neglected due to the testing procedure necessitating imposing the desired constant displacement in a prescribed time, i.e. at a prescribed loading rate, from which depended the maximum peak of stress and possibly the final stress value. Consequently, three factors were envisaged in total.

In the ageing factor, the low temperature effects were not regarded and the attention was principally focused on elevated temperatures, humidity and UV-radiation. The artificial ageing method of the ISO 11431 [4.4] was applied as it combined the three aforementioned environmental conditions. The complete procedure, lasting three weeks, is detailed in section 4.2.1.2.

For the loading rate applied until the desired displacement, only two values were retained, i.e. a low one at 5mm/min and an elevated at 15mm/min. These rates were adopted with regard to the previous quasi-static shear tests. While the highest rate was assimilated to the maximum one of the quasi-static experiments, the lowest one covered an intermediate range to provide additional information.

The imposed displacements were applied in several steps with a first loading until two different values of 0,5mm and 1,5mm, corresponding respectively to about a sixth and a half of the maximum displacement authorized by the test set-up. After waiting for 600s, a second displacement of 2,95mm was applied on all the specimens and from their already deformed shapes, see Fig. 4.94. This second loading would allow estimating the dependency on the loading path.

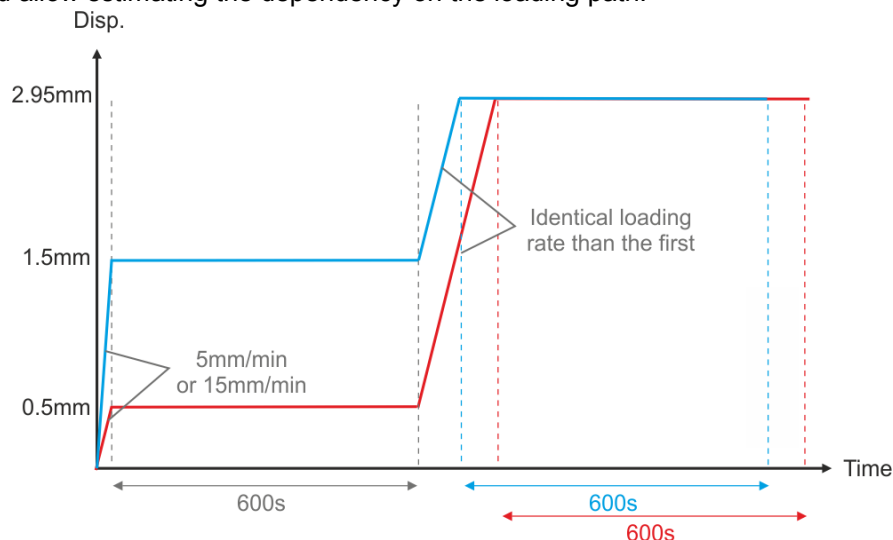


Figure 4.94- Complete test procedure for the acrylic long-term shear tests

### Choice of the Taguchi table

With the grouping of the environment parameters into one factor and the separation of the imposed displacements, three factors at two levels were examined:

- Ageing, a qualitative Boolean factor at two levels, i.e. the presence or absence of ageing.

- B. Loading rate, a quantitative continuous factor at two levels, i.e. 5mm/min and 15mm/min.  
 C. Imposed displacement, possessing the same attributes than the loading rate with two levels 0,5mm and 1mm.

| Standard Test n° | Factors |   |   | Samples to be tested |
|------------------|---------|---|---|----------------------|
|                  | A       | B | C | Test series          |
| 1                | 1       | 1 | 1 | AS-1                 |
| 2                | 2       | 1 | 1 | AS-9                 |
| 3                | 1       | 2 | 1 | AS-3                 |
| 4                | 2       | 2 | 1 | AS-13                |
| 5                | 1       | 1 | 2 | AS-4                 |
| 6                | 2       | 1 | 2 | AS-16                |
| 7                | 1       | 2 | 2 | AS-6                 |
| 8                | 2       | 2 | 2 | AS-14                |

|         |          |          |       |
|---------|----------|----------|-------|
| Level 1 | Not Aged | 5mm/min  | 0,5mm |
| Level 2 | Aged     | 15mm/min | 1,5mm |

**Table 4.47-** Design of experiments for acrylic shear samples under long-term loading

The Taguchi table  $L_8(2)^7$  was established with the help of Appendix B, see Table 4.47. According to this selected design of experiments, 8 tests in total were needed as no repetition of the test series was envisaged. The specimens were randomly distributed in the table to eliminate any parasite parameters coming from the fabrication process. With the low number of tests to be done, the influences of the interaction of the factors were neglected for this analysis to save some degrees of liberties for the variance analysis based on the ANAVAR method.

### Description of the tests

The long-term shear tests were carried out on the 10kN INSTRON mobile hydraulic press equipped with the system described in Fig. 4.89. The applied force was measured with an external sensor of 10kN, while the displacement was recorded by the machine and assimilated to the displacement of the steel punch. The geometry of this last element imposed a maximum displacement of 2,95mm and a constant tested thickness of 1,5mm. As evoked in the previous section 4.3.2.2, the specimens were first installed on the punch before being positioned on the lower part of the rigid matrix. The upper part of the matrix was then added to completely close the system with 4 screws. Finally this whole set-up was placed between the parallel steel plates installed on the machine. A pre-contact was achieved between the punch and the upper steel plate to ensure that the displacement imposed was equivalent for all samples. This method was validated with the help of pilot tests before carrying out all the tests of the previous design of experiments during a minimum duration of 600s.

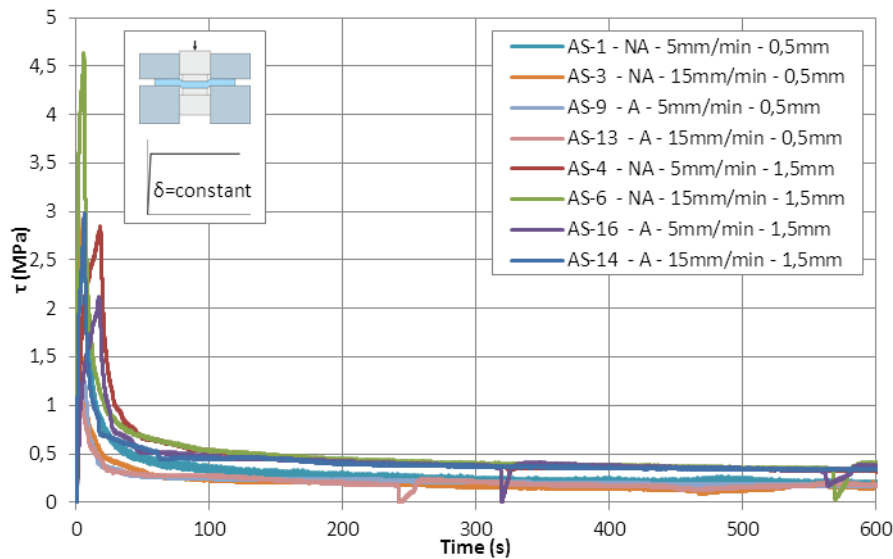
After these first 600s, a single displacement of 3mm was imposed on the deformed positions of all the specimens for another 600s. The loading rate employed for the first loading was conserved to reach the new imposed deformation so that the design of experiments shown in Table 4.47 was preserved. The meaning of the last column accounting for the imposed displacement changed, as 3mm was imposed on all the samples, and was then considered as an indicator for the loading path.

### Tests results

To ensure of the proper reproduction of the tests, the imposed displacements were controlled for each configuration. Shear stress-time diagrams were achieved by dividing the applied force by the tested area equivalent to the lateral area of the cylinder delimited by the diameter of the matrix hole. A distinction was operated between the first loading until the imposed displacements of Table 4.47 and the second loading until the displacement of 3mm.

i. First loading until the imposed displacement of the DOE of Table 4.47

All the curves corresponding to the first imposed displacements of 0,5mm and 1,5mm were plotted and superposed to obtain the final diagram of Fig. 4.95.



**Figure 4.95-** Stress-time diagram – DOE of Table 4.47 – acrylic long-term shear

The scattering in the stress peaks at the beginning were due to the different loading rates and the first evolutions of the stresses before these maximums were not regarded. As for the long-term tensile behaviour, an important loss was remarked and a close proximity was found for the final stresses at 600s. However, the evaluation of the influence of the different factors could not be made directly and an ANAVAR procedure was only performed on the stresses discretized at several times. The time of each stress peak was assimilated to the beginning of the relaxation and the stress were recorded at the peak, after 60s of relaxation, 120s, 240s, 360s, 480s and 600s. These stress results were all stored in Table 4.48.

| Test n° | A      | B                     | C                  | Stress (MPa)  |                |                 |                 |                 |                 |                 |
|---------|--------|-----------------------|--------------------|---------------|----------------|-----------------|-----------------|-----------------|-----------------|-----------------|
|         | Ageing | Loading rate (mm/min) | Imposed disp. (mm) | $\tau_{\max}$ | $\tau_{t=60s}$ | $\tau_{t=120s}$ | $\tau_{t=240s}$ | $\tau_{t=360s}$ | $\tau_{t=480s}$ | $\tau_{t=600s}$ |
| 1       | NA     | 5                     | 0,5                | 2,842         | 0,398          | 0,307           | 0,255           | 0,215           | 0,234           | 0,172           |
| 2       | A      | 5                     | 0,5                | 1,249         | 0,260          | 0,241           | 0,222           | 0,192           | 0,182           | 0,169           |
| 3       | NA     | 15                    | 0,5                | 3,124         | 0,269          | 0,219           | 0,192           | 0,150           | 0,112           | 0,143           |
| 4       | A      | 15                    | 0,5                | 2,365         | 0,276          | 0,258           | 0,171           | 0,177           | 0,142           | 0,177           |
| 5       | NA     | 5                     | 1,5                | 2,855         | 0,581          | 0,477           | 0,400           | 0,359           | 0,344           | 0,314           |
| 6       | A      | 5                     | 1,5                | 2,120         | 0,501          | 0,451           | 0,389           | 0,384           | 0,348           | 0,355           |
| 7       | NA     | 15                    | 1,5                | 4,631         | 0,625          | 0,509           | 0,421           | 0,384           | 0,358           | 0,396           |
| 8       | A      | 15                    | 1,5                | 2,977         | 0,453          | 0,452           | 0,386           | 0,362           | 0,347           | 0,333           |

**Table 4.48-** Stress results at the discretized times – DOE of Table 4.47 – acrylic long-term shear

The large differences existing between the peak values and the stresses at the first discretized time of 60s forced to analyze separately the stress peaks. Furthermore, these maximum values were issued from the first quasi-static loading until the desired constant displacement. Thus, according to the final results found for the quasi-static tests, a distinction in terms of loading rate and imposed displacement was done. The mean values for the four configurations were calculated and exposed in Table 4.49.

Four distinct values were then observed and the lowest was naturally detected at 5mm/min for a total displacement of 0,5mm, while the highest was discovered for 15mm/min until a displacement of

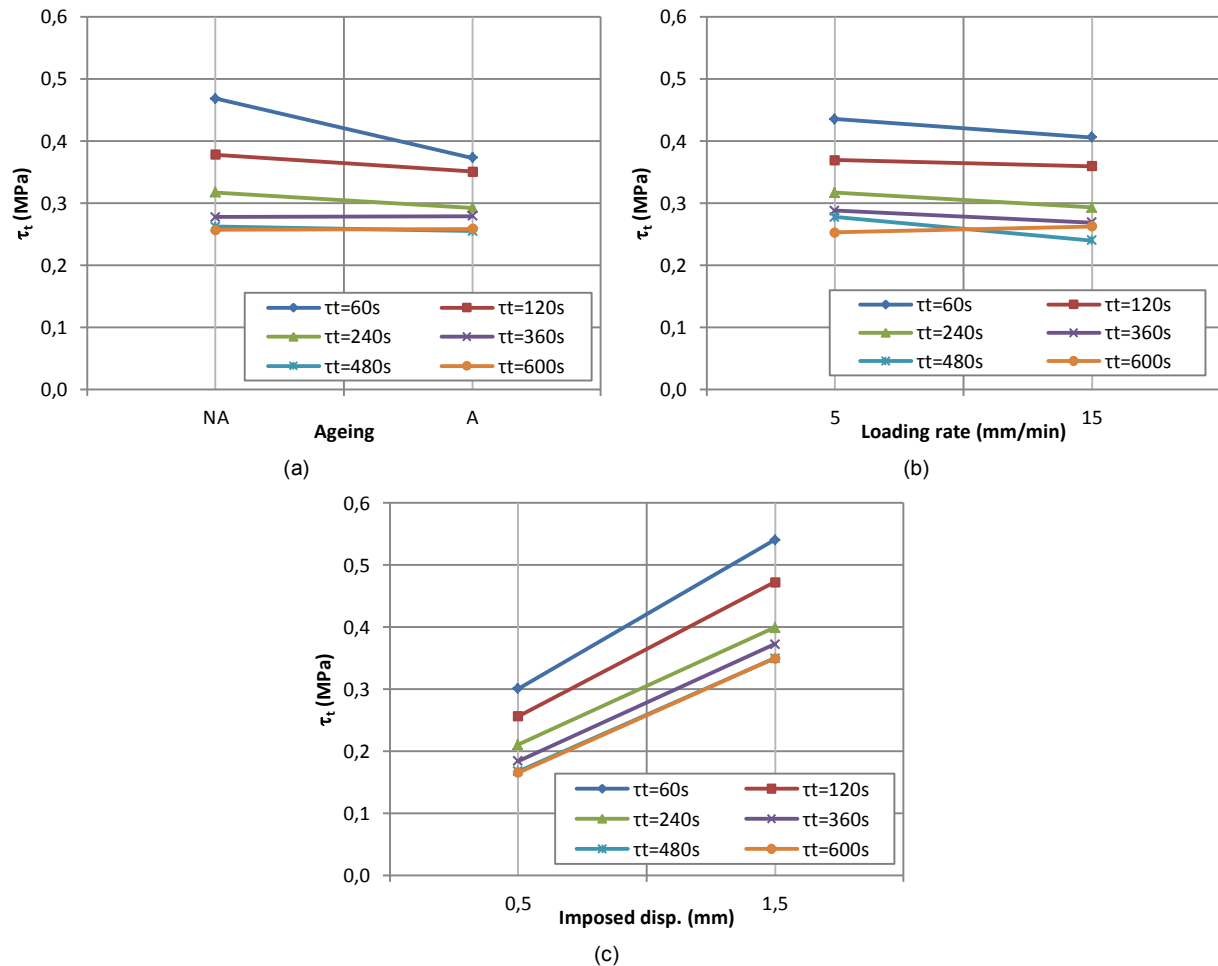


1,5mm. These results again validated the dependency of the stress peak to these both factors.

| Test n° | A      | B                     | C                  | Maximum stress (MPa) |       |
|---------|--------|-----------------------|--------------------|----------------------|-------|
|         | Ageing | Loading rate (mm/min) | Imposed disp. (mm) | $\tau_{\max}$        | Aver. |
| 1       | NA     | 5                     | 0,5                | 2,842                | 2,045 |
| 2       | A      | 5                     | 0,5                | 1,249                |       |
| 3       | NA     | 15                    | 0,5                | 3,124                | 2,745 |
| 4       | A      | 15                    | 0,5                | 2,365                |       |
| 5       | NA     | 5                     | 1,5                | 2,855                | 2,488 |
| 6       | A      | 5                     | 1,5                | 2,120                |       |
| 7       | NA     | 15                    | 1,5                | 4,631                | 3,804 |
| 8       | A      | 15                    | 1,5                | 2,977                |       |

**Table 4.49-** Stress peaks evaluation – DOE of Table 4.47 – acrylic long-term shear

The stresses discretized from 60s to 600s were then employed to establish the total effect diagrams of each factor, see Fig. 4.96.

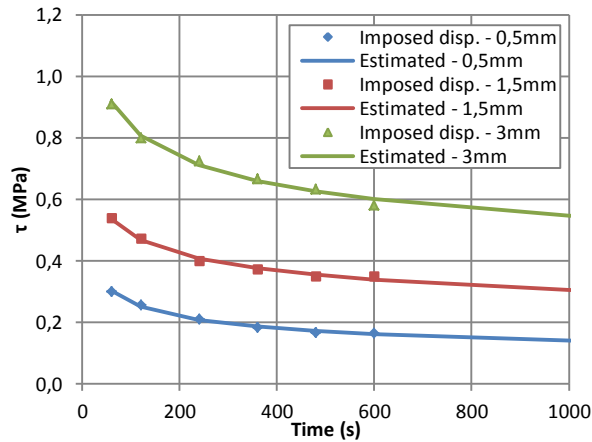


**Figure 4.96-** Total effect of (a) Ageing, (b) Loading rate and (c) Imposed displacement on the discretized stresses

Graphically, only the imposed displacement seemed to impact the stresses over all the test duration, while the two others factors presented non-uniform negligible variations. This would imply that the loading rate effect, influencing the stress peaks, disappeared before the first 60s. For a given imposed displacement and independently of the maximum stress reached during the loading under different rates, the stresses dropped to attain a single value. To confirm this phenomenon, two ANAVAR



analyses were performed on the stresses discretized at 60s and at 600s, see Appendix C.15. These two studies corroborated these graphical observations and only the imposed displacement was demonstrated as influent. Consequently, the results could have been split in two categories according to this factor, i.e. separate the specimens tested until 0,5mm and 1,5mm. Hence, the discretized stresses were averaged for each time and each imposed displacement to draw the following diagram.



| Imposed disp. | Power coefficients |        | Correlation coefficient |
|---------------|--------------------|--------|-------------------------|
|               | a                  | b      |                         |
| 0,5mm         | 0,934              | -0,274 | 0,993                   |
| 1,5mm         | 1,217              | -0,200 | 0,989                   |
| 3mm           | 1,944              | -0,184 | 0,986                   |

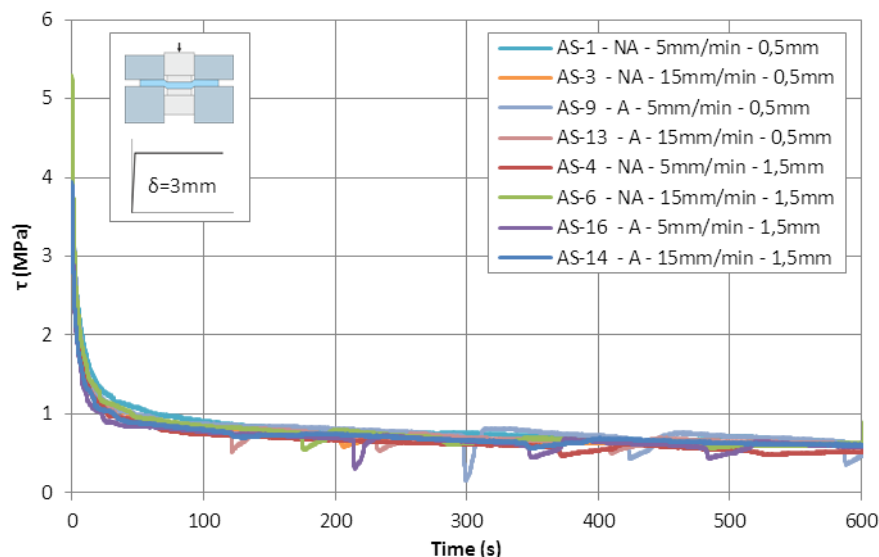
**Table 4.50-** Power law coefficients for the 3 imposed disp.

**Figure 4.97-** Estimation of the stress loss – 3 imposed disp.

An approximation with the power function (Pow) presented in section 4.2.1.4 was undertaken for these two imposed displacements and a good confidence was found with correlation coefficients close to 1, see Table 4.50. The stresses after 25 years of use under these prescribed conditions were estimated with the power function coefficients, i.e. for 0,5mm a final stress of 0,0034MPa was obtained and for 1,5mm the final stress was of 0,0203MPa.

ii. Second loading for an imposed displacement of 3mm

The same protocol was applied on the second portion of the curves for which the samples were all subjected to an imposed displacement of 3mm. All the curves were plotted, from the beginning of the relaxation by neglecting the loading path until the desired constant displacement, see Fig. 4.98.



**Figure 4.98-** Stress-time diagram for an imposed disp. of 3mm – DOE of Table 4.47 – acrylic long-term shear

The stress-time diagrams were all relatively well superposed, which tended to confirm the results acquired for the first loading, i.e. the only influence of the imposed displacement. Furthermore, the loading path, with a first displacement of 0,5mm or of 1,5mm, did not seem to impact the stresses. To ensure of these assumptions, the stresses were picked up at discretized time to later conduct a

variance analysis, i.e. at 0s, 60s, 120s, 240s, 360s, 480s and 600s. In this case, the time at 0s was assimilated to the stress peak. All the results were inserted in the design of experiments of Table 4.47 with the notion of loading path for the imposed displacement of 0,5mm and 1,5mm, see Table 4.51.

| Test n° | A      | B                     | C                  | Stress (MPa) – imposed disp of 0,3mm |                |                 |                 |                 |                 |                 |
|---------|--------|-----------------------|--------------------|--------------------------------------|----------------|-----------------|-----------------|-----------------|-----------------|-----------------|
|         | Ageing | Loading rate (mm/min) | Imposed disp. (mm) | $\tau_{t=0s} = \tau_{max}$           | $\tau_{t=60s}$ | $\tau_{t=120s}$ | $\tau_{t=240s}$ | $\tau_{t=360s}$ | $\tau_{t=480s}$ | $\tau_{t=600s}$ |
| 1       | NA     | 5                     | 0,5                | 4,069                                | 1,025          | 0,872           | 0,749           | 0,720           | 0,681           | 0,605           |
| 2       | A      | 5                     | 0,5                | 3,825                                | 0,972          | 0,861           | 0,788           | 0,774           | 0,732           | 0,531           |
| 3       | NA     | 15                    | 0,5                | 4,911                                | 0,876          | 0,799           | 0,727           | 0,612           | 0,623           | 0,592           |
| 4       | A      | 15                    | 0,5                | 4,412                                | 0,902          | 0,803           | 0,715           | 0,681           | 0,674           | 0,581           |
| 5       | NA     | 5                     | 1,5                | 3,567                                | 0,857          | 0,729           | 0,653           | 0,601           | 0,568           | 0,517           |
| 6       | A      | 5                     | 1,5                | 3,014                                | 0,846          | 0,749           | 0,729           | 0,664           | 0,566           | 0,578           |
| 7       | NA     | 15                    | 1,5                | 5,296                                | 0,943          | 0,834           | 0,728           | 0,682           | 0,592           | 0,634           |
| 8       | A      | 15                    | 1,5                | 3,936                                | 0,865          | 0,748           | 0,716           | 0,604           | 0,637           | 0,614           |

**Table 4.51-** Stress results at the discretized times for an imposed disp. of 3mm – DOE of Table 4.47 – acrylic long-term shear

The stresses at 0s were evaluated independently of the other discretized stresses as these values were mainly governed by the quasi-static loading at either 5mm/min or 15mm/min. As the imposed displacement was the same for all the specimens, the only distinction was realized according to the loading rate, see Table 4.52 in which was revised the order of the tests.

| Test n° | A      | B                     | C                  | Maximum stress (MPa)      |       |
|---------|--------|-----------------------|--------------------|---------------------------|-------|
|         | Ageing | Loading rate (mm/min) | Imposed disp. (mm) | $\tau_{t=0} = \tau_{max}$ | Aver. |
| 1       | NA     | 5                     | 0,5                | 4,069                     | 3,619 |
| 2       | A      | 5                     | 0,5                | 3,825                     |       |
| 5       | NA     | 5                     | 1,5                | 3,567                     |       |
| 6       | A      | 5                     | 1,5                | 3,014                     |       |
| 3       | NA     | 15                    | 0,5                | 4,911                     | 4,638 |
| 4       | A      | 15                    | 0,5                | 4,412                     |       |
| 7       | NA     | 15                    | 1,5                | 5,296                     |       |
| 8       | A      | 15                    | 1,5                | 3,936                     |       |

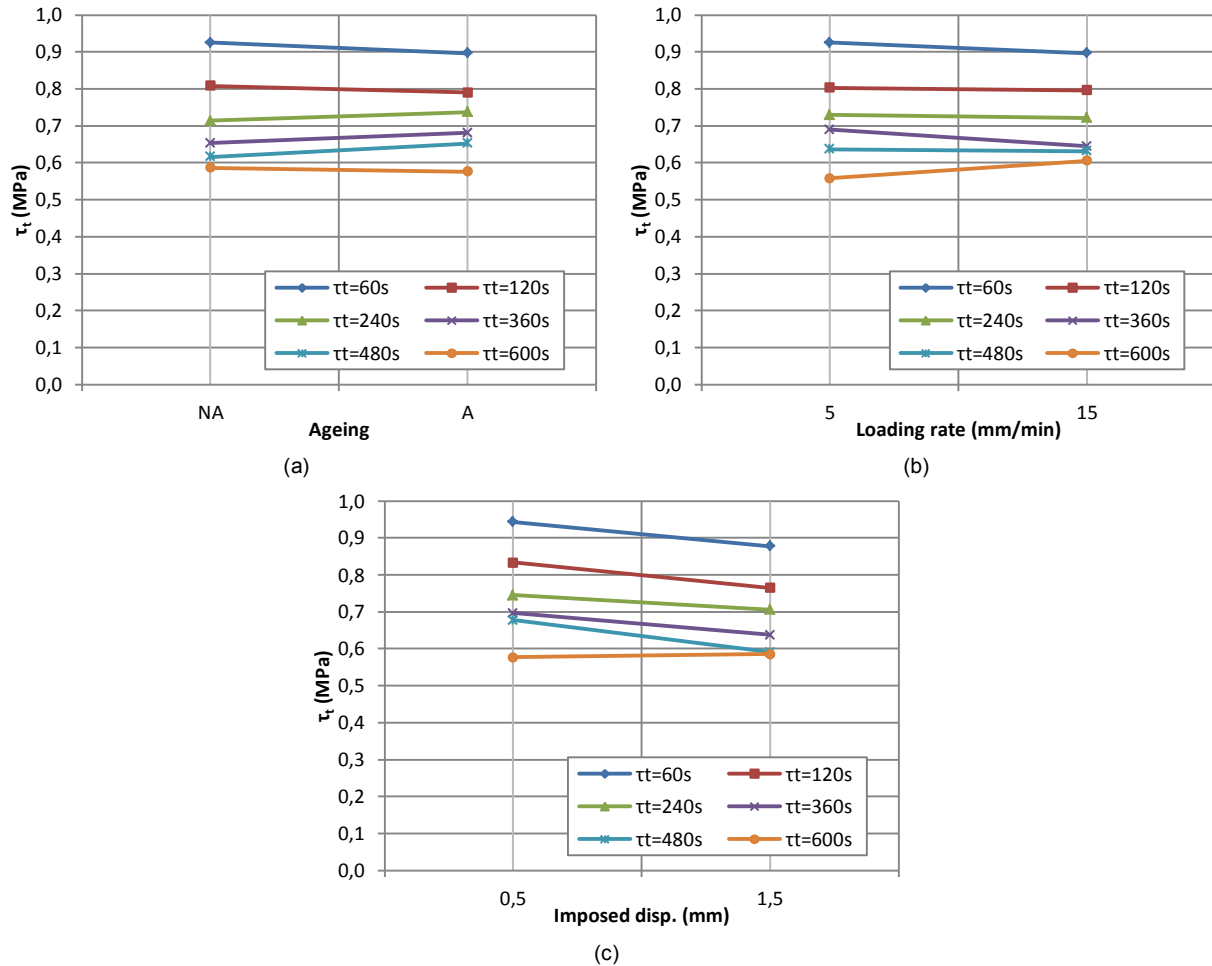
**Table 4.52-** Stress peaks evaluation for an imposed disp. of 3mm – DOE of Table 4.47 – acrylic long-term shear

A large difference was noticed between the mean values of the two imposed loading rates confirming the dependency of the maximum shear stress to the loading rate.

The evolution of the discretized stresses was then assessed with the help of the total effect diagrams of the three factors, i.e. the ageing, the loading rate and the imposed displacement envisaged as the loading path effect, see Fig. 4.97. For all the three diagrams almost no variations could have been seen over all the test duration of 600s. These factors could then be considered as non-influent on the relaxed stresses for an imposed displacement of 3mm. Nevertheless, two ANAVAR analyses were carried out with the discretized stresses at 60s and 600s, see Appendix C.16. From these two studies, the invariance of the stress towards the three factors was proved. It was then conclude that the final stresses of relaxation tests did not vary with the presence of the ageing and the previous encountered loading path. Furthermore, even if elevated loading rates increased the quasi-static stresses before the long-term action, the final stresses dropped to an identical value.

For a specific discretized time, the mean stress was calculated by averaging all the regrouped stress values independently of the investigated factors. This operation was repeated for each time in order to

superpose, to the existing curves for the imposed displacements of 0,5mm and 1,5mm, the evolution of the stress for a constant displacement of 3mm, see Fig. 4.97. This last curve was approximated with the power function which gave a good concordance with the experimental results, see Table 4.50. The prediction of the stress for a total duration of 25 years, corresponding to the expected lifetime of adhesively bonded joint, was estimated to 0,045MPa for this imposed displacement of 3mm. This value was judged very low as for the long-term tension results on the same acrylic. In consequence, this adhesive should not be used as thick joint of about 2mm for system inducing long-term actions.



**Figure 4.99-** Total effect of (a) Ageing, (b) Loading rate and (c) Imposed displacement on the discretized stresses at 3mm

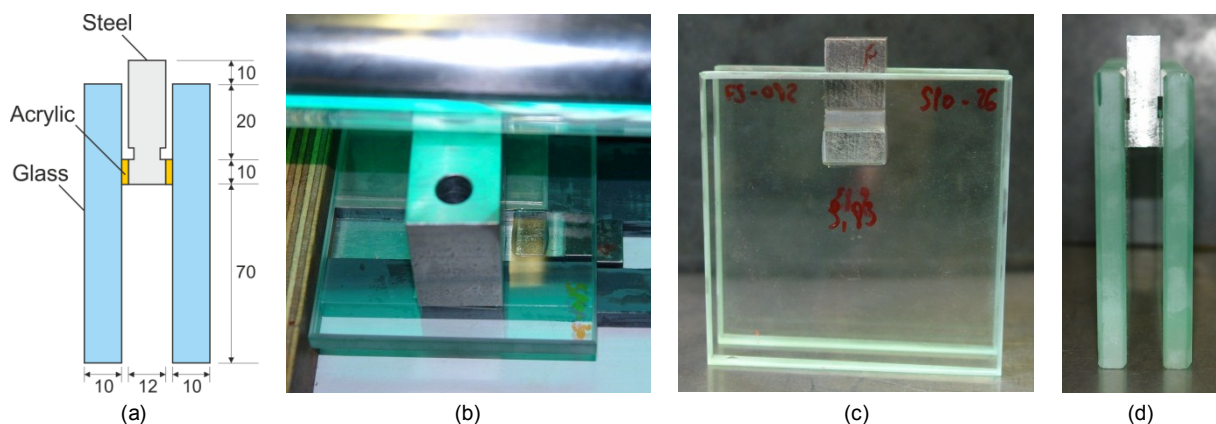
The long-term stress evolution was assessed for three different imposed displacements up to 3mm with the help of the power function. Thus, the variations of the parameters “a” and “b” of the power law could in their turn be approximated with some functions. Therefore, the two diagrams representing these parameters in function of the imposed displacements were drawn. While for the parameter “a”, a simple linear function allowed to describe its evolution ( $a = 0,410 \delta_{imp} + 0,682$ ) for the parameter “b” a power function was employed ( $b = -0,230 \delta_{imp}^{-0,230}$ ).

### 4.3.3 Push-out shear tests

The interest of the previous modified shear test was to determine the behaviour of the acrylic adhesive only, with absolutely no consideration to the adherends. However, basing a complete joint design with these properties could not be undertaken, as it supposes a 100% cohesive failure. This mode of failure, validated for silicone adhesive, depends strongly on the adherend types for the selected UV-acrylic. Therefore, some small-scale tests comprising all the components, i.e. glass and steel materials as well as the adhesive, had to be conducted.

#### 4.3.3.1 Manufacturing of the samples

The concept of double lap-joint assemblies employed to appraise the pure shear properties of silicone elastomer was adopted for these experiments on acrylic. With this type of connection, unwanted peel stresses were absent and the real shear behaviour was evaluated. Two outer glass plates for one inner steel plate were required to build the specimens. This layering was estimated more efficient in this configuration as the applied load was transmitted in the brittle adherends through a total larger area. The dimensions of all the elements were chosen with regards to the characteristics of the adhesive but also with regards to the capacity of the mobile hydraulic press of 10kN. The outer glass plates, measuring 100x100x10 mm, were constituted by annealed glass chamfered all around the edges to prevent any stress concentrations engendering their failure. Due to its viscosity and curing process, the thickness of the adhesive was realized as small as possible to fit the range of 0.08mm to 0.5mm advised by the manufacturer. The two bonding areas were estimated with the shear modulus found with the previous modified shear experiments and were of 20x10mm each to respect the maximum load of the hydraulic press. Hence, the total final bonded section was of 400mm<sup>2</sup>. The dimensions of the steel part 40x20x12mm were imposed by the size of the bonding area to avoid undesired lateral connection between glass and steel. Further, two slots of 8mm height and 1mm thick were machined to delimit the bonded zone and allow the surplus of acrylic penetrating inside, see Fig. 4.100 (a). With these modifications, constant glued areas were achieved for all the push-out samples.



**Figure 4.100-** (a) Dimensions of the acrylic push-out; (b) Manufacturing; (c) Front and (d) lateral view of the finished sample

The positioning, i.e. vertically and horizontally, of the steel part was done with the help of calibrated plastic pieces, see Fig. 4.100 (b). The steel and glass surfaces were then degreased with a solvent provided by the adhesive producer before applying, with a needle of 1,37mm of diameter, a small quantity of acrylic on the steel element. The adhesive was stretched with the needle in order to eliminate the surplus. The glass was then installed in the fixed system ensuring a correct positioning. A steel weight was disposed at the top to apply a certain pressure during the curing phase for one hour. This procedure, comprising the installation of the calibrated plastic pieces, the cleaning of the surfaces with solvent, the application of the adhesive and the curing for another hour, was repeated on the other side of the steel. A particular attention was devoted to the parallelism of the bottom glass surfaces of the push-out assembly. The produced samples were stored during 24hours at ambient temperature, humidity and shielded from the light.

As for the other acrylic samples, a visual inspection was performed on the 9 produced specimens to verify the correct bonding and the absence of air bubble. The dimensions of the final products were compared to the dimensions of each element measured separately to deduct the thicknesses of the adhesive, see Appendix A.7. From this study, it was observed that the average acrylic thickness of one side, assimilated to the total adhesive thickness divided by 2, was of 0,17mm with a standard deviation of 0,04mm, i.e. within the thickness range defined by the manufacturer.

#### 4.3.3.2 Quasi-static

Push-out quasi-static tests were carried out to evaluate the failure mode, either cohesive or adhesive, of steel to glass connections and to compare the results with the previous modified shear tests. The Taguchi procedure, applied to set up the complete design of experiments, is detailed below.

##### Definition of the objectives

The objectives described for the modified shear tests on the only acrylic could be conserved for the push-out experiments and the study of the failure mode could be added. These experiments also completed the lack of information concerning the maximum force at breakage, as the setup employed for the previous shear tests was not adapted. The complete list of objectives to meet was:

- Establish force-displacement diagrams to ensure of the correct testing of the specimens and acquire sufficient information for a later comparison with the prior shear results.
- The influence of parameters, e.g. some environmental factors or loading rate, had to be considered as they could impact the adhesion to the adherents.
- Define the maximum force authorized by the acrylic for the specific conditions evoked in the previous objective. This would allow designing a glass to steel connection subjected to shear.
- Analyze the failure mode, either adhesive or cohesive, to foresee some further improvements in case of adhesive failure.

##### Selection of the influent factors

The push-out shear tests aimed to corroborate the results obtained with the shear tests on the acrylic only. Thus, similar factors were envisaged, i.e. the loading rate and the artificial ageing. However, the ageing realized according to the ISO 11431 [4.4] was demonstrated as non-influent on the shear properties, see section 4.3.2.1. Consequently, only the loading rate factor was investigated. Three different speeds were selected in relation to the ones already exerted on the other shear configuration, i.e. a very low one at 0,6mm/min, chosen in reason to the very small thicknesses of the adhesive, a medium at 1mm/min, identical to the antecedent loading rate on shear tests, and a high one at 5mm/min, whose behaviour was assessed during the first loading of relaxation shear tests.

##### Choice of the Taguchi table

| Standard Test n° | Factors          | Samples to be tested |               |               |
|------------------|------------------|----------------------|---------------|---------------|
|                  | A = Loading rate | Test series 1        | Test series 2 | Test series 3 |
| 1                | 1                | 1 (20/01/19)         | 2 (18/02/21)  | 3 (22/03/23)  |
| 2                | 2                | 4 (24/04/25)         | 5 (26/05/27)  | 6 (28/06/29)  |
| 3                | 3                | 7 (31/07/30)         | 8 (32/08/33)  | 9 (34/09/35)  |
| Level 1          | 0,6mm/min        |                      |               |               |
| Level 2          | 1mm/min          |                      |               |               |
| Level 3          | 5mm/min          |                      |               |               |

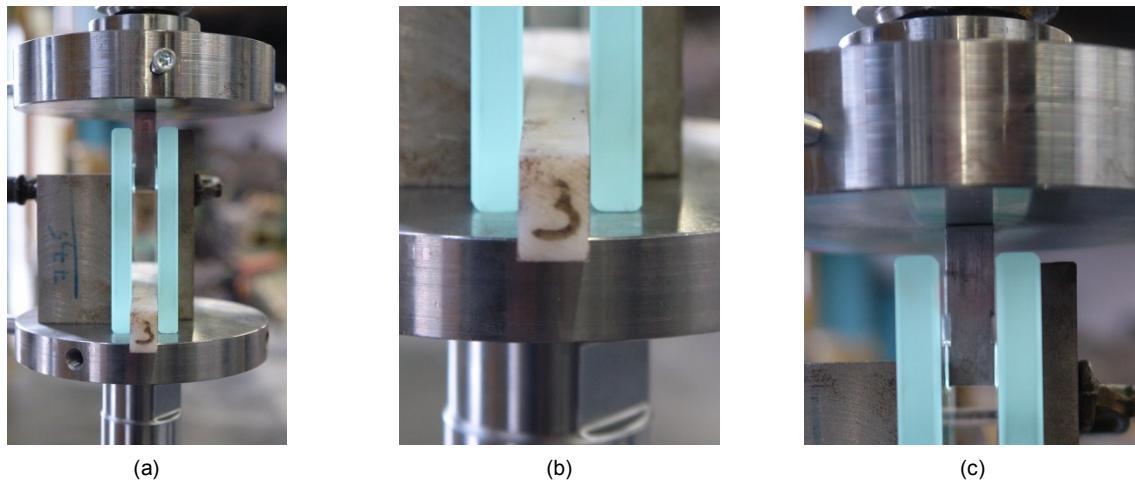
**Table 4.53-** Design of experiments for acrylic push-out quasi-static shear tests (Front glass/Steel/Back glass)

Only one factor A, the loading rate, possessing three levels, i.e. 0,6m/min, 1mm/min and 5mm/min,

was examined. The Taguchi table contained one column for this factor, see Table 4.53. Three test series were repeated for each loading rate to have a better confidence in the final force-displacement curves.

### Description of the tests

The acrylic push-out shear tests, presenting a lower total bonded area than the silicone samples, were carried out on the 10kN INSTRON mobile hydraulic piston. The two parallel steel plates used for the compressive experiments on silicone were installed on the press, see Fig 4.101 (a). A relatively rigid polyamide spacer 12mm thick was inserted between the glass plates at the bottom of the sample to perfectly fit the remaining gap. Lateral steel supports were clamped around the push-out specimen to avoid any glass opening. The combination of the polyamide spacer and the two steel supports allowed ensuring transmission of pear shear actions in the acrylic adhesive.



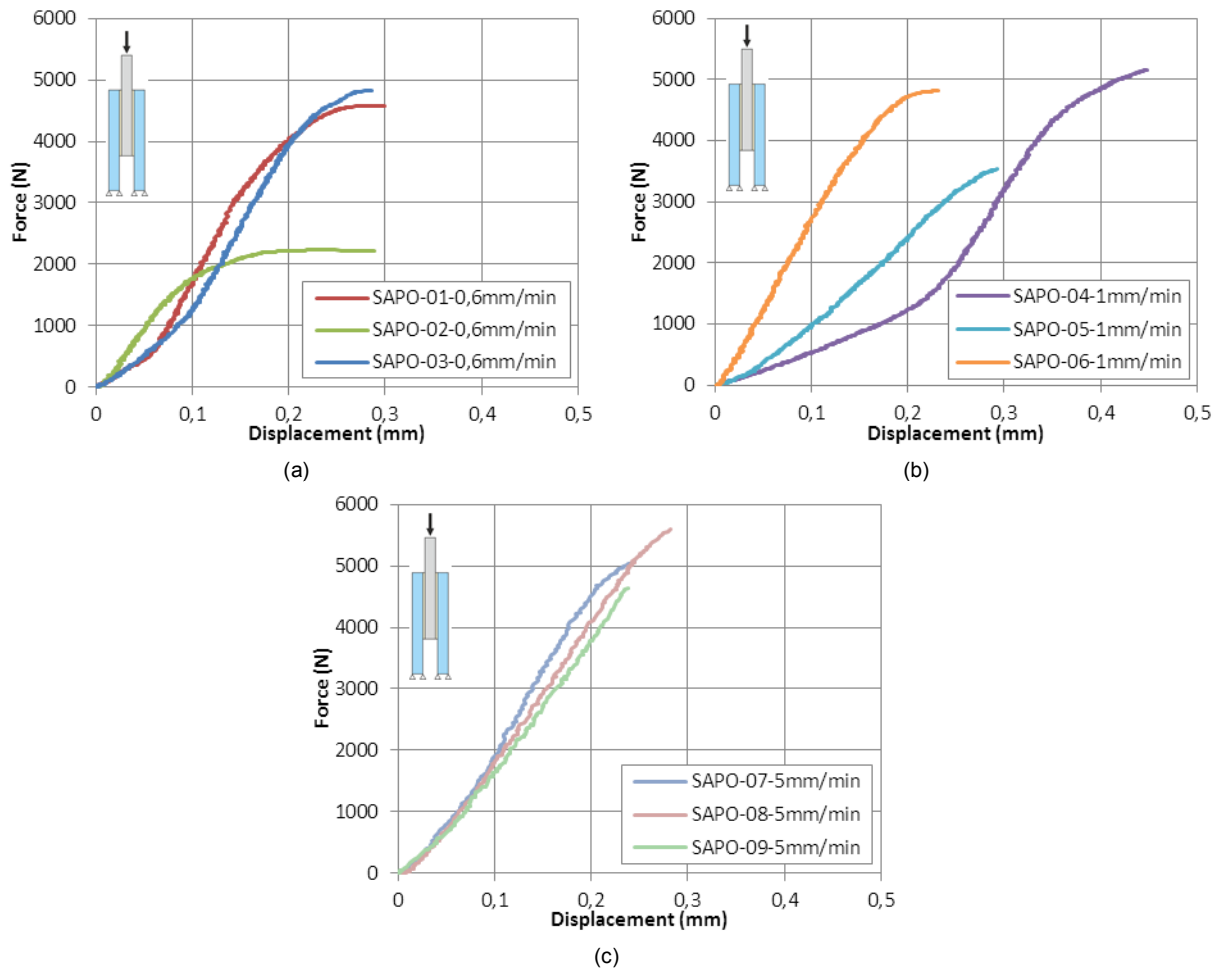
**Figure 4.101-** (a) Acrylic push-out shear layout; Details of the (b) bottom and (c) top of the test setup

The total applied force was measured with the help of an external force sensor of 10kN, while the displacements between the steel plates by the internal sensor of the hydraulic piston. To prevent any parasite effect in the measurements and with regards to the estimated low applied force, no additional material was inserted under or over the specimen, Fig. 4.101 (b) & (c). Furthermore, the glass and steel plates were designed to expose negligible deformations, so that the recorded displacements always corresponded to the displacements of the inner steel plate. All the nine tests of the previous design of experiments of Table 4.53 were conducted until breakage with this layout.

### Tests results

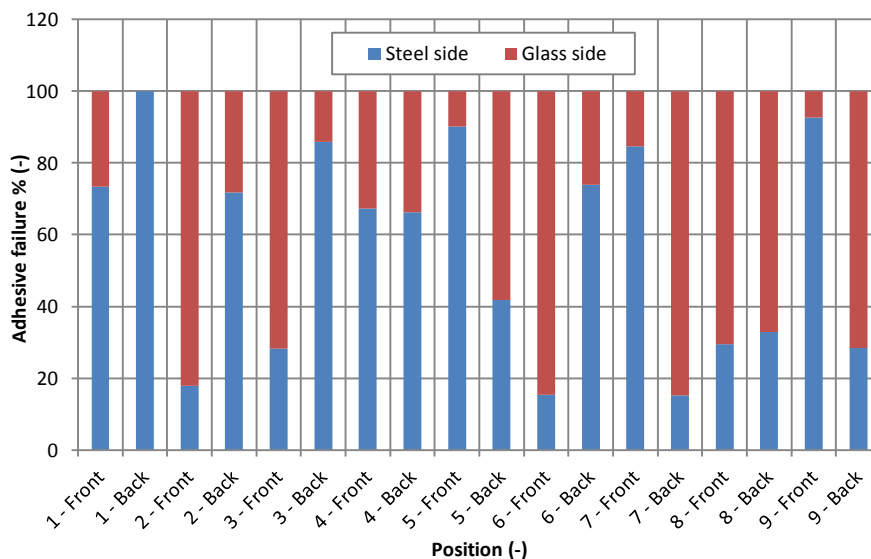
The force-displacement curves were obtained by directly exploiting and combining the data recorded by the two sensors. These curves were superposed for the same applied loading rate in order to better appraise the evolution of the force, see Fig. 4.102.

While the curves were linear and well superposed for the highest loading rate of 5mm/min, certain dispersions were observed for the two other loading rates. Indeed, the samples 1 and 3 subjected to 0,6mm/min showed a first low linear behaviour until a displacement of about 0,7mm and then became stiffer with a steeper slope. The same phenomenon was remarked for the sample 4 under a loading rate of 1mm/min, which presented a second slope identical to the slope of the sample 6. This was interpreted by the non-flatness of the supporting glass surfaces and a possible offset of few tenths of millimeters between these latters inducing a transmission of the load though only one acrylic joint. Therefore, for the low and medium rate, the first portions of the curves were not exploitable as the shear did not start at the same moment in both acrylic sections. The end point of each curve always coincided with the failure of the specimens and so even if the displacements attained were not correct, the maximum force could be exploitable.

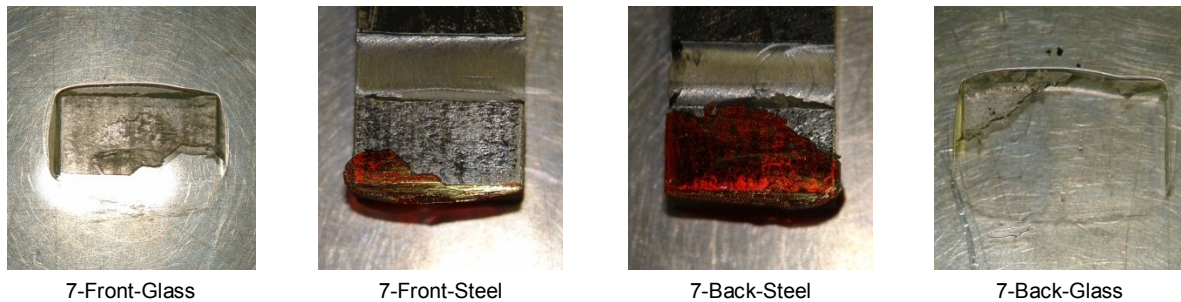


**Figure 4.102-** Force-displacement diagrams obtained for a loading rate of (a) 0,6mm/min, (b) 1mm/min and (c) 5mm/min

Nevertheless, a validation of the results obtained for elevated displacements was necessary to make sure of the correct values of the maximum forces. Hence, a complete analysis of the failure mode was conducted for all the nine specimens. For each push-out, the inner steel part was entirely free at the end of the experiments, indicating that once the maximum force was reached both acrylic sections broke together. The areas of the remaining acrylic residues left on the four surfaces, i.e. on the front glass and steel and the back steel and glass, were then measured with an image-processing program. Except for the back side of sample 1, all steel and glass surfaces presented important marks of acrylic.







**Figure 4.103-** Analysis of the failure mode of the push-out acrylic samples and detailed example of specimen n°7

The adhesive residues left on the glass were never superimposable to the residues of the steel plate, meaning that the failure was adhesive partially on the steel side and on the glass side. These results were stored in the diagram of Fig. 4.103, giving the percentages of the real bonded area which either failed on the steel side or on the opposite glass side. By averaging these values, it was found that the adhesion was lost approximately equally between glass (43,6%) and steel. Consequently, the final values of the force represented correctly the resistance of the push-out shear tests and could not be increased with specific mechanical or chemical treatments.

The maximum forces at breakage were recorded for each test in Table 4.54 and the mean values were calculated for the different loading rates. Due to relatively low local data for the samples tested at 0,6mm/min and 1mm/min, no conclusion on the influence of the loading rate could have been set with sufficient confidence level, even if the load seemed to increase with the loading rate. Furthermore, by considering the stiffness of the acrylic adhesive and the small bonded height of 10mm, the calculation of the stress consisting in simply dividing the applied force by the total glued area might be completely wrong with regards to the theory of the double lap-joint assembly developed by Volkersen [4.8]. Indeed this division would suppose a uniform distribution of the stress along the bonded length, which does not seem to be valid. A detailed explanation of this exception is provided in section 6.3.2.

| Test n° | A            | Maximum force (N) |               |               | Average (N) |
|---------|--------------|-------------------|---------------|---------------|-------------|
|         | Loading rate | Test series 1     | Test series 2 | Test series 3 |             |
| 1       | 0,6mm/min    | 4582,703          | 2229,248      | 4820,679      | 3877,543    |
| 2       | 1mm/min      | 5156,800          | 3535,706      | 4817,261      | 4503,255    |
| 3       | 5mm/min      | 5076,050          | 5592,407      | 4643,555      | 5104,004    |

**Table 4.54-** Maximum force at breakage – DOE of Table 4.53 – acrylic quasi-static push-out test

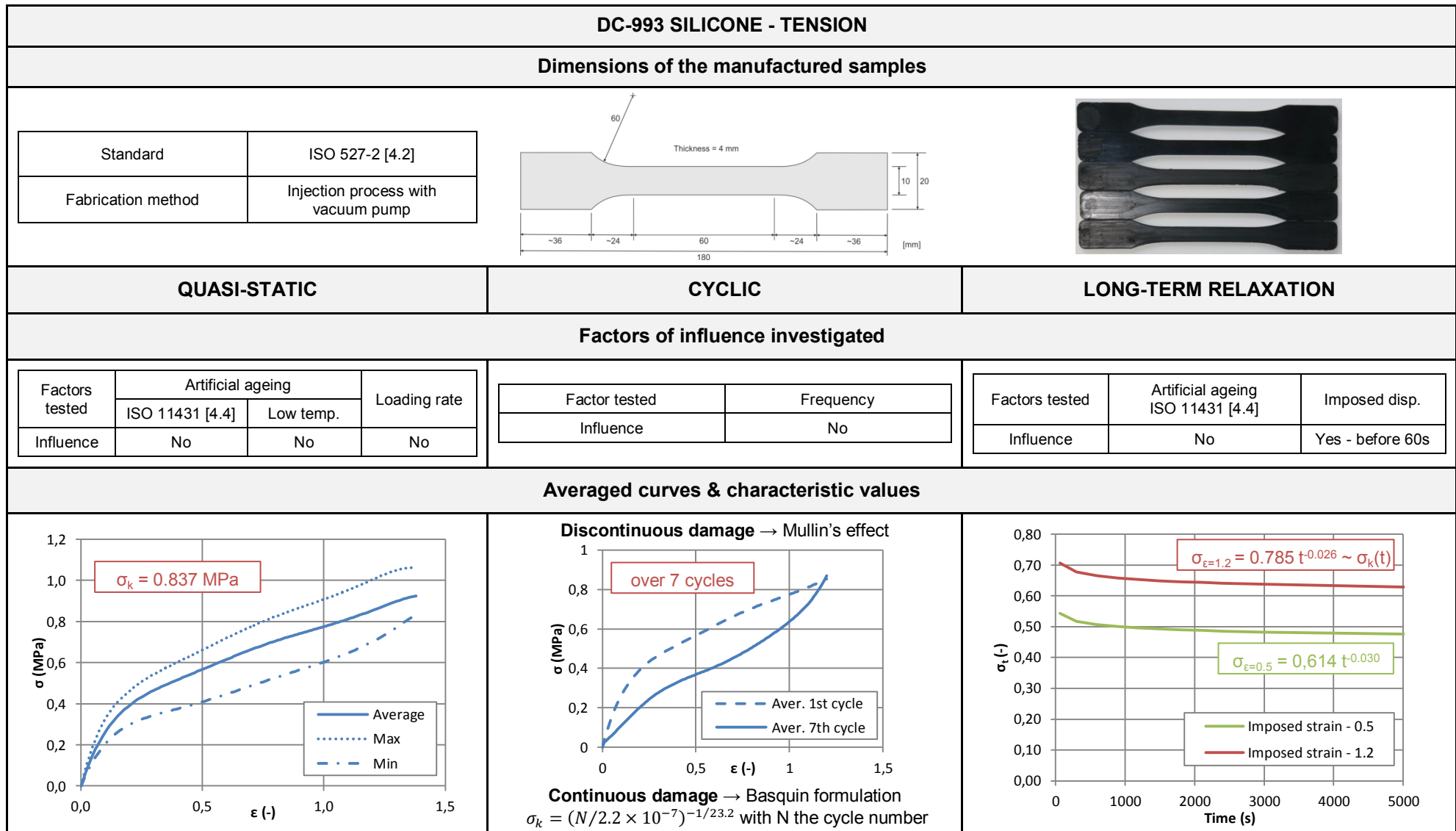
Finally the stiffnesses of all the curves were evaluated for a comparison with the stiffnesses estimated with the modified acrylic shear results of the previous section. The stiffnesses determination of the current push-out tests was each time assessed during the second slope for which both acrylic joints were subjected, at the same time, to shear forces. All these stiffnesses of the envisaged design of experiments were stored in Table 4.55. For a given loading rate, these last stiffnesses were averaged and compared to the stiffnesses calculated with the shear modulus of the modified shear tests. The shear modulus of 5mm/min was obtained by analyzing the loading of the long-term tests. No influence of the loading rate could have been postulated but the stiffnesses of both tests coincided well.

| Push-out shear tests |              |                    |          |          |                | Modified shear tests |          |                    |
|----------------------|--------------|--------------------|----------|----------|----------------|----------------------|----------|--------------------|
| Test n°              | A            | Stiffness K (N/mm) |          |          | Average (N/mm) | G(MPa)               | K (N/mm) | Relative error (%) |
|                      | Loading rate | Series 1           | Series 2 | Series 3 |                |                      |          |                    |
| 1                    | 0,6mm/min    | 29249,7            | 20839,1  | 26539,0  | 25542,6        | -                    | -        | -                  |
| 2                    | 1mm/min      | 25859,9            | -        | 22163,2  | 24011,6        | 8,648                | 23879,6  | 0,6                |
| 3                    | 5mm/min      | 28050,7            | 22188,5  | 22548,8  | 24262,7        | 13,441               | 25218,9  | -3,8               |

**Table 4.55-** Stiffnesses – DOE of Table 4.53 – acrylic quasi-static push-out test & Comparison to modified shear stiffnesses



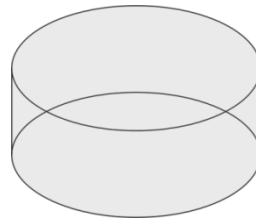
## 4.4 SUMMARY AND CONCLUSION



## DC-993 SILICONE - COMPRESSION

## Dimensions of the manufactured samples

|                    |                        |
|--------------------|------------------------|
| Standard           | -                      |
| Fabrication method | Simple pouring process |



## QUASI-STATIC

## CYCLIC

## LONG-TERM RELAXATION

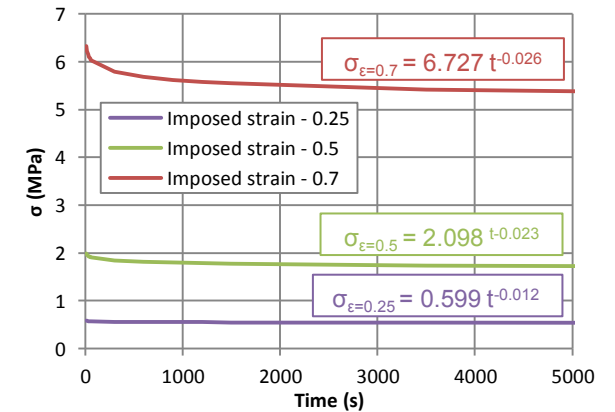
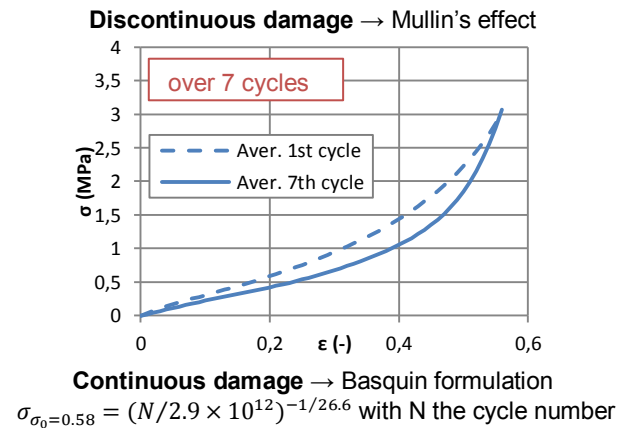
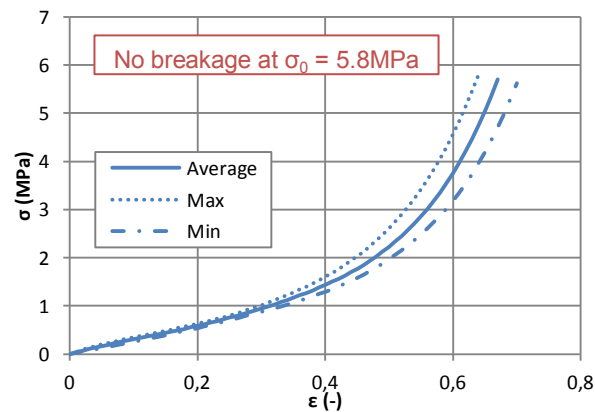
## Factors of influence investigated

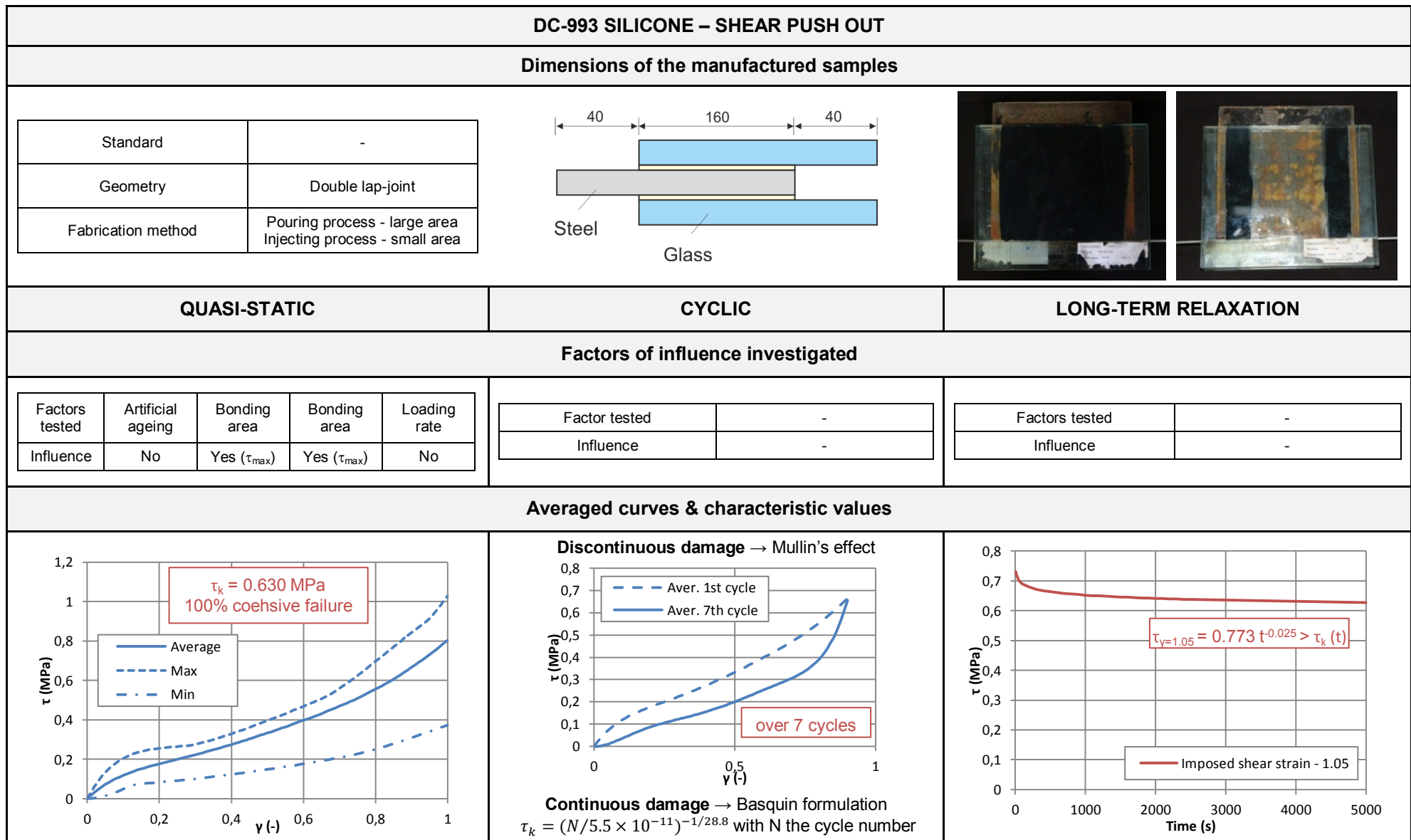
| Factors tested | Artificial ageing |           | Loading rate |
|----------------|-------------------|-----------|--------------|
|                | ISO 11431 [4.4]   | Low temp. |              |
| Influence      | No                | No        | No           |

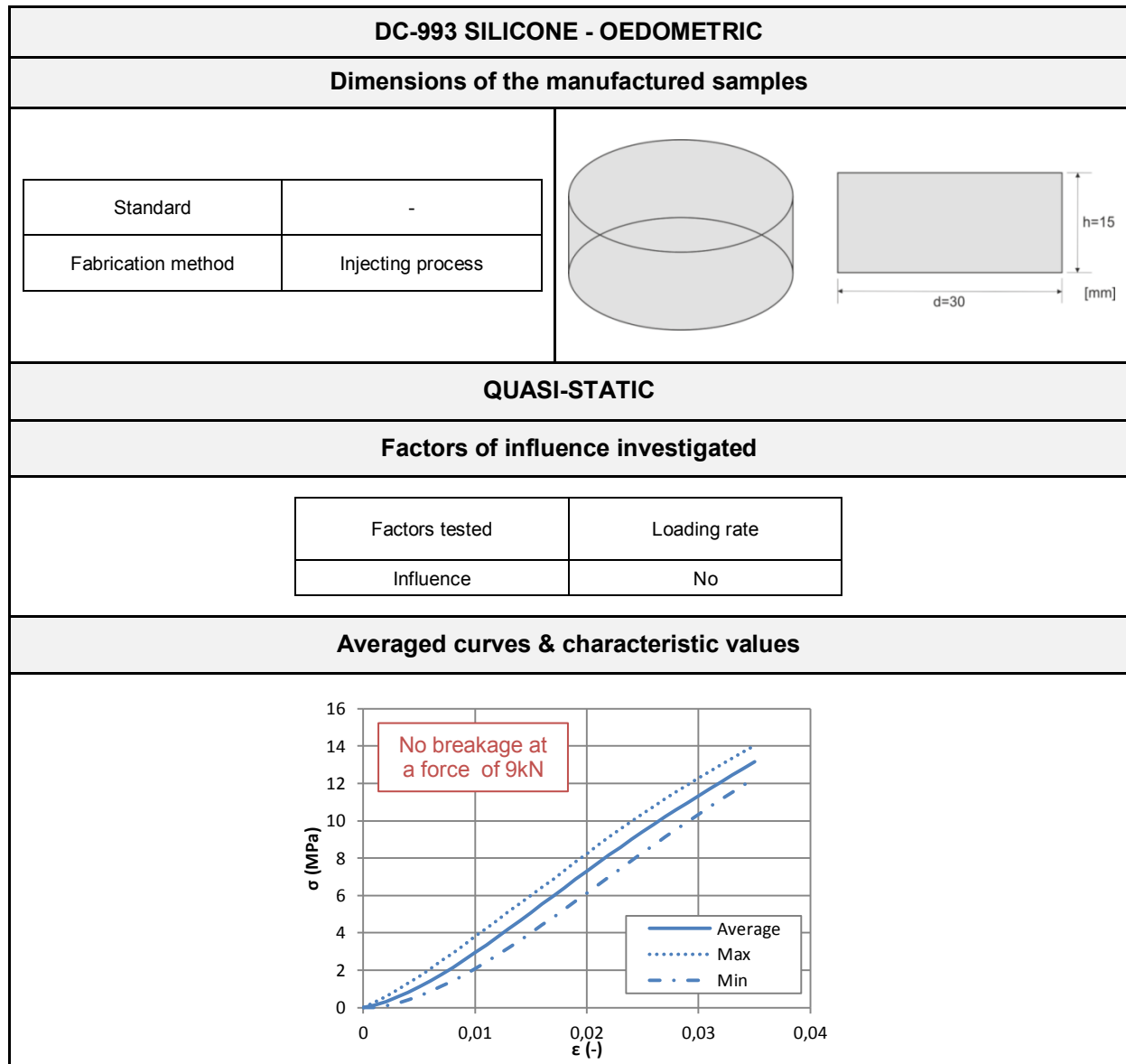
| Factor tested | Frequency |
|---------------|-----------|
| Influence     | No        |

| Factors tested | Artificial ageing<br>ISO 11431 [4.4] | Imposed disp.    |
|----------------|--------------------------------------|------------------|
| Influence      | No                                   | Yes - before 60s |

## Averaged curves &amp; characteristic values



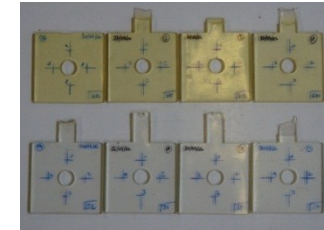
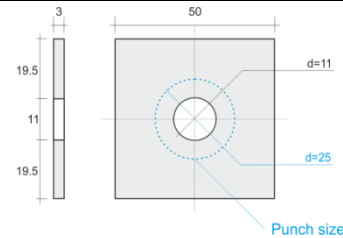






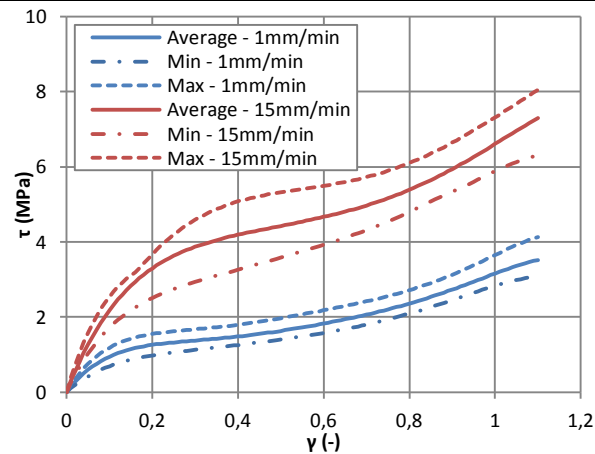
**MV 760 UV-ACRYLIC – MODIFIED SHEAR****Dimensions of the manufactured samples**

|                    |                   |
|--------------------|-------------------|
| Standard           | ASTM D732 [4.10]  |
| Fabrication method | Injection process |

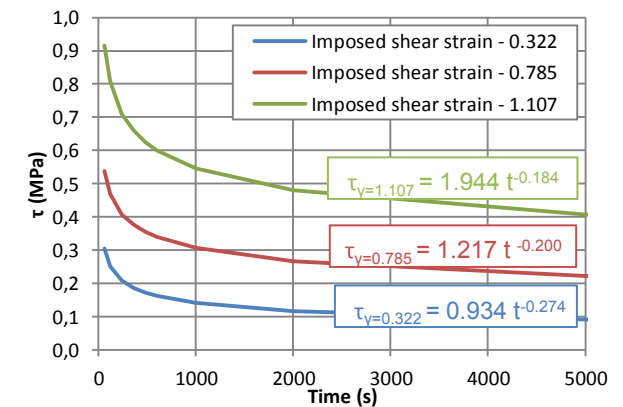
**QUASI-STATIC****LONG-TERM RELAXATION****Factors of influence investigated**

| Factors tested | Artificial ageing<br>ISO 11431 [4.4] | Loading rate |
|----------------|--------------------------------------|--------------|
| Influence      | No                                   | Yes          |

| Factors tested | Artificial ageing<br>ISO 11431 [4.4] | Imposed disp. |
|----------------|--------------------------------------|---------------|
| Influence      | No                                   | Yes           |

**Averaged curves & characteristic values**

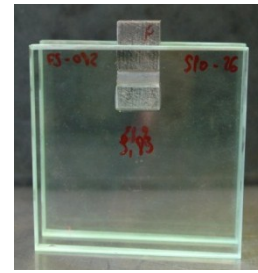
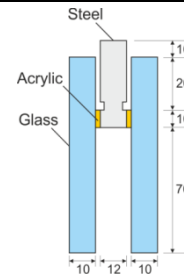
| Loading rate<br>(mm/min) | Shear modulus<br>$G_0$ (MPa) |       | Maximum stress<br>$\sigma_{\gamma=1,10}$ (MPa) |       |
|--------------------------|------------------------------|-------|------------------------------------------------|-------|
|                          | Aver.                        | Std.  | Aver.                                          | Std.  |
| 1                        | 8,648                        | 3,926 | 3,488                                          | 0,511 |
| 15                       | 24,751                       | 3,966 | 7,202                                          | 0,840 |



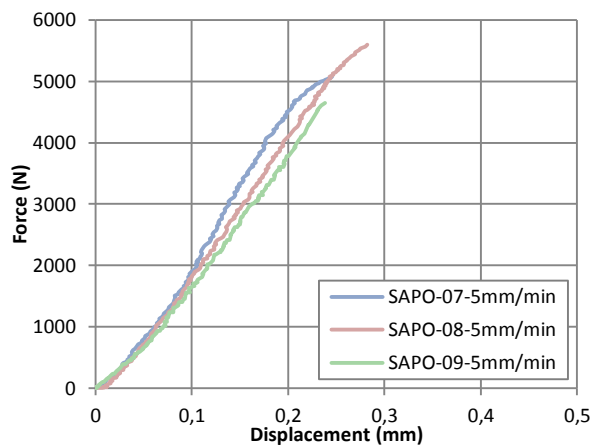
Valid for all loading rates (first 60s excluded)

**MV 760 UV-ACRYLIC – SHEAR PUSH OUT****Dimensions of the manufactured samples**

|                    |                  |
|--------------------|------------------|
| Standard           | -                |
| Geometry           | Double lap-joint |
| Fabrication method | Pouring process  |

**QUASI-STATIC****Factors of influence investigated**

|                |                        |
|----------------|------------------------|
| Factors tested | Loading rate           |
| Influence      | Not fully demonstrated |

**Averaged curves & characteristic values**

| Loading rate<br>(mm/min) | Stiffness K (N/mm) |        | Maximum force (N) |        |
|--------------------------|--------------------|--------|-------------------|--------|
|                          | Aver.              | Std.   | Aver.             | Std.   |
| 0,6                      | 25542,6            | 4292,9 | 3877,5            | 1432,4 |
| 1                        | 24011,6            | 2613,9 | 4503,3            | 854,9  |
| 5                        | 24262,7            | 3285,5 | 5104,0            | 475,0  |

Linear behaviour corresponding to the first portion of the modified shear curve (identical initial stiffnesses)

100% adhesive failure equally distributed between the steel and glass adherends

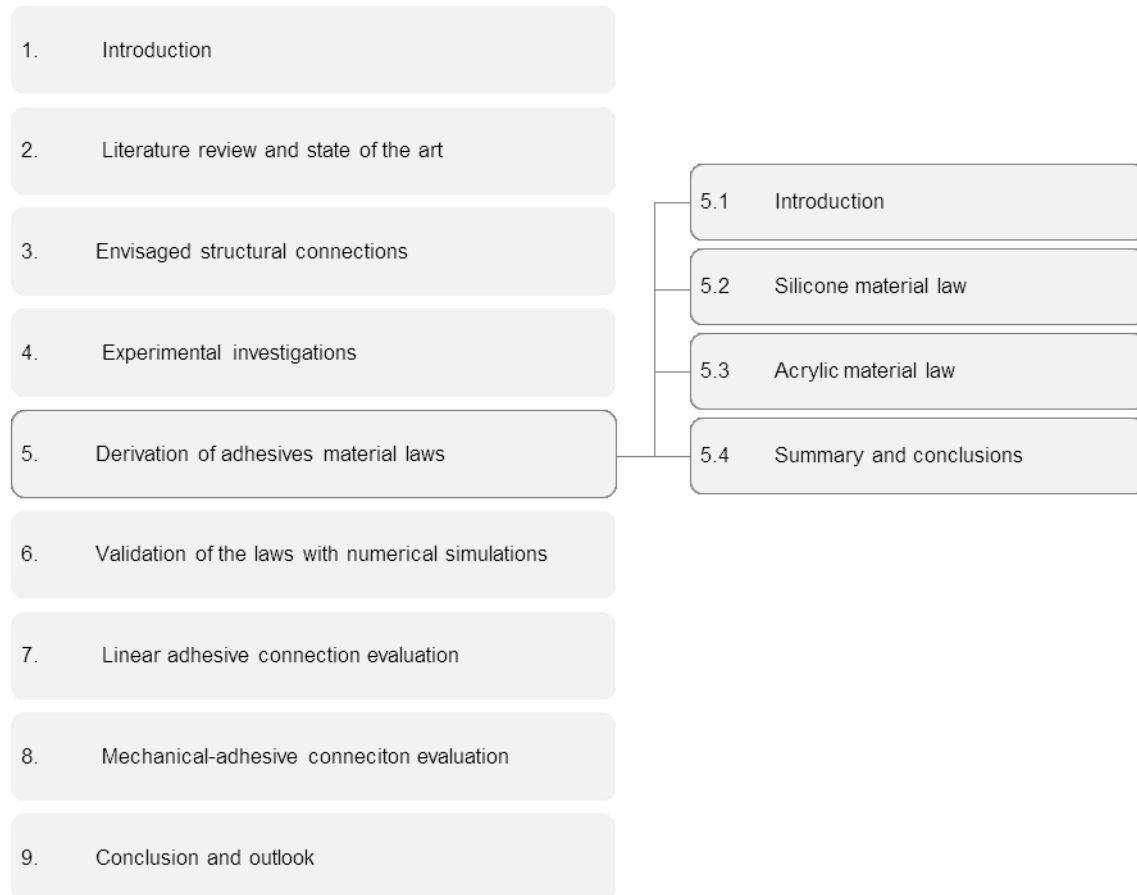




## 5. DERIVATION OF ADHESIVE MATERIAL LAWS

### 5.1 INTRODUCTION

Material laws for the two investigated adhesives, i.e. silicone elastomer and UV-acrylic thermoset, are developed in this chapter. The suitability of the existing models, regrouped in chapter 2, is discussed and their inconsistencies to model the two adhesives engender the development a new constitutive law.



**Figure 5.0-** Organization chart of chapter 5

**Silicone material law.** The existing isochoric strain energy potentials are evaluated with the tests data obtained in the previous chapter. All are inapt to represent the strong non-linearity in the stress values under small strains. Therefore, a new potential function is developed and compared to the isochoric results. For the volumetric part, an existing function is fitted to the oedometric experiments. The different material coefficients determinations with the non-linear Levenberg-Marquardt are presented in this section too.

**Acrylic material law.** Two one-dimensional models are considered for the representation of the rate dependent tension and shear properties of the selected UV-acrylic. The classical Ramberg-Osgood model is used for the uniaxial tension, while a self-developed law is extracted from the silicone law for the shear behaviour. In both models, the loading rate dependency is included by modifying the material parameters.

**Summary and conclusion.** The 3D hyperelastic material law for the silicone, including the softening occurring after the Mullin's effect, and the two 1D models for the tension and shear representation of the acrylic behaviour are gathered in the conclusion.

## 5.2 SILICONE MATERIAL LAW

In section 2.4.2 were presented the current and most often employed material laws for silicone elastomers, i.e. the phenomenological model and the probabilistic models. Even if these two models were established with different starting points, they both necessitated the determination of material coefficients by fitting experimental stress-strain curves. Furthermore, as it was intended to implement the final constitutive material law in the finite element software Abaqus®, the first investigation concerned the phenomenological models already existing within the material library of this software. The fundamental equations of this theory based on the formulation of the strain energy potential, decoupled in an isochoric part depending on the invariants of the deviatoric stretch tensor  $\bar{\mathbb{B}}$  and in a volumetric part depending on the Jacobian  $J$  of the deformation tensor, were repeated below:


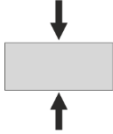
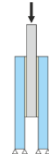
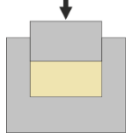
$$W(\bar{\mathbb{B}}) = W_{iso}(\bar{\mathbb{B}}) + W_{vol}(J) = W_{iso}(\bar{I}_1(\bar{\mathbb{B}}), \bar{I}_2(\bar{\mathbb{B}})) + W_{vol}(J) \quad (5.1)$$

$$\bar{I}_1(\bar{\mathbb{B}}) = \text{Tr}(\bar{\mathbb{B}}) \quad (5.2 \text{ a})$$

$$\bar{I}_2(\bar{\mathbb{B}}) = \frac{1}{2} [\text{Tr}(\bar{\mathbb{B}})^2 - \text{Tr}(\bar{\mathbb{B}}^2)] \quad (5.2 \text{ b})$$

$$J = \det(\bar{\mathbb{F}}) \quad (5.2 \text{ c})$$

The main difficulty consisted in finding correct mathematical formulations of the strain energy isochoric  $W_{iso}$  and volumetric  $W_{vol}$  parts fitting the best experimental curves. These last curves were achieved in section 4.2 as stress-strain diagrams for four different actions, i.e. tension, compression, shear and multiaxial oedometric. According the volume change induced by these tests, they were useful for the evaluation of either the isochoric part of the strain energy potential or for the volumetric part. While for the uniaxial tension and compression as well as push-out shear, no volume variation was remarked, for the oedometric tests, minor changes were observed. Hence, two categories of experimental results were considered, see Table 5.1.

| Determination of $W_{iso}(\bar{I}_1(\bar{\mathbb{B}}), \bar{I}_2(\bar{\mathbb{B}}))$ |                                                                                     |                                                                                     | Determination of $W_{vol}(J)$                                                         |
|--------------------------------------------------------------------------------------|-------------------------------------------------------------------------------------|-------------------------------------------------------------------------------------|---------------------------------------------------------------------------------------|
| Uniaxial tension                                                                     | Uniaxial compression                                                                | Push-out shear                                                                      | Oedometric tests                                                                      |
|   |  |  |  |
| Quasi-static<br>Mullins' effect                                                      | Quasi-static<br>Mullins' effect                                                     | Quasi-static<br>Mullins' effect                                                     | Quasi-static                                                                          |

**Table 5.1-** Repartition of the tests according to the determination of the strain energy isochoric and volumetric parts

The three types of tests, allowing the assessment of the strain energy isochoric part, were conducted under three different type of actions, i.e. quasi-static, cyclic and relaxation long-term. For the quasi-static experiments, the averaged curves gathered in section 4.4 were taken into account for this study. For the cyclic tests, a distinction between the continuous and discontinuous damages was operated and only this last damage, representing the Mullin's effect and ending after a defined number of cycles, i.e. 7 cycles for each test type, was envisaged. The averaged last 7<sup>th</sup> stress-strain curves, also recorded in section 4.4, were examined to characterize the Mullin's effect. The relaxation long-term stresses were predicted for specific strains and did not need to be numerically simulated.

The stress-strain diagrams of the oedometric tests necessary to appraise the form of the strain energy volumetric part were only created for quasi-static actions. Due to the very small deformations accepted by this confined material and with regard to the damage theories assuming a rupture of the molecular chains or a sliding at their connecting nodes, no stress softening was supposed under cyclic actions. The strain energy volumetric part was therefore judged as invariant and constant between quasi-static and cyclic actions.

In consequence, the principal objective was to propose a unique mathematical formulation of the strain energy potential able to describe the instantaneous behaviour of silicone adhesive, but also its behaviour under a finite number of cycles by modifying the material parameters.

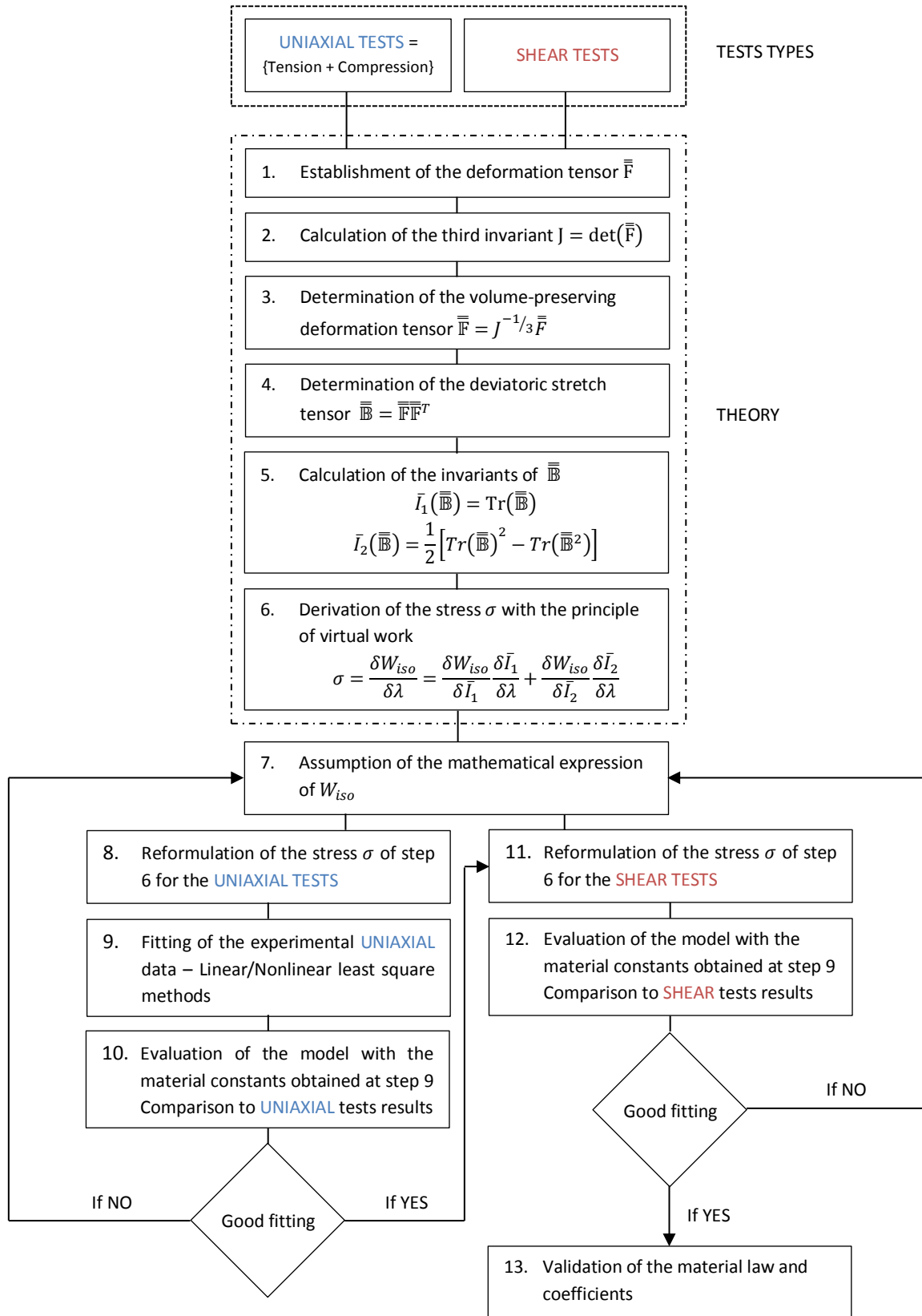


Figure 5.1- Algorithm for the determination of the strain energy isochoric part

### 5.2.1 Formulation of the isochoric part of the strain energy potential

The first investigation had to be centered on the evaluation of the isochoric part formulation, as for the invoked experiments no volume change was noted. This, with the proposed decoupling of the strain energy potential and the normalization condition, induced a nil volumetric part ( $J = 1$ ) with:

$$W(\bar{\mathbf{B}}) = W_{iso}(\bar{\mathbb{B}}) = W_{iso}(\bar{I}_1(\bar{\mathbb{B}}), \bar{I}_2(\bar{\mathbb{B}})) = W_{iso}(I_1(\bar{\mathbf{B}}), I_2(\bar{\mathbf{B}})) \quad (5.3)$$

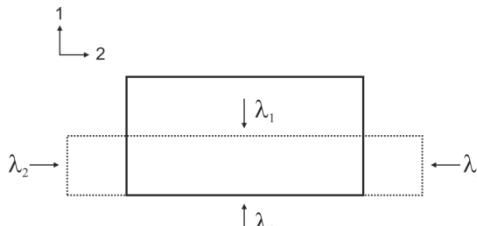
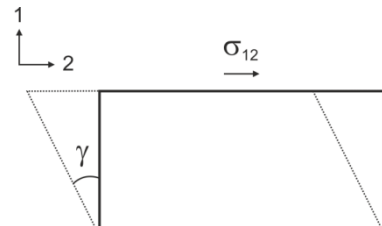
#### 5.2.1.1 Algorithm of resolution

The complete procedure leading to the determination of the isochoric strain energy is presented in Fig. 5.1. This algorithm could have been divided in two main steps:

- A theoretical step, in which the stresses of each test were expressed in function of the a priori unknown isochoric strain energy of Eq. (5.3) derived by the deviatoric strain invariants. This equation, based on the principle of the virtual work, also demonstrated the dependency of the stresses to the deviatoric strain invariants derived by the elongations. The stresses were thus directly related to the deviatoric stretch tensor  $\bar{\mathbb{B}}$  and to the volume-preserving deformation tensor  $\bar{\mathbb{F}}$ . Knowing the dependency to this last tensor, the tensile and compressive stress-strain results were regrouped in one uniaxial class as both exposed an identical deformation tensor. The two theoretical types of stresses, i.e. for the uniaxial and shear tests, were finally established, see section 5.2.1.2.
- An assumption and trial step, for which different isochoric strain energy forms were proposed, fitted to the uniaxial experimental results for material coefficients estimation and compared to uniaxial and shear tests results for complete validation. The different tested isochoric strain energy functions are detailed in section 5.2.1.3 for the existing ones and 5.2.1.4 for the new one.

#### 5.2.1.2 Evaluation of the stresses for the different tests (Steps 1 to 6 of Fig. 5.1)

The first six theoretical steps of the algorithm of Fig. 5.1 were conducted for the uniaxial and shear tests to summarize the final expression of the stresses in Table 5.2. After reaching this objective, no further continuation could have been done without assuming and testing different forms of the isochoric strain energy potential.

| UNIAXIAL TEST                                                                                                                                                                                                            | SHEAR TEST                                                                                                  |
|--------------------------------------------------------------------------------------------------------------------------------------------------------------------------------------------------------------------------|-------------------------------------------------------------------------------------------------------------|
|                                                                                                                                       |                         |
| $\bar{\mathbf{F}} = \begin{pmatrix} \lambda_1 & 0 & 0 \\ 0 & \lambda_2 & 0 \\ 0 & 0 & \lambda_3 \end{pmatrix} = \begin{pmatrix} \lambda_1 & 0 & 0 \\ 0 & \lambda_1^{-1/2} & 0 \\ 0 & 0 & \lambda_1^{-1/2} \end{pmatrix}$ | $\bar{\mathbf{F}} = \begin{pmatrix} 1 & \gamma & 0 \\ 0 & 1 & 0 \\ 0 & 0 & 1 \end{pmatrix}$                 |
| $J = \det(\bar{\mathbf{F}}) = \lambda_1 \lambda_2 \lambda_3 = 1$                                                                                                                                                         | $J = \det(\bar{\mathbf{F}}) = 1$                                                                            |
| $\bar{\mathbb{F}} = \bar{\mathbf{F}}$                                                                                                                                                                                    | $\bar{\mathbb{F}} = \bar{\mathbf{F}}$                                                                       |
| $\bar{\mathbb{B}} = \begin{pmatrix} \lambda_1^2 & 0 & 0 \\ 0 & \lambda_1^{-1} & 0 \\ 0 & 0 & \lambda_1^{-1} \end{pmatrix}$                                                                                               | $\bar{\mathbb{B}} = \begin{pmatrix} 1 + \gamma^2 & \gamma & 0 \\ \gamma & 1 & 0 \\ 0 & 0 & 1 \end{pmatrix}$ |

|                                                                                                                                                          |                                                                                                                          |
|----------------------------------------------------------------------------------------------------------------------------------------------------------|--------------------------------------------------------------------------------------------------------------------------|
| $\begin{aligned}\bar{I}_1(\bar{\mathbb{B}}) &= 2\lambda_1^{-1} + \lambda_1^2 \\ \bar{I}_2(\bar{\mathbb{B}}) &= \lambda_1^{-2} + 2\lambda_1\end{aligned}$ | $\begin{aligned}\bar{I}_1(\bar{\mathbb{B}}) &= 3 + \gamma^2 \\ \bar{I}_2(\bar{\mathbb{B}}) &= 3 + \gamma^2\end{aligned}$ |
| $\sigma_{11} = 2(1 - \lambda_1^{-3}) \left[ \lambda_1 \frac{\delta W_{iso}}{\delta \bar{I}_1} + \frac{\delta W_{iso}}{\delta \bar{I}_2} \right]$         | $\sigma_{12} = 2\gamma \left[ \frac{\delta W_{iso}}{\delta \bar{I}_1} + \frac{\delta W_{iso}}{\delta \bar{I}_2} \right]$ |

**Table 5.2-** Derivation of the stresses for the two related experiments (steps 1 to 6 of Fig. 5.1)

### 5.2.1.3 Study of the existing isochoric formulations

#### Principal assumptions

One of the major assumptions, adopted in the existing formulations, was proposed by Obata [5.1] and Kawabata [5.2], who also verified experimentally that the derivatives of the isochoric strain energy  $W_{iso}$  with respect to the first  $\bar{I}_1$  and second  $\bar{I}_2$  deviatoric invariants were decoupled, so that  $\delta W_{iso}/\delta \bar{I}_1$  only depended on  $\bar{I}_1$  and  $\delta W_{iso}/\delta \bar{I}_2$  on  $\bar{I}_2$ . With the introduction of two functions  $f_1$  and  $f_2$ , the following equations were established:

$$\frac{\delta W_{iso}}{\delta \bar{I}_1} = f_1(\bar{I}_1) \qquad \frac{\delta W_{iso}}{\delta \bar{I}_2} = f_2(\bar{I}_2) \qquad (5.4)$$

Thus, with the above Eq. (5.4), the isochoric strain energy potential could be written as the sum of the integrals of the two functions  $f_1$  and  $f_2$  and the research of the general form of  $W_{iso}$  could be reported to the researches of these last two functions.

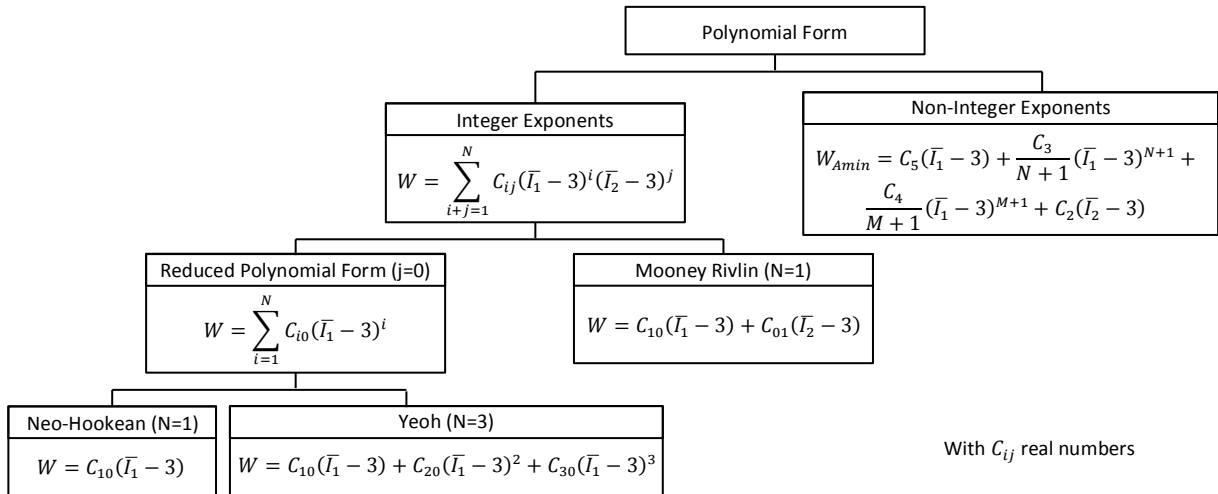
Another conjecture commonly approved consisted in expressing the respective functions  $f_1$  and  $f_2$  as the sums of polynomial terms of  $\bar{I}_1$  and  $\bar{I}_2$ . With respect to the normalization condition, for which the strain energy potential and consequently the isochoric strain energy for the current experiments had to vanish in the reference configuration, i.e.  $W(I) = W_{iso}(I) = 0$  with  $I$  the identity matrix, the function  $W_{iso}$  was rewritten as:

$$W_{iso} = \sum_{i=1}^M A_i (\bar{I}_1 - 3)^i + \sum_{j=1}^N B_j (\bar{I}_2 - 3)^j \qquad (5.5)$$

With  $A_i$  and  $B_j$  material constants and  $M$  and  $N$  integers.

#### Existing models (Steps 7, 8, 11 of Fig. 5.1)

The most common forms of the isochoric strain energy potential exposed in section 2.4.2.2 were summarized in tree structure to appraise their interdependencies, see Fig.5.2.



**Figure 5.2-** Tree structure of the most employed isochoric energy potential forms  $W_{iso}$  (step 7 of Fig. 5.1)

In spite of the general polynomial form breaking the principle of the first assumption and coupling the first and second deviatoric invariants by multiplying polynomials composed by these last two terms, the other laws respected the two stated hypotheses. Indeed, the equation Eq. (5.5) constituted the basis of the reduced polynomial ( $B_j = 0$ ), the Mooney-Rivlin ( $M = 1; N = 1$ ), the Yeoh ( $M = 3; B_j = 0$ ) and the Neo-Hookean ( $M = 1; B_j = 0$ ) forms.

To cover a large range, the last three aforementioned models were envisaged as well as the more global polynomial form for which  $N$  was chosen equal to 2 to keep the number of material coefficient to be determined lower than five. For all these considered isochoric strain energy potentials, the steps 8 and 11 of the algorithm of Fig. 5.1, consisting in reformulating the stresses according to the tests types, were performed see Table 5.3.

| $W_{iso}$ models                                                                                                                                                                    | UNIAXIAL TEST                                                                                                                                                                                                                                     | SHEAR TEST                                                                     |
|-------------------------------------------------------------------------------------------------------------------------------------------------------------------------------------|---------------------------------------------------------------------------------------------------------------------------------------------------------------------------------------------------------------------------------------------------|--------------------------------------------------------------------------------|
| Neo-Hookean<br>$W_{iso} = C_{10}(\bar{I}_1 - 3)$                                                                                                                                    | $\sigma_{11} = 2C_{10}\lambda_1(1 - \lambda_1^{-3})$                                                                                                                                                                                              | $\sigma_{12} = 2C_{10}\gamma$                                                  |
| Yeoh<br>$W_{iso} = C_{10}(\bar{I}_1 - 3) + C_{20}(\bar{I}_1 - 3)^2 + C_{30}(\bar{I}_1 - 3)^3$                                                                                       | $\sigma_{11} = 2\lambda_1(1 - \lambda_1^{-3})[C_{10} + 2C_{20}(2\lambda_1^{-1} + \lambda_1^2 - 3) + 3C_{30}(2\lambda_1^{-1} + \lambda_1^2 - 3)^2]$                                                                                                | $\sigma_{12} = 2\gamma[C_{10} + 2C_{20}\gamma^2 + 3C_{30}\gamma^4]$            |
| Mooney-Rivlin<br>$W_{iso} = C_{10}(\bar{I}_1 - 3) + C_{01}(\bar{I}_2 - 3)$                                                                                                          | $\sigma_{11} = 2(1 - \lambda_1^{-3})[C_{10}\lambda_1 + C_{01}]$                                                                                                                                                                                   | $\sigma_{12} = 2\gamma[C_{10} + C_{01}]$                                       |
| Polynomial form ( $N = 2$ )<br>$W_{iso} = C_{10}(\bar{I}_1 - 3) + C_{20}(\bar{I}_1 - 3)^2 + C_{01}(\bar{I}_2 - 3) + C_{02}(\bar{I}_2 - 3)^2 + C_{11}(\bar{I}_1 - 3)(\bar{I}_2 - 3)$ | $\sigma_{11} = 2(1 - \lambda_1^{-3})\{\lambda_1[C_{10} + 2C_{20}(2\lambda_1^{-1} + \lambda_1^2 - 3) + C_{11}(\lambda_1^{-2} + 2\lambda_1 - 3)] + C_{01} + 2C_{02}(\lambda_1^{-2} + 2\lambda_1 - 3) + C_{11}(2\lambda_1^{-1} + \lambda_1^2 - 3)\}$ | $\sigma_{12} = 2\gamma[C_{10} + C_{01} + 2(C_{20} + C_{02} + C_{11})\gamma^2]$ |

**Table 5.3-** Stresses reformulations acc. to the tests types for different isochoric strain potentials (step 8 and 11 of Fig. 5.1)

### Material constants evaluations (Step 9 of Fig. 5.1)

As it could be remarked with the previous table, higher was the degree of the polynomial and more complex was the equation of the stress. Nevertheless, despite this complexity, the stresses were always linear in terms of the material constants. Therefore, a simple linear least squares method, minimizing the relative error between the theoretical stresses and the experimental stresses was employed for the determination of these parameters. This procedure, corresponding to step 9 of the algorithm of Fig. 5.1, was only achieved with the data issued from the uniaxial tests. The measure of the relative error was done with the help of the following function:

$$E = \sum_{i=1}^n \left( 1 - \frac{\sigma_i^{Th}}{\sigma_i^{Test}} \right)^2 \quad (5.6)$$

$n$  the total number of experimental uniaxial stress-strain data,

With  $\sigma_i^{Th}$  the expression of theoretical uniaxial stress (Table 5.3) associated to the  $i^{th}$  strain,

$\sigma_i^{Test}$  the experimental uniaxial stress associated to the  $i^{th}$  strain.

The material constants of each model were calculated by solving the systems of equations formed by the minimization of the relative error by each  $C_{ij}$ , i.e. the derivatives of  $E$  towards each  $C_{ij}$  had to be nil:

$$\frac{\delta E}{\delta C_{ij}} = 0 \quad \forall i, j \quad (5.7)$$

As example, for the Mooney-Rivlin law, two material constants were unknown and so a system formed by two equations obtained with Eq. (5.7) had to be solved:

$$\begin{cases} \frac{\delta E}{\delta C_{10}} = 0 \\ \frac{\delta E}{\delta C_{01}} = 0 \end{cases} \equiv \begin{cases} \sum_{i=1}^n \frac{2(1-\lambda_i^{-3})^2 \lambda_i^2}{\sigma_i^{Test^2}} C_{10} + \sum_{i=1}^n \frac{2(1-\lambda_i^{-3})^2 \lambda_i}{\sigma_i^{Test^2}} C_{01} = \sum_{i=1}^n \frac{2(1-\lambda_i^{-3}) \lambda_i}{\sigma_i^{Test}} \\ \sum_{i=1}^n \frac{2(1-\lambda_i^{-3})^2 \lambda_i}{\sigma_i^{Test^2}} C_{10} + \sum_{i=1}^n \frac{2(1-\lambda_i^{-3})^2}{\sigma_i^{Test^2}} C_{01} = \sum_{i=1}^n \frac{(1-\lambda_i^{-3})}{\sigma_i^{Test}} \end{cases} \quad (5.8)$$

The sums preceding the material coefficients were implemented in an Excel file under matrix form to be inverted and multiplied by the results of the equations. This allowed calculating the two coefficients  $C_{10}$  and  $C_{01}$ .

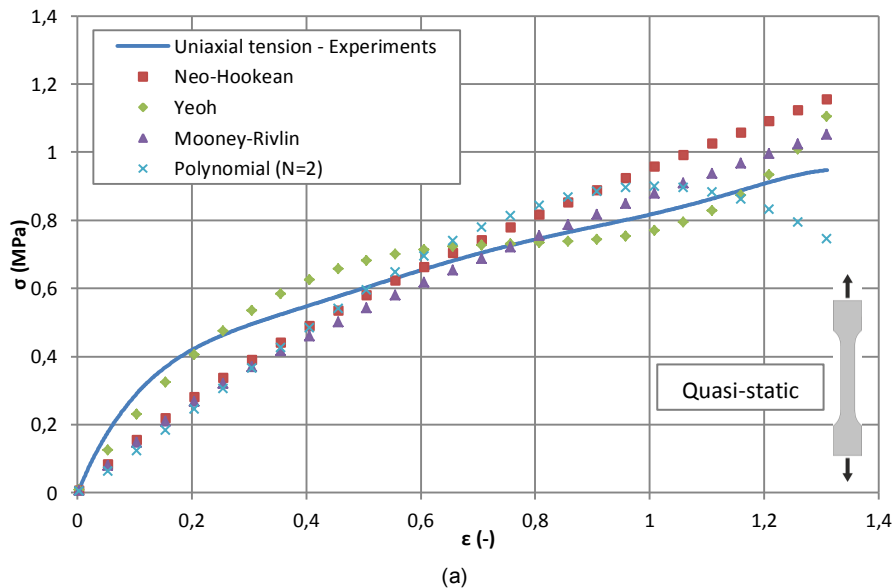
This principle was applied to each model of Table 5.3 and for the quasi-static and the Mullin's effect (curve of the 7<sup>th</sup> cycle) stress-strain experimental data. The following material constants were found:

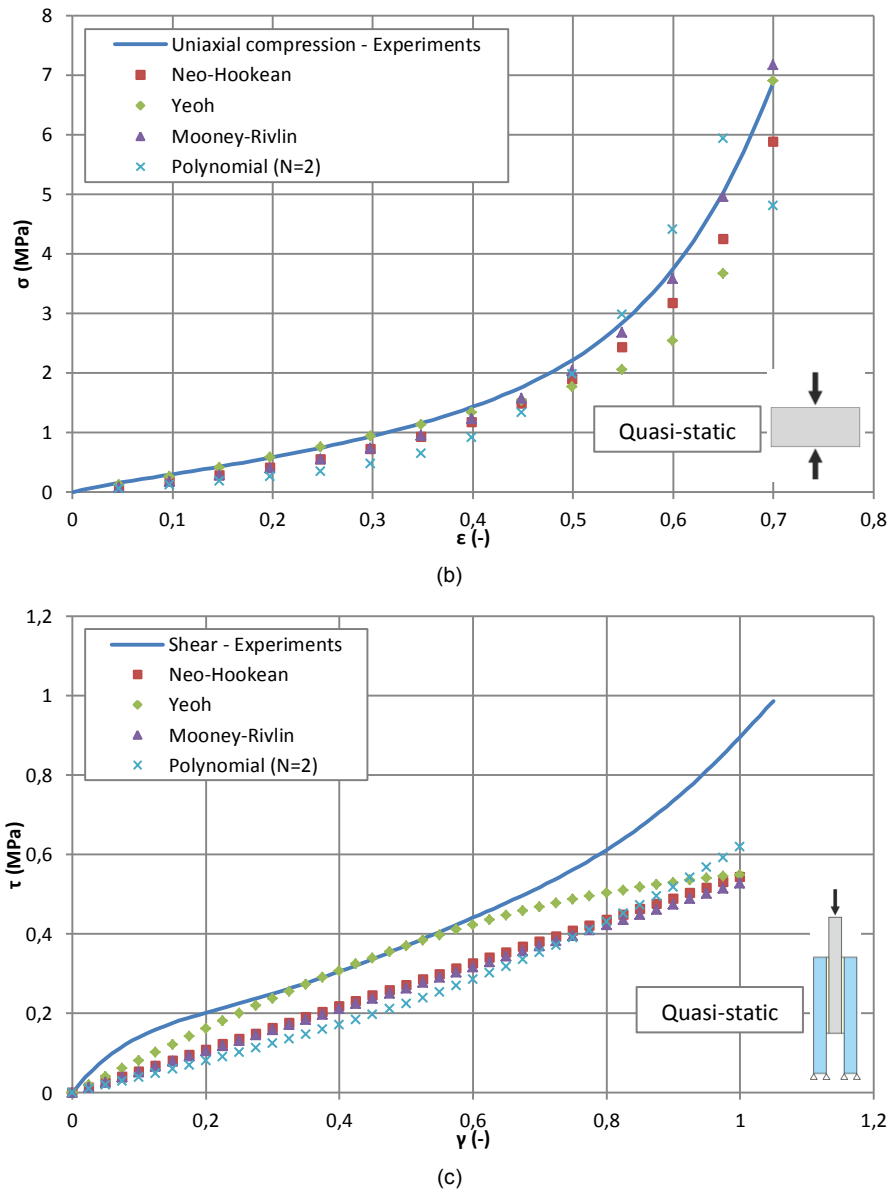
| $W_{iso}$ models            | Action       | Material constants (-) |          |          |          |          |          |
|-----------------------------|--------------|------------------------|----------|----------|----------|----------|----------|
|                             |              | $C_{10}$               | $C_{20}$ | $C_{30}$ | $C_{01}$ | $C_{02}$ | $C_{11}$ |
| Neo-Hookean                 | Quasi-static | 0,27203                | -        | -        | -        | -        | -        |
|                             | Mullins      | 0,19901                | -        | -        | -        | -        | -        |
| Yeoh                        | Quasi-static | 0,41168                | -0,08902 | 0,01361  | -        | -        | -        |
|                             | Mullins      | 0,23423                | -0,04007 | 0,00916  | -        | -        | -        |
| Mooney-Rivlin               | Quasi-static | 0,23500                | -        | -        | 0,02895  | -        | -        |
|                             | Mullins      | 0,13951                | -        | -        | 0,07029  | -        | -        |
| Polynomial form ( $N = 2$ ) | Quasi-static | 0,38238                | -0,12986 | -        | -0,18503 | -0,06824 | 0,25411  |
|                             | Mullins      | 0,13360                | 0,44226  | -        | 0,25569  | 0,39660  | -1,04636 |

**Table 5.4-** Material coefficients associated to each model of Table 5.3 and to each type of action (step 9 of Fig. 5.1)

### Evaluation of the existing models (Steps 10, 12 of Fig. 5.1)

As the quasi-static curves and the 7<sup>th</sup> cyclic curves were different for the three types of loading, i.e. tension, compression and shear, their material coefficients were also different for a given model. Hence, to appraise the degree of fitting of the existing isochoric energy potentials to the experimental stress-strain diagrams, a separation according to the type of action was realized. Furthermore, the uniaxial tension and compression were ungrouped to better apprehend each behaviour. These evaluations with the material coefficients of Table 5.4, corresponding to the steps 10 and 12 of Fig. 5.1, were gathered in Fig. 5.3 for the quasi-static results and Fig. 5.4 for the 7<sup>th</sup> cyclic curves.





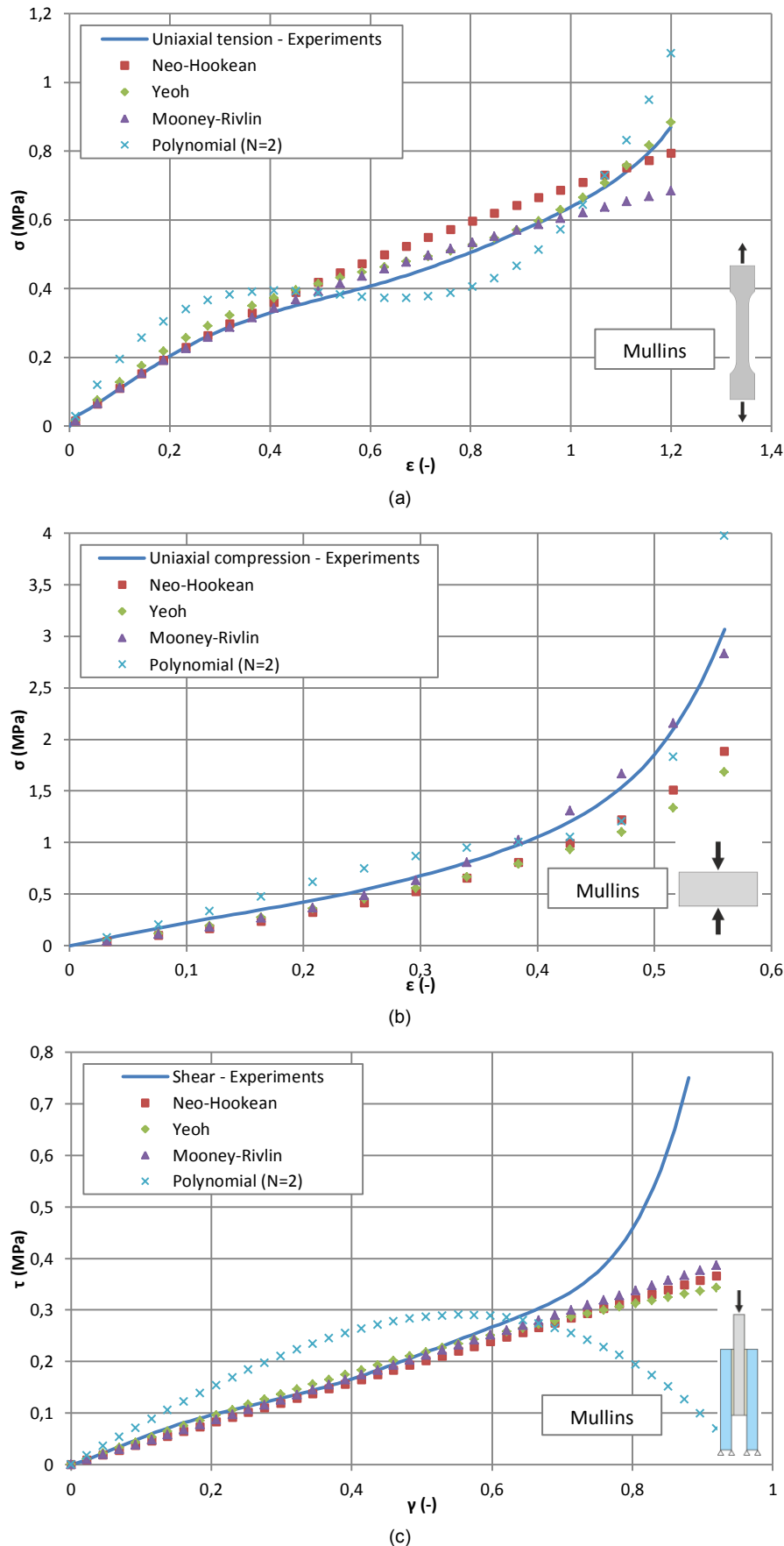
**Figure 5.3-** Evaluation of the curve fittings for quasi-static (a) tension, (b) compression and (c) shear – Existing models

The three diagrams of Fig. 5.3 were achieved by fitting the experimental uniaxial quasi-static curve. A good concordance was therefore envisaged for the tension and compression data. However, it was noticed that the tensile behaviour at small strain, i.e. under  $\epsilon = 0,4$ , was underestimated for three of the four isochoric strain energy models. For this small strains range, only the Yeoh law exposed an accurate representation of the tensile stresses. For strains larger than  $\epsilon = 0,4$ , this last model showed non-negligible oscillations, invalidating its use for numerical simulations. Additionally, the three others did not demonstrate a better agreement to the tensile quasi-static experimental curve. For the compression, good correlations were found for the full tested strains range with the exception of the second order polynomial form, for which an important decrease in stress was seen at  $\epsilon = 0,7$ . The closest model to the compressive experimental curve was in this case the Mooney-Rivlin.

For the quasi-static shear behaviour, no curve fitting was done and the stresses were calculated by simply injecting the coefficients of the Table 5.4, issued from the uniaxial fitting, in the shear stresses expressions of Table 5.3. With this procedure, greater variations were consequently foreseen. For the Neo-Hookean, Mooney-Rivlin and second order polynomial, a linear stress-strain behaviour largely underestimating the test data was observed. For the Yeoh law a more parabolic diagram approaching the real stresses for strain comprised between 0,4 and 0,6 was distinguished. Nevertheless, for both small and large strains, the approximated shear stresses were lower than the experimental ones.



In conclusion, none of the four existing and studied isochoric strain energies were able to properly represent all the three quasi-static tension, compression and shear behaviour of silicone elastomer.



**Figure 5.4-** Evaluation of the curve fittings of the 7<sup>th</sup> cyclic curve in (a) tension, (b) compression and (c) shear – Existing models

As for the quasi-static case, the diagrams of Fig. 5.4 were based on the fitting of the experimental uniaxial 7<sup>th</sup> cyclic curve regrouping tension and compression results. The tensile stress-strain diagram arising from the test and accounting for the Mullins' effect appeared more linear than the first loading. Thus, the small strain behaviour was better modeled with the studied isochoric strain energy forms, except for the second order polynomial, again exhibiting important oscillations. Nevertheless, the Yeoh law gave the better closeness to tensile experimental curve for all the strains range. For compression, even if the stresses at small strains were well described by the four models, only the Mooney-Rivlin was accurate at large strains. For shear, the linearity of the stress-strain diagram was well represented until strains up to 0,6 by the Neo-Hookean, Yeoh and Mooney-Rivlin forms. The polynomial second order was concave and could not approach the experimental data. In conclusion, the Mooney-Rivlin was the most efficient (larger strains range) to characterize the 7<sup>th</sup> cyclic tensile, compressive and shear curves. However, large strains could not be described with this last isochoric strain energy potential.

The capacities of the existing laws to model tension, compression and shear under quasi-static action or after the cyclic stress softening associated to the Mullins' effect were gathered in Table 5.5. None of the laws were able to fully represent without strains conditions, the integrality of the silicone behaviour and therefore a new isochoric strain energy potential had to be developed.

|                        | Quasi-static |                                   |       | Mullins' effect consideration     |                                   |                              |
|------------------------|--------------|-----------------------------------|-------|-----------------------------------|-----------------------------------|------------------------------|
|                        | Tension      | Compression                       | Shear | Tension                           | Compression                       | Shear                        |
| Neo-Hookean            | -            | +<br>(until $\varepsilon = 0.5$ ) | -     | +<br>(until $\varepsilon = 0.4$ ) | +<br>(until $\varepsilon = 0.3$ ) | +<br>(until $\gamma = 0.6$ ) |
| Yeoh                   | -            | +<br>(until $\varepsilon = 0.5$ ) | -     | +                                 | +<br>(until $\varepsilon = 0.3$ ) | +<br>(until $\gamma = 0.6$ ) |
| Mooney-Rivlin          | -            | +                                 | -     | +<br>(until $\varepsilon = 1$ )   | +                                 | +<br>(until $\gamma = 0.6$ ) |
| Polynomial ( $N = 2$ ) | -            | -                                 | -     | -                                 | -                                 | -                            |

**Table 5.5-** Summary of the capacities of the existing isochoric strain energy forms to model the quasi-static and Mullins actions ("+" for accurate representation and "-" for inappropriate)

#### 5.2.1.4 Proposition of a new isochoric formulation

As a new law had to be established, a return to step 7 of the algorithm of Fig. 5.1 was necessary to later repeat the following steps until validation. However, before postulating a new model, a precise understanding of the failure reasons of the existing ones was essential. The study mainly concerned the shear stresses, as they were not fitted with the experimental data and so completely dependent on the mathematical form of the isochoric strain energy potential. From the previous section, the quasi-static and Mullins stress representations were inaccurate in each case and exhibited an almost perfect linear behaviour. To apprehend the origin of this linearity, the most general form, obtained by going backwards in the tree structure of Fig. 5.2, was conserved. The polynomial law with integer exponents was so employed to set the global expression of the shear stresses:

$$\sigma_{12} = 2\gamma \sum_{i+j=1}^N C_{ij} (i+j) \gamma^{2i+2j-2} = 2\gamma [C_{10} + C_{01} + 2(C_{20} + C_{02} + C_{11})\gamma^2 + 3C_{30}\gamma^4 + \dots] \quad (5.9)$$

With the shear stress definition given in equation Eq. (5.9), two problems arose:

- For low polynomial order, the stress was automatically linear. Indeed, for a degree  $N = 1$ , Eq. (5.9) corresponded to the Mooney-Rivlin shear stress exposed in Table 5.3, which was simply linear in terms of strain. Hence, the non-linearity of the experimental quasi-static shear behaviour at small strains and the stress hardening at large strains of the 7<sup>th</sup> cyclic curve ending the Mullins' effect could not have been approached with a small polynomial order.
- Independently of the polynomial order, difficulties came at small strains due to the formulation of the isochoric strain energy itself. By only considering very small deformations under  $\gamma = 0,2$ ,

the quasi-static shear behaviour exposed in Fig. 5.3 (c) presented an inflection point, where a change of concavity occurred. Furthermore, under these very low strains, it was assumed that  $\gamma^2 = \gamma^3 = \dots = \gamma^N = 0$ , as all these monomials in gamma possessing a degree superior or equal to 2 exposed a horizontal tangent at the origin. Thus, with this conjecture, Eq. (5.9) became completely linear in terms of strain:

$$\sigma_{12} = 2\gamma[C_{10} + C_{01} + 2(C_{20} + C_{02} + C_{11})\gamma^2 + 3C_{30}\gamma^4 + \dots] \sim 2(C_{10} + C_{01})\gamma \quad (5.10)$$

The only remaining coefficient  $2(C_{10} + C_{01})$  was consequently assimilated to the tangent at the origin of the curve. Due to this linearity in the equation, it was not possible to characterize the experimental inflexion point. To corroborate this effect with the conducted fitting estimation of the previous section, the polynomial second order form was taken as example, as it possessed the larger number of material constants. The linear and non-linear monomials in  $\gamma$  were separately plotted to apprehend the influence of each material parameter, see Fig. 5.5. The slope of the resulting linear part of the stress was naturally increasing ( $2(C_{10} + C_{01}) > 0$ ) and the resulting non-linear part was convex ( $4(C_{20} + C_{02} + C_{11}) > 0$ ) after the horizontal tangent at the origin. The final polynomial law was achieved by summing the linear and non-linear resulting parts, see Fig. 5.5 (c). This confirmed that the initial stiffness was bore by the linear term and that the stress hardening was accomplished by the non-linear terms.

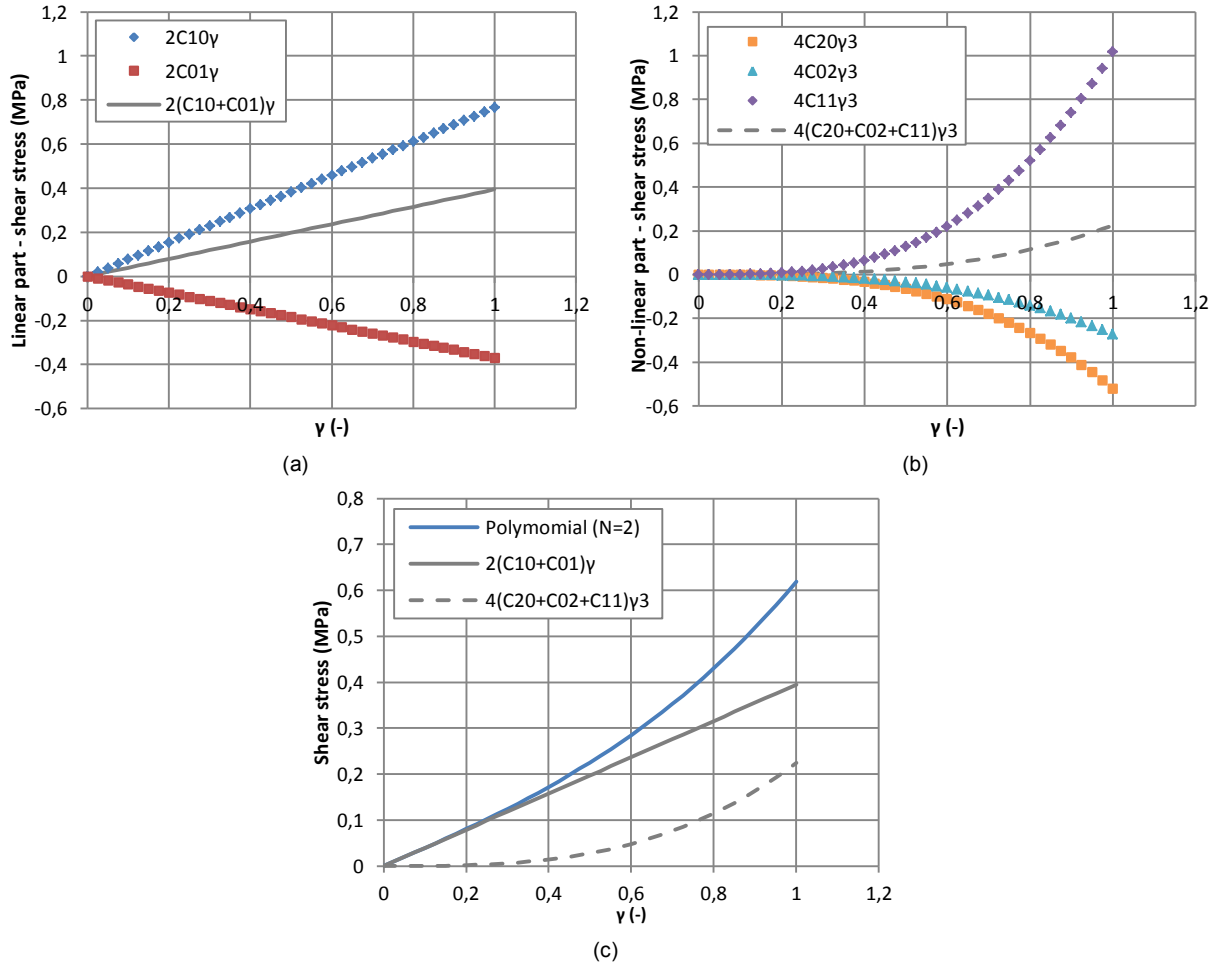


Figure 5.5- Evolution of (a) the linear part and of (b) the non-linear part of the shear stress; (c) Polynomial form obtaining

#### New model proposition (Steps 7, 8, 11 of Fig. 5.1)

Knowing the two aforementioned problems concerning the existing polynomial forms of the isochoric strain energy potential, a new model based completely on the assumption of Eq. (5.4) and partially on

Eq. (5.5) was developed. To account for the non-linearity appearing at small strains, the hypothesis consisting in only expressing the functions  $f_1$  and  $f_2$  as the sums of polynomial terms of  $\bar{I}_1$  and  $\bar{I}_2$  could not be entirely exploited. Therefore, the main idea was not to get rid of the polynomial forms but to complete them. As for the previous identification of the problems, the data in shear were at first investigated. With the superposition principle showed in Fig. 5.5 (c), the expected shear stresses were decomposed in three main parts, i.e. one representing the effects at small strains  $\sigma_{12}^I$ , one at medium strains  $\sigma_{12}^{II}$  and a last one at large strains  $\sigma_{12}^{III}$ , see Eq. (5.11).

$$\sigma_{12} = \sigma_{12}^I + \sigma_{12}^{II} + \sigma_{12}^{III} \quad (5.11)$$

The two last stresses for medium and large strains were directly established by considering the existing isochoric strain energy potentials converted in stresses with the principle of virtual work:

- The stresses  $\sigma_{12}^{II}$  were assimilated to the linear shear stresses provided by the Mooney-Rivlin model, which gave the better concordance to the experimental results as demonstrated in the previous section, see Eq. (5.12) where  $a$  and  $c$  were material constants. This choice was also motivated by the parallelism occurring between the quasi-static stresses issued from the tests and from this model for shear strains from 0,2 up to 0,6 and by the fine fitting to the 7<sup>th</sup> cyclic curve until a strain of 0,6.

$$\sigma_{12}^{II} = 2(a + c)\gamma \quad (5.12)$$

- The stresses  $\sigma_{12}^{III}$  implied the use of non-linear terms in  $\gamma^3$  to approach the stress hardening manifesting at large strains. In order to limit the determination of the material constants to a minimum and with regards to the identical behaviour of the functions plotted on Fig. 5.5 (b), only one non-linear term was allocated to these stresses, see Eq. (5.13) where  $b$  was a material constant. This induced a polynomial of one deviatoric invariant raised to square in the expression of the isochoric strain energy.

$$\sigma_{12}^{III} = 4b\gamma^3 \quad (5.13)$$

After these two choices and without the definition of the first stress of Eq. (5.11), the total shear curve was not different to the one obtained in Fig. 5.5 (c) for the second order polynomial model. Hence, the definition of  $\sigma_{12}^I$  was essential to reproduce the experimental inflection point. The function describing these last stresses had to obey certain rules:

$$\begin{aligned} \sigma_{12}^I(\gamma = 0) &= 0 \\ \lim_{\gamma \rightarrow \infty} \sigma_{12}^I(\gamma) &= 0 \end{aligned} \quad (5.14 \text{ a})$$

$$\left\{ \frac{\delta \sigma_{12}^I(\gamma)}{\delta \gamma} > 0 \quad \text{for } \gamma \leq \gamma_0 \right. \quad (5.14 \text{ b})$$

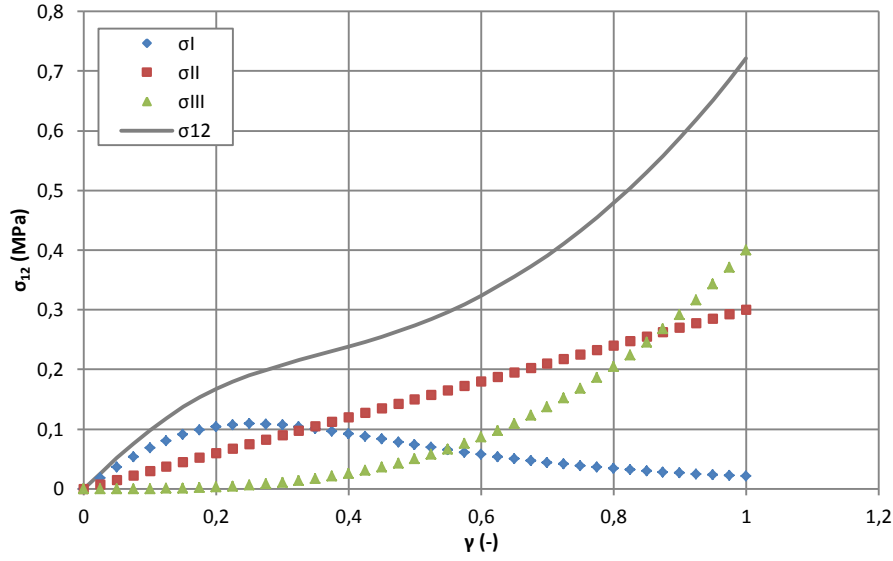
$$\left\{ \frac{\delta \sigma_{12}^I(\gamma)}{\delta \gamma} < 0 \quad \text{for } \gamma > \gamma_0 \right. \quad (5.14 \text{ c})$$

Several mathematical functions were investigated and the one giving the best adequacy to these rules was of the form:

$$\sigma_{12}^I(\gamma) = \frac{2d\gamma}{(\gamma^2 + e)^2} \quad (5.15)$$

With  $d$  and  $e$  non-nil positive real constants and  $\gamma_0 = \sqrt{e/3}$ . The denominator was set to a power 2 to accelerate the convergence to 0 and so diminish the impact of these stresses at large strains. This function was plotted with  $d = 0,015$  and  $e = 0,2$  as example on Fig. 5.7. This allowed checking the conditions given in Eq. (5.14 c), i.e. a first increase until  $\gamma_0$  followed by a decreased to a stress value close to zero. The two other stresses  $\sigma_{12}^{II}$  and  $\sigma_{12}^{III}$  were also drawn with random material constants

on the diagram of Fig. 5.7 for complete validation of the overall combination. The behaviour obtained by summing the evoked stresses was judged more adequate to represent the shear experimental results.



**Figure 5.6-** Example of superposition of the three shear stresses representing the new proposed model

The full equation of the shear stress was then achieved by injecting the three established individual stresses in Eq. (5.11). A last reformulation was also operated to get an expression comparable to the one recorded in Table 5.2 for the shear tests.

$$\sigma_{12} = 2(a + c)\gamma + 4b\gamma^3 + \frac{2d\gamma}{(\gamma^2 + e)^2} = 2\gamma \left[ a + c + 2b\gamma^2 + \frac{d}{(\gamma^2 + e)^2} \right] = 2\gamma [f_1(\bar{I}_1) + f_2(\bar{I}_2)] \quad (5.16)$$

As the final objective was to propose an isochoric strain energy potential, from which could be derived all types of stress, the order of the steps 5 to 6 of the algorithm of Fig. 5.1 was inverted with the above Eq. (5.15) as starting point. A proper identification of the functions  $f_1(\bar{I}_1)$  and  $f_2(\bar{I}_2)$  was consequently inevitable. With the Mooney-Rivlin definition of the stresses at medium strains, one material constant had to be attributed to function  $f_1(\bar{I}_1)$  while the other to function  $f_2(\bar{I}_2)$ . For the two other stresses at small and large strains, no particular belonging to  $f_1$  or  $f_2$  was imposed. Therefore several trials were conducted and so different isochoric strain energy functions were postulated to later be compared to the uniaxial experimental results. The better concordance was found with the following repartition:

$$f_1(\bar{I}_1) = \frac{\delta W_{iso}}{\delta \bar{I}_1} = a + 2b\gamma^2 \quad f_2(\bar{I}_2) = \frac{\delta W_{iso}}{\delta \bar{I}_2} = c + \frac{d}{(\gamma^2 + e)^2} \quad (5.17)$$

With the expression of the deviatoric invariants for shear experiments, exposed in Table 5.2, and by integration of these two functions, two parts of the isochoric strain energy were obtained:

$$W_{iso}(\bar{I}_1) = a(\bar{I}_1 - 3) + b(\bar{I}_1 - 3)^2 + y \quad W_{iso}(\bar{I}_2) = c(\bar{I}_2 - 3) - \frac{d}{(\bar{I}_2 - 3 + e)} + z \quad (5.18)$$

With  $y$  and  $z$  integration constants. The mathematical equation of the new isochoric strain energy was finally accomplished by summing the two terms of Eq. (5.18):

$$W_{iso} = a(\bar{I}_1 - 3) + b(\bar{I}_1 - 3)^2 + c(\bar{I}_2 - 3) - \frac{d}{(\bar{I}_2 - 3 + e)} + x \quad (5.19)$$

With  $x = y + z$  integration constant. Nevertheless, the normalization condition, for which the energy potential had to be nil under no deformation, was not respected with the above Eq. (5.19). Therefore, the constant  $x$  was chosen equal to  $d/e$  to cancel the effect of the last term for the description of the stress at small strains, see Eq. (5.20).

$$W_{iso} = a(\bar{I}_1 - 3) + b(\bar{I}_1 - 3)^2 + c(\bar{I}_2 - 3) - \frac{d}{(\bar{I}_2 - 3 + e)} + \frac{d}{e} \quad (5.20)$$

Knowing the final formulation of the isochoric strain energy, the steps 8 and 11 of the algorithm of Fig. 5.1 were repeated again, see Table 5.6.

| $W_{iso}$ model                  | UNIAXIAL TEST                                                                                                                                                            | SHEAR TEST                                                                      |
|----------------------------------|--------------------------------------------------------------------------------------------------------------------------------------------------------------------------|---------------------------------------------------------------------------------|
| New proposed model<br>Eq. (5.20) | $\sigma_{11} = 2(1 - \lambda_1^{-3}) \left[ a\lambda_1 + 2b\lambda_1(2\lambda_1^{-1} + \lambda_1^2 - 3) + c + \frac{d}{(\lambda_1^{-2} + 2\lambda_1 - 3 + e)^2} \right]$ | $\sigma_{12} = 2(a + c)\gamma + 4b\gamma^3 + \frac{2d\gamma}{(\gamma^2 + e)^2}$ |

**Table 5.6-** Stresses reformulations acc. to the tests types for the proposed isochoric strain potential (step 8 and 11 of Fig. 5.1)

### Material constants evaluations (Step 9 of Fig. 5.1)

In contrary to the classical polynomial laws of section 5.2.1.3, both stresses of Table 5.6 were not linear in terms of the material constants, i.e. the last term regrouped two coefficients. Hence, as a simple linear least square method could not be used to minimize the relative error in stresses, the non-linear least square of Levenberg-Marquardt [5.3] was employed. This method was based on a descent direction iterative process for which the constants to be determined were first assumed. At the end of each iterative step, small increments, calculated from the minimization of the error function, were added to these constants. This operation was repeated until no further evolution was reached. The procedure was carried out on the uniaxial experimental data regrouping tension and compression results (step 9 of Fig. 5.1). The measure of the error was done with the help of the following function:

$$F(x_j) = \frac{1}{2} \sum_{i=1}^n [\sigma_i^{Test} - \sigma_i^{Th}(x_j)]^2 = \frac{1}{2} \sum_{i=1}^n [f_i(x_j)]^2 = \frac{1}{2} \mathbf{f}^T \mathbf{f} \quad (5.21)$$

$n$  the total number of experimental uniaxial stress-strain data,  
 $\sigma_i^{Th}$  the expression of theoretical uniaxial stress (Table 5.6) associated to the  $i^{\text{th}}$  strain,  
 With  $\sigma_i^{Test}$  the experimental uniaxial stress associated to the  $i^{\text{th}}$  strain,  
 $x_j$  the material constants to be determined ( $x_1 = a$ ;  $x_2 = b$ ; ...),  
 $\mathbf{f}$  the column vector of the  $n$  differences between testing and theoretical stresses.

In order to simplify the notations, a matrix arrangement was considered. The material constants to be determined and the increments to be added at the end of each iterative step were stored under column vectors respectively noted  $\mathbf{x}$  and  $\mathbf{h}$ . The variations in the error functions were symbolized by:

$$F(\mathbf{x} + \mathbf{h}) = \frac{1}{2} \mathbf{f}(\mathbf{x} + \mathbf{h})^T \mathbf{f}(\mathbf{x} + \mathbf{h}) \quad (5.22)$$

The vector  $\mathbf{f}$  was composed by functions differentiable and sufficiently smooth to apply the Taylor expansion, so that Eq. (5.22) became:

$$F(\mathbf{x} + \mathbf{h}) = \frac{1}{2} [\mathbf{f}(\mathbf{x}) + \mathbf{J}(\mathbf{x})\mathbf{h}]^T [\mathbf{f}(\mathbf{x}) + \mathbf{J}(\mathbf{x})\mathbf{h}] \quad (5.23)$$

With  $\mathbf{J}(\mathbf{x})$  the Jacobian,  $(\mathbf{J}(\mathbf{x}))_{ij} = \frac{\delta f_i}{\delta x_j}(\mathbf{x})$ .

By developing Eq. (5.23) and by observing that  $F(\mathbf{x}) = (1/2) \mathbf{f}(\mathbf{x})^T \mathbf{f}(\mathbf{x})$ , it was then possible to set:

$$F(\mathbf{x} + \mathbf{h}) = F(\mathbf{x}) + \mathbf{h}^T \mathbf{J}(\mathbf{x})^T \mathbf{f}(\mathbf{x}) + \frac{1}{2} \mathbf{h}^T \mathbf{J}(\mathbf{x})^T \mathbf{J}(\mathbf{x}) \mathbf{h} \quad (5.24)$$

Finally, as the constants vector  $\mathbf{x}$  was always known either from the first initial assumption or from the previous iteration, the above equation was minimized with regards to the increments vector  $\mathbf{h}$ . This minimization was achieved by nullifying the derivative of Eq. (5.24).

$$F'(\mathbf{x} + \mathbf{h}) = \mathbf{J}(\mathbf{x})^T \mathbf{f}(\mathbf{x}) + \mathbf{J}(\mathbf{x})^T \mathbf{J}(\mathbf{x}) \mathbf{h} = 0 \quad (5.25)$$

With this last equation, the increments vector  $\mathbf{h}$  minimizing the error function could have been easily deducted. However, a damping factor  $\mu$  was inserted to increase the convergence rate of the method. This factor each time evolved with the iteration and was selected according to the maximum value of the matrix  $\mathbf{J}^T \mathbf{J}$  such as  $\mu = 10^{-6} \max\{(\mathbf{J}^T \mathbf{J})_{ij}\}$ . Thus, the final expression of the vector  $\mathbf{h}$  was:

$$\mathbf{h} = (\mathbf{J}(\mathbf{x})^T \mathbf{J}(\mathbf{x}) + \mu \mathbf{I})^{-1} (-\mathbf{J}(\mathbf{x})^T \mathbf{f}(\mathbf{x})) \quad (5.26)$$

Where  $\mathbf{I}$  was the identity matrix. With the above Eq. (5.26), the calculation of the  $\mathbf{h}$  vector was simply realized in an Excel file. As all the required data were exposed, the complete Levenberg-Marquardt algorithm, leading to the estimation of the five material constants, was summarized in Fig. 5.7. The repetition of the procedure was repeated until each components of the vector  $\mathbf{h}$  did not present a variation of more than  $10^{-5}$ .

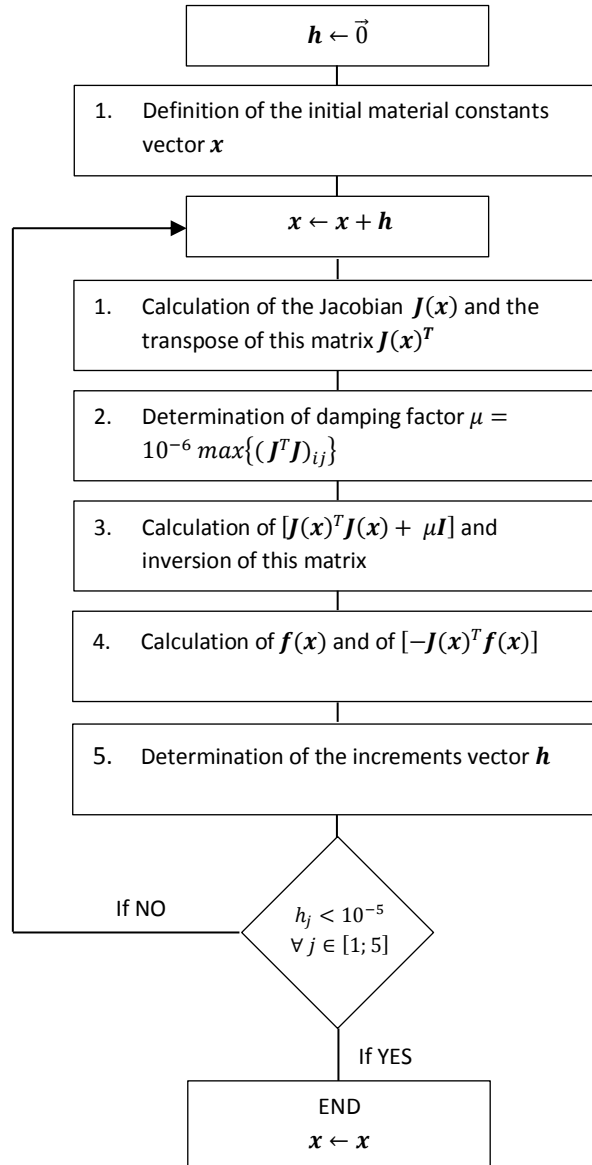


Figure 5.7- Algorithm of the Levenberg-Marquardt method for the determination of the material coefficients

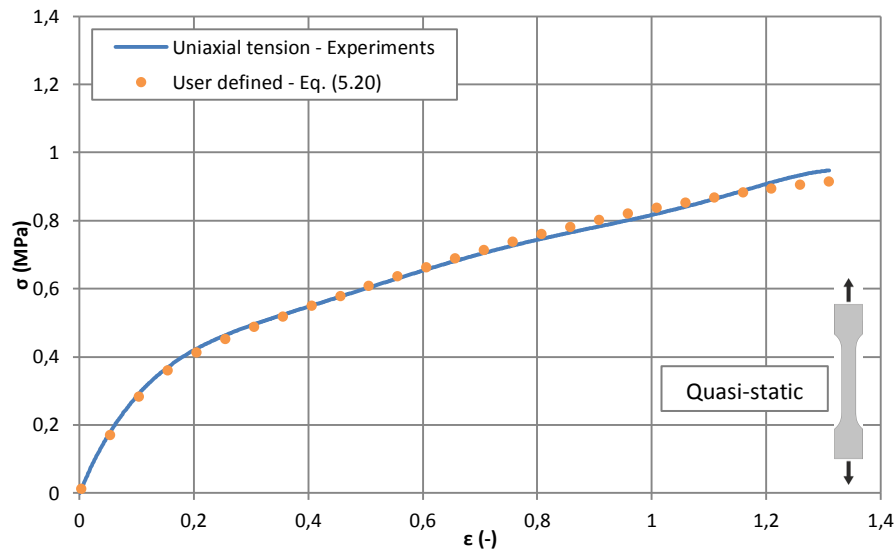
This algorithm was applied on the uniaxial test results for the quasi-static and the Mullins' effect cases. The five material constants associated to each types of action were recorded in Table 5.7.

| $W_{iso}$ model                  | Action       | Material constants (-) |          |         |         |         |
|----------------------------------|--------------|------------------------|----------|---------|---------|---------|
|                                  |              | $a$                    | $b$      | $c$     | $d$     | $e$     |
| New proposed model<br>Eq. (5.20) | Quasi-static | 0,24415                | -0,00751 | 0,04113 | 0,01577 | 0,22733 |
|                                  | Mullins      | 0,05776                | 0,02106  | 0,07467 | 0,04177 | 0,49856 |

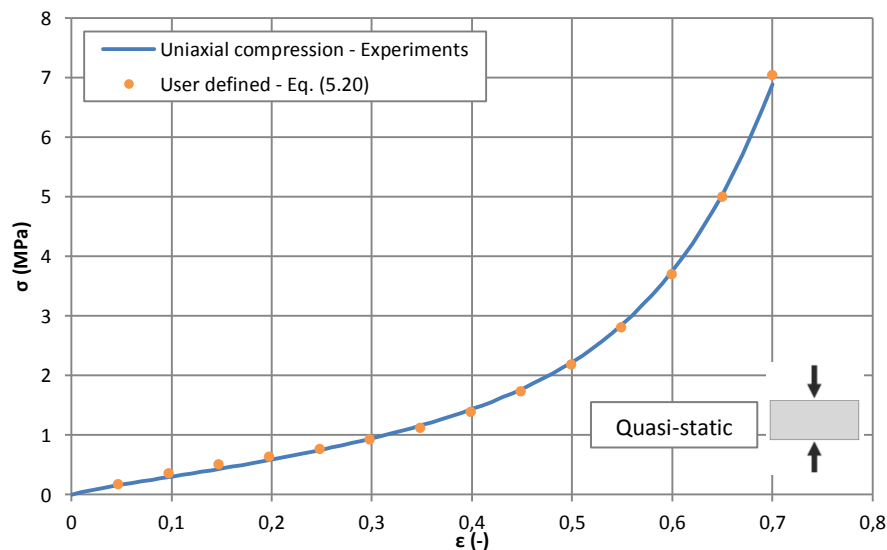
**Table 5.7-** Material coefficients associated to the self-developed isochoric strain energy for the two types of action

### Evaluation of the model (Steps 10, 12 of Fig. 5.1)

For validation of the new proposed isochoric strain energy potential, a distinction between the types of action was necessary. Graphical comparisons between the quasi-static experimental results and the theoretical stresses of the new model were envisaged. These last theoretical stresses were calculated by injecting the first set of coefficients of Table 5.7 in the uniaxial and shear stress expressions of Table 5.6. A separation between the tensile and compressive data was again done to better appraise the existing differences. The three diagrams corresponding to the three types of behaviour were given in Fig.5.8.

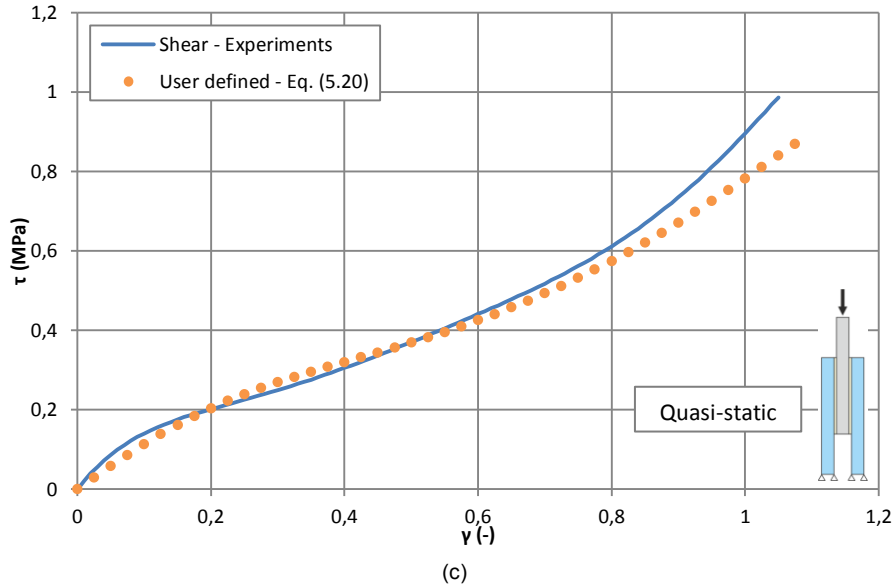


(a)



(b)



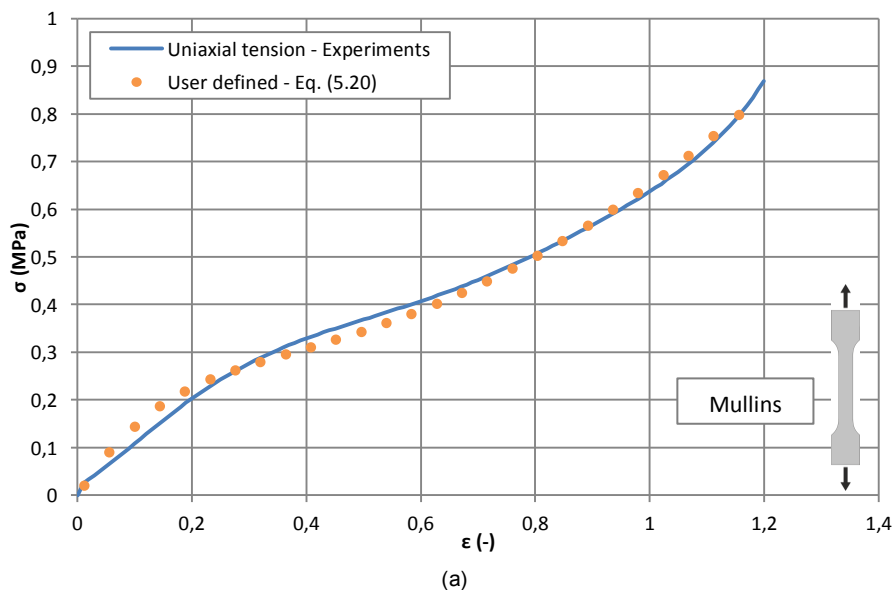


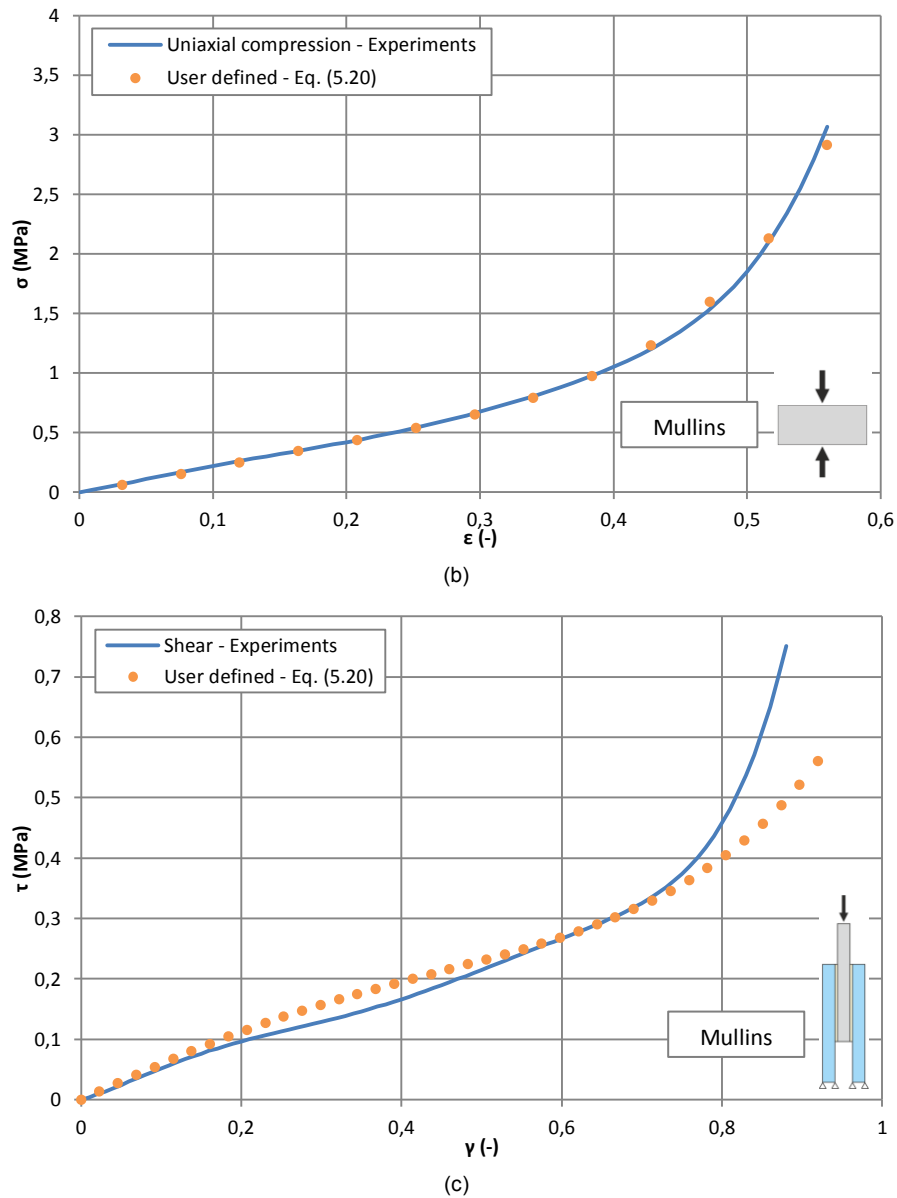
**Figure 5.8-** Evaluation of the curve fittings for quasi-static (a) tension, (b) compression and (d) shear – User model

As already mentioned, the three above figures were achieved by fitting the uniaxial experimental data regrouping tension and compression. In consequence, good concordances to these two types of behaviour were expected. The graphical comparisons between test and theory of Fig. 5.8 (a) and (b) allowed confirming this postulate. Indeed, the estimated tensile and compressive stresses matched perfectly the real stresses for all the strains ranges. For the tensile behaviour, the strong non-linearity at small deformations was clearly better represented with the new model than with the existing ones showed in Fig. 5.3 (a).

Even if no curve fitting was carried out on the shear experimental stress-strain data for the material constants determination, a good correlation was obtained by injecting the coefficients issued from the uniaxial quasi-static analysis into the shear stress equation of Table 5.6. The two curves were superposed until a strain of 0,8 and then a slight divergence was found. The difference in stresses appeared at a stress of about 0,6MPa, i.e. approximately the maximum allowable value determined from the shear experiments. Furthermore, compared to the existing laws, the proposed model was undoubtedly closer.

The same graphical verification was conducted with the tests data concerning the Mullins' effect, for which the second set of coefficients of Table 5.7 was injected in the equations of Table 5.6.





**Figure 5.9-** Evaluation of the curve fittings of the 7<sup>th</sup> cyclic curve in (a) tension, (b) compression and (c) shear – User model

The tensile and compressive results, accounting for the Mullins' effect, were well represented by the proposed model over all the strains ranges. This was not achieved by the existing models, which partially represented the behaviour until specific strains, see Table 5.5. For the shear, the estimated stresses were relatively close to the test results until a strain of 0,75. Then, as for the quasi-static behaviour, a divergence was observed. For this action, the principal difference with the exiting strain energy potentials came from the strains ranges. Indeed, a correct fitting of the 7<sup>th</sup> cyclic shear curve was only reached until a strain of 0,6 for the existing laws.

In conclusion to the two evaluations, the developed isochoric strain energy potential was more suited to model the quasi-static and the Mullins' effect behaviour of silicone elastomer subjected to tension, compression and shear.

## 5.2.2 Formulation of the volumetric part of the strain energy potential

To find the most appropriate form of the volumetric part of the strain energy potential, the results of the oedometric tests were needed. For this type of experiment, volume variations were recorded, so that  $W_{vol}(J)$  was not nil. With this second study, the complete form of Eq. (5.1) could thus be known.

### 5.2.2.1 Algorithm of resolution

The procedure leading to the determination of the volumetric strain energy is presented in Fig. 5.10. A separation in two parts could have been noticed:

- A first theoretical part during which the isochoric stress was calculated based on the proposed isochoric form of Eq. (5.20) and on the steps 1 to 5 of the algorithm of Fig. 5.1. The quasi-static coefficients exposed in Table 5.7 were considered. Hence, for this computational part, the isochoric stress was known and no fitting had to be realized.

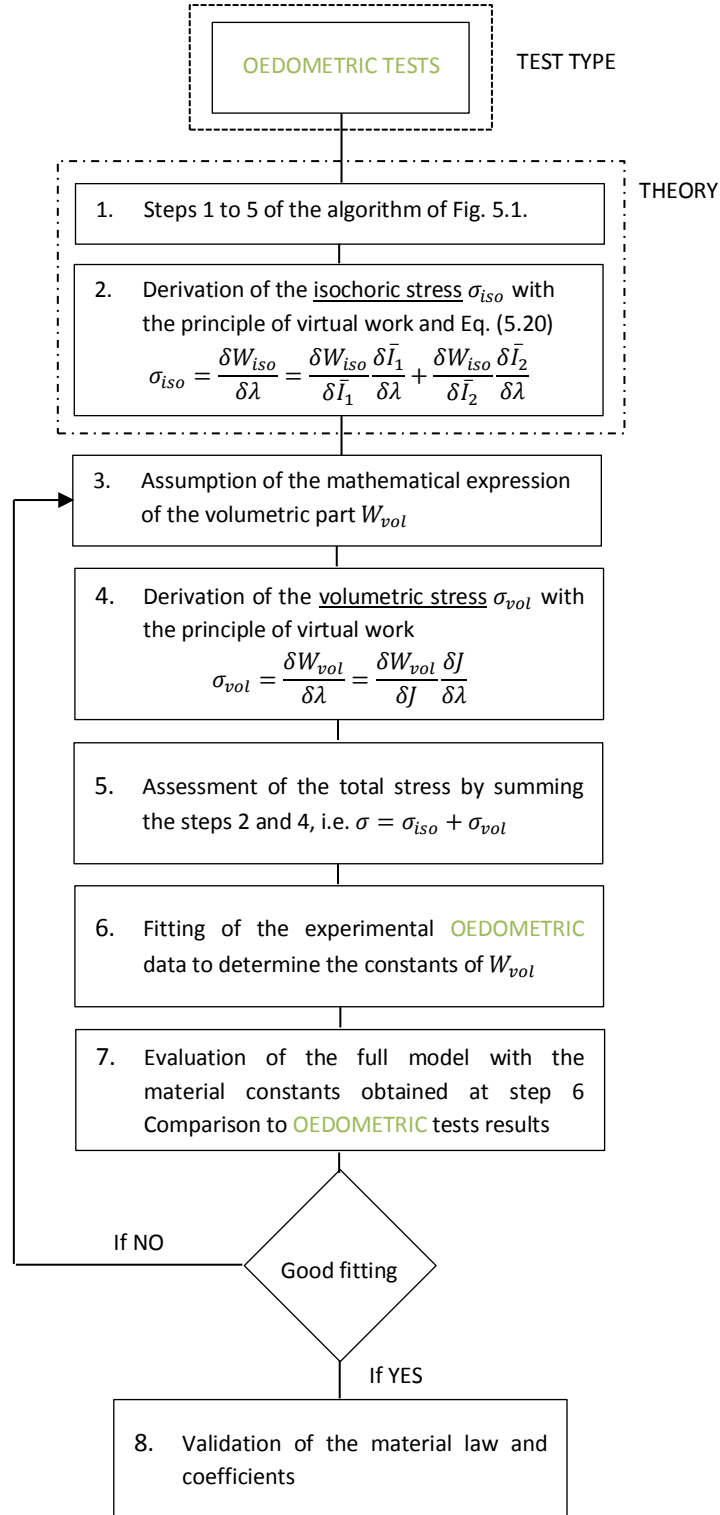


Figure 5.10- Algorithm for the determination of the strain energy volumetric part

- An assumption and trial part, for which the existing volumetric strain energy potential of Table 2.9 were fitted to the oedometric experimental data and compared to the curve issued from the tests for validation.

### 5.2.2.2 Evaluation of the stresses for the oedometric tests (Steps 1, 2 and 4 of Fig. 5.10)

To fit and confront identical data, the isochoric strain energy potential was converted to stress with the principle of virtual work and a partial formulation of the volumetric stress was also deduced, see Table 5.8. After finalizing these steps, no further continuation could have been made without choosing a volumetric strain energy equation.

| OEDOMETRIC TEST                                                                                                                                                                                                                                                                                                                                  |
|--------------------------------------------------------------------------------------------------------------------------------------------------------------------------------------------------------------------------------------------------------------------------------------------------------------------------------------------------|
|                                                                                                                                                                                                                                                                                                                                                  |
| $\bar{\mathbf{F}} = \begin{pmatrix} \lambda_1 & 0 & 0 \\ 0 & 1 & 0 \\ 0 & 0 & 1 \end{pmatrix}$                                                                                                                                                                                                                                                   |
| $J = \det(\bar{\mathbf{F}}) = \lambda_1$                                                                                                                                                                                                                                                                                                         |
| $\bar{\bar{\mathbf{F}}} = J^{-1/3} \bar{\mathbf{F}} = \begin{pmatrix} \lambda_1^{2/3} & 0 & 0 \\ 0 & \lambda_1^{-1/3} & 0 \\ 0 & 0 & \lambda_1^{-1/3} \end{pmatrix}$                                                                                                                                                                             |
| $\bar{\mathbb{B}} = \bar{\bar{\mathbf{F}}} \bar{\bar{\mathbf{F}}}^T = \bar{\mathbf{F}}^2 = \begin{pmatrix} \lambda_1^{4/3} & 0 & 0 \\ 0 & \lambda_1^{-2/3} & 0 \\ 0 & 0 & \lambda_1^{-2/3} \end{pmatrix}$                                                                                                                                        |
| $\bar{I}_1(\bar{\mathbb{B}}) = \lambda_1^{4/3} + 2\lambda_1^{-2/3}$ $\bar{I}_2(\bar{\mathbb{B}}) = \lambda_1^{-4/3} + 2\lambda_1^{2/3}$                                                                                                                                                                                                          |
| $\sigma_{iso} = \left[ a + 2b \left( \lambda_1^{4/3} + 2\lambda_1^{-2/3} - 3 \right) \right] \left[ \frac{4}{3} \lambda_1^{1/3} - \frac{4}{3} \lambda_1^{-5/3} \right]$ $+ \left[ c + \frac{d}{\left( \lambda_1^{-4/3} + 2\lambda_1^{2/3} - 3 + e \right)^2} \right] \left[ \frac{4}{3} \lambda_1^{-1/3} - \frac{4}{3} \lambda_1^{-7/3} \right]$ |
| $\sigma_{vol} = \frac{\delta W_{vol}}{\delta J}$                                                                                                                                                                                                                                                                                                 |

Table 5.8- Derivation of the isochoric and volumetric stresses for the oedometric test (step 1, 2 and 4 of Fig. 5.10)

### 5.2.2.3 Selection of the volumetric part

#### Existing models (Steps 3 and 4 of Fig. 5.10)

Three of the four volumetric models presented in section 2.4.2.2 were envisaged, as they necessitated the determination of only one factor. Instead of carrying the steps 3 to 7 for each material law one after another, they were studied in parallel for a direct selection of the best fitting one. These models were gathered in Table 5.9 and the volumetric stresses were calculated for each.

|                       | Sussman and Bathe [2.60]<br>SB    | Simo, Taylor and Pister [2.61]<br>STP               | Simo and Miehe [2.63]<br>SM                                    |
|-----------------------|-----------------------------------|-----------------------------------------------------|----------------------------------------------------------------|
| $W_{vol}$ models      | $W_{vol} = \frac{K}{2}(J - 1)^2$  | $W_{vol} = \frac{K}{2}(\ln(J))^2$                   | $W_{vol} = \frac{K}{2}(J^2 - 1 - 2\ln(J))$                     |
| Stress $\sigma_{vol}$ | $\sigma_{vol} = K(\lambda_1 - 1)$ | $\sigma_{vol} = K \frac{\ln(\lambda_1)}{\lambda_1}$ | $\sigma_{vol} = K\left(\lambda_1 - \frac{1}{\lambda_1}\right)$ |

**Table 5.9-** Stress reformulations of the different volumetric strain potentials (step 4 of Fig. 5.10)

### Material constant evaluation (Step 6)

The total theoretical stresses for the oedometric tests were obtained by simply summing the common isochoric stresses to the volumetric stresses for each of the three selected models (Fig. 5.10 – step 5). As the coefficients of the isochoric strain energy potential were already evaluated with volume-preserving tests, the associated stresses were known. Consequently, only one factor  $K$ , belonging to the volumetric part, had to be assessed. Furthermore, the volumetric expressions of the stresses were linear in terms of this last constant. Therefore, a simple linear regression, minimizing the relative error between the experimental stresses and the total theoretical stresses, was conducted. This procedure, corresponding to step 6 of the algorithm, was performed with the following measure of the relative error:

$$E = \frac{1}{2} \sum_{i=1}^n (\sigma_i^{Test} - \sigma_i^{Th})^2 = \frac{1}{2} \sum_{i=1}^n (\sigma_i^{Test} - \sigma_i^{iso} - \sigma_i^{vol})^2 \quad (5.27)$$

$n$  the total number of experimental uniaxial stress-strain data,

With  $\sigma_i^{Test}$  the experimental stress associated to the  $i^{th}$  strain,

$\sigma_i^{Th}$  the theoretical stress associated to the  $i^{th}$  strain, with  $\sigma_i^{Th} = \sigma_i^{iso} + \sigma_i^{vol}$ .

The material constant, of each law of Table 5.9, was then calculated by deriving the relative error  $E$  of Eq. (5.27) towards the unknown factor  $K$ :

$$\frac{\delta E}{\delta K} = 0 \quad (5.28)$$

With the linearity of the volumetric stress  $\sigma_{vol} = K g(\lambda)$ , a global solution was established for the three models and implemented in an Excel file, see Eq. (5.29).

$$K = \frac{\sum g(\lambda_i) [\sigma_i^{Test} - \sigma_i^{iso}]}{\sum g(\lambda_i)} \quad (5.29)$$

Only the quasi-static coefficients of the isochoric strain energy were used, as the oedometric tests were also carried under this type of action. However, as already mentioned, it was assumed that the factor  $K$  was invariant towards the quasi-static or cyclic actions for the oedometric set-up, due to the very small imposed strains. Therefore, the value of the material constant exposed in Table 5.10 could be employed to characterize the instantaneous response of the material or the impact of the Mullins' effect. Compared to the isochoric strain energy potential, the material coefficients of the volumetric part  $K$  were quite higher. So even under very small elongation, the ascendancy of these coefficients was such that the isochoric stresses were quasi-negligible.

| $W_{vol}$ models              | $K (-)$   |
|-------------------------------|-----------|
| Sussman and Bathe - SB        | 367,04682 |
| Simo, Taylor and Pister - STP | 381,55733 |
| Simo and Miehe - SM           | 185,89864 |

**Table 5.10-** Material coefficient associated to each model of Table 5.9 (step 6 of Fig. 5.10)

### Evaluation of the existing models (Steps 7 and 8 of Fig. 5.10)

Graphical comparisons between the experimental oedometric tests and the theoretical stresses were achieved by injecting the quasi-static coefficients of Table 5.7 into the isochoric stress expression of Table 5.8 and the coefficients of Table 5.10 into the volumetric stress equations of Table 5.9. All the corresponding curves were plotted on Fig. 5.11.

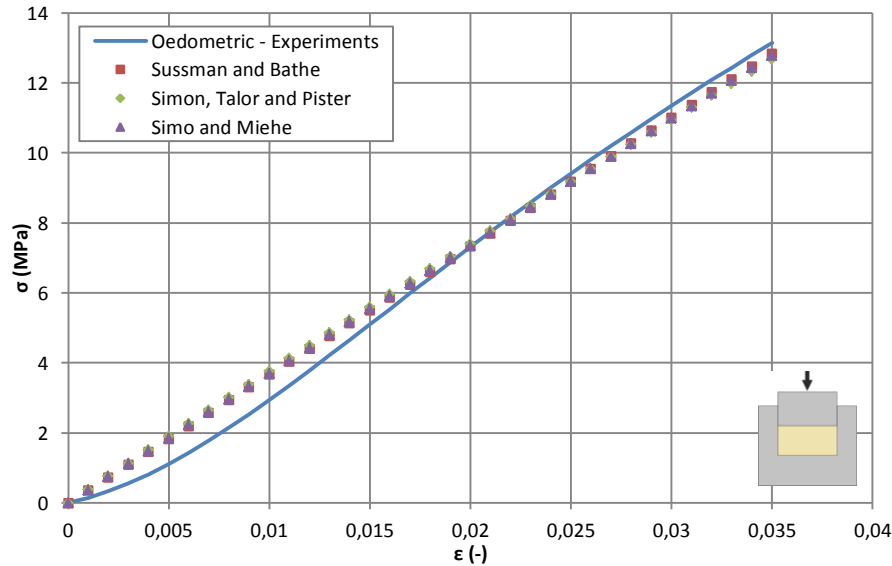


Figure 5.11- Evaluation of the oedometric curve fittings for the different volumetric models

The three estimated curves were linear for the small range of deformations and well superposed. Despite the fact that they slightly overestimated the stress for strains until 0,015, they represented correctly the experimental oedometric results. Thus, the three examined volumetric energy potentials could be employed to model the restrained behaviour of silicone elastomer. Nevertheless, the law of Sussman and Bathe [2.60] was chosen for its simplicity and its common used in finite element software, such as Abaqus®.

### 5.2.3 Final proposed model

The self-developed isochoric strain energy potential was summed to the volumetric energy potential of Sussman and Bathe to propose a model describing the selected silicone elastomer, see Table 5.11. This new law could be employed to characterize the quasi-static behaviour as well as to account for the Mullins' effect by representing the last stress-strain curve ending it. The coefficients associated to these two actions were naturally different, except for the material constant of the volumetric part.

| Strain energy potential for silicone elastomer ( $W = W_{iso} + W_{vol}$ )                                                          |         |          |         |         |         |           |
|-------------------------------------------------------------------------------------------------------------------------------------|---------|----------|---------|---------|---------|-----------|
| $W = a(\bar{I}_1 - 3) + b(\bar{I}_1 - 3)^2 + c(\bar{I}_2 - 3) - \frac{d}{(\bar{I}_2 - 3 + e)} + \frac{d}{e} + \frac{K}{2}(J - 1)^2$ |         |          |         |         |         |           |
| Coefficients                                                                                                                        | $a$     | $b$      | $c$     | $d$     | $e$     | $K$       |
| Quasi-static                                                                                                                        | 0,24415 | -0,00751 | 0,04113 | 0,01577 | 0,22733 | 367,04682 |
| Mullins' effect                                                                                                                     | 0,05776 | 0,02106  | 0,07467 | 0,04177 | 0,49856 |           |

Table 5.11- Final proposed model with corresponding coefficients for quasi-static actions and Mullins' effect consideration

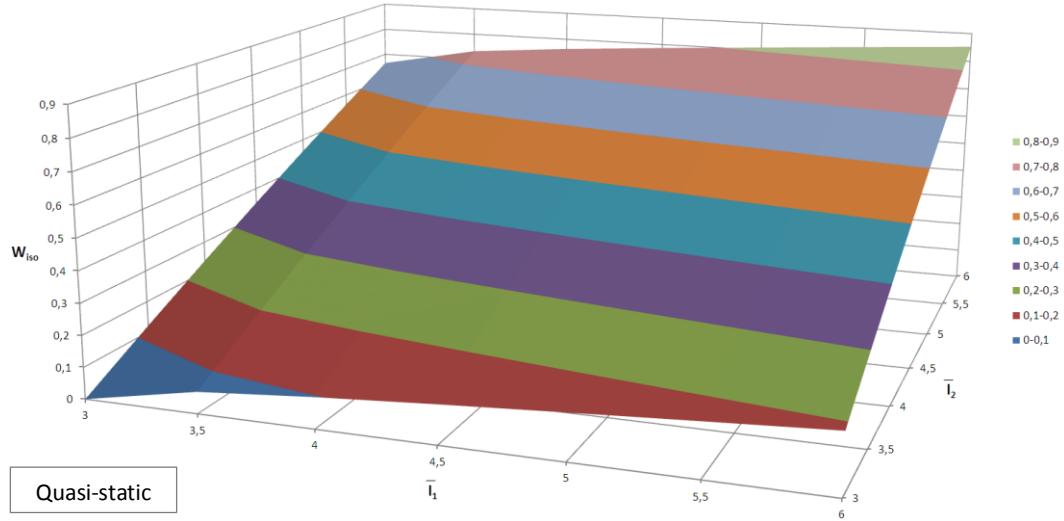
The full form of the strain energy potential and the two sets of material coefficients were established with the help of simple tests, i.e. uniaxial tension, compression, shear and oedometric experiments. Therefore, to ensure of the validity of the law for general loading types, the normalization and the positivity conditions had to be checked:

- Normalization condition

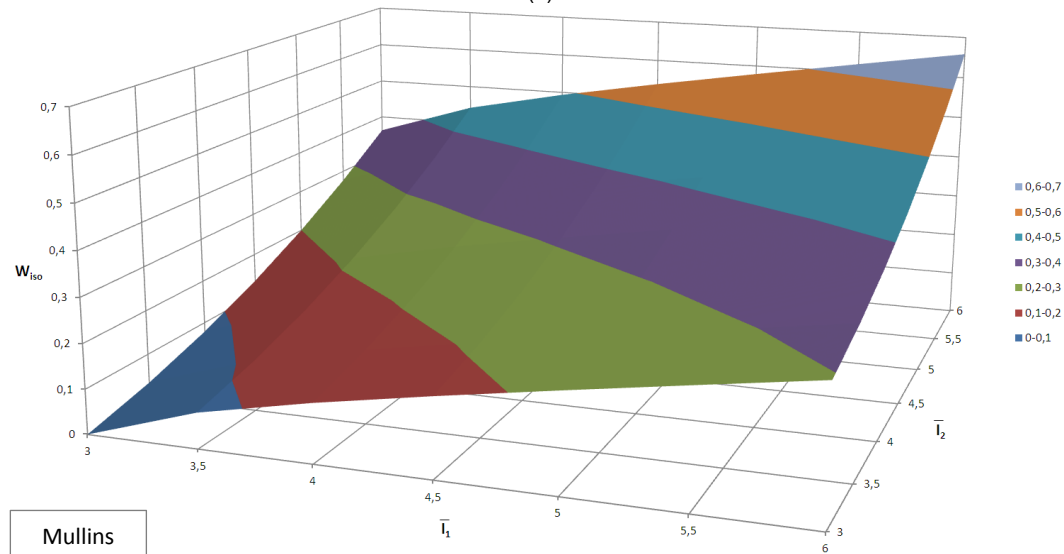
The normalization condition implied that the strain energy potential had to be nil, when no deformation was imposed on the material, i.e.  $W(\bar{\mathbf{I}}) = 0$  with  $\bar{\mathbf{I}}$  the identity tensor. With no regards to the material coefficients, the isochoric strain energy potential respected this condition with the two last terms compensating each other. In addition, for a non-deformed state, the volume was preserved and the Jacobian of the transformation was equal to one. This induced a nil volumetric strain energy potential independently of the constant  $K$ . Consequently, the normalization condition was always verified with the proposed constitutive material law.

- Positivity condition

The positivity condition implied that the strain energy function should increase with the deformation, i.e.  $W(\bar{\mathbf{F}}) = W(\bar{\mathbf{I}}_1 + \bar{\mathbf{I}}_2 + J) > 0$ . With the positive value of the coefficient  $K$  and the mathematical formulation of the Jacobian, the positivity of the volumetric strain energy potential was achieved. Hence, only the positivity of the isochoric strain energy had to be analysed for the two sets of coefficients. To confirm this criterion for the quasi-static and the Mullins definition, the isochoric part was plotted versus the two invariants  $\bar{\mathbf{I}}_1$  and  $\bar{\mathbf{I}}_2$ , see Fig. 5.12. Both diagrams validated the positivity and showed an increase of the isochoric strain energy with the increase of the deviatoric invariants.



(a)



(b)

**Figure 5.12-** Verification of the positivity condition for the quasi-static and the Mullins' effect coefficients

### 5.3 ACRYLIC MATERIAL LAW

As for the determination of a silicone constitutive material law, only the quasi-static properties of the UV-acrylic adhesive were examined. Three different types of experiments, i.e. uniaxial tension on dog-bone specimens, modified shear on adhesive alone and push-out shear tests with the presence of adherents, were conducted. A strong dependency to the loading rate was observed in each case. Furthermore, a link between the modified shear and the push-out shear results was found, i.e. the initial stiffness of the modified shear experiments always corresponded to the stiffness of the push-out shear tests for a given loading rate. Thus, the characterization of the modified shear behaviour under various loading rate could be sufficient to apprehend the behaviour of push-out shear assemblies. In consequence, the two sets of data to be analyzed were the tensile stress-strain diagrams and the modified shear curves. With regards to the respective test layouts, the two experiments were carried out on non-coincident loading rates and links, at small strains, between the elastic and shear modulus could not be established. Therefore, they were studied separately in order to find one-dimensional constitutive models.

#### 5.3.1 Tension characterization

##### 5.3.1.1 One-dimensional material law and essential prerequisites

As aforementioned, the tensile tests results on the UV-acrylic, limiting to the breakage for brittle curves type I or to the necking for curves type II, demonstrated dependency to the loading rate, i.e. higher was the loading rate and higher was the stress-strain diagram. Nevertheless, the behaviour of this adhesive was divided in two parts, evolving both with the loading rate, i.e. a first linear elastic part followed by non-linear viscoelastic properties. One of the models presented in section 2.4.3.2 able to account for this effect was the Ramberg-Osgood model, see the following Eq. (5.30).

$$\varepsilon = \frac{\sigma}{E} + K \left( \frac{\sigma}{E} \right)^n \quad (5.30)$$

With  $K$  and  $n$  material constants and  $E$  the Young modulus. McLellan [2.71] supposed, with the help of tensile experiments, the dependencies of  $E$  and  $K$  to the loading rate and also the invariance of the factor  $n$ . However, for the current acrylic adhesive, no assumption was a priori made. The full form of Eq. (5.30) was conserved with a differentiation in loading rate operated on the data only, i.e. the two unknown coefficients  $K$  and  $n$  were evaluated for each loading rate. The relations existing between the Young modulus and the loading rate and between the two material coefficients and the loading rate had to be analyzed a posteriori. This procedure consequently necessitated carrying tensile tests under a third loading rate at least to deduce tendencies for the three parameters.

Five acrylic dog bone samples, prepared in accordance to the manufacturing procedure exposed in section 4.3.1.1, were employed to acquire sufficient stress-strain information. As for the previous experiments, two factors were considered, i.e. the loading rate and the artificial ageing realized in agreement with the ISO 11431 [4.4]. As results were already obtained for medium and high loading rates of 50mm/min and 250mm/min, a low one of 5mm/min was envisaged.

| Test n° | Factors    | Samples to be tested |               |               |
|---------|------------|----------------------|---------------|---------------|
|         | A = Ageing | Test series 1        | Test series 2 | Test series 3 |
| 1       | 1          | A-29                 | A-30          | A-33          |
| 2       | 2          | A-28                 | A-34          | -             |
| Level 1 | Not aged   |                      |               |               |
| Level 2 | Aged       |                      |               |               |

**Table 5.12-** Design of experiments of acrylic samples tested under a loading rate of 50mm/min



The five dog-bone samples were randomly distributed in Table 5.12, for which only the ageing factor evolved as a unique loading rate was regarded. The test set-up used for the tensile experiments was conserved as well as the testing procedure. Standard stress-strain diagrams were achieved by dividing the total applied forces by the tested cross section, see Appendix A.5, and the displacements by the initial tested length of 60mm. All the curves corresponded to type II, i.e. ductile behaviour with yielding, and only the first portion to the necking was kept. The average and the extreme curves were superposed to the stress-strain diagrams of section 4.3.1, see Fig. 5.13. Finally, the characteristic points associated to the loading rate of 5mm/min were recorded in Table 5.13.

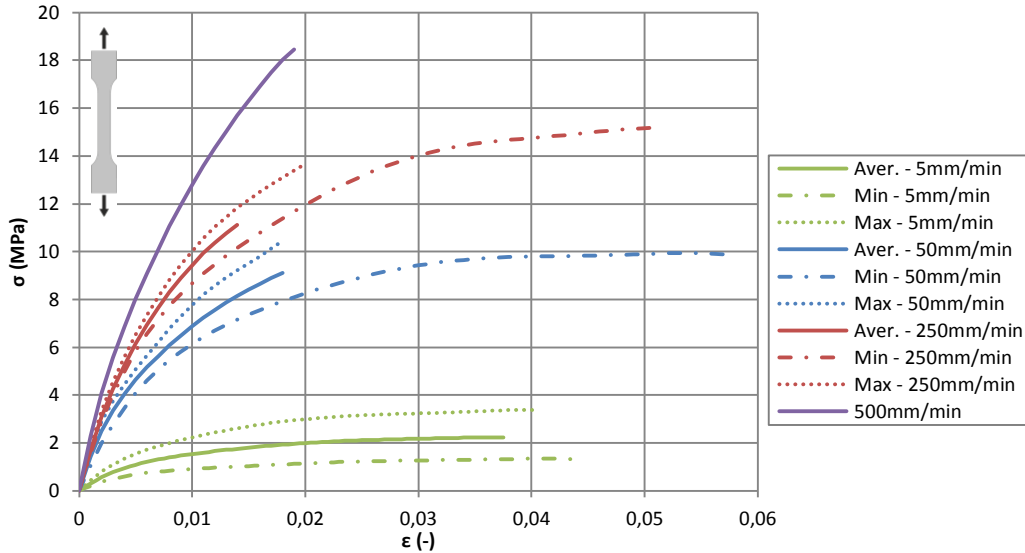


Figure 5.13- Stress-strain diagrams superposition for the different tested loading rates

| Loading rate<br>(mm/min) | Ageing | Curve type | Chord modulus<br>$K_0$ (MPa) |        | Strength/Yield<br>$\sigma_{max}$ (MPa) |       | Strain at break/yield $\epsilon_{max}$ (-) |       |       |
|--------------------------|--------|------------|------------------------------|--------|----------------------------------------|-------|--------------------------------------------|-------|-------|
|                          |        |            | Aver.                        | Std.   | Aver.                                  | Std.  | Aver.                                      | Min   | Max   |
| 5                        | NA     | II         | 256,856                      | 94,997 | 2,293                                  | 0,973 | 0,053                                      | 0,044 | 0,063 |
|                          | A      | II         |                              |        |                                        |       | 0,039                                      | 0,038 | 0,040 |

Table 5.13- Characteristic points according to the factors of influence –acrylic quasi-static dog-bone tests low loading rate

In addition to this study at a low loading rate of 5mm/min, another test was carried out at a rate of 500mm/min to later make a comparison between experimental and predicted data. The resulting curve was also plotted on Fig. 5.13 and demonstrated a brittle behaviour (curve I) as for the elevated rate of 250mm/min.

### 5.3.1.2 Determination of the coefficients

With this last analysis, sufficient stress-strain data were acquired for three different influent loading rates. The specimens subjected to an artificial ageing at low temperature were treated separately, as they exposed consequent stiffening. Hence, a separation of the results in three classes, i.e. 5mm/min, 50mm/min and 250mm/min, was done in order to apply the Ramberg-Osgood law, see Eq. (5.30). The Young's modulus, associated to a chord modulus between strains of 0,05% and 0,25% and calculated for each tested specimen, was preserved. The remaining unknown coefficients were thus  $K$  and  $n$ . To assess these two factors, a linearization of Eq. (5.30) was accomplished with the logarithmic function.

$$\log \left( \epsilon - \frac{\sigma}{E} \right) = \log(K) + n \log \left( \frac{\sigma}{E} \right) \quad (5.31)$$

For each tested samples, the stress-strain data and the proper Young's modulus, not the averaged one of Tables 4.39 or 5.13, were employed to appraise the values of  $\log(\epsilon - \sigma/E)$  and of  $\log(\sigma/E)$ .

Then, these values were regrouped for all the specimens belonging to the same class, e.g. 5mm/min, to perform a simple linear regression as the coefficients were linearly independent. The factors  $n$  and  $K$  were obtained with the following Eq. (5.32).

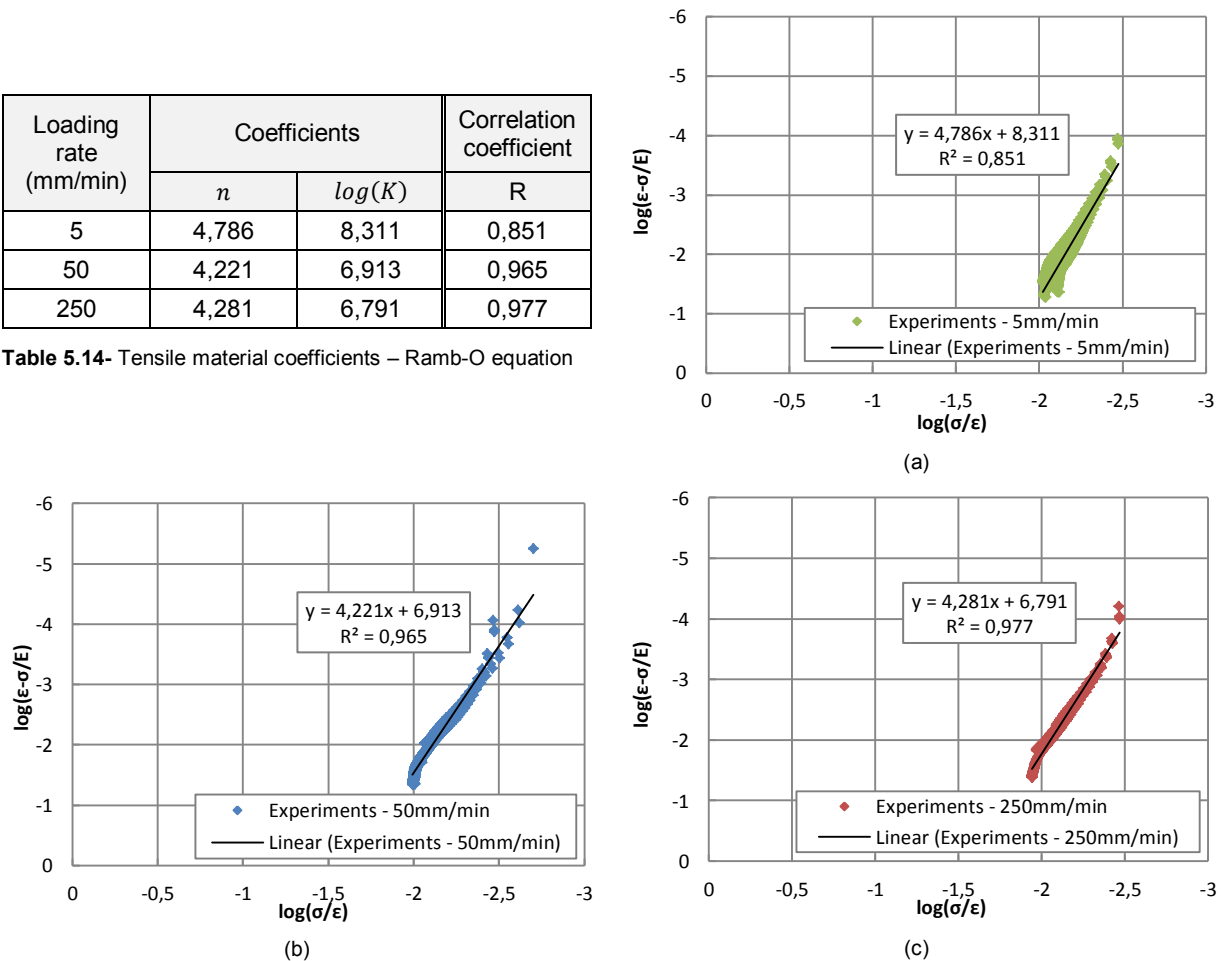
$$n = \frac{m \sum \log\left(\frac{\sigma_i}{E}\right) \log\left(\epsilon_i - \frac{\sigma_i}{E}\right) - \sum \log\left(\frac{\sigma_i}{E}\right) \sum \log\left(\epsilon_i - \frac{\sigma_i}{E}\right)}{m \sum \left[\log\left(\frac{\sigma_i}{E}\right)\right]^2 - \left[\sum \log\left(\frac{\sigma_i}{E}\right)\right]^2} \quad (5.32 \text{ a})$$

$$\log(K) = \frac{\sum \log\left(\epsilon_i - \frac{\sigma_i}{E}\right) - n \sum \log\left(\frac{\sigma_i}{E}\right)}{n} \quad (5.32 \text{ b})$$

With  $m$  the total number of values. These equations were implemented in an Excel file to determine these two parameters for the three classes of loading rates. Table 5.14 gathered the  $n$  and  $\log(K)$  values as well as the correlation coefficients. Trendlines were drawn with these data and superposed to experimental points for comparison, see Fig. 5.14.

| Loading rate<br>(mm/min) | Coefficients |           | Correlation coefficient<br>R |
|--------------------------|--------------|-----------|------------------------------|
|                          | $n$          | $\log(K)$ |                              |
| 5                        | 4,786        | 8,311     | 0,851                        |
| 50                       | 4,221        | 6,913     | 0,965                        |
| 250                      | 4,281        | 6,791     | 0,977                        |

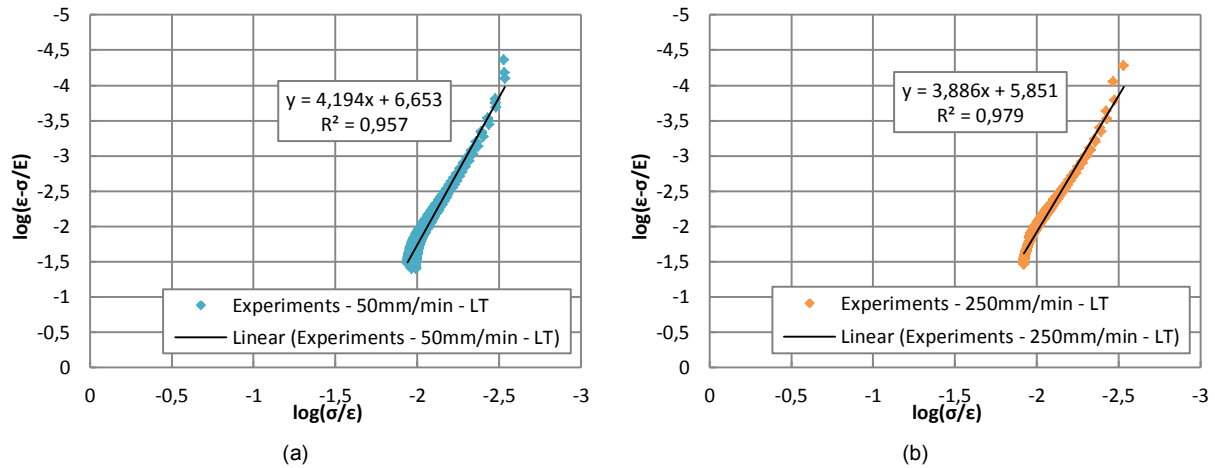
**Table 5.14-** Tensile material coefficients – Ramb-O equation



**Figure 5.14-** Linear fitting of the tensile experimental data for specimens under (a) 5mm/min, (b) 50mm/min and (c) 250mm/min

As it could have been observed, good correlations were found for the three loading rates, validating the procedure and coefficients. Consequently, a fitting of the averaged stress-strain curves for a specific loading rate could be realized with the help of the coefficient of Table 5.14 and the averaged Young's modulus all injected in Eq. (5.30).

Despite the small number of specimens subjected to an artificial ageing at low temperature, the whole method was conducted with regards to the two loading rates, i.e. 50mm/min and 250mm/min. With the linearization of the Ramberg-Osgood equation, the coefficients  $n$  and  $\log(K)$  were evaluated with the Eq. (5.32), resulting from a simple linear regression. Their values and the correlation coefficient were given in Fig. 5.15, in which were also plotted the comparison curves.

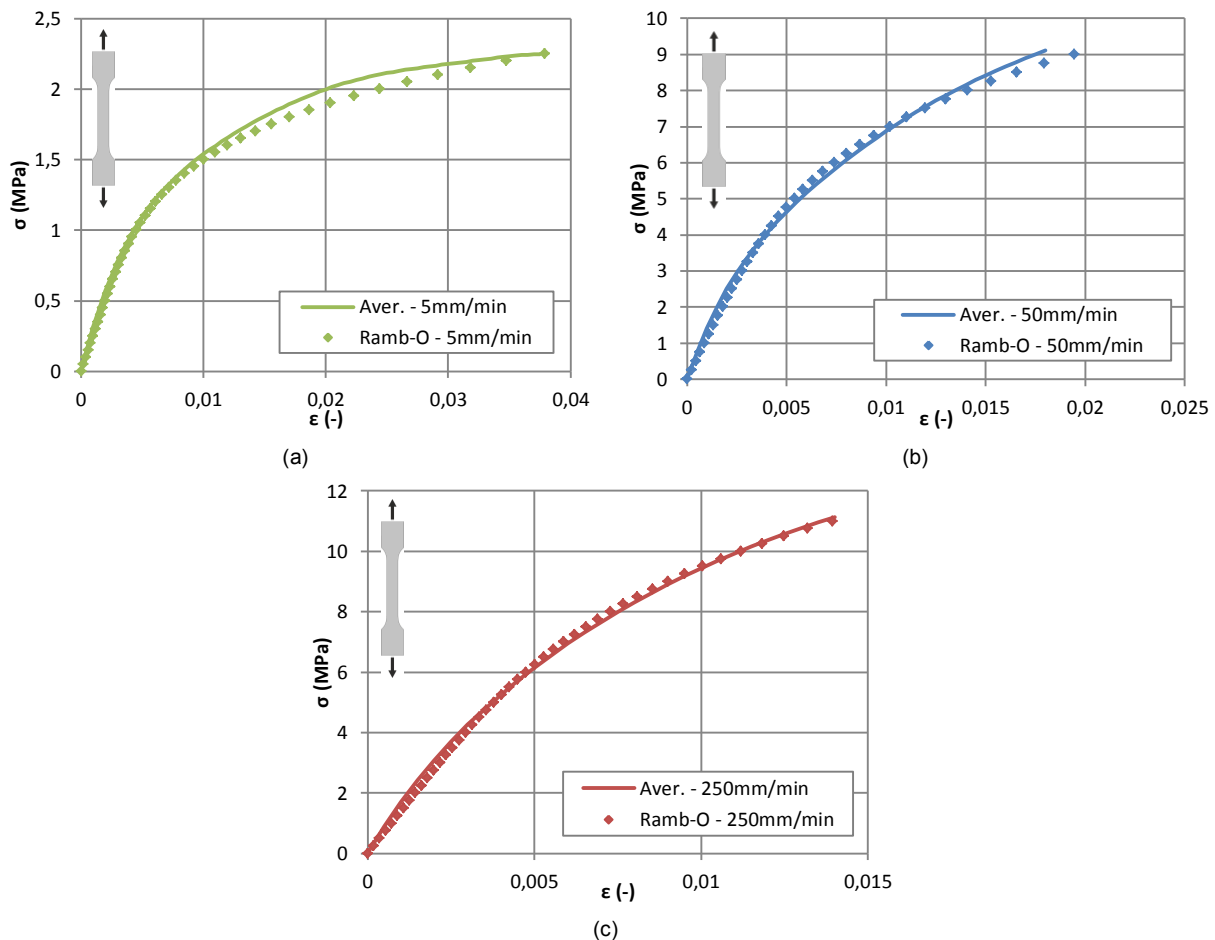


**Figure 5.15-** Linear fitting of the experimental data for low temperature aged specimens under (a) 50mm/min, (b) 250mm/min

As for the previous analysis, the correlation coefficients were close to one, indicating a good fitting of the data. Combined to the averaged Young's modulus of Table 4.39, these values would allow estimating the stress-strain curves of low-temperature aged specimens.

### 5.3.1.3 Evaluation and predicted curves

To properly assess the fitting of the Ramberg-Osgood equation to the averaged experimental curves, the different sets of parameters established in the previous section were employed. Theoretical stress-strain diagrams were, for each loading rate, compared to the stress-strain diagrams issued from the tests, see Fig. 5.16.

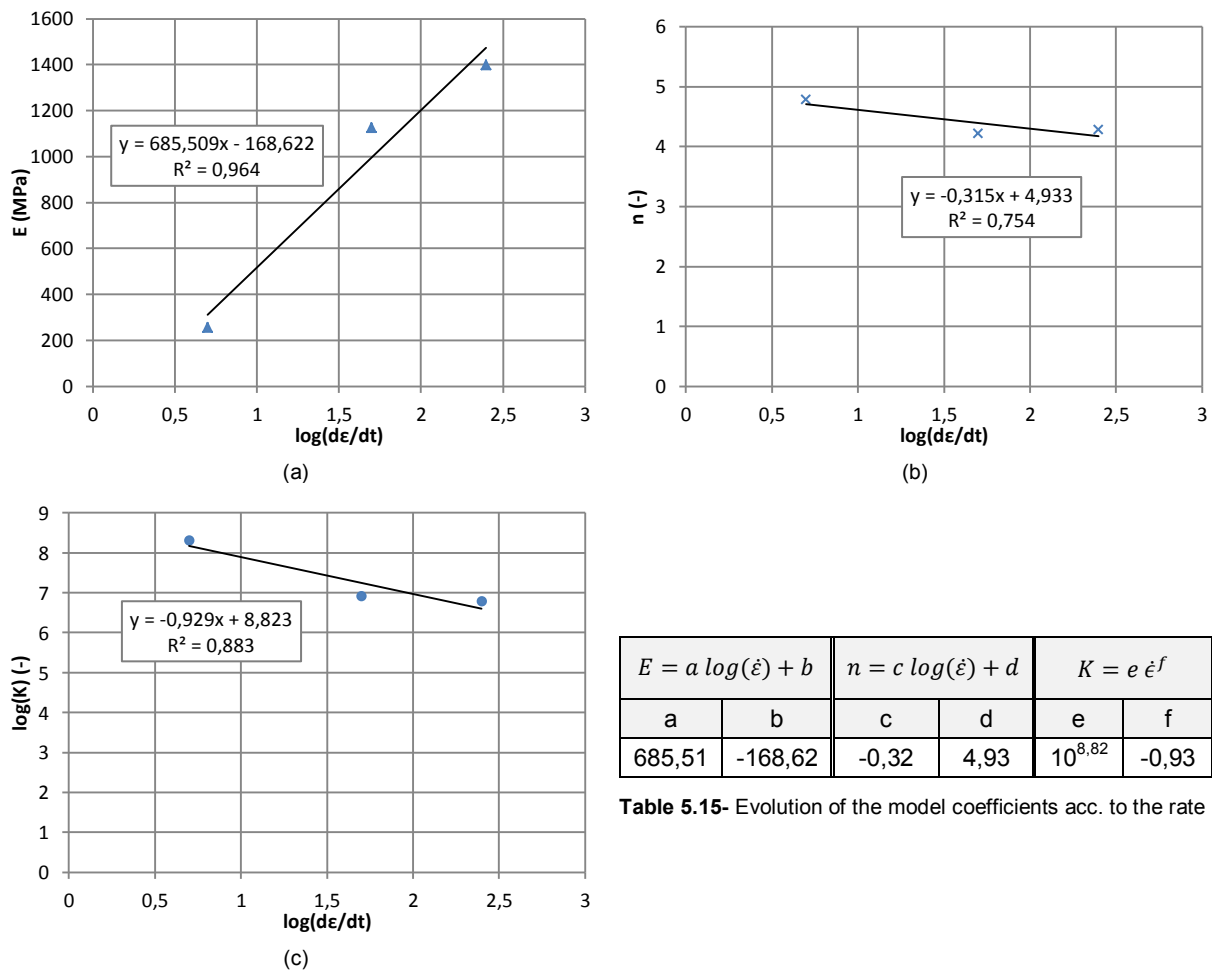


**Figure 5.16-** Theoretical (Ramb-O) and experimental stress-strain diagrams for (a) 5mm/min, (b) 50mm/min and (c) 250mm/min

With the chosen model, the three experimental curves were well fitted and no divergence was found. Nevertheless, the established coefficients were only valid for the three investigated loading rates and could not be used to describe the tensile behaviour of acrylic adhesive under other rates. To predict the evolution of the stress in function of the strain rate, a study concerning the dependency in loading rate of the three material parameters, i.e.  $E$ ,  $K$  and  $n$ , was performed. Several functions, such as the ones postulated by McLellan, see Eq. (2.27), were tested. However, the better concordance was attained by expressing  $E$  and  $n$  in function of  $\log(\dot{\epsilon})$  and  $K$  in terms of a power function, see Eq. (5.33).

$$\begin{aligned} E(\dot{\epsilon}) &= a \log(\dot{\epsilon}) + b \\ n(\dot{\epsilon}) &= c \log(\dot{\epsilon}) + d \\ K(\dot{\epsilon}) &= e \dot{\epsilon}^f \end{aligned} \quad (5.33)$$

With  $a, b, c, d, e$  and  $f$  material constants. For  $E$  and  $n$ , the coefficients were evaluated by determining the slope and the ordinate at the origin of the functions plotted under a logarithmic x-axis, while for  $K$ , double logarithmic axes were necessary. The corresponding curves were drawn on Fig. 5.17 and the resulting material constants recorded in Table 5.15.



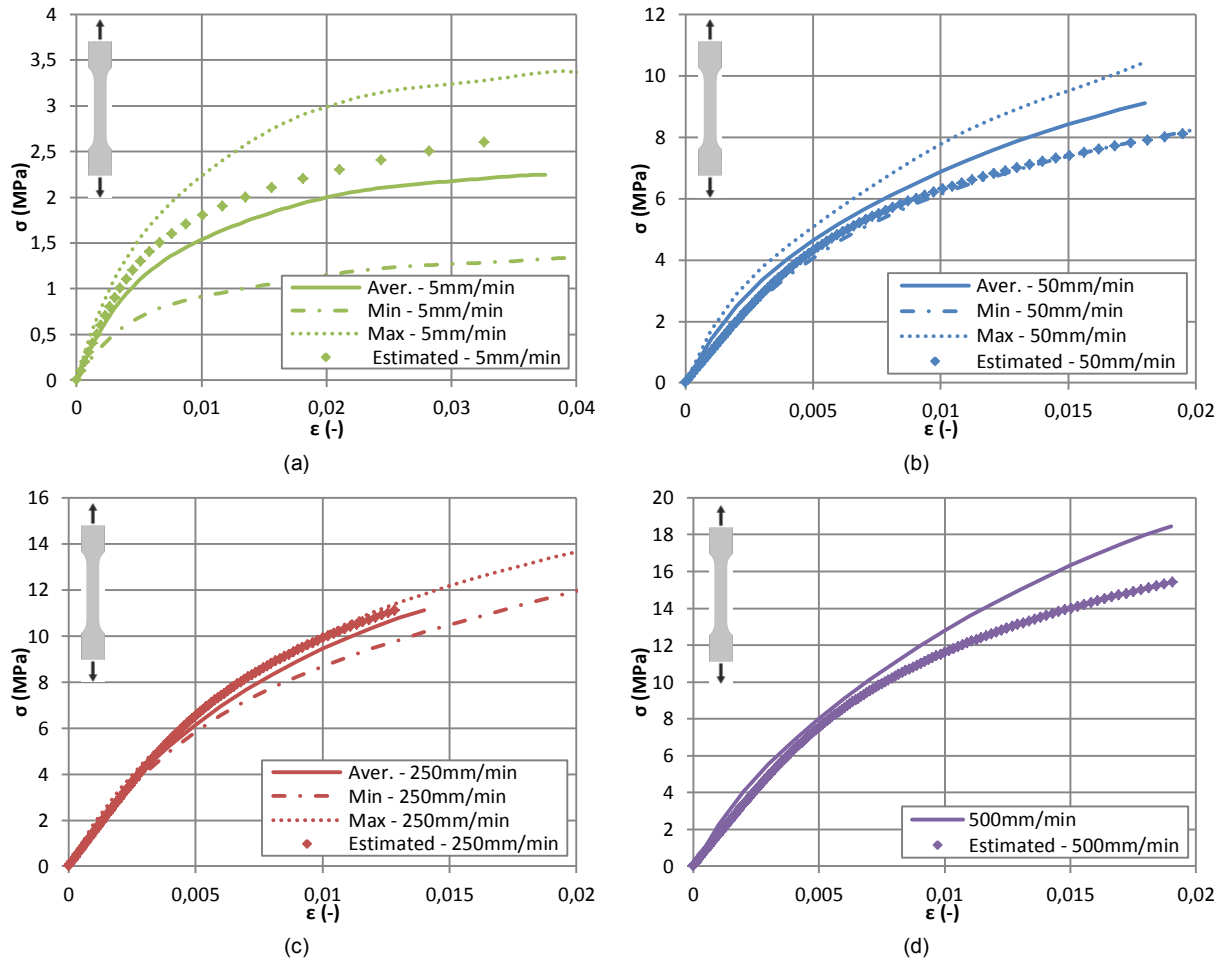
**Table 5.15-** Evolution of the model coefficients acc. to the rate

**Figure 5.17-** Fitting of the evolution of the 3 material coefficients according to the loading rate with the laws of Eq. (5.33)

While a good correlation coefficient was found for the Young's modulus estimation, lower ones were observed for  $K$  and  $n$ . To appraise the deviations induced by these approximations, the relative errors between the parameters of the Ramberg-Osgood model of Table 5.14 and the ones estimated with the Eq. (5.33) were calculated, see Table 5.16. The global errors for the coefficients  $n$  and  $\log(K)$  were globally inferior to 5%, with maximums values reached for 50mm/min. For the estimated Young's modulus, the errors were always superior to 5%, with a maximum of about 20% for the lowest loading rate of 5mm/min. Despite this large gap, graphical examinations were conducted for a comparison to the averaged experimental stress-strain curves, see Fig. 5.18.

| Loading rate<br>(mm/min) | $E$    |            |      | $n$    |            |     | $\log(K)$ |            |     |
|--------------------------|--------|------------|------|--------|------------|-----|-----------|------------|-----|
|                          | Ramb-O | Eq. (5.33) | %    | Ramb-O | Eq. (5.33) | %   | Ramb-O    | Eq. (5.33) | %   |
| 5                        | 256,9  | 310,5      | 20,9 | 4,786  | 4,713      | 1,5 | 8,311     | 8,174      | 1,6 |
| 50                       | 1126.5 | 996,0      | 11,6 | 4,221  | 4,397      | 4,2 | 6,913     | 7,245      | 4,8 |
| 250                      | 1398.4 | 1475,2     | 5,5  | 4,281  | 4,177      | 2,4 | 6,791     | 6,596      | 2,9 |

**Table 5.16-** Relative errors between the coefficients of the Ramberg-Osgood model and the estimated ones with Eq. (5.33)



**Figure 5.18-** Estimated/experimental stress-strain diagrams for (a) 5mm/min, (b) 50mm/min, (c) 250mm/min and (d) 500mm/min

For 5mm/min and 250mm/min, the coefficients estimated with Eq. (5.33) and injected in the Ramberg-Osgood Eq. (5.30) overestimated the experimental averaged stress-strain curves, while for 50mm/min and 500mm/min it was the opposite. The errors in stresses for the maximum strains were of about 20% for 5mm/min, 13,5% for 50mm/min and of 3,5% for 250mm/min. Thus, the best stress-strain representation occurred for a loading rate of 250mm/min. Nevertheless, for the three first rates, the estimated diagrams were always within the min/max range assessed during the experiments. At a rate of 500mm/min, the behaviour under a strain of 0,0075 was correctly approached with the estimated coefficients but certain dispersion was noticed after and a relative error in stresses of about 16,5% was recorded at the maximum strain.

The low-temperature aged specimens were also fitted with the Ramberg-Osgood equation and the corresponding material coefficients were given in Fig. 5.15. To evaluate the closeness between the theoretical stress-strain behaviour and the averaged experimental data, a superposition of the curves was realized on Fig. 5.19. A good concordance between the curves was remarked for the two loading rates with no dispersion. Consequently the set of coefficients presented in section 5.3.1.2 combined with the Young's modulus of Table 4.39 were sufficient to describe the acrylic behaviour after a low-

temperature ageing for loading rates of 50mm/min and 250mm/min. Furthermore, as only two rates were investigated no prediction curves could be proposed in this case.

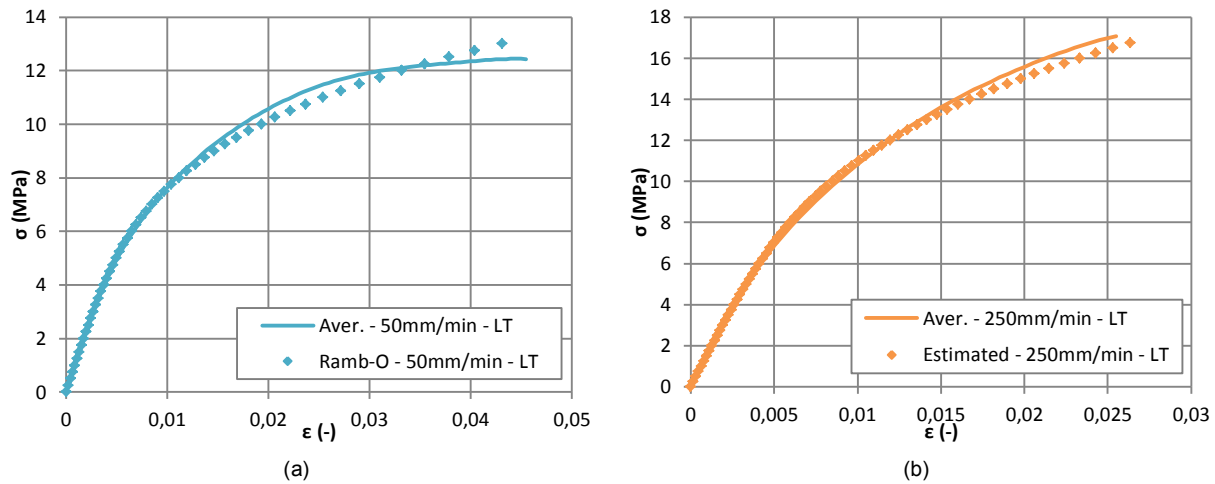


Figure 5.19- Theoretical and experimental diagrams for low temperature aged specimens under (a) 50mm/min, (b) 250mm/min

## 5.3.2 Modified shear characterization

### 5.3.2.1 One-dimensional modified Ramberg-Osgood fitting

As aforementioned, no relation could have been directly done between the elastic parts of the tensile and modified shear results, as both dependent on the loading rate, provided information for dissimilar rates. Nevertheless, as for the tensile results representations, the form of the Ramberg-Osgood law of Eq. (5.30) was conserved, see Eq. (5.34).

$$\gamma = \frac{\tau}{G_0} + K' \left( \frac{\tau}{G_0} \right)^{n'} \quad (5.33)$$

With  $G_0$  the shear modulus associated to a chord modulus evaluated between  $\gamma=0,01$  and  $\gamma=0,05$ . From the quasi-static tests, stress-strain diagrams were obtained for two loading rates, i.e. 1mm/min and 15mm/min. These data were completed with the ones acquired during the modified long-term shear tests with the first loading, i.e. before reaching the constant displacement plateau, at 5mm/min. Hence, the shear behaviour of acrylic adhesive was assessed under three different loading rates, which bestowed sufficient data for later prediction under various loading rates. These averaged curves were summarized in Fig. 5.20 and their characteristic points recorded in Table 5.17.

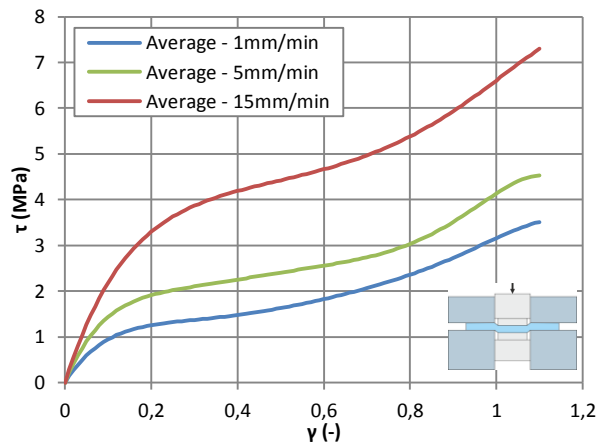


Figure 5.20- Stress-strain diagrams – acrylic modified shear

| Loading rate<br>(mm/min) | Shear modulus<br>$G_0$ (MPa) |       | Maximum stress<br>$\sigma_{\gamma=1,10}$ (MPa) |       |
|--------------------------|------------------------------|-------|------------------------------------------------|-------|
|                          | Aver.                        | Std.  | Aver.                                          | Std.  |
| 1                        | 8,648                        | 3,926 | 3,488                                          | 0,511 |
| 5                        | 15,113                       | 6,425 | 4,530                                          | -     |
| 15                       | 24,751                       | 3,966 | 7,202                                          | 0,840 |

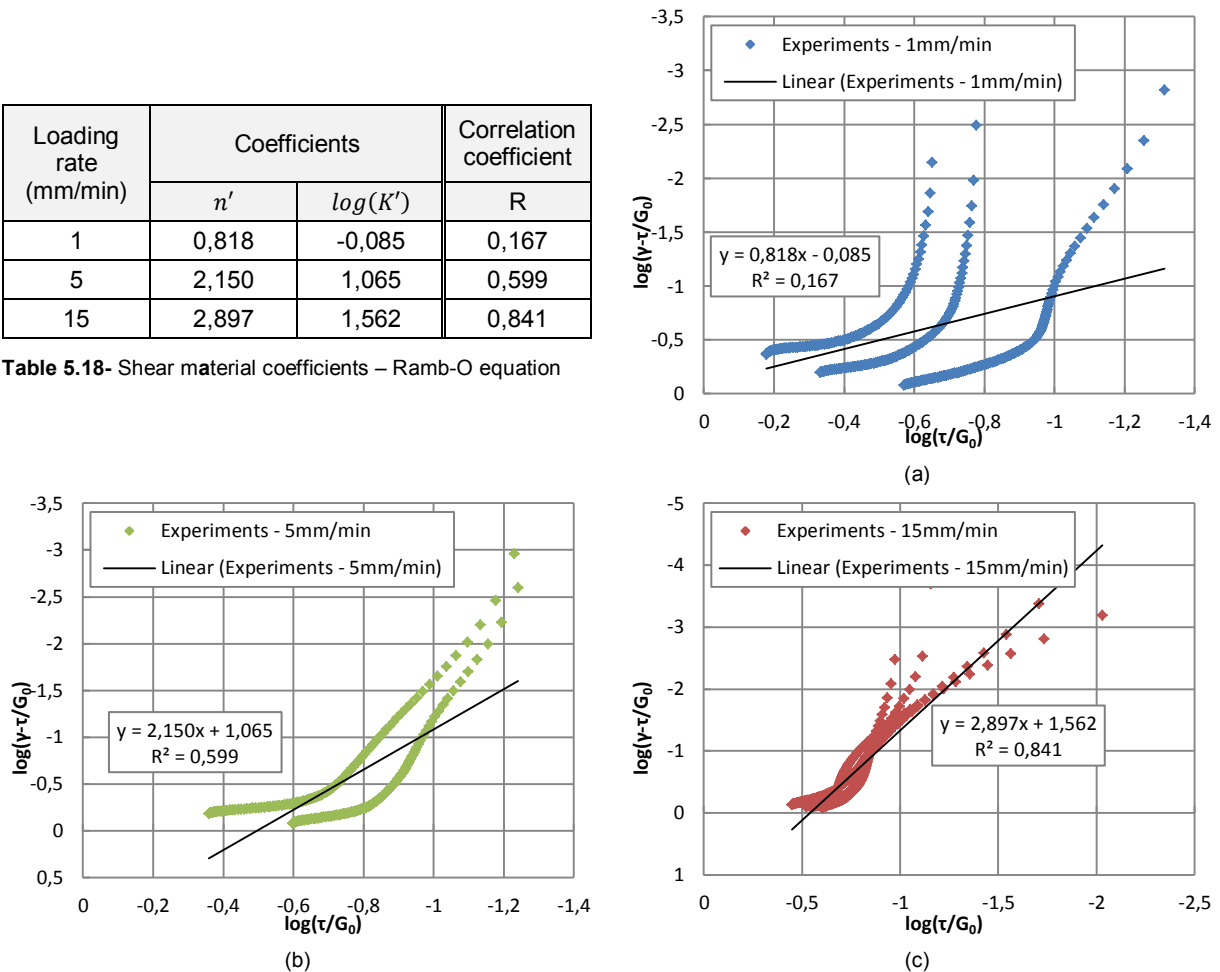
Table 5.17- Characteristic points – acrylic modified shear

For the determination of the material coefficients, the results were split in three classes according to the loading rate. The Eq. (5.32), adapted to the present shear formulation, was used over all the data

of one class with their respective shear modulus (not the averaged ones of Table 5.17), in order to calculate the unknown  $n'$  and  $\log(K')$ . These estimated parameters were then gathered in Table 5.18 and the fitting curves exposed on Fig. 5.21.

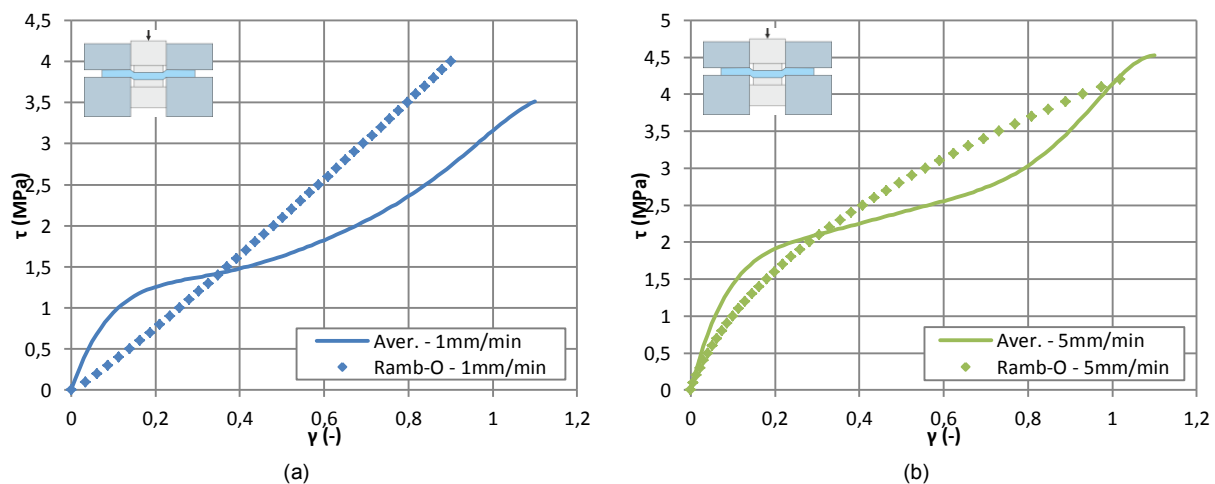
| Loading rate<br>(mm/min) | Coefficients |            | Correlation coefficient<br>R |
|--------------------------|--------------|------------|------------------------------|
|                          | $n'$         | $\log(K')$ |                              |
| 1                        | 0,818        | -0,085     | 0,167                        |
| 5                        | 2,150        | 1,065      | 0,599                        |
| 15                       | 2,897        | 1,562      | 0,841                        |

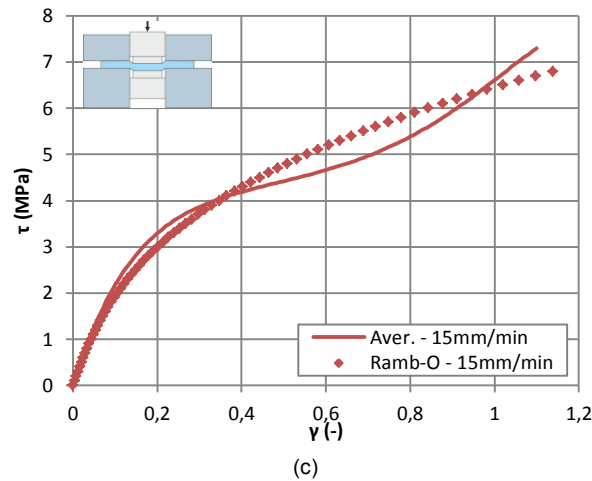
**Table 5.18-** Shear material coefficients – Ramb-O equation



**Figure 5.21-** Linear fitting of the shear experimental data for specimens under (a) 1mm/min, (b) 5mm/min and (c) 15mm/min

Poor coefficients of correlation were obtained, except for the highest loading rate of 15mm/min. This implied that the Ramberg-Osgood form applied to the shear results was not relevant and could not be employed to represent this type of action. To completely confirm this postulate the theoretical curves were superposed to the experimental shear curves for all the loading rates, see Fig. 5.21. The theoretical curves were achieved by injecting the material parameters of Table 5.18 and the averaged Young's modulus of Table 5.17 in Eq. (5.33). While for 1mm/min and 5mm/min, the theoretical curves did not approach the experimental ones, a better concordance was found for 15mm/min.





**Figure 5.22-** Theoretical (Ramb-O) and experimental stress-strain diagrams for (a) 1mm/min, (b) 5mm/min and (c) 15mm/min

However, the strong non-linearities arising in the shear stress-strain behaviour were not accounted by this material law for all the loading rates. Judged as inapt no further continuations were done with this one dimensional law.

### 5.3.2.2 One-dimensional proposed model

By examining the global stress variations of the experimental shear stress-strain curves of UV-acrylic, similarities with the shear behaviour of the structural silicone studied in section 5.2 were remarked. Indeed, an inflection point at small strains was followed by consequent hardening at large strains. Because of this observation, it was decided to investigate a shear formulation identical to the one presented in Table 5.6. This equation was rewritten below by regrouping the factors  $a$  and  $c$ , as they possessed the same function:

$$\tau = 2A\gamma + 4B\gamma^3 + \frac{2C\gamma}{(\gamma^2 + D)^2} \quad (5.34)$$

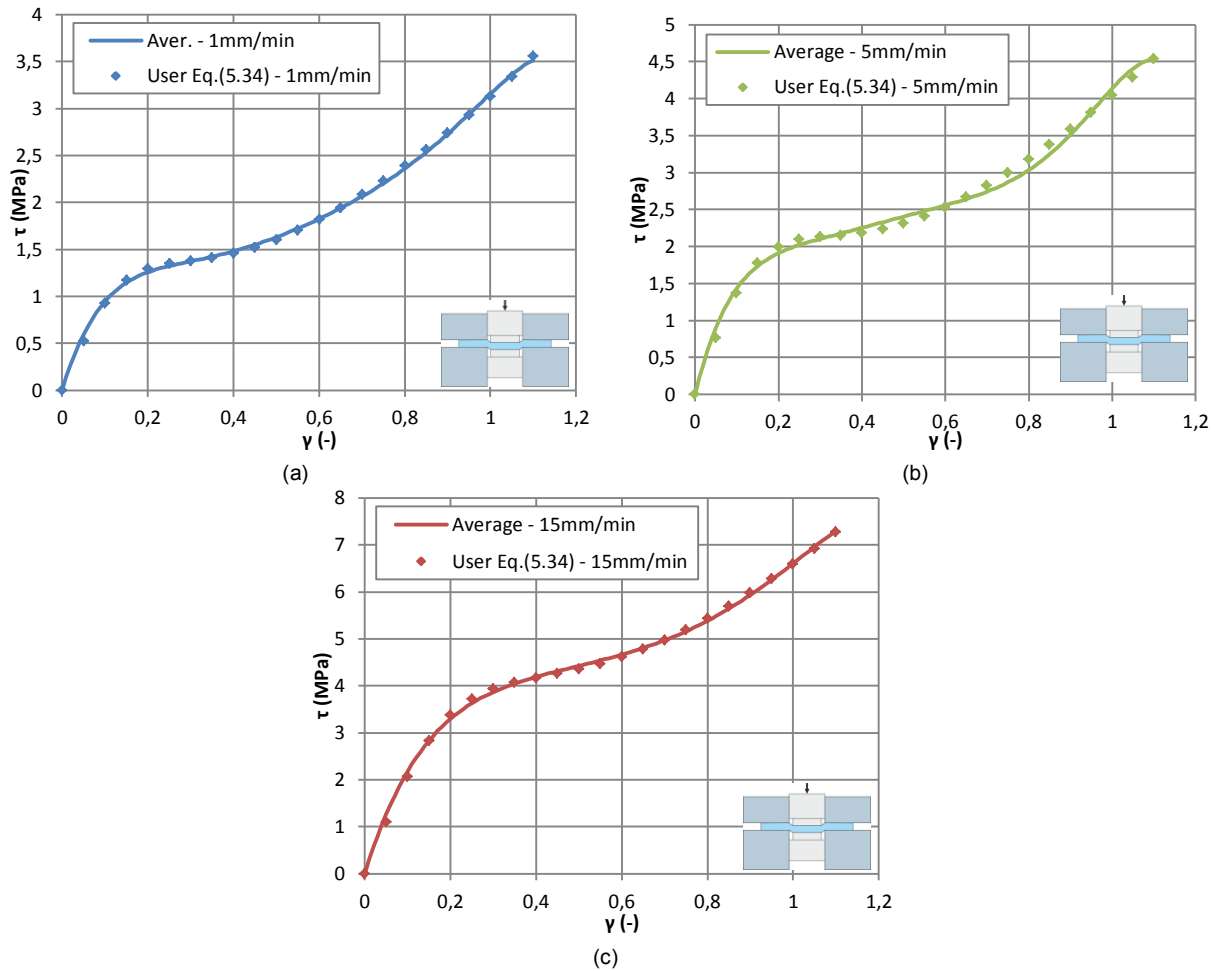
Where  $A, B, C$  and  $D$  material parameters. With the shear stress definition of Eq. (5.34), the coefficients were not linearly independent and a simple linear least square method could not have been used. Therefore, the non-linear least square method of Levenberg-Marquardt was employed. The principle of this procedure and the different steps to be carried out were already evoked in section 5.2.1.4. The four coefficients were consequently evaluated, for each loading rate and for the averaged stress-strain diagrams of Fig. 5.20, by following the algorithm of Fig. 5.7, see Table 5.19.

| Loading rate<br>(mm/min) | Material constants (-) |         |         |         |
|--------------------------|------------------------|---------|---------|---------|
|                          | $A$                    | $B$     | $C$     | $D$     |
| 1                        | 1,24852                | 0,14398 | 0,03210 | 0,08750 |
| 5                        | 1,67071                | 0,14515 | 0,07312 | 0,10872 |
| 15                       | 2,79236                | 0,15234 | 0,27717 | 0,18201 |

**Table 5.19-** Shear material coefficients for the three loading rates – stress formulation of Eq. (5.34)

To fully validate the formulation and the associated coefficients, the experimental shear stress-strain curves were individually compared to the theoretical curves assessed by injecting the data of Table 5.19 in Eq. (5.34), see Fig. 5.23. A good correlation was found between the curves with no dispersion, which proved the ability of the proposed model to represent the shear behaviour of acrylic adhesive under different loading rates by simply changing the material parameters. Even if these coefficients were established for three different rates, predictions of their evolutions could have been made to later determine the shear stress variations under random loading rates.



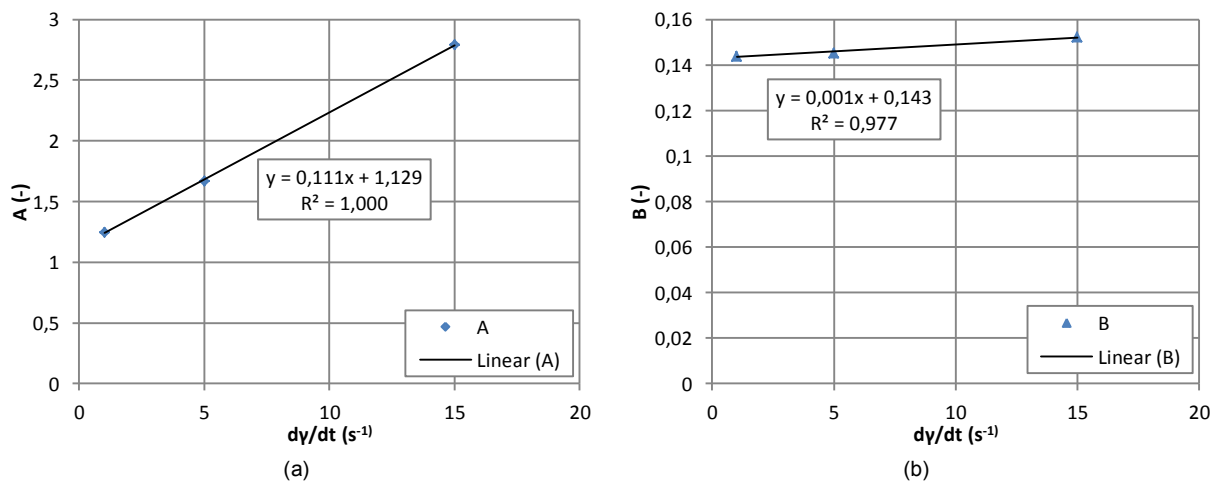


**Figure 5.23-** Theoretical (Eq. (5.34)) and experimental stress-strain diagrams for (a) 1mm/min, (b) 5mm/min and (c) 15mm/min

To apprehend the dependency of the material parameters to the loading rate, the first step consisted in plotting each of them according to the investigated rates, see Fig. 5.24. Then, simple linear fitting, see example of Eq. (5.35), were realized for all the constants and relatively good coefficients of correlation, close to one, were obtained in each case.

$$A = k\dot{\gamma} + l = 0.111\dot{\gamma} + 1.129 \quad (5.35)$$

Nevertheless, to ensure of small deviations between the parameters directly fitted from the averaged experiments and the estimated parameters with the linear equations of Fig. 5.24, the relative errors were calculated, see Table 5. 20.



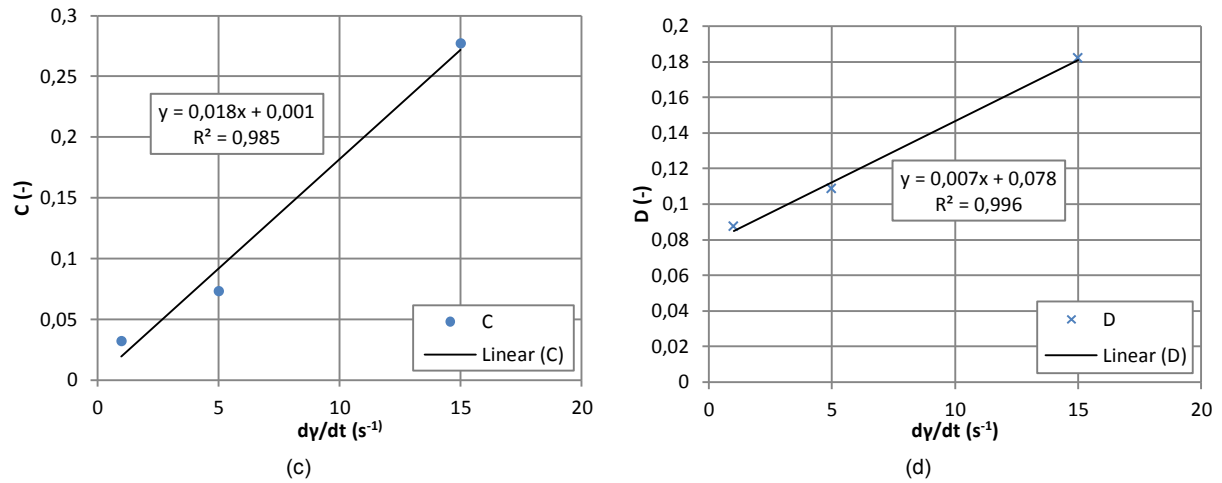


Figure 5.24- Linear fitting of the evolution of the 4 material coefficients of Eq. (5.34) according to the loading rates

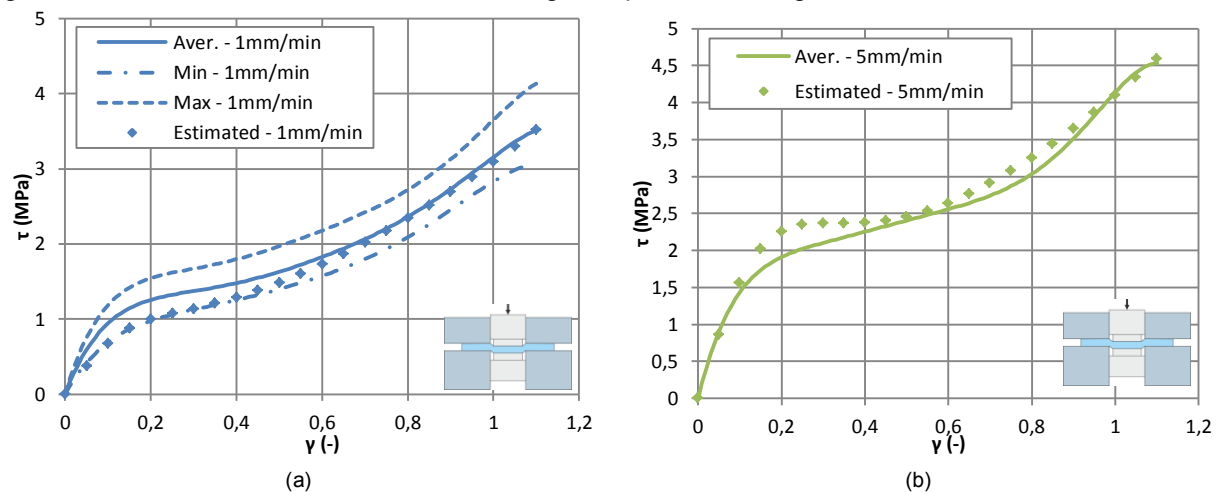
| Loading rate<br>(mm/min) | A                            |               |     | B                            |               |     |
|--------------------------|------------------------------|---------------|-----|------------------------------|---------------|-----|
|                          | Direct fitting<br>Eq. (5.34) | Linear estim. | %   | Direct fitting<br>Eq. (5.34) | Linear estim. | %   |
| 1                        | 1,24852                      | 1,24004       | 0,7 | 0,14398                      | 0,14344       | 0,4 |
| 5                        | 1,67071                      | 1,6826        | 0,7 | 0,14515                      | 0,14592       | 0,5 |
| 15                       | 2,79236                      | 2,789         | 0,1 | 0,15234                      | 0,15212       | 0,1 |

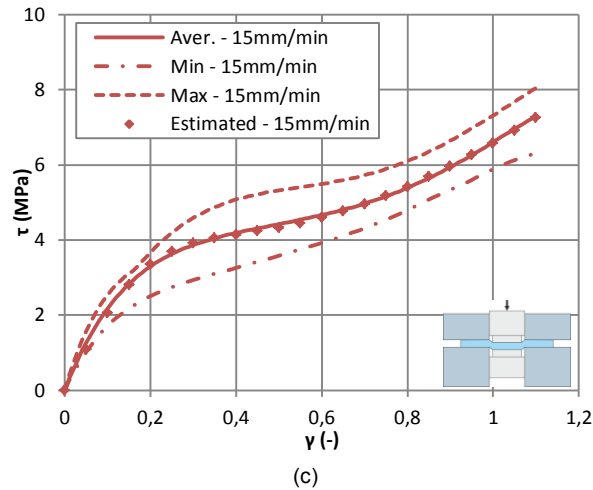
  

| Loading rate<br>(mm/min) | C                            |               |      | D                            |               |     |
|--------------------------|------------------------------|---------------|------|------------------------------|---------------|-----|
|                          | Direct fitting<br>Eq. (5.34) | Linear estim. | %    | Direct fitting<br>Eq. (5.34) | Linear estim. | %   |
| 1                        | 0,03210                      | 0,01909       | 40,5 | 0,08745                      | 0,0849        | 3,0 |
| 5                        | 0,07312                      | 0,09133       | 24,9 | 0,10872                      | 0,11234       | 3,3 |
| 15                       | 0,27717                      | 0,27193       | 1,9  | 0,18201                      | 0,18094       | 0,6 |

Table 5.20- Relative errors between the coefficients of the proposed model of Eq. (5.34) and the estimated ones with Eq. (5.35)

The main deviations occurred for the coefficients  $C$ , especially for the lowest loading rate, while almost no differences were noticed for the others parameters. These variations should also be nuanced with regards to the values orders, which were very small. Thus, to properly assess the existing differences, graphical comparisons were necessary. For a given loading rate, the two stress-strain curves were achieved by injecting the two sets of coefficients in Eq. (5.34), see Fig. 5.25. As it could have been noted for the imposed rate of 1mm/min, the first elastic part, between 0 and 0,05 underestimated the averaged experimental elastic part but complied with the minimum resulting curve. For larger strains, good concordances in stresses with the averaged experimental diagram were seen.





**Figure 5.25-** Estimated/experimental shear stress-strain diagrams for (a) 1mm/min, (b) 5mm/min and (c) 15mm/min

For 5mm/min, the initial stiffnesses of the estimated and experimental curves were identical, but some differences in stresses followed between strains of 0,1 and 0,4. Nevertheless, the last non-linear part was well represented. For 15mm/min, the best coincidence with the averaged curve issued from the modified shear tests was observed. Consequently, in reason to the small dispersions, the proposed model of Eq. (5.34) combined to the linear approximation of the material coefficients were validated to appraise the shear behaviour of UV-acrylic under any imposed loading rate.

## 5.4 SUMMARY AND CONCLUSION

Only the quasi-static properties of both adhesives were considered to propose proper material laws. While for the silicone elastomer, a 3D constitutive material law accounting for the slight compressibility and for the Mullins' effect was provided, for the UV-acrylic, only 1D models were found to describe the respective tensile and shear behaviour.

For silicone, the 3D material law, written under a strain energy potential form, and the appropriate constants were summarized in the following Table 5.26. The postulated equation, implemented in finite element software, would allow modeling any types of quasi-static actions arising in silicone joints of structural glass façade.

| Strain energy potential for silicone elastomer                                                                                      |         |          |         |         |         |           |
|-------------------------------------------------------------------------------------------------------------------------------------|---------|----------|---------|---------|---------|-----------|
| $W = a(\bar{I}_1 - 3) + b(\bar{I}_1 - 3)^2 + c(\bar{I}_2 - 3) - \frac{d}{(\bar{I}_2 - 3 + e)} + \frac{d}{e} + \frac{K}{2}(J - 1)^2$ |         |          |         |         |         |           |
| Coefficients                                                                                                                        | $a$     | $b$      | $c$     | $d$     | $e$     | $K$       |
| Quasi-static                                                                                                                        | 0,24415 | -0,00751 | 0,04113 | 0,01577 | 0,22733 | 367,04682 |
| Mullins' effect                                                                                                                     | 0,05776 | 0,02106  | 0,07467 | 0,04177 | 0,49856 |           |

**Table 5.21-** Complete 3D constitutive material law for silicone elastomer

For acrylic, sensitive to the imposed loading rate, a separation between tension and shear had to be operated to envisage one-dimensional models. While the well-known Ramberg-Osgood equation was efficient to reproduce the experimental tensile behaviour, a new law, based on the established silicone model, was advanced. As three different loading rates were tested for each type of action, the evolutions of the material coefficients according to the loading rates were approximated with simple mathematical functions. This concept allowed predicting the one-dimensional behaviour of the acrylic under any rates, see Table 5.22.

| Action                | TENSION                                                                                                                                                     | SHEAR                                                                                                                           |
|-----------------------|-------------------------------------------------------------------------------------------------------------------------------------------------------------|---------------------------------------------------------------------------------------------------------------------------------|
| 1D model              | Ramberg-Osgood                                                                                                                                              | Self-developed                                                                                                                  |
|                       | $\varepsilon = \frac{\sigma}{E} + K \left( \frac{\sigma}{E} \right)^n$                                                                                      | $\tau = 2A\gamma + 4B\gamma^3 + \frac{2C\gamma}{(\gamma^2 + D)^2}$                                                              |
| Material coefficients | $E = 685.509 \log(\dot{\varepsilon}) - 168.622$ $n = -0.315 \log(\dot{\varepsilon}) + 4.933$ $K(\dot{\varepsilon}) = 10^{8.823} \dot{\varepsilon}^{-0.929}$ | $A = 0.111\dot{\gamma} + 1.129$ $B = 0.001\dot{\gamma} + 0.143$ $C = 0.018\dot{\gamma} + 0.001$ $D = 0.007\dot{\gamma} + 0.078$ |

**Table 5.22-** Separate 1D material laws for the tensile and shear characterization of the loading rate-dependent UV-acrylic

## 6. VALIDATION OF THE LAWS WITH NUMERICAL SIMULATIONS

### 6.1 INTRODUCTION

The aim of this chapter is to implement the own developed material laws of the two adhesives in finite element software and validate them by modeling the conducted tests. This would ensure of the correctness of the developed user-subroutines for later numerical simulations on more complex geometries. The organization chart of this chapter is presented in Fig. 6.0.

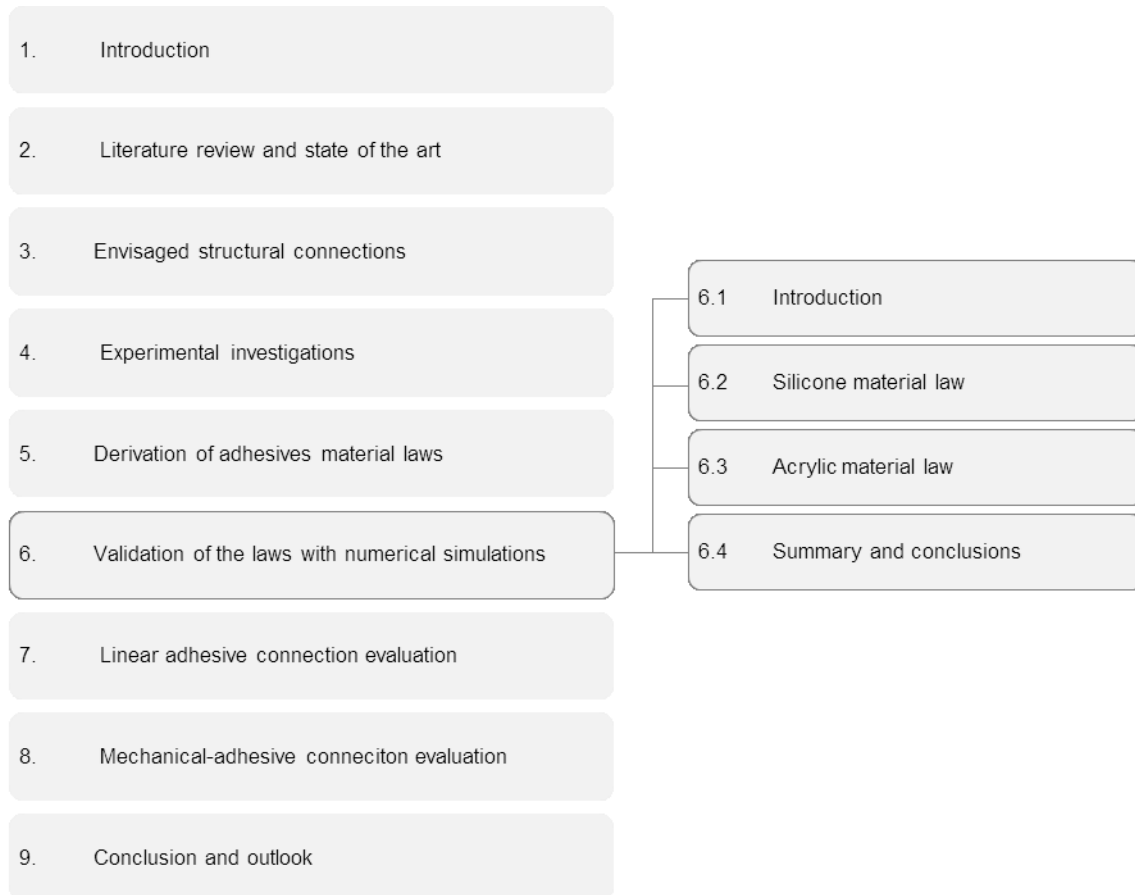


Figure 6.0- Organization chart of chapter 6

**Silicone material law.** According to the solving procedure, either implicit or explicit, two FORTRAN subroutines are written to insert the developed silicone material law in finite element software. The uniaxial tension, compression and shear isochoric tests are modeled with both subroutines to fully validate them. The isochoric tests are also modeled with the two solving procedures. The results of all the conducted numerical calculations are detailed in this section. The peak stress problem, noticed with the direct shear stress record was investigated by three procedures, which are also evoked in this section.

**Acrylic material law.** The self-developed shear 1D model for the acrylic material is incorporated by modifying the coefficients of the implicit subroutine written for the silicone. The numerical simulations of the modified shear tests are performed and compared to the experimental results.

**Summary and conclusions.** At the end of this chapter, the different realized steps are summarized and the problems observed reminded.

## 6.2 SILICONE MATERIAL

### 6.2.1 Implementation in the finite element software Abaqus®

In the finite element software Abaqus®, two possibilities were commonly offered to implement a material law, i.e. by selecting a model already present in the software's library or writing an external FORTRAN user-subroutine called during the analysis. While the standard hyperelastic constitutive laws, such as the polynomial, the Yeoh, the Mooney-Rivlin and the Neo-Hookean forms, belonged to Abaqus' library and only necessitated the definition of the  $C_{ij}$  material coefficients, the new proposed strain energy model of Table 5.21 implied the creation of a subroutine. The writing of this last file was directly dependent on the solving method, which had to account for the non-linear large deformations of silicone material. Within, the chosen finite element software, two solving methods were available, i.e. an iterative implicit method, referred as Abaqus/Standard, and an explicit method, associated to Abaqus/Explicit. The differences between these two methods and their advantages/drawbacks were summarized in Appendix E.1. In consequence, one subroutine was made for each solving procedure.

#### 6.2.1.1 Abaqus/Standard - UHYPER definition

In Abaqus/Standard, isotropic hyperelastic behaviour could be implemented through a user-subroutine called UHYPER, for which only the definitions of the strain energy potential and its derivatives towards the deviatoric strain invariants were of importance. Hence, the total expression of the strain energy function of Table 5.21 was employed with the associated set of coefficients. The complete subroutine, written with the imposed FORTRAN formalism, was detailed in Appendix E.2. The Cauchy 3D stress tensor was calculated for all the iterations of an increment by the software to finally provide the stress distribution at the end of the analysis.

#### 6.2.1.2 Abaqus/Explicit - VUMAT definition

In Abaqus/Explicit, the insertion of a hyperelastic law appeared more complex, as the definition of the strain energy function was not sufficient and no equivalence to the UHYPER subroutine existed. Therefore, a general subroutine VUMAT, allowing implementing all kind of material behaviour, was used. To properly define this user-routine, all the components of the Cauchy stress tensor expressed in a corotational framework were needed. These Cauchy stresses were extracted from the developed strain energy potential of Table 5.21. However, in the proposed formulation, the strain energy potential was dependent on the deviatoric invariants, themselves dependent on the Cauchy-Green deformation tensor and on the deformation gradient  $F = RU$ . Yet, this last tensor already incorporated the rotations, which was redundant with the corotational framework definition automatically accounting for rigid body rotations. Thus, to avoid including the rotations two times, it was decided to express the stresses directly in function of the stretch tensor  $U$ .

To determine the Cauchy stress from the strain energy potential, the following equation Eq. (6.1) had to be used. In this equation were injected the fundamental Eq. (2.25) in order to split the stress into an isochoric and a volumetric part.

$$\sigma = 2J^{-1}\bar{\bar{B}} \frac{\delta W(\bar{\bar{B}})}{\delta \bar{\bar{B}}} = 2J^{-1}\bar{\bar{B}} \frac{\delta W_{iso}(\bar{\bar{B}})}{\delta \bar{\bar{B}}} + 2J^{-1}\bar{\bar{B}} \frac{\delta W_{vol}(J)}{\delta \bar{\bar{B}}} = \sigma_{iso} + \sigma_{vol} \quad (6.1)$$

With the previous separation of the Cauchy stress, the general expression of the volumetric stress was first investigated:

$$\sigma_{vol} = 2J^{-1}\bar{\bar{B}} \frac{\delta W_{vol}(J)}{\delta \bar{\bar{B}}} = 2J^{-1}\bar{\bar{B}} \frac{\delta W_{vol}(J)}{\delta J} \frac{\delta J}{\delta \bar{\bar{B}}} = 2J^{-1}\bar{\bar{B}} \frac{\delta W_{vol}(J)}{\delta J} \frac{J}{2} \bar{\bar{B}}^{-1} = \frac{\delta W_{vol}(J)}{\delta J} \bar{\bar{I}} \quad (6.2)$$

With  $\bar{\bar{I}}$  the identity tensor. Consequently, the final formulation of the volumetric stress was achieved by simply injecting the chosen isochoric strain energy potential into Eq. (6.2) and deriving it according to

the Jacobian of the transformation. The obtained result presented the configuration of a tensor, see Eq. (6.3).

$$\sigma_{vol} = K(J - 1) \begin{pmatrix} 1 & 0 & 0 \\ 0 & 1 & 0 \\ 0 & 0 & 1 \end{pmatrix} \quad (6.3)$$

The above equation depended on the Jacobian of the transformation and so on the deformation tensor with the relation  $J = \det(F) = \det(RU) = \det(R)\det(U) = \det(U)$ . In this way, no rearrangement was necessary to write the volumetric stress in function of the stretch tensor  $U$ . Knowing one of the two components composing the general Cauchy stress, the study was then focused on the isochoric stress, whose formulation was rewritten as:

$$\sigma_{iso} = 2J^{-1}\bar{B} \frac{\delta W_{iso}(\bar{\mathbb{B}})}{\delta \bar{\mathbb{B}}} \frac{\delta \bar{\mathbb{B}}}{\delta \bar{B}} = 2J^{-1}\bar{B}J^{-2/3} \left( J - \frac{1}{3}\bar{B} \otimes \bar{B}^{-1} \right) : \frac{\delta W_{iso}(\bar{\mathbb{B}})}{\delta \bar{\mathbb{B}}} \quad (6.4)$$

Where  $J$  was the fourth-order unit tensor,  $\otimes$  the tensor product and  $:$  the contraction. By reformulating the previous expression, it was possible to deduct:

$$\sigma_{iso} = \bar{B} \left( J^{-2/3} J - \frac{1}{3}\bar{B}^{-1} \otimes \bar{\mathbb{B}} \right) \bar{\mathbb{B}}^{-1} : 2J^{-1} \frac{\delta W_{iso}(\bar{\mathbb{B}})}{\delta \bar{\mathbb{B}}} \bar{\mathbb{B}} = \mathbb{P} : \bar{\sigma} \quad (6.5)$$

$$\mathbb{P} = J - \frac{1}{3}\bar{I} \otimes \bar{I}$$

With

$$\bar{\sigma} = 2J^{-1} \frac{\delta W_{iso}(\bar{\mathbb{B}})}{\delta \bar{\mathbb{B}}} \bar{\mathbb{B}}$$

Finally, a last rearrangement was operated to provide the following general form of the isochoric stress only depending on the introduced stress  $\bar{\sigma}$ :

$$\sigma_{iso} = \bar{\sigma} - \frac{1}{3}Tr(\bar{\sigma})\bar{I} \quad (6.6)$$

According to the definition of Eq. (6.5), the stress  $\bar{\sigma}$  was based on the derivative of the isochoric part of the strain energy potential towards the deviatoric stretch tensor  $\bar{\mathbb{B}}$ . This last derivative was estimated with the help of Eq. (5.2) implemented in

$$\frac{\delta W_{iso}(\bar{\mathbb{B}})}{\delta \bar{\mathbb{B}}} = \left[ a - 6b + \left( 2b + c + \frac{d}{X} \right) Tr(\bar{\mathbb{B}}) \right] \bar{I} - \left( c + \frac{d}{X} \right) \bar{\mathbb{B}} \quad (6.7)$$

With

$$X = \left[ \frac{1}{2} \left( Tr(\bar{\mathbb{B}})^2 - Tr(\bar{\mathbb{B}}^2) \right) - 3 + e \right]^2$$

By injecting the Eq. (6.7) in the definition of  $\bar{\sigma}$  and considering that  $\bar{\mathbb{B}} = \bar{\mathbb{F}}\bar{\mathbb{F}}^T = R\bar{\mathbb{U}}\bar{\mathbb{U}}^T R^T = R\bar{\mathbb{U}}^2 R^T$  with  $\bar{\mathbb{U}} = J^{-1/3}\bar{\mathbb{U}}$  and also that  $\det(\bar{\mathbb{B}}) = \det(\bar{\mathbb{U}}^2)$ , it was possible to set:

$$\bar{\sigma} = R \left\{ 2J^{-1} \left[ a - 6b + \left( 2b + c + \frac{d}{X} \right) Tr(\bar{\mathbb{U}}^2) \right] \bar{\mathbb{U}}^2 - 2J^{-1} \left( c + \frac{d}{X} \right) \bar{\mathbb{U}}^4 \right\} R^T \quad (6.8)$$

The combination of the term inside the curly brackets of Eq. (6.8), excluding the orthogonal tensor  $R$ , and the complete Eq. (6.6) allowed evaluating the isochoric stress, which had to be summed with Eq. (6.3) to appraise all the components of the Cauchy stress tensor written in function of the modified stretch tensor  $\bar{\mathbb{U}}$ . With this set of equations, the VUMAT subroutine was established, see Appendix E.3. The different steps conducted in this subroutine were summarized below:

- i. Determination of the Jacobian of the transformation with  $J = \det(U)$ , the stretch components being provided at each increment by the Abaqus/Explicit algorithm.
- ii. Evaluation of the volumetric stress with the help of Eq. (6.3).
- iii. Calculation of the modified stretch tensor  $\bar{\mathbb{U}}$  such as  $\bar{\mathbb{U}} = J^{-1/3}\bar{\mathbb{U}}$ .
- iv. With the previous step, it was possible to assess  $\bar{\mathbb{U}}^2$  and its Trace  $Tr(\bar{\mathbb{U}}^2)$ .

- v. The same operation was made for  $\bar{\mathbb{U}}^4$  and its Trace  $Tr(\bar{\mathbb{U}}^4)$ .
- vi. Evaluation of different parameters X, Y and Z defined as follow:

$$X = \left[ \frac{1}{2} \left( Tr(\bar{\mathbb{U}}^2)^2 - Tr(\bar{\mathbb{U}}^4) \right) - 3 + e \right]^2$$

$$Y = 2J^{-1} \left[ a - 6b + \left( 2b + c + \frac{d}{X} \right) Tr(\bar{\mathbb{U}}^2) \right] \quad (6.9)$$

$$Z = 2J^{-1} \left( c + \frac{d}{X} \right) \bar{\mathbb{U}}^4$$

- vii. Determination of the isochoric stress with the past steps and Eq. (6.6)
- viii. Assessment of Cauchy stress by summing the results of steps ii. and vii.

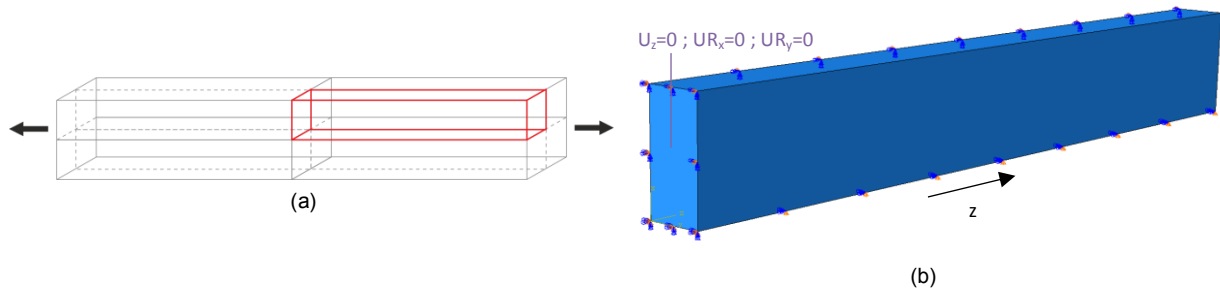
## 6.2.2 Uniaxial numerical simulations

Two sets of coefficients, i.e. one for the quasi-static case and one for the Mullin's effect impact, were obtained by fitting the developed isochoric strain energy potential to the uniaxial experimental results regrouping tension and compression. In this section, a distinction between the uniaxial actions was however operated in order to test the ability of the two written subroutines, UHYPER and VUMAT, to represent separately quasi-static and Mullin's impact tension/compression.

### 6.2.2.1 Tension

#### Definition of the geometry and boundary conditions

The tensile experiments on silicone elastomer, exposed in chapter 4 and either quasi-static or cyclic, were performed on dog-bone specimens installed between self-closing wedge clamps so that only the constant cross section was free and so that the radii between the heads and the core were non-tested. The dimensions of this section were in accordance to the ISO 527-2 [4.2], i.e. a cross section of 10x4mm and a length of 60mm. With the isotropic assumption of the silicone material and in reason of the symmetries of the boundary conditions, only one eighth of the parallelepiped, i.e. a section of 5x2mm and length of 30mm, was model, see Fig. 6.1.



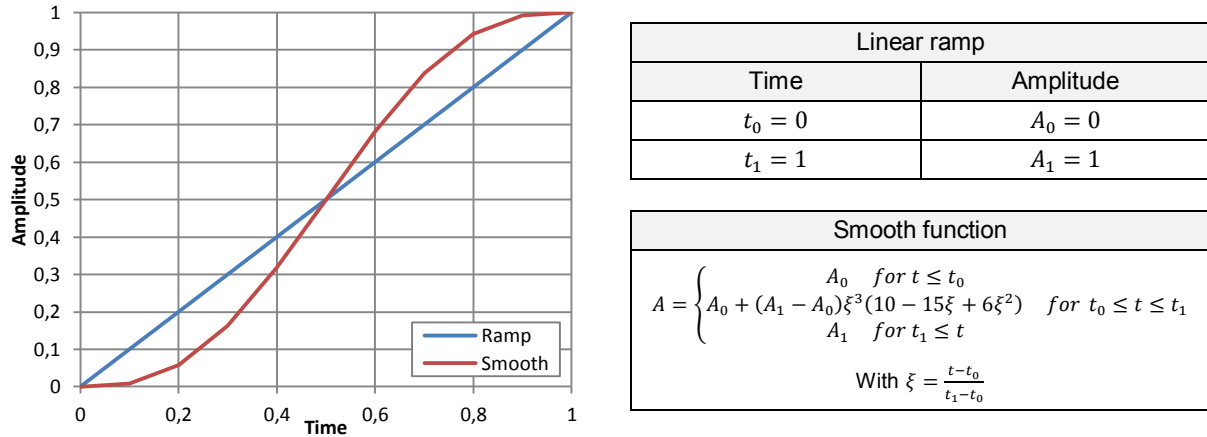
**Figure 6.1-** (a) 1/8<sup>th</sup> of the tested zone of the silicone dog bone sample and (b) Model in Abaqus with boundary conditions

As only 1/8<sup>th</sup> of the tested zone of the dog-bone sample was represented, boundary conditions had to be applied on the three faces theoretically in contact with the rest of the specimen. These boundary conditions were standard symmetries for which the displacements along the perpendicular to the surface were fixed as the rotations around the axes defining this surface, see example of Fig. 6.1 (b).

The loading was inserted as a simple displacement imposed to the bottom face, as the studied silicone was found invariant to the loading rate. To cover the whole quasi-static and Mullin's tested strain ranges, a displacement of 42mm, equivalent to a strain of 1.4, was considered. While, this displacement was assigned as a ramp during the increment over the selected time period in Abaqus /Standard, several possibilities were available in Abaqus/Explicit. In spite of the large choice, only the ramp and the smooth amplitude functions, see Fig. 6.2, were envisaged for this last solving method. As it can be observed, the main differences between these two functions occurred at the beginning



and at the end of the time increment, i.e. in the zones where the acceleration should vary slightly to no cause stress waves and inaccuracy of the solution. The results generated by these two amplitude functions will be discussed in the following paragraphs.



**Figure 6.2-** Comparison between Ramp/Smooth amplitude functions for the application of the displacement in Abaqus/Explicit

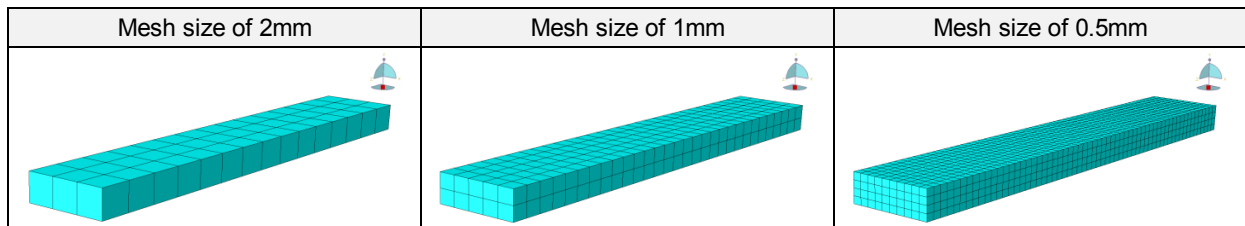
### Material behaviour

With the imposed boundary conditions, only the silicone material was modeled. The quasi-static and Mullin's behaviour were investigated separately with the hyperelastic material law and associated coefficients gathered in Table 5.21. The constitutive model was first implemented via the developed UHYPER subroutine of Abaqus/Standard and then via the VUMAT subroutine of Abaqus/Explicit. In consequence, four distinctive cases stood out:

- Quasi-static representation with the UHYPER subroutine,
- Mullin's effect consideration with the UHYPER subroutine,
- Quasi-static representation with the VUMAT subroutine,
- Mullin's effect consideration with the VUMAT subroutine.

### Meshing

The mesh elements should be chosen according to the solving method and specific libraries existed for both, i.e. a standard library for Abaqus/Standard and explicit library for Abaqus/Explicit. In spite of this distinction, 3D hexahedral elements were available in the two libraries, i.e. 8-node linear or 20-node quadratic bricks. Due to the quasi-incompressible nature of the silicone material, the reduced integration was avoided and hybrid elements, using a mix formulation of displacement and stress variables, had to be selected in the standard library. Thus, for Abaqus/Standard and with regards to the linear or quadratic order of the element, two different types were investigated, i.e. C3D8H and C3D20H. In Abaqus/Explicit, only linear C3D8 and quadratic C3D10M bricks were offered. In addition, to the selection of the elements, different mesh sizes were tested, i.e. three cubic sizes of 0,5mm, 1mm and 2mm of length for Abaqus/Standard and two cubic sizes of 1mm and 2mm of length for Abaqus/Explicit, see Fig. 6.3.



**Figure 6.3-** Different mesh sizes (2mm/1mm/0.5mm) for the numerical simulation of silicone dog-bone samples

All the different investigated elements and mesh sizes were summarized in the following Table 6.1.

| Element order | Abaqus/Standard                                    | Abaqus/Explicit            |
|---------------|----------------------------------------------------|----------------------------|
| Linear        | C3D8H hybrid elements<br>Mesh size: 2mm/1mm/0.5mm  | C3D8<br>Mesh size: 2mm/1mm |
| Quadratic     | C3D20H hybrid elements<br>Mesh size: 2mm/1mm/0.5mm | C3D10M<br>Mesh size: 2mm   |

**Table 6.1-** Summary of the elements and mesh sizes according to the two numerical methods of resolution

### Solution procedures

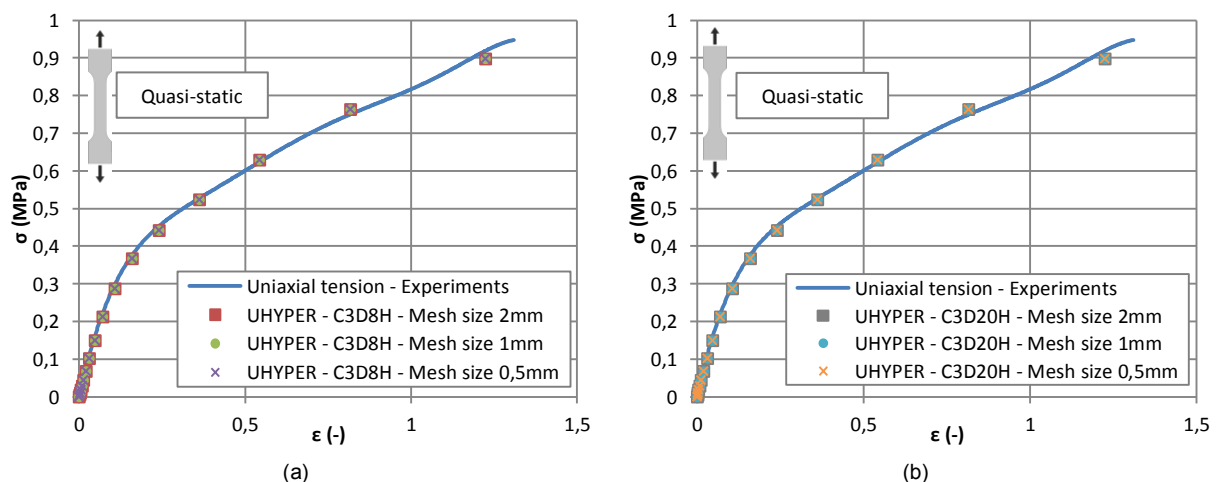
In Abaqus/Standard and Explicit, non-linear geometries were expected and so the corresponding option “nlgeom” was incorporated in all the models. Furthermore, as the studied silicone was found completely invariant towards the loading rate, the definition of the time period was arbitrary made for the standard implicit method of resolution. Only the initial increment size was lowered to 0,001 for this procedure. However, for the explicit algorithm, the full analysis was undertaken in two steps with a first determination of the lowest natural frequency with the help of the frequency tool provided Abaqus/Standard followed by the resolution of the problem with the explicit method. The evaluation of the fundamental frequency was primordial to define a proper time period in order to prevent local distortions of the mesh due to a too small period or too long calculation engendered by a too large period. A frequency of 436,8Hz was obtained, inducing a minimal time period of 0,002s. Despite this last value, the recommendation advised by the Abaqus documentation consisted in stating the explicit calculation with this period and progressively increasing it by 10 to 50 times until noticing appropriate results from an energy balance point of view. Thus, time periods of 0,1s and 0,2s were also assessed for the explicit examination.

### Analysis of the results

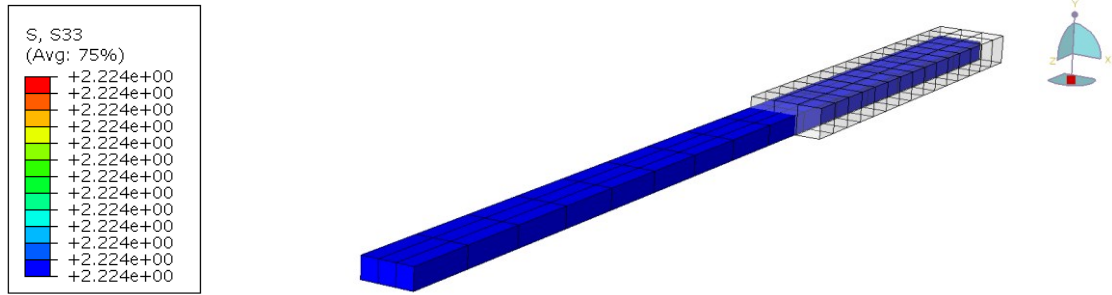
The results of the numerical simulations of silicone dog-bone samples were split according to the method of resolution and consequently to the employed subroutine. The stress-strain curves acquired with the UHYPER subroutine were first examined for the different envisaged mesh elements and sizes. This operation was then repeated with the diagrams issued from the VUMAT subroutine. In both cases, Abaqus returned the true stress data, i.e. the force divided by the actual deformed section. These true stresses were converted in engineering stresses for comparison to the experimental results assessed by dividing the applied force by the initial and constant cross section.

- Abaqus/Standard – UHYPER

The UHYPER subroutine was first employed in combination to the quasi-static set of coefficients of Table 5.21 to evaluate this type of action.



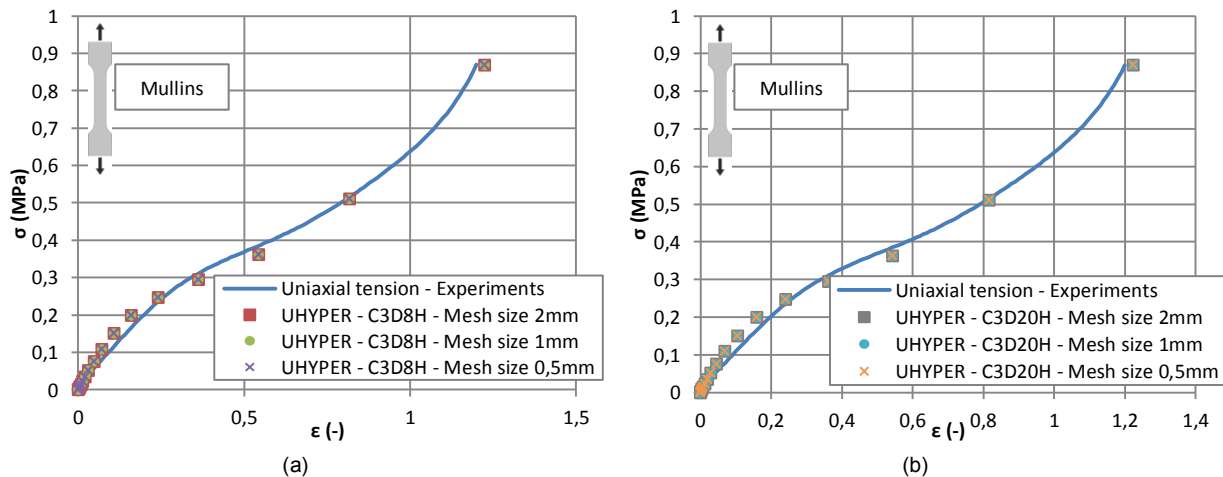
**Figure 6.4-** Engineering stress-strain diagrams for (a) linear and (b) quadratic elements – Silicone quasi-static tension



**Figure 6.5-** True stress final result of UHYPER-C3D8H-Mesh size 2mm – Silicone quasi-static tension

The two selected mesh elements and the three associated mesh sizes were gathered in Fig. 6.4. For the linear mesh elements C3D8H, no difference was seen between the three mesh sizes, indicating that even a coarse mesh was apt to model the quasi-static tensile behaviour of silicone. The same observation could have been done for the quadratic elements C3D20H, for which no variation in the stress-strain behaviour was assessed for the three mesh sizes. A very good concordance between all the numerical simulations and the real tensile behaviour was recorded, validating the UHYPER subroutine for this type of action.

The UHYPER subroutine was then used with the Mullin's effect coefficients of Table 5.21 to conduct the same analysis. For the two considered element orders, linear and quadratic, the three mesh sizes were investigated, see Fig. 6.6.

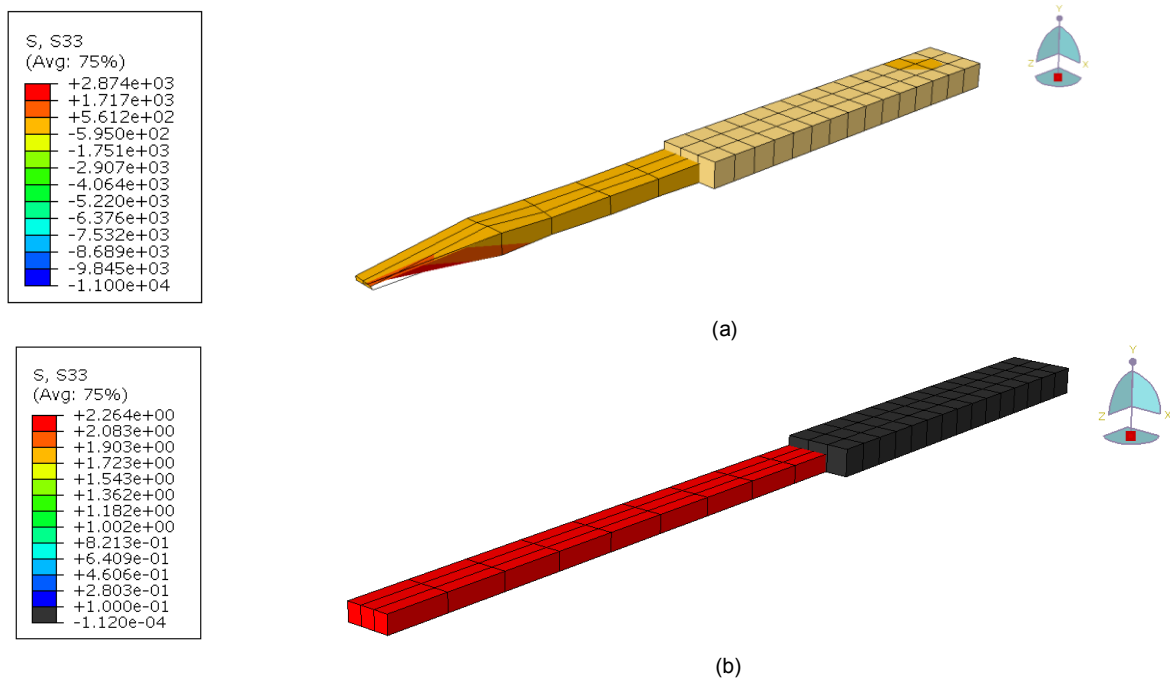


**Figure 6.6-** Engineering stress-strain diagrams for (a) linear and (b) quadratic elements – Silicone Mullin's tension

For the two types of elements, i.e. C3D8H or C3D20H, and for the different sizes of the mesh, all the numerical simulations were clearly superposed to the averaged experimental curve over the whole strains range. Hence, neither the types of element nor the mesh sizes were of influence for this simple tension representation. The subroutine UHYPER was therefore validated to model the stress-strain behaviour of silicone material after the Mullin's effect.

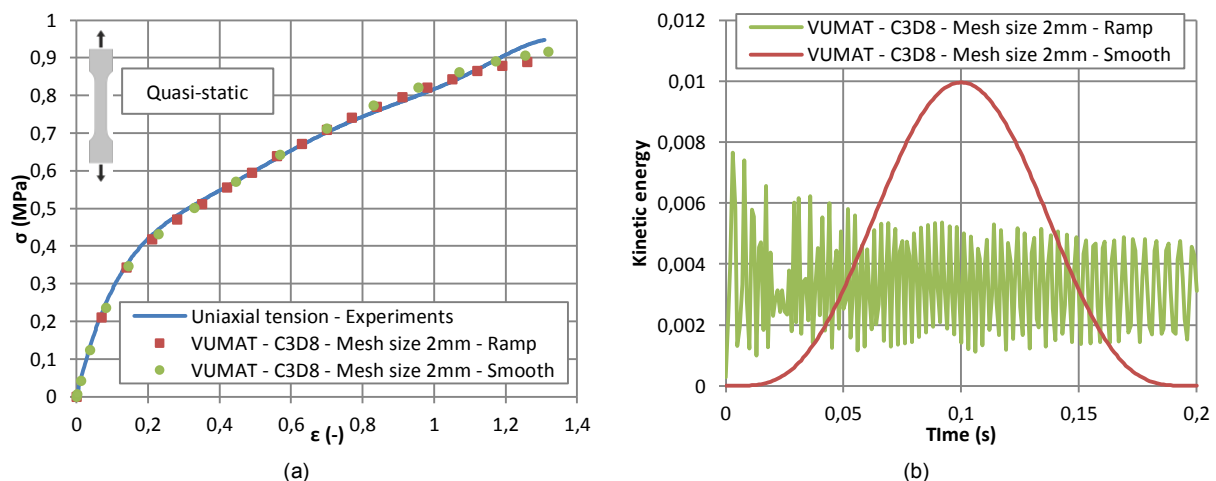
- Abaqus/Explicit – VUMAT

The written VUMAT subroutine was used at first to reproduce the quasi-static experimental results. However, before evaluating the convergence of the mesh, by studying linear/quadratic elements or reducing the size of the mesh, the determination of the correct time period was essential for this explicit resolution. As aforementioned, three periods were examined, i.e. 0,002s, 0,1s and 0,2s. While the calculation for linear elements of 2mm of size combined to a smooth application of the imposed displacement aborted with severe distortions on several elements for the shorter period, the other two, for greater periods, ran until the end and provided true stresses close to the ones got with the standard resolution, see Fig. 6.7 for the extreme cases.



**Figure 6.7-** True stress final results – Time period of (a) 0.002s and (b) 0.2s – VUMAT-C3D8-Mesh size 2mm-Smooth

With regards to the short time of calculation, the maximum period of 0,2s was conserved to appraise the influence of the amplitude function, i.e. either a ramp or a smooth function, applied on the imposed displacement of 42mm. In the present case and for both functions, the total time period of 0,2s was attributed to the value  $t_1$  of the equations of Fig. 6.2. Even, if the numerically obtained stress-strain diagrams were superposed and perfectly matched the experimental data, a difference appeared by comparing the kinematic energy, which had to be negligible for these quasi-static tests. For the ramp amplitude, chaotic variations of the kinetic energy were remarked and for the smooth amplitude, a more “Gaussian” function was achieved, see Fig. 6.8. As the ramp amplitude did not generate a smooth kinetic result, this option was judged as inappropriate for the application of the imposed displacement. Thus, only the smooth amplitude was preserved.



**Figure 6.8-** (a) Engineering stress-strain diagrams – Linear elements; (b) Kinetic energy vs. time – Ramp/Smooth comparison

Finally, with the choices of the time period of 0,2s and the application of the displacement via the smooth amplitude function, the importance of the mesh refinement could be investigated. Two mesh sizes were tested for the linear elements and one mesh size for the quadratic ones, see Fig. 6.9. The numerical results were again superposed and close to the real quasi-static tensile behaviour, demonstrating the independence of the final data towards the regarded mesh parameters. In addition, the kinetic energy diagrams also coincided, confirming this observation. In conclusion, the VUMAT

subroutine implemented in Abaqus/Explicit accurately described the quasi-static behavior of dog bone samples.

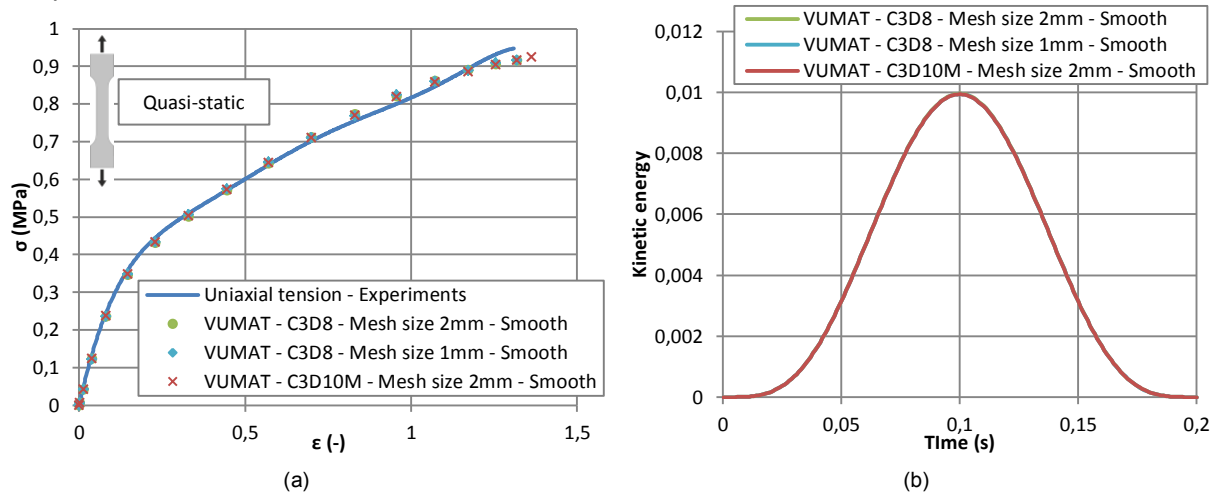


Figure 6.9- (a) Engineering stress-strain diagrams and (b) Kinetic energy vs. time – Silicone quasi-static tension

As for the UHYPER subroutine, the VUMAT was employed to represent the Mullin's effect with the corresponding coefficients of Table 5.21. The time period of 0,2s and the smooth amplitude function for the application of the desired displacement, both determined as optimum for the quasi-static case in Abaqus/Explicit, were conserved. To evaluate the convergence of the mesh, two element types were tested, i.e. linear and quadratic. While for the linear type, two mesh sizes of 1mm and 2mm were investigated, only one of 2mm was examined for the quadratic element. The results of these numerical simulations and the kinetic energy diagrams validating them were presented in Fig. 6.10.

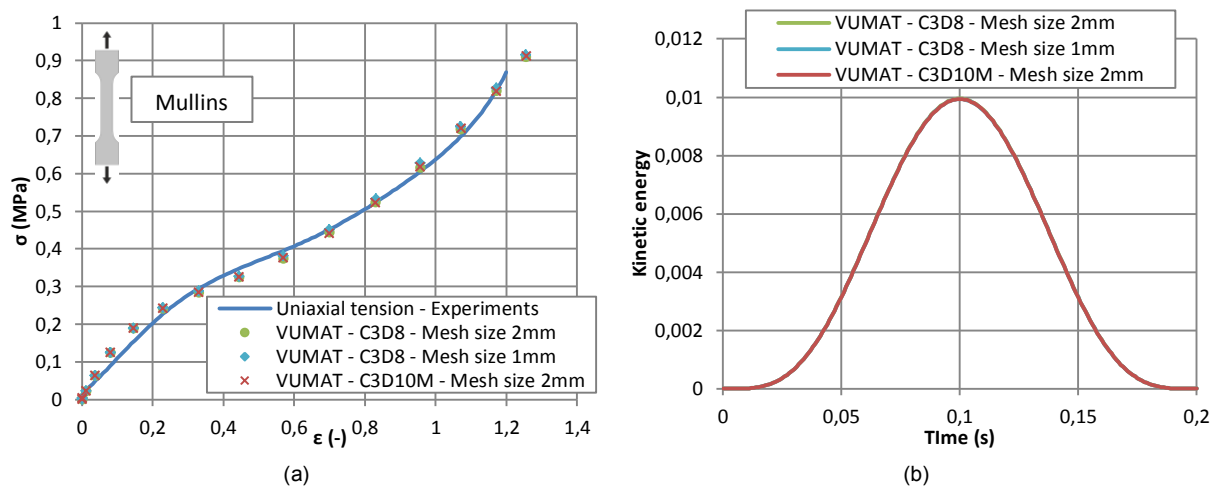


Figure 6.10- (a) Engineering stress-strain diagrams and (b) Kinetic energy vs. time – Silicone Mullin's tension

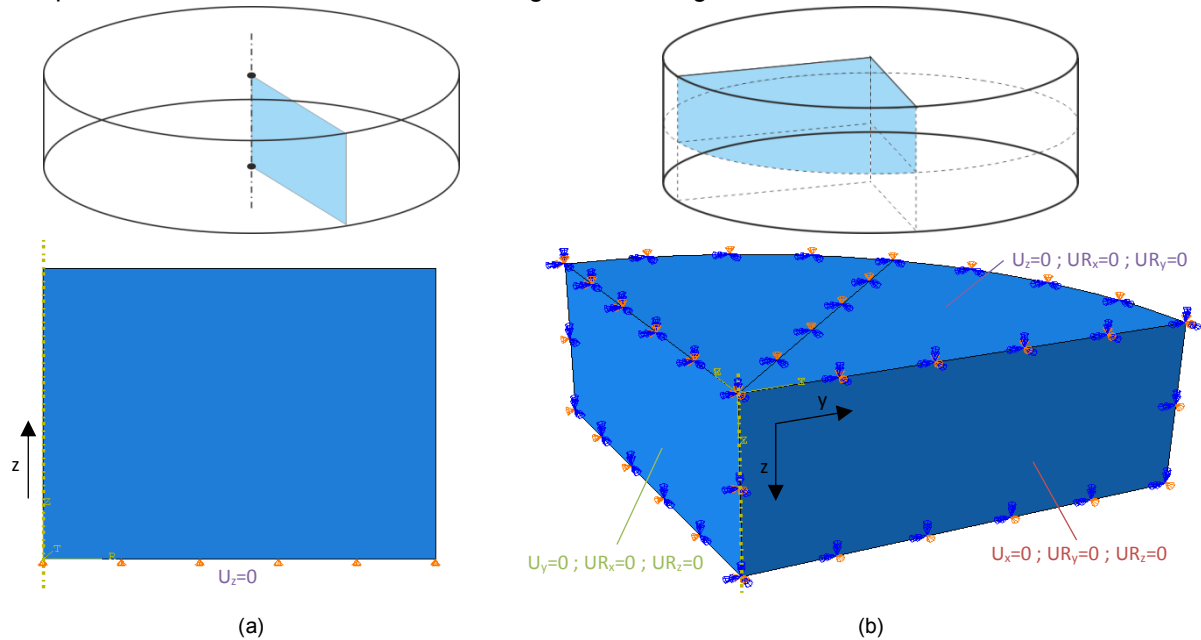
All the curves issued from the numerical calculations perfectly fitted the experimental averaged curve, indicating that the convergence was already reached for the coarse linear mesh. This also confirmed the validity of the developed VUMAT subroutine for tensile simulations.

### 6.2.2.2 Compression

#### Definition of the geometry and boundary conditions

The uniaxial compressive experiments were conducted on cylindrical specimens of 20mm of height and 45mm of diameter. With the employed testing procedure, no friction at the top and bottom extremities of the samples occurred, allowing free lateral expansions. Consequently, only the silicone part was modeled as the friction was considered nil. Furthermore, as this material was assumed isotropic and with regards to the symmetries of the boundary conditions, a simple axisymmetric

representation was envisaged. This last method was however only available in Abaqus/Standard, for which no mass had to be defined to proceed to the calculation. In Abaqus/Explicit, one eighth of the silicone sample, radius of 22,5mm and height of 10mm, was represented as a 3D deformable solid. The particularities of these two models were gathered in Fig. 6.11.



**Figure 6.11-** (a) Axisymmetric representation in Abaqus/Standard and (b) 3D representation of 1/8<sup>th</sup> in Abaqus/Explicit

For the axisymmetric model of Abaqus/Standard, only one boundary condition was applied on the lower edge to restrain the vertical displacement, but also authorize the sliding of the sample. The load was introduced as a simple displacement applied on the opposite edge with ramp amplitude over the increments. The value selected for this displacement was of 14mm corresponding to a strain of 0,7 and equivalent to the maximum deformation resulting from the quasi-static experiments.

For the 3D model of Abaqus/Explicit, at least three boundary conditions, applied on the cut surfaces, were necessary. Standard symmetries, restraining the displacements along the perpendicular of the surface and the rotations around the axes defining it, were used. The load was inserted on the upper flat surface as a displacement combined to a smooth amplitude, see Fig. 6.2. As 1/8<sup>th</sup> of the total compressive specimen was modeled, the assigned value was of 7mm for both quasi-static and Mullins numerical simulations.

### Material behaviour

As for the uniaxial tension, only the silicone material behaviour was implemented and four different cases stood out according to the type of action and to the solving method:

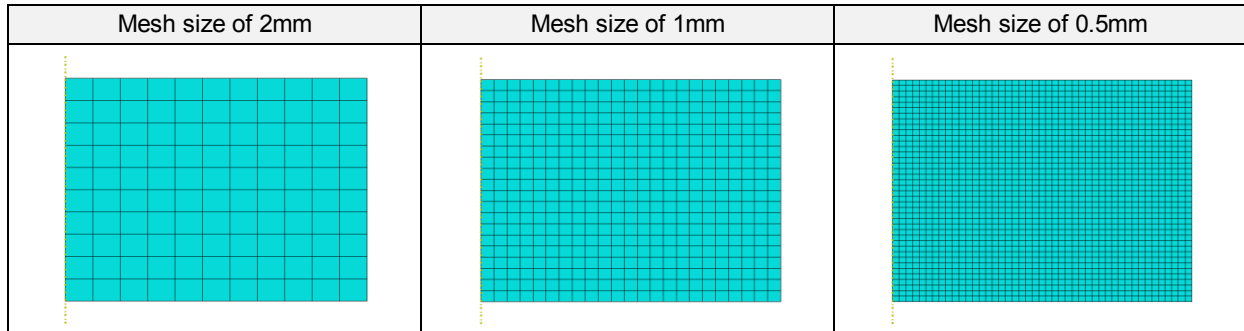
- Quasi-static representation with the UHYPER subroutine,
- Mullin's effect consideration with the UHYPER subroutine,
- Quasi-static representation with the VUMAT subroutine,
- Mullin's effect consideration with the VUMAT subroutine.

The two subroutines were given in Appendix E and the material coefficients for the instantaneous and Mullin's effect characterization in Table 5.21.

### Meshing

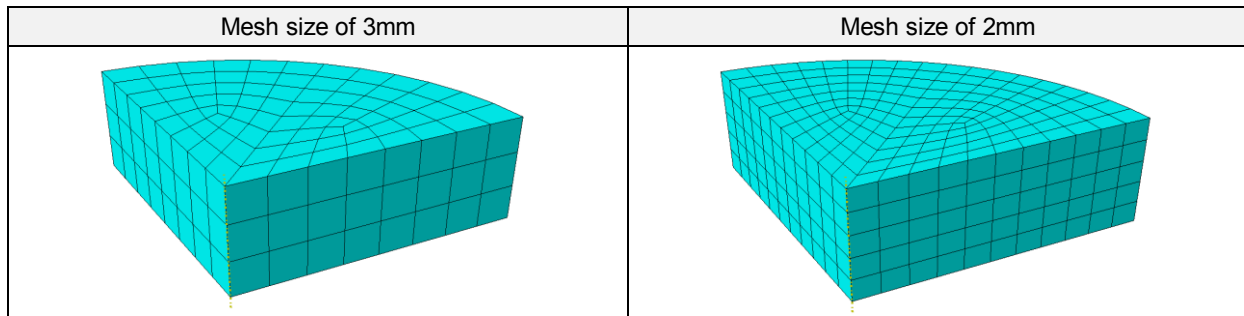
The possibilities offered by the axisymmetric elements library of Abaqus/Standard were analyzed. While the reduced integration elements were avoided, the hybrid formulation had to be employed for the present quasi-incompressible silicone. Furthermore, the convergence of the mesh was evaluated

by using linear CAX4H and quadratic CAX8H elements, but also by reducing the size of the mesh starting from 2mm to 0,5mm, see Fig. 6.12.



**Figure 6.12-** Different mesh sizes for the numerical simulation of silicone compressive samples – Abaqus/Standard

In Abaqus/Explicit, linear and quadratic 3D elements were tested for the geometry defined on Fig. 6.11 (b). As the hybrid formulation was absent for this type of analysis, convergence difficulties coming from the mesh were expected. Due to the cylindrical geometry of the compressive sample, the elements were non identical in size and did not present perpendicular angles, see Fig. 6.13. This combined with the large compression, during which the volume of each element rapidly decreased to almost zero, generated instabilities in the explicit solving method. Therefore, only two larger mesh sizes of C3D8 elements were studied in this case, i.e. 3mm and 2mm, see Fig. 6.13.



**Figure 6.13-** Different mesh sizes for the numerical simulation of silicone compressive samples – Abaqus/Explicit

### Solution procedures

From the compressive experimental investigations presented in chapter 4, the complete invariance of the silicone properties towards the loading rate was demonstrated. Thus, as for the tensile numerical simulations, the definition of the time period in Abaqus/Standard was arbitrary made and the default value offered by the software was conserved. The initial increment size was however decreased to 0,001s to appraise the evolution of the calculation.

The lowest natural frequency was once more estimated with the frequency tool of Abaqus/Standard in order to determine the proper time period to implement in Abaqus/Explicit for the resolution of the current problem. The obtained frequency was of 544,8Hz inducing a minimal time period of about 0,002s. Consequently, this last time period was considered in Abaqus/Explicit, as well as larger ones of 0,1s and 0,2s as recommended by the Abaqus documentation. As for the implicit resolution, the non-linear geometry option “nlgeom” was incorporated in this model.

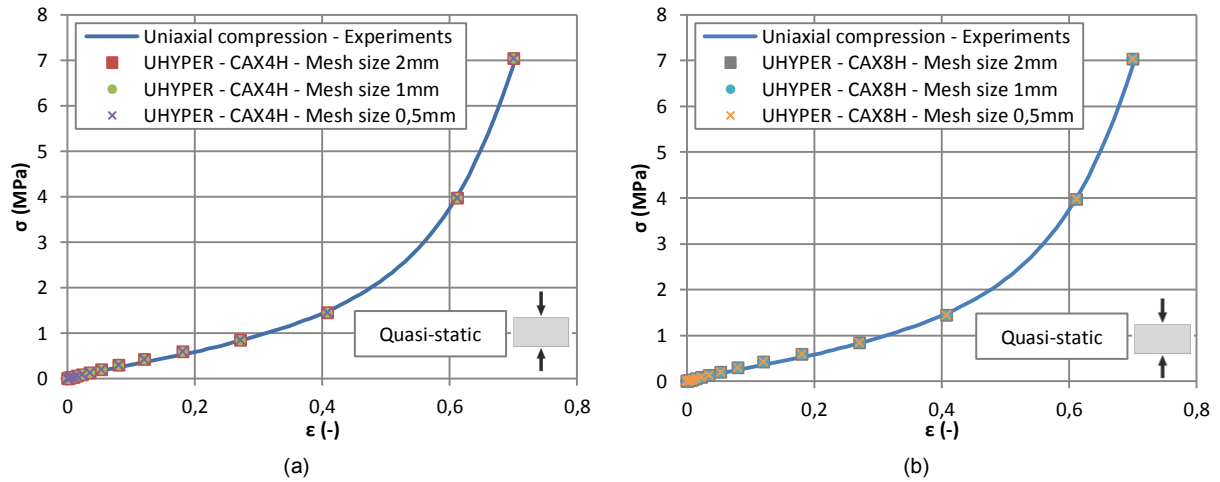
### Analysis of the results

For each method of resolution, based either on the UHYPER or the VUMAT subroutine, the two types of behaviour characterizing the selected elastomer, i.e. instantaneous and including the Mullin's effect, were analyzed. In both cases, the resulting true stresses were converted in engineering stresses for a direct comparison with the averaged experimental results.

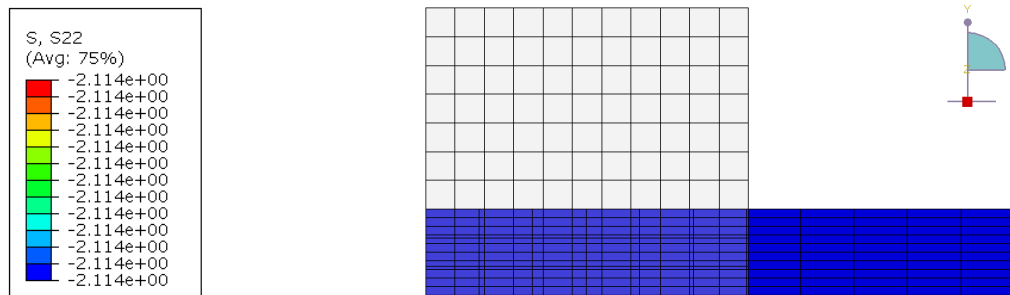


- Abaqus/Standard – UHYPER

The first study with the UHYPER subroutine concerned the reproduction of the quasi-static behaviour issued from the uniaxial compressive tests. The numerically achieved stress-strain diagrams for the different mesh orders and sizes were superposed to the real one for comparison, see Fig. 6.14.

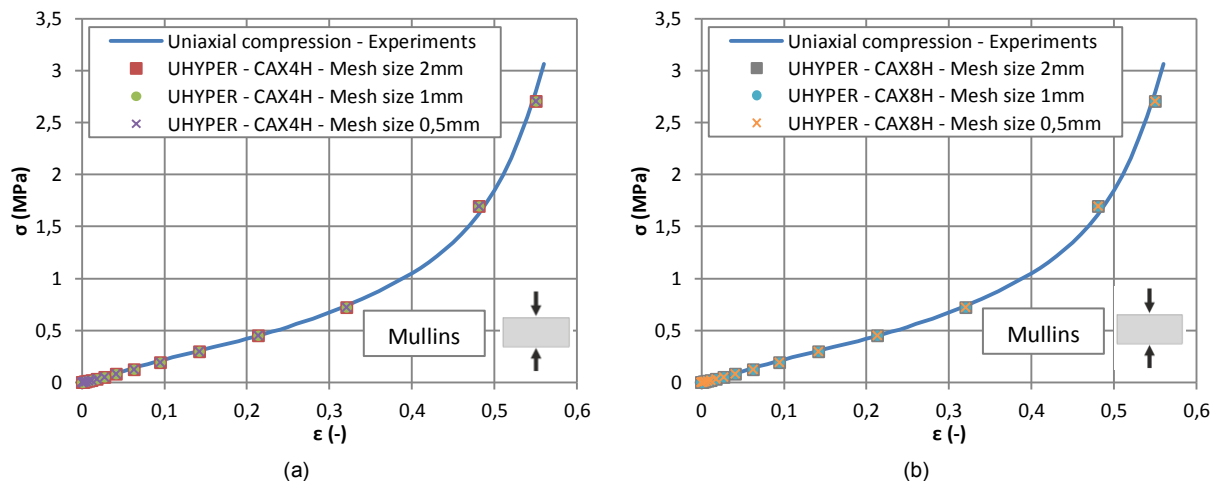


**Figure 6.14-** Engineering stress-strain diagrams for (a) linear and (b) quadratic elements – Silicone quasi-static compression



**Figure 6.15-** True stress final result of UHYPER-CAX4H-Mesh size 2mm – Silicone quasi-static compression

For the linear order element CAX4H, all the different mesh sizes gave the same stress-strain curves perfectly matching the experimental one on the whole strain range. Identical results could be extracted from the observation of the stress-strain curves attained with the quadratic elements CAX8H. Hence, even with a coarse linear mesh, good results were achieved, as no variation was remarked with smaller elements. This allowed concluding on the validity of the developed subroutine UHYPER for the representation of the quasi-static compressive silicone behaviour.



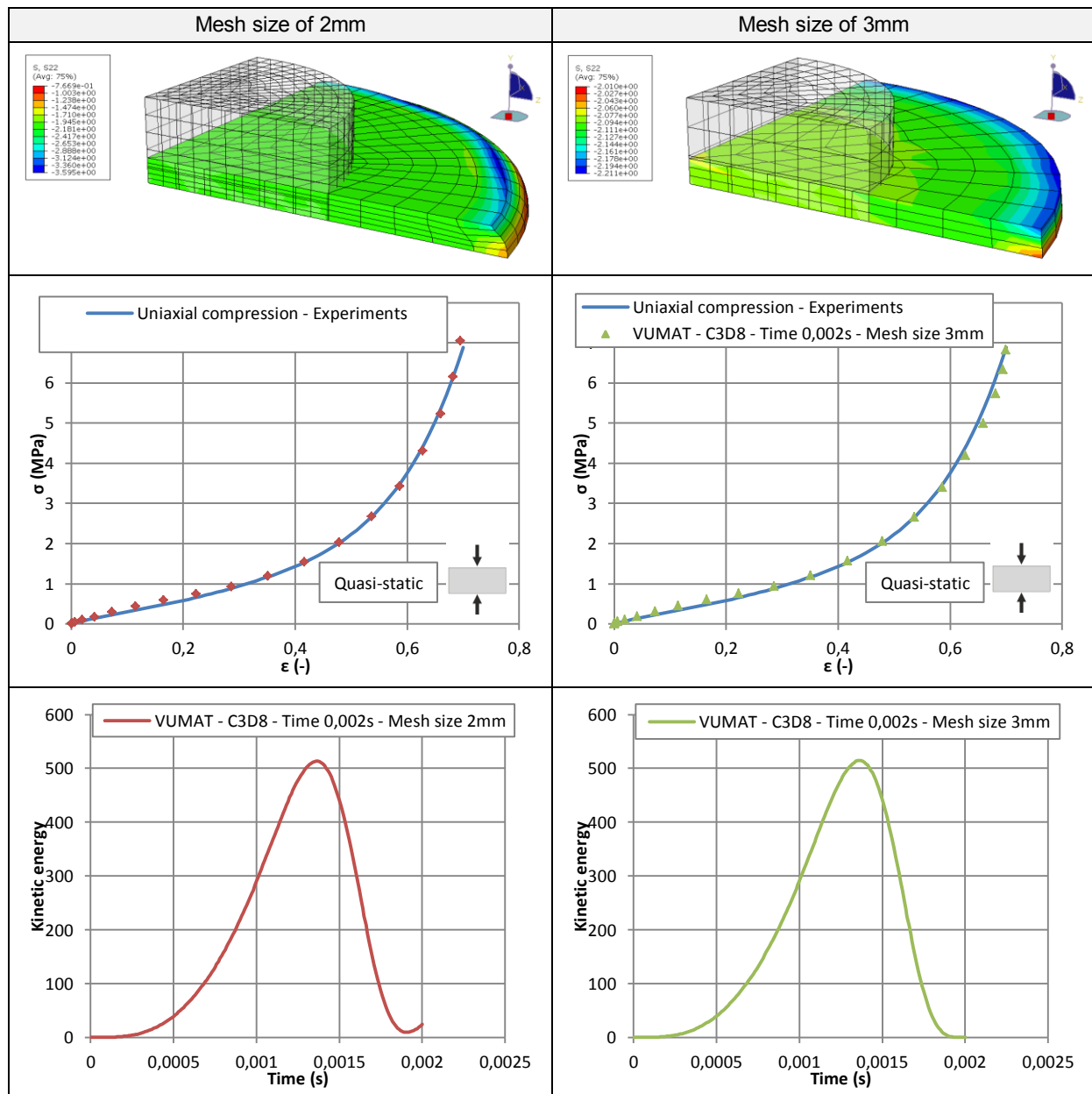
**Figure 6.16-** Engineering stress-strain diagrams for (a) linear and (b) quadratic elements – Silicone Mullin's compression



To account for the variations in stress-strain curve after discontinuous damage lasting 7 cycles, i.e. Mullin's effect, the second set of coefficients of Table 5.21 was used in combination with the UHYPER subroutine. The obtained diagrams were again compared to the experimental one, see Fig. 6. 16. For the linear and quadratic elements, no distinction between the stress-strain curves could have been done, as they were alike and superposed to the curve arising from the tests. The mesh sizes and the orders of the elements were consequently judged as non-influent. With the good concordance between all the results, the UHYPER subroutine was estimated apt to represent the behaviour of the silicone after the Mullin's effect.

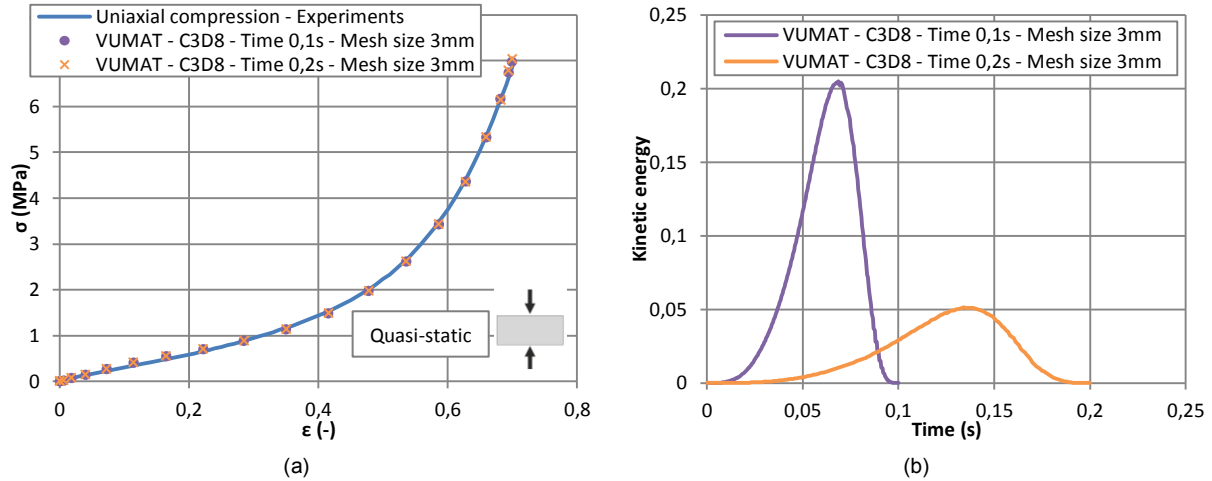
- Abaqus/Explicit – VUMAT

The subroutine VUMAT was also employed at first to represent the quasi-static behaviour of silicone subjected to uniaxial compression. As aforementioned, due to the mesh dependency of the studied system, the calculation was performed for two mesh sizes of 2mm and 3mm and also for three time periods, i.e. 0,002s, 0,1s and 0,2s. To properly assess the importance of the mesh on the results, the time period was fixed to 0,002s and the two mesh sizes were tested, see Table 6.2.



**Table 6.2-** Influence of the mesh size on the accuracy of the results under Abaqus/Explicit – Silicone quasi-static compression

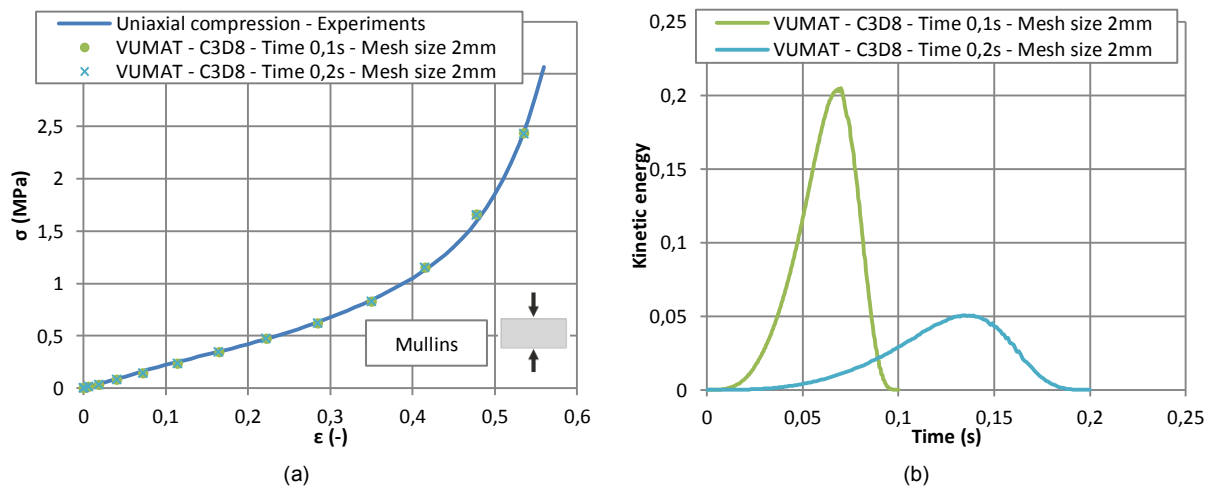
As it could be observed, the stress-strain curves achieved with the numerical simulations accurately matched the one issued from the numerical simulations for both mesh sizes. However, a closer look to the kinetic energy diagrams allowed identifying a last burst and the non-return to zero at the end of the time period for the 2mm mesh. This resulted in important deformations of the elements at the free extremity of the sample, not present for the larger mesh of 3mm. Therefore, a too small mesh could lead to erroneous numerical data and only an analysis of the energy balance could let apprehend this phenomenon. Furthermore, an important peak of kinetic energy was noted indicating that the applied time period of 0,002s was too low. The calculation was thus redone with the two periods of 0,1s and 0,2s for the mesh size of 3mm, see Fig. 6.17.



**Figure 6.17-** (a) Engineering stress-strain diagrams and (b) Kinetic energy vs. time – Silicone quasi-static compression

For the larger periods, the maximum peaks of kinetic energy were negligible and the curves returned to zero validating the results. The experimental behaviour was properly represented over the whole deformation range validating the written VUMAT subroutine for the quasi-static case.

Then, the behaviour at the end of the Mullin's effect was considered. The explicit subroutine and the corresponding coefficients were implemented to reproduce the experimental data. The load was again introduced as a displacement applied with the help of a smooth amplitude. As for the quasi-static investigations, a mesh size of 3mm was chosen and the two larger time periods of 0,1s and 0,2s were tested, see Fig. 6.18.



**Figure 6.18-** (a) Engineering stress-strain diagrams and (b) Kinetic energy vs. time – Silicone Mullin's compression

The evaluation of the kinetic energy, low maximum value and return to zero at the end of the time period, allowed ensuring of the accuracy of the results. The stress-strain curves coming from the numerical simulations were then compared to the experimental one. Good concordances were found,

demonstrating the proper selection of the time period and the correct definition of the material law through the VUMAT subroutine for the representation of the compressive silicone behaviour including the Mullin's effect.

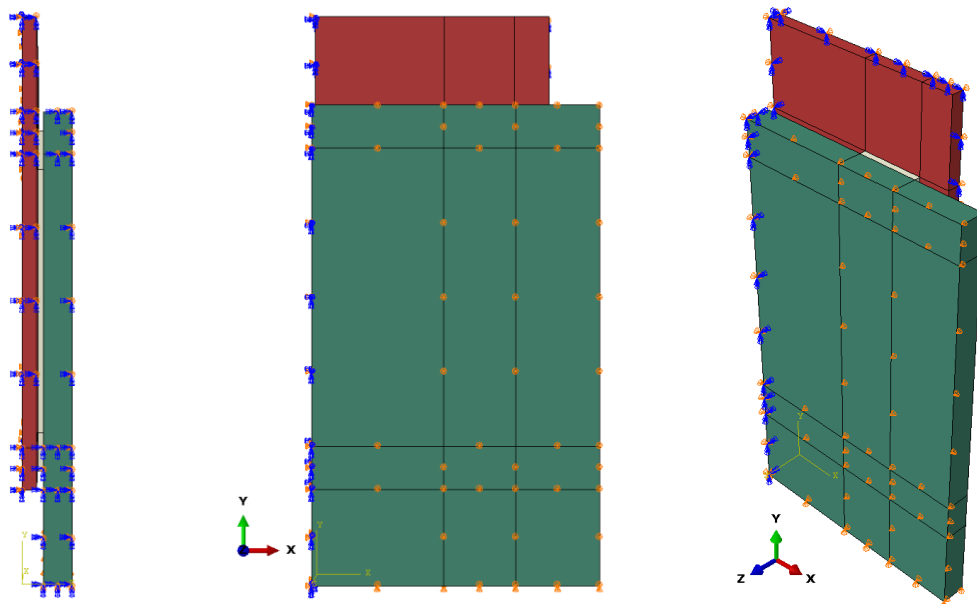
### 6.2.3 Shear numerical simulations

The uniaxial numerical simulations were followed by shear investigations as experimentally performed. While no variation in the silicone sample sizes were undertaken for the tensile and compressive tests, different adhesive geometries, i.e. in terms of bonding area and thickness, were examined with the push-out specimens. Nevertheless, these specificities were only demonstrated influent on the final strength and not on the global stress-strain behaviour. Therefore, only one configuration was at first considered and implemented in finite element software to evaluate the validity of the developed material law. From, this analysis a stress numerical singularity appeared. This last phenomenon and its real occurrence were also checked and presented in this section.

#### 6.2.3.1 Material law verification

##### Definition of the geometry and boundary conditions

With respect to the geometry of the push-out experiments and involved materials, a three dimensional representation was regarded. Indeed, even if a 2D representation could well represent the behaviour of the inner core of the adhesive joint, it was judged as inapt to account for the lateral deformations arising at its edges. Furthermore, for two of the four tested push-out assemblies, the adhesive repartition was discontinuous with four strips of 30mm width. As aforementioned, due to the invariance of the silicone shear stress-strain properties towards geometric changes, only one 3D configuration was kept and modeled in Abaqus, i.e. the smallest bonded area of 4x(160x30mm) and thickness of 3mm. As for the other arrangements, two axes of geometrical and material symmetry existed allowing inspecting only one fourth of the total assembly, see Fig. 6.19.



**Figure 6.19-** 3D representation of 1/4<sup>th</sup> of the push-out assembly (160x30x3mm) for both Abaqus/Standard and Abaqus/Explicit

With this representation, two boundary conditions had to be applied to reproduce the behaviour of the whole element, i.e. two standard symmetries limiting the displacements along the perpendicular of the surface and the rotations around the axes defining the latter. These symmetries were simply placed on the surfaces theoretically in contact. During the test, the rotations of the glass plates around their supporting edges were restrained with the help of lateral steel supports and with an inner Polyamide spacer fitting at the bottom the gap remaining between the two outer adherends. To incorporate these

conditions in the numerical model, the displacements perpendicular to the outer glass plate were simply fixed thereby avoiding, in combination with the symmetry boundary on the inner steel plate, any opening. Finally, the bottom steel support acting on the glass edges of the assembly was inserted by restricting the vertical displacements, see Fig. 6.19.

The displacement loading was applied on the upper edge of the inner steel plate with no consideration of the loading rate as the silicone shear properties were found independent of this parameter. To cover a large strain range, a displacement of 5,23mm, corresponding to a strain of 1,05 was inserted for the evaluation of the quasi-static behaviour and another one of 3,63mm, equivalent to a strain of about 0,88, for the Mullin's effect. While in Abaqus/Standard, a default standard ramp amplitude during the increment was used for the application of the desired displacement, a smooth amplitude was employed in Abaqus/Explicit.

### Material behaviour

In contrary to the previous uniaxial numerical simulations, other materials than the studied silicone were implemented in the present model. With regards to the large cross sections, the glass and steel properties were considered fully linear, without plasticity for the steel element. Only the definition of the Young's modulus and the Poisson's coefficient were thus needed for both standard and explicit resolutions, see Table 6.3.

| Material | Young's modulus E (MPa) | Poisson's ratio (-) | Density (ton/mm <sup>3</sup> ) |
|----------|-------------------------|---------------------|--------------------------------|
| Steel    | 210000                  | 0,3                 | 2,5E-009                       |
| Glass    | 70000                   | 0,23                | 7,85E-009                      |

**Table 6.3-** Linear material properties of the steel and glass elements composing the push-out numerical model

For the silicone material, the quasi-static and Mullin's behaviour were also considered via the two solving methods and consequently the two developed subroutines, generating four distinct analyses:

- Quasi-static representation with the UHYPER subroutine,
- Mullin's effect consideration with the UHYPER subroutine,
- Quasi-static representation with the VUMAT subroutine,
- Mullin's effect consideration with the VUMAT subroutine.

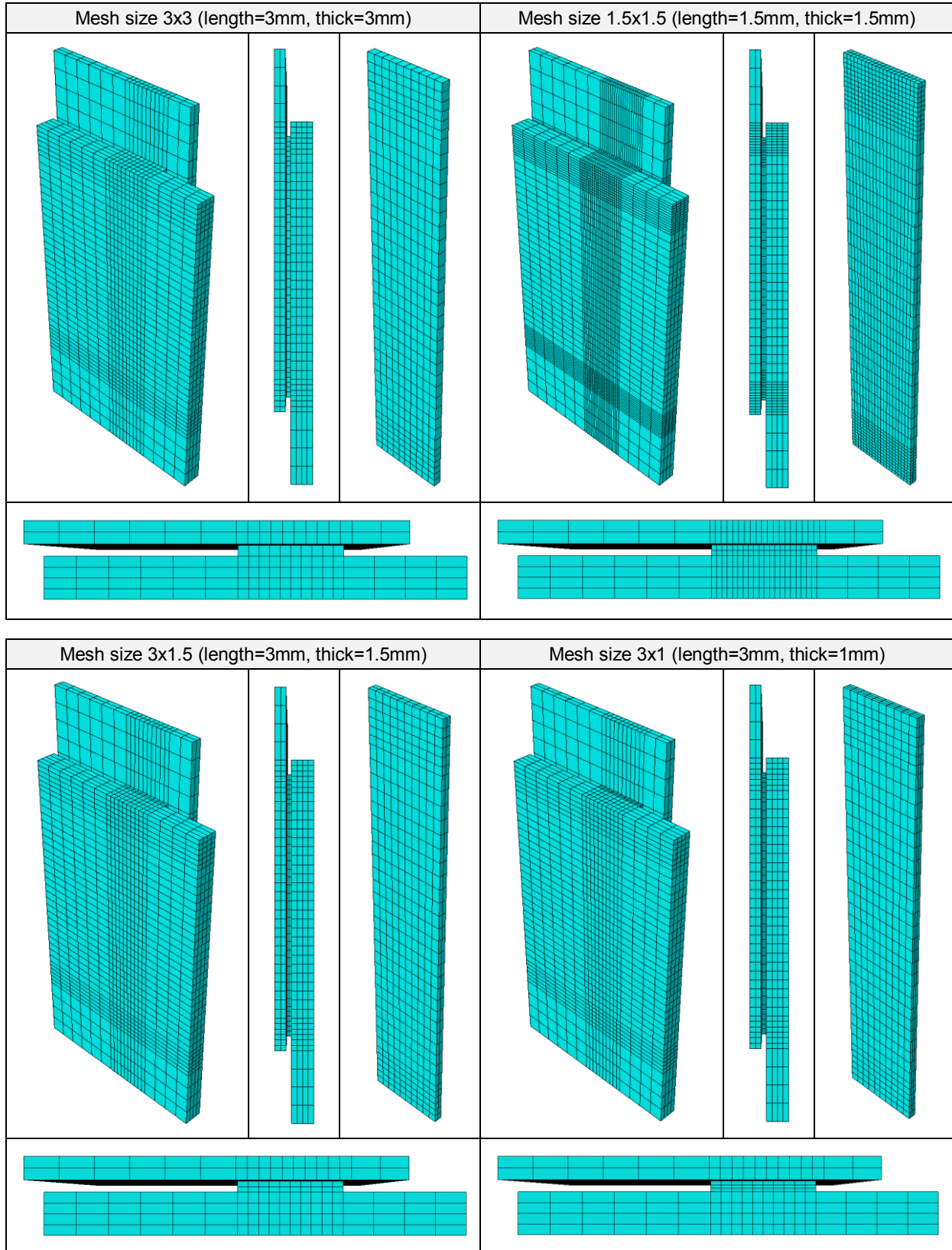
The two subroutines were given in Appendix E and the material coefficients for the instantaneous and Mullin's effect characterization in Table 5.21.

### Meshing

With no regards to the solving method or to the silicone properties, 3-dimension hexahedral elements were used in each case. Beside the definition of the shape, the choice of the element type was mainly dependent on the solving method and on the material. Indeed, the hybrid elements for incompressible or quasi-incompressible materials were only available in Abaqus/Standard. Reduced integration elements were nonetheless avoided for the two methods of resolution. Furthermore, with the large imposed deformations, important variations in the mesh angles were expected as well as distortions. Therefore, to prevent that some elements curled up on themselves, only 8-node linear bricks were envisaged for the silicone and consequently for the other components. Hence, in Abaqus/Standard, C3D8 linear elements were administrated to the steel and glass parts and hybrid C3D8H to the elastomer adhesive. In Abaqus/Explicit, only C3D8 elements were assigned to all the constituents, even to the silicone.

The influence of the mesh size on the results was examined too by essentially concentrating on the silicone. The number of elements along the thickness of the glass and of the steel always remained identical (fixed size of 3mm), i.e. four elements for the glass and two for the steel. For the free end regions of these two parts, the length of the mesh was fixed to 10mm. Two partitions over the whole

piece were made horizontally to mark out two zones of 18mm of length near the extremities of the adhesive. In the core region comprised between these two partitions, the length was continually set to 5mm. The length, width and thickness of the mesh at the extremities of the silicone were varied by keeping the ratio length over width equal to one (square face). The four cases studied under Abaqus/Explicit were summarized on Fig. 6.20. For Abaqus/Standard, only the mesh case 1x1mm was added.



**Figure 6.20-** Different mesh sizes for the numerical simulation of silicone push-out samples – based on Abaqus/Explicit models

## Solution procedures

With the invariance of the silicone shear properties towards the loading rate, no particular attention had to be paid to the definition of the time period and the default value proposed by Abaqus/Standard of 1s was conserved for the implicit resolution. Only the increment size was lowered to 0,001s to appraise the correct evolution of the calculation. The non-linear geometry option “nlgeom” was again selected for the job conduction.

The lowest natural frequency was evaluated to 224,2Hz with the help of the frequency tool provided by Abaqus/Standard. This allowed defining the proper time period, preventing local distortions and too long calculation, for the explicit resolution. Indeed, with this obtained frequency, the lowest period to be considered was of about 0,005s. Nevertheless, a value of 0,01s was envisaged to importantly decrease the kinetic energy compared to the internal one. The definition of the smooth amplitude combined to the application of the load was adapted in consequence.

## Analysis of the results

As aforementioned in the material behaviour section, the two developed subroutines were respectively employed with the quasi-static and Mullin's coefficients with the aim to validate the material law for the silicone elastomer. Hence, the results presented in the paragraph will be centered on the numerical stress-strain diagrams returned by this material. The stresses of these last diagrams were acquired by summing the vertical reaction forces measured at each node of the bottom glass surface and dividing it by the bonding area. Due to the large involved deformations, the strains were assessed by taking the arctangent of the ratio formed by the displacement of the inner steel plate over the constant thickness of 3mm. It is important to note that the shear stresses were not regarded directly along the overlap length of the adhesive at its interface with the steel adherend.

- Abaqus/Standard – UHYPER

The UHYPER subroutine was at first used with the quasi-static coefficients to ensure of the validity of the instantaneous shear behaviour of silicone. The stress-strain results achieved for the different investigated mesh sizes were gathered in Fig. 6.21.

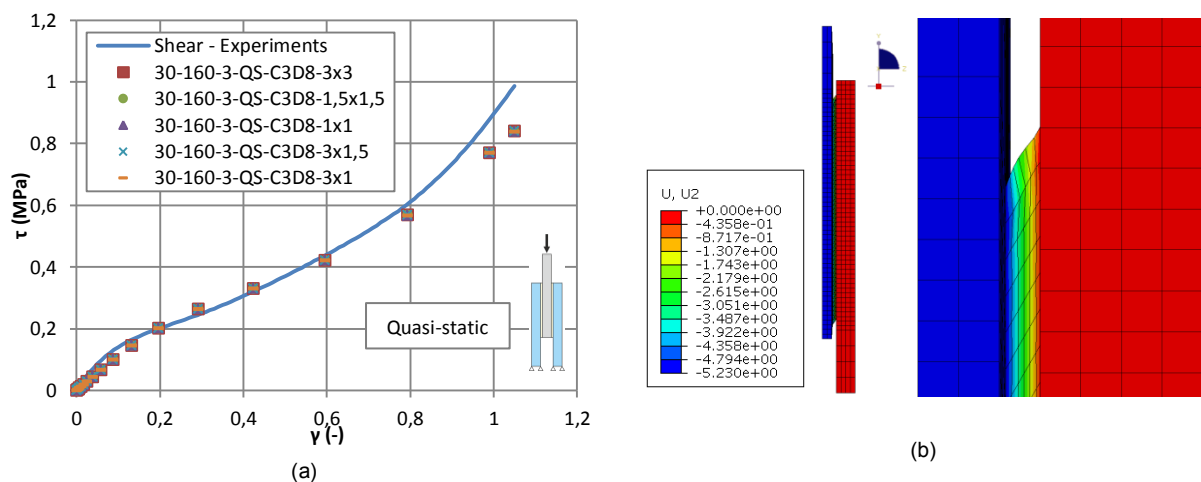


Figure 6.21- (a) Stress-strain diagrams for different mesh sizes and (b) displacements – Silicone quasi-static shear

Form the above diagram, it could have been observed that the different mesh sizes gave identical results with a perfect superposition. Finer meshes were also tested but the calculations aborted due to too important distortions at the adhesive extremities. According to this evaluating procedure, the influence of the mesh on the stress-strain curve appeared nil. While a good concordance was observed until a strain of 0,8, a small divergence compared to the experimental results occurred at larger strains. This difference was already remarked during the determination of the quasi-static

coefficients by fitting the stress-strain data. Nevertheless, the reproduction of the instantaneous behaviour by the developed UHYPER subroutine was acceptable.

The Mullin's coefficients were then injected in the UHYPER subroutine to model the shear behaviour after 7 cyclic cycles. The results of the five examined meshes were all summarized on Fig. 6.22.

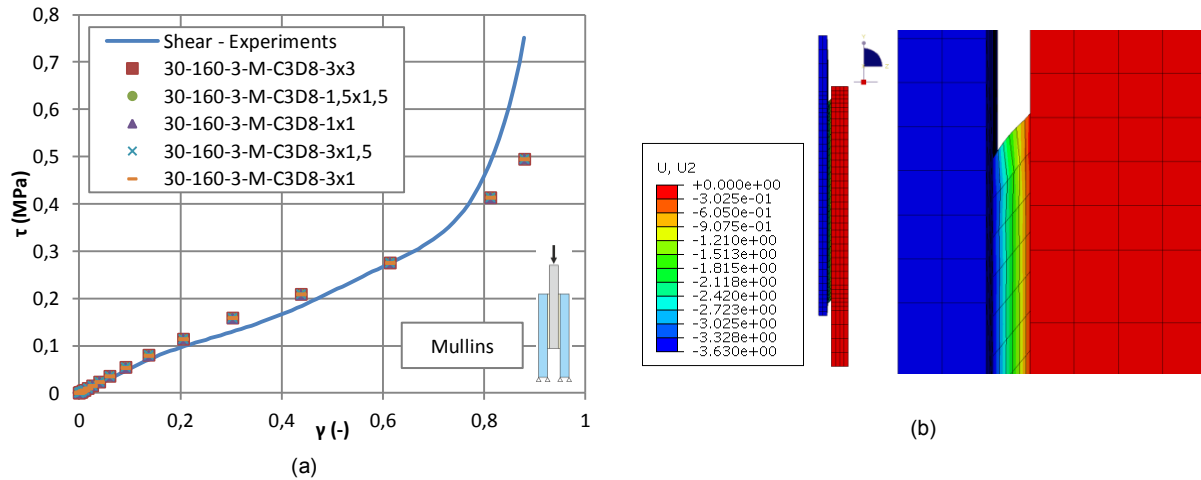


Figure 6.22- (a) Stress-strain diagrams for different mesh sizes and (b) displacements – Silicone Mullin's shear

No variation appeared in the stress-strain curves resulting from the numerical simulations, letting envisage that the mesh size of the silicone part was not influent. In addition, they were relatively close to the curve coming from the shear experiments until a strain of about 0,8, indicating that the written UHYPER subroutine combined with the Mullin's coefficient was appropriate to represent this specific behaviour.

- Abaqus/Explicit – VUMAT

The VUMAT subroutine was also regarded for validation with the quasi-static coefficients. For the selected time period and for each mesh size, the maximum value of the kinetic energy and its return to zero at the end of the calculation were carefully checked. The stress-strain curves determined with the four meshes were gathered on Fig. 6.23.

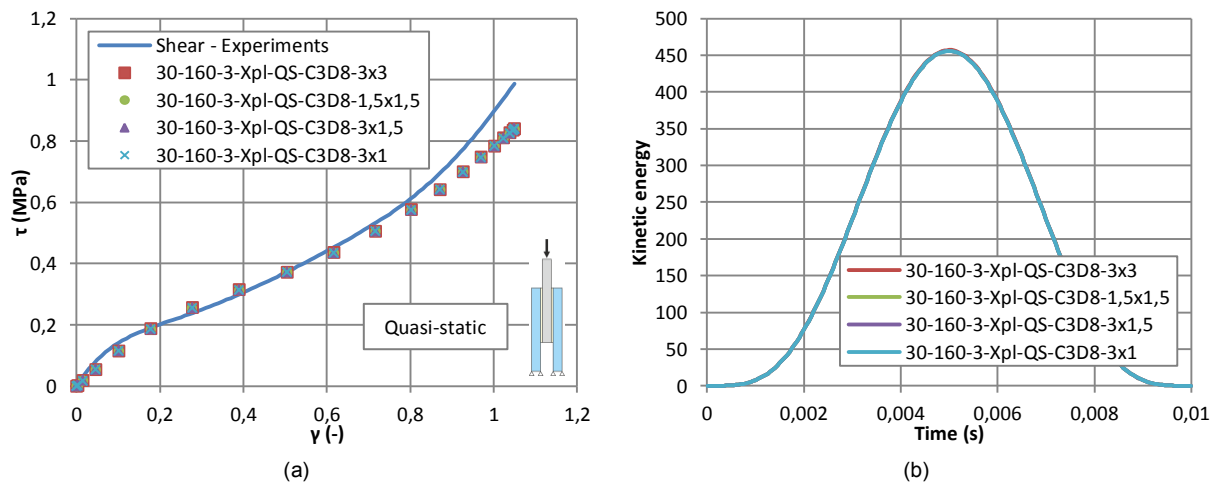


Figure 6.23- (a) Shear stress-strain diagrams and (b) Kinetic energy vs. time – Silicone quasi-static shear

The results of the numerical simulations were again well superposed on the whole strains range, meaning that, with this evaluation method based on the reaction force divided by the bonded area and not directly on the measurement of the stresses along the overlap length, the mesh was not influent. Even if a small gap was seen between the experimental and numerical curves at large strains, a good concordance was remarked until a strain of 0,8, which corresponded to the fitting exposed on Fig. 5.8



of section 5.2.1.4. Consequently, the written VUMAT subroutine was also estimated efficient to model the shear quasi-static behaviour of silicone.

The Mullin's coefficients were then inserted in the explicit subroutine to apprehend the stress-strain results returned by the software. The established curves issued of the four different meshes were regrouped for comparison on Fig. 6.24.

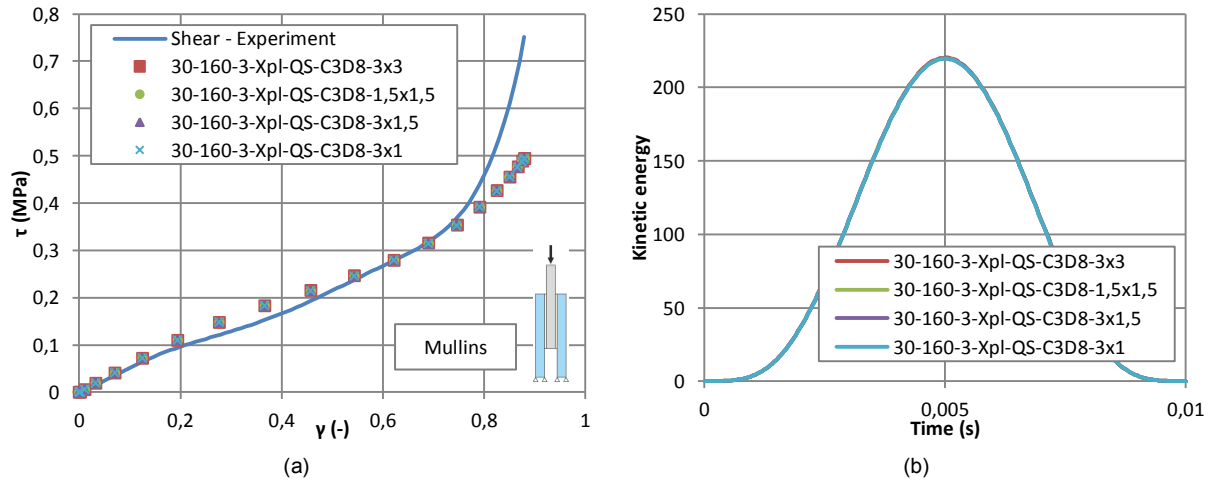


Figure 6.24- (a) Shear stress-strain diagrams and (b) Kinetic energy vs. time – Silicone Mullin's shear

The form of the kinetic energy and its return to zero for each mesh size confirmed the validity of the acquired stress-strain curves. The latter were again hidden one by another and a certain divergence occurred at large strains with the test data. This difference was already noticed and conceded during the estimation of the material coefficients. Hence, the VUMAT subroutine with the Mullin's coefficient was also apt to model the behaviour of the elastomer after 7 cycles.

### 6.2.3.2 Peak stress problem

#### Identification

For the four principal cases studied in the previous section, the shear stresses were determined by dividing the reaction force recorded at the bottom of the assembly by the constant bonding area. While this method allowed approving the material law, another approach was also considered. Indeed, the shear stresses were directly measured along specific paths in the direction of the overlap length at the silicone/steel interface, see example of Fig. 6.25. In general, seven paths were spread over the width of the adhesive to recreate a 3D distribution of the shear stresses and appraise the position of the maximum.

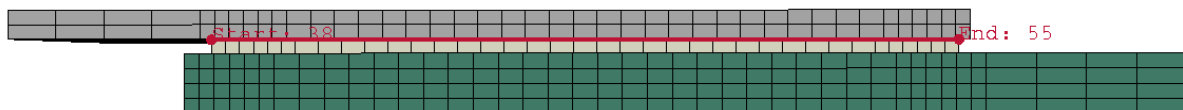


Figure 6.25- Example of path along the overlap length for the direct measurement of the shear stresses in the silicone

- Abaqus/Standard – UHYPER

The results of the numerical simulations of the instantaneous behaviour of silicone presented in the previous section were operated again. At first, only the UHYPER subroutine was inspected with the quasi-static coefficients. The mesh dependency was still investigated and the main curves exhibiting the evolution of the shear stress  $\tau$  along the overlap length plotted, see examples of Fig. 6.26 for which only four paths from 0mm (extremity closest to the center of the push-out assembly) to 15mm (middle of the adhesive joint) were superposed.



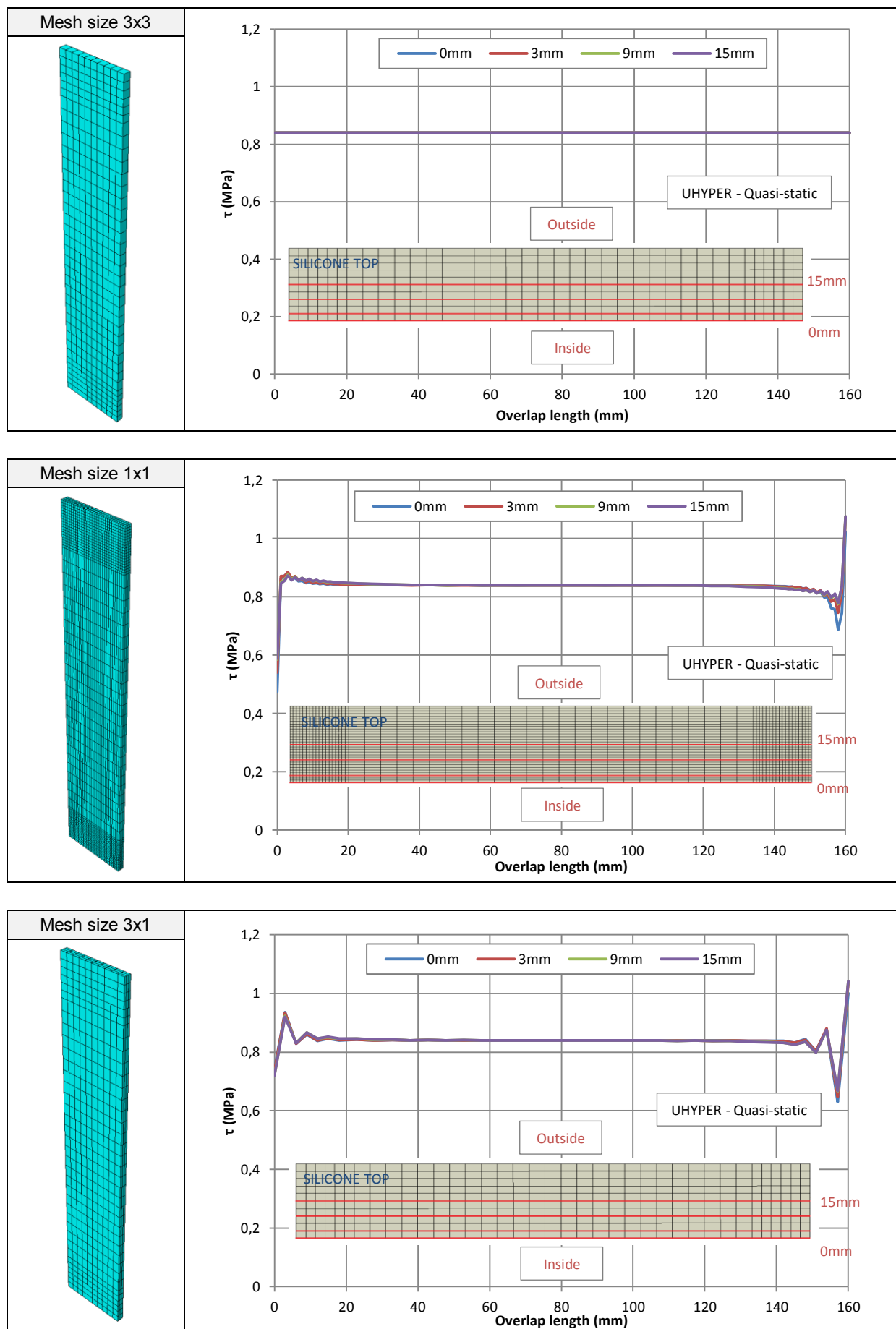
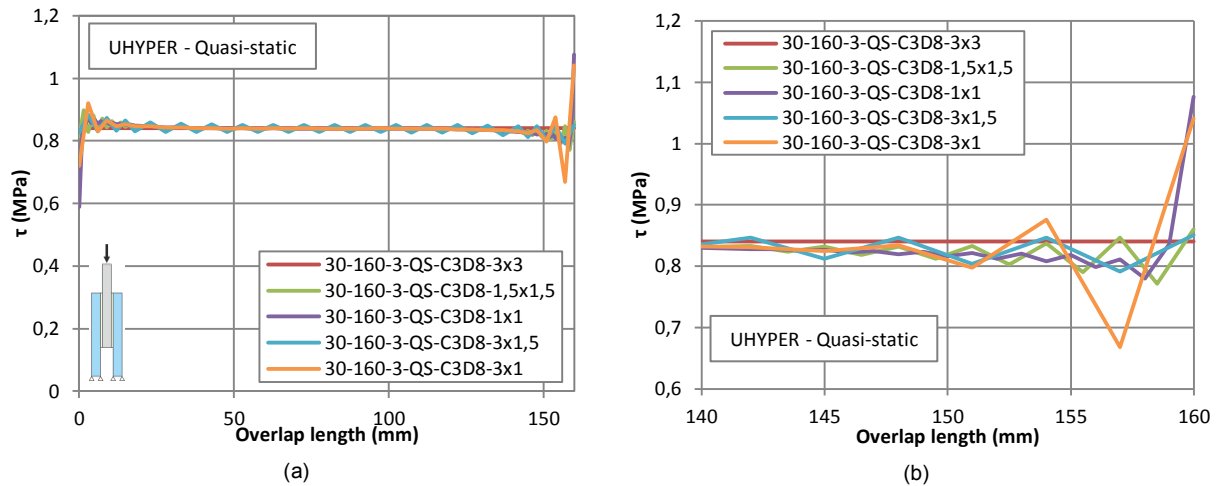


Figure 6.26- Evaluation of the peak stress according to the mesh size – UHYPER subroutine – Silicone quasi-static shear

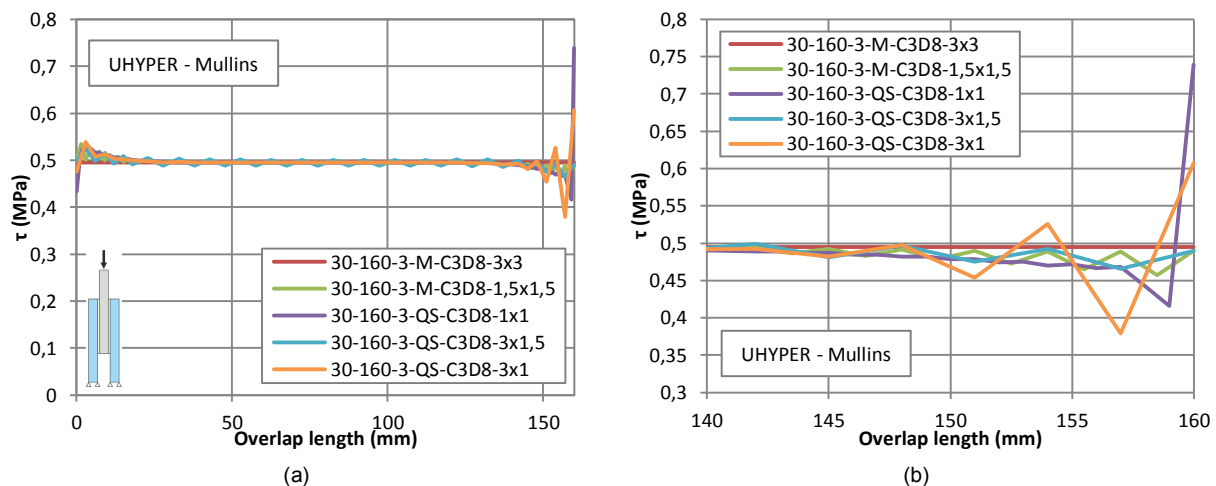
For the coarse mesh 3x3mm (1 element along the thickness), the shear stress was found horizontal and quasi-constant over the whole bonding length. For this mesh configuration, the position of stress measurement was judged irrelevant as the results of the four paths were well superposed. However, for finer mesh, such as 1x1mm or 3x1mm, large stress peaks developed at the extremities of the adhesive, while the stress at the core was constant. Further, the position of the maximum peak was dependent on the selected path, i.e. the higher stress was always reached in the center (at 15mm). Hence, to better apprehend the influence of the mesh on the peak, this last position was regarded, see Fig. 6.27 (a).



**Figure 6.27-** Comparison of the maximum stress peaks (at 15mm) for the different mesh combinations – (a) global and (b) local

As observed on Fig. 6.27 (b), the scattering of the shear stresses over the last 20mm was relatively low, i.e. less or about 0,5MPa, for meshes strictly larger than 1mm. For smaller elements, e.g. 1x1mm, or narrower thickness, e.g. 3x1mm, the stress peak attained a value of 1,05MPa, representing nearly 1,25 times the expected plateau value of 0,841MPa located in the core of the bond. Hence, the decreasing of the mesh induced an important increasing of the shear stresses at the extremities of the adhesive, synonymous of a numerical singularity. Simulations with thinner elements, e.g. 0,5x0,5mm or 1,5x0,5mm, were performed but none could be performed until the end due to too large mesh distortions aborting the calculations.

To ensure that the problem was not caused by the quasi-static coefficients of the proposed material, the results of the Mullin's effect simulation with the UHYPER subroutine were again analyzed. For each configuration, the path giving the maximum peak was the one separating the joint in two equal proportions. This stresses along this path were extracted for the different mesh and then superposed, see Fig. 6.28.

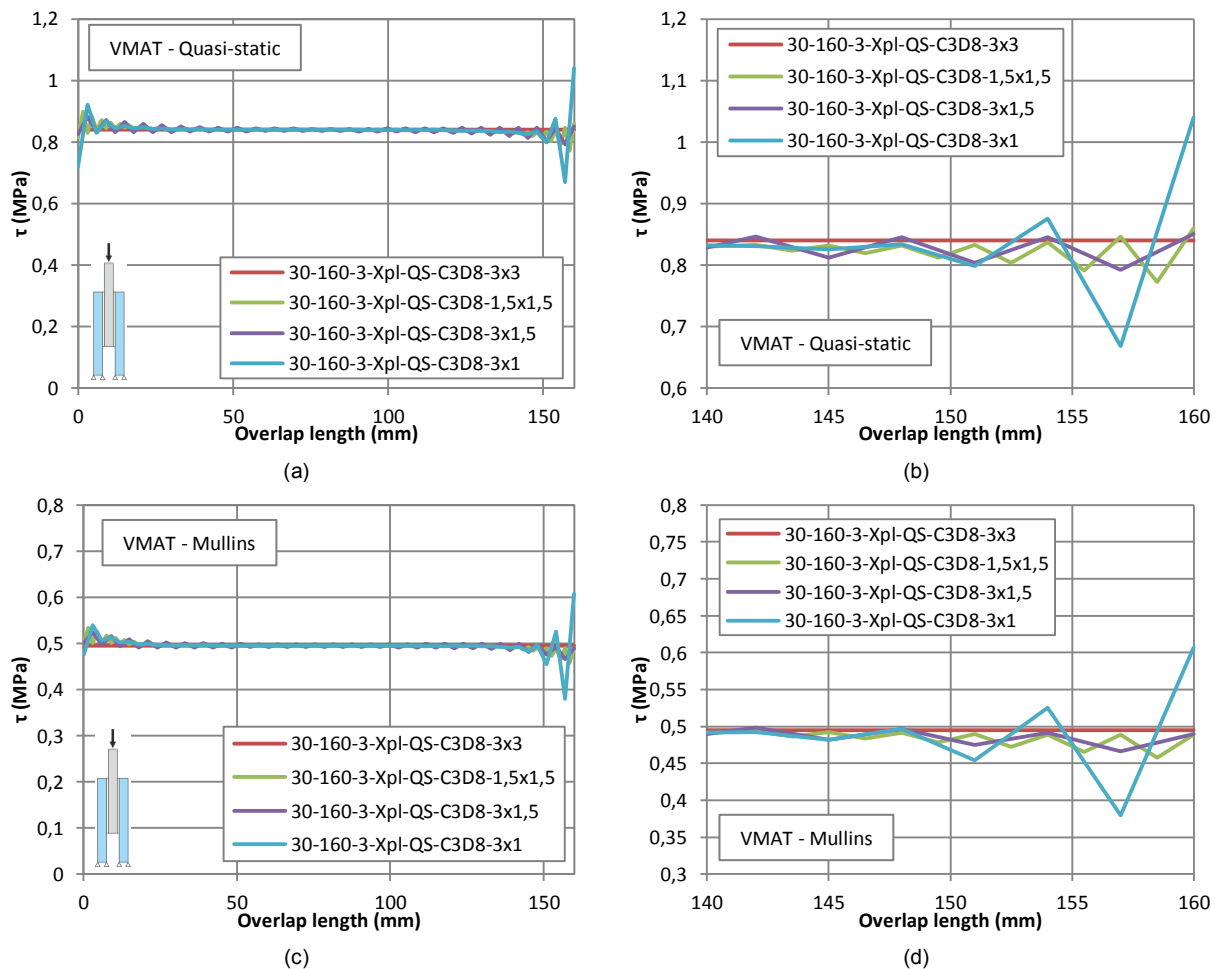


**Figure 6.28-** Comparison of the maximum stress peaks (at 15mm) for the different mesh combinations – (a) global and (b) local

Stress peaks were noticed at the free end of the adhesive, while a plateau was perceived in the core. The peak appeared strongly dependent on the mesh, as finer elements gave the maximum stress values, see Fig. 6.28 (b). In addition, no convergence seemed to be reached by reducing the mesh, attesting of the evoked numerical singularity. As similarities existed in the curves issued from the cyclic and quasi-static set of constants, this last phenomenon was not influenced by the injected material coefficients.

- Abaqus/Explicit – VUMAT

The same procedure than the one conducted for the UHYPER subroutine was repeated for the explicit method of resolution, i.e. the two sets of coefficients were injected in the VUMAT subroutine. At least seven paths were created to identify the one supplying the maximum values and and, as for the precedent study, the middle path provided the higher stress peaks in each case. The development of the stresses along this last were consequently retrieved and compared for the different mesh sizes, see Fig. 6.29.



**Figure 6.29-** (a) & (c) Global and (b) & (d) local stress peaks for the quasi-static and Mullin's set of coefficients (mid path)

Independently of the set of coefficients, the peak stresses appeared at the extremities of the adhesive, demonstrating once more than the acquired shear stress results were not affected by this parameter. Finer was the mesh and higher was the stress peak, indicating the absence of convergence and so the apparition of a numerical singularity. By analogy to the calculations conducted with the UHYPER subroutine, the presence of this phenomenon let envisaged that the method of resolution, either implicit or explicit, could not constitute a mean to overcome this problem.

In conclusion, none of the set of coefficients or of the method of resolution was of influence on the peak stress distribution. Only the mesh size was of a real importance.

## Parameters of influence

The variations of the shear stresses were evaluated with only one specific geometry of 4x(160x30mm) under one imposed displacement. Hence, the possible dependencies of the stress peak towards these two types of parameters were not assessed. Further, the important changes of rigidities between the adhesive and both adherents could also lead to higher or lower stress peaks. In consequence, three categories should be investigated, i.e. the geometry, the material properties and the load intensity. To properly inspect the influence of each one, only one solving procedure associated to the quasi-static set of coefficients was considered, i.e. the implicit method with the UHYPER subroutine. Additionally, the mesh elements and sizes were always fixed, i.e. a size of 3x1mm, see Fig. 6.20, composed by C3D8 elements for the adherents and C3D8H for the silicone.

- Geometry influence

The push-out shear experiments were conducted according a Taguchi design of experiments in which the thickness and width were envisaged as influent factors. For the numerical simulations, these two factors were conserved and the influence of the overlap length added. The three studied factors were thus the following ones:

- The adhesive thickness, a quantitative continuous factor with two levels, i.e. 3mm and 6mm.
- The adhesive width, whose values were selected according to the tests carried out, i.e. 30mm and 170mm. This factor, as the previous one, was quantitative and continuous.
- The overlap length, for which one value corresponded to the tests, i.e. 160mm, while the other one of 80mm was chosen according to the maximum width to respect a ratio of about 2:1.

All the three parameters possessed two levels, which allowed establishing the design of experiments presented in Table 6.4.

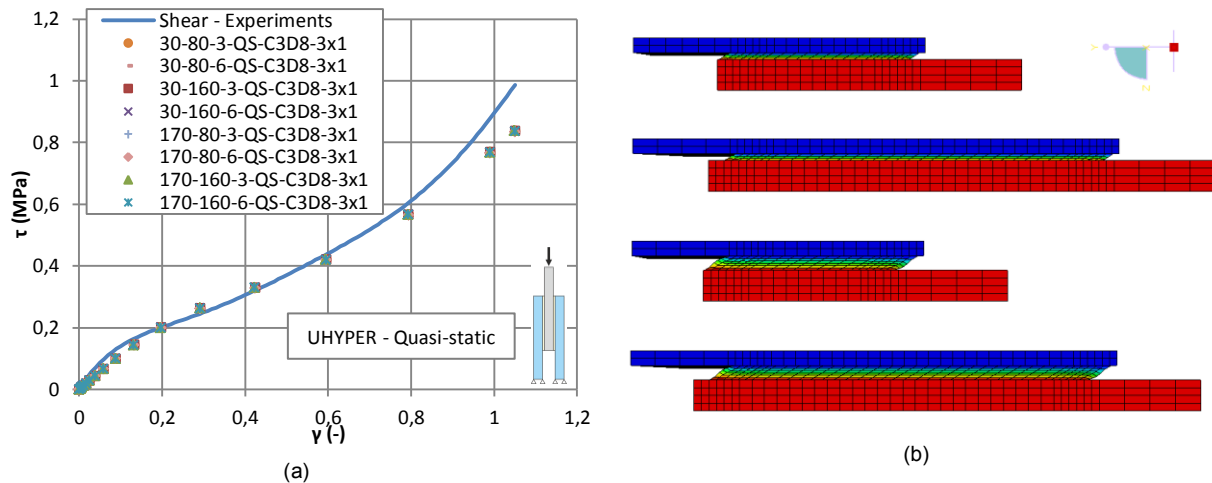
| Standard Test n° | Factors |       |       | Numerical simulations |
|------------------|---------|-------|-------|-----------------------|
|                  | A       | B     | C     |                       |
| 1                | 1       | 1     | 1     | 30-80-3               |
| 2                | 2       | 1     | 1     | 30-80-6               |
| 3                | 1       | 2     | 1     | 170-80-3              |
| 4                | 2       | 2     | 1     | 170-80-6              |
| 5                | 1       | 1     | 2     | 30-160-3              |
| 6                | 2       | 1     | 2     | 30-160-6              |
| 7                | 1       | 2     | 2     | 170-160-3             |
| 8                | 2       | 2     | 2     | 170-160-6             |
| Level 1          | 3mm     | 30mm  | 80mm  |                       |
| Level 2          | 6mm     | 170mm | 160mm |                       |

**Table 6.4-** Design of experiments to numerically evaluate the dependency of the peak stress towards geometrical variations

As the double lap-joint specimens possessed two axes of geometrical and material symmetry, only 1/4<sup>th</sup> of the model was represented. The boundary conditions evoked in the previous section and detailed on Fig. 6.19 were conserved. As the load was introduced as a displacement imposed on the upper surface of the inner steel adherend and as two different thicknesses were envisaged, two different values for the displacement were adopted to end up with the same shear strain and so the same shear stress of 0,841MPa, i.e. 5,23mm for the joint thickness of 3mm and 10,46mm for 6mm. The default time period of 1s proposed by Abaqus/Standard was conserved and only the initial increment size was decreased to 0,001s.

The eight numerical simulations of Table 6.4 were then conducted with these specificities and the first verification concerned the validity of the stress-strain diagram obtained by recording the reaction force at the bottom of the assembly and dividing it by the bonding area. The direct measurement of the

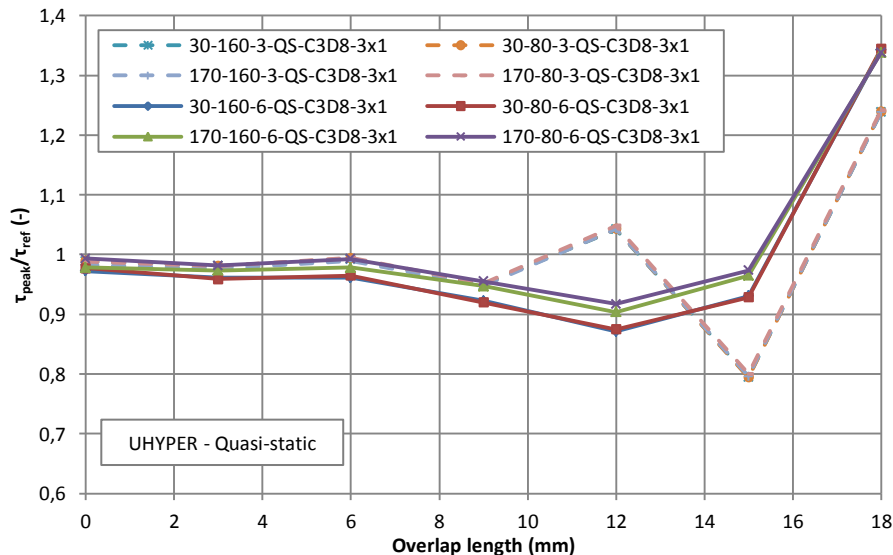
stresses was initially and as previously not necessary to ensure of the correctness of the results. The stress-strain curves of all the tests of the Taguchi design of experiments were gathered on Fig. 6.30.



**Figure 6.30-** (a) Shear stress-strain diagrams of numerical simulations – DOE of Table 6.4 and (b) Displacements diagrams

No difference could be noted between the results of the numerical simulations letting suppose that the geometry of the bonded joint did not impact the shear properties. Further, these results were relatively close to the experimental stress-strain diagram proving the reliability of the simulations.

The evolution of the stress along the overlap length was however examined by creating at least seven paths over the thickness, see example of Fig. 6.25. By studying each configuration independently, the central path cutting the joint in two equal parts provided the maximum stress values. Hence, the stresses along this path were extracted and compared to the reference value of 0,841MPa arising in the core of the adhesive joint. This comparison was achieved by calculating the ratio formed by the stress recorded along the path over this last reference stress. As the scattering and the stress peak occurred generally within the final 18mm of the bond, only this distance was contemplated, see Fig. 6.31.



**Figure 6.31-** Evolution of the stresses ratio along the last 18mm of overlap length – DOE of Table 6.4 – UHYPER subroutine

With the above diagram, one factor was clearly preponderant on the other, i.e. the thickness. Indeed, the evolution of the stresses ratios were well matched for a given thickness and independently of the width or the overlap length. Furthermore, the maximum stress peak values at the free extremities were regrouped according to this parameter. Larger was the thickness and higher was the stress peak. Nevertheless, these findings had to be qualified as the thickness of the adhesive was augmented

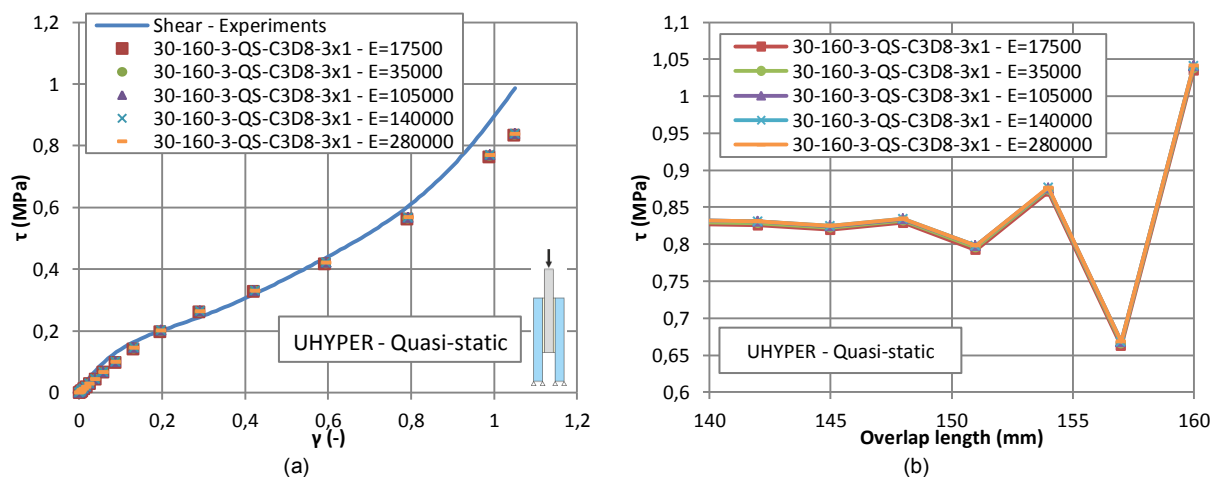
without varying the size of the mesh element along this direction. The thickness was doubled while the element thickness was fixed to 1mm, which could lead to some variations in reason of the mesh dependency. It was however possible to affirm that the peak was not influenced by the width or the overlap length of the joint.

- Material properties influence

Important changes of rigidity occurred at the steel/silicone and glass/silicone interfaces. To assess if these brutal variations of stiffness between the adhesive and its adherends impacted the stress peak value, it was decided to homogenize, in terms of material properties, the push-out shear assembly. Indeed, instead of defining two different kinds of adherends, only one material was affected to both sides, so that the outer and inner adherends possessed the same linear properties, i.e. Young's modulus and Poisson's ratio. While the Poisson's coefficient was kept constant and equal to 0,23 (same as the glass) for these numerical simulations, the Young's modulus was varied to evaluate the deviation in the stress peak. Five different values were envisaged, i.e. 17500MPa, 35000MPa, 105000MPa, 140000MPa and 280000MPa.

In order to avoid parasite influences arising from the mesh or eventually from the thickness, only one configuration was employed, i.e. the reference of 4x(160x30mm). The boundary conditions described earlier were conserved as only 1/4<sup>th</sup> of the specimen was modeled. Only the quasi-static properties of silicone were inserted in Abaqus/Standard via the UHYPER subroutine. The mesh was composed by C3D8 elements for both adherends and C3D8H for the adhesive. The only mesh size considered for this study was 3x1mm, see Fig. 6.20. The default time period of 1s provided by the implicit resolution was applied and the initial increment size changed to 0,001s to remain coherent with the already performed analyzes.

The five numerical simulations were conducted with the aforementioned specificities. The verification of the calculation was achieved by checking the concordance of the stress-strain diagrams obtained by dividing the reaction force at the bottom of the assembly by the bonding area, see Fig 6.32 (a). As remarked, all the numerical curves were properly superposed and close to the experimental one, which tended to validate the results. The stresses were then directly measured along predefined paths along the overlap joint. The middle path separating the adhesive in two equal sections appeared to be the one giving the maximum stress values. Thus, this path was selected for the extraction and the superposition of the stresses for the different adherent rigidities, see Fig. 6.32. (b).



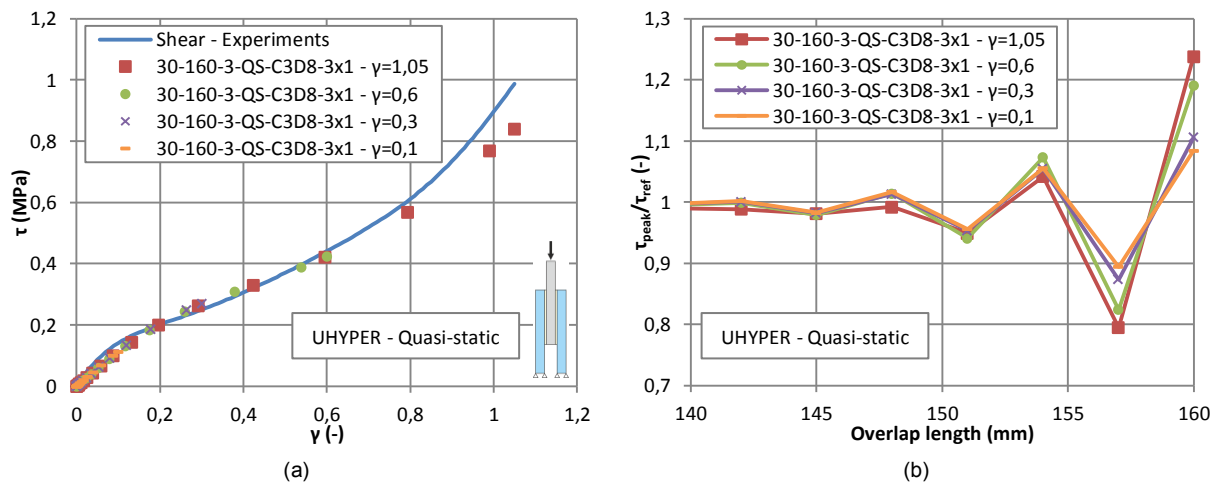
**Figure 6.32-** (a) Shear stress-strain diagrams and (b) Stress evolution along the overlap length – Adherent rigidity influence

Stress peaks occurred independently of the adherend rigidity and seemed to be identical in each case. The curves converged towards an identical value at the free end of the joint and were so close that no distinction was possible. In conclusion, the rigidity of the adherend in the chosen range did not induce changes in the maximum stress value.

- Load intensity influence

The last possible influent factor studied was the load intensity, which was applied as a displacement imposed on the upper surface of the inner steel adherend. Up until now, the imposed deformation was equivalent to a strain of 1,05. To determine the consequences of this parameter on the stress peak, three others displacements corresponding to a strain of 0,1, 0,3 and 0,6 were also examined. Only the quasi-static properties inserted in Abaqus/Standard via the UHYPER subroutine was inquired. The geometry of the assembly was 4x(160x30mm), but only 1/4<sup>th</sup> was modeled with appropriate boundary conditions. The mesh was composed by two types of elements, C3D8 for the adherends and C3D8H for the adhesive. The size of the elements was fixed to 3x1mm as exposed in Fig. 6.26.

The verification of the stress-strain diagrams issued from the measure of the reaction force at the bottom of the assembly allowed approving the numerical simulations, see Fig. 6.33 (a). The middle path, giving the maximum stress values, was regarded, especially over the last 18mm, to appraise the divergence in the peaks, see Fig. 6.33 (b). Lower was the imposed displacement and lower was the maximum peak stress. Nevertheless, even for a very small imposed deformation of one tenth of the thickness, the phenomenon occurred. This indicated that the load intensity obviously contributed to the magnitude of the peak but were not the origin of this effect.



**Figure 6.33-** (a) Shear stress-strain diagrams and (b) Stress evolution along the overlap length – Load intensity influence

### Validity of the peak

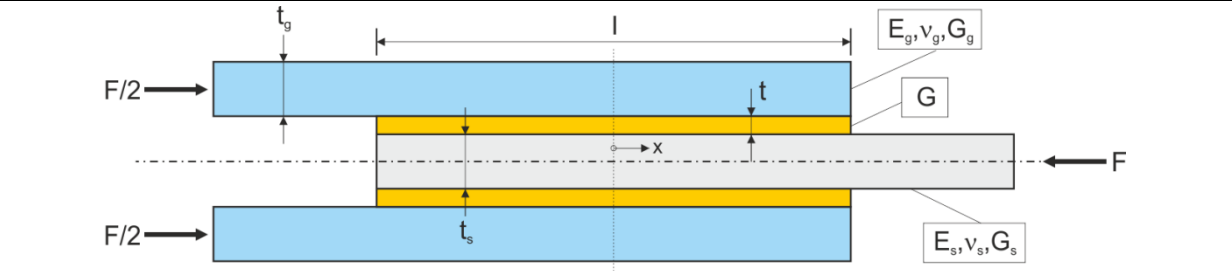
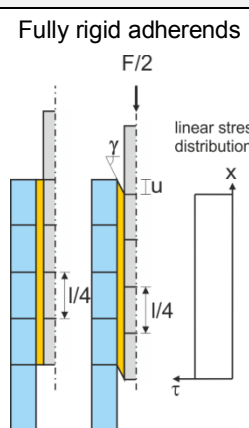
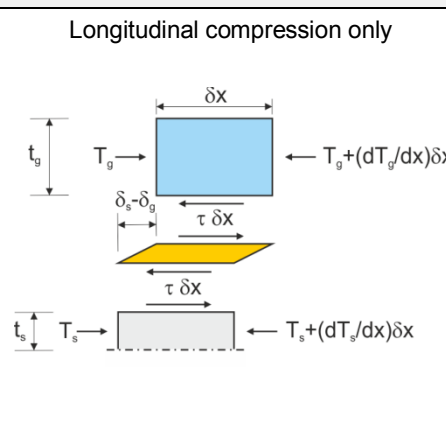
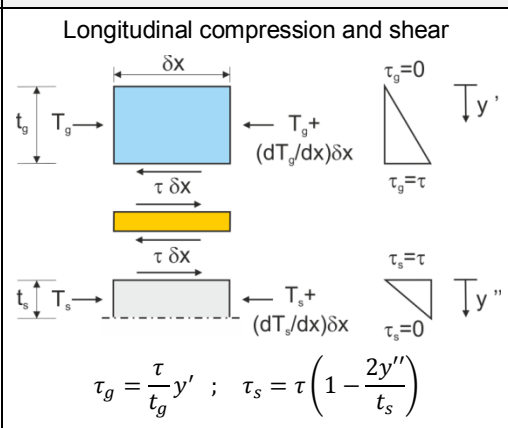
The stress peak problem was presented as a numerical problem due to its strong dependency to the mesh size. However, to fully confirm this assertion for which this phenomenon occurred only in the numerical calculations, three parallel researches were managed, i.e. the first one concerned the existing theories for double lap joint assemblies, another one was an in-depth study of the previous numerical simulation from an energetic point of view and the last one was centered on some small-scale experiments.

- Theoretical point of view

In this paragraph, three basic 2D theories, allowing establishing the stress distribution along the overlap length of the shear push-out tests, were gathered. The 2-dimensional characterization was judged correct as the maximum stresses appeared in the middle path of the joint. All of these were based on the assumption of linear properties for the adhesive. Thus, only the shear modulus and Poisson's coefficient were needed to fully describe the joint behaviour. However, the carried out shear experiments demonstrated the non-linear behaviour of the selected silicone elastomer. To have a correspondence between theory and real behaviour, a simple linear regression was applied on the experimental quasi-static stress-strain curve, in order to approximate a shear modulus. With this procedure, the shear stiffness  $G$  was found equal to 0,811MPa with a correlation coefficient of 0,966.



For all the models, pure shear was the only action transmitted through the adhesive and peel stresses were completely excluded. The distinctions existing between the theories came from the adherends and more particularly to the type of actions transferred, see Table 6.5.

| Double lap-joint shear assembly (Pure shear actions)                                                                         |                                                                                                                                                                                                                                                                                                                                                                                                                                                                                  |                                                                                                                                                                                                                                                                                                                                                                                                                                                                                                                                                                                                                                               |
|------------------------------------------------------------------------------------------------------------------------------|----------------------------------------------------------------------------------------------------------------------------------------------------------------------------------------------------------------------------------------------------------------------------------------------------------------------------------------------------------------------------------------------------------------------------------------------------------------------------------|-----------------------------------------------------------------------------------------------------------------------------------------------------------------------------------------------------------------------------------------------------------------------------------------------------------------------------------------------------------------------------------------------------------------------------------------------------------------------------------------------------------------------------------------------------------------------------------------------------------------------------------------------|
|                                            |                                                                                                                                                                                                                                                                                                                                                                                                                                                                                  |                                                                                                                                                                                                                                                                                                                                                                                                                                                                                                                                                                                                                                               |
| Linear shear distribution                                                                                                    | Volkersen [6.1]                                                                                                                                                                                                                                                                                                                                                                                                                                                                  | Tsai and Hill [6.2]                                                                                                                                                                                                                                                                                                                                                                                                                                                                                                                                                                                                                           |
| <p>Fully rigid adherends</p>               | <p>Longitudinal compression only</p>                                                                                                                                                                                                                                                                                                                                                           | <p>Longitudinal compression and shear</p>                                                                                                                                                                                                                                                                                                                                                                                                                                                                                                                  |
| $\tan(\gamma) = \frac{u}{t}$<br>$\tau = \gamma G$                                                                            | $\begin{cases} \frac{dT_g}{dx} + \tau = 0 \\ \frac{dT_s}{dx} - 2\tau = 0 \end{cases}; \begin{cases} \frac{d\delta_g}{dx} = \frac{T_g}{E_g t_g} \\ \frac{d\delta_s}{dx} = \frac{T_s}{E_s t_s} \end{cases}$ $\tau = \frac{G(\delta_s - \delta_g)}{t}$ <p>By injecting the terms in brackets into the last eq. derived 2 times</p> $\frac{d^2\tau}{dx^2} - \lambda^2\tau = 0$ <p>With <math>\lambda^2 = \frac{G}{t} \left( \frac{1}{E_g t_g} + \frac{2}{E_s t_s} \right)</math></p> | $\begin{cases} \frac{dT_g}{dx} + \tau = 0 \\ \frac{dT_s}{dx} - 2\tau = 0 \end{cases}; \begin{cases} T_g = E_g t_g \left( \frac{d\delta_g}{dx} - \frac{t_g}{3G_g} \frac{d\tau}{dx} \right) \\ T_s = E_s t_s \left( \frac{d\delta_s}{dx} - \frac{t_s}{6G_s} \frac{d\tau}{dx} \right) \end{cases}$ $\tau = \frac{G(\delta_s - \delta_g)}{t}$ <p>By injecting the terms in brackets into the last eq. derived 2 times</p> $\frac{d^2\tau}{dx^2} - \beta^2\tau = 0$ <p>With <math>\beta^2 = \frac{\frac{G}{t} \left( \frac{1}{E_g t_g} + \frac{2}{E_s t_s} \right)}{1 + \frac{G}{t} \left( \frac{t_g}{3G_g} + \frac{t_s}{6G_s} \right)}</math></p> |
| <p>Linear stress distribution</p> $\tau = \frac{F}{2lw} \text{ (MPa)}$ <p>With w the width of the adhesive over one face</p> | $\tau = A \sinh(\lambda x) + B \cosh(\lambda x)$ <p>With <math>A = \frac{\frac{F\lambda}{4} \left( 1 - \frac{E_s t_s}{2E_g t_g} \right)}{\cosh\left(\frac{\lambda l}{2}\right) \left( 1 + \frac{E_s t_s}{2E_g t_g} \right)}</math></p> <p>And <math>B = \frac{\frac{F\lambda}{4}}{\sinh\left(\frac{\lambda l}{2}\right)}</math></p>                                                                                                                                              | $\tau = A \sinh(\beta x) + B \cosh(\beta x)$ <p>With <math>A = \frac{\frac{F\beta}{4} \left( 1 - \frac{E_s t_s}{2E_g t_g} \right)}{\cosh\left(\frac{\beta l}{2}\right) \left( 1 + \frac{E_s t_s}{2E_g t_g} \right)}</math></p> <p>And <math>B = \frac{\frac{F\beta}{4}}{\sinh\left(\frac{\beta l}{2}\right)}</math></p>                                                                                                                                                                                                                                                                                                                       |

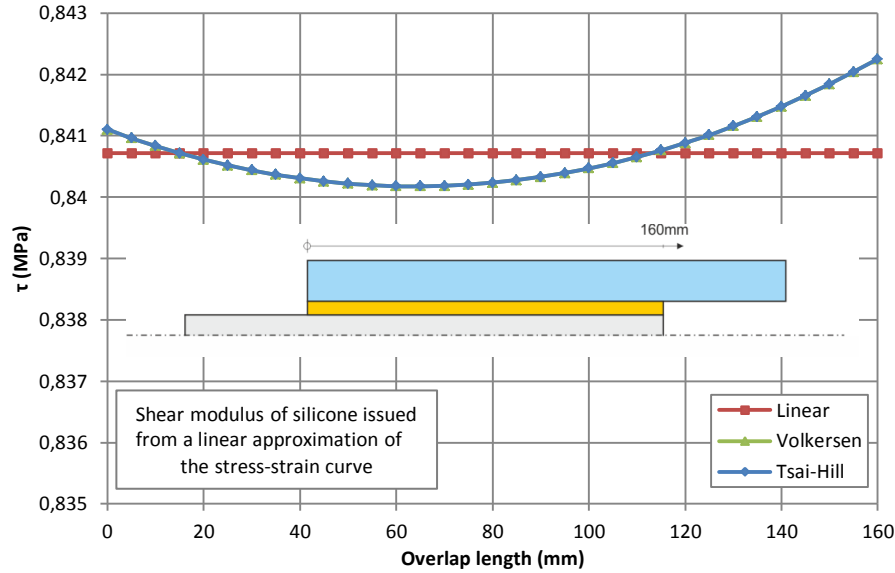
**Table 6.5-** Details of the three envisaged theories for the description of the shear stress distribution along the overlap length

In contrary to the Volkersen and Tsai and Hill theories, the stress of the linear distribution was directly expressed in MPa, as the width was incorporated. However, the correspondence could be achieved for the last two models by simply dividing the expressions of the stress exposed in Table 6.5 by the adhesive width. The main difference arising between the Volkersen and the Tsai and Hill models came



from the expression of the coefficient inside the two hyperbolic functions, i.e. either  $\lambda$  or  $\beta$ . The latter included the shear modulus of both adherends. While the linear stress distribution could be assumed when the rigidities of the adherends were greatly higher than the rigidity of the silicone, the last two had to be used for stiff adhesive involving high loads.

For the present analysis, the dimensions of the push-out specimens described in section 4.2.3.1 were regarded. The reference bonding area of 4x(160x30mm), numerically simulated, was investigated. The total load  $F$  applied on the global system was of 16,15kN to approach the one developing in the simulations. The results provided by the three laws were superposed on Fig. 6.34.



**Figure 6.34-** Stress evolution along the overlap length according to the three considered theories – Silicone shear quasi-static

While for the linear distribution the shear stress remained flat, slight increases at the extremities of the joint were noticed with the Volkersen and Tsai and Hill theories. Nevertheless, these variations were sufficiently small to be neglected and to consider a linear distribution of the stress over the whole adhesive length. Consequently, the stress peak emerging with the numerical simulations did not stand within the results of the existing double lap joint theories.

- Energy study – numerical simulations

The results of the Taguchi design of experiments, detailed in Table 6.4, were reused in this section to check the stress variations along the overlap length. The quasi-static shear behaviour of silicone was modeled in Abaqus/Standard via the UHYPER-subroutine. A particular attention was paid to the end of the adhesive joints, especially to the last 18mm, as the stress scatterings started in these zones independently of the solving method, the mesh size, the geometry or the magnitude of the applied load. In these regions, the shear stresses were linearized with the following formula:

$$\tau_{lin} = \frac{1}{l} \int_0^l \tau dx \quad (6.10)$$

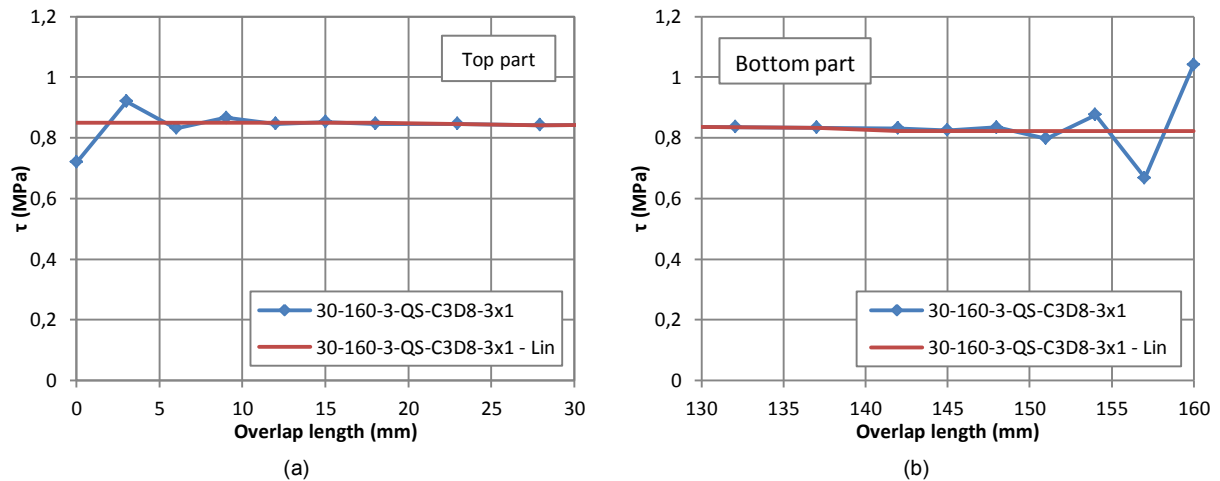
Where  $l$  represents the overlap zone on which the linearization of the measured shear stress  $\tau$  should be operated. In other words, it consisted in calculating the area under the stress-overlap length curve limited to the first or last partition and dividing it by the length of the studied region, i.e. 18mm. This procedure was conducted over the eight specimens of the design of experiments of Table 6.4. Furthermore, and as for the peak analyses of Fig. 6.31, the linearized stress were compared to the reference stress of 0,841MPa arising in the core of the adhesive bond. This comparison was achieved by calculating the ratio formed by the linearized stress over the reference stress. The corresponding data were thus stored in Table 6.6 with a distinction between the top and bottom part of the silicone joint.

| Standard Test<br>n° | A         | B     | C              | $\tau_{lin}/\tau_{ref}$ (-) |             |
|---------------------|-----------|-------|----------------|-----------------------------|-------------|
|                     | Thickness | Width | Overlap length | Top part                    | Bottom part |
| 1                   | 3mm       | 30mm  | 80mm           | 1,011                       | 0,979       |
| 2                   | 6mm       | 30mm  | 80mm           | 1,019                       | 0,968       |
| 3                   | 3mm       | 170mm | 80mm           | 1,009                       | 0,982       |
| 4                   | 6mm       | 170mm | 80mm           | 0,995                       | 0,998       |
| 5                   | 3mm       | 30mm  | 160mm          | 1,011                       | 0,979       |
| 6                   | 6mm       | 30mm  | 160mm          | 1,020                       | 0,967       |
| 7                   | 3mm       | 170mm | 160mm          | 1,012                       | 0,977       |
| 8                   | 6mm       | 170mm | 160mm          | 1,005                       | 0,988       |

**Table 6.6-** Ratio of the linearized shear stress of the reference stress – DOE of Table 6.4 – Silicone quasi-static shear

Independently of the top or bottom studied position, the stress ratio was close to one for each case, indicating that the linearization of Eq. (6.10) tended to minimize the gap existing with the reference stress representing the state of the core of the joint. In addition, the influence of the thickness noticed during the evaluation of the stress peak completely disappeared with the linearization, which let suppose that the stress peak variations were entirely due to the size of the mesh.

The linearized stresses were assumed constant over the top and bottom 18mm zones and to ensure that no discontinuity arose with the surrounding stresses, a visual inspection of the stress evolution in extended zones was done, see example of Fig. 6.35.



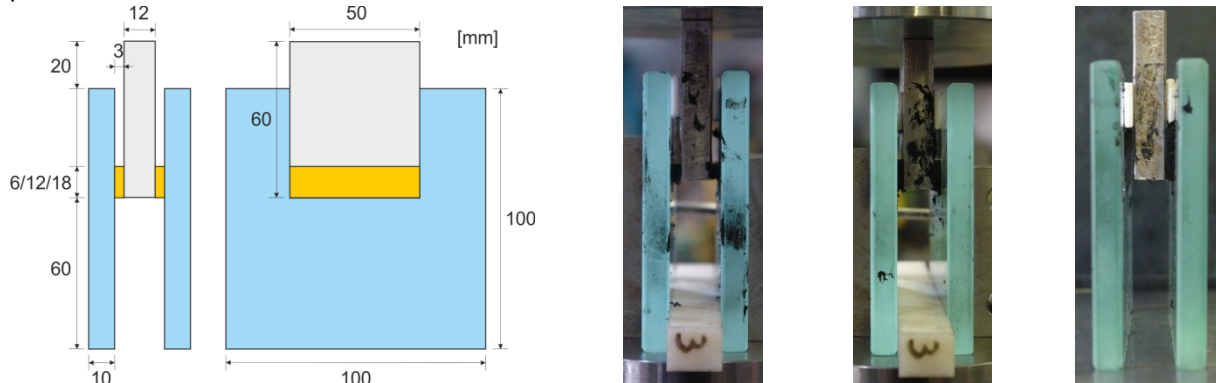
**Figure 6.35-** Example of linearized stress distribution with consideration of the (a) top and (b) bottom parts of the joint

- Small-scale experiments

As deduced from the results of the two prior analyses on the validity of the stress peak, it was advanced that this phenomenon occurred only in the numerical simulation and not during the experiments. To confirm this assumption, some small-scale shear tests concentrating only on the 18mm zone, in which the peak appeared, were performed. Thus, for this small overlap joint and if the peak happened in reality, the shear behaviour of silicone should clearly be determined by the peak and lower stress-strain curves should ensue. Smaller would be the overlap length and lower would be the stress-strain diagram. However, if this effect was simply a numerical problem, the same shear behaviour as the one found for the standard push-out specimens of section 4.2.3 should be noticed.

For this test campaign, three different overlap lengths were envisaged, i.e. 18mm, 12mm and 6mm. The silicone thickness, non-influent on the behaviour, was kept constant to 3mm. As the bonding lengths were relatively short, the global size of the assembly was reduced. The outer glass plates were lowered to 100x100x10mm and the inner steel plate to 60x50x12mm in order to keep a sufficient

width to not alter the final results, see details on Fig.6.36. Between the upper faces of the outer and inner plates, an offset of 20mm was created to press on the central part with sufficient stroke length. The silicone was placed on the lower part of the steel profile and close to the center of the outer glass plates.

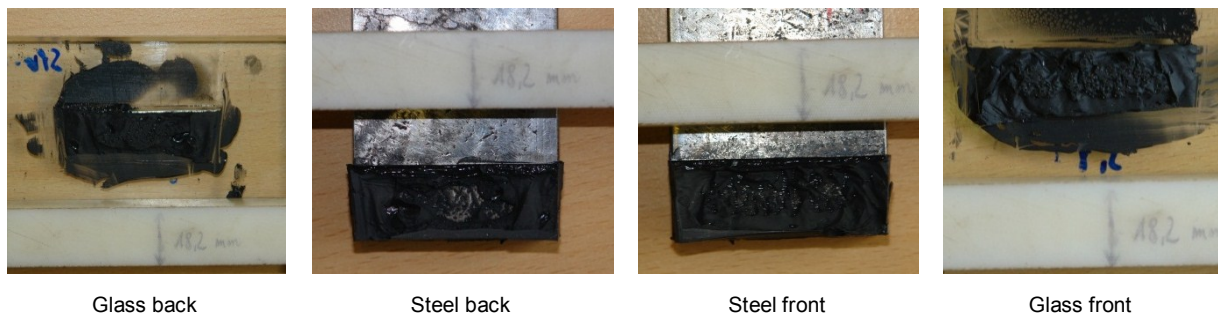


**Figure 6.36-** Details of the dimensions of the small-scale push tests and lateral view of the three silicone thicknesses

To manufacture these samples, 3mm thick Teflon plates were disposed on both sides of the inner steel plate to leave free the regions to be bonded. The silicone was simply poured at these extremities and the covering glass plates were then added. Calibrated pieces were then inserted in the remaining gap between the glass plates to support the steel to guarantee the respect of the desired dimensions. Three assemblies were produced for each overlap length. The nine realized samples were stored during 24 hours at ambient temperature and humidity shielded from the light. A control of the silicone thickness was operated to verify the reproducibility of the manufacturing procedure, see Appendix A.8.

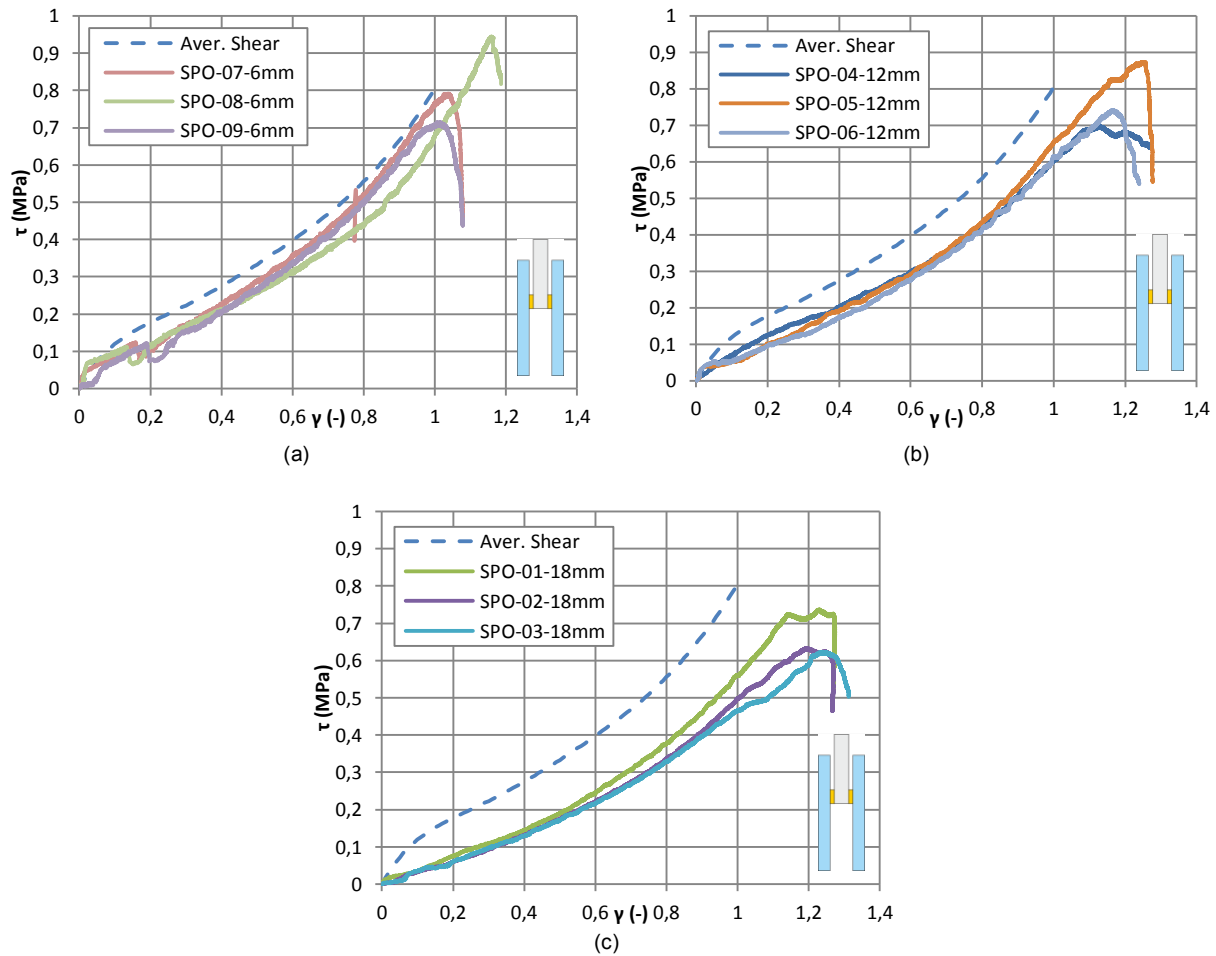
These tests were conducted on the 10kN INSTRON mobile hydraulic piston, as the small-scale push-out acrylic tests. Due to the large cross-sections of the inner and outer adherends, no longitudinal elongations were expected, so that the imposed deformation only developed in the adhesive joint. Thus, no additional device measuring the relative displacement between the glass and the steel part was needed. Further, in contrary to the larger push-out tests of section 4.2.3, no supporting Teflon plate was inserted under the assembly. The displacement of the silicone hence corresponded to the displacement applied by the machine. The total load was recorded with the help of an external force sensor of 10kN. To make sure of the pure shear action, a polyamide spacer fitting the gap between the glass plates was placed at the bottom, as well as 3mm thick Teflon pieces between the steel and glass at the top, see Fig. 6.36. Two lateral rigid steel supports were also placed to definitely prevent any rotation of the glass plates around their supporting edges.

All the experiments were conducted until the adhesive breakage, which allowed verifying the mode of failure. As for the larger silicone push-out tests, portions of adhesive remained on all the surfaces of each specimen, concluding on a 100% cohesive failure, see the example of Fig. 6.37 (test No. 1). With this mode of failure, the net bonding area, excluding air bubbles, was measured with an image-processing program. With this process, the shear stresses  $\tau$  were obtained by dividing the applied force by the net bonding area.



**Figure 6.37-** Mode of failure of the push-out silicone sample – peak stress evaluation – Test No. 1

The strains were calculated by dividing the average of the measured displacements by the half of the total thickness and then taking the arctangent of this value. The acquired stress-strain curves were then superposed to the averaged one obtained during the larger push-out shear tests, see Fig. 6.38.



**Figure 6.38-** Stress-strain diagrams for an overlap of (a) 6mm, (b) 12mm and (c) 18mm – Silicone peak stress verification

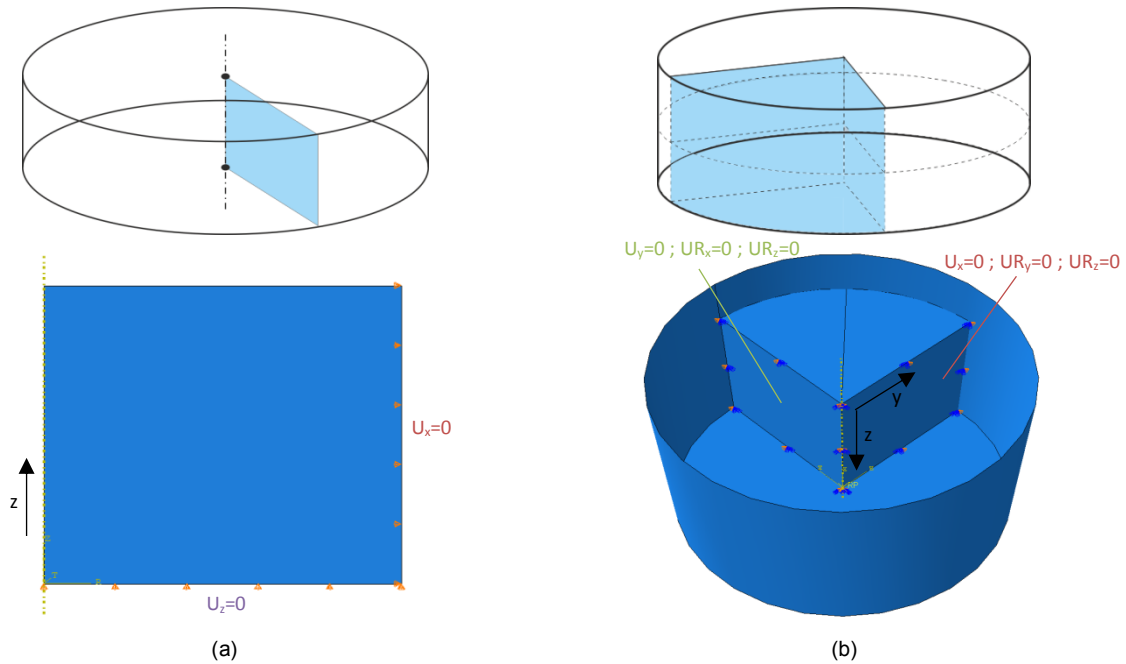
For the smaller overlap length of 6mm, the stress-strain curves issued from this test campaign were close to the averaged one from the larger push-out tests. Then, higher was the overlap length and lower were the stress diagrams, see both Fig. 6.38 (b) and (c). This was obviously contradictory to what was anticipated, i.e. the stress-strain curve had to be lower for lower bonding length if the stress peak really existed. The net areas for the larger overlap lengths could not include all the air bubbles trapped inside the adhesive, which could explain the captured data. However, with the current results, it was not possible to conclude on the truthfulness of the stress peak. Others tests, possessing a continuous adhesive length (butt-bonded hollow cylinder) as described in the DIN EN 14869-1 [6.3], should be carried out for comparison.

## 6.2.4 Oedometric simulations

The last type of action experimentally investigated and characterizing the quasi-incompressible behaviour of the selected silicone elastomer corresponded to the oedometric tests. Based on this test, a specific term accounting for the volume variations was added to the isochoric strain energy potential. Only one material parameter, i.e. the constant  $K$ , was necessary to define this term. Further, with the assumption made concerning the damage, it was postulated that this coefficient was invariant towards the type of action, i.e. quasi-static or cyclic. Thus, no difference should be remarked between the numerical representations of the oedometric tests with the two sets of coefficients of Table 5.21.

### Definition of the geometry and boundary conditions

The geometry of the oedometric samples was identical to the one of the compressive specimens subjected to uniaxial loading with only a difference of size, i.e. the height of the oedometric sample was limited to 15mm with a diameter of 30mm. With the symmetry of revolution in terms of geometry and boundary conditions but also with the isotropy assumption of the material, a simple axisymmetric model was envisaged. While this representation was available in Abaqus/Standard, it was not possible in Abaqus/Explicit due to the definition of the mass. Thus, a 3D deformable model had to be created for the explicit resolution. The dimensions and particularities of the two parts implemented in the finite element software were gathered on Fig. 6.39.



**Figure 6.39-** (a) Axisymmetric representation in Abaqus/Standard and (b) 3D representation of 1/8<sup>th</sup> in Abaqus/Explicit

Two boundary conditions, each limiting the displacement in only one direction, were imposed on two consecutive edges of the axisymmetric model done in Abaqus/Standard to reproduce the action of the rigid steel matrix. With this method, only the silicone was represented. The vertical displacement of the upper horizontal edge was the only one authorized and no friction on the vertical right edge was introduced. Thus, the upper edge remained perfectly flat during the application of the loading. The load was assigned on the latter as a simple displacement increasing linearly over the time period, i.e. as a linear ramp. The value selected for this displacement was assimilated to the maximum value found during the testing, i.e. 0,525mm equivalent to a strain of 0,035.

For the 3D model of Abaqus/Explicit, only one fourth of the real sample was displayed in reason of the aforementioned symmetry. Standard symmetries, only restraining the displacement along the perpendicular of the surface and the rotations around the axes defining it, were applied on the two faces theoretically in contact with the rest of the specimen. At first, only boundary conditions were used to simulate the action of the rigid matrix, but incompatibilities between them arose at all the jointing edges generating unwanted local displacements going through the “matrix”. Therefore, to prevent this phenomenon, the steel matrix was implemented as an analytical rigid shell undergoing no deformation. Surface to surface explicit contact characterized by hard contact without friction was then employed to restrain the silicone. The loading was inserted on the upper surface as a displacement combined to a smooth amplitude see Fig. 6.2. The value chosen for the displacement was the same than the one of the implicit model, i.e. 0,525mm.

### Material behaviour

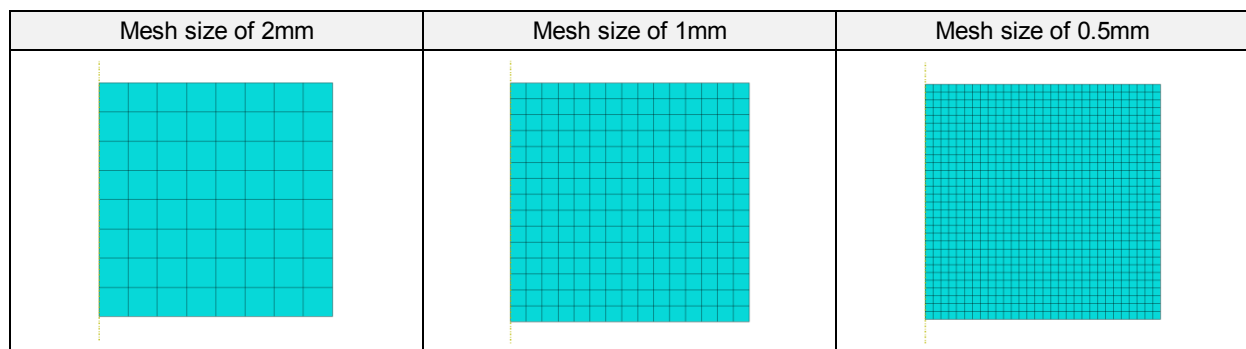
The type of action, quasi-static or cyclic, was assumed as non-influent on the oedometric behaviour. However, even if this postulate was valid from a physical point of view, some differences could appear in the results of the numerical simulations with the two set of coefficients presented in Table 5.21. Hence, the four cases, set according to the type of action and the solving method and already studied for the uniaxial and shear behaviour, were considered once again:

- Quasi-static representation with the UHYPER subroutine,
- Mullin's effect consideration with the UHYPER subroutine,
- Quasi-static representation with the VUMAT subroutine,
- Mullin's effect consideration with the VUMAT subroutine.

The two subroutines were given in Appendix E and the material coefficients for the instantaneous and Mullin's effect characterization in Table 5.21.

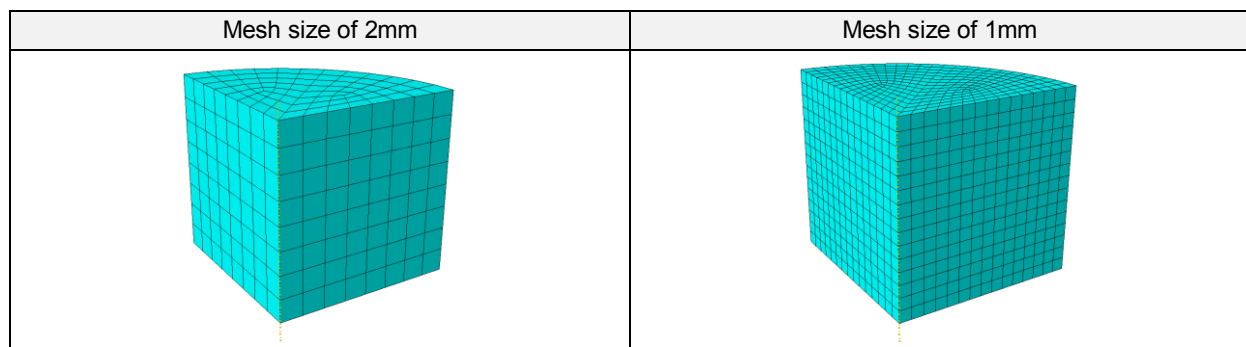
### Meshing

The different axisymmetric elements offered by the library of Abaqus/Standard were analyzed and some restrictions induced by the behaviour of the material were made. Indeed, the reduced integration elements had to be avoided in reason of the possible apparition of the Hourglass effect engendered by the strong quasi-incompressibility and the hybrid formulation had to be adopted. Linear CAX4H and quadratic CAX8H mesh elements were both envisaged to evaluate the convergence of the results. In addition, three element sizes were examined, i.e. 2mm, 1mm and 0.5mm, see Fig. 6.40.



**Figure 6.40-** Different mesh sizes for the numerical simulation of silicone oedometric samples – Abaqus/Standard

As for the meshing in Abaqus/Standard, the different possibilities offered by the Abaqus/Explicit library were analyzed. However, in contrary to the previous one, no hybrid formulation was available and only linear or quadratic 3D elements were applicable. The generated mesh was not composed by pure bricks presenting rectangular angles. Nevertheless, the difficulties encountered for the uniaxial compressive case were not expected as the displacement imposed was relatively small and no important volume decrease was foreseen. To assess the influence of the mesh on the final results, linear C3D8 and quadratic C3D10M as well as two mesh sizes were investigated, see Fig. 6.41.



**Figure 6.41-** Different mesh sizes for the numerical simulation of silicone oedometric samples – Abaqus/Explicit



## Solution procedures

The oedometric behaviour of the silicone was experimentally demonstrated as invariant towards the loading rate and thus the definition of the time period in Abaqus/Standard was not necessary. The default time period of 1s was so conserved and only the minimal starting increment was lowered to a value of 0,001s to appraise the evolution of the calculation. Even if the imposed deformation was very low, the geometric nonlinearity option "nlgeom" was selected.

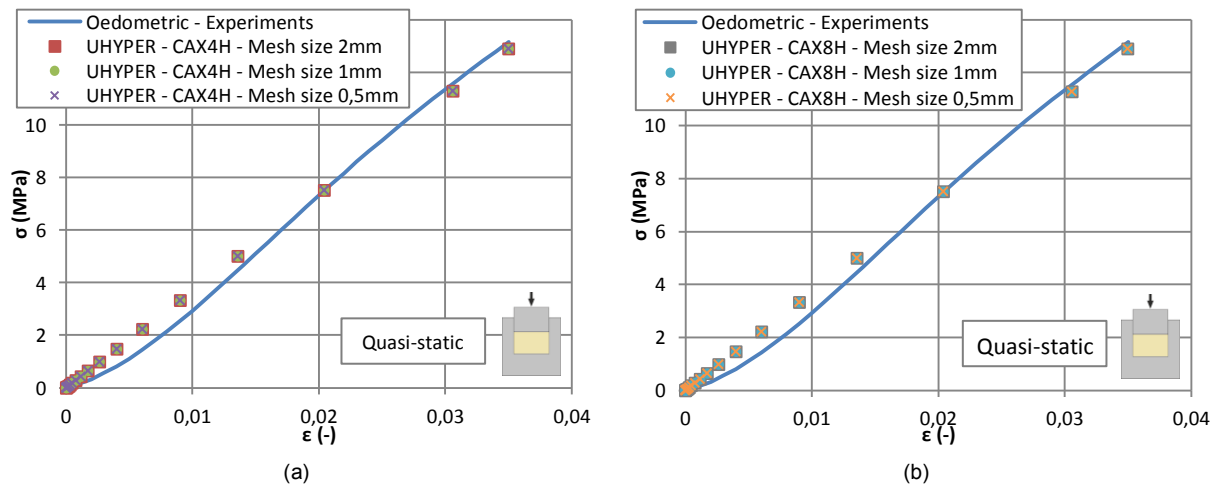
Before proceeding to the explicit resolution, the time period had to be properly defined. To meet this objective, the lowest natural frequency was estimated with the frequency tool provided by the implicit resolution. The determined frequency was higher than the one of the compressive test, i.e. 1218,5Hz inducing a minimal time period of 0,001s. As recommended by the Abaqus documentation, this period was implemented in Abaqus/Explicit for calculation, as well as higher ones 0,05s and 0,1s. The smooth amplitude acting on the imposed displacement was also modified according to these values.

## Analysis of the results

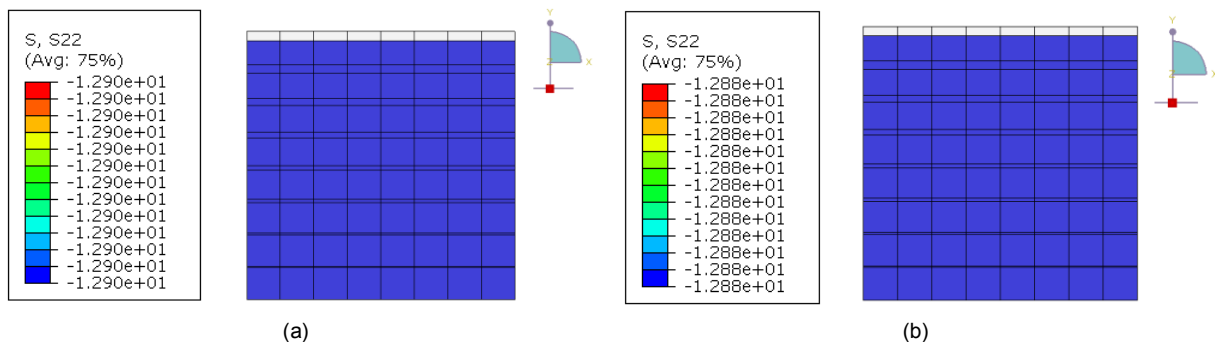
The two sets of coefficients, corresponding to the two examined types of action, were injected in the developed UHYPER and VUMAT subroutines in order to confront the stress-strain curves obtained experimentally and numerically. As the lateral expansions of the oedometric specimens were restrained, the true stresses and the engineering stresses were identical, so that the results returned by the software were directly comparable to the tests data.

- Abaqus/Standard – UHYPER

The quasi-static coefficients were combined to the UHYPER subroutine to assess the instantaneous behaviour of the studied silicone. For the two element orders and three mesh sizes, the diagrams acquired by the numerical simulations were superposed to the real one, see Fig. 6.42.



**Figure 6.42-** Engineering stress-strain diagrams for (a) linear and (b) quadratic elements – Silicone quasi-static oedometric

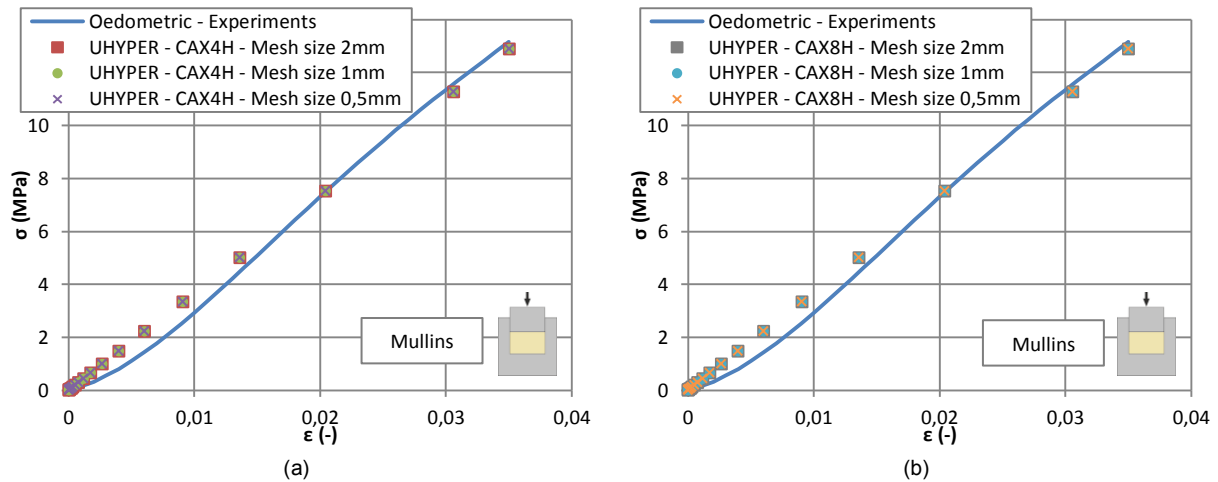


**Figure 6.43-** True stress final result of UHYPER-CAX4H-Mesh size 2mm – Silicone (a) quasi-static and (b) Mullin's oedometric

For the linear element CAX4H, a perfect concordance was observed between the stress-strain curves issued from the three mesh sizes, meaning that this last factor did not impact the result. For the very first strains, a small gap existed with the experimental data, but was entirely due to the definition of the volumetric part of the strain energy potential, which was already approved. Consequently, the real oedometric stress-strain curve was considered correctly represented by the linear element. The same conclusion could be drawn from the analysis of the quadratic CAX8H elements results. This indicated that the convergence was already reached for the coarse linear mesh and validated the UHYPER subroutine with the quasi-static set of coefficients for the representation of the oedometric behaviour.

The same subroutine was conserved with the Mullin's coefficients gathered in Table 5.21. Identical stress-strain curves were expected as the principal coefficient K describing the slight compressibility of the silicone remained invariant according to the type of action. The obtained stress-strain diagrams were again plotted on the experimental diagram for comparison, see Fig. 6.44.

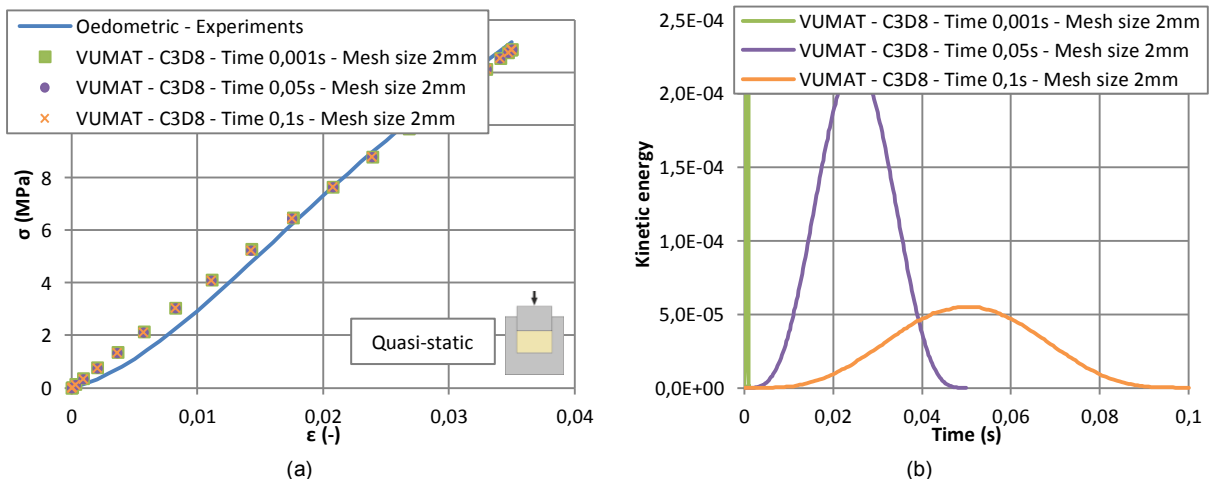
As for the quasi-static coefficients, no distinction could have been made between the different attained stress-strain curves, whose fittings to the test data were relatively correct in spite of the little gap noticed at small strains. Hence, the convergence of the model was also reached for the coarse linear mesh of 2mm, whose final stress was strictly equal to the one assessed with the quasi-static coefficients, see Fig. 6.43. The UHYPER subroutine was consequently fully approved to characterize the quasi-incompressible behaviour.



**Figure 6.44-** Engineering stress-strain diagrams for (a) linear and (b) quadratic elements – Silicone Mullin's oedometric

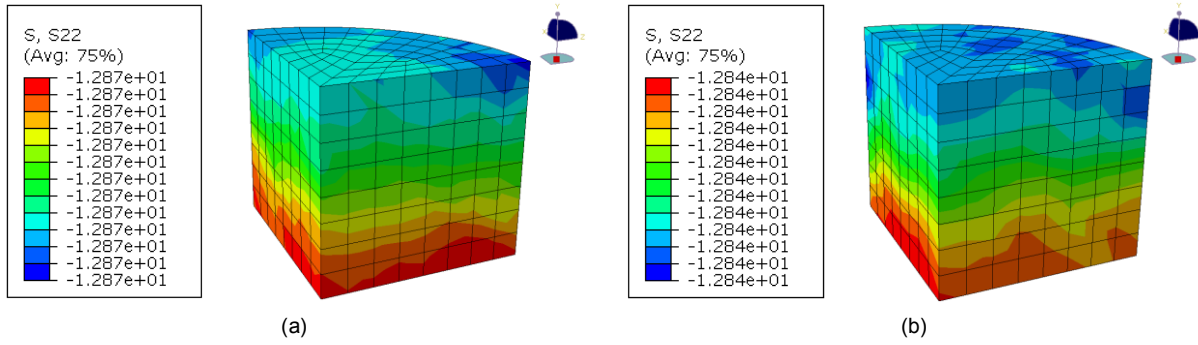
- Abaqus/Explicit – VUMAT

The VUMAT subroutine was also employed at first with the quasi-static set of coefficients to model the oedometric experiments in order to ensure of the validity of this written function.



**Figure 6.45-** (a) Stress-strain diagrams and (b) Kinetic energy vs. time – Time period influence –Quasi-static oedometric

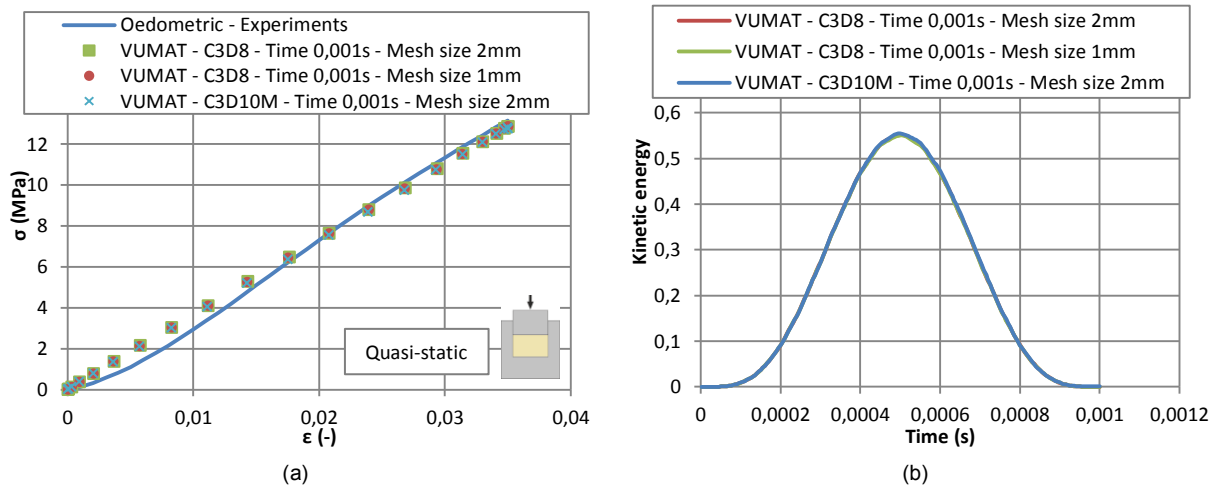




**Figure 6.46-** True stresses of VUMAT-C3D8-Time 0.001s-Mesh size 2mm – Silicone (a) quasi-static and (b) Mullin's oedometric

Three time periods, 0,001s, 0,05s and 0,1s, were envisaged and two types of elements, linear and quadratic, were used as well as two mesh sizes, 2mm and 1mm. The size and order of the mesh elements were initially fixed to appraise the influence of the time period. Indeed, the first analyzes were centered on linear elements of 2mm for which the three time periods were varied. The stress-strain curves and the kinetic energy balance were drawn to apprehend the accuracy of the numerical results, see Fig. 6.45.

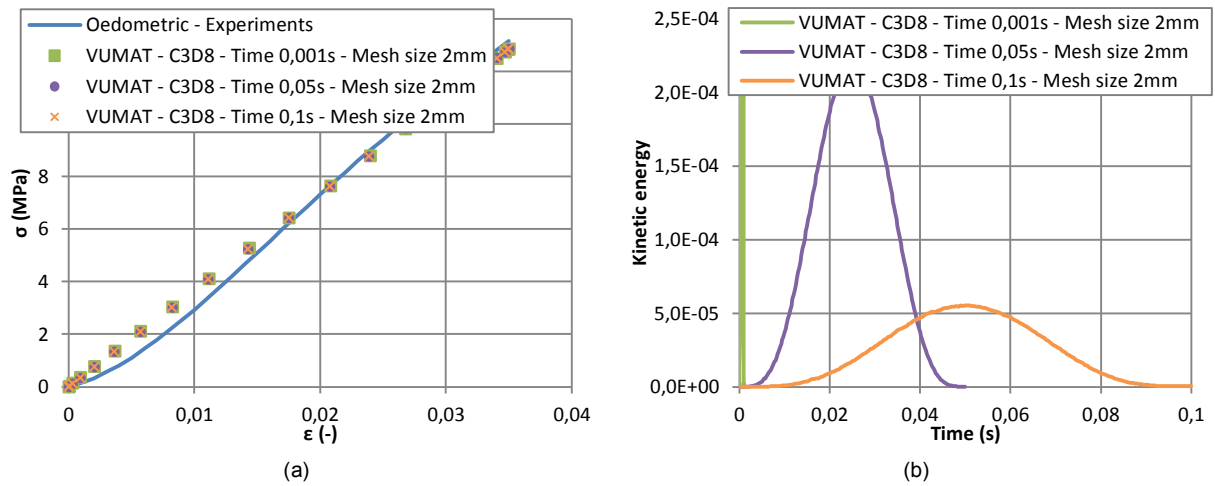
The kinetic energy was low for the three time periods and always returned to zero at the end, which allowed accepting the results. The analytical stress-strain curves were well superposed and matched correctly the experimental one. A last visual check on the deformed shape concluded on the efficiency of the model, as no senseless element distortion occurred, see Fig. 6.46. As no dispersion was observed, it was also concluded that the time period was not of influence with regards to the small imposed displacement. Therefore, the possible influence of the mesh, i.e. element order and size, was then investigated by conserving the smallest time period of 0,001s, see Fig. 6.47.



**Figure 6.47-** (a) Stress-strain diagrams and (b) Kinetic energy vs. time – Mesh influence – Quasi-static oedometric

The kinetic energy again indicated that the acquired results were relevant and could be compared to the tests data. With this study concerning the influence of the mesh, it was remarked that the stress-strain curves were independent of the element size and order as they were all alike. This confirmed that the proper results were already reached for the linear coarse mesh of 2mm and that the developed VUMAT subroutine associated to the quasi-static coefficients returned a correct slightly compressible behaviour.

The Mullin's set of coefficients was then inserted in the VUMAT subroutine for numerical simulations of the oedometric tests. The three time periods evoked previously were conserved and their possible influences analyzed by fixing the mesh size to 2mm and limiting to linear element, i.e. the worth mesh case, see Fig. 6.48.



**Figure 6.48-** (a) Stress-strain diagrams and (b) Kinetic energy vs. time – Time period influence –Mullin's oedometric

The stress-strain curves did not present any variations and closely matched the real behaviour coming from the experiments. The validity of the calculation was corroborated by the form of the kinetic energy, which came back to zero for each period. Additionally, no difference in final stresses was found with the previous study with the quasi-static coefficients, see Fig. 6.46. In conclusion, as the convergence was already attained for the coarse mesh, the VUMAT subroutine with the Mullin's coefficients was considered as accurate to model the oedometric behaviour.

## 6.3 ACRYLIC MATERIAL

The acrylic properties were described by two 1D material laws according to the type of action, i.e. the Ramberg-Osgood formulation was employed for the tensile behaviour, while a self-developed model based on the silicone one was used for shear. Further, due to the loading rate dependency of this adhesive, several coefficients were proposed as well as some equations allowing evaluating them for specific rates for which the behaviour was a priori unknown. In this section, only the shear properties simulations were of real interest, as they represented the main actions arising in the envisaged steel-glass composite beam.

### 6.3.1 Implementation in the finite element software Abaqus®

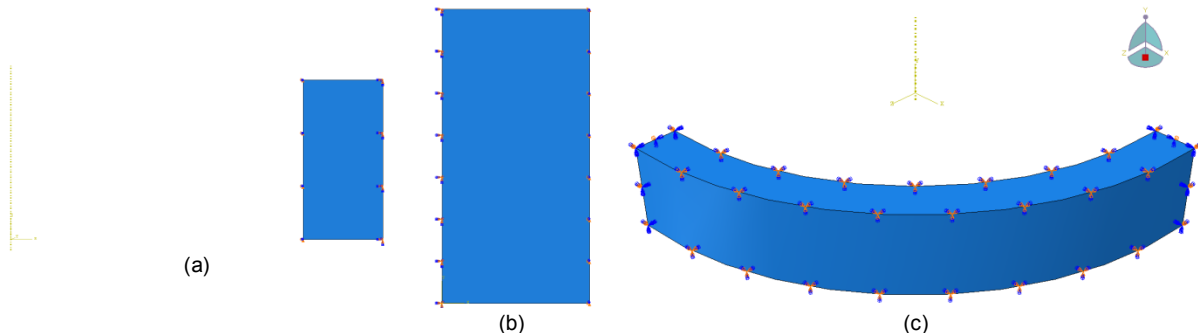
The envisaged one-dimensional shear material law summarized in Table 5.22 necessitated the writing of an external FORTRAN subroutine, as no equivalence was found in the existing software's library. Only one solving method was chosen to model the acrylic even if some mesh distortions could appear in reason of the large undertaken deformations, i.e. the implicit method of Abaqus/Standard. This choice was motivated by the simplicity of this solving method showing no convergence problem and for which no preliminary frequency analysis was needed. As the acrylic law was extracted from the 3D constitutive model characterizing the silicone, the UHYPER subroutine written for the latter was reused and adjusted to match the acrylic shear behaviour. The volumetric coefficients  $K$  of Table 5.21 was remove from the equation, as the acrylic was not incompressible. The coefficients  $a$  and  $c$  were redundant and only one had to be defined. Hence, the coefficient  $c$  was set to zero and consequently only four parameters were implemented. The complete subroutine and the different set of coefficients corresponding to the three estimated loading rates were gathered in Appendix E.4.

### 6.3.2 Modified shear simulations

To check the validity of the user subroutine explained in section 6.3.1, numerical simulations of the quasi-static modified shear experiments were performed. The small-scale push-out tests could not be modeled as the adhesive thickness was not well known (too thin) and could influence importantly the final results.

#### Definition of the geometry and boundary conditions

The investigated square samples of 50mm length and 3mm thick were fully detailed in Fig. 4.88. The tested zone was however circular and properly defined by the punch size. The adhesive thickness subjected to shear was of 1,5mm and the maximum displacement authorized by the test set-up was of 2,95mm, see Fig. 4.89 (b). Hence, by only concentrating on the tested zone (material geometry) and assuming a complete material symmetry, this experiment could be represented by an axisymmetric model, see Fig. 6.49 (a). Only the shear zone was simulated with appropriate boundary conditions, i.e. the outer right edge, at the opposite of the symmetry axis, was fully fixed (encastre) and the maximum displacement of 2,95mm was imposed on the inner vertical edge.



**Figure 6.49-** (a) Axisymmetric (b) 2D and (c) 3D representation of the quasi-static modified shear experiments on acrylic





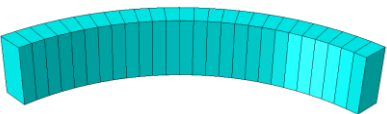
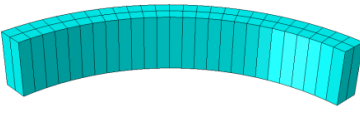
Nevertheless, the axisymmetric representation was not the only one studied. Indeed, as the material law was intended to be one-dimensional and as the one inserted in the finite element software was based on a 3D model, some extended numerical simulations on 2D and 3D parts had to be performed to ensure of the correctness of the resulting behaviour, see Fig. 6.49 (b)&(c). The 2D representation consisted in considering a straight joint of the same section (3x1,5mm) and boundary conditions than the one of the axisymmetric case. For the 3D, only one fourth of the modified shear specimen was inspected and two additional symmetry boundary conditions were inserted at the extremities to fix the displacements along the perpendicular to the surface and the rotations around their middle horizontal axes. In both cases, a displacement of 2,95mm was imposed on the inner edge/surface.

### Material behaviour




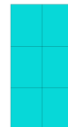
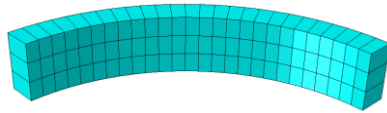
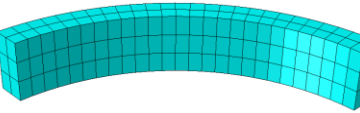
With the three envisaged models and boundary conditions, the only material implemented was the acrylic and thus only its quasi-static behaviour was used via the UHYPER subroutine for an implicit resolution. However, three loading rates were examined by modifying the material coefficients directly in the subroutine, i.e. 1mm/min, 5mm/min and 15mm/min.

### Meshing

For the three studied cases, the reduced integration elements were again avoided while the hybrid formulation was selected when available, as the material law was inserted through the hyperelastic option. For the axisymmetric model, only linear rectangular CAX4H mesh elements were regarded as quadratic elements could curl up on themselves due to the large imposed displacement. For the 2D part, the same linear order was chosen with rectangular CPS4 plane stress elements. Finally for the 3D instance, 8-node linear hybrid bricks C3D8H were employed. The convergence of the results according to the mesh size were once more investigated, see Fig. 4.50.

| Representation | Mesh size 3x1.5mm                                                                   | Mesh size 3x0.75mm                                                                    |
|----------------|-------------------------------------------------------------------------------------|---------------------------------------------------------------------------------------|
| Axisymmetric   |  |  |
| 2D             |  |  |
| 3D             |  |   |

| Representation | Mesh size 1x1.5mm                                                                   | Mesh size 1x0.75mm                                                                    |
|----------------|-------------------------------------------------------------------------------------|---------------------------------------------------------------------------------------|
| Axisymmetric   |  |  |
| 2D             |  |  |
| 3D             |  |   |

**Figure 6.50-** Different mesh sizes corresponding to the three representations of the quasi-static modified acrylic shear tests

For the 3D models, 26 elements were created in the circular areas corresponding to an element width of about 0,75mm, i.e. the minimum width along the thickness. The mesh was relatively coarse as large distortions, leading the calculation to a prematurely, were expected for this small cross section.

### Solution procedures

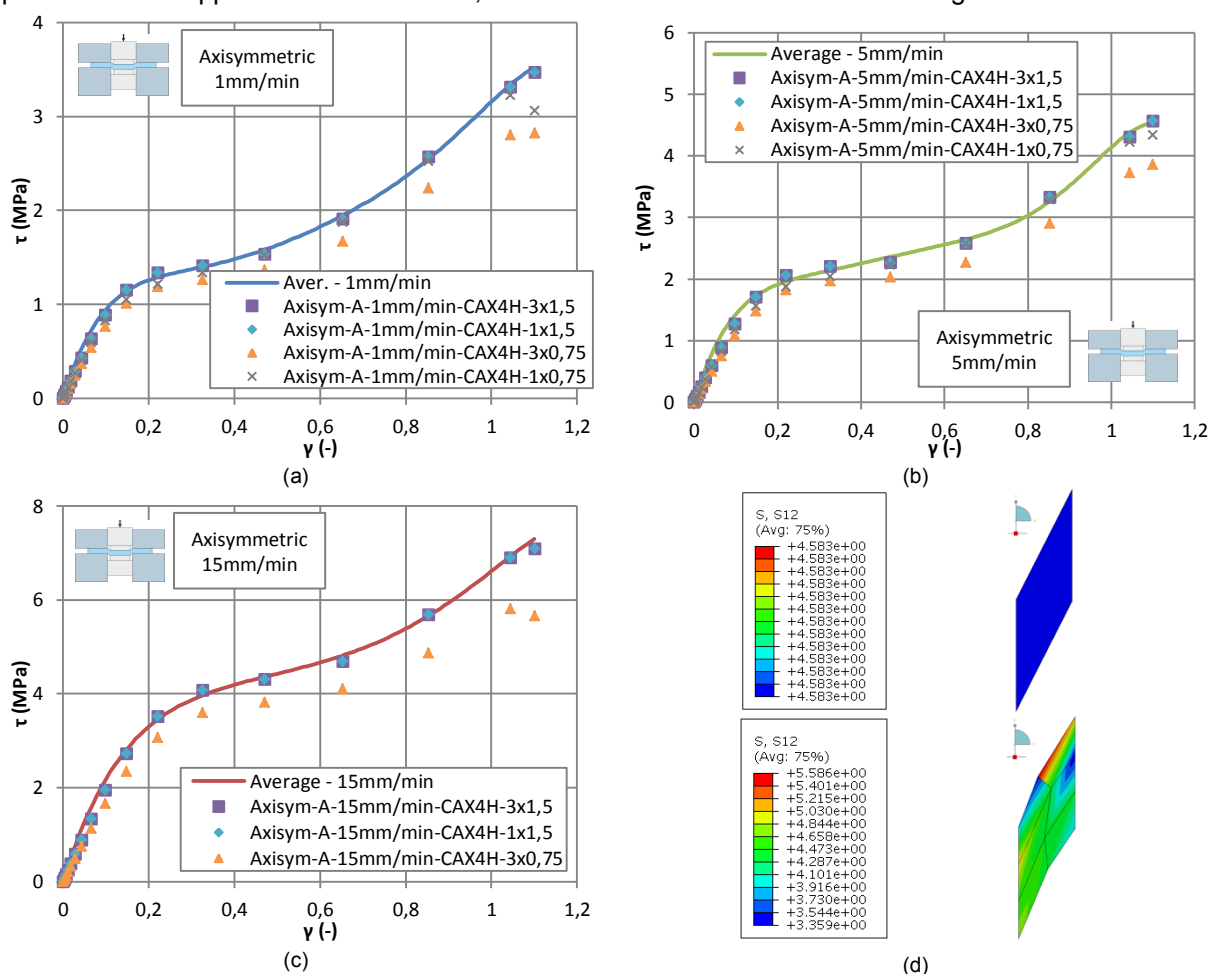
As the loading rate dependency was accounted in the material law by the definition of the material coefficients, no particular attention had to be paid to the time period. Thus, the standard time period of 1s offered by Abaqus/Standard was conserved and only the initial increment size was lowered to 0,001s to better appraise the evolution of the calculation. The geometrical non-linear option “nlgeom” was also applied.

### Analysis of the results

The obtained stress-strain results were divided into three categories according to the representation mode and then according to the loading rate.

- Axisymmetric representation

The stress-strain curves were achieved by summing the reaction forces measured at all the nodes placed along the fully fixed vertical edge and dividing it by the tested thickness and by  $4\pi^2$ . This procedure was applied to all mesh sizes, see stress-strain results recorded on Fig. 6.51.



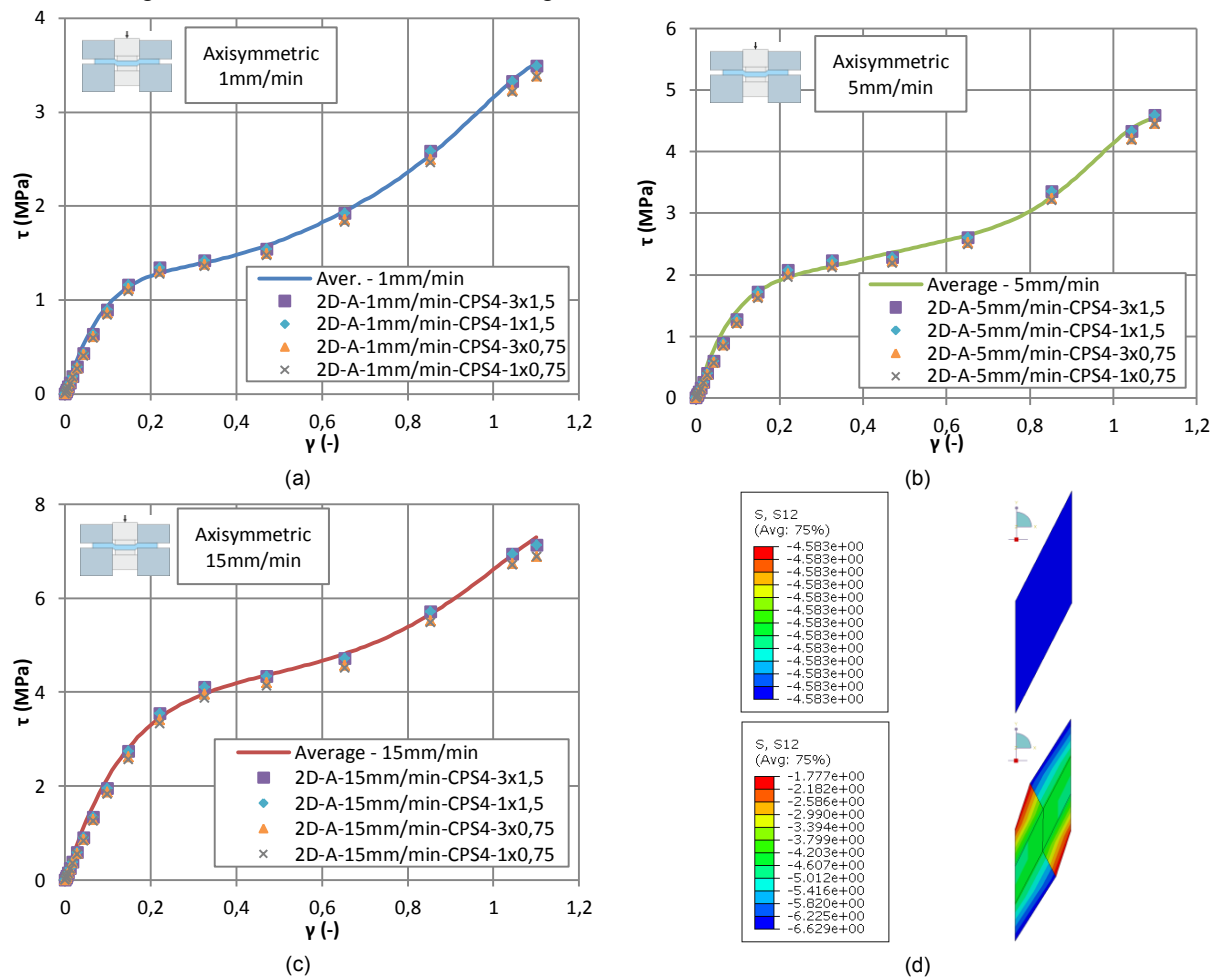
**Figure 6.51-** Stress-strain diagrams of the three rates (a) 1mm/min, (b) 5mm/min and (c) 15mm/min – (d) Shear deformation

For the highest loading rate and the finer mesh, the calculation could not be conducted until the end as too large distortions were encountered. Furthermore, even if the other jobs well succeeded, all the

acquired stress-strain curves did not match the averaged experimental ones. This was especially true for the mesh size of 3x0,75mm and independently of the loading rate. Nevertheless, the shear stress-strain curves were well represented by the larger mesh elements 3x1,5mm and 1x1,5mm, as no important distortion arose, see example of Fig. 6.51 (d) for a rate of 5mm/min. In conclusion, the developed UHYPER subroutine, modified for the acrylic adhesive, was judged apt to model its shear behaviour by paying however attention to the mesh size.

- 2D representation

For the 2D representation, the stress data were calculated by dividing the reaction force measured along the fully fixed edge by the thickness of 3mm. The stress-strain diagrams were thus done for each loading rate and each mesh size, see Fig. 6.52.



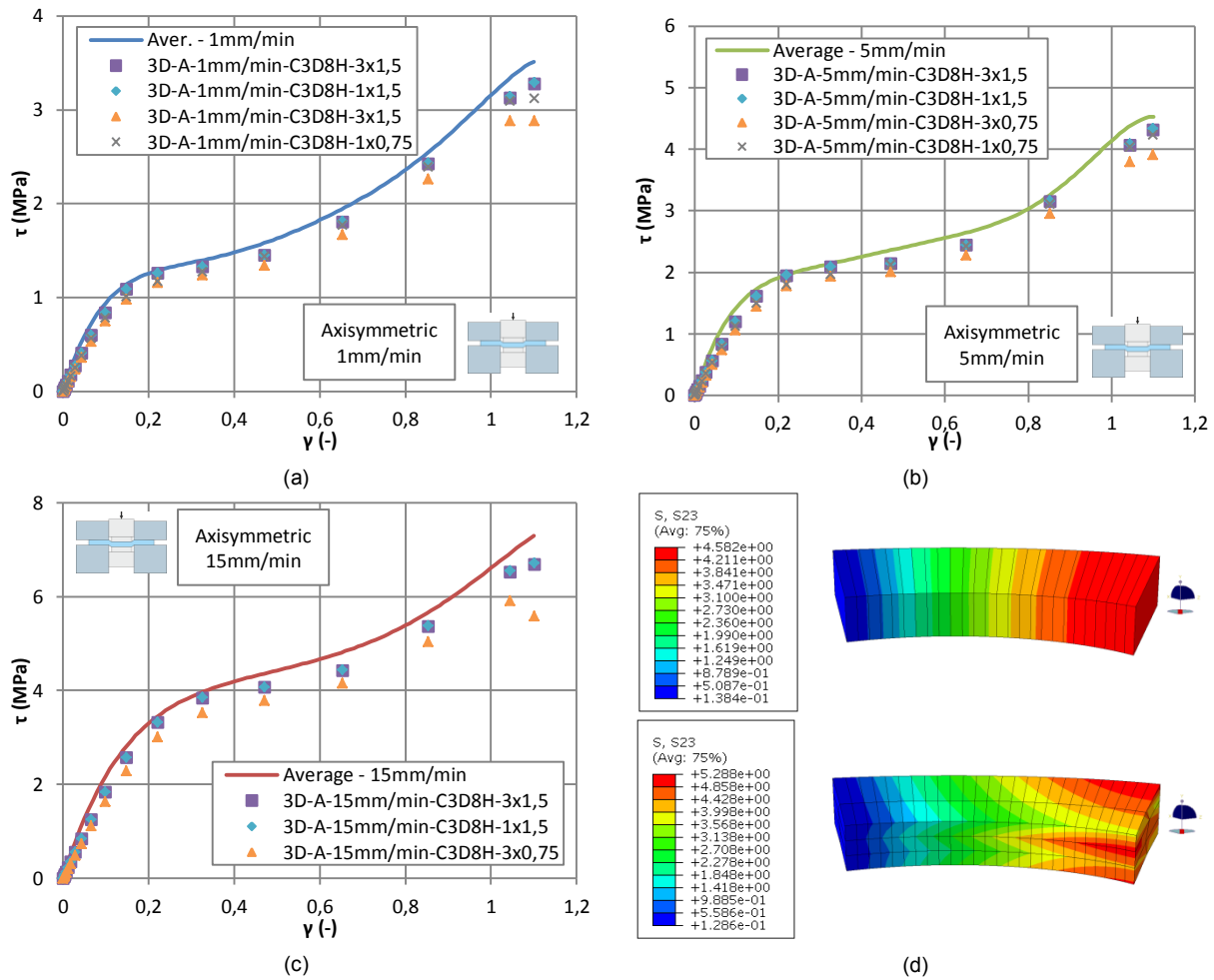
**Figure 6.52-** Stress-strain diagrams of the three rates (a) 1mm/min, (b) 5mm/min and (c) 15mm/min – (d) Shear deformation

In contrary to the axisymmetric representation, all the calculations were carried until the end. For the three loading rates, the estimated stress-strain curves closely corresponded to the experimental ones independently of the mesh size. While a direct measurement of the shear stress was available for the coarser mesh containing only one element, large variations were noticed for finer meshes, see Fig. 6.52 (b). The distortions, induced by the large imposed deformations, again appeared as a problem in terms of element stability. Nevertheless, as the developed subroutine returned the correct stress-strain behaviour, it was appraised as valid for the 2D numerical simulations.

- 3D representation

The stress values of the 3D representation were determined by dividing the reaction force recorded at all the nodes along the fixed edge by the lateral area at the same position, while the strains were

evaluated by calculating the arctangent of the displacement assessed on the inner lateral face divided by the thickness of 1,5mm. The stress-strain curves of each loading rate were exposed on Fig. 6.53.



**Figure 6.53-** Stress-strain diagrams of the three rates (a) 1mm/min, (b) 5mm/min and (c) 15mm/min – (d) Shear deformation

As for the axisymmetric model, only one simulation did not succeed, i.e. for the highest loading rate and finer mesh of 1x0,75mm. The reason evoked previously was still valid with too large distortions of the mesh elements. For the other jobs, the final time period was completed, even if the stress-strain curves did not perfectly matched the experimental ones, e.g. for the mesh size of 3x0,75mm as for the axisymmetric case. Nevertheless, the good concordance for larger meshes between the numerical and experimental diagrams allowed validating the use of the developed UHYPER subroutine for the 3D representation of the acrylic shear behaviour. The mesh size should however be controlled and different calculations always performed to assess the convergence of the results.

## 6.4 SUMMARY AND CONCLUSION

The developed silicone and acrylic adhesive material laws, presented in chapter 5, were converted in FORTRAN subroutines implemented in Abaqus. For the silicone 3D constitutive material law, the two solving methods proposed by the finite element software, i.e. an implicit and an explicit resolution, were envisaged as this material tended to largely distorted. Both presented advantages, such as the stability for the standard one and the distortion control and the ALE method for the explicit one. In consequence, two subroutines were created depending on the solving procedure, i.e. an UHYPER subroutine for Abaqus/Standard and a VUMAT subroutine for Abaqus/Implicit. For the acrylic material law, in reason of its extraction from the developed silicone material, the implicit subroutine was employed.

The three isochoric deformations, uniaxial tension, compression and shear, imposed to the silicone were successively modeled with the two subroutines and by evaluating the convergence of the results in function of the mesh elements and sizes. Even with coarse mesh, the obtained results perfectly matched the experiments in the three cases. However, for the push-out shear tests, the silicone shear stresses could not be directly analyzed at the material itself due the presence of singularities and important peaks. In this specific case, the stress-strain diagrams were achieved by recording the reaction force at the bottom of the glass plate and dividing it by the bonded area. Nevertheless, to study the validity of the shear stress peaks, three distinct methods were employed, i.e. by considering the existing theories, by evaluating the parameter of influence of the peaks with numerical calculations and by conducting small-scale tests. According to the Volkersen and Hart & Smith theories, the peaks were not present and only some negligible increase of the stress occurred at the silicone extremities. The numerical simulations demonstrated that finer was the mesh and higher were the peak values. Further, the width, length and thickness of the joint were non-influent on the peaks. Based on this last method, a linearization of the stress, over a length 6 times greater than the silicone thickness, allowed finding the constant stress in the core of the joint. This indicated that the stress peaks were certainly due to a numerical singularities and were absent from the real behaviour. However, the small-scale tests nuanced the results as differences were observed between different geometries. The variations were low and could be induced by the manufacture of the specimens, which was relatively difficult with regards to the small joint dimensions.

The volumetric oedometric tests were also modeled with the two subroutine and solving methods. The results matched the experimental ones even for the coarser mesh. This last step definitely validated the two written UHYPER and VUMAT subroutines, which could be employed to model more general joints and type of actions.

As aforementioned, the acrylic material was modeled by slightly modifying the UHYPER subroutine intended for the silicone representation. The implicit solving method was used to model the modified shear tests. As this material was dependent on the loading rate, the coefficients of the material laws were adapted for the three investigated rates. Further, as the law was one dimensional, three types of modeling were accounted, i.e. with an axisymmetric representation, in two dimensions and in three dimensions. The influence of the mesh size on the results was also checked for these three models. Nevertheless, the shear behaviour, issued from the three numerical simulations, perfectly matched the experimental results. The push-out shear tests could not be implemented in the Abaqus software, as the thickness of the joint were not perfectly known and some small deviations could lead to great changes.



## 7. LINEAR ADESIVE CONNECTION EVALUATION

### 7.1 INTRODUCTION

The principal objective of this chapter is to assess the behaviour of the linear adhesive composite beams. The results issued from the partial connection theories are compared to the results of the numerical simulations. Large-scale tests are performed to fully validate the proposed analytical and numerical models. The organization of this chapter is detailed in Figure 7.0.

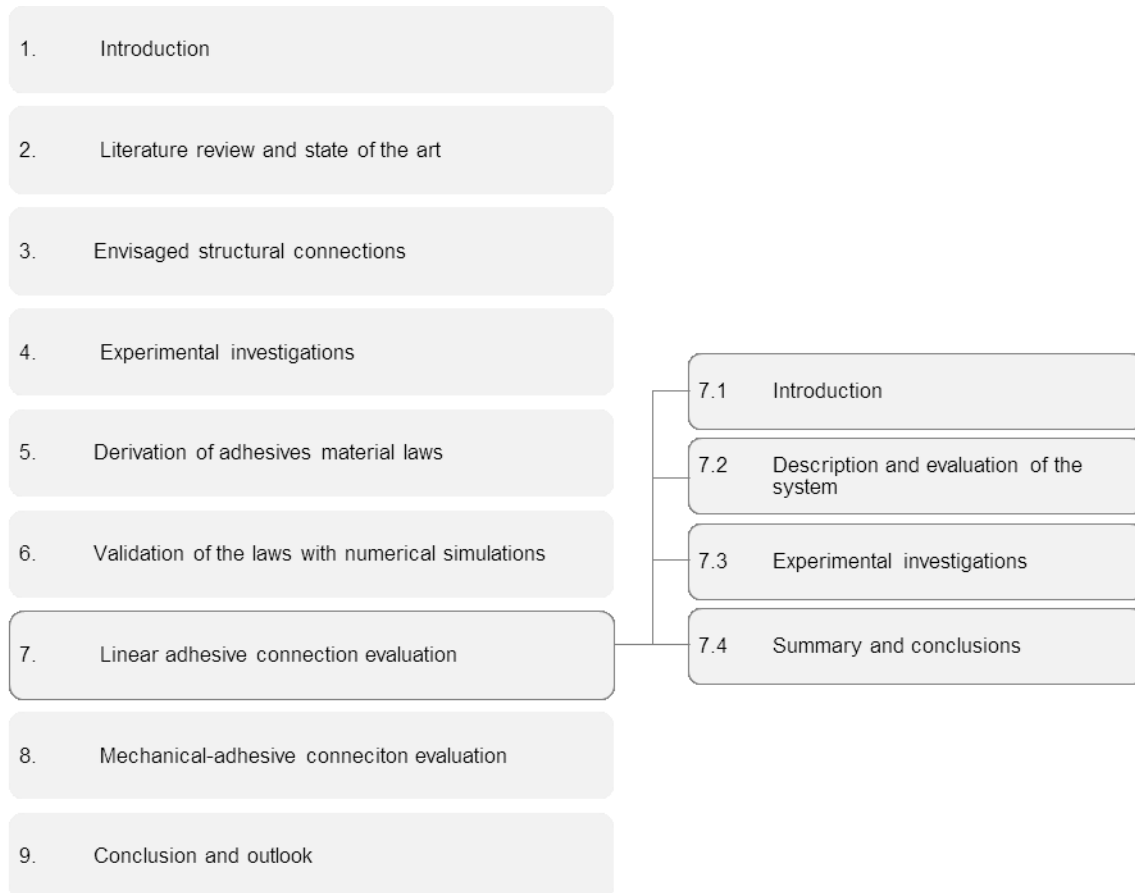


Figure 7.0- Organization chart of chapter 7

**Description and evaluation of the system.** The dimensions given to the envisaged linear adhesive connections are given in this section. The partial connection theory of Lebet is first employed to assess the behaviour of this system. In parallel, are conducted several numerical simulations, which allow providing comparison charts between fully connected, unconnected and the actual assembly, in order to determine the degree of connection.

**Experimental investigations.** The manufacture of the three large-scale beams to be tested is explained. The global testing layout and the employed instrumentations are detailed. A comparison of all the results is made for the validation of the existing analytical and numerical theories.

**Summary and conclusion.** The origin of the observed differences between the experimental results and theoretical ones is proposed in the conclusion.

## 7.2 DESCRIPTION AND EVALUATION OF THE SYSTEM

### 7.2.1 Description of the composite beam

The linear adhesive system, composed by three different material types, was described in section 3.3. The two adhesive studied in chapter 4 were the possible candidates to join the steel beam and the glass plate. However, the tensile and shear properties of the Bohle UV-acrylic MV 760 were found greatly reduced by long-term actions, which made it unfit for this connection. Consequently, only the thermally and mechanically stable Dow Corning DC993 silicone was considered. For the different configurations, vertical or horizontal non accessible glazing, the intensity of the out-of-plane actions was estimated more decisive for the composite beam than the in-plane loads, essentially caused by the differences of thermal coefficients. Hence, to assess the rigidity of the assembly and the degree of connection, only 4-point bending tests were envisaged. The 3-point bending tests were excluded, as they did not offer a large zone of constant bending stress between the two load application points.

- Global system

The length of the beam and the locations of the two load application points were detailed on Fig. 7.1. While the tested length was of 3300mm, divided in three equal portions by the loads, the total length of the assembly measured 3500mm. This over dimensioning was done to anticipate the large rotations and displacements at the supports.

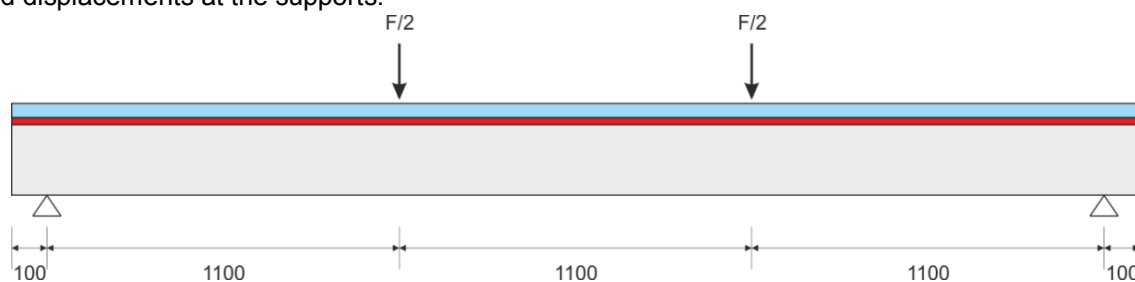


Figure 7.1- Description of the global system – Dimensions and position of the loads

- Cross-section dimensions

The width of the fully tempered glass (FTG) panel was set to about 1/3 the tested length of the beam. A thick monolithic element of 15mm was employed instead of a laminated glazing, as this latter could introduce parasite partial interaction between two panels. The S355 steel profile was a rectangular hollow section of 150mm of height and 100mm of width, corresponding to one tenth of the glass width. This last section was chosen in order to limit the instabilities such as the lateral buckling. The bonding area of the adhesive was provided by the width and length of the steel profile and the thickness was made as small as possible, i.e. 3mm as it was achieved with the small-scale shear tests.

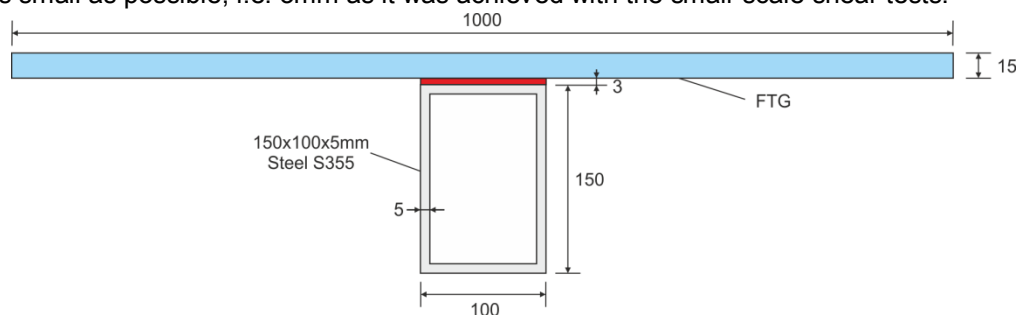


Figure 7.2- Composition and dimensions of the cross section of the linear adhesive composite beam

In an ideal system, the glass plate would only be subjected to non-crucial compressive forces, i.e. the neutral axis should be in the steel profile. The position of the latter could be determined for a perfect

connection with the procedure exposed in Appendix F. For the present system, assuming a complete interaction between the members, the position of the neutral axis was found 18,8mm under the upper surface of the steel profile.

- Material properties

Only the linear properties of steel were at first regarded to approximate, with the theories presented in Appendix F, the behaviour of the steel-glass composite beam. The isolated steel beam subjected to the four-bending test would start to plasticize under a total load of 61,9kN, meaning that this linear assumption of the steel remained at least valid until this load. The glass properties were fully linear and exposed in Table 7.1. For the first numerical simulations, the non-linear silicone behaviour was entirely described by the developed material law with the quasi-static set of coefficients, as the beams were directly tested after the manufacturing. For the evaluation with the partial connection theories, a simple linear regression was applied on the experimental quasi-static shear stress-strain curve in order to calculate a shear stiffness  $G$  fitting the best the real data. Thus, only for the theories, the silicone was assumed linear with a shear modulus of 0,811MPa, as already determined for the peak stress theories.

| Steel (S355)      |           |                             | Glass   |           |                             | Silicone                               |
|-------------------|-----------|-----------------------------|---------|-----------|-----------------------------|----------------------------------------|
| Linear properties |           |                             |         |           |                             | Non-linear properties                  |
| E (MPa)           | $\nu$ (-) | $\rho$ (kg/m <sup>3</sup> ) | E (MPa) | $\nu$ (-) | $\rho$ (kg/m <sup>3</sup> ) | Hyperelastic law                       |
| 210000            | 0,3       | 7850                        | 70000   | 0,23      | 2500                        | Table 5.21 – quasi-static coefficients |

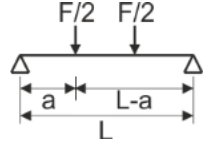
**Table 7.1-** Material properties inserted in finite element analysis for the prediction of the composite beam behaviour

## 7.2.2 Theoretical and numerical analysis

To evaluate the degree of connection of the considered system, some reference configurations were first assessed, i.e. the steel beam only, a state of no connection between the glass and steel elements and a perfect connection. The proposed arrangement of Fig. 7.2 was then superposed to the three previous ones for comparison. The estimation of the behaviours of all the entities was achieved by two distinct methods, i.e. theoretical analyzes presented in Appendix F and numerical simulations. As aforementioned, the adherends were only linear and the plasticity of the steel was thus neglected. With this linear hypothesis, the total force applied on each system was identical and equal to 100kN. The correlation between the two general methods was first done for each case:

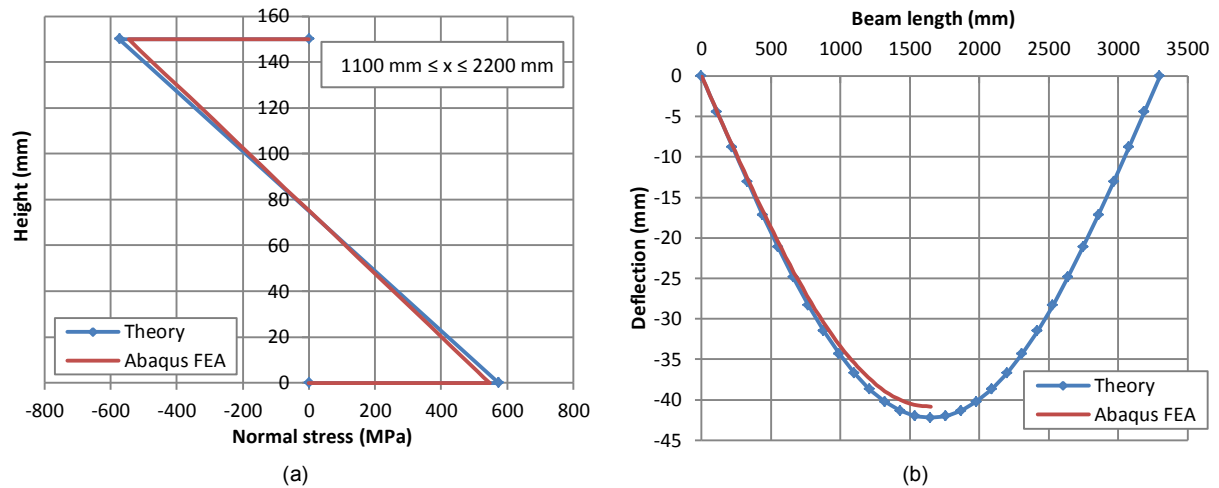
- Steel beam only

The points of application of the two loads, as well as the dimensions of the steel beam evoked in the previous section remained the same, i.e. the glass plate and the silicone were simply removed. The standard beam theory was employed to theoretically determine the maximum stress distribution in the steel profile. The displacements according to the length of the beam were obtained with the following equations:



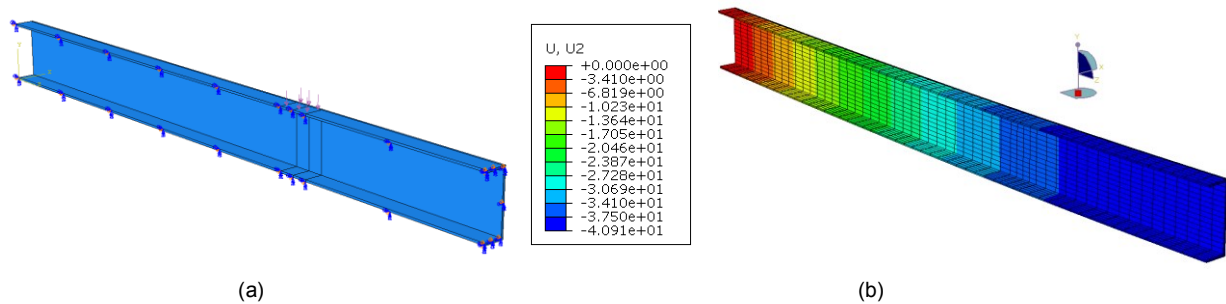
$$\begin{aligned}
 0 \leq x \leq a & \quad y = \frac{F(L-a)x}{12EIL}(L^2 - (L-a)^2 - x^2) + \frac{Fax}{12EIL}(L^2 - a^2 - x^2) \\
 a \leq x \leq L-a & \quad y = \frac{Fa(L-x)}{12EIL}(x(2L-x) - a^2) + \frac{Fax}{12EIL}(L^2 - a^2 - x^2) \\
 L-a \leq x \leq L & \quad y = \frac{Fa(L-x)}{12EIL}(x(2L-x) - a^2) + \frac{F(L-a)(L-x)}{12EIL}(x(2L-x) - (L-a)^2)
 \end{aligned}$$

The theoretical maximum normal stress distribution in the steel profile and the deflection of the beam according to the length were plotted on Fig. 7.3. As observed, for a force of 100kN, the ultimate stress of the S355 steel was already exceeded and large displacements up to about 42mm were reached.



**Figure 7.3-** (a) Normal stress distribution in the steel profile and (b) Deflection according to the beam length

For the numerical simulation, only one fourth of the model was modeled in reason of the isotropy of the material and the geometrical symmetries. Only the tested length was considered, neglecting the 100mm at each extremity. Symmetry boundary conditions were applied on the faces theoretically in contact with the rest of the beam. The vertical displacements at the supports were restrained along the edges. Some partitions were also created around the load application point (at 40mm) to introduce a pressure on the model, see Fig. 7.4. Different mesh sizes and elements order were tested to ensure the convergence of the mesh under Abaqus/Standard. The quadratic bricks C3D20 elements were employed. The wall thickness of the steel beam was composed by two elements while the flange contained four and the web fourteen. Along the length, the size of the mesh was set to 30mm, except between the partition (load application zone) where 20mm were regarded. The results of the calculation were superposed to the theoretical ones on Fig. 7.3. The stress distribution was recorded at the center of the beam and a path was made to measure the displacements along the length. A relatively good concordance between the theory and the numerical simulation was noticed validating the results.



**Figure 7.4-** (a) Boundary conditions and load application on the model and (b) Vertical displacements of the steel beam

- Unconnected system

Compared to the previous case, the glass plate was disposed on the top of the steel beam and the connection was completely neglected. The classical beam theory could not be used due to this layering. Therefore, the Lebet theory was employed by adjusting the rigidity of the connection to a very low value. The shear modulus was chosen equal to  $10^{-5}$  MPa, as no changes in terms of stresses and displacements were remarked for lower values. The maximum normal stress distribution under the load application point and the deflection along the length acquired with this theoretical model were plotted on Fig. 7.5. The addition of the glass plate on the top of the beam did not increase significantly the rigidity of the assembly, as the maximum deflection of the beam was of about 41mm. Furthermore, the maximum normal stress again exceeded the ultimate strength and was close to the one achieved for the steel beam alone. In addition to these two curves, the Lebet model, based on the sliding equilibrium equation, allowed the estimation of the relative displacements at the steel-glass interface. This data was plotted along the length of the beam on Fig. 7.6.

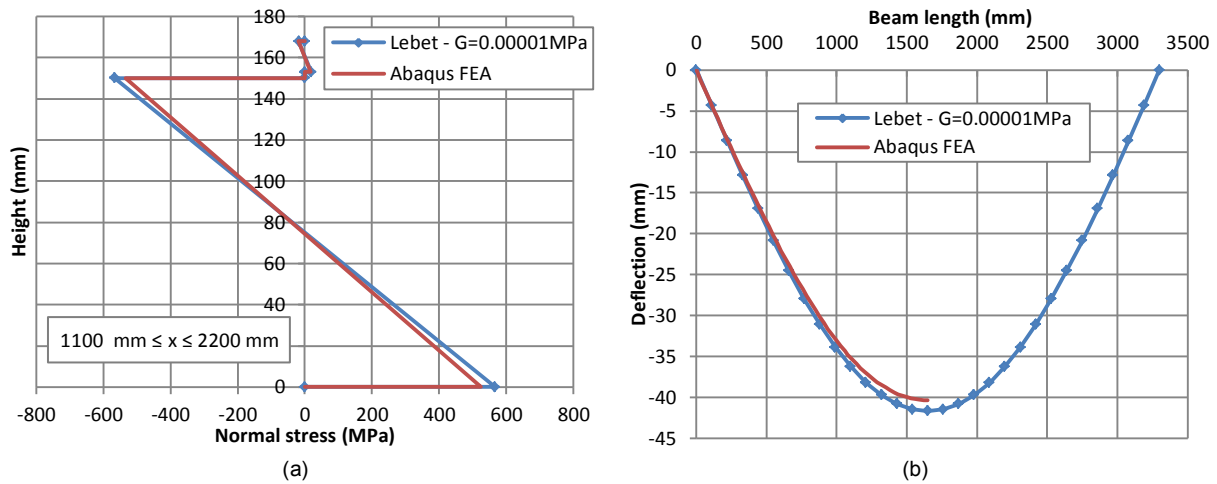


Figure 7.5- (a) Normal stress distribution in the non-connected assembly and (b) Deflection according to the beam length

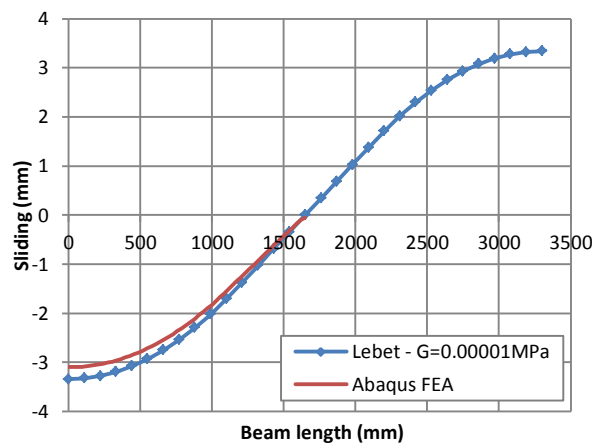


Figure 7.6- Sliding at the steel-glass interface in function of the length of the beam – Assembly with no connection

As for the simple steel beam,  $1/4^{\text{th}}$  of the total system, excluding the 100mm at the extremities, was represented with appropriate boundary conditions. This model was possible in reason of the isotropy of the two materials and of the geometrical symmetries. The support of the beam was accounted by vertically restraining one of the bottom edges of the steel. Symmetry boundary conditions were applied on the parts virtually in contact with the rest, even for the glass plate. Partitions were again made at the proximity of the load application line (at 40mm on both side), see Fig. 7.7. A hard and frictionless contact was inserted between the touching zones of the steel and glass parts. Further, the two pieces were not allowed to vertically separate once the contact was achieved, which prevent any dissociation possibly appearing at the end of the beam. The load was introduced through an analytical rigid hollow section of 80mm of width and 500mm of length. This part was allowed to rotate around its own axis and move along the vertical direction. A hard and frictionless contact was also implemented between the rigid body and the glass plate. The calculation was performed under Abaqus/Standard with the implicit method of resolution and the convergence of the results according the mesh was checked. All the elements were quadratic C3D20 bricks and the mesh size presented for the steel beam alone was conserved.

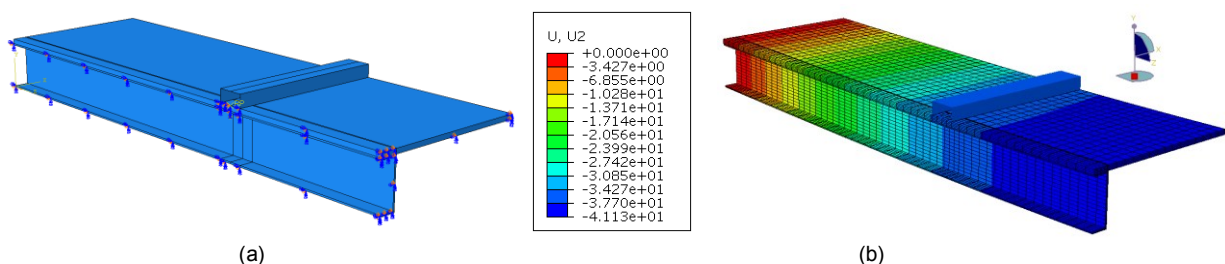
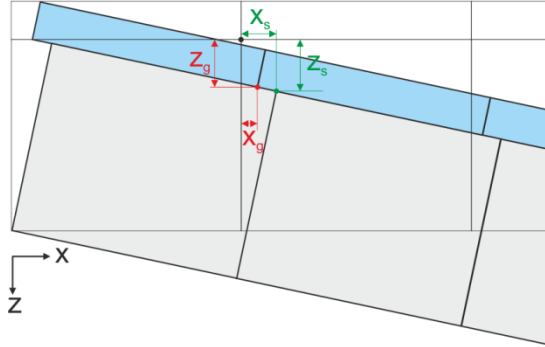


Figure 7.7-(a) Boundary conditions and load application on the unconnected model and (b) Vertical displacements

For the glass plate, 4 elements along the thickness were selected and 30x30mm elements established on the free zone. At the contact zone, the steel mesh size was reproduced on the glass. The results of the simulation were added to the theoretical ones on Fig. 7.5. The small existing gaps between the two methods of calculation were close enough to confirm the validity of the Lebet theory. The sliding at the interface was calculated by extracting the displacements at the steel and glass nodes with the following procedure:



For a shared node at the start of the increment.

At the end of the calculation:

$$Sliding = \sqrt{(z_s - z_g)^2 + (x_s - x_g)^2}$$

With  $z_s$  the vertical displacement of the steel node.

$z_g$  the vertical displacement of the glass node.

$x_s$  the horizontal displacement of the steel node.

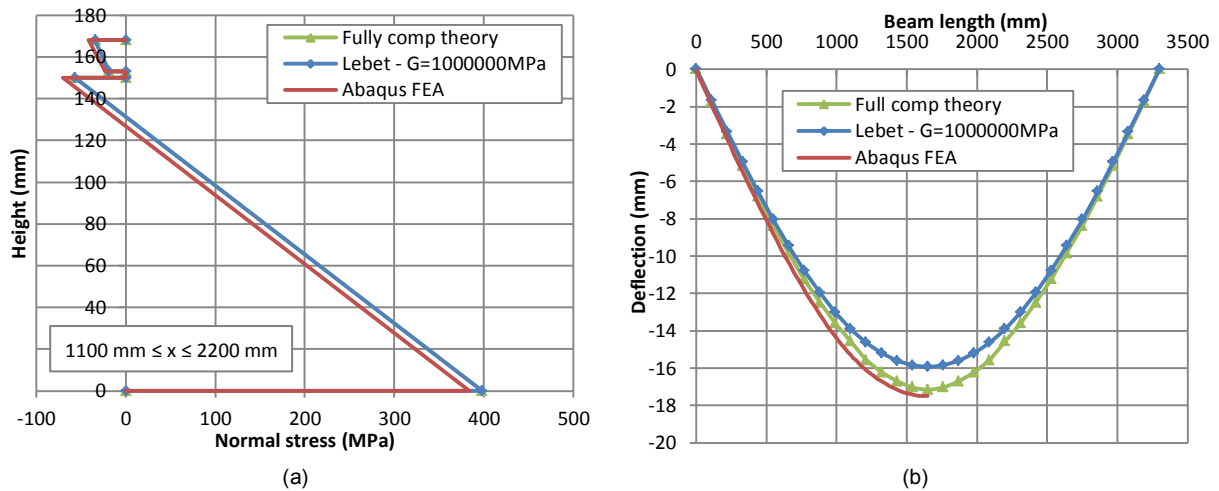
$x_g$  the horizontal displacement of the glass node.

**Figure 7.8-** Procedure allowing evaluating the sliding at the steel-glass interface for the numerical simulations

The numerical sliding was relatively closed to the theoretical one with an error of about 7% at the end of the beam. The Lebet theory was thus approved to predict the behaviour of the unconnected beam.

- Fully connected system

At the opposite of the unconnected system, the full connection was investigated. For the theories, two possibilities arose, i.e. the full composite beam theory evoked in Appendix F and the Lebet theory in which a large shear modulus should be injected. For the latter, a shear modulus  $G$  of  $10^6$  MPa was employed, as for higher values no evolution was noted. For both, the normal stress distribution and the displacement along the length of the beam were determined, see Fig. 7.9. In terms of stress, the fully composite beam theory gave the same results than the Lebet theory. However the maximum deflection was slightly underestimated by the last model, but the deviation was not so important, which seemed to confirm the validity of the Lebet theory. Only compression force developed in the glass element corresponding to the ideal case. In addition, the maximum tensile stress in the steel was clearly reduced with the 100% connection and was inferior to the ultimate strength.



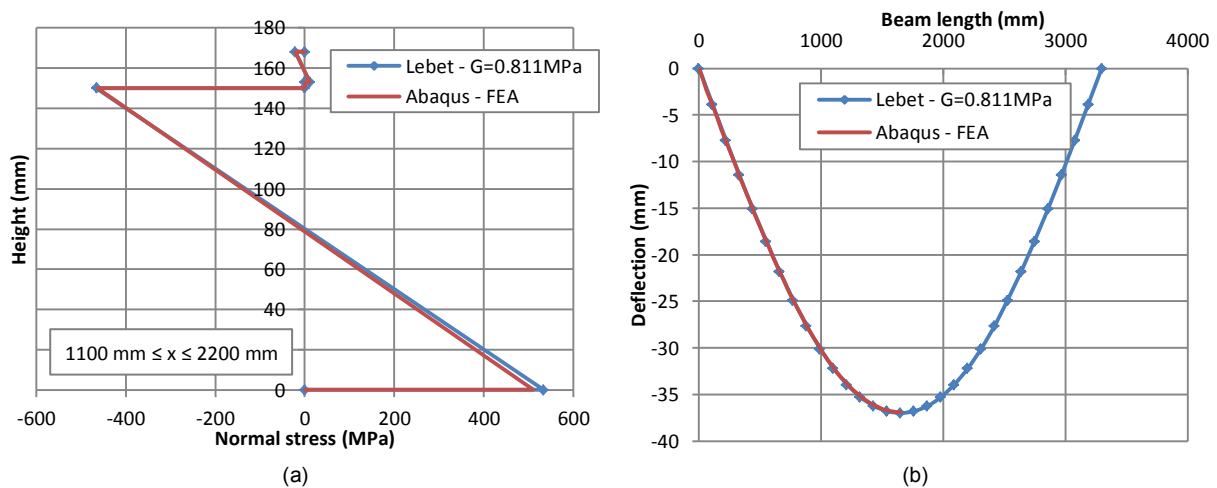
**Figure 7.9-** (a) Normal stress distribution in the fully connected assembly and (b) Deflection according to the beam length

One fourth of the system was represented in Abaqus as a unique part, in which was defined the two materials. The boundary conditions evoked for the unconnected system remained however the same, as well as the realized partitions. The load was again introduced through an analytical rigid hollow

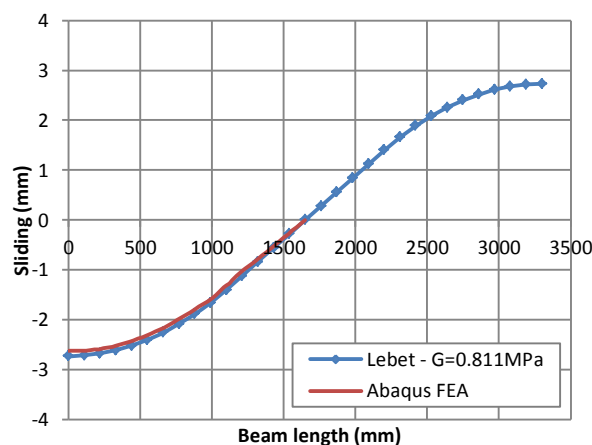
section of 80mm of width, for which the rotation around its principal axis was allowed in order to ensure a uniform pressure. A hard frictionless contact was created between this rigid part and the glass plate. The implicit resolution was regarded and the convergence of the results towards the mesh size assessed. The quadratic C3D20 bricks were reused and the mesh described previously conserved. The deflection and stress distribution results were superposed to the two theories of Fig. 7.9. The tensile stresses at the bottom of the assembly were slightly lower for the numerical simulation although the maximum deflection was higher.

- System of Fig. 7.2

The two previous analyzes constituted the extreme cases allowing visualizing the degree of the partial connection detailed in Fig. 7.2. The Lebet theory was applied with the already mentioned linear shear stiffness of 0,811MPa for the adhesive. The stress distribution and deflection along the length of the beam were drawn on Fig. 7.10. As observed, only a small portion of the glass plate would be under tensile forces, i.e. about one third of the thickness. The tensile stress in the steel would approach the ultimate limit strength. The sliding at the interface was also estimated along the length and plotted on Fig. 7.11. With this diagram, the maximum relative displacement at the end of the beam was found lower than the one of the unconnected beam.



**Figure 7.10-** (a) Normal stress distribution in the envisaged assembly (Fig. 7.2) and (b) Deflection according to the beam length

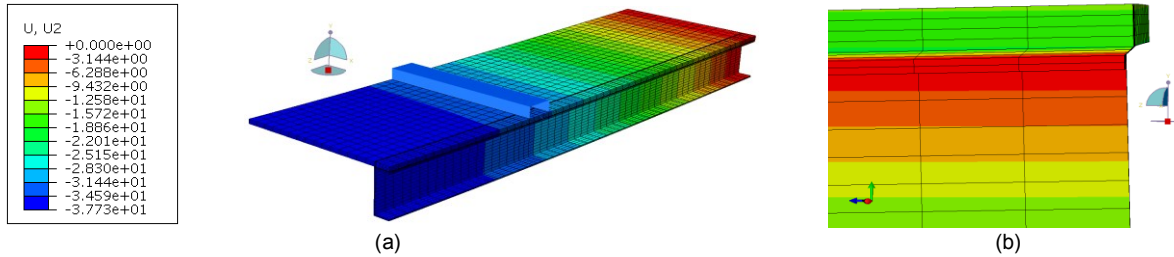


**Figure 7.11-** Sliding at the steel-glass interface in function of the length of the beam – Envisaged assembly of Fig.7.2

The one fourth model represented in Abaqus was made out of one part on which were assigned the three different materials. While the steel and glass elements were fully linear, the non-linearity of the silicone material was implemented through the developed UHYPER subroutine, as the implicit method of resolution was envisaged. The boundary conditions detailed previously were conserved and applied to the silicone for the symmetry ones. The two partitions defining the zone for the introduction of the



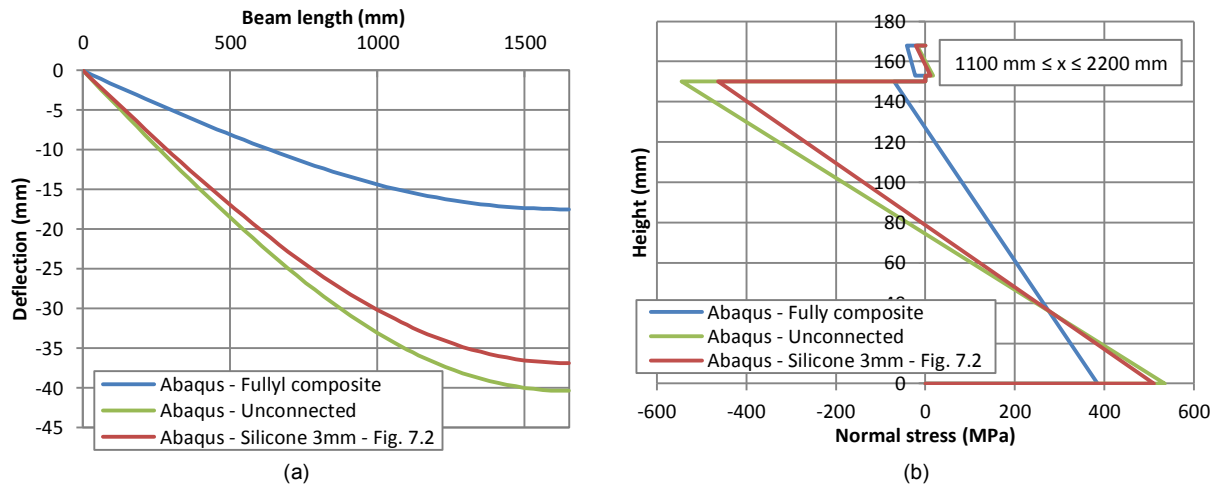
load were reproduced and the analytical rigid hollow section maintained with its specific boundary conditions and hard frictionless contact. The size of the C3D20 elements disposed on the glass and steel parts were similar to the one employed heretofore. For the silicone, the repartition of the mesh over the large surface was dictated by the mesh size of the outer adherends. On the thickness, three elements were at least necessary to achieved correct results, see Fig. 7.12.



**Figure 7.12-** (a) Vertical displacements and (b) sliding at the interface for the envisaged assembly of Fig. 7.2

The stress distribution and the deflection obtained with the numerical simulation were superposed to the theoretical ones on Fig. 7.10. For both studies, the results of the two methods were well matched, which proved the validity of the Lebet theory combined to a linear approximation of the silicone shear behaviour. The sliding values along the length of the beam were assessed with the procedure evoked in Fig. 7.8 and added to Fig. 7.11 for comparison. Again no difference was observed between the two sliding curves.

The three degrees of steel to glass connection were evaluated with numerical simulations and the Lebet theory. The two methods provided the same results in terms of deflection and maximum normal stresses. Hence, only one was selected to situate the envisaged connection of Fig. 7.2 between the two extreme cases, see Fig. 7.13. As the shear stiffness of silicone was low and the thickness limited to 3mm, the contribution of the glass plate to the global rigidity of the assembly was not sufficient to approach the perfect connection. Nevertheless, for the same load intensity, the deflection of the beam was less than the one of the unconnected system. Furthermore, the maximum tensile stress in the glass was also lower.



**Figure 7.13-** (a) Comparison of the deflection curves and (b) of the stress distribution for the three degrees of connection

## 7.3 EXPERIMENTAL INVESTIGATIONS

To definitely approve the preceding theoretical and numerical evaluations, three large scale beams were manufactured according to the dimensions presented in Fig. 7.1 and 7.2. This test campaign had for objectives to:

- Evaluate the rigidity of the system by analyzing the deflection at defined positions.
- Measure the sliding at the steel-glass interface along several positions along the length for comparison to the Lebet theory.



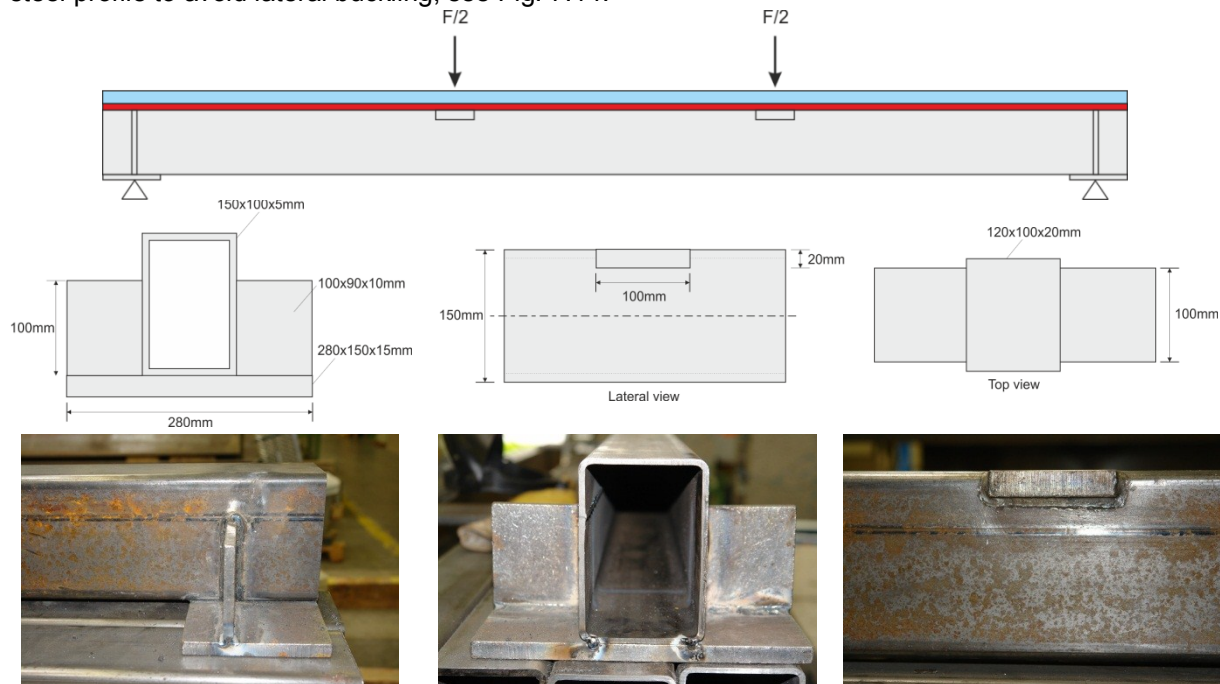
- Achieve force-displacement curve to obtain a general vision of the beam behaviour.

### 7.3.1 Manufacturing of the beam

Several operations, as well as measurements, were separately conducted on the steel beam and on the glass plate before realizing the final bonded assembly. These different actions were gathered in the following paragraphs.

#### Steel beam modifications

The length and cross section of the steel hollow profile were detailed on Fig. 7.1 and 7.2. As important forces were expected, some modifications were made in order to avoid possible instabilities arising at the supports and at the force introduction positions. To allow the large rotation and displacements of the beam at the two supports, the use of rollers of 30mm of diameters was envisaged. With this configuration, the reaction forces would be transmitted through lines and not over sufficiently large surfaces. This would cause very local bending of the steel cross section in reason of its small wall thickness of 5mm. Therefore, to prevent this phenomenon, a thick plate of 15mm was welded at these two locations. Furthermore, two plates 10mm thick were vertically welded on the latters and on the steel profile to avoid lateral buckling, see Fig. 7.14.



**Figure 7.14-** Local modifications of the steel beam at the support and load introduction positions to prevent instabilities

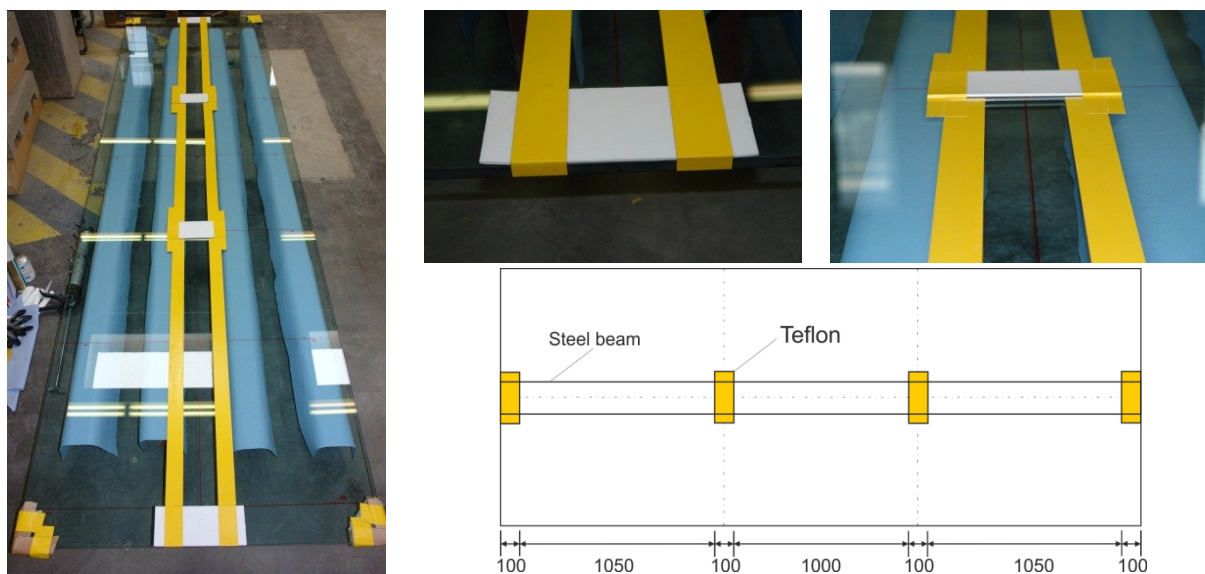
As for the supports, the introduction of the load on the total system remained a problem, as it had to be transmitted through the glass plate sensible to local stress concentration peaks. In consequence, the rollers could not be employed and steel plates of 80mm of width were considered. With the thin wall thickness of the steel, recesses were still possible. Hence, the upper part of the steel beam was cut on 100mm and over 20mm in depth and replaced by a welded thick steel plate, see Fig. 7.14. The welding was always achieved on the side and not on the top of the beam, as it would introduce longitudinal tensile forces bending the beam and making unachievable the realization of an adhesive constant thickness. Compared to the load introduction steel plate, this last welded element was 20mm longer (10mm on each side) to ensure a proper transmission of the load in the steel profile.

As the top flange of the beam had to be bonded to the glass plate, the protective oxide was removed all along the length with a grinder and then degreased with solvent. The application of the primer was realized just before the pouring of the silicone to prevent its complete drying.

### Glass preparation

Fully tempered and chamfered glass of 15mm was employed for these four-point bending tests and consequently, besides the standard measurement concerning the length, width and thickness, the prestress had to be measured in several positions to check the homogeneity of the tempering process. The record of all the information was gathered in Appendix G.1.

In contrary to the steel element, no particular mechanical machining was operated on the glass. The bonding width, equivalent to the steel beam flange width, was delimited with the help of adhesive tape, set over the whole length of the plate, see Fig. 7.15. Additionally, to prevent the adhesion at both extremities of the beam, i.e. within the first and last 100mm, Teflon plates of 3mm of thickness were placed at these specific zones. Two other Teflon plates were also disposed under the load application points and thus replaced the silicone, which could have been compressed during the manufacturing of the assembly. Hence, these last elements were also responsible for the adhesive constant thickness of 3mm.

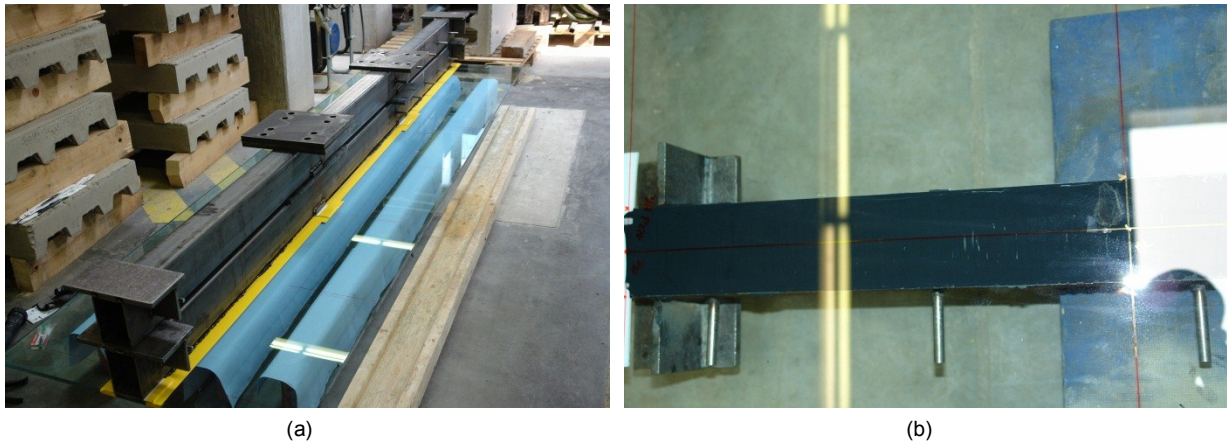


**Figure 7.15-** Preparation of the glass plates and definition of the bonding thickness and area with Teflon plates

The zone delimited by the adhesive tapes was carefully cleaned with solvent to prevent dust particles affecting the bonding. As for the steel beam, the primer was only applied few minutes after the pouring of the adhesive.

### Assembly

To achieve the final composite assembly, the prepared glass plate was placed, tin side on the top, on four supporting wood beams covered by paper to prevent any hard contact, see Fig. 7.15. After, the application of the primer, the silicone was poured, with manual handguns, on two central zones at the same time to quickly finish the process and avoid any curing of the adhesive before positioning the steel beam. Continuous beads were carefully formed in order to not trap large air bubbles inside the core of the elastomer. The steel beam was reversed and then centered on the silicone. To apply sufficient pressure to evacuate the surplus of adhesive, another beam was added on the bonded one to put a constant and uniform pressure, see Fig. 7.16 (a). This system was let in position during 24 hours at ambient temperature and humidity to ensure of the correct curing, which was also validated by the complete curing of the butterfly tests conducted at each cartridge opening. After this period, six strain gauges were glued on predefined locations of the glass plate to record the tensile stress. The adhesive tape was finally removed and the complete assembly returned before being tested 24 hours later. An example of bonding was presented on Fig. 7.16 and some imperfections, essentially small air bubbles, were trapped in the core of the silicone.



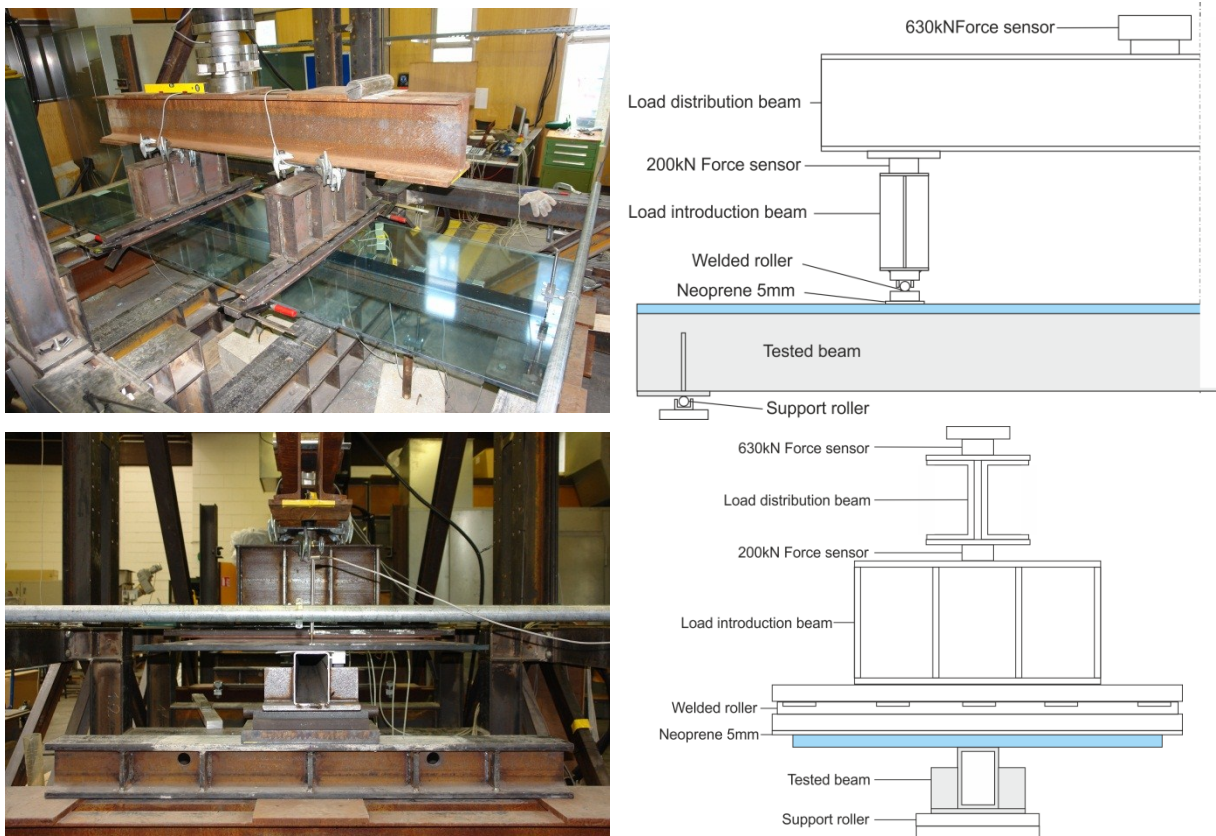
**Figure 7.16-** (a) Dead weight on the top of the assembly for constant adhesive thickness and (b) Silicone bonding example

With the nature of the fully tempered glass plate, a transparent adhesive film of vinyl was placed on the compressive upper surface of the glass to retain the fragments after the complete breakage of the latter. No influence on the stress distribution was introduced by this film as it was installed on the compressive zone.

### 7.3.2 Description of the tests

#### Test layout

The large-scale tests on the linear adhesive composite beams were conducted on a 630kN mobile hydraulic press on which was attached a force sensor of equivalent maximum value. To this sensor was also fixed a kneecap allowing hanging up the horizontal load distribution beam composed by two U-profiles, see Fig. 7.17. This intermediary element was responsible for the correct repartition of the load between the two envisaged positions, as the rest of the upper set-up was fixed.



**Figure 7.17-** Test set-up for the large-scale beam tests and details of the complete load introduction system

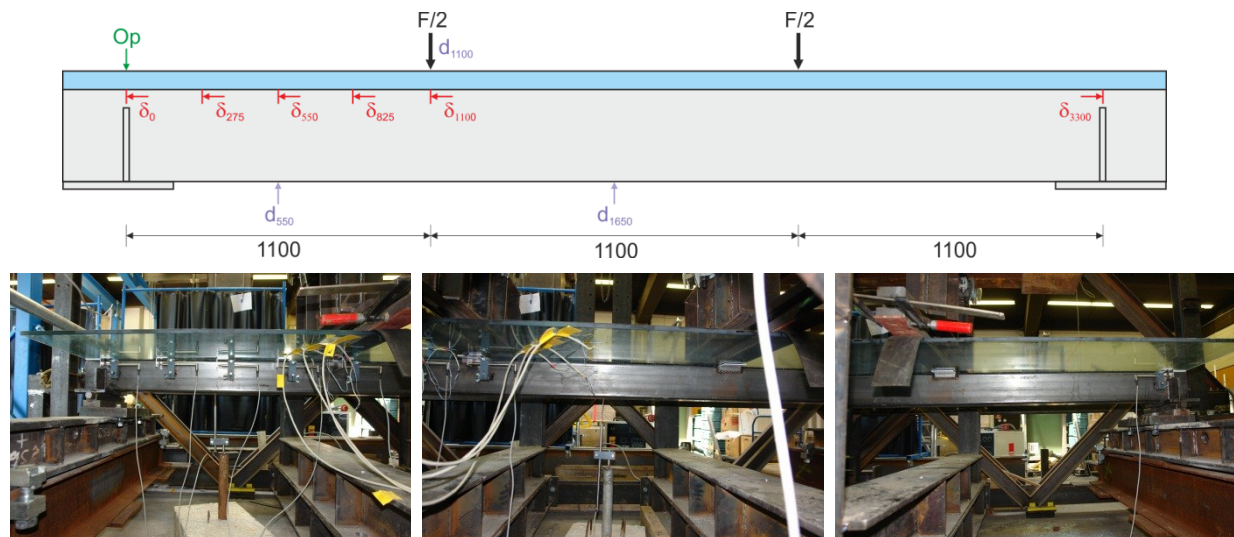


The verification of the equivalent load distribution was checked with the help of two 200kN force sensors jointing the load distribution beam and the load introduction beam. This last was made of a reinforced I-profile. Under the lower surface of the load introduction beam was welded a rigid steel bar of 1200mm of length, 80mm of width and 30mm of thickness. This bar could not be used to directly introduce the force in the system, as large deformations were expected. Hence, to uniformly apply the force, the rotation along the width had to be permitted. This was achieved by welding a roller on another rigid steel section of 1200x80x30mm and placing it under the load introduction beam, as detailed on Fig. 7.17. Further, to prevent steel to glass contact, a Neoprene interlayer 5mm thick was inserted between this last element and the glass plate.

For the lower part of the test set-up under the beam, only two rollers of 30mm of diameter rotating in U-profiles were employed. The latters were welded on steel plates of 40mm of thickness, fixed to rigid steel beams. In contrary to the upper part, no additional interlayer was added between the composite beam and the rollers.

### Instrumentation

As aforementioned, one principal force sensor of 630kN was directly installed on the hydraulic press to measure the total force applied on the system. In addition, as the load was introduced in two distinct points, two others force sensors of 200kN were positioned at these locations to ensure of the correct load distribution. The displacement of the press was recorded by an internal sensor and so was assimilated to the deflection of the beam at 1100mm and 2200mm of the tested length, see Fig. 7.18. Besides, as it was intended to compare the theoretical deflection of the beam along the length to the experimental one, two other displacements sensors of 50mm and 100mm were placed under the beam at respectively 550mm and 1650mm. With these measurements in three different points, the global experimental deflection could be estimated over the first half of the beam, the other half being symmetric with respect to the center.



**Figure 7.18-** Positions of the displacement sensors along the linear adhesive composite beam

The sliding at the steel-glass interface was assessed in six positions with 20mm displacement sensors fixed to the steel beam and measuring the relative displacement of the glass plate. Five were put on the first 1100mm of the composite beam at 0mm, corresponding to the start of the silicone bonding, at 275mm, 550mm, 875mm and 1100mm. As the maximum relative displacement should occur at the extremities of the tested beam, another displacement sensor was horizontally fixed at 3300mm to compare its values to the ones of the sensor at 0mm. Different amounts would mean that the bonding of the areas, comprised between the support and the load introduction point, was not equal. Finally, a last 20mm sensor was vertically installed over the beam at the support to verify that no separation between the glass and the steel happened. Dissociation would invalidate the considered theories.

To assess the elongations of the glass plate according to the total applied force, six strain gauges were employed. Three were positioned at 1100mm, i.e. under the load application zone, while three other at the center of the beam. Starting from the edge, they were each at a distance of 150mm, except for the closest one to the beam, for which the interval was reduced to 120mm to allow a correct bonding. The shear lag could be evaluated with this method and a correct definition of the effective glass width proposed.

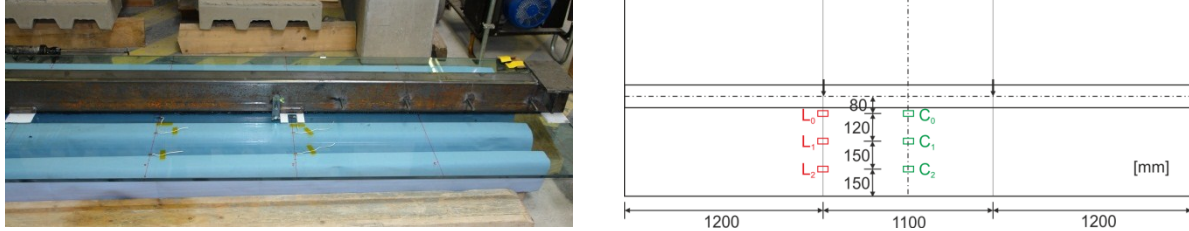


Figure 7.19- Positions of the six strain gauges along the linear adhesive composite beam

### 7.3.3 Tests results

All the tests were conducted in displacement control until glass failure, even if it was not achieved with the first loading in reason of important deflections, larger than the maximal allowed displacement of the press. Therefore, they were carried out in two steps with a first loading until about 90mm, then unloaded to insert some aluminum bars of 1200x80x40mm and followed by a second loading until breakage. A detailed example of total applied force versus machine displacement was exposed, for the linear adhesive composite beam No.2 (LAC-2), on Fig. 7.20. As observed, the first loading curve was linear until a force of about 50kN and then became non-linear. At the end of the unloading, a large plastic deformation was reached and a difference of 40mm was found with the original configuration. In this state, the glass plate curvature was identical to the one of the steel beam as the silicone kept these two elements together. The slope of the second loading was identical to the slope of the linear portion of the first loading until reaching the previous maximum force. After this point, the force-displacement curve corresponded to the continuity of the first loading curve.

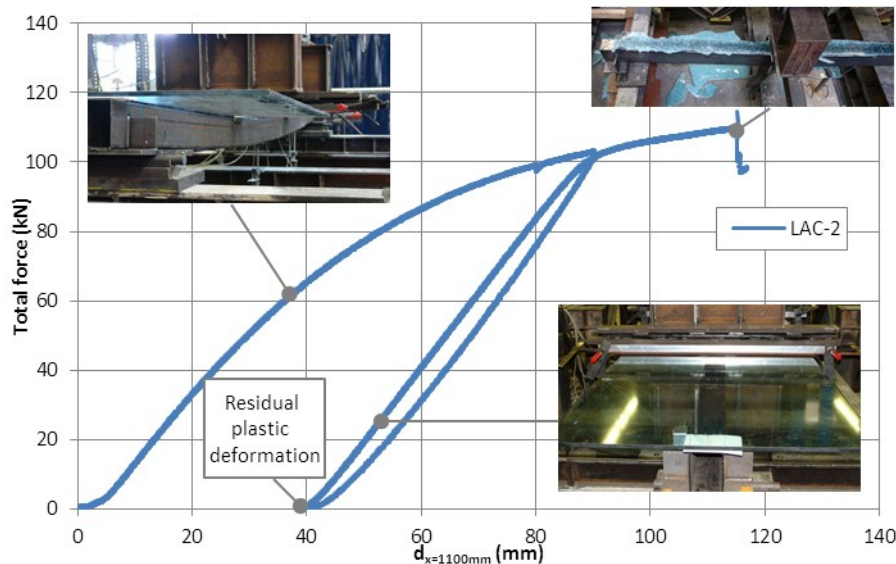


Figure 7.20- Example of total force versus machine displacement ( $x=1100\text{mm}$ ) curve – linear adhesive composite beam

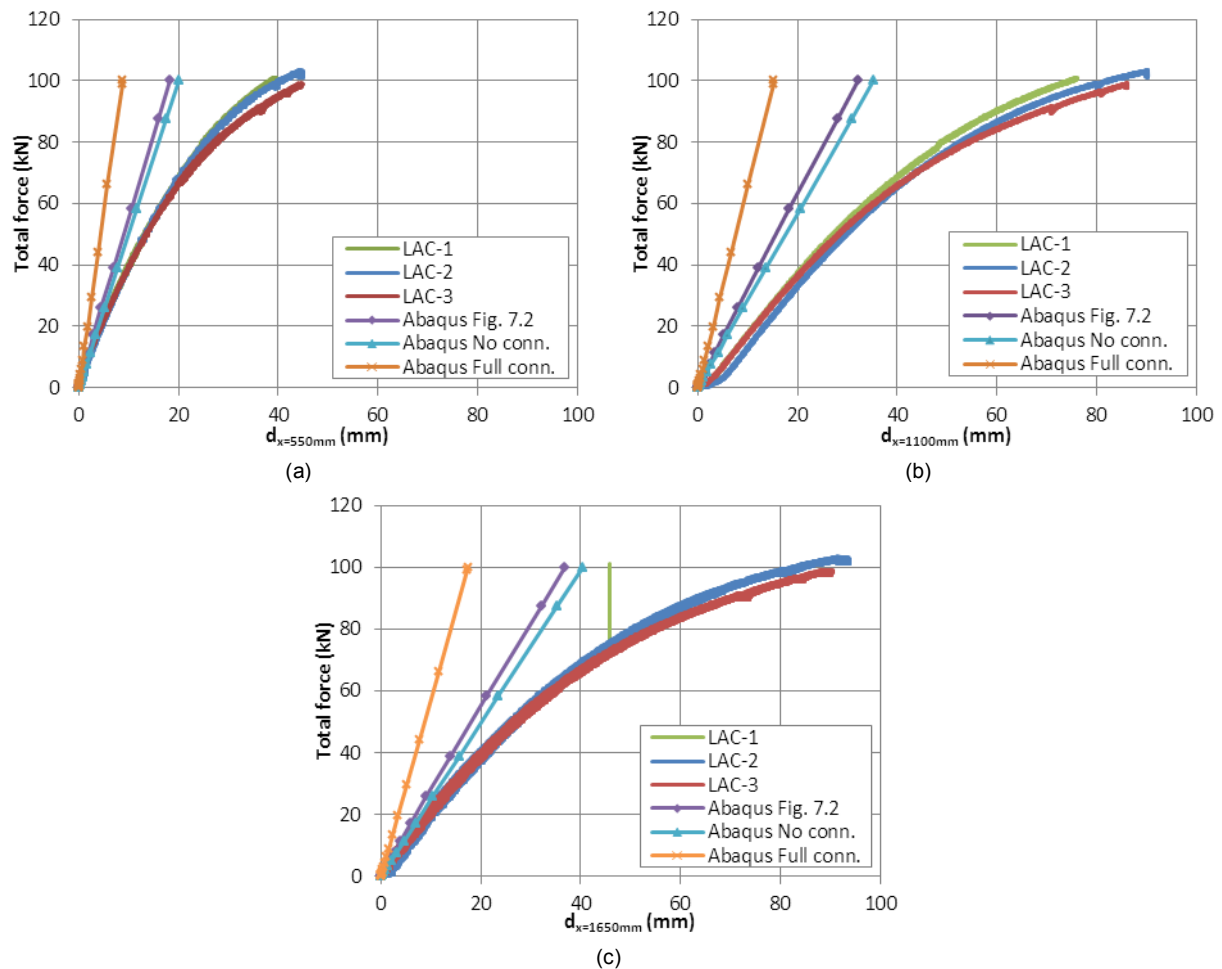
| Composite beam | 1 <sup>st</sup> loading |                      | 2 <sup>nd</sup> loading |                      |
|----------------|-------------------------|----------------------|-------------------------|----------------------|
|                | Max. force (kN)         | Max. $d_{1100}$ (mm) | Max. force (kN)         | Max. $d_{1100}$ (mm) |
| LAC-1          | 100,9                   | 76,2                 | 115,2                   | 141,8                |
| LAC-2          | 102,1                   | 89,9                 | 110,1                   | 115,4                |
| LAC-3          | 99,1                    | 85,8                 | 98,1                    | 90,0                 |

Table 7.2- Maximum forces and displacements after the 1<sup>st</sup> and 2<sup>nd</sup> loading – linear adhesive composite beam

The maximum loads and machine displacements of the first loading were quite close to the forces and displacements at breakage, except for the first beam for which the second loading took place 24 hours after the first one (long-term action in the adhesive decreasing its properties), see Table 7.2. Hence in the following paragraphs, only the first loading was considered to plot curves comparable to the ones obtained with the theoretical and numerical calculations.

### Force-deflection curves

For the three composite assemblies, the deflections at the three selected positions detailed on Fig. 7.18 were recorded and plotted against the total applied force, see LAC curves of Fig. 7.21. All the experimental curves were relatively well matched for all the deflection ranges, indicating that the rigidity of the three beams was equivalent in spite of some possible differences of bonding area due to air bubbles. While the deflections at 1650mm and 1100mm were alike for a given force, they were about two times lower at 550mm.

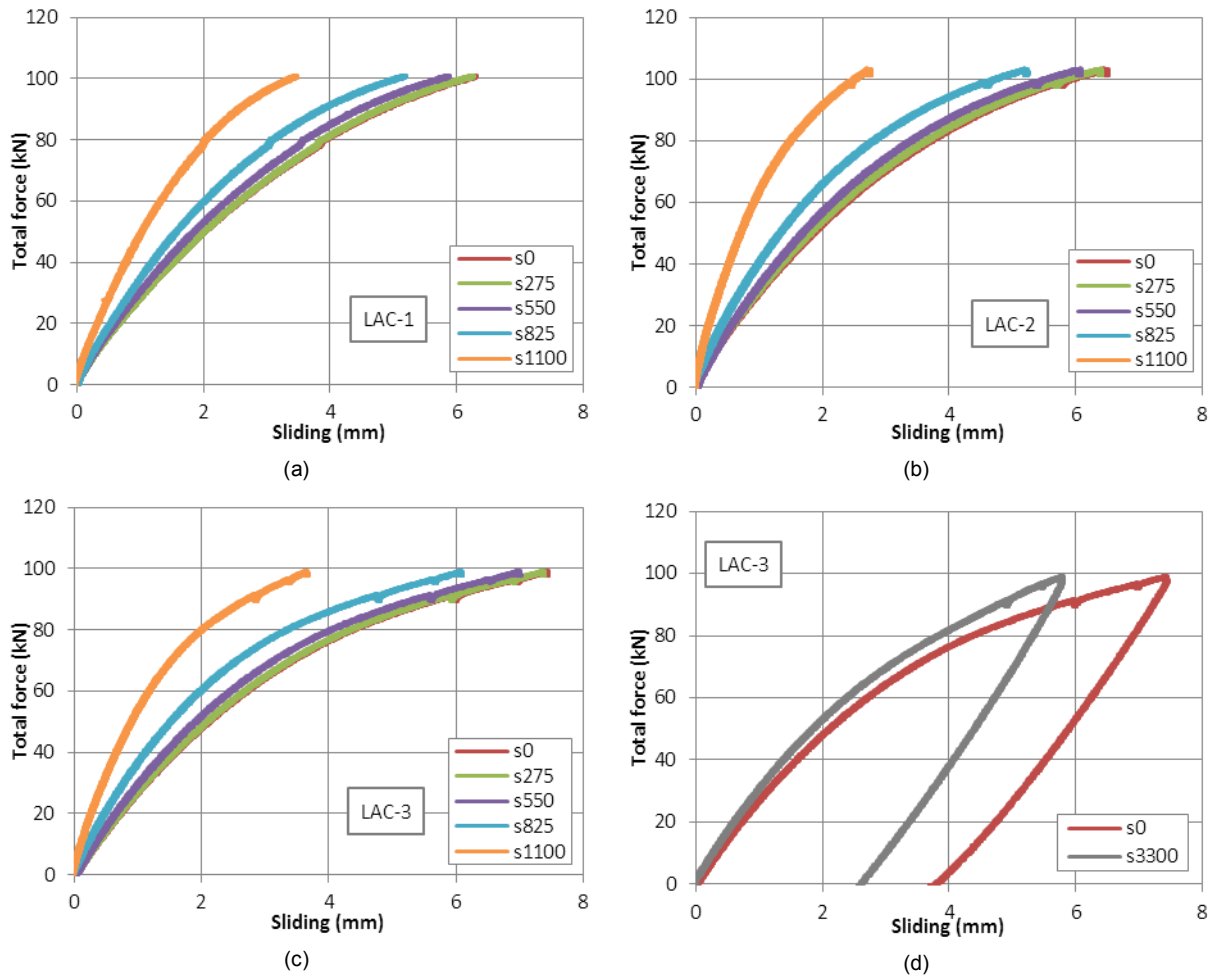


**Figure 7.21-** Total applied force vs. deflection at (a) 550mm, (b) 1100mm and (c) 1650mm – linear adhesive composite beam

The theoretical and numerical results were acquired with the assumption of a linear behaviour for the steel material, which did not represent the real case. Consequently the experimental curves could not be correctly matched for large imposed displacements. This was observed on the previous diagrams, on which were superposed the results issued from the numerical simulations, i.e. a non-connected, a fully connected beam and the system presented in Fig. 7.2. Additionally, the first linear portion was also overestimated by the final results of Abaqus even for an unconnected element. This implied that an external factor, not related to the quality of the bonding, was responsible for the rigidity decrease. An origin of this effect is proposed in section 7.3.4.

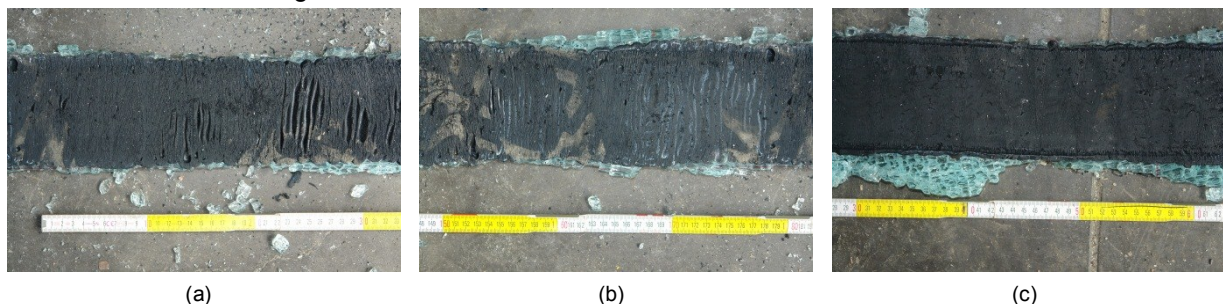
### Force-sliding curves

The sliding measurements also constituted vital information for the comparison of the experimental and numerical results. The total applied force versus relative displacements at the interface diagrams were plotted for the three assemblies individually to ensure of the correct increase of the values, see Fig. 7.22.



**Figure 7.22-** Total applied force versus sliding at the interface for (a) LAC-1, (b) LAC-2, (c) LAC-3; (d) Sliding at the extremities

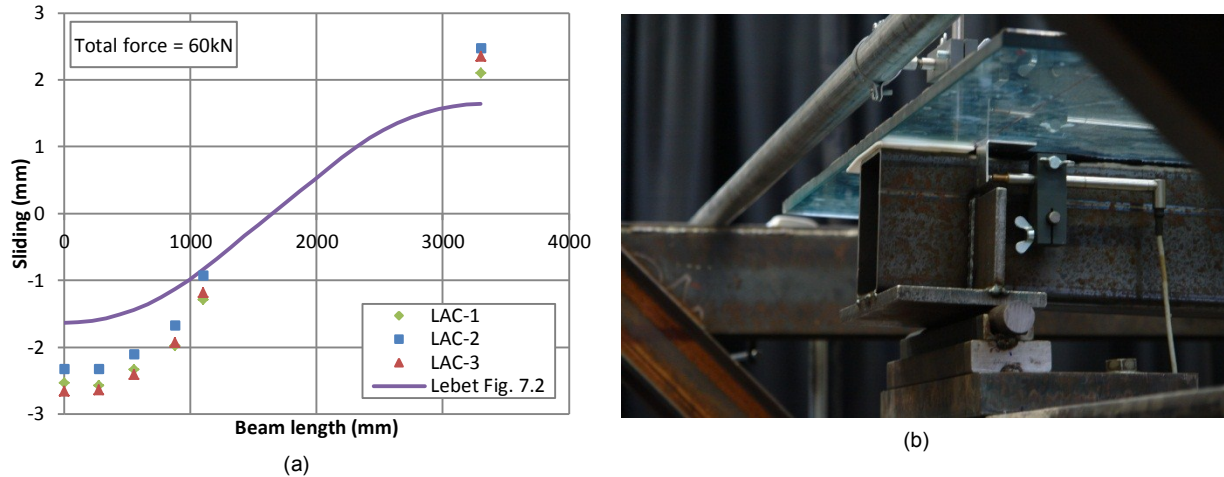
The global form of these curves was identical to the previous force-deflections curves with a first linear part followed by a certain non-linearity. The displacements at the extremities were clearly higher than the ones in the central zone, i.e. a maximum sliding of about 7mm was observed at  $x=0$ mm for a total load of 100kN against approximately 3mm under the load application point. The control of the relative displacements at the two extremities of the beams exposed different final values under the maximum force of the first loading but similar slopes, see Fig. 7.22 (d). These slight deviations were certainly due to non-equitable bonding areas between the opposing portions of the composite assembly. This was confirmed by the cut of the silicone after the complete failure of the LAC-3 specimen, for which the more consequent trapped bubbles of air were located on the first portion of the beam, i.e. within the first 1100mm, see Fig. 7.23.



**Figure 7.23-** Silicone net bonded area for (a) the first, (b) the central and (c) the last portions of the composite beam LAC-3



To compare these sliding data to the theoretical/numerical ones, a load was chosen to retrieve the different relative displacement values, which were then be plotted according to the length of the beam. A total force of 60kN, corresponding to the limit of elasticity of the steel beam alone tested with the current 4-point bending test, was selected. The results of the Lebet theory, identical to the ones obtained with Abaqus, served as references, see Fig. 7.24 (a). The relative displacements measured during the 3 experiments were in the same range with no major variation and were clearly higher than the theoretical estimation, i.e. about 1mm larger at the ends. These displacements were sufficiently consequent to be directly observable with the camera, see Fig. 7.24 (b).

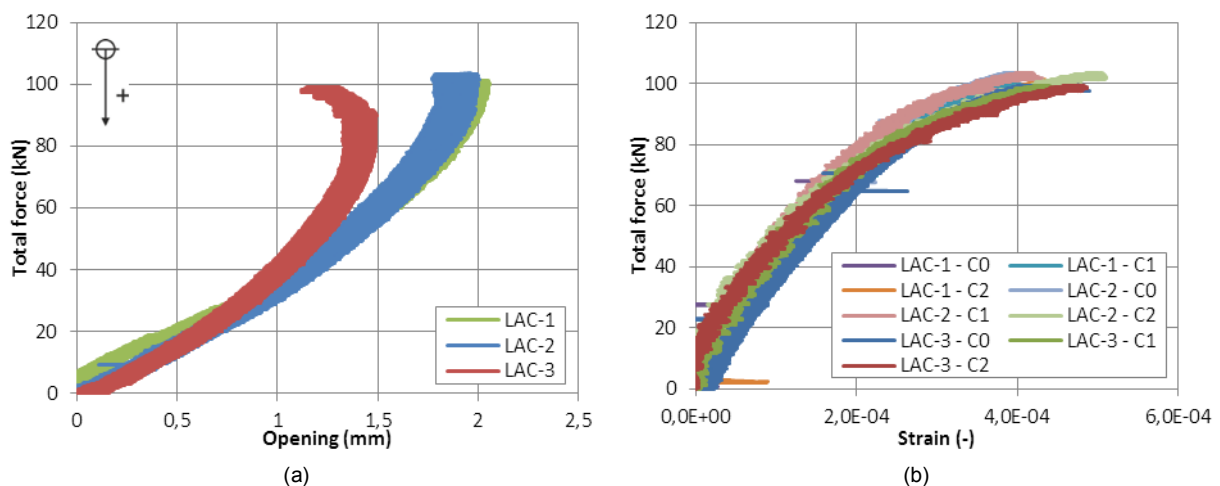


**Figure 7.24-** (a) Sliding along the beam length for a force of 60kN and (b) Relative displacement at the end of the beam

By intersecting the line formed by the relative displacements at 875 and 1100mm and the horizontal axis of Fig. 7.24(a), it could have been noted that the zero sliding value did not occur at the center of the composite beam but before and this for the three large-scale tests. This phenomenon could be induced by the modifications of the beams operated under the load applications points.

### Force-Opening curves

The last displacement sensors installed on the system measured the opening between the glass and steel elements at the end of the composite beam. The data recorded from this sensor were plotted for the three systems against the total applied load to verify the validity of the applied theories, see Fig. 7.25 (a). However, the obtained diagrams exposed positive displacements comprised between 1,25 and 2mm, meaning that the movements occurred towards the bottom direction synonymous of a closing. This type of measurement was not relevant as the glass plate moved along the steel profile and rotated around the support. This last phenomenon was particularly visible on the third tested beam with an important change of curvature. A control of the rotation would have been better.

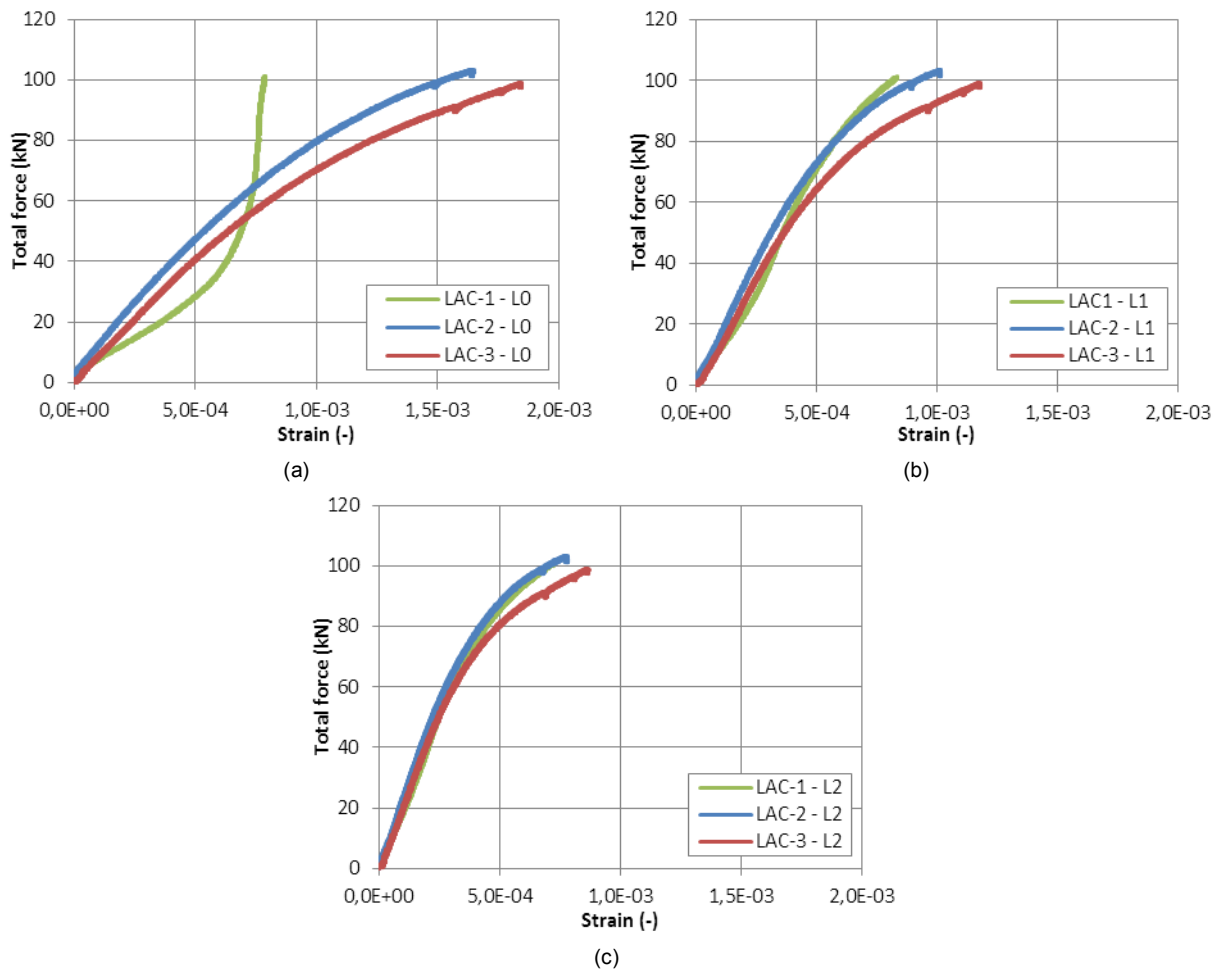


**Figure 7.25-** (a) Force versus opening displacements for the 3 beams and (b) Force versus strains at the center of the glass



### Force-glass elongations curves

The strains were strongly dependent on the considered position, i.e. consequent differences existed between the values at the center and at the load application line, see Fig. 7.25 (b) and 7.26. Nevertheless, no variation was noticed in the strains curves at the center which ended at the same values of about 0,004 under a force of 100kN. This indicated that the elongations of the glass plate were identical with no regards to the proximity to the steel beam. However, under the load application, the strains varied from the edge to the steel beam. Indeed, according to the set of Fig. 7.26 (a) to (c), the strains were larger near the center of the beam at  $L_0$ . This effect could have been explained by a concentrated transfer of the load at the more rigid location, i.e. at the steel beam flange. The Teflon was locally compressed and the glass bent, which caused higher values. The introduction of the force on the system was consequently a crucial point.

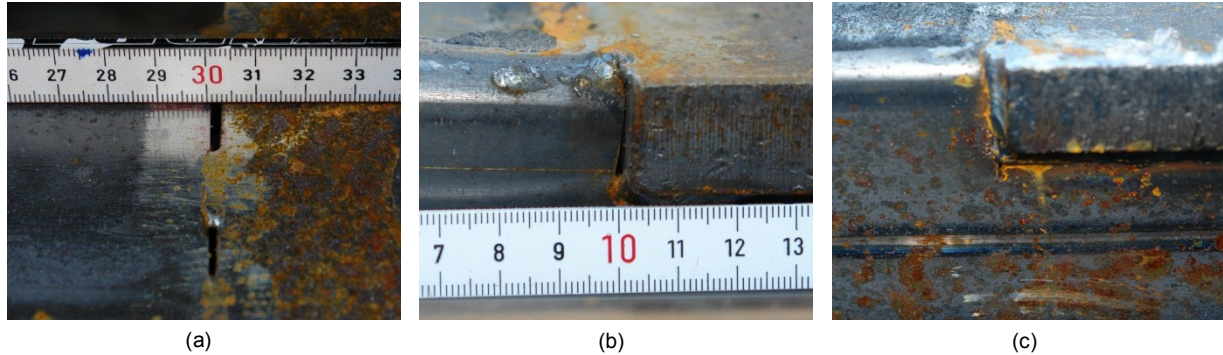


**Figure 7.26-** Total applied force versus strains under the load position at (a) 150mm, (b) 300mm and (c) 420mm from the edge

### 7.3.4 Discussion of the results

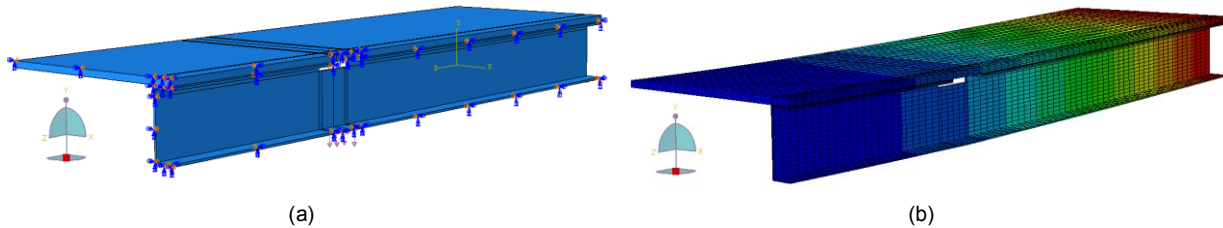
The comparison of the experimental results to the theoretical and numerical ones, especially for the force-deflection diagrams and the sliding along the beam length, demonstrated that the manufactured assemblies bent more. This effect was not simply due to the imperfection of the bonding but could be induced by the operations realized on the steel beam and more particularly at 1100mm and 2200mm under the load applications points. At these locations, the upper part of the steel beam was cut 20mm in the height and 100mm in the thickness, with the aim to add a rigid plate of the same dimensions. The details of all these operations were presented on Fig. 7.14. Nevertheless, they necessitated a lot of precision and were not simple tasks. After the end of the tests, an inspection of these zones was done and some defects were observed, see Fig. 7.27. Indeed, important horizontal openings of approximately 3mm appeared on the upper zone after the elastic return of the plasticized steel beam.

For other assemblies, the top flange of the steel pushed against the added rigid plate creating openings comprised between 1 and 2mm on the side of the beam. Moreover, some profiles also showed imperfections during the cutting of the upper steel beam, which was too deep compared to the expected 20mm. In consequence, the action wanted for the steel plate was not effective and it was assumed that the behaviour of the global assembly corresponded to the one composed by a steel beam possessing holes instead of rigid plates.



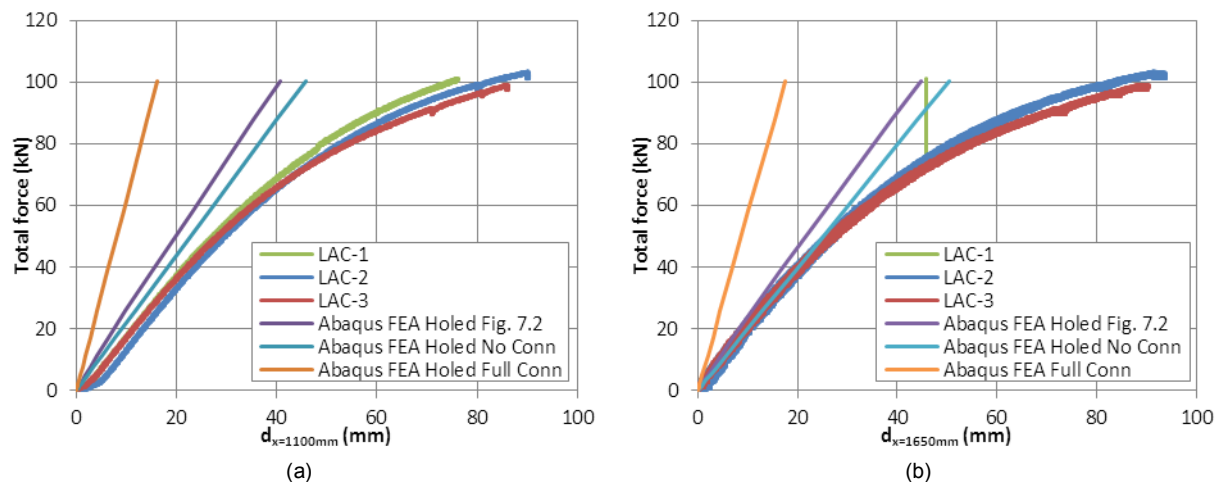
**Figure 7.27-** (a) Horizontal opening after the test; (b) Opening on the side after the test; (c) Too long cut for the plate positioning

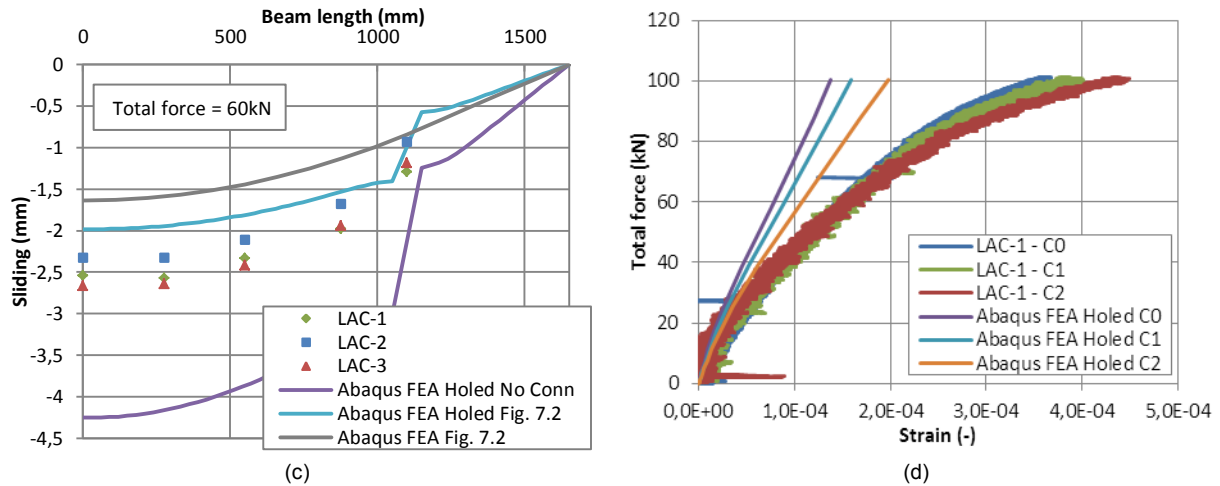
Numerical simulations were conducted with Abaqus to verify this assumption. The model exposed in Fig. 7.12 was reused and modified to let appear one hole of 100mm of width and 20mm of height in the top steel flange under the load application. At this position, the silicone was also removed, which matched the reality as a Teflon plate was employed instead of adhesive to transfer the load. The three boundary conditions applied on the surfaces theoretically in contact and on the edge to reproduce the support were conserved. The load application with the analytical rigid hollow section was however suppressed and introduced as a negative pressure under the beam, see Fig. 7.28. The silicone was thus in charge to accommodate the curvature of the glass to the curvature of the steel, which was different to reality. The C3D20 mesh elements as well as the different mesh size remained naturally unchanged. The calculation was performed under Abaqus/Standard using the developed UHYPER subroutine for the silicone.



**Figure 7.28-** (a) Boundary conditions and load application on the holed beam system and (b) Vertical displacements

The results of these last numerical simulations allowed plotting the main diagrams acquired with the previous experiments, see Fig. 7.29.





**Figure 7.29-** Total force versus deflections at (a) 1100mm and (b) 1650mm; (c) Sliding along the beam; (d) Force versus strains

The experimental force-deflections diagrams were better matched with the holed beam, especially for the center position (comparison between Fig. 7.21 (c) and 7.29 (b)). The differences remarked for the deflections at 1100mm were probably due to the application of the load under the steel beam flange in the numerical model and not on the glass plate. Nevertheless, the slopes were closer for the linear portions of the curves which tended to validate the previous assumption. The sliding values were extracted for a load of 60kN and plotted along the beam length. From the Fig. 7.29 (c), it was evident that the holed beam was closer than the perfect system exposed on Fig. 7.2. Furthermore, a discontinuous rise appeared for the holed systems, which reminded the effect observed with the experiments, i.e. the zero sliding value seemed to not occur at the center of the beam synonymous of a discontinuity. The last data regarded was the evolution of the strains according the applied force, see Fig. 7.29 (d). The strains were not considered at 1100mm under the load application, as in the model the load was not inserted through the glass but at the bottom of the beam and thus the local phenomenon noticed with the tests could not arise. The strains in the central position were nevertheless relatively close to the experimental ones.

In conclusion, the differences between the theoretical/numerical calculations and the tests results were probably induced by the manufacturing of the steel beams. Other tests on unmodified steel beams alone should be performed to compare the deflections to the theory and ensure of the steel properties. Additionally, tensile tests should be carried on steel dog-bone samples cut from the non-tested zones of the steel beams in order to properly determine the Young's modulus, the yield point and the plasticity stress-strain behaviour.

## 7.4 SUMMARY AND CONCLUSION

The characteristics of the linear adhesive composite beams were detailed in this chapter, as well as their manufacture, necessitating a large quantity of the silicone. For this connection, the silicone was simply poured on the glass and the reversed steel beam added on top of it. The production of these beams was relatively difficult, especially for the constant silicone thickness realization, which was achieved by using four equally spaced Teflon interlayers of 3mm.

To evaluate the rigidity of these beams, a classical four-point bending tests was carried out. The realization of the large-scale tests was preceded by first theoretical and linear numerical calculations. Indeed, as the silicone was principally subjected to shear forces, the properties of each material were known. While, the non-linearity of the silicone was accounted by the developed material law implemented in Abaqus software, a linear approximation of the shear was made for the Lebet theory. The results of these two analyzes were well superposed, demonstrating that the behaviour of a linear adhesive composite beam could be evaluated by one of those two methods. A parametric study could be performed with these models to design a composite beam and optimize the dimensions of each component. The silicone thickness could not, for manufacturing reasons, be less than 3mm. For comparison, the degrees of rigidity a fully composite and an unconnected beam were superposed to the obtained diagrams for the current assembly. It was observed that the behaviour of the linear adhesive beam was closer to the behaviour of the unconnected system. However, by regarding the normal stress distribution in the elements, it was remarked that the zone subjected to tensile stresses in the glass was reduced.

To valid the theoretical and numerical calculations, three large-scale beam tests were undertaken. The principal diagrams, i.e. force-deflection curves and sliding along the beam, were established. The obtained diagrams were well superposed, demonstrating the beams were produced in the same conditions. The rigidities issued from the experiments were however greatly lowers than the theoretical and numerical ones and the sliding larger. The observed differences were attributed to the steel beams modification under the load application points, for which the upper part was cut over 20mm and replaced by a welded thicker plate. The latter could not be welded against the top steel flange, as it was intended to keep the steel profile flat and straight for a correct application and control of the silicone thickness. This assumption was confirmed by numerical simulations of linear adhesive beams in which were cut the upper part modified part of the beam. Nevertheless, unmodified and modified steel beams alone should be subjected to the same 4-point bending test than the composite beam to fully validate this hypothesis. The characteristic of the steel, especially its plastic properties, should also be assessed with tensile tests on dog bone samples.

In conclusion, the theoretical calculations, based on a fully elastic shear modulus, and the numerical simulations, with the correct silicone representation, gave an identical rigidity. The latter was, however, different to the experimental one, in reason of the modifications operated on the steel beam. A test series should be redone to confirm this postulate.

## 8. MECHANICAL-ADHESIVE CONNECTION EVALUATION

### 8.1 INTRODUCTION

In this chapter, the mechanical-adhesive composite beam behaviour is determined with the help of partial connection theories, numerical simulations and large-scale experiments. A comparison of these different methods is made for validation. The organization of this chapter is presented in Fig. 8.0.

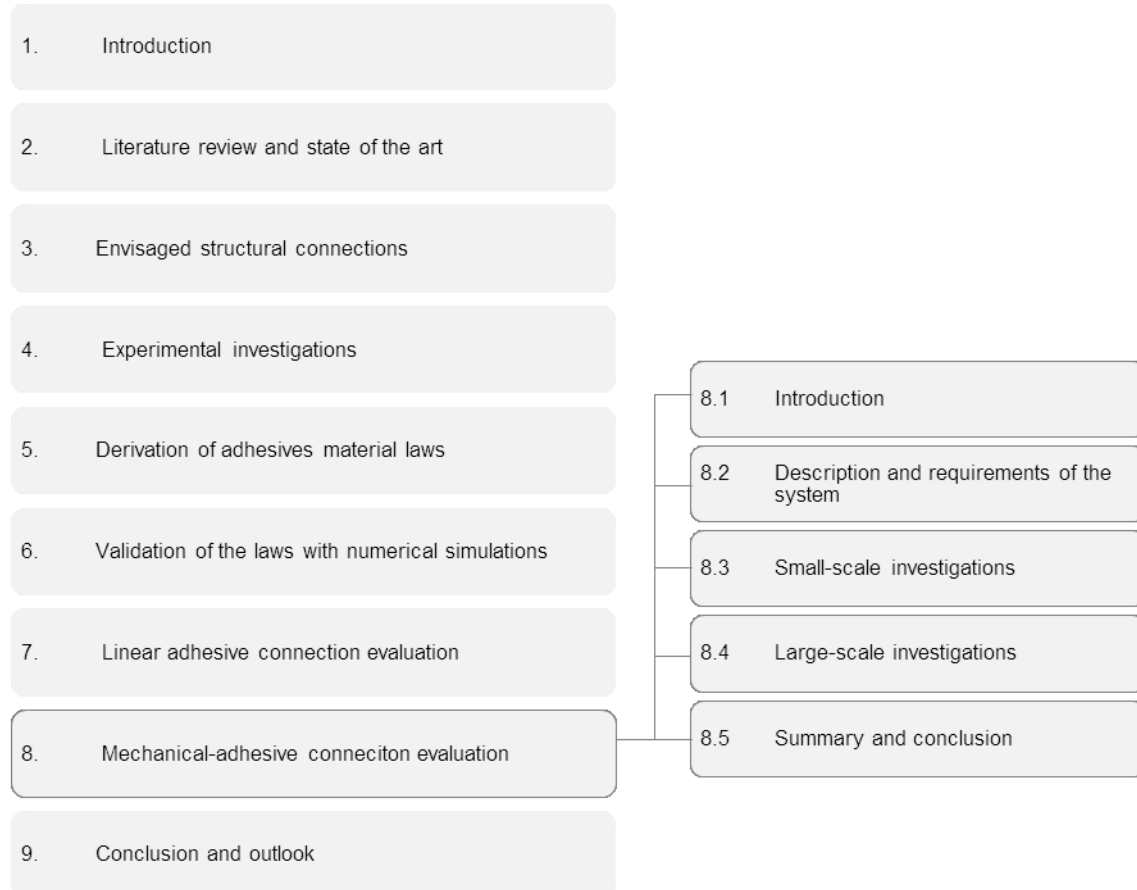


Figure 8.0- Organization chart of chapter 8

**Description and requirements of the system.** The cross-section and length of the total beam to be tested are first described. The requirements necessary to the application of the partial connection theories are also detailed.

**Small-scale investigations.** This section is divided in two parts, with an evaluation of the rigidity of a one holed connection by numerical simulation and by small-scale tests. The limits of the numerical modeling, including the different techniques proposed by the Abaqus software, are demonstrated and experimentally supported.

**Large-scale investigations.** Following the evaluation of the rigidity for one hole, the analytical models accounting for the partial interaction, are analyzed and numerical simulations performed in parallel. The results, obtained with both methods, are recorded in this section and compared to large-scale experiments.

**Summary and conclusions.** The origin of the slight differences occurring between the theories and the experiments are explained in the conclusion.

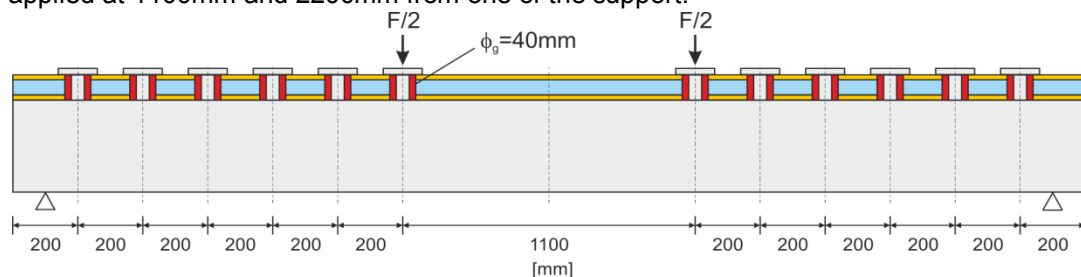
## 8.2 DESCRIPTION AND REQUIREMENTS OF THE SYSTEM

### 8.2.1 Description of the composite beam

The mechanical-adhesive connection was composed by more elements than the linear adhesive connection, i.e. in addition to the glass plate, the steel beam and the adhesive were also employed several covering steel plates, Teflon interlayers and bolts. Hence, more operations had to be made to achieve the final assembly. As it was intended to mainly use the adhesive in compression and not in shear, an in-fill elastomer possessing high incompressibility had to be selected. Therefore, only the DC993 Dow Corning silicone was considered. As evoked in section 7.2.1, the principal external actions, consistently affecting the properties of the connections, were the out-of plane loads. Therefore the rigidity of the assembly and the degree of connection were assessed with the help of a standard four-point bending test.

- Global system

The dimensions of the global system remained the same than for the linear adhesive connection. The total length of the composite beam was of 3500mm, while the tested length was reduced to 3300mm. At each extremity, 100mm were let free to compensate for the large rotations and displacements at the supports, see Fig. 8.1. The assembly was divided in three equal portions of 1100mm and the loads were applied at 1100mm and 2200mm from one of the support.

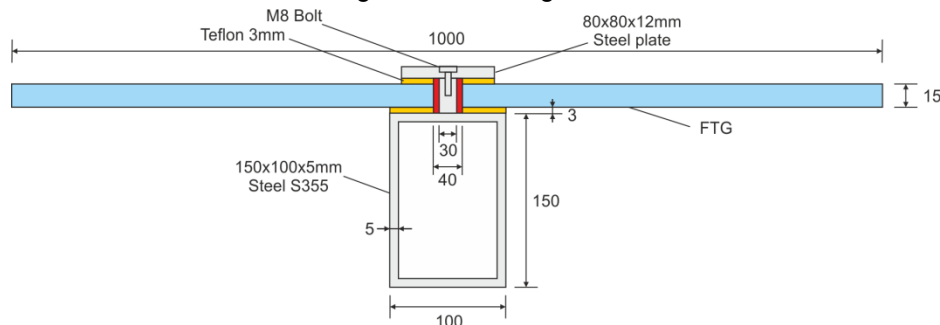


**Figure 8.1-** Description of the global system – Dimensions and position of the load – Mechanical adhesive connection

For the current system, twelve holes of 40mm of diameter were drilled in the glass plate with 6 in the first portion, each distant of 200mm, and 6 others in the last. Twelve corresponding steel studs were necessary. Their diameters were chosen equal to 30mm, generating a silicone thickness of 5mm all around the hole. The contacts between the steel beam/covering plates and the glass were prevented by anti-adhesive Teflon elements 3mm thick, so that no additional friction could be induced at the interfaces. The main advantage compared to the previous system was the introduction of the loads, which was transmitted through covering steel plates and not directly in the glass.

- Cross-section dimensions

The width of the fully tempered monolithic glass plate remained unchanged, i.e. 1000mm, equivalent to about 1/3<sup>rd</sup> of the total tested beam length. Laminated glass was avoided for the actual evaluation.



**Figure 8.2-** Composition and dimensions of the cross section of the mechanical-adhesive composite beam

The steel beam was a hollow rectangular profile of 150x100x5mm made out of S355 steel. The hole of the glass plate was 10mm larger than the one of the welded studs to inject the silicone in-between. The layering formed on top of the steel beam was closed with the help of rigid steel plate limiting the squeezing out of the silicone. These last plates should be neglected for the design of such composite beam as they did not increase the global rigidity. Thus, the position of the neutral axis for a perfect connection should be of 18,8mm, meaning that only compression would act on the glass.

- Material properties

The glass was by nature fully linear and the only definition of its Yong's modulus, Poisson's ratio and density were sufficient for the numerical simulations but also for the partial theory developed by Lebet. As for the linear adhesive connection, only the linear properties of the steel were regarded for the first evaluation of the composite beam. This linear consideration was assumed true until 61,9kN, i.e. the total applied force generating a yielding of the steel beam alone for the 4-point bending configuration. The characteristics of these two materials were regrouped in Table 7.1. For the numerical simulations, the silicone properties were modeled with the developed material law with the quasi-static set of coefficients, as no action was applied on the system prior to the testing, see Table 5.21.

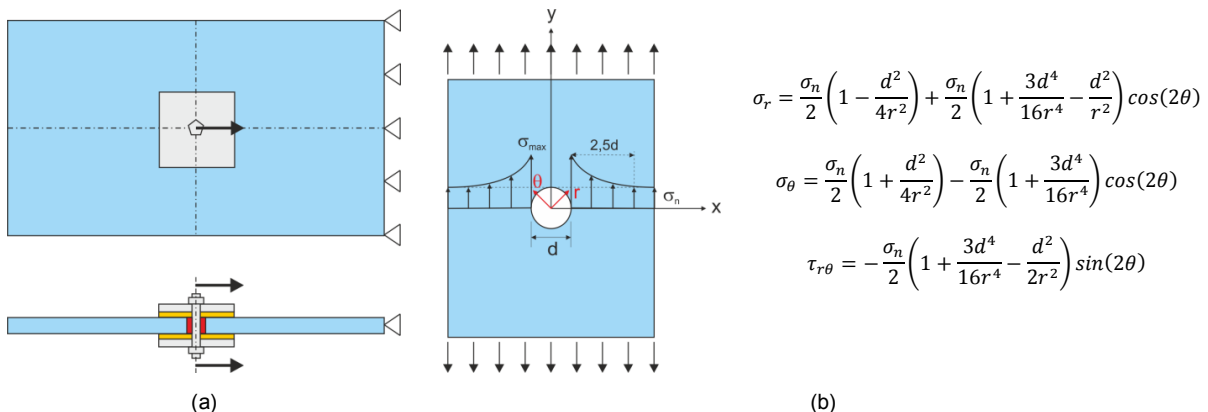
## 8.2.2 Theory requirements

The partial connection theories, such as the Lebet theory exposed in Appendix F.4, necessitated the definition of the rigidity of the connection. While this was feasible for the linear adhesive connection as the transmission of the load occurred by simple shear, it was not directly available for the mechanical-adhesive connection due to the complexity of the geometry and due to the 3D quasi-incompressible behaviour of the silicone. Two distinct methods could be employed to determine the required rigidity, i.e. by numerically modeling the connection in Abaqus or by carrying out small-scale tests. These two possibilities were examined in the next section.

## 8.3 SMALL-SCALE INVESTIGATIONS

### 8.3.1 Numerical simulations

To avoid the full representation of the composite beam for the evaluation of the connection stiffness, a simplification was done assuming that the rigidity of these twelve fixations was equivalent to 12 times the rigidity of one fixation. Further, the steel beam was also estimated unnecessary for this analysis. Consequently, a system formed by only one holed glass plate symmetrically covered on the two sides by 3mm thick Teflon plates and closed by two rigid steel plates was required. The load could simply be introduced in the plane of the glass through a rigid steel bolt pressing against the silicone, see Fig. 8.3 (a). The dimensions to be given to the glass plate were depending on several factors, such as the size of the hole, the proximity of the edge or the silicone thickness.



**Figure 8.3-** (a) simplification of the studied system; (b) Analytical solution of an infinite holed plate under uniaxial tensile loading



To prevent the influence of one of the aforementioned factors on the final results, the existing theories were regarded to design the glass plate. The only well-known analytical solution concerned a holed plate of infinite dimensions subjected to uniaxial in-plane tensile force. The stresses resulting from this system were recalled on Fig. 8.3 (b). According to these equations, the stress concentrations on one side disappeared along the width at distance of 5 times the radius of the hole. For the envisaged hole of 40mm, this would imply a total width of minimum 200mm to appraise the nominal stress with a complete disappearance of the stress peaks. Other solutions were developed for finite-width holed plate subjected to the same loading type. The latters were essentially based on the establishment of stress concentration factors as proposed by Howland [8.1]. With this method, Frocht and Hill also advanced a stress concentration factor for finite width holed plate loaded through a perfectly fitting pin:

$$K_n = 12.882 - 52.714 \left( \frac{d}{H} \right) + 89.762 \left( \frac{d}{H} \right)^2 - 51.667 \left( \frac{d}{H} \right)^3 \quad (8.1)$$

Where d represented the diameter of the hole and H the total width of the plate (hole included). This expression was valid for d/H ratios comprised between 0,15 and 0,75 with a height two times higher than the width. The maximum value of the stress at the rim of the plate was obtained with:

$$\sigma_{max} = K_n \sigma_n = K_n \frac{P}{(H - d)h} \quad (8.2)$$

With P the load applied through the pin and h the thickness of the plate. This solution was conserved for the calibration of the mesh of the glass plate during the numerical simulations and also constituted a reference for later comparison.

Thus, by considering the validity of the two mentioned theories and the vanishing of the stress peak at a distance of 5 times the diameter of the hole for an infinite plate subjected to tension, the width of the system to be modeled was of 240mm ( $\geq 200$ mm) and the height of 480mm, corresponding to the lower condition of the Frocht and Hill theory.

### 8.3.1.1 Abaqus/Standard resolution

The first numerical simulations of the system presented on Fig. 8.3 (a) were made with the most stable and unconditional method of resolutions, i.e. the implicit resolution. The different steps leading to the analyses of the results were detailed below.

#### Definition of the geometry and boundary conditions

The material and geometrical symmetries of the assembly allowed modeling only one fourth of the system, so that the dimensions of the glass plate were reduced to a height of 480mm for a width of 120mm. The semi-hole in the glass had a radius of 20mm and the steel bolt of 15mm. The thickness of the silicone was therefore equal to 5mm. Only one part was created for these three elements and some partitions were made to correctly assign the different materials. The covering steel plate was not implemented as it was assumed completely rigid and fix.

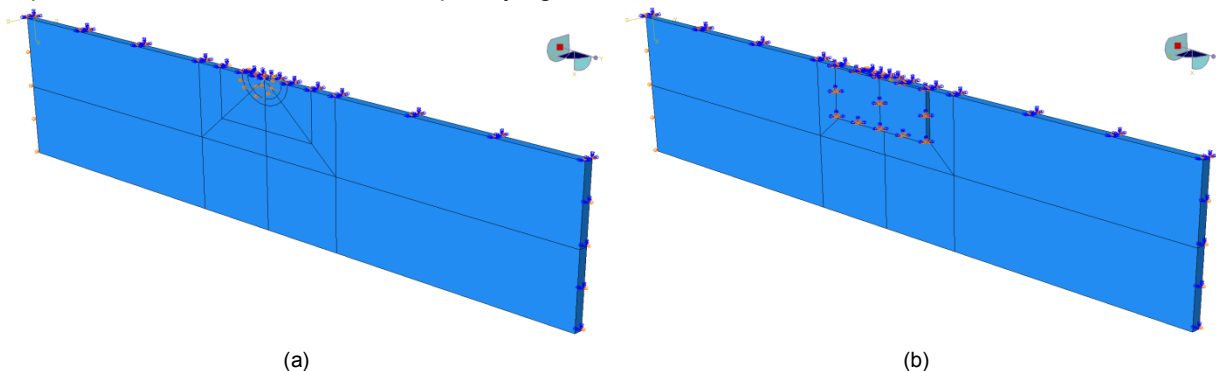


Figure 8.4- (a) 2D analytical rigid fully fixed and (b) 3D deformable representation of the 3mm thick covering Teflon plate



The 3mm Teflon plate was independently conceived and two different possibilities were envisaged to achieve it, i.e. with a 2D analytical rigid plate fully fixed and with a 3D representation including the compression of the material, see Fig. 8.4. The real case was nevertheless envisaged closer to the 3D model. In both configurations, the surface of the Teflon plate was of 80x40mm.

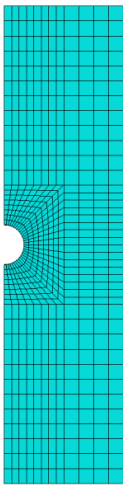
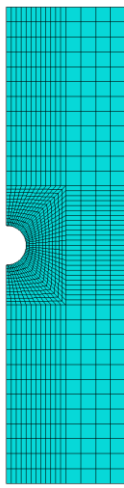
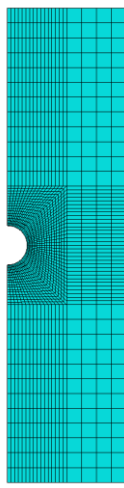
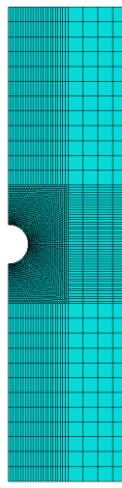
Without accounting for the Teflon plate and as only  $1/4^{\text{th}}$  of the model was realized, two symmetrical boundary conditions had to be set on the surfaces theoretically in contact with the rest of the system. One was inserted on the edge along the length, while the other one was positioned on the back over the steel, glass and silicone materials. At the bottom of the model, the displacements of the nodes in the direction of the load were restrained with simply supported conditions. For the 2D representation of the Teflon plate, the definition of a reference point was necessary and the fully fixed conditions applied onto it. For the 3D representation, the external face of this material was also fully fixed. A surface to surface hard frictionless contact was implemented in both cases between the inner Teflon face and the silicone one. The loading was introduced as a displacement of 3mm imposed on the steel bolt only with the assumption of loading rate independency.

### Material behaviour

Four different material properties had to be defined in total even if only three were really employed for the 2D representation of the Teflon. The linear glass and steel properties presented in Table 7.1 were conserved for the numerical simulations. The non-linear behaviour of the silicone was inserted in the software with the help of the developed UHYPER subroutine combined with the quasi-static set of coefficients of Table 5.21. The Teflon was assumed fully linear and the only definitions of the Young's modulus of 500MPa and of the Poisson's ratio of 0,46 were sufficient.

### Meshing

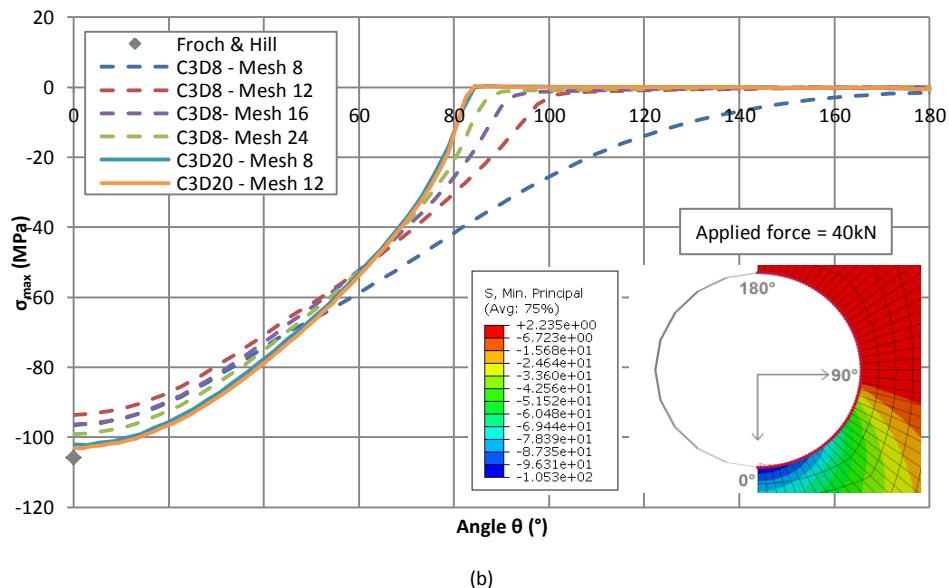
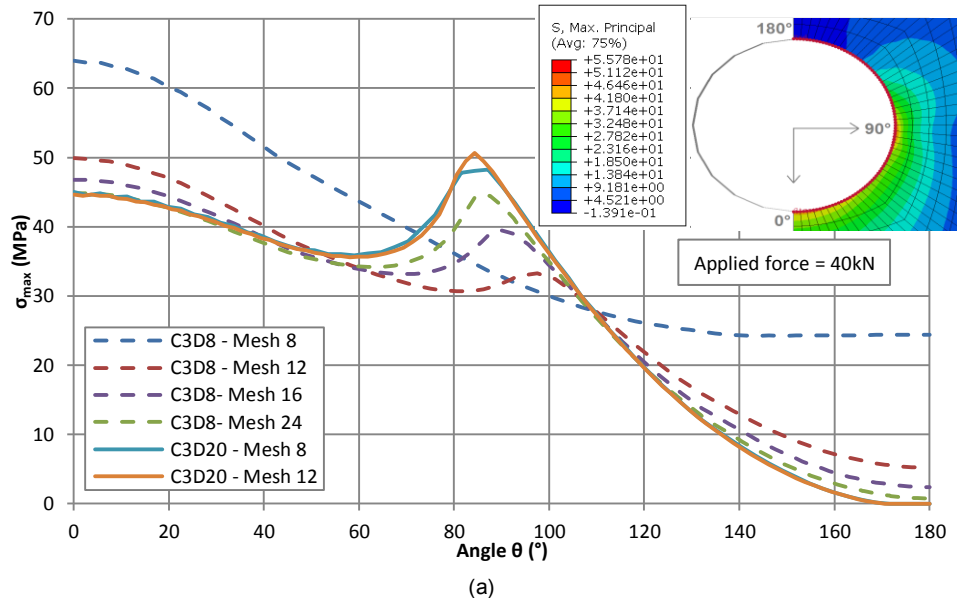
The central part containing three different materials, as well as the 3D deformable representation of the Teflon plate, were composed by 3D hexahedral brick elements. However, the 2D analytical rigid modeling of this last element did not require the definition of a mesh. The geometrical singularity of the glass (hole) could generate convergence difficulties and therefore the reduced integration elements were never used for the whole system, Teflon included in reason of its contact with the silicone. Some additional partitions, helping to the manual control of the mesh size, were made to define 60mm of length square zone around the center of the bolt, see Fig. 8.4. The diagonals starting from the center of the assembly were also created in these square regions.

| Mesh size 8                                                                         | Mesh size 12                                                                        | Mesh size 16                                                                         | Mesh size 24                                                                          |
|-------------------------------------------------------------------------------------|-------------------------------------------------------------------------------------|--------------------------------------------------------------------------------------|---------------------------------------------------------------------------------------|
|  |  |  |  |
| Linear/Quadratic                                                                    | Linear/Quadratic                                                                    | Linear                                                                               | Linear                                                                                |

**Table 8.1-** Different mesh sizes and orders for the numerical simulation of a glass plate loaded thorough a perfectly fitting pin

The glass plate was at first considered separately to assess the convergence of the results according to the mesh element orders and sizes. The configuration investigated was formed by a glass plate of identical dimensions than the one of the final system to be modeled and an infinitely rigid pin perfectly fitting the glass hole. The pin was realized with a revolved analytical rigid shell and a hard frictionless contact was incorporated with the rim of the plate. The system envisaged was thus identical to the one studied by Frocht and Hill for the determination of the stress concentration factor of Eq. (8.1). Four elements were always disposed along the thickness, as lower values would reduce the accuracy of the solution. With the undertaken partitions, four equal zones were defined around the center. In these zones, the mesh was uniformly distributed, i.e. the radius the horizontal and vertical edges as well as the diagonals possessed the same number of elements along their total length. This allowed obtaining a mesh whose consecutive lines did not expose too small angles. In these zones, 8, 12, 16 and 24 elements were envisaged, as shown in table 8.1. For the less critical external portions, a global mesh size of 15mm was chosen.

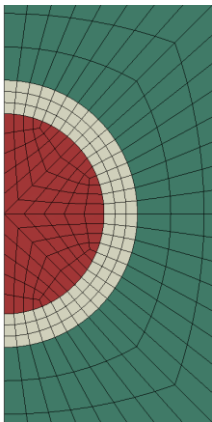
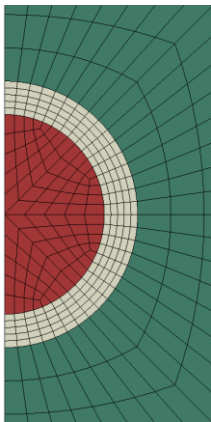
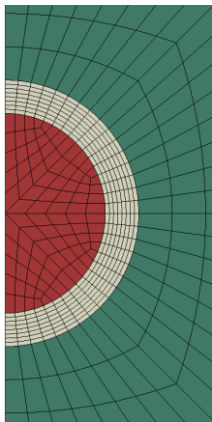
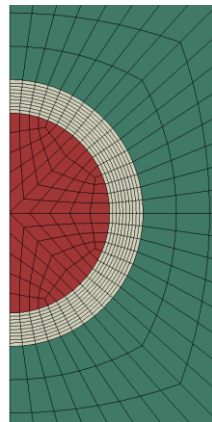
All the calculations were performed for an applied force of 40kN with the implicit solving method and no modifications of the time period and initial increment was made as the linear glass material was assumed independent on the loading rate. The maximum and minimum principal stresses were extracted with the help of paths created on the hole of the glass. The principal results were gathered on Fig. 8.5 (a) and (b) in which the load direction corresponded to 0°.



**Figure 8.5-** (a) Maximum and (b) Minimum stress along the hole – Implicit – Glass plate loaded through a perfectly fitting pin

By reducing the size of the linear C3D8 mesh elements, the maximum stress at  $0^\circ$  rapidly decreased and a stress peak appeared at  $90^\circ$ . The C3D20 mesh provided however the same values, indicating that the convergence of the maximum principal stress was already reached for the coarser mesh. For the minimum stress, the quadratic elements converged towards the theoretical value calculated with the Frocht and Hill theory of Eq. (8.1) and (8.2). Again large variations were remarked for the linear elements, which however tended to be closer to the quadratic ones for finer meshes. In conclusion, the linear mesh elements were not employed for the glass modeling of the studied system of Fig. 8.3 (a). The quadratic elements with the larger mesh size, defined by 8 elements along the length, were consequently the only ones conserved.

This selected mesh size for the glass element was transmitted to those underlying, i.e. to the silicone and to the steel bolt. As the stiffness of the bolt was largely higher than the one of the silicone and as it was not a crucial part, only 5 elements were envisaged along the vertical and horizontal edges. For the silicone different mesh sizes over the thickness were tested to ensure of the convergence of the results, see Table 8.2. Hybrid elements C3D20H were only applied to the silicone material.

| Mesh 3 elts (1.667mm)                                                              | Mesh 5 elts (1mm)                                                                  | Mesh 8 elts (0.625mm)                                                               | Mesh 10 elts (0.5mm)                                                                 |
|------------------------------------------------------------------------------------|------------------------------------------------------------------------------------|-------------------------------------------------------------------------------------|--------------------------------------------------------------------------------------|
|  |  |  |  |

**Table 8.2-** Different mesh sizes of the silicone element for the numerical simulations of the envisaged system of Fig. 8.3

For the 3D deformable representation of the Teflon plate, similar partitions than the ones made on the glass part were realized to have a perfect correspondence of the nodes in contact with the silicone at the beginning of the calculation. The 3D Teflon plate was hence meshed as exposed in Table 8.2.

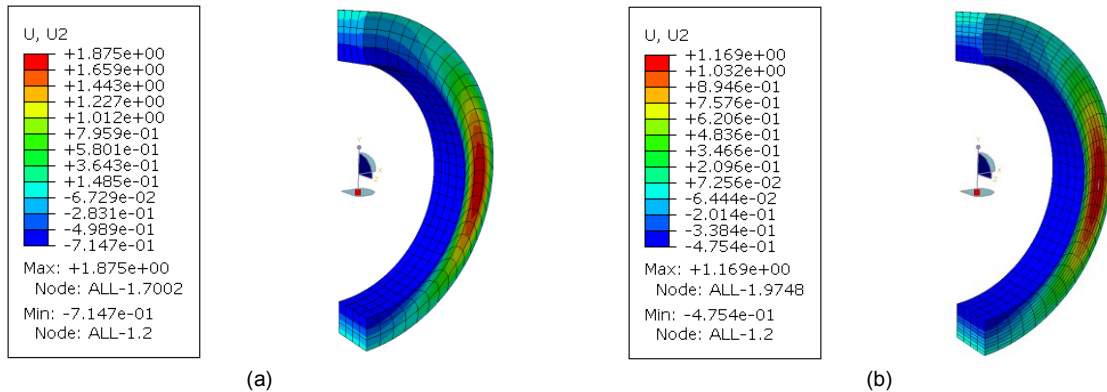
### Solution procedures

The complete assembly was supposed invariant towards the loading rate and thus no modification was made on the default time period and initial increment offered by Abaqus/Standard. The non-linear geometry option “nlgeom” was considered, as large displacements of 3mm were imposed on the steel bolt, which generated important deformations in the silicone.

### Analysis of the results

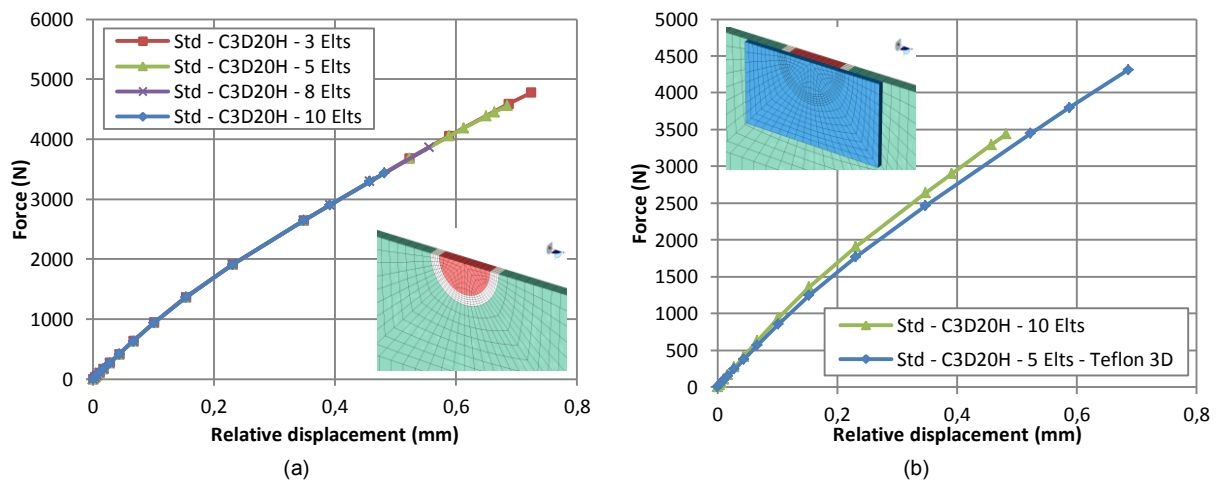
None of the calculations, independently of the representation of the Teflon, could be performed until the end as too large distortions in the silicone occurred. On the imposed displacement of 3mm, hardly 20% was correctly achieved. Furthermore, finer was the mesh and sooner was the abortion of the job. This last observation was clearly visible on the reached displacements at the untimely termination of the calculation, see Fig. 8.6. The nodes of the internal and external faces of the silicone were fixed to the nodes of its adherents as the whole was conceived in one part. Thus, with regards to the rigidity of the different elements, the silicone nodes in contact with the glass remained quasi-fixed while the nodes shared with the steel bolt moved in the direction of the imposed displacement. Nevertheless, all these nodes were not authorized to move along the radii. At the opposite, the nodes in the core of the

adhesive were free to evolve. The quasi-incompressibility of the silicone generated important motions as the volume of each element barely changed. Hence, as it could be observed on Fig. 8.6, the central part of the adhesive, at  $90^\circ$  with respect to the load application direction, moved more than the current imposed displacement.



**Figure 8.6-** Final displacement values of the silicone at the last valid increment for (a) Mesh 3 elts and (b) Mesh 10 elts

The relative displacement of the silicone in the compression zone (at  $0^\circ$ ) was measured by summing the displacements of the two silicone nodes belonging respectively to the steel bolt and the glass plate. The total resulting force was measured by summing the reaction forces measured on the lower edge of the glass and by multiplying the obtained values by four, as only  $1/4^{\text{th}}$  of the model was implemented. Standard force versus relative displacement diagrams, assimilated to the rigidity of the connection, were then plotted for the different envisaged mesh sizes and Teflon representations, see Fig. 8.7.

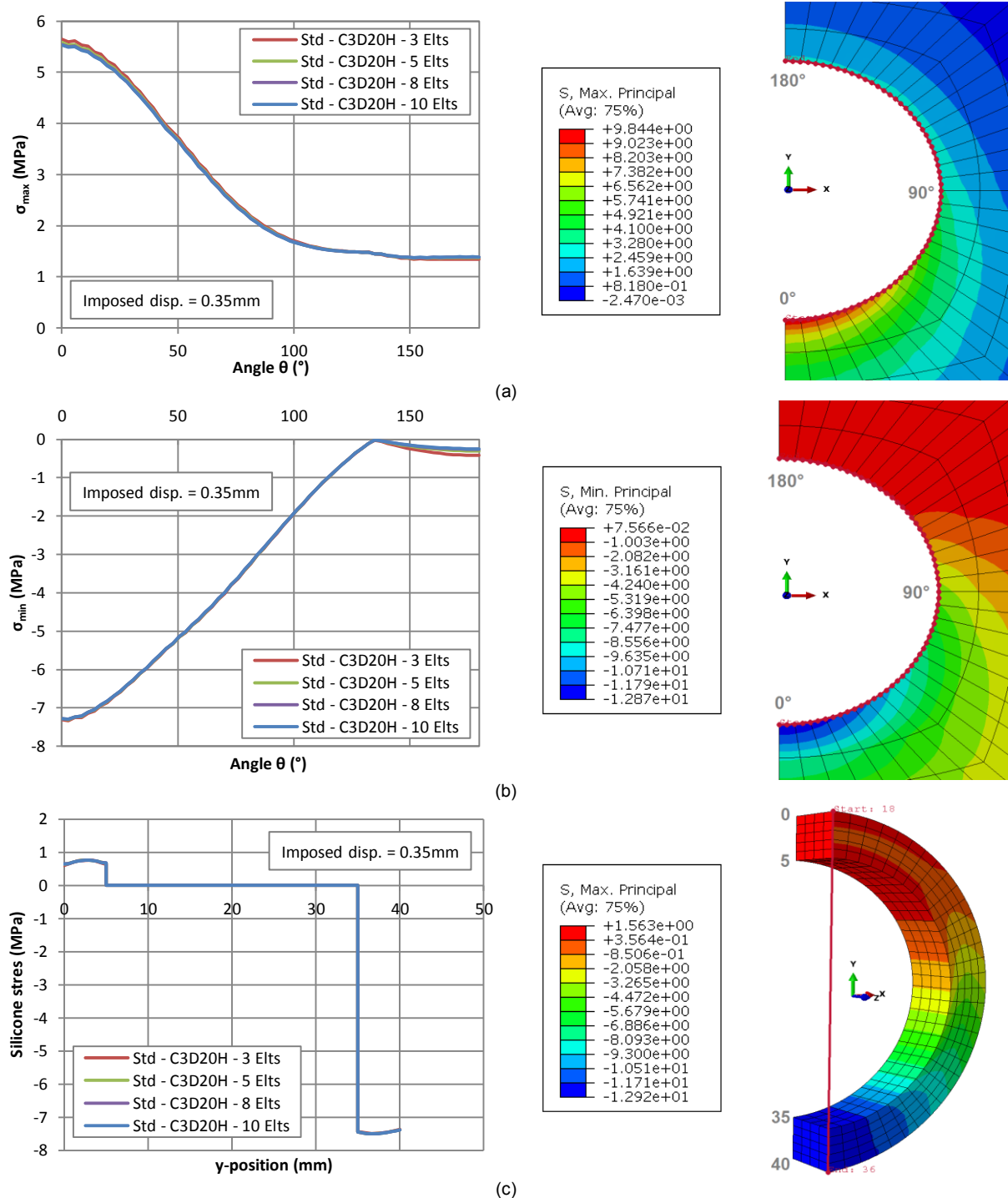


**Figure 8.7-** Total force versus silicone relative displacement diagram for (a) the 2D- and (b) the 3D-representation of the Teflon

For the 2D representation of the Teflon plate, the force-displacement curves were well superposed, demonstrating the invariance of the global behaviour towards the size of the mesh for the silicone part. For the obtained displacements, the rigidity of the connection exposed on Fig. 8.3 seemed linear and equal to about 6600N/mm. A comparison of rigidities with a full representation of the system with a 3D deformable Teflon plate was provided on Fig. 8.7 (b). The rigidity was slightly reduced by accounting for the deformations of the covering Teflon element. Nevertheless, the difference between the two curves was not significant for the acquired displacements. The less time consuming calculation with the analytical rigid plate was therefore only regarded in the following paragraphs.

The influence of the mesh size of the silicone was simply analyzed from a general point of view and the maximum/minimum principal stresses in the silicone and glass were not examined. These data could however vary according to the dimensions of the mesh. Therefore, two different paths were done to retrieve these information, i.e. a circular one was created around the glass hole, as made for the stress assessment of the glass plate loaded thorough a perfectly fitting pin, and another one was

undertaken on the silicone material at an angle of  $0^\circ$  with respect to the load direction. As all the models did not end at the same increment, these results were retrieved for the last stable one shared by all the calculations, see Fig. 8.8.



**Figure 8.8-** (a) Maximum and (b) Minimum principal stresses according to the position on the radius; (c) Silicone stress at  $\theta=0^\circ$

For the regarded displacement of 0,35mm, corresponding to the displacement at the last increment, the size of the silicone mesh was not found as influent on the maximum/minimum principal stresses in the glass. Indeed, the variations were too small to be visually appraised, but the coarser mesh gave the higher tensile stress and the lower compressive stress. Concerning the stress distribution in the silicone, no visual difference was noticed for the maximum stresses as well as for the minimum ones. Thus, it could have been conclude, that the size of the silicone mesh was not influent. Nevertheless, as the calculations did not reach the total time period, these observations should be nuanced and another solving method employed for possible improvement.

### 8.3.1.2 Abaqus/Explicit resolution

The explicit method of resolutions was tested in order to check if the total time increment could be reached with one of the procedures detailed in Appendix E.1, i.e. with a control of the distortion or with the Arbitrary Lagrangian Eulerian (ALE) method.

#### Definition of the geometry and boundary conditions

The model presented on Fig. 8.4 (a) with the 2D representation of the Teflon plate was conserved for the explicit resolution. The dimensions and boundary conditions of the different elements remained identical. Only an arbitrary mass had to be defined at the reference point of the Teflon plate and its surface to surface hard and frictionless contact with the silicone was managed with a finite sliding kinematic method.

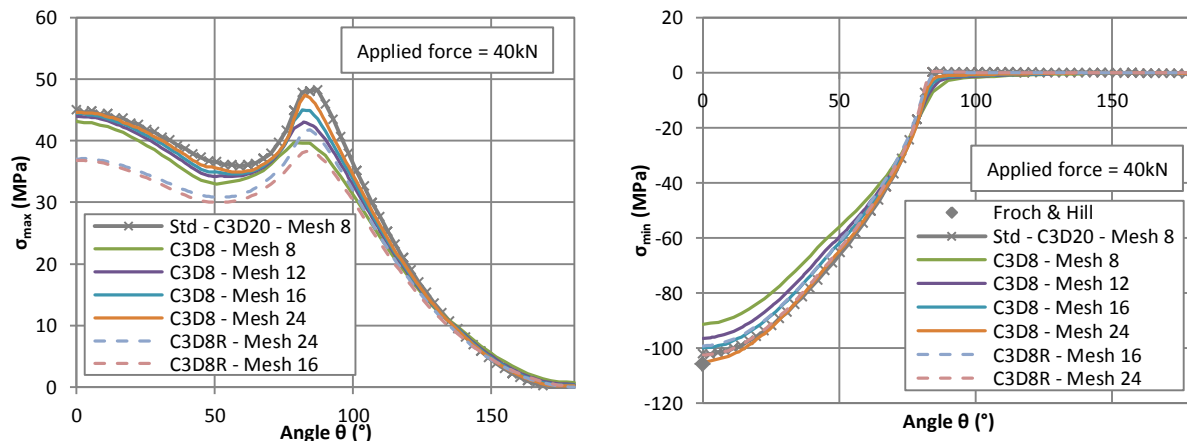
#### Material behaviour

The linear properties of glass and steel exposed in Table 7.1 were unchanged and the non-linear silicone behaviour was implemented through the developed VUMAT subroutine with the quasi-static set of coefficients detailed in Table 5.21. The density of each component had to be properly inserted for these calculations.

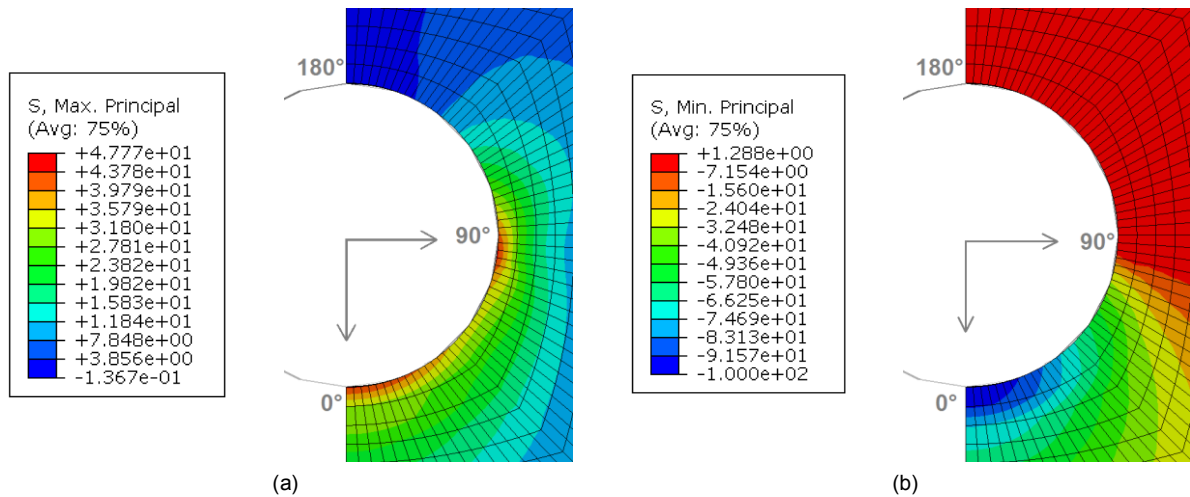
#### Meshing

The central part containing the three different deformable materials was meshed with 3D hexahedral brick elements, while the analytical rigid Teflon plate was not meshed. With the geometrical singularity of the glass plate, the convergence of the results according to the mesh size and element could lead to some difficulties. Furthermore, even if the distortion control did not require some specific elements, the ALE method was only applicable to reduced integration elements. Hence a finer mesh should be assigned to the mesh for this last method. The partitions operated on the main system to define the three material regions were completed by others around the center to delimit two square zones of 60mm helping for the mesh allocation. The diagonals starting from the center of the piece were also made for the meshing, see Fig. 8.4 (a).

The glass plate was isolated from the rest to evaluate the convergence of the results in function of the mesh. A completely rigid pin fitting perfectly the glass hole was made with an analytical rigid revolved shell. A hard frictionless contact was inserted between the inner diameter of the glass hole and the outer face of the pin. The load of 40kN was introduced in the glass through the reference point of the pin. The comparison with the Frocht and Hill theory evoked in Eq. (8.1) was thus conceivable. The different mesh distributions described for the implicit analyses and gathered in Table 8.1 were conserved with the modification of the element orders. Indeed, as the quadratic elements were not considered, only linear elements remained.







**Figure 8.9-** (a) Maximum and (b) Minimum stress along the hole – Explicit – Glass plate loaded through a perfectly fitting pin

The four mesh sizes were modeled with C3D8 elements and only the last two, i.e. mesh sizes 16 and 24, were used with the C3D8R reduced elements. Several time periods were investigated and the most efficient one in term of accuracy and rapidity was of 0,003s (five times the inverse of lowest natural frequency equal to 1691Hz). The maximum/minimum principal stresses around the hole were extracted with corresponding paths and regrouped on Fig. 8.9. The results issued from the implicit resolution of the quadratic elements served as reference. As remarked for the C3D8 meshes, larger was the number of elements and closer were the stresses to the implicit results. Indeed for the mesh size 24, a difference of approximately 1,3% was observed with the maximum stresses at 90° to the load direction and almost none for the minimum stresses. Nevertheless, the duration of the calculation was consequent and a mesh size of 16 was preferred. This last size gave a minimum stress close to the Frocht and Hill theory with a difference of 1,2% with the implicit minimum stress. For the maximum stress a gap of about 6% existed with the implicit stresses. However, the reduced elements C3D8R underestimated the maximum stresses and were not so far from the minimum reference stresses. Therefore, these last elements should be avoided or used with the finer possible size.

Consequently, the glass plate should at least be modeled with the mesh size 16 presented in Table 8.1. For the classical calculation method and for the control of the distortion, C3D8 elements had to be employed, while C3D8R elements were needed for the ALE method. The envisaged glass mesh size was transmitted to the underlying silicone and steel material. For the bolt, 8 elements were always assigned along the vertical and horizontal central edges. Three different sizes were tested over the silicone thickness, i.e. 3, 5 and 8 elements as showed in Table 8.2, in order to assess the influence of this factor on the maximum/minimum stress in all the components.

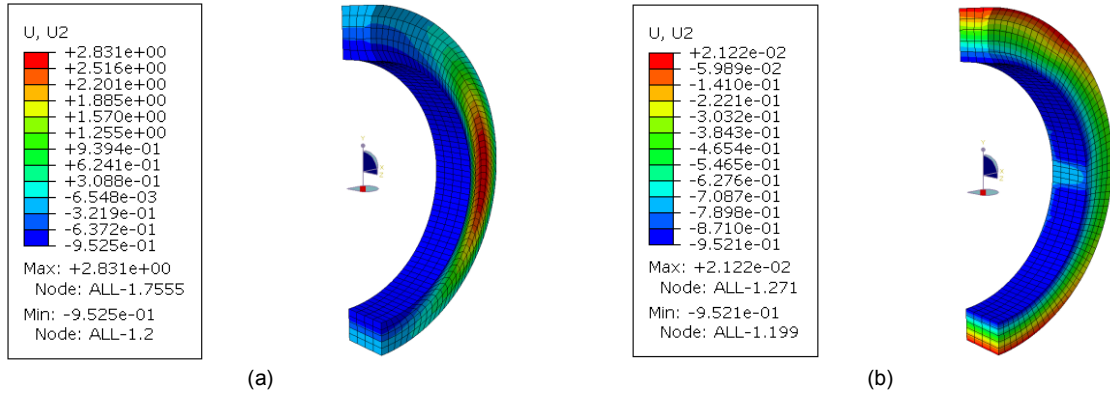
### Solution procedures

The lowest natural frequency of the complete assembly was first determined with the frequency tool of Abaqus/Standard. The frequency found was of 2033Hz inducing a minimum time period of 0,0005s. Nevertheless, a period six times higher of 0,003s was preferred and provided a better form of the kinetic energy over the increments. To impose the displacement of 3mm on the steel bolt a smooth amplitude function was implemented. For all the calculations, the non-linear geometry option “nlgeom” was applied.

### Analysis of the results

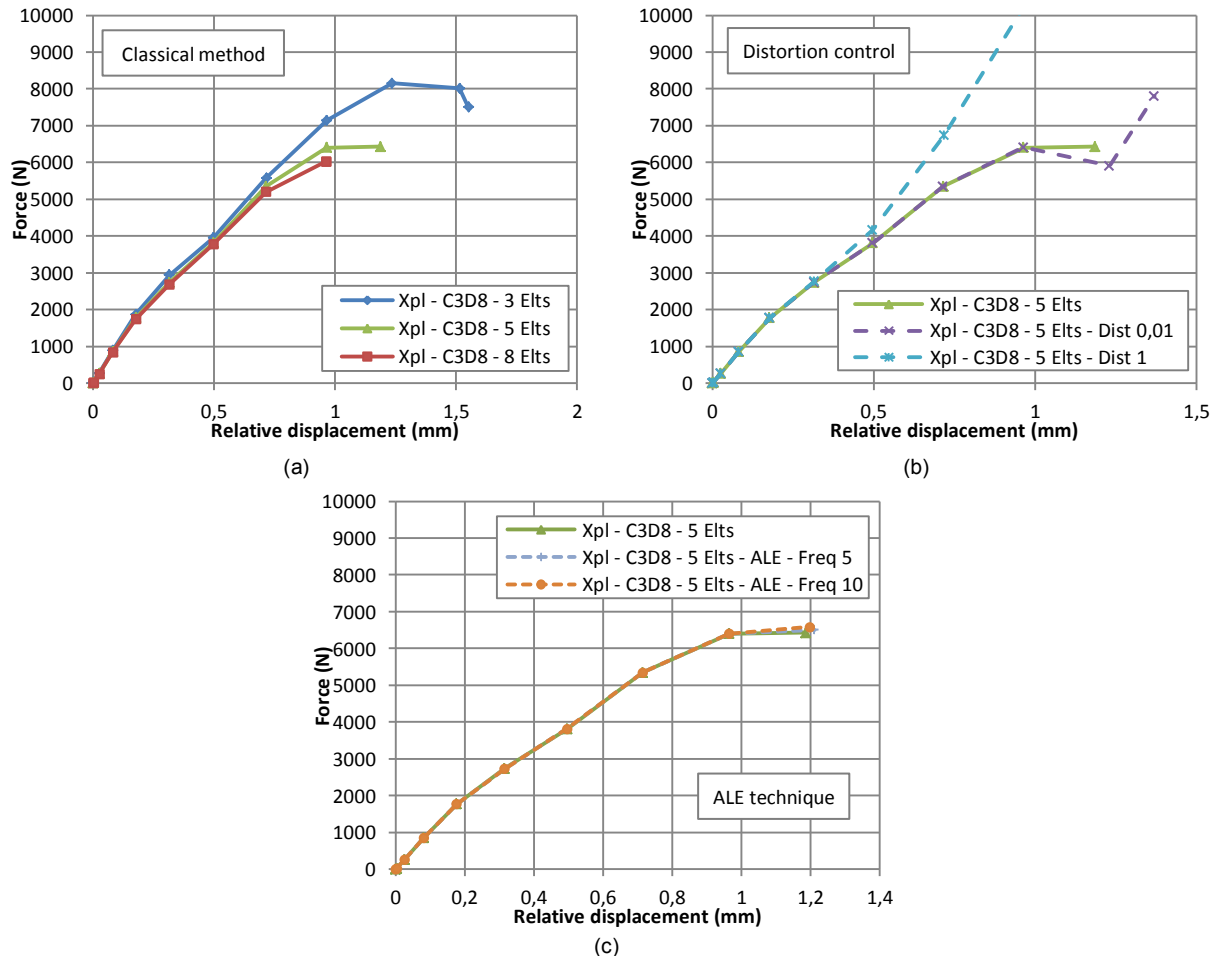
From all the numerical investigations made, only one reached the end, i.e. by controlling the distortion with a penalty value of 1. Nevertheless, its results did not reflect the reality as a locking of the mesh occurred. For the other jobs, a displacement of nearly 1mm, equivalent to one third of the imposed displacement, was successfully attained before a premature end. For the classical modeling without

using specific procedures, such as the distortion control or the ALE, this termination was essentially due to too large distortions appearing in the core of the adhesive as remarked for the results of the implicit method, see Fig. 8.10. For the ALE procedure, the limit was dictated by the too important volume variations combined to a too small mesh. The angles between two consecutive elements decreased rapidly and nearly tended to zero just before that the adaptative remeshing could have been redone. With this last technique, the uplifting of the core of the silicone at 90° of the load application could not be assessed as the displacements were measured on repositioned nodes, whose variations were almost inexistent.



**Figure 8.10-** Final displacement values of the silicone at the last valid increment for (a) classical and (b) ALE explicit resolution

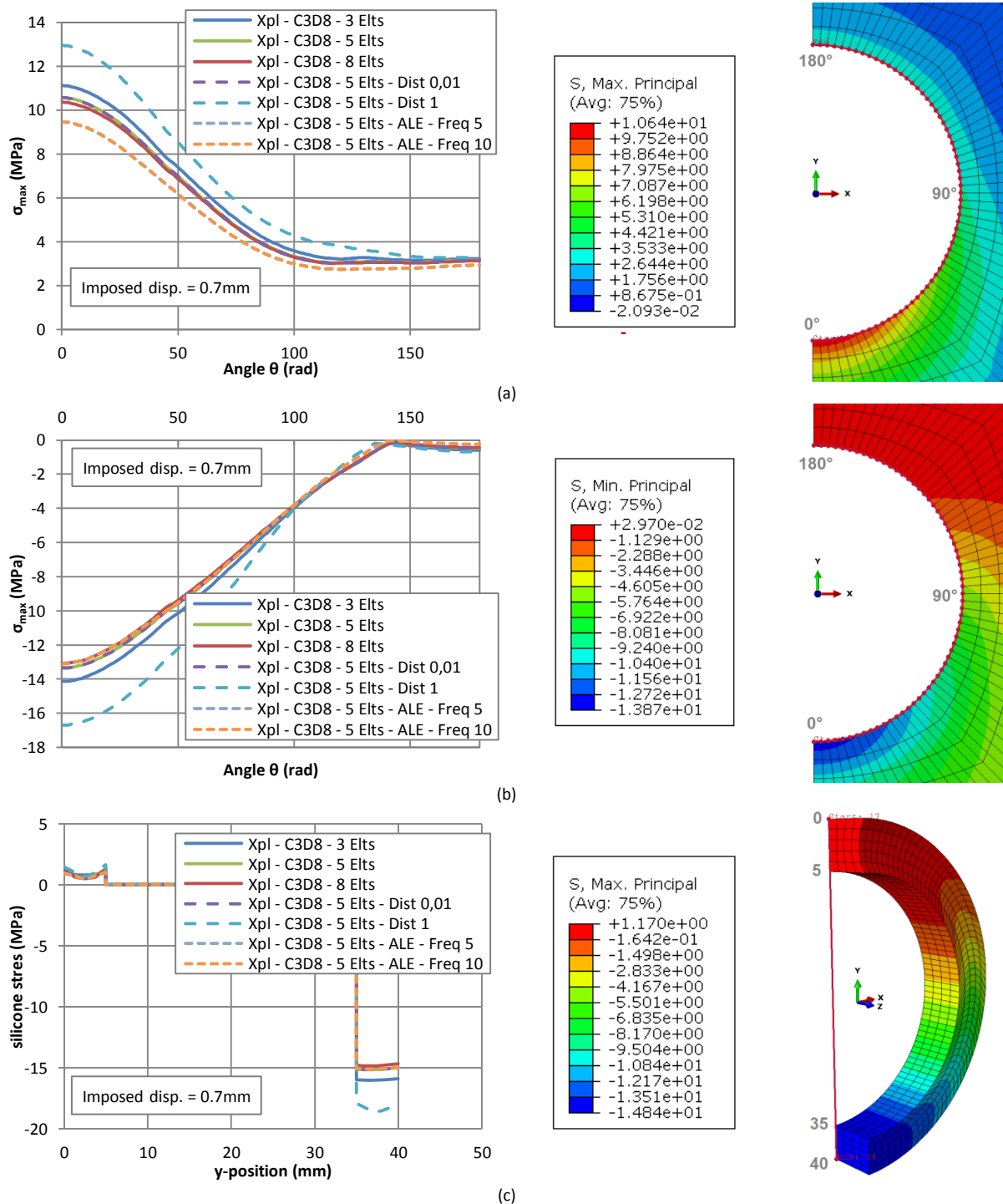
For all the models the form and the return to zero of the kinetic energy curve over the increments was controlled. The relative displacement of the silicone in the compression zone was recorded with the same protocol than for the implicit resolution. The total force again corresponded to the reaction force at the bottom of the glass multiplied by four to reproduce the full model of Fig. 8.3.



**Figure 8.11-** Total force versus silicone relative displacement diagrams – (a) classical, (b) Distortion control and (c) ALE



The rigidity of the connection was then evaluated by regarding the slopes of the force versus silicone relative displacements diagrams. All the curves were gathered according to the technique employed, see Fig. 8.11. For the classical method, i.e. without the use of specific remeshing techniques, higher were the sizes of the elements and higher were the relative displacements numerically attained. Nevertheless, the curves started to diverge at around 1mm due to the large distortions. The slope of these curves and consequently the rigidity of the connection was of 7250N/mm, which was slightly higher to the one obtained with the implicit method. With the distortion control, an important penalty of 1 lead to a considerable stiffening of the silicone away from reality, i.e. for a displacement of 3mm the total load was of 100,8kN. Finally the ALE technique provided exactly the same curve than the normal calculation, independently of the remeshing frequency.



**Figure 8.12-** (a) Maximum and (b) Minimum principal stresses according to the position on the radius; (c) Silicone stress at  $\theta=0^\circ$

The influence of the silicone mesh on the stresses of the surrounding materials were also investigated by considering the maximum/minimum stresses around the glass hole, see Fig. 8.12. Furthermore, the stresses in the silicone itself were also investigated for the stable increment common to all the jobs. For this increment, the total reached displacements were two times higher than the one of the implicit resolution and as remarked the tensile and compressive stresses in the glass were two times higher. The same observation could have been made for the compressive stress in the silicone.

In conclusion, even if higher relative displacements were acquired with the explicit solving, none of the techniques proposed by Abaqus were able to achieve the complete imposed deformation. Only approximation of the rigidity of the connection based on a linear assumption with the current results were available. To confirm this hypothesis, small-scale tests on the system described in Fig. 8.3 were needed.

### 8.3.2 Experiments

As for the numerical simulation the aim of these small-scale experiments was essentially to assess the rigidity of the connection by studying one layered hole, but also to confirm the assumption consisting in assimilating the rigidity of twelve connections to twelve times the rigidity of only one. This hypothesis implied that the proximity to the edge or to another hole did not influence the global behaviour. To ensure of this postulate, the system presented in Fig. 8.3 (a) was first tested and then another system of two holes inspected.

#### 8.3.2.1 One hole – System of Fig. 8.3 (a)

##### Manufacturing of the samples

The dimensions of the glass plates matched the ones of the numerically modeled system, i.e. a total width of 240mm with a length two times higher of 480mm. The thickness of these plates was of 12mm and the glass was non-tempered for these experiments, as an earlier silicone failure was expected. Chamfers of 1mm were only made around the edges of the glass plates and not around the hole. This last was of 40mm of diameter and drilled in the middle of the plate. Two distinct silicone thicknesses were envisaged to evaluate its influence on the rigidity of the connection. Thus, besides the modeled thickness of 5mm, another one of 10mm was chosen. To respect this dimension and avoid constantly changing the bolt for the conduction of the tests, some circular rigid steel rings were machined. The diameter of the bolt was of 16mm, which was assimilated to the inner diameter of the steel ring.

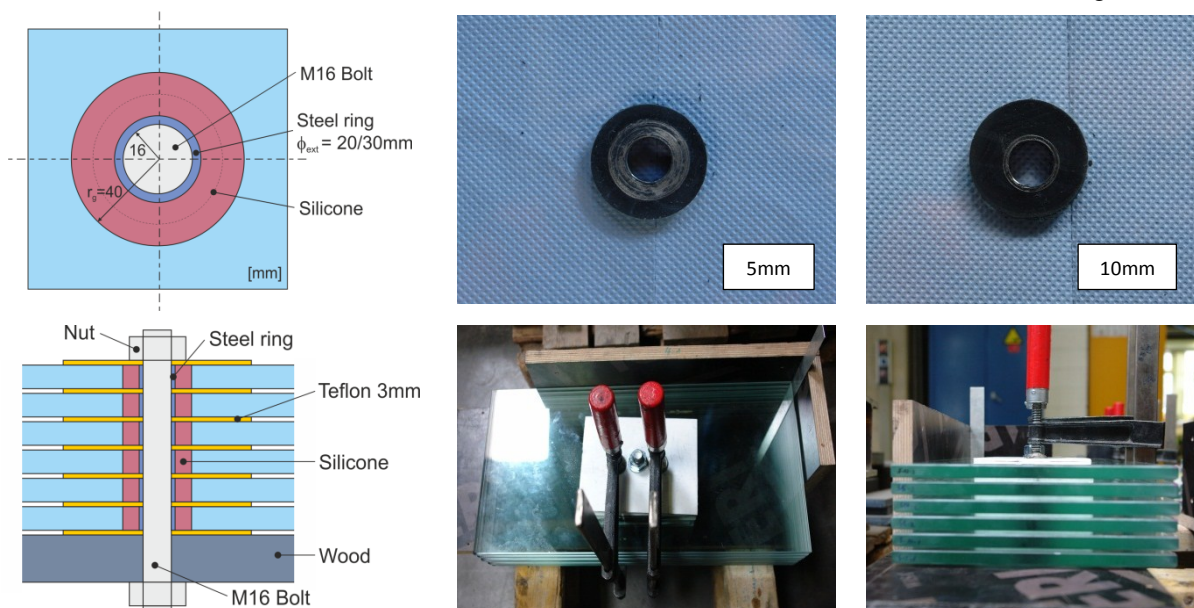


Figure 8.13- Composition of the small-scale mechanical-adhesive connection (1 hole) and production details

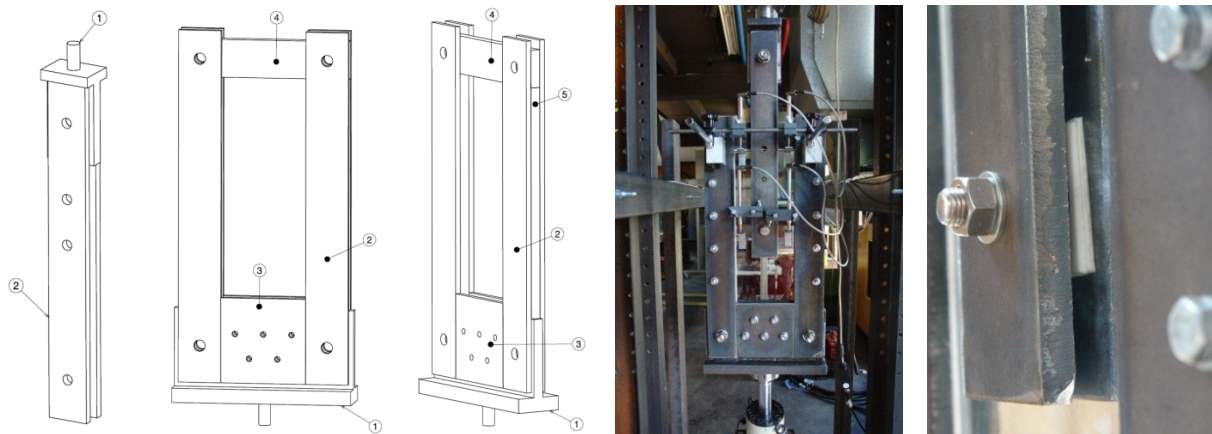
The external diameter of the ring was consequently of 20mm for the silicone thickness of 10mm and of 30mm for the silicone thickness of 5mm, see Fig. 8.13. To manufacture six plates at a time, a layering process was established. A calibrated support made out of wooden plates generally used for concrete casting and possessing perpendicular surfaces was constructed. A hole was drilled right in the middle of the lower plate to insert a long M16 bolt serving as reference for the positioning of the ring before the silicone pouring. The different steps were carried out:

- A first Teflon plate 3mm thick was placed around the bold and in contact of the wood plate.
- The first glass plate was then positioned on top of this last element. The centering simply achieved by pressing the one angle of the plate against the calibrated vertical wooden plates.
- The ring, corresponding to the desired silicone thickness, was then fitted on the bolt and the gap with the glass hole verified.
- The silicone was then injected between the last two assembled components by applying more quantity than necessary to be sure of the correct repartition.
- A covering Teflon plate of 3mm was then added to close the first injection and the previous operation repeated until the 6<sup>th</sup> glass plate.

The whole system was closed with a nut, which allowed, with the self-weight of the different elements, evacuating the surplus of the silicone and obtaining straight lateral surfaces. The layering was left in the current state during 24 hours to cure at ambient temperature and humidity. With the disposition of the Teflon plate, no shielding against light was judged necessary. In total, three assemblies of each silicone thickness were produced. The silicone compression zone during the tests were measured with a digital caliber and variations of about less than 10% of the thickness were noticed.

### Description of the tests

The small-scale tests of the mechanical-adhesive connection were conducted on a 10kN mobile hydraulic press on which was fixed a force sensor of the same capacity. To reproduce properly the principle of the test exposed on Fig. 8.3 (a), a steel layout had to be manufactured, see Fig. 8.14. This construction was composed by two structures. Attached to the force sensor on the immobile part of the frame, a structure composed by two parallel steel plates 15mm thick and 80mm wide was created. A constant gap of 24mm was achieved to install in-between the glass and two covering Teflon plates at each side.



**Figure 8.14-** Details of the test set-up and final installed assembly with complete instrumentation – Small scale tests MAC

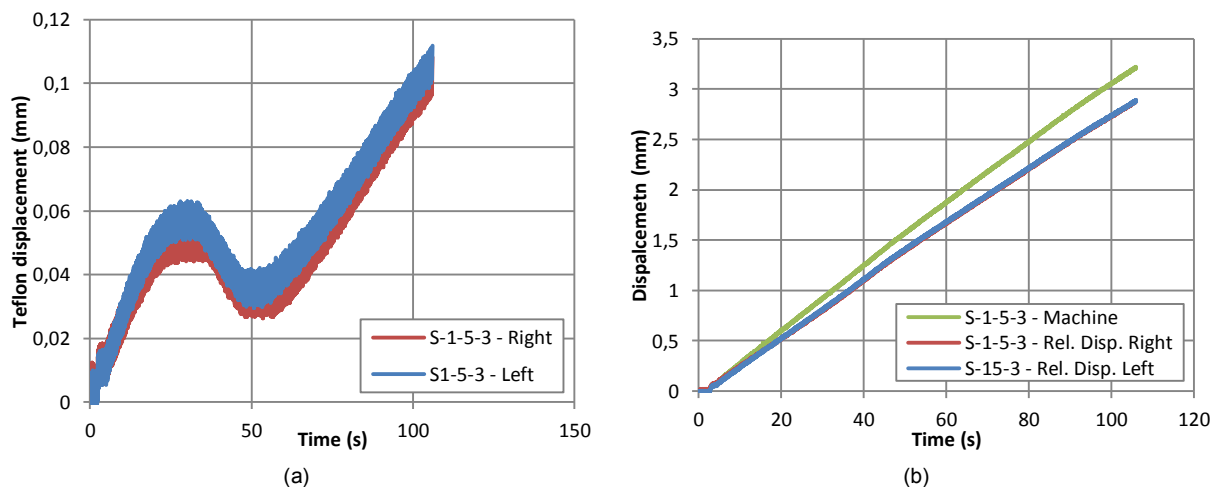
At the bottom of the test set-up, a complete steel frame, made to retain the glass, was attached to the mobile piston. This frame was composed by five main parts, such as a rigid support (1), whose vertical plate defined a gap of 22mm between the four vertical 12mm thick steel plates (2). As each plate was attached with one bolt to the bottom support (1), two square plates 12mm thick (3) fitted the gap existing on one side between them. The vertical steel plates were reinforced by inserting two rigid steel profiles of 22mm of thickness (5). At the top was tightly screwed a rigid steel plate (5) of 80mm of height. As the mobile press could only be operated downwards, the upper zone of the glass was under compression and this last component was thus subjected to important loads. The bolts employed to

link all the elements perfectly fitted the machined holes to prevent parasite influence on the total displacement measured by the machine. On all inner surfaces of this bottom structure were disposed some 3mm thick Teflon plates preventing any direct steel to glass contact. The central bolt closing the system and connecting the glass plate to the upper structure was tightly screwed to preventing any loosening during the test.

As aforementioned, the total force was measured with an external force sensor of 10kN and the total displacement by the machine. However, the most relevant information was the relative displacement between the bolt and the glass plate, i.e. the deformation of the silicone assimilated to the rigidity of the connection. This relative displacement was recorded in two different positions with displacement sensors of 20mm. These sensors were attached to the fixed upper part as close as possible to the bolt and recorded the displacements of steel plates bonded on the glass, see Fig. 8.14. Two measuring devices were used as it allowed assessing the possible rotation of the glass plate and consequently the non-uniformity of the applied loading. The deformations of the Teflon plate located between the part (4) of the lower structure and the glass edge were also evaluated in two positions with 10mm displacement sensors.

### Tests results

All the six tests were conducted in displacement control until either silicone complete breakage for the 10mm silicone thickness samples or until reaching the 10kN maximum capacity of the press. The displacements recorded with the 10mm sensors and measuring the compression in the Teflon plate placed at the top of the assembly were negligible, as less than one tenth of millimeter was found in each case, see Fig. 8.15 (a) for the results of the third sample of 5mm silicone thickness.



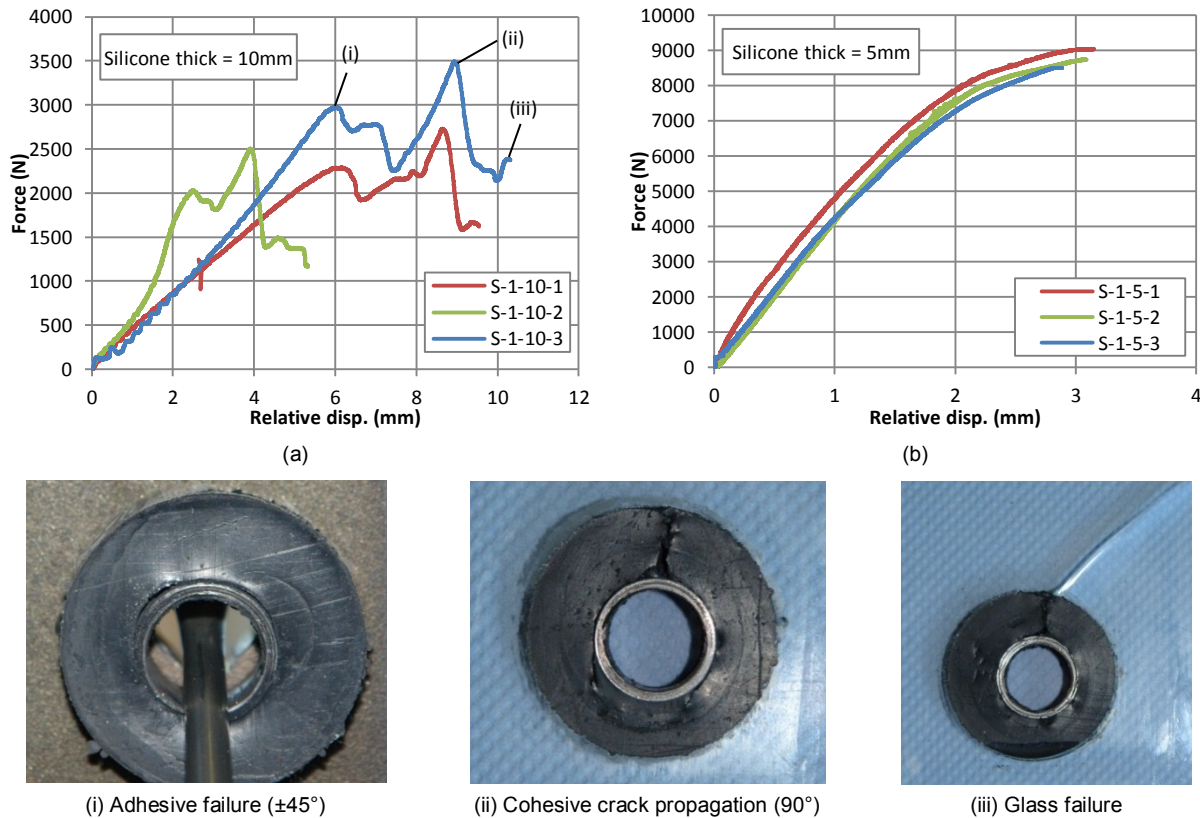
**Figure 8.15-** (a) Displacements in the Teflon and (b) Relative displacements in the silicone acc. to the time – Silicone 5mm thick

Thus, only the relative displacements in the silicone and the total applied force sensors provided relevant information. For all the tests, the results of the two 20mm sensors accounting for the silicone displacements were plotted versus time, to ensure that no rotation of the specimen occurred during the test, see Fig. 8.15 (b) for the third sample of 5mm silicone thickness. As observed, no difference could have been made between these two curves for all the studied specimens and consequently no rotation happened.

The rigidity of the connection was assessed by drawing the force according to the averaged relative displacements. These six curves were established and exposed for the two investigated silicone thicknesses on Fig. 8.16. For the 10mm thickness, one curve was stiffer and diverged from the two others, which were, in contrary, close. Nevertheless, the global form of the three curves was similar, with a first linear increase until a first adhesive failure on the steel side (i) occurring at  $\pm 45^\circ$  to the load application direction. This failure started at the steel ring as its radius was lower than the glass one and larger angle variations should took place. After this first peak, the force decreased slightly and



became constant corresponding to the propagation and jointing at  $0^\circ$  of the two adhesive failures. Once achieved, the silicone was fully dissociated from the ring in the compressive zone and the force started to increase again until quasi-instantaneous failure of the silicone in the direction of the load (ii). Finally, as the silicone was push to the side by the bolt, the ring entered in contact with the glass plate, which led to its failure (iii).



**Figure 8.16-** Force versus relative displacements for (a) 5mm and (b) 10mm silicone thickness – Detail of the failure for 10mm

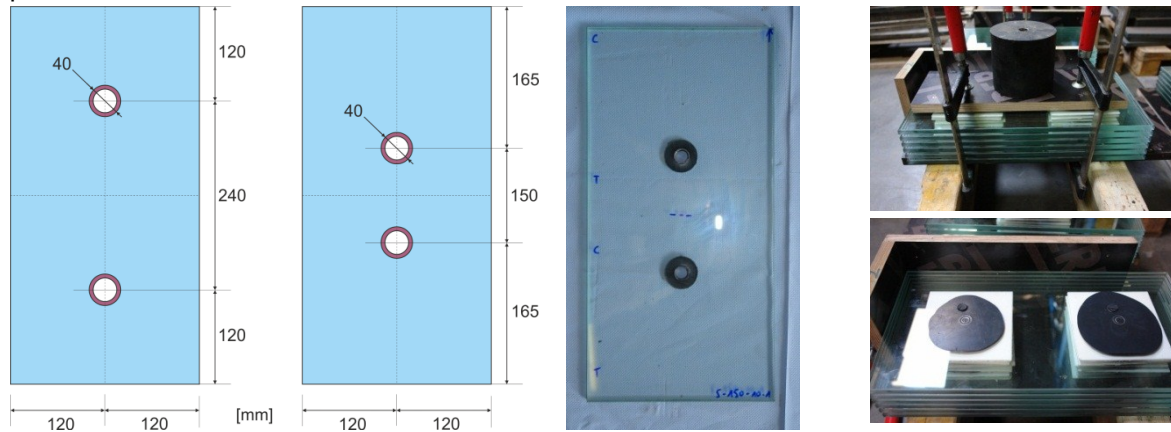
For the 5mm silicone thickness, the maximum force of the press was applied and no failure appeared at the end of the tests. The force-relative displacements curves were presented on Fig. 8.16 (b). No dispersion was remarked indicating a better reproducibility of the results with this smaller thickness. The rigidity of the connection could be assimilated linear until a displacement of 1.5mm. It however became non-linear after this displacement. For the linear part, the averaged rigidity was estimated to 4125N/mm, which was lower than the one of 6600N/mm assessed with the numerical simulations. For the 10mm silicone thickness, the approximation of the linear part until a displacement of 4mm and excluding the diverging curve was found equal to 440N/mm, which represented less than 9 times the one of the 5mm silicone thickness. Consequently, by dividing by two the adhesive thickness, the maximum authorized force was almost multiplied by 10.

### 8.3.2.2 Two holes

#### Manufacturing of the samples

The principal aim of this second series of tests was to evaluate the possible influences of the proximity to the edge or the proximity of another hole on the rigidity of the connection, by ensuring that the force carried by two holes was equal two times the one of hole. The two silicone thicknesses previously employed for one hole, i.e. 5mm and 10mm, were conserved for this study. The external dimensions of the glass plate were unchanged, 480x240x12mm, to conform to the prior manufactured steel test frame. Further, the diameters of the glass holes were of 40mm independently of the desired silicone thickness. By varying the distance between the two holes, the closeness to the edges was also varied. Consequently, two distances between the holes were inspected, i.e. 150mm and 240mm. The four

different configurations and associated dimensions were gathered in Fig. 8.17 and Table 8.3. For each configuration, at least three tests were conducted to valid the results. Hence, twelve specimens were produced in total.



**Figure 8.17-** Dimensions of the small-scale mechanical-adhesive connections (2 holes) and production details

| Standard Test n° | Factors       |                    | Samples to be tested |               |               |
|------------------|---------------|--------------------|----------------------|---------------|---------------|
|                  | Hole distance | Silicone thickness | Test series 1        | Test series 2 | Test series 3 |
| 1                | 1             | 1                  | S-150-5-1            | S-150-5-2     | S150-5-3      |
| 2                | 1             | 2                  | S-150-10-1           | S-150-10-2    | S-150-10-3    |
| 3                | 2             | 1                  | S-240-5-1            | S-240-5-2     | S-240-5-3     |
| 4                | 2             | 2                  | S-240-10-1           | S-240-10-2    | S-240-10-3    |
| Level 1          | 150mm         | 5mm                |                      |               |               |
| Level 2          | 240mm         | 10mm               |                      |               |               |

**Table 8.3-** Design of experiments for the small-scale mechanical-adhesive connections (2 holes)

As the test set-up remained unchanged, the diameter of the bolt transmitting the force in the system was of 16mm and the concept of steel rings was still conserved. For a silicone thickness of 10mm, the outer diameter of the ring was of 20mm and, for a thickness of 5mm, the ring measured 30mm. The layering process explained for the construction of one bolt was reused. In the bottom calibrated wooden plates were drilled, with the required spacing, the two holes allowing inserting the long M16 bolts serving as references. Two wooden assemblies were consequently necessary. The different steps leading to the production of six plates was again applied and for a uniform closing of the system, a wood plate was placed on top of the layering. The surplus of silicone was evacuated by disposing an important weight and two clamping systems, see Fig. 8.17. The remaining silicone bonded on the surface was very thin and easily removed. As for the case of one hole, slight eccentricity less than 10% of the thickness appeared but were judged as non-crucial.

### Description of the tests

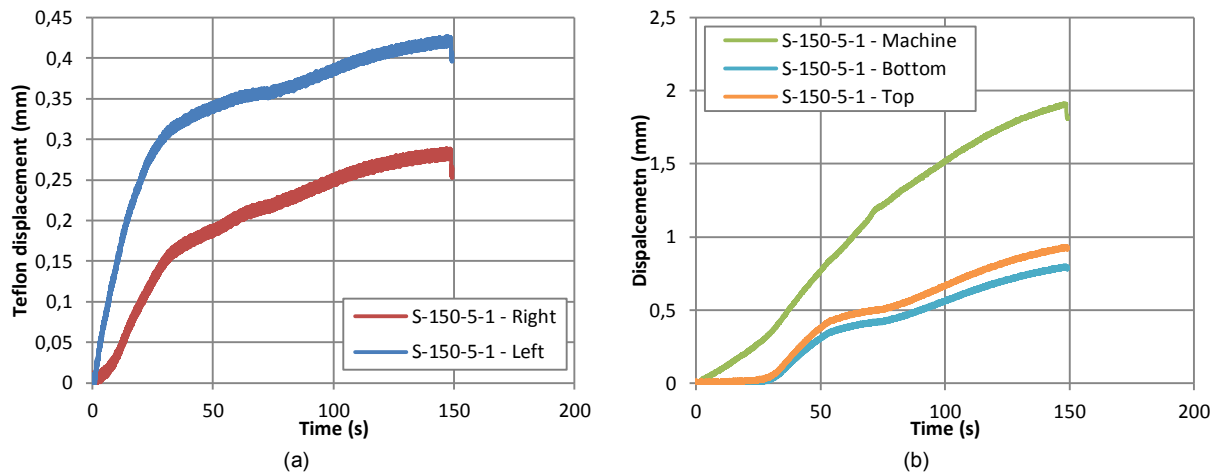
These tests were conducted on the same 10kN INSTRON mobile hydraulic press employed for the experiments on one holed plate. The steel frame detailed previously was conserved, as the external dimensions of the glass were identical. Nevertheless, due to the presence of the two holes, certain modifications were made on the upper part. Indeed, two additional holes of 16mm of diameters were drilled in the two parallel steel plates of 80mm of width. These holes were necessary to introduce the two bolts fitting the steel rings of the specimens. To link the top steel frame to the sample and restrain the lateral displacement of the silicone perpendicularly to the load introduction direction, two Teflon plates of 3mm thick were needed on each side and for each bolt.

The total applied force was recorded by an external force sensor of 10kN and the total displacement by the internal sensor of the machine. Two additional displacement sensors were responsible for the

measurement of the relative displacement of the silicone. As two bolts were considered for these tests, one sensor was responsible for the upper bolt, while the other for the bottom connection. The compression in the Teflon plate was recorded by two external sensors of 10mm.

### Tests results

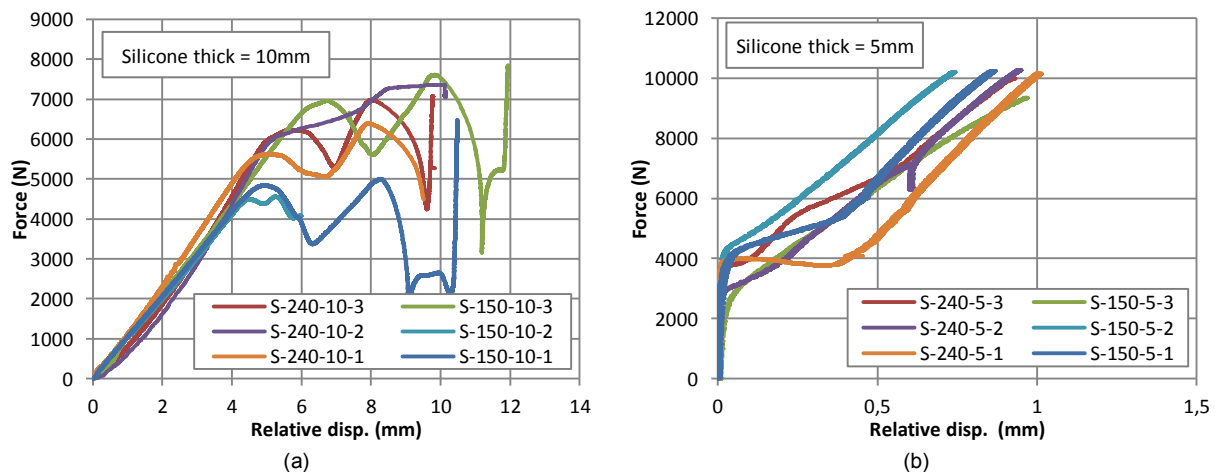
The twelve tests of the design of experiments exposed in table 8.3 were carried out in displacement control until either breakage of the glass plate or until reaching the maximum capacity of the press. The compression in the Teflon plate was larger than the one assessed for one bolt, but remained lower than one half of millimeter in the worst scenario, see Fig. 8.18 (a) for the Teflon displacement versus time diagram of specimen S-150-5-1. The differences observed between the two regarded positions demonstrated a very small rotation of the plate accommodating to the steel frame at the beginning, i.e. during the first 20s. However, this did not impact the final results.



**Figure 8.18-**(a) Displacements in the Teflon and (b) Relative displacements in the silicone acc. to the time – 2 bolts system

For the relative displacements measured at the upper and lower bolts, some differences were noticed, but independently of the position, i.e. sometimes the relative displacements in the lower bolt were lower than the ones of the upper bolts and sometimes it was the opposite, see Fig. 8.18 (b). These variations were mainly due to the slight eccentricity of one of the bolt. Furthermore, these gaps were clearly lower than the distance to the displacements of the machine.

The rigidities of the four systems were classified according the silicone thicknesses, see Fig. 8.19. For the 10mm thickness, the behaviour of the connection was identical to the one bolt configuration with the same propagation of the failure until glass failure. The linear portion of these curves seemed to be identical independently of the distances between the two bolts and the averaged slope was equal to 1088,8N/mm, which was 2,5 times higher than the rigidity of one bolt with the same silicone thickness.

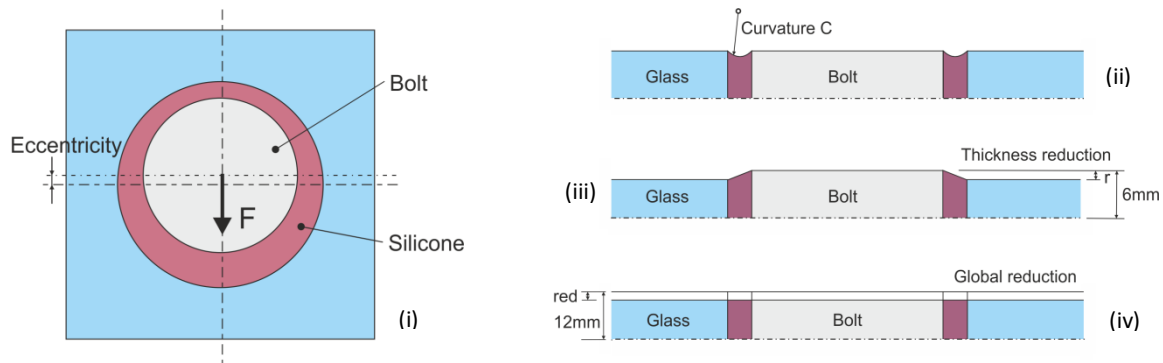


**Figure 8.19-** Force versus silicone relative displacements for (a) 5mm and (b) 10mm silicone thicknesses – 2 bolts system

For the 5mm silicone thickness an important rigidity occurred at the very beginning with almost no variation in the relative displacements. This great stiffness lasted until a force of about 4kN before dropping and finally reaching a force of 10kN for a displacement of approximately 0,9mm. For a given force, the attained displacements with the 2 bolts system were 3 times less than the ones of the one bolt system for the same silicone thickness. As an important scattering in the displacements appeared for the different configurations, the influence of the distance between two holes could not be assessed. The assumption consisting in assimilating the rigidity of a connection formed by 2 bolts to two times the rigidity of a one bolt connection was therefore estimated conservative.

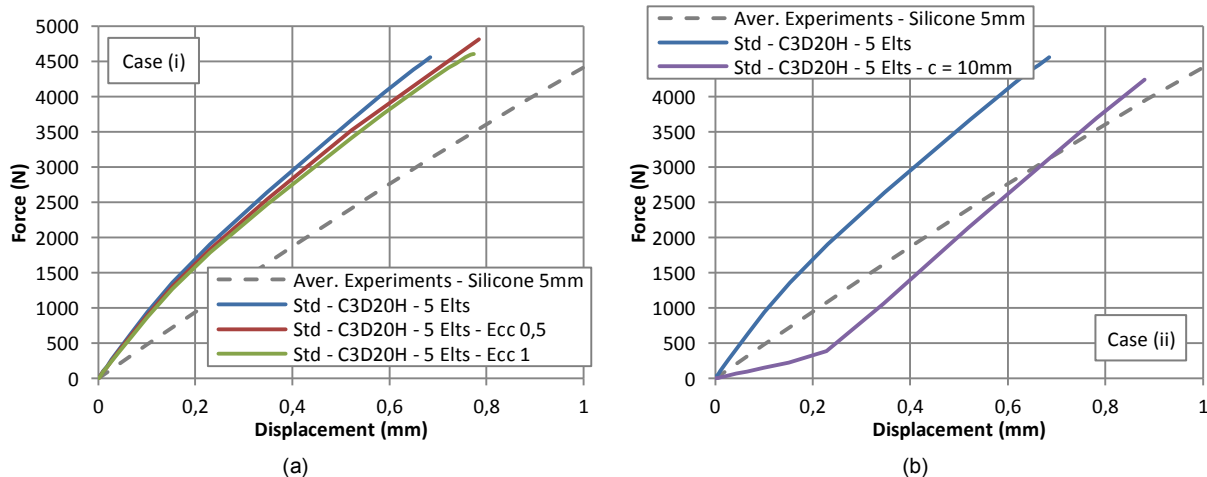
### 8.3.3 Discussion of the results

The difference between the rigidities obtained with the experiments and the numerical simulations for the one bolt connection with a 5mm silicone thickness were relatively consequent. Indeed, with the numerical simulations, the rigidity was of 6600N/mm compared to 4125N/mm from the experiments, which represented a relative error of 60%. To determine the origin of this error, further numerical simulations were conducted by modifying some dimensions of the elements constituting the specimen, see details on Fig 8.20.

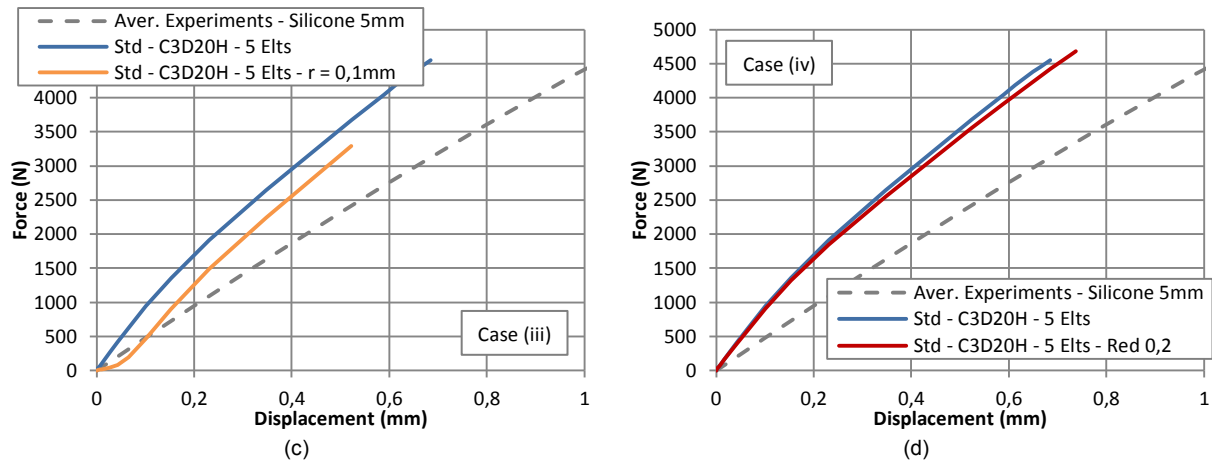


**Figure 8.20-** Geometrical modifications to the numerical simulations for the case of one bolt with 5mm silicone thickness

- (i) An eccentricity in the position of the bolt was incorporated to the model by keeping unchanged all the other dimensions. This was made to increase the compression zone of the silicone.
- (ii) A curvature was created all around the silicone surface, so that no uniform contact with the Teflon plate was present at the beginning of the calculation.
- (iii) The glass thickness was reduced by conserving the dimensions of the bolt. This also induced a slope all around the silicone. The difference compared to the (ii) configuration came from the non-restraining of the bottom nodes, which could move downwards.
- (iv) A complete reduction of the whole thickness was operated. All the elements still possessed the same thickness. The aim of this reduction was to diminish the compression zone without changing the silicone thickness.







**Figure 8.21-** Force versus relative disp. curves – Numerical simulations of the geometrical modifications presented on Fig. 8.20

The calculations were performed under Abaqus/Standard with quadratic elements, as the stresses in the glass were more accurate with this model. Five elements were always considered over the silicone thickness, even for the eccentric case (i). As for the previous numerical simulations, none of the model could reach the end due to the presence of too large distortions. Nevertheless, the force-displacement curves characterizing the rigidity of the connection were plotted on Fig. 8.21, as the main concern was the initial slope.

The averaged results constituted the reference coming from the experiments and the previous numerical calculation on an ideal geometry with a silicone thickness of 5mm (Std-C3D20H-5 Elts) was the numerical reference. As it could have been noticed for the case (i), the creation of an eccentricity at the bolt, up to 20% of the silicone thickness (1mm), did not influence importantly the rigidity of the connection, i.e. less than 0.5mm of difference was found with the numerical simulations of the perfect geometry for the maximum force of 4,5kN. For the case (ii), the curvature in the surface of the silicone modified the initial slope as the silicone was not fully in contact with the Teflon plate. Thus, over the first 0,2mm, the rigidity was low and then, once the whole silicone section was in contact with the Teflon an increase of rigidity occurred. This second linear slope matched the one of the ideal silicone representation. For the case (iii), the same conclusion than for the silicone curvature could be done. Finally, with the total thickness reduction of the specimen, no better results were observed and the rigidity did not approach the one coming from the experiments.

In conclusion, the variations observed between the rigidities of the experiments and of the numerical simulations were not due to some geometrical imperfections. Therefore, it was supposed that the manufacturing process, based on a simple pouring of the silicone in the remaining gap, was the main responsible. The volumetric coefficients  $K$  of the developed material law was based on the oedometric tests results, for which an injecting process was employed instead of a simple pouring process. Thus, the coefficient  $K$  was established in ideal conditions and could not be directly used for the numerical calculations. As the relative error between the analytical and experimental methods was of 60%, a reduction of the  $K$  factor by this value would lead to similar results. Nonetheless, only the rigidity found with the tests of 4125N/mm for the 5mm silicone thickness was the one conserved in the following paragraphs.

## 8.4 LARGE-SCALE INVESTIGATIONS

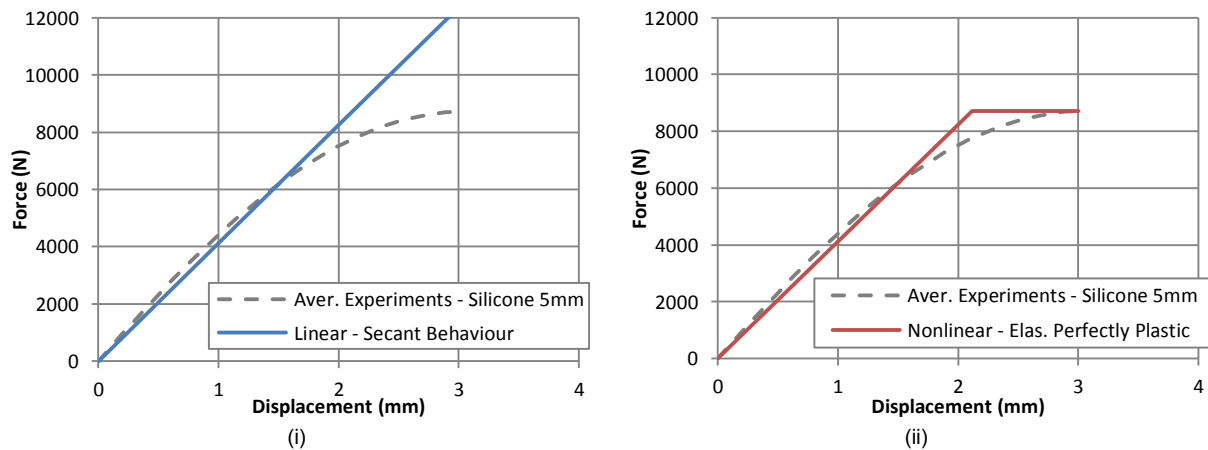
### 8.4.1 Numerical simulations

#### 8.4.1.1 Connection simplifications

The mechanical-adhesive large-scale beams exposed on Fig. 8.1 & 8.2 were designed with a silicone thickness of 5mm. In consequence, only the rigidity of the corresponding connection was considered,

i.e. Fig. 8.16 (b). Further, as none of the numerical simulation of the small-scale tests, implying only one hole, could be conducted until the end, a complete 3D representation of the composite beam including the silicone was not envisaged. Instead, as the connection behaviour was experimentally assessed, it was easier to implement its rigidity through springs positioned at the same location than the bolts, i.e. each 200mm in the longitudinal shear zones. Two different possibilities were investigated to account of the rigidity of the connection:

- (i) With a linear assumption based on a secant evaluation of the slope of the averaged force-relative displacement curves at  $u=1,5\text{mm}$ , see Fig. 8.22 (b). This also served to define the ratio rigidity over action length  $K/e$  required by the Lebet theoretical model described in Appendix F.4. This representation was however only valid until a displacement of 1,5mm was a divergence with the real behaviour appeared beyond.
- (ii) By assimilating the rigidity to an elastic-perfectly plastic law, see Fig. 8.22 (b). The slope of the elastic part remained identical to the one of the fully elastic representation (i) and once the maximum force at 3mm was reached the slope changed and became nil. The force at then hypothetically end before silicone breakage was clearly lower than the one for the first elastic representation.



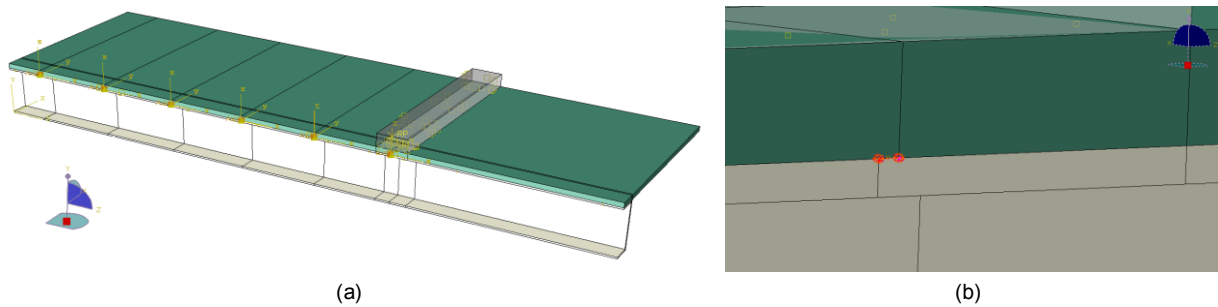
**Figure 8.22-** (i) Linear elastic and (ii) Nonlinear elastic-perfectly plastic representations of the rigidity of the connection in FEA

While a standard spring could be used in Abaqus software for the first linear case, a specific connector was employed for the nonlinear behaviour. The details of the two models, as well as the obtained results, were provided in section 8.4.1.2.

#### 8.4.1.2 Evaluation of the composite beam

##### Definition of the geometry and boundary conditions

With the spring representation of the connection, only the glass plate and the steel beam had to be modeled. Further, no particular modification had been made on the steel beam, as the welded bolts were not needed. As the silicone failed first in the connection, the stresses arising around the glass holes were not crucial and this material implementation was done without including the holes. A uniform and monolithic glass plate was thus regarded. The material and geometrical symmetries of the so-formed beam allowed accounting for only one fourth of the total model, as for the unconnected and fully connected system of section 7.2.2. Only the tested length was considered and the 100mm at the extremities neglected. Two symmetry boundary conditions were applied on the surfaces theoretically in contact with the rest of the material and the nodes at the support were vertically restrained. A hard and frictionless contact, preventing the vertical separation, was defined between the top flange of the steel beam and the glass plate (similar to the Teflon plates' actions). The load of 25kN (100kN over the whole beam) was introduced on a width of 80mm with an analytical rigid hollow section of 500mm of length, equivalent to the glass width. Another hard and frictionless contact was inserted between the latter and the glass plate. In addition, to reproduce a real load application, the rigid hollow section was free to move in the vertical direction and rotate around its principal axis only, see Fig. 8.23.



**Figure 8.23-** (a) Global model of the mechanical-adhesive composite beam and (b) Local definition of the connection behaviour

Several partitions were made on the two elements of the model to assign the six springs or connectors representing the connection behaviour. A clearance was operated between the partitions of the glass plate and of the steel beam to activate these elements and start the calculations, see Fig. 8.23 (b).

### Material behaviour

The linear properties of steel and glass materials gathered in Table 7.1 were implemented and the rigidity of the connection was either represented by a spring for the linear elastic behaviour (i) or by an axial connector for the elastic-perfectly plastic behaviour (ii). Specific coordinate systems were created and placed at each spring/connector position to ensure of the correct transfer of the load during the deflection of the beam.

### Meshing

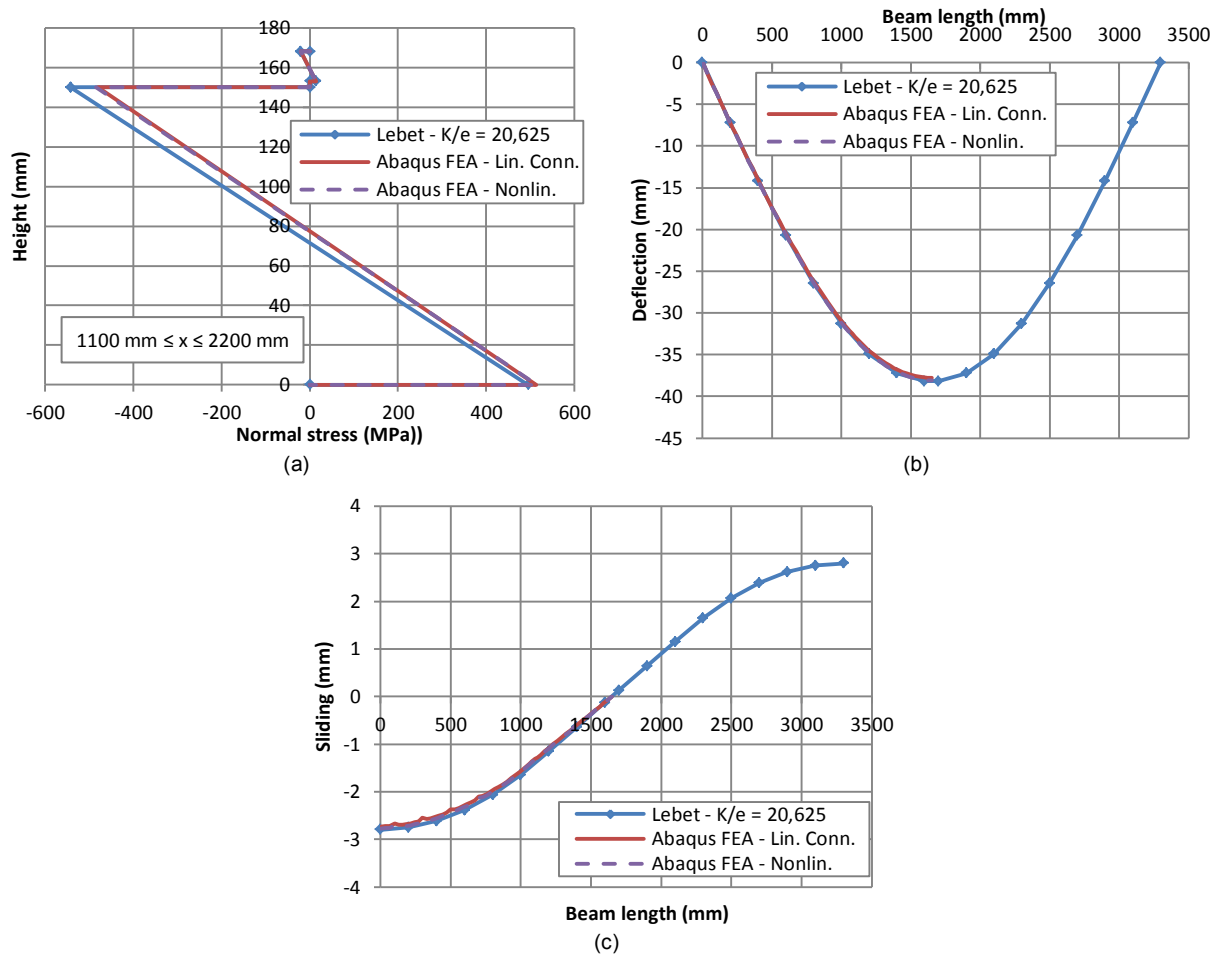
The mesh employed for the evaluation of the fully composite and the unconnected beams remained unchanged. For the steel cross section, a least two elements were imposed on the wall thickness of 5mm, four elements along the flange width and fourteen elements over the web length. Along the length the dimensions of the mesh was of 30mm. For the glass, four elements were selected over the thickness and along the width the mesh of the steel was transmitted to the glass plate. In the other regions a mesh size of 30x30mm was applied. Only C3D20 quadratic bricks were employed for the two components of the beam, as they were more appropriate for this 4-point bending test.

### Solution procedures

The calculations were performed under Abaqus/Standard, as the implicit solving method was sufficient with the absence of the silicone. Both materials were assumed independent of the loading rate, so that the time period and initial increment proposed by default by Abaqus were conserved.

### Analysis of the results

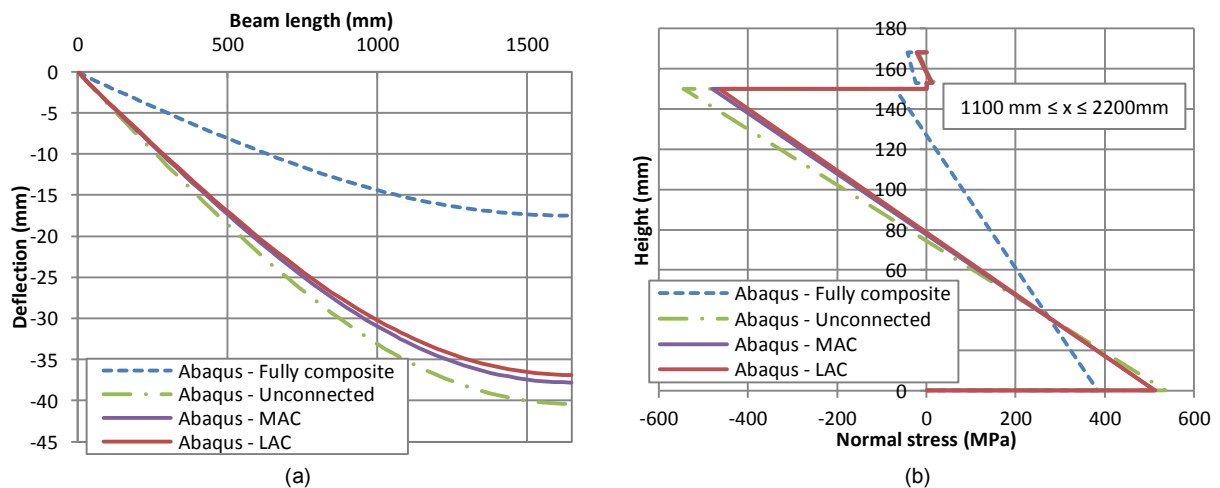
All the calculations were successfully conducted until the end for the imposed total force of 100kN. For the two rigidity representations, paths were made to retrieve the maximum normal stress distribution in the whole system, the deflection according to the length position and the relative displacements at the steel-glass interface. These three diagrams were regrouped in Fig. 8.24 and compared to the theory developed by Lebet. For the latter, the definition of the rigidity was identical to the linear elastic case (i) with a stiffness per length unit of  $20,625\text{N/mm}^2$ . The stress distribution in the composite assembly of Fig. 8.1 and 8.2 for the central position was independent of the representation of the connection for the numerical simulations. Indeed, the linear elastic and elastic-perfectly plastic implemented rigidities gave the same stresses in both steel and glass materials. Compared to the Lebet theory, the glass stresses errors for the low and upper surfaces were of about 1%. However, while the tension in the steel was correct, a relative error of 11% was found in the flange under compression. This effect could have been due to a propagation of local effect induced by the spring definition on one node. It could nonetheless be conclude that the three methods gave close normal stresses.



**Figure 8.24-** (a) Normal stress distribution in the composite section (Fig. 8.1); (b) Deflection and (c) Sliding acc. to the length

The deflection of the beam along its length was identical for the three methods, which confirmed the validity of the methods and the non-influence of the representation of the rigidity. For the sliding, the same conclusion was drawn, even if the plastic part was activated over the first 800mm (activation after a sliding of 2,1mm). In conclusion, the three methods could be used to obtain an approximation of the real composite beam behaviour.

To locate the degree of connection of the beam, the perfect connection and the unconnected models served as references. The deflection was plotted over the beam length for the mechanical-adhesive connection (MAC) but also for the linear adhesive connection (LAC), see Fig. 8.25 (a). While the two envisaged connections presented similar behaviours, they were closer to the unconnected model.



**Figure 8.25-** Comparison of the deflection curves and (b) of the stress distributions for the four types of connection

The normal stress distribution provided the same type of results, with a small zone of tension in the glass. Nevertheless, even if the mechanical-adhesive connection was slightly lower than the linear adhesive one, some improvements could be brought, e.g. by reducing the silicone thickness from 5 to 3mm or increasing the number of bolts. For the linear adhesive connection, as the whole steel flange was bonded and as the silicone could not be reduced to a thickness inferior to 3mm, no increase of rigidity could be possible.

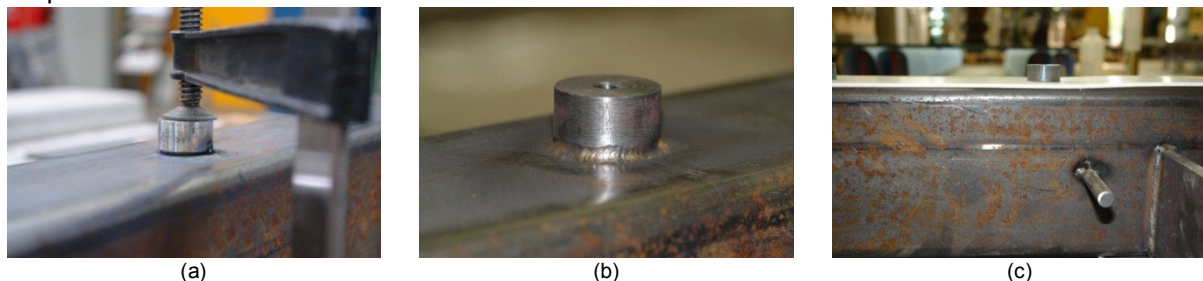
## 8.4.2 Experiments

The principal objective of the large-scale experiments was to confirm the different results acquired with the Lebet theory and the numerical simulations. The rigidity of the connection should be analyzed by plotting the deflection according to the position along the length, as well as the sliding. The standard force-deflection curve was also an important results. The manufacture and the complete tests of the mechanical-adhesive composite beams were detailed in the following sections.

### 8.4.2.1 Manufacturing of the beams

#### Steel beam modifications

The modifications made on the steel beam for the linear adhesive large-scale tests were reproduced for this new connection type, cf. section 7.3.1. At the supporting rollers, steel plate 15mm thick were welded under the extremities of the beam to prevent any local crushing of the beam wall thickness. In addition, to ensure that no instabilities, such as lateral buckling, could occur during the tests other reinforcing steel plates 10mm thick were vertically welded on this last element and on the main beam. At the load introduction positions, the upper parts of the steel beam were removed on 20mm to insert and weld thicker steel plates of corresponding thickness. The dimensions of these plates were chosen in relation to the rigid steel bars introducing the load in the system. As these bars were 80mm wide, the plates were set to 100mm.



**Figure 8.26-** (a) Chamber at the bolt, (b) Final welded and cleaned bolt and (c) Insertion of the fitting Teflon plate

In contrary to the small-scale tests, for which the bolt had to be removable, it was completely fixed and welded to the steel beam. The principle of rings, defining the silicone thickness, was thus not needed. The diameter of the steel stud, replacing this bolt, was constant of 30mm and its height was of 18mm to be at the same level than the glass plate. A chamfer of 3mm was machined at their bottoms to create a weld of the same thickness, see Fig. 8.26. To adapt the M8 bolts closing the complete system and restraining the silicone, central holes were drilled on each stud. These elements were then cleaned to adapt predrilled Teflon plates closely fitting the bolts diameters. Three plates 3mm thick were employed over the whole beam, as it can be observed on Fig. 8.27



**Figure 8.27-** Repartition of the three Teflon plates fitting the welded steel studs of the mechanical adhesive connection



As the side of the studs had to be bonded to the glass plate holes, they were cleaned with abrasive paper and cleaned with solvent. The application of the primer was realized just before the injection of the silicone to prevent its complete drying.

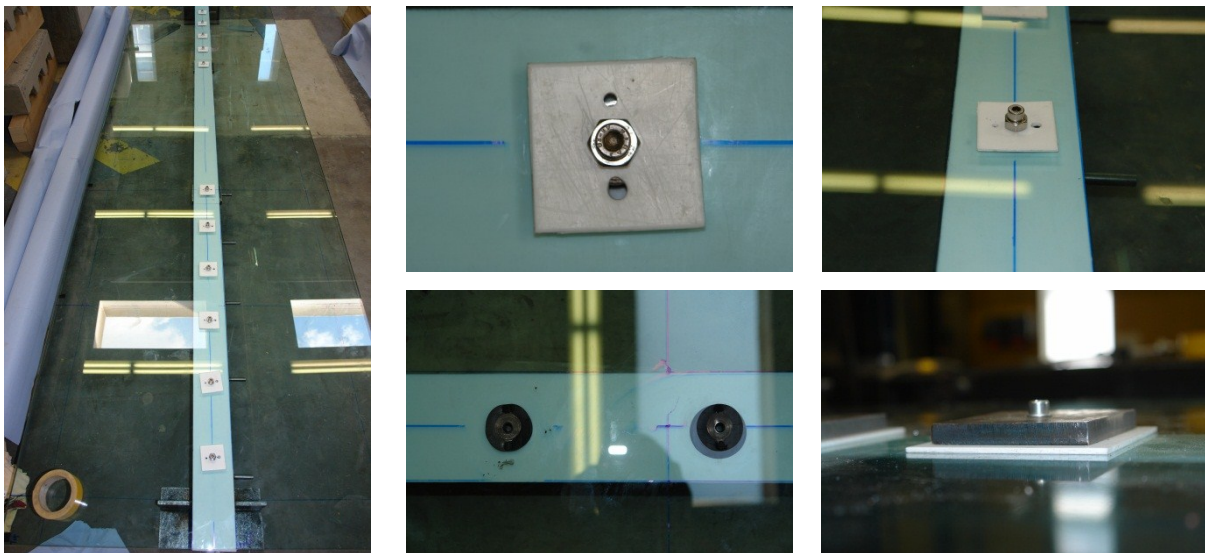
### Glass preparations

The glass employed for the mechanical adhesive composite beam was fully tempered (FTG) and the inherent prestress had to be measured in several positions, as the holes could slightly influence these data. The dimensions of the holes were controlled with a caliper but did not constitute fundamental information, in contrary to the values of the compression zone of the silicone for the final assembly bolt inserted. The length and width were simply controlled with tape measure and the thickness with the help of a digital caliper. All these recorded data were gathered in Appendix G.2.

No mechanical process was realized on the glass plate and the addition of the surrounding elements was performed after the silicone injection. Before proceeding to the latter, the rim of the glass holes were cleaned with solvent and as for the beam, the primer was applied just before this operation.

### Assembly

For the realization of the assembly, the steel beams were disposed on the floor and their horizontal positions were obtained by inserting some steel wedges. On the steel beam was adapted the first layer in Teflon as exposed on Fig. 8.27. Then, the glass plate was positioned, tin side towards the bottom, and centered on the steel beam. During this operation, the remaining gap between the studs and the glass holes were visually controlled. At each stud was tightly screwed a Teflon plate of small dimensions for the injection of the silicone, see Fig. 8.28. A large hole was drilled on one side of these plates and a small one diametrically opposed. The larger one was used for the injection of the silicone and the small one for the evacuation of the air. The horizontality of the glass plate was checked after the injection and readjusted if necessary with weights. The silicone cured during 24 hours at ambient temperature and humidity. With the disposed Teflon plate, no shielding against UV-light was undertaken.



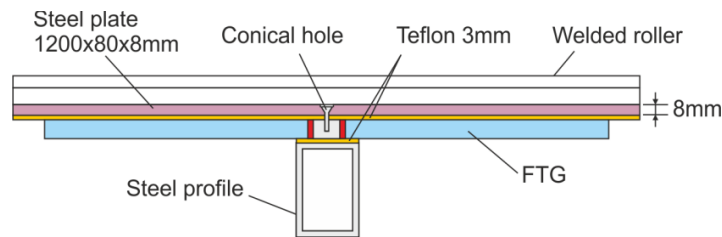
**Figure 8.28-** Steps leading to the injection of the silicone and to the final assembly of the mechanical adhesive connection

Once the complete curing was achieved the temporary Teflon plates were removed and the silicone dimensions in the compressive zone measured with a digital caliper. These information were recorded in Appendix G.2. Before conducting the tests, the final covering Teflon plates of 3mm and steel plates of 12mm were disposed at each hole. In contrary to the Teflon plates employed for the injection, the latter perfectly covered and restrained the silicone. All the M8 bolts fixing the layering system were screwed with the same torque of 10N/m just before the installation of the composite beam in the test frame.

### 8.4.2.2 Description of the tests

#### Test layout

The large-scale tests on the mechanical adhesive composite beams were all conducted on the same 630kN INSTRON mobile hydraulic press than the linear adhesive composite beams. The global test set-up fixed to the main frame supporting the piston was conserved, see Fig. 7.17. The lower part of the tested beams rested on rollers of 30mm of diameter allowing the rotations. The rollers were inserted in U-profiles attached to the steel frames and so could not displace. For the upper part, the two load application points were achieved by fixing on the load distribution beam fixed to the kneecap of the piston, two load introduction beams. In-between were installed two force sensors of 200kN. The welded rollers of the upper system were kept but the Neoprene spacers were replaced by another system, see Fig. 8.29.



**Figure 8.29-** Test set-up for the large-scale mechanical adhesive beam tests and details of the system under the load

With the design of the composite beam, one stud was always situated under each load application point. Hence, the load could not be directly introduced with the previous configuration employed for the linear adhesive beam due to the presence of a M8 bolt, i.e. with the roller welded on the rigid steel bar. Therefore, at this specific location, the covering system composed by the covering steel plate and M8 bolt was changed. A thinner steel plate of 1200x80x8mm, longer than the glass width, replaced the standard covering piece. In this steel plate was drilled a conical hole allowing the insertion of a bolt of identical geometry. The head of the conical bolt was 1mm deeper than the surface of the long steel plate, in order to apply uniformly the load and not directly through the bolt. A second Teflon layer covering the width of the glass plate was inserted under this steel plate to prevent contact.

#### Instrumentation

The total applied force was measured by the external sensor of 630kN installed on the piston. As the load was introduced on two different positions on the beam, a control of each transmitter force was achieved with two sensors of 200kN situated between the load introduction and distribution beams, see Fig. 7.17. The total displacement, assimilated to the deflection of the beam at 1100 and 2200mm, was recorded by the internal sensor of the machine. To approximate the deflection of the beam along the length, two others vertical sensors were positioned, i.e. one of 100mm was installed at mid-span and one of 50mm at one sixth of the tested length, see Fig. 7.18.

The sliding at the steel-glass interface was obtained with the help of six 20mm displacements sensors. While five were equally spaced on the first portion of the beam ( $x \leq 1100\text{mm}$ ), the last one was installed at the other extremity to control the uniformity of the rigidity of the two sections subjected to the shear forces. Finally, the last employed sensor measured the vertical dissociation of the glass plate at the first extremity of the beam.

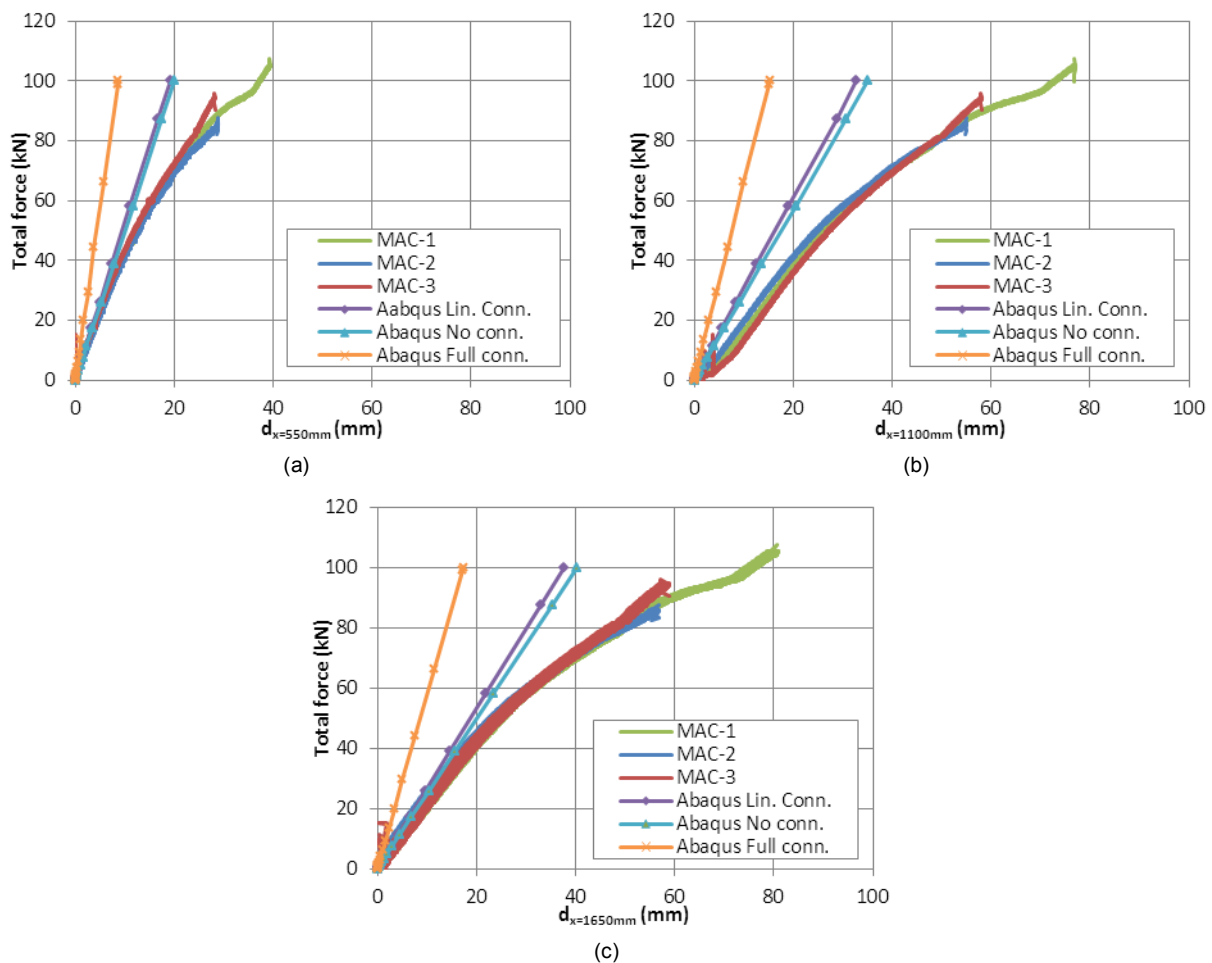
The elongations in the glass plate were also assessed in six positions, i.e. three strain gauges were put under the load application line and three at the middle of the plate. The positions of these strain gauges were identical to the ones of the previous composite beam, see Fig. 7.19.

### 8.4.2.3 Tests results

The three large-scale tests were carried out in displacement control until glass failure, associated to a contact between on bolt and the hole of the glass. In contrary to the linear adhesive composite beam, the total deflections of the three experiments were lower than the displacement of the machine, which allowed conducting the experiments with one loading only. The principal results were exposed in the following paragraphs.

#### Force-deflection curves

For the three composite beams, the deflection at the three positions detailed on Fig. 7.18 were plotted against the total applied force, see the MAC curves of Fig. 8.30. As it could have been remarked, the experimental force-deflection diagrams were well matched independently of the regard position, indicating that the rigidities of the three manufactured beams were equivalent. Hence, the small variations in silicone thickness observed in the compression zone did not influent on the behaviour of the beams. Only one test presented a higher forces and displacements, i.e. the first beam MAC-1 which presented at the extremities the larger silicone thickness.



**Figure 8.30-** Total applied force vs. deflection at (a) 550mm, (b) 1100mm and (c) 1650mm – Mechanical adhesive connection

As the theoretical or numerical methods of evaluation of such composite beams provided identical results, only one was conserved as a reference, i.e. the numerical analysis employing the fully elastic definition of the rigidity. Except for the displacements under the load application point at 1100mm, the



very first portion of the curves were similar, indicating that for loads up to 50kN the were correctly represented by the numerical model. The effect under the load application was certainly engendered by a local compression of the Teflon plates, as the measurement was made by the machine and not an external displacement sensor positioned under the beam. However, even if the modifications on the steel beam were identical between the linear adhesive and the mechanical-adhesive composite beams, the softening of the experimental results was less consequent.

For the maximum applied load, the bolts at the extremities were subjected to important sliding at the interface and the breakage of the silicone described for the small-scale tests occurred. The failures of the beams were due to the contact between the steel bolt and the glass plate, as showed on Fig. 8.31. A V-pattern was observed with the remaining fragments of the glass confirming the contact. At the opposite, under the load application points, where the sliding was less important, the silicone broke but the bolt did not came in contact with the glass, see Fig.8.31 (c).

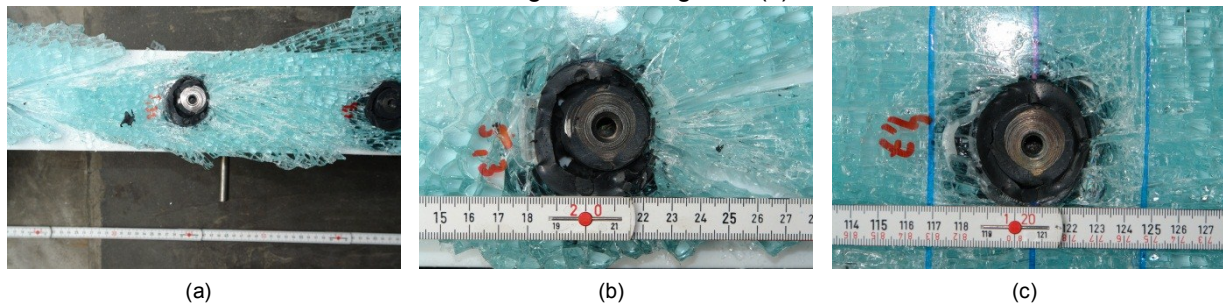


Figure 8.31- (a) V-crack in the glass at (b) the bolt-glass contact; (c) Silicone failure under the load application point

### Force-sliding curves

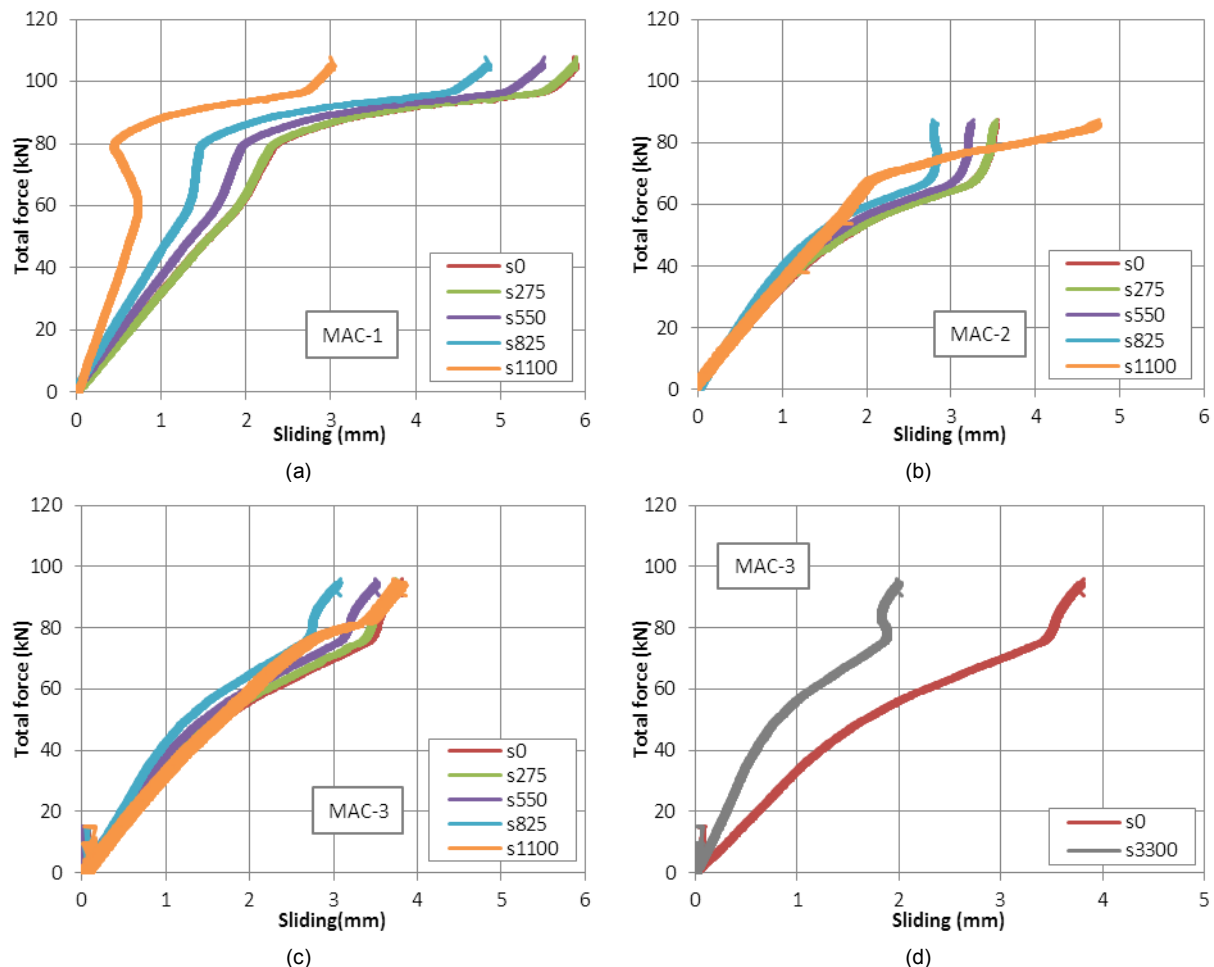


Figure 8.32- Total force versus sliding at the interface for (a) MAC-1, (b) MAC-2 and (c) MAC-3; (d) Sliding at the extremities

As for the theoretical and numerical results the sliding occurring at the interface was experimentally investigated. The total applied force was plotted, for each mechanical-adhesive composite beam, in function of the five sliding values recorded on the first part of the beam, see Fig. 8.32. The sliding form was different for the three tests but also for the different positions. For the first composite beam MAC-1, the higher displacements were found at the extremity of the beam, while the lower near the center and the load application location. On these curves the sliding decreased after a force of 60kN, which was possibly due to the jointing of the silicone adhesive failures at 45° around the bolt, case (i) of Fig. 8.16. After the horizontal peak, the sliding brutally increased, as the silicone was pushed on the side by the bolt until complete silicone failure, case (ii). The last increased of stiffness at 100kN should be induced by the steel to glass contact, case (iii). For the composite beam MAC-2 and MAC-3, the failure type (ii) of the silicone was certainly instantaneous as the global sliding behaviour was different. The data recorded for the bolt under the load application point were non-relevant for these both beams. As for the linear adhesive beam, sliding differences were also noticed according to the first or last portion of the beam. These differences were explained by the eccentricities generated by the manufacturing.

To compare the theory/numerical simulations to the experiments, a total force of 60kN was considered as it corresponded to the force plasticizing the steel beam alone for this 4-point bending test. The sliding values were plotted according to the length of the beam on Fig. 8.33 (a). As remarked, on the first portion of the beams, the experimental relative displacements were higher than the one estimated by the Lebet method. However, on the other portion, the sliding values were lower than the estimation. The proximity of these values was however better than for the linear adhesive connection.

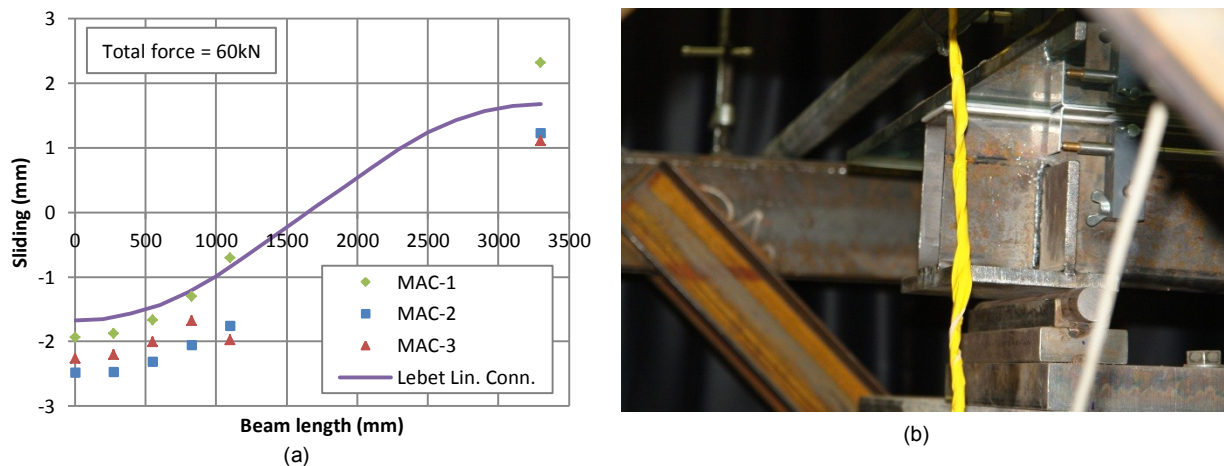


Figure 8.33- (a) Sliding along the beam length for a force of 60kN and (b) Relative displacement at the end of the beam

### Force-opening curves

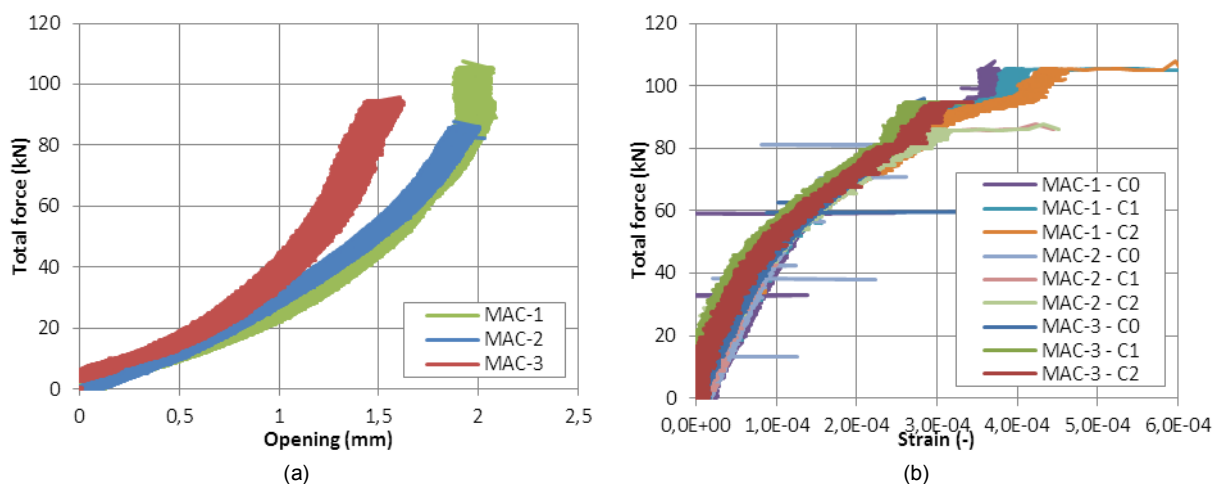
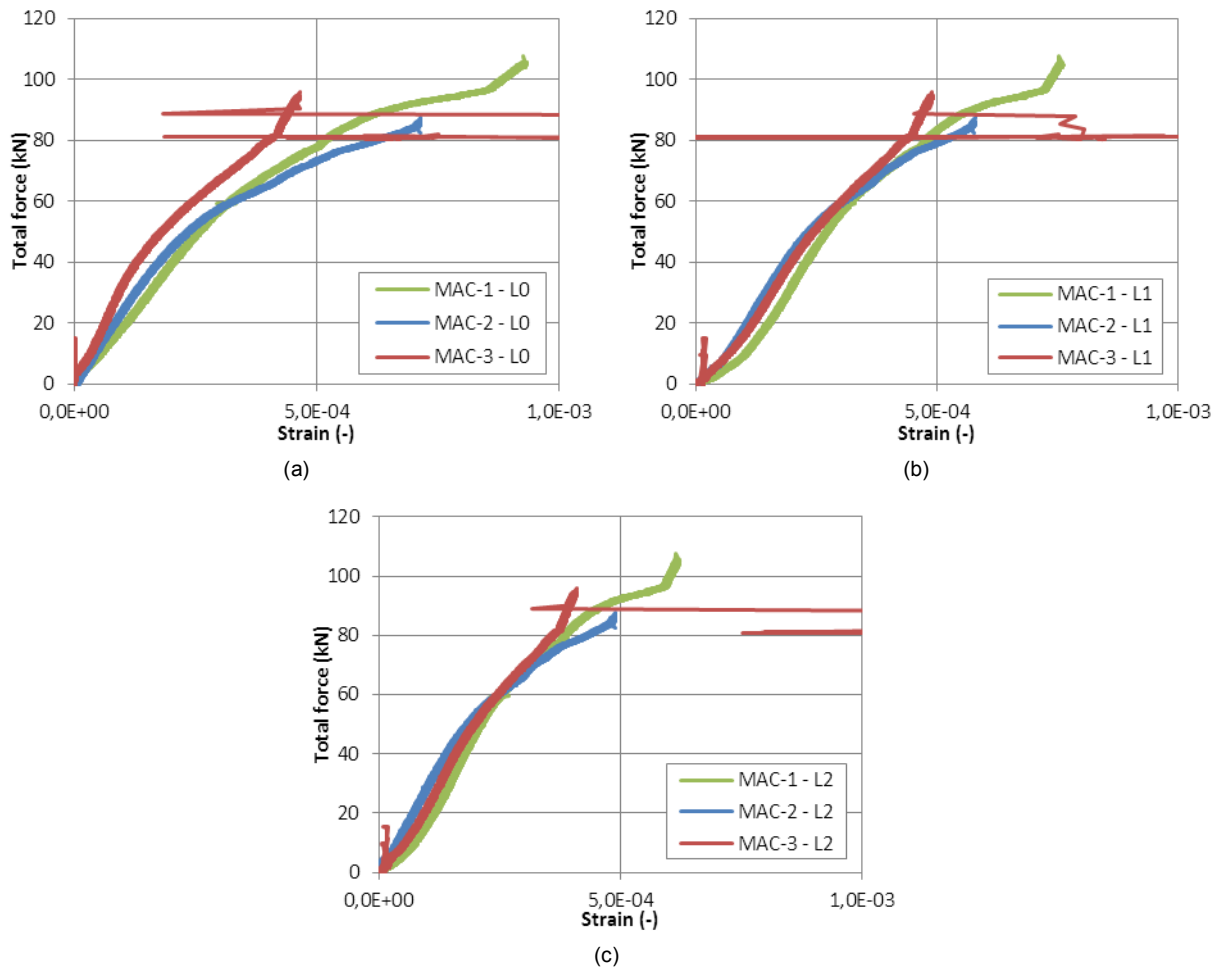


Figure 8.34- (a) Force versus opening displacements for the 3 beams and (b) Force versus strains at the center of the glass

The values recorded by the last displacement sensors were also used to plot total applied force versus opening displacements curves for the three composite beams, see Fig. 8.34. All the curves showed a positive displacement, meaning that the glass plate moved downwards in the direction of the steel beam and not at the opposite as expected. This behaviour could have been due to the displacements and rotations of the beam at the support which were both combined. Hence, the measurement of this sensor was not relevant and a control of the rotation would have been appreciated.

### Force-glass elongations curves

The strains data, measured in six positions were split according to their positions, i.e. either under the load application point or at the center of the beam. The total force- strain diagrams were plotted on Fig. 8.34 (b) for the central position for the three beams and on Fig. 8.35 for the load position. As for the linear adhesive connection, the stresses in the center of the glass beam were independent of the regarded width, meaning that they were uniform along the glass width. Further, as for the deflections, they were superposed for the three beams. For the strains at the load application point, a distinction was made according to the proximity to the steel beam. As remarked, all the manufactured beams exposed the same diagrams with almost no dispersion. The horizontal peaks were came from the acquisition and were not to be considered. By comparing the three diagrams for a same force, e.g. for 80kN, it was noticed that the strains were equivalent, i.e. about 0,0005. Hence, in contrary to the adhesive connection, the elongations along the glass width under the load position were independent on their location. This proved that the differences obtained for the mechanical adhesive composite beams were due to a more important transfer of the load at the steel beam. For the actual mechanical adhesive composite beam this uniformity was acquired with the modification of the load introduction at a steel bolt as detailed in section 8.4.2.2.



**Figure 8.35-** Total applied force versus strains under the load position at (a) 150mm, (b) 300mm and (c) 420mm from the edge

## 8.5 SUMMARY AND CONCLUSION

In this chapter, the dimensions of the envisaged mechanical-adhesive composite beam as well as its manufacture were detailed. Compared to the linear adhesive connection, even if more operations had to be made on the steel beams with the welding of the studs and on the glass plate with the drilling of holes, the final assembly was easier to performed with the silicone injection procedure. Additionally, a smaller quantity of silicone was necessary.

To assess the global behaviour of this composite beam with the existing theory and more particularly with the Lebet theory, the analysis of one holed system was investigated with the help of the numerical simulations and of small-scale tests. This configuration was based on the assumption that a plate connected with two holes presented the same stiffness than two one holed glass plates. The general dimensions given to this system were deduced from the existing theory to neglect the influence of the edges or of the proximity of another hole on the final rigidity. The force-displacement diagrams were first determined with numerical simulations. However, even if different techniques were employed with an implicit and an explicit solving, none of e calculations could reach the end due to the apparition of too large distortions of the silicone at the bolt. Therefore, small-scale experiments were conducted to calculate the stiffness of one holed assembly. No dispersion was found for the envisaged silicone thickness of 5mm, which allowed calculating an averaged stiffness of the first linear portion of the force-displacement curves. This stiffness was lower than the initial stiffness get from the numerical results and different geometry imperfections, such as eccentricity or reduction of surfaces, were modeled to assess their influences. However, none were relevant and could explain the large gap observed. The only remaining possibility arose from the manufacturing method, for which a simple pouring was performed instead of an injection as made for the evaluation of the volumetric factor of the developed material. Same force-displacement diagrams could be obtained with the simulations for a reduction of 60% of the volumetric factor  $K$ .

With the acquired stiffness from the small-scale tests, the Lebet theory and numerical simulations were undertaken on the regarded dimensions of the mechanical-adhesive connection. From both, analytical and numerical methods, similar results were observed and thus an approximation of a composite beam possessing other dimensions, but the same silicone thickness of 5mm could be made with one of these procedures. The envisaged beam was investigated with both and a comparison to the fully and unconnected system showed the degree of connection, which was identical to the one of the linear adhesive composite beam. Nevertheless, some improvements could be operated to increase the global rigidity and end with less displacements, as for example reducing the silicone thickness to 3mm or increasing the number of studs. The linear adhesive connection, dependent on the flange of the steel beam, could not be improved as the silicone thickness could not be reduce to a dimension inferior to 3mm.

To valid the theories, three large-scale experiments on the final mechanical adhesive beams were conducted. The force-deflection diagrams were relatively close but not perfectly superposed. The same observation was made with the sliding diagrams along the length. In both case, the values provided by the real tests were larger than the theoretical ones. This, as for the linear adhesive beam, was certainly due to the modifications operated on the steel beams by the cutting of the upper part for the insertion of a more rigid welded plate. Therefore, to ensure of this assumption, some tests should be first done on steel beams alone to determine their properties and then on modified steel beams for comparison. Furthermore, the steel properties, especially for the plasticity, should also be obtained with dog-bone samples. Nevertheless, better correspondence was found between the real mechanical adhesive beams and the theory than between the linear adhesive beam and the theory. This could be also induced by the less quantity of silicone used.

## 9. CONCLUSION AND OUTLOOK

### 9.1 CONCLUSION

Glass linear properties and recent researches on its structural stability as well as existing assemblies, involving steel material and more particularly steel beam, were detailed in ([Chapter 2](#)). The glass exposed important in-plane capacity and an elevated compressive strength. These characteristics were not considered in the actual steel to glass connections, for which the glass was essentially used as a tertiary element, whose role was to act as a non-structural barrier between outdoor and indoor conditions. In this configuration, its failure did not affect the global supporting structure.

To plainly use the intrinsic properties of glass element, two types of connection were envisaged for the realization of a steel-glass composite beam. Both methods of connection, presented in ([Chapter 3](#)), were established by analogy to the existing steel-concrete beams, in which the upper slab/plate acted in compression, while the lower steel beam acted in tension. To achieve such distribution of normal stress in the different components, the rigidity of the connection mean was crucial. A high rigidity would allow transferring important loads between the glass and the steel, but could also lead to a premature glass failure in case of important in-plane actions, such as the ones induced by the temperature variations. The two selected connections were estimated sufficiently rigid to transfer shear loading and also sufficiently soft to accommodate for the difference in thermal expansion coefficients. A first linear adhesive connection, using either a well-known certified silicone or a stiff UV-acrylic, was advanced. The contact zone of the glass plate and the steel beam had to be fully adhesively bonded to transfer the shear forces between the adherents through the adhesive only. A second connection, refereed as mechanical-adhesive connection in reason of the use of adhesive but also welded steel bolts, was also proposed. In the latter, the shear forces were mainly transferred to the steel beam by compression of the adhesive, fitting the gap existing between the glass holes and the bolts. An infill silicone adhesive was specifically chosen for this assembly. Further, to prevent its squeezing out and to increase the rigidity, the adhesive was restrained in all direction by covering stiff plates.

The two anticipated connections necessitated the use of specific adhesives, i.e. a silicone elastomer and an UV-acrylic thermoset. Even if the principal characteristic values of these two adhesives, i.e. tensile strength, shear strength and elongations at failure, were provided by the manufacturers, no proper constitutive material laws existed. Therefore, several experiments were carried out in order to develop models implementable in finite element software. Four experiments were conducted on silicone elastomer and three experiments on the UV-acrylic. These tests were all detailed in ([Chapter 4](#)). For the elastomer, three isochoric tests in uniaxial tension, compression and shear were performed and were also completed by oedometric tests characterizing the slight compressibility exposed by this material. Except for the last volumetric tests, the behaviour of the silicone was found non-linear up to large strains before returning to the original dimensions after unloading. The Mullins effect inherent to the elastomer was also accounted with the help of cyclic tests, as well as the evolution of the behaviour under long-term relaxation tests. The general properties of the silicone were found independent of the loading rate and of the environmental conditions, i.e. temperature, humidity and UV-light. The acrylic was tested in uniaxial tension and under shear with two different layouts. Its stress-strain behaviour was found strongly dependent on the loading rate for the two types of action, i.e. higher rates generated a stiffer behaviour. However, even if the instantaneous properties of the thermoset were better than the one of the elastomer, they strongly decreased under long-term loading. This loss was so important that the acrylic could not be employed in connection subjected to long-term loading, such as the proposed composite beam relying on a full linear adhesive connection.

Based on the different properties established for the silicone with the previous experiments, a three-dimensional hyperelastic constitutive material law was developed in ([Chapter 5](#)). For this model, the isochoric and volumetric data were divided in two, to provide strain energy functions accounting for

both behaviours. While a new isochoric functions was proposed to include the strong non-linearity occurring under very low strains, an existing model was employed for the volumetric function. The assessment of all the isochoric coefficients was done by fitting the law to the experimental data with the nonlinear least square method of Levenberg-Maquardt. For the UV-acrylic, two one-dimensional models were considered to respectively represent the uniaxial tension and the shear behaviour. While the existing Ramberg-Osgood proved to be efficient for the tension, a new law, based on the one established for the silicone, was proposed for the shear. The loading rate dependencies were accounted by expressing the different coefficients of these two laws in function of the rate. The prediction of the acrylic behaviour under a chosen rate could thus be made.

The developed material laws were implemented in Abaqus software by writing and compiling user-subroutines. Due to the large expected deformations of silicone, important meshes distortions were foreseen and a full use of the two implicit and explicit solving methods, offered by the software, were regarded (Chapter 6). The insertion of the user-subroutine was dependent on the method of resolution and therefore a UHYPER subroutine and a VUMAT subroutine were respectively written for the implicit and the explicit procedures. The two subroutines were tested by modeling the conducted isochoric tension, compression and shear tests, but also the volumetric oedometric experiments. Both were thus validated with this methodology and could henceforth be employed to model complex joints involving silicone. For the acrylic, only the shear behaviour was controlled by comparing the tests results to numerical simulations achieved by modifying the form of the UHYPER subroutine coefficients. The rate-dependency was accounted by adjusting the material law parameters. The different stress-strain experiments were well represented by this method.

The first envisaged and investigated composite beam was the linear adhesive connection, as the material properties of all the elements were known. The partial connection theory developed by Lebet and linear numerical simulations of the whole system were compared and identical stiffnesses were observed (Chapter 7). The latters were closer to the one of an unconnected steel-glass beam than to the stiffness of a fully connected assembly. However, the stress distribution in the most critical section showed that the glass plate, of the envisaged connection, was less subjected to tensile stresses. The conducted large-scale tests all demonstrated lower stiffnesses than the ones attained with numerical and theoretical analyses. This difference was explained by the modifications made on the upper part of the steel beams in order to prevent instabilities. Further tests should be carried out on modified and unmodified steel beams alone to fully validate this assumption. Other complete linear bonded systems with no modification should also be tested to confirm the theory.

The large-scale experiments on the mechanical-adhesive composite beams were preceded by first evaluations of one holed systems. Numerical simulations were performed on this complex system and none of them, including different techniques such as distortion control or ALE method, reached the total time period. The premature ends were imposed by the too large distortions of the mesh elements attached to the steel bolt. Therefore, small-scale experiments on identical system were made allowing the determination of the connection rigidity. This stiffness was incorporated in the Lebet theory to pre-evaluate the composite beam behaviour and in numerical simulations as springs. The analytical and numerical results were superposed in (Chapter 8). Tests were carried out on three beams and a lower stiffness, for the elastic part of the force-deflection curve, was found in comparison to the ones arising from the two last approaches. As for the linear adhesive composite beam, this was attributed to the modifications operated on the steel beam.

With the actual design of the linear adhesive and mechanical-adhesive composite beams, the degrees of connection were almost identical. Both exposed rigidities similar to the one of an unconnected steel-glass beam. However, the tensile stresses in the glass were reduced by about one third compared to the latter. While some improvements could be done on the mechanical-adhesive connection by reducing the silicone thickness or increasing the number of bolts, no better results could be achieved with the linear adhesive one as the silicone thickness could not be lowered to values inferior to 3mm.

## 9.2 OUTLOOK

The different unsolved points encountered during the previous chapters were gathered in the following paragraphs.

### **Peak stress problem**

The stress peak problem arising during the numerical simulations was not completely demonstrated as a singularity appearing only in the calculations, even if the existing theories and modeling let suppose that this assumption was correct. Hence, further tests should be carried out on other geometries, such as the butt-bonded hollow cylinder described in the DIN EN 14869-1. In this system, no discontinuity occurred in the silicone, which should be uniformly distributed over the whole tested area. The comparison of the strength obtained with the double lap-joint shear tests and the one achieved with the latter method should prove the fact the peaks did not appear in reality.

### **Small-scale beam tests**

As only two silicone thicknesses, 5mm and 10mm, were investigated with the small-scale one holed system of the mechanical-adhesive connection, no prediction concerning smaller thicknesses could have been done. Numerical simulations could only give a first approximation, but only tests would allow ensuring of the obtained rigidities. At least two other thicknesses should be regarded, such as 3mm and 8mm.

### **Large-scale beam tests**

As the large scale-beam tests were influenced by the operations made on the steel beams, another test series should be carried out with beam presenting no modifications. A comparison to the results provided by theories and to the results achieved with numerical calculations, including the non-linear behaviour of steel, would allow validating these last two methods. Then, some parametric studies could be undertaken by varying several parameters, such as the silicone thickness of the linear adhesive connection or the number of bolts for the mechanical adhesive connections. Some design rules and limits could then be extracted.

### **Laminated glass plates**

For all the conducted experiments, only thick monolithic glass plates were used. However, this did not correspond to a real case, especially for accessible glazing necessitating at least three glass plates. The changes induced by this increase of thickness should also be examined with experiments and numerical simulations. In addition, the laminated plate stress distribution could also be changed by the connection.





## REFERENCES

### Chapter 2

- [2.1] ZARZYCKI J. *Les verres à l'état vitreux*, Masson, France 1982.
- [2.2] EN 572-1:2012, *Glass in building – Basic soda lime silicate glass products – Part 1: Definitions and general physical and mechanical properties*, European Standard, 2012.
- [2.3] EN 1748-1-1, *Glass in building - Special basic products - Borosilicate glasses - Part 1-1: Definitions and general physical and mechanical properties*, European Standard, 2012.
- [2.4] SEDLACEK G., BLANK K., LAUFS W., GÜSGEN J. *Glas im Konstruktiven Ingenieurbau*, Ernst & Sohn, Berlin, 1999.
- [2.5] HALDIMANN M., LUIBLE A., OVEREND M. *Structural Use of Glass*, IABSE, ETH Zürich, 2008.
- [2.6] EN 1288-5, *Determination of the bending strength of glass – Part 5: Coaxial double ring test on flat specimens with small test surface areas*, European Standard, 2000.
- [2.7] EN 1288-3, *Determination of the bending strength of glass – Part 3: Test with specimen supported at two points (four point bending)*, European Standard, 2000.
- [2.8] MENKENHAGEN J. *Bautabellen für Ingenieure – Glas im konstruktiven Ingenieurbau*, Schneider Auflage 17, p. 7-38, Werner Verlag, 2006.
- [2.9] TRLV, *Technische Regeln für die Verwendung von linienförmig gelagerten Verglasungen*, Germany, 2006.
- [2.10] DIN 1249-10, *Flachglas im Bauwesen – Teil 10: Chemische und physikalische Eigenschaften*, German Standard, 1990.
- [2.11] FINK A. *Ein Beitrag zum Einsatz von Floatglas als dauerhaft tragender Konstruktionswerkstoff im Bauwesen*, Universität Darmstadt, Darmstadt, 2000.
- [2.12] LUIBLE A. *Stabilität von Tragelementen aus Glas*, EPFL, Lausanne, 2004.
- [2.13] DIN EN 673, *Determination of thermal transmittance (U value) - Calculation method*, European Standard, 2011.
- [2.14] ACHILLES A., NAVRATIL D. *Construire en verre*, Birkhäuser Basics, France, 2008.
- [2.15] EN 12600, *Glass in building - Pendulum tests - Impact test method and classification for flat glass*, European Standard, 2003.
- [2.16] EN 12150-1, *Glass in building - Thermally toughened soda lime silicate safety glass - Part 1: Definition and description*, European Standard, 2012.
- [2.17] EN 12150-2, *Glass in building - Thermally toughened soda lime silicate safety glass - Part 2: Evaluation of conformity*, European Standard, 2005.

- [2.18] EN 14179-1, *Glass in building - Heat soaked thermally toughened soda lime silicate safety glass - Part 1: Definition and description*, European Standard, 2005.
- [2.19] EN 1863-1, *Glass in building - Heat strengthened soda lime silicate glass - Part 1: Definition and description*, European Standard, 2000.
- [2.20] EN 1863-2, *Glass in building - Heat strengthened soda lime silicate glass - Part 2: Evaluation of conformity/Product standard*, European Standard, 2004.
- [2.21] EN 12337-1, *Glass in building - Chemically strengthened soda lime silicate glass. Part1: Definition and description*, European Standard, 2000.
- [2.22] EN 12337-2, *Glass in building - Chemically strengthened soda lime silicate glass. Part2: Evaluation of conformity*, European Standard, 2004.
- [2.23] ISO 12543-1, *Glass in building - Laminated glass and laminated safety glass – Part 1: Definitions and description of component parts*, European Standard, 2008.
- [2.24] ISO 12543-2, *Glass in building - Laminated glass and laminated safety glass – Part 2: Laminated safety glass*, European Standard, 2008.
- [2.25] EN 1279-1, *Glass in building - Insulating glass units – Part 1: Generalities, dimensional tolerances and rules for the system description*, European Standard, 2004.
- [2.26] EN 1279-5, *Glass in building - Insulating glass units – Part 5: Evaluation of conformity*, European Standard, 2005.
- [2.27] CSTB 3488, *Vitrages extérieurs collés – Cahier de prescriptions techniques – Annexe B*, Centre Scientifique et Technique du Bâtiment, France, 2003.
- [2.28] OSAMU A. *Vacuum Glazing for Transparent Thermal Insulating Material*, Nippon Sheet Glass Co. Ltd, Glass Proceeding Days 2003, p. 623-625.
- [2.29] EN 1991, *Eurocode 1: Einwirkungen auf Tragwerke*, European Standard, 2002.
- [2.30] EN 1990, *Eurocode: Grundlagen der Tragwerksplanung*, European Standard, 2002.
- [2.31] TRLV 2006, *Technische Regeln für die Verwendung von linienförmig gelagerten Verglasungen*, German technical rule, 2006.
- [2.32] TRAV 2003, *Technische Regeln für die Verwendung von absturzsichernden Verglasungen*, German technical rule, 2003.
- [2.33] DIN 1055-100, *Einwirkungen auf Tragwerke - Teil 100: Grundlagen der Tragwerksplanung - Sicherheitskonzept und Bemessungsregeln*, German Standard, 2010.
- [2.34] FELDMEIER F. *Klimabelastung und Lastverteilung bei Mehrscheiben-Isolierglas*, Stahlbau 75, Heft 6, p. 467-478, Ernst & Sohn, 2006.
- [2.35] DIN 18008-1, *Glas im Bauwesen – Bemessungs- und Konstruktionsregeln – Teil 1: Begriffe und allgemeine Grundlagen*, German Standard, 2010.

- [2.36] prEN 13474-3, *Glass in building - Determination of the strength of glass panes - Part 3: General method of calculation and determination of strength of glass by testing*, European draft Standard, 2009.
- [2.37] PANAIT A. *Étude expérimentale et numérique des problèmes de contact unilatéral et de frottement sec dans les assemblages verriers*, Dissertation, Cahier 3519 - Mars 2005.
- [2.38] BRENDLER S., SCHNEIDER S. *Bemessung von punktgelagerten Verglasungen mit verifizierten Finite-Elementen-Modellen*, DIBt Mitteilungen 6/2004, p. 196-202.
- [2.39] TRPV 2006, *Technische Regeln für die Bemessung und die Ausführung punktförmig gelagerter Verglasungen*, German technical rule, 2006.
- [2.40] SIEBERT B. *Beitrag zur Berechnung punktgehaltener Gläser*, Dissertation, TU-München, München, 2004.
- [2.41] KASPER R. *Berechnungskonzept für die Bemessung von punktförmig gelagerter Glasscheiben*, Stahlbau 75 (2006), Heft 6, p. 454-461, Ernst & Sohn Verlag, Berlin, 2006.
- [2.42] Z-70.2-90, *Punktgehaltene Verglasung mit Glassline-Tellerhaltern PH705, PH707, PH791, PH793, PH794, PH800, PH103, PH104 und PH106*, Deutsches Institut für Bautechnik, 2009.
- [2.43] BEYER J. *Ein Beitrag zum Bemessungskonzept für punktgestützte Glastafeln*, Dissertation, TU-Darmstadt, Institut für Statik, Darmstadt, 2007.
- [2.44] ETAG 002, *Structural Sealant Glazing Systems (SSG)*, EOTA, January, 2002.
- [2.45] ASTM C1401, *Standard Guide for Structural Sealant Glazing*, ASTM International, 2002.
- [2.46] SIGURDE S. *TSSA - Transparent Structural Silicone Adhesive - a next generation product*, COST Action TU0905 Workshop Meeting, February, 2011.
- [2.47] FELDMANN M., ABELN B., BAITINGER M. *INNOGLAST-Project: Development of innovative steel-glass-structures in respect to structural and architectural design*, RWTH-Aachen, Germany, 2010.
- [2.48] LOUTER C. *Fragile yet Ductile - Structural Aspects of Reinforced Glass Beams*, Dissertation, Faculty of Architecture, Delft University of Technology, Netherlands, April 2011.
- [2.49] CARVALHO P. *Connecting Through Reinforcement - Experimental Analysis of a Glass Connection Using Perforated Steel Plates*, Challenging Glass Conference 3, Delft, Netherlands, June 2012.
- [2.50] WELLER B. et al. *Kleben im konstruktiven Glasbau*, Stahlbau Kalender 2011.
- [2.51] PETRIE M. *Handbook of adhesives and sealants*, Mc Graw-Hill Handbook, 1999.
- [2.52] AMIN AFMS. *Hyperelasticity Model for Finite Element Analysis of Natural and High Damping Rubbers in Compression and Shear*. Journal of Engineering Mechanics, Vol. 132, No. 1, January 2006, pp. 54-64.
- [2.53] G. L. BRADLEY, P.C. CHANG, G.B. McKenna. *Rubber modeling using uniaxial test data*, J. Appl. Polym. Sci. 81 (2001) 837-848.

- [2.54] C. MIEHE. *Discontinuous and continuous damage evolution in Ogden-type large-strain elastic materials*. Eur. J. Mech. A/Solids, 14(5):697–720, 1995.
- [2.55] BUECHE, F. (1961). *Mullins effect and rubber–filler interaction*. J. Appl. Polym. Sci., 5: 271–281. doi: 10.1002/app.1961.070051504.
- [2.56] OGDEN RW. *Large deformation isotropic elasticity – on the correlation of theory and experiment for incompressible rubber solids*. Proceedings of the Royal Society of London. Series A, Mathematical and Physical Sciences, Volume 328, Issue 1575, pp. 567-583.
- [2.57] WANG MC, GUTH E. *Statistical Theory of Networks of Non-Gaussian Flexible Chains*. J. Chem. Phys. 20, 1144 (1952); <http://dx.doi.org/10.1063/1.1700682>.
- [2.58] ARRUDA EM. *Characterization of the strain hardening response of amorphous polymers*, Dissertation, Massachusetts Institute of Technology, 1992.
- [2.59] FLORY PJ. *Thermodynamic relations for high elastic materials*. Trans. Faraday Soc., 1961, 57, p. 829-838.
- [2.60] SUSSMAN T., BATHE KJ. *A finite element formulation for nonlinear incompressible elastic and inelastic analysis*. Computer & Structures 26, 1987, 357-409.
- [2.61] SIMO, J.C., TAYLOR, R.L., PISTER, K.S. *Variational and projection methods for the volume constraint in finite deformation elastoplasticity*. Computational Methods in Applied Mechanics Engineering, 51, p. 177–208 (1985).
- [2.62] OGDEN, R.W. *Large deformation isotropic elasticity. On the correlation of theory and experiment for incompressible rubberlike solid*. Proceedings of the Royal Society of London A328, 1972, p. 567-583.
- [2.63] SIMO, J.C., MIEHE C. *Associative coupled thermoplasticity at finite strains: Formulation, numerical analysis and implementation*. Computer Methods in Applied Mechanics and Engineering 85, 1992, p. 273-310.
- [2.64] OGDEN, R. W., and D. G. ROXBURGH. *A Pseudo-Elastic Model for the Mullins Effect in Filled Rubber*, Proceedings of the Royal Society of London, Series A, vol. 455, p. 2861–2877, 1999.
- [2.65] ASTM D638, *Standard Test Method for Tensile Properties of Plastics*, ASTM International, 2010.
- [2.66] EN ISO 527-1, *Plastics - Determination of tensile properties - Part 1: General principles*, European Standard, 2012.
- [2.67] LITTELL, J., RUGGERI, C., GOLDBERG, R., ROBERTS, G., ARNOLD, W., BINIENDA, W. (2008). *Measurement of Epoxy Resin Tension, Compression, and Shear Stress–Strain Curves over a Wide Range of Strain Rates Using Small Test Specimens*. J. Aerosp. Eng. 21, SPECIAL ISSUE: Impact Mechanics of Composite Materials for Aerospace Application, p. 162–173.
- [2.68] CHIU WK., JONES R. *Unified constitutive model for thermoset adhesive, FM73*, International Journal of Adhesion and Adhesives, Volume 15, Issue 3, July 1995, p. 131–136.

- [2.69] ASTM D 2990, *Standard Test Methods for Tensile, Compressive, and Flexural Creep and Creep-Rupture of Plastics*, American Standard, 2009.
- [2.70] RAMBERG W., OSGOOD W. *Description of stress-strain curves by three parameters*, National Advisory Committee for Aeronautics (NASA), Technical Note No. 902, July 1943.
- [2.71] MCLELLAN DL (1969) Appl. Polym. Symp. 12, p 137.
- [2.72] RENIERI MP, HERAKOVICH CT, BRINSON HF. *Rate and time dependent behavior of structural adhesives*. Virginia Polytechnic Institute and State University, College of Engineering Report No. VPI-E-76-7, 1976.
- [2.73] RAMASWAMY VG. *A Constitutive Model for the Inelastic Multiaxial Cyclic Response of a Nickel Base Superalloy Rene 80*. University of Cincinnati. NASA Contractor Report 3998. 1986.
- [2.74] HAWARD RN., THACKRAY G. *The use of mathematical model to describe isothermal stress-strain curves in glassy thermoplastics*, Proc. Roy. Soc. A., vol. 302, p. 453-472, 1968.
- [2.75] BERGSTROM JS., BOYCE MC. *Constitutive Modeling of the Large Strains Time-Dependent Behavior of Elastomers*, J. Mech. Phys. Solids, Vol. 46, No. 5, pp. 931-954, 1998.
- [2.76] BERGSTROM JS., BOYCE MC. *Mechanical Behavior of Particle Filled Elastomers*, Rubber Chem. Technol., Vol. 72, pp. 633–656, 1999.
- [2.77] BERGSTROM JS., BOYCE MC. *Large-Strain Time-Dependent Behavior of Filler Elastomers*, Mechanics and Materials, Vol. 32, pp. 627–644, 2000.
- [2.78] BERGSTROM JS., BOYCE MC. *Constitutive Modeling of the Time-dependent and Cyclic Loading of Elastomers and Application to Soft Biological Tissues*, Mechanics of Materials, Vol. 33, pp. 523–530, 2001.

### Chapter 3

- [3.1] MOCIBOB D. *Glass Panel under Shear Loading – Use of Glass Envelopes in Building Stabilization*, Thèse No. 4185, Ecole Polytechnique fédérale de Lausanne, 2008.
- [3.2] DIN 18008-2, *Glass in Building - Design and construction rules - Part 2: Linearly supported glazings*, German Standard, 2010.
- [3.3] EN 1991-1-4, *Eurocode 1: Actions on structures - Part 1-4: General actions - Wind actions*, European Standard, 2010.
- [3.4] EN 1991-1-3, *Eurocode 1: Actions on structures - Part 1-3: General actions - Snow loads*, European Standard, 2010.
- [3.5] EN 1991-1-1, *Eurocode 1: Actions on structures - Part 1-1: General actions - Densities, self-weight, imposed loads for buildings*, European Standard, 2010.
- [3.6] SOBEK W. *Glass-steel connection using acrylate adhesives*, Challenging Glass, Conference on Architectural and Structural Applications of Glass, 2008.

## Chapter 4

- [4.1] HAGL A. *Silicone Bonded Point Supports – Behaviour under Cyclic Loading, Engineering Transparency*, Düsseldorf, Germany, 2010.
- [4.2] EN ISO 527-2, *Plastics - Determination of tensile properties - Part 2: Test conditions for moulding and extrusion plastics*, European Standard, 2012.
- [4.3] DIN ISO 23529, *Rubber - General procedures for preparing and conditioning test pieces for physical test methods*, German Standard, 2010.
- [4.4] EN ISO 11431, *Building construction - Jointing products - Determination of adhesion/cohesion properties of sealants after exposure to heat, water and artificial light through glass*, European Standard, 2002.
- [4.5] VIGIER MG. *Pratique des Plans d'Expériences - Méthologie Taguchi*, ISBN : 2-7081-0850-6, Les Editions d'Organisation, 1988.
- [4.6] KUHLMAYER M. *Statistische Auswertungsmethoden für Ingenieure: mit Praxisbeispielen*, Springer Verlag, ISBN-13: 978-3540410973, 2001.
- [4.7] BOUKAMEL A. *Modélisation Mécaniques et Numériques des Matériaux et Structures en Elastomères*, Mémoire d'Habilitation à Diriger des Recherches, Université de la Méditerranée, 2006.
- [4.8] HART-SMITH LJ. *Adhesive - Bonded Double-Lap Joint*, Technical Report, National Aeronautics and Space Administration (NASA), 1973.
- [4.9] ASTM D638, *Standard Test Method for Tensile Properties of Plastics*, American Standard, 2010.
- [4.10] ASTM D732, *Standard Test Method for Shear Strength of Plastics by Punch Tool*, American Standard, 2010.

## Chapter 5

- [5.1] OBATA Y., KAWABATA S., KAWAI H. *Mechanical properties of natural rubber vulcanizates in finite deformation*. J. Polym. Sci., A-28, p. 903–919, 1970.
- [5.2] KAWABATA S., KAWAI H. *Strain energy density functions of rubber vulcanizates from biaxial extension*. Adv. Polym. Sci., 24, p. 90-124, 1977.
- [5.3] MADSEN K., NIELSEN HB., TINGLEFF O. *Methods for Non-linear Least Square Problems*, Technical University of Denmark, p. 24-29, April 2004.

## Chapter 6

- [6.1] HART-SMITH LJ. *Adhesive - Bonded Double-Lap Joint*, Technical Report, National Aeronautics and Space Administration (NASA), p. 86-94, 1973.

- [6.2] TSAI MY., OPLINGER DW., MORTON, J. *Improved Theoretical Solutions for Adhesive Lap Joints*, Int. J. Solids Structures Vol. 35, No. 12, p. 1163-1185, 1998.
- [6.3] DIN EN 14869-1, *Structural adhesives - Determination of shear behaviour of structural bonds - Part 1: Torsion test method using butt-bonded hollow cylinders*, German Standard, 2011.

## **Chapter 8**

- [8.1] PILKEY WD., PILKEY DF. *Peterson's Stress Concentration Factors*, ISBN-13: 978-0470048245, Wiley, 3<sup>rd</sup> edition, 2008.





## LIST OF FIGURES

|                                                                                                                                         |    |
|-----------------------------------------------------------------------------------------------------------------------------------------|----|
| <b>Figure 1.1-</b> Greenhouses of (a) the Kew gardens palm house in London and (b) the Bicton gardens dating from the 19th century .... | 1  |
| <b>Figure 1.2-</b> Organization diagram of the thesis .....                                                                             | 4  |
| <b>Figure 2.0-</b> Organization chart of Chapter 2 .....                                                                                | 5  |
| <b>Figure 2.1-</b> Coaxial double ring tests - EN 1288-5 .....                                                                          | 8  |
| <b>Figure 2.2-</b> Four point bending test - EN 1288-3 .....                                                                            | 8  |
| <b>Figure 2.3-</b> Summary of the principal properties of glass employed in structural applications .....                               | 10 |
| <b>Figure 2.4-</b> Examples and compositions of monolithic, laminated and insulating glass units .....                                  | 12 |
| <b>Figure 2.5-</b> Summary of the current design methods for the glass elements .....                                                   | 14 |
| <b>Figure 2.6-</b> Mechanically and linearly supported glass façade – General and detailed view .....                                   | 20 |
| <b>Figure 2.7-</b> Mechanically and locally clamped fixation – General and detailed view .....                                          | 20 |
| <b>Figure 2.8-</b> Assembly by friction in glass fins [2.37] – General and detailed view .....                                          | 21 |
| <b>Figure 2.9-</b> Through glass point fixations for cylindrical and conical holes (Source: Glasströsch) .....                          | 23 |
| <b>Figure 2.10-</b> Undercut point fitting (Fisher FZP-G-Z) – General and detailed view .....                                           | 24 |
| <b>Figure 2.11-</b> SSGS of the Zeppelin University, Germany .....                                                                      | 26 |
| <b>Figure 2.12-</b> SSGS layout (with IGU) .....                                                                                        | 26 |
| <b>Figure 2.13-</b> Trapezoidal deformations in SSGS .....                                                                              | 27 |
| <b>Figure 2.14-</b> Adhesive point fixing (TSSA) .....                                                                                  | 28 |
| <b>Figure 2.15-</b> TSSA transparency (front view) .....                                                                                | 28 |
| <b>Figure 2.16-</b> Jointing details of hybrid steel-glass beams [2.47] .....                                                           | 28 |
| <b>Figure 2.17-</b> Details of the adhesively bonded and laminated reinforced glass beams investigated by Louter [2.47] .....           | 29 |
| <b>Figure 2.18-</b> Summary of the actual steel-to-glass connections .....                                                              | 30 |
| <b>Figure 2.19-</b> Shear strength (issued from tensile lap-joint shear tests) versus elongation at break [2.50] .....                  | 31 |
| <b>Figure 2.20-</b> Rigidity of the adhesives versus temperatures .....                                                                 | 33 |
| <b>Figure 2.21-</b> Characteristic tensile stress-strain curve [2.52] .....                                                             | 34 |
| <b>Figure 2.22-</b> Volumetric compression test results [2.53] .....                                                                    | 34 |
| <b>Figure 2.23-</b> Discontinuous damage (Mullins) .....                                                                                | 34 |
| <b>Figure 2.24-</b> Continuous damage (unloading only) .....                                                                            | 34 |
| <b>Figure 2.25-</b> Typical stress-strain diagrams of thermosets .....                                                                  | 44 |
| <b>Figure 2.26-</b> Tensile (a), Compressive (b) and Shear (c) stress-strain diagrams for Epoxy E862 [2.67] .....                       | 45 |
| <b>Figure 2.27-</b> Relaxation test on thermoset adhesive FM73 [2.68] .....                                                             | 45 |
| <b>Figure 2.28-</b> 3D rheological model .....                                                                                          | 49 |
| <b>Figure 2.29-</b> Uniaxial behaviour from the stress superposition .....                                                              | 49 |
| <b>Figure 2.30-</b> Materials laws summary .....                                                                                        | 49 |
| <b>Figure 3.0-</b> Organization chart of chapter 3 .....                                                                                | 51 |
| <b>Figure 3.1-</b> Steel-concrete composite beam .....                                                                                  | 52 |
| <b>Figure 3.2-</b> Steel-glass composite beam .....                                                                                     | 52 |
| <b>Figure 3.3-</b> Detail of the linear adhesive connection – (a) Isometric view – (b) Cross section – (c) Side view .....              | 57 |
| <b>Figure 3.4-</b> Comparison between the tensile (a) and shear (b) properties of acrylic adhesives [3.6] .....                         | 58 |
| <b>Figure 3.5-</b> Detail of the mechanical-adhesive connection – (a) Isometric view – (b) Cross section – (c) Side view .....          | 59 |
| <b>Figure 3.6-</b> Possible mechanical-adhesive connection for system class (iii) .....                                                 | 60 |
| <b>Figure 4.0-</b> Organization chart of chapter 4 .....                                                                                | 63 |
| <b>Figure 4.1-</b> (a) Dimensions of the silicone dog-bone samples according to ISO 527-2 and (b) Manufactured samples .....            | 64 |
| <b>Figure 4.2-</b> (a) POM C mold for dog-bone samples production and (b) Vacuum pump installation and (c) Injection part .....         | 65 |
| <b>Figure 4.3-</b> Ishikawa diagram for dog-bone quasi-static tests .....                                                               | 66 |
| <b>Figure 4.4-</b> Detail of the artificial ageing procedure for elevated temperatures .....                                            | 67 |
| <b>Figure 4.5-</b> Water and UV- exposure .....                                                                                         | 67 |
| <b>Figure 4.6-</b> Heat exposure in oven .....                                                                                          | 67 |

|                                                                                                                                               |     |
|-----------------------------------------------------------------------------------------------------------------------------------------------|-----|
| <b>Figure 4.7-</b> (a) Pilot tests on aluminum, (b) Installation of a silicone dog-bone sample and (c) Deformed silicone sample .....         | 69  |
| <b>Figure 4.8-</b> Stress-strain diagram corresponding to the design of experiments of Table 4.1 (NA=non-aged, A=aged) .....                  | 69  |
| <b>Figure 4.9-</b> Surface plot of the defined stress versus the ageing and loading rate for silicone dog-bone samples of Table 4.1 .....     | 70  |
| <b>Figure 4.10-</b> Example of linearized curve – sample S-04-50mm/min-NA (Top x axis only for dashed lines) .....                            | 71  |
| <b>Figure 4.11-</b> Surface plot of the initial stiffness versus the ageing and loading rate for silicone dog-bone samples of Table 4.1 ..... | 72  |
| <b>Figure 4.12-</b> Stress-strain diagram corresponding to the design of experiments of Table 4.2 (LT=Low Temperature) .....                  | 73  |
| <b>Figure 4.13-</b> Total effect of the loading rate on (a) the maximum stress and (b) the initial stiffness for DOE Table 4.2 .....          | 74  |
| <b>Figure 4.14-</b> Stress-strain diagram comparing the first and second DOE .....                                                            | 74  |
| <b>Figure 4.15-</b> Cyclic tension stress-strain diagram for silicone sample under a frequency of 1Hz .....                                   | 77  |
| <b>Figure 4.16-</b> Evaluation of the dissipated energy for samples (a) at low frequency and (b) at high frequency .....                      | 77  |
| <b>Figure 4.17-</b> Comparison between the averaged 1st cycle and the limiting 7th cycle of the Mullins' effect .....                         | 78  |
| <b>Figure 4.18-</b> Initial stiffness versus the cycle number .....                                                                           | 78  |
| <b>Figure 4.19-</b> Total effect of loading rate on the initial stiffness .....                                                               | 78  |
| <b>Figure 4.20-</b> Evolution of the maximum allowable stress with the increase of cycles .....                                               | 79  |
| <b>Figure 4.21-</b> Wöhler curve representation with Basquin form .....                                                                       | 80  |
| <b>Figure 4.22-</b> Comparison between the averaged Basquin formulation and the tensile tests results .....                                   | 80  |
| <b>Figure 4.23-</b> Stress-time diagrams for an imposed displacement of (a) 30mm and (b) 72mm .....                                           | 82  |
| <b>Figure 4.24-</b> Total effect of (a) the ageing and (b) the imposed displacement for long-term dog-bone tests in tension (Table 4.9) ..    | 83  |
| <b>Figure 4.25-</b> Reduction stress factor with comparison to (a) the reference stress at 60s and (b) to the quasi-static stress .....       | 84  |
| <b>Figure 4.26-</b> Total effect of (a) the ageing and (b) the imposed disp. on the stress reduction compared to quasi-static results .....   | 84  |
| <b>Figure 4.27-</b> Estimation of the stress loss – 2 imposed disp. ....                                                                      | 85  |
| <b>Figure 4.28-</b> (a) Dimensions of the silicone compressive samples and (b) Manufactured sample .....                                      | 86  |
| <b>Figure 4.29-</b> Pilot compression tests with (a) Teflon plates, (b) with pulverized Teflon spray and (c) deformed shape .....             | 88  |
| <b>Figure 4.30-</b> Stress-strain diagram –silicone under quasi-static compression (NA=non-aged, A=aged, LT=low temperature) .....            | 89  |
| <b>Figure 4.31-</b> Surface plot of the initial stiffness versus ageing and loading rate - silicone quasi-static compressive tests .....      | 90  |
| <b>Figure 4.32-</b> Surface plot of the strains versus ageing and loading rate - silicone quasi-static compressive tests .....                | 91  |
| <b>Figure 4.33-</b> Cyclic compression stress-strain diagram for silicone sample under a frequency of 0.1Hz .....                             | 93  |
| <b>Figure 4.34-</b> Evaluation of the dissipated energy for samples under cyclic compression .....                                            | 94  |
| <b>Figure 4.35-</b> Comparison between the averaged 1st cycle and the limiting 7th cycle of the Mullins' effect – cyclic compression .....    | 94  |
| <b>Figure 4.36-</b> Initial stiffness versus the cycle number .....                                                                           | 95  |
| <b>Figure 4.37-</b> Total effect of loading rate on the initial stiffness .....                                                               | 95  |
| <b>Figure 4.38-</b> Evolution of the maximum stress at a given strain of 0.58 with the increase of cycles .....                               | 95  |
| <b>Figure 4.39-</b> Wöhler curve representation with Basquin form .....                                                                       | 96  |
| <b>Figure 4.40-</b> Comparison between the tests results and the averaged Basquin for (a) all the samples (b) excepted SC-34 .....            | 96  |
| <b>Figure 4.41-</b> Stress-time diagrams for an imposed displacement of (a) 5mm and (b) 10mm – silicone long-term compression .....           | 99  |
| <b>Figure 4.42-</b> Stress-time diagrams for an imposed displacement of 14mm – silicone long-term compression .....                           | 99  |
| <b>Figure 4.43-</b> Total effect of (a) the ageing and (b) the imposed displacement – silicone long-term compression (Table 4.20) .....       | 100 |
| <b>Figure 4.44-</b> Total effect of imposed disp. for all specimens .....                                                                     | 100 |
| <b>Figure 4.45-</b> Reduction stress factor compared to $\sigma_{t=60s}$ .....                                                                | 100 |
| <b>Figure 4.46-</b> Total effect of imposed disp. for all specimens .....                                                                     | 101 |
| <b>Figure 4.47-</b> Reduction stress factor compared to $\sigma_{quasi-static}$ .....                                                         | 101 |
| <b>Figure 4.48-</b> Estimated stress-time diagrams – disp. of 5mm.....                                                                        | 102 |
| <b>Figure 4.49-</b> Estimated stress-time diagrams for an imposed disp. of (a) 5mm and (b) 10mm – silicone long-term compression ...          | 102 |
| <b>Figure 4.50-</b> (a) Double-lap joint geometry to test shear and (b) (c) Manufactured samples .....                                        | 103 |
| <b>Figure 4.51-</b> Pouring process for large area .....                                                                                      | 104 |
| <b>Figure 4.52-</b> (a) Injector and (b) Injecting process for small area .....                                                               | 104 |
| <b>Figure 4.53-</b> (a) Double lap-joint shear layout, (b) Relative displacement sensors and (c) Opening displacement sensors .....           | 106 |
| <b>Figure 4.54-</b> (a) Relative disp. versus time; (b) Opening disp. versus time; (c) Lateral disp. versus time; (d) Force versus time ....  | 107 |
| <b>Figure 4.55-</b> Mode of failure of the push-out silicone sample – Test n°12 of Table 4.24 .....                                           | 108 |
| <b>Figure 4.56-</b> Stress-strain diagrams- silicone under quasi-static shear .....                                                           | 108 |
| <b>Figure 4.57-</b> Total effect of (a) ageing, (b) bonding area, (c) bonding thickness and (d) loading rate on the initial stiffness .....   | 109 |
| <b>Figure 4.58-</b> Total effect of (a) ageing, (b) bonding area, (c) bonding thickness and (d) loading rate on the strength .....            | 111 |

|                                                                                                                                               |     |
|-----------------------------------------------------------------------------------------------------------------------------------------------|-----|
| <b>Figure 4.59-</b> (a) Opening displacement versus time and (b) Lateral displacement versus time - silicone cyclic shear .....               | 113 |
| <b>Figure 4.60-</b> Mode of failure of the push-out silicone subjected to cyclic shear – (a) glass side and (b) steel side .....              | 113 |
| <b>Figure 4.61-</b> Cyclic shear stress-strain diagram for silicone push-out sample under a frequency of 0.1Hz .....                          | 114 |
| <b>Figure 4.62-</b> (a) Dissipated area versus cycle numbers and (b) Initial stiffness versus cycle numbers - silicone cyclic shear .....     | 114 |
| <b>Figure 4.63-</b> Comparison between the averaged 1st cycle and the limiting 7th cycle of the Mullins' effect - silicone cyclic shear ..    | 115 |
| <b>Figure 4.64-</b> Evolution of the maximum allowable stress with the increase of cycles - silicone cyclic shear .....                       | 115 |
| <b>Figure 4.65-</b> Wöhler curve representation with Basquin form .....                                                                       | 116 |
| <b>Figure 4.66-</b> Comparison between the averaged Basquin formulation and the tests results - silicone cyclic shear .....                   | 116 |
| <b>Figure 4.67-</b> (a) Opening displacement versus time and (b) Lateral displacement versus time - silicone long-term shear .....            | 118 |
| <b>Figure 4.68-</b> Stress-time diagrams for an imposed strain of $\gamma=1.05$ – silicone long-term shear .....                              | 118 |
| <b>Figure 4.69-</b> Reduction stress factors – tests and estimations .....                                                                    | 119 |
| <b>Figure 4.70-</b> Estimated stress-time diagrams – silicone long-term shear .....                                                           | 119 |
| <b>Figure 4.71-</b> (a) Oedometric test layout; (b) Manufactured samples and (c) dimensions; (d) Injecting mold in Teflon .....               | 120 |
| <b>Figure 4.72-</b> (a) Punch; Rigid steel matrix (b) side view and (C) bottom view; (d) Final oedometric assembly .....                      | 122 |
| <b>Figure 4.73-</b> Stress-strain diagram corresponding to the DOE of Table 4.31 – silicone oedometric quasi-static tests .....               | 122 |
| <b>Figure 4.74-</b> Total effect of the loading rate on the stiffness .....                                                                   | 123 |
| <b>Figure 4.75-</b> Average stress-strain diagram – oedometric test .....                                                                     | 123 |
| <b>Figure 4.76-</b> (a) Dimensions of the acrylic dog-bone samples according to ISO 527.2 and (b) Manufactured samples .....                  | 124 |
| <b>Figure 4.77-</b> (a) Layering of the acrylic mold; (b) Self-manufactured mold pre-installed and (c) Curing of the adhesive .....           | 125 |
| <b>Figure 4.78-</b> (a) Centering pins and covering aluminum plates; (b) Installed and (c) tested dog-bone sample .....                       | 127 |
| <b>Figure 4.79-</b> Stress-strain diagrams regrouping (a) the brittle type I curves and (b) the ductile with yielding type II curves .....    | 127 |
| <b>Figure 4.80-</b> Surface plot of the initial stiffness versus ageing and loading rate – DOE Table 4.33 – acrylic quasi-static tension .... | 129 |
| <b>Figure 4.82-</b> Surface plot of the stress versus ageing and loading rate – DOE Table 4.33 - acrylic quasi-static tension .....           | 130 |
| <b>Figure 4.83-</b> Stress-strain diagrams versus loading rate for (a) ambient/high temperatures and (b) for low-temperature ageing ....      | 131 |
| <b>Figure 4.84-</b> Stress-time diagram for the two imposed displacements – acrylic long-term tension .....                                   | 133 |
| <b>Figure 4.85-</b> Total effect of (a) ageing and (b) imposed displacement on the stress ratio – acrylic long-term tension .....             | 134 |
| <b>Figure 4.86-</b> Total effect of (a) ageing and (b) imposed disp. on the stress ratio quasi-stat. reference – acrylic long-term tension .  | 135 |
| <b>Figure 4.87-</b> Evolution of the stress reduction factor .....                                                                            | 135 |
| <b>Figure 4.88-</b> (a) Dimension of the acrylic shear samples; (b) Manufactured mold and (c) aged and non-aged samples .....                 | 137 |
| <b>Figure 4.89-</b> (a) Dimensions of the punch; (b) Details and (c) Position of the specimen; (d) Whole assembly; (d) Test set-up .....      | 139 |
| <b>Figure 4.90-</b> Shear stress-strain diagram – UV-acrylic under quasi-static shear (NA/A=non-aged/aged) .....                              | 140 |
| <b>Figure 4.91-</b> Surface plot of the initial stiffness versus ageing and loading rate – DOE Table 4.43 – acrylic quasi-static shear .....  | 141 |
| <b>Figure 4.92-</b> Surface plot of the maximum stress versus ageing and loading rate – DOE Table 4.43 – acrylic quasi-static shear ..        | 142 |
| <b>Figure 4.93-</b> Mean stress-strain diagrams – load. rate distinction .....                                                                | 142 |
| <b>Figure 4.94-</b> Complete test procedure for the acrylic long-term shear tests .....                                                       | 143 |
| <b>Figure 4.95-</b> Stress-time diagram – DOE of Table 4.47 – acrylic long-term shear .....                                                   | 145 |
| <b>Figure 4.96-</b> Total effect of (a) Ageing, (b) Loading rate and (c) Imposed displacement on the discretized stresses .....               | 146 |
| <b>Figure 4.97-</b> Estimation of the stress loss – 3 imposed disp. ....                                                                      | 147 |
| <b>Figure 4.98-</b> Stress-time diagram for an imposed disp. of 3mm – DOE of Table 4.47 – acrylic long-term shear .....                       | 147 |
| <b>Figure 4.99-</b> Total effect of (a) Ageing, (b) Loading rate and (c) Imposed displacement on the discretized stresses at 3mm .....        | 149 |
| <b>Figure 4.100-</b> (a) Dimensions of the acrylic push-out; (b) Manufacturing; (c) Front and (d) lateral view of the finished sample .....   | 150 |
| <b>Figure 4.101-</b> (a) Acrylic push-out shear layout; Details of the (b) bottom and (c) top of the test setup .....                         | 152 |
| <b>Figure 4.102-</b> Force-displacement diagrams obtained for a loading rate of (a) 0.6mm/min, (b) 1mm/min and (c) 5mm/min .....              | 153 |
| <b>Figure 4.103-</b> Analysis of the failure mode of the push-out acrylic samples and detailed example of specimen n°7 .....                  | 153 |
| <b>Figure 5.0-</b> Organization chart of chapter 5 .....                                                                                      | 163 |
| <b>Figure 5.1-</b> Algorithm for the determination of the strain energy isochoric part .....                                                  | 165 |
| <b>Figure 5.2-</b> Tree structure of the most employed isochoric energy potential forms $W_{iso}$ (step 7 of Fig. 5.1) .....                  | 167 |
| <b>Figure 5.3-</b> Evaluation of the curve fittings for quasi-static (a) tension, (b) compression and (c) shear – Existing models .....       | 170 |
| <b>Figure 5.4-</b> Evaluation of the curve fittings of the 7th cyclic curve in (a) tension, (b) compression and (c) shear – Existing models   | 171 |
| <b>Figure 5.5-</b> Evolution of (a) the linear part and of (b) the non-linear part of the shear stress; (c) Polynomial form obtaining .....   | 173 |
| <b>Figure 5.6-</b> Example of superposition of the three shear stresses representing the new proposed model .....                             | 175 |

|                                                                                                                                              |     |
|----------------------------------------------------------------------------------------------------------------------------------------------|-----|
| <b>Figure 5.7-</b> Algorithm of the Levenberg-Marquardt method for the determination of the material coefficients .....                      | 177 |
| <b>Figure 5.8-</b> Evaluation of the curve fittings for quasi-static (a) tension, (b) compression and (d) shear – User model .....           | 179 |
| <b>Figure 5.9-</b> Evaluation of the curve fittings of the 7th cyclic curve in (a) tension, (b) compression and (c) shear – User model ..... | 180 |
| <b>Figure 5.10-</b> Algorithm for the determination of the strain energy volumetric part .....                                               | 181 |
| <b>Figure 5.11-</b> Evaluation of the oedometric curve fittings for the different volumetric models .....                                    | 184 |
| <b>Figure 5.12-</b> Verification of the positivity condition for the quasi-static and the Mullins' effect coefficients .....                 | 185 |
| <b>Figure 5.13-</b> Stress-strain diagrams superposition for the different tested loading rates .....                                        | 187 |
| <b>Figure 5.14-</b> Linear fitting of the tensile experimental data for specimens under (a) 5mm/min, (b) 50mm/min and (c) 250mm/min .....    | 188 |
| <b>Figure 5.15-</b> Linear fitting of the experimental data for low temperature aged specimens under (a) 50mm/min, (b) 250mm/min .....       | 189 |
| <b>Figure 5.16-</b> Theoretical (Ramb-O) and experimental stress-strain diagrams for (a) 5mm/min, (b) 50mm/min and (c) 250mm/min .....       | 189 |
| <b>Figure 5.17-</b> Fitting of the evolution of the 3 material coefficients according to the loading rate with the laws of Eq. (5.33) .....  | 190 |
| <b>Figure 5.18-</b> Estimated/experimental stress-strain diagrams for (a) 5mm/min, (b) 50mm/min, (c) 250mm/min and (d) 500mm/min .....       | 191 |
| <b>Figure 5.19-</b> Theoretical and experimental diagrams for low temperature aged specimens under (a) 50mm/min, (b) 250mm/min .....         | 191 |
| <b>Figure 5.20-</b> Stress-strain diagrams – acrylic modified shear .....                                                                    | 191 |
| <b>Figure 5.21-</b> Linear fitting of the shear experimental data for specimens under (a) 1mm/min, (b) 5mm/min and (c) 15mm/min .....        | 193 |
| <b>Figure 5.22-</b> Theoretical (Ramb-O) and experimental stress-strain diagrams for (a) 1mm/min, (b) 5mm/min and (c) 15mm/min .....         | 194 |
| <b>Figure 5.23-</b> Theoretical (Eq. (5.34)) and experimental stress-strain diagrams for (a) 1mm/min, (b) 5mm/min and (c) 15mm/min .....     | 195 |
| <b>Figure 5.24-</b> Linear fitting of the evolution of the 4 material coefficients of Eq. (5.34) according to the loading rates .....        | 196 |
| <b>Figure 5.25-</b> Estimated/experimental shear stress-strain diagrams for (a) 1mm/min, (b) 5mm/min and (c) 15mm/min .....                  | 197 |
| <b>Figure 6.0-</b> Organization chart of chapter 6 .....                                                                                     | 199 |
| <b>Figure 6.1-</b> (a) 1/8th of the tested zone of the silicone dog bone sample and (b) Model in Abaqus with boundary conditions .....       | 202 |
| <b>Figure 6.2-</b> Comparison between Ramp/Smooth amplitude functions for the application of the displacement in Abaqus/Explicit .....       | 203 |
| <b>Figure 6.3-</b> Different mesh sizes (2mm/1mm/0.5mm) for the numerical simulation of silicone dog-bone samples .....                      | 203 |
| <b>Figure 6.4-</b> Engineering stress-strain diagrams for (a) linear and (b) quadratic elements – Silicone quasi-static tension .....        | 204 |
| <b>Figure 6.5-</b> True stress final result of UHYPER-C3D8H-Mesh size 2mm – Silicone quasi-static tension .....                              | 205 |
| <b>Figure 6.6-</b> Engineering stress-strain diagrams for (a) linear and (b) quadratic elements – Silicone Mullin's tension .....            | 205 |
| <b>Figure 6.7-</b> True stress final results – Time period of (a) 0.002s and (b) 0.2s – VUMAT-C3D8-Mesh size 2mm-Smooth .....                | 206 |
| <b>Figure 6.8-</b> (a) Engineering stress-strain diagrams – Linear elements; (b) Kinetic energy vs. time – Ramp/Smooth comparison .....      | 206 |
| <b>Figure 6.9-</b> (a) Engineering stress-strain diagrams and (b) Kinetic energy vs. time – Silicone quasi-static tension .....              | 207 |
| <b>Figure 6.10-</b> (a) Engineering stress-strain diagrams and (b) Kinetic energy vs. time – Silicone Mullin's tension .....                 | 207 |
| <b>Figure 6.11-</b> (a) Axisymmetric representation in Abaqus/Standard and (b) 3D representation of 1/8th in Abaqus/Explicit .....           | 208 |
| <b>Figure 6.12-</b> Different mesh sizes for the numerical simulation of silicone compressive samples – Abaqus/Standard .....                | 209 |
| <b>Figure 6.13-</b> Different mesh sizes for the numerical simulation of silicone compressive samples – Abaqus/Explicit .....                | 209 |
| <b>Figure 6.14-</b> Engineering stress-strain diagrams for (a) linear and (b) quadratic elements – Silicone quasi-static compression .....   | 210 |
| <b>Figure 6.15-</b> True stress final result of UHYPER-CAX4H-Mesh size 2mm – Silicone quasi-static compression .....                         | 210 |
| <b>Figure 6.16-</b> Engineering stress-strain diagrams for (a) linear and (b) quadratic elements – Silicone Mullin's compression .....       | 210 |
| <b>Figure 6.17-</b> (a) Engineering stress-strain diagrams and (b) Kinetic energy vs. time – Silicone quasi-static compression .....         | 212 |
| <b>Figure 6.18-</b> (a) Engineering stress-strain diagrams and (b) Kinetic energy vs. time – Silicone Mullin's compression .....             | 212 |
| <b>Figure 6.19-</b> 3D representation of 1/4th of the push-out assembly (160x30x3mm) for both Abaqus/Standard and Abaqus/Explicit .....      | 213 |
| <b>Figure 6.20-</b> Different mesh sizes for the numerical simulation of silicone push-out samples – based on Abaqus/Explicit models .....   | 215 |
| <b>Figure 6.21-</b> (a) Stress-strain diagrams for different mesh sizes and (b) displacements – Silicone quasi-static shear .....            | 216 |
| <b>Figure 6.22-</b> (a) Stress-strain diagrams for different mesh sizes and (b) displacements – Silicone Mullin's shear .....                | 217 |
| <b>Figure 6.23-</b> (a) Shear stress-strain diagrams and (b) Kinetic energy vs. time – Silicone quasi-static shear .....                     | 217 |
| <b>Figure 6.24-</b> (a) Shear stress-strain diagrams and (b) Kinetic energy vs. time – Silicone Mullin's shear .....                         | 218 |
| <b>Figure 6.25-</b> Example of path along the overlap length for the direct measurement of the shear stresses in the silicone .....          | 218 |
| <b>Figure 6.26-</b> Evaluation of the peak stress according to the mesh size – UHYPER subroutine – Silicone quasi-static shear .....         | 219 |
| <b>Figure 6.27-</b> Comparison of the maximum stress peaks (at 15mm) for the different mesh combinations – (a) global and (b) local .....    | 220 |
| <b>Figure 6.28-</b> Comparison of the maximum stress peaks (at 15mm) for the different mesh combinations – (a) global and (b) local .....    | 220 |
| <b>Figure 6.29-</b> (a) & (c) Global and (b) & (d) local stress peaks for the quasi-static and Mullin's set of coefficients (mid path) ..... | 221 |
| <b>Figure 6.30-</b> (a) Shear stress-strain diagrams of numerical simulations – DOE of Table 6.4 and (b) Displacements diagrams .....        | 223 |
| <b>Figure 6.31-</b> Evolution of the stresses ratio along the last 18mm of overlap length – DOE of Table 6.4 – UHYPER subroutine .....       | 223 |

|                                                                                                                                                     |     |
|-----------------------------------------------------------------------------------------------------------------------------------------------------|-----|
| <b>Figure 6.32-</b> (a) Shear stress-strain diagrams and (b) Stress evolution along the overlap length – Adherend rigidity influence .....          | 224 |
| <b>Figure 6.33-</b> (a) Shear stress-strain diagrams and (b) Stress evolution along the overlap length – Load intensity influence .....             | 225 |
| <b>Figure 6.34-</b> Stress evolution along the overlap length according to the three considered theories – Silicone shear quasi-static .....        | 227 |
| <b>Figure 6.35-</b> Example of linearized stress distribution with consideration of the (a) top and (b) bottom parts of the joint .....             | 228 |
| <b>Figure 6.36-</b> Details of the dimensions of the small-scale push tests and lateral view of the three silicone thicknesses .....                | 229 |
| <b>Figure 6.37-</b> Mode of failure of the push-out silicone sample – peak stress evaluation – Test No. 1 .....                                     | 229 |
| <b>Figure 6.38-</b> Stress-strain diagrams for an overlap of (a) 6mm, (b) 12mm and (c) 18mm – Silicone peak stress verification .....               | 230 |
| <b>Figure 6.39-</b> (a) Axisymmetric representation in Abaqus/Standard and (b) 3D representation of 1/8th in Abaqus/Explicit .....                  | 231 |
| <b>Figure 6.40-</b> Different mesh sizes for the numerical simulation of silicone oedometric samples – Abaqus/Standard .....                        | 232 |
| <b>Figure 6.41-</b> Different mesh sizes for the numerical simulation of silicone oedometric samples – Abaqus/Explicit .....                        | 232 |
| <b>Figure 6.42-</b> Engineering stress-strain diagrams for (a) linear and (b) quadratic elements – Silicone quasi-static oedometric .....           | 233 |
| <b>Figure 6.43-</b> True stress final result of UHYPER-CAX4H-Mesh size 2mm – Silicone (a) quasi-static and (b) Mullin's oedometric .....            | 233 |
| <b>Figure 6.44-</b> Engineering stress-strain diagrams for (a) linear and (b) quadratic elements – Silicone Mullin's oedometric .....               | 234 |
| <b>Figure 6.45-</b> (a) Stress-strain diagrams and (b) Kinetic energy vs. time – Time period influence –Quasi-static oedometric .....               | 234 |
| <b>Figure 6.46-</b> True stresses of VUMAT-C3D8-Time 0.001s-Mesh size 2mm – Silicone (a) quasi-static and (b) Mullin's oedometric .....             | 235 |
| <b>Figure 6.47-</b> (a) Stress-strain diagrams and (b) Kinetic energy vs. time – Mesh influence – Quasi-static oedometric .....                     | 235 |
| <b>Figure 6.48-</b> (a) Stress-strain diagrams and (b) Kinetic energy vs. time – Time period influence –Mullin's oedometric .....                   | 236 |
| <b>Figure 6.49-</b> (a) Axisymmetric (b) 2D and (c) 3D representation of the quasi-static modified shear experiments on acrylic .....               | 237 |
| <b>Figure 6.50-</b> Different mesh sizes corresponding to the three representations of the quasi-static modified acrylic shear tests .....          | 238 |
| <b>Figure 6.51-</b> Stress-strain diagrams of the three rates (a) 1mm/min, (b) 5mm/min and (c) 15mm/min – (d) Shear deformation .....               | 239 |
| <b>Figure 6.52-</b> Stress-strain diagrams of the three rates (a) 1mm/min, (b) 5mm/min and (c) 15mm/min – (d) Shear deformation .....               | 240 |
| <b>Figure 6.53-</b> Stress-strain diagrams of the three rates (a) 1mm/min, (b) 5mm/min and (c) 15mm/min – (d) Shear deformation .....               | 241 |
| <b>Figure 7.0-</b> Organization chart of chapter 7 .....                                                                                            | 243 |
| <b>Figure 7.1-</b> Description of the global system – Dimensions and position of the loads .....                                                    | 244 |
| <b>Figure 7.2-</b> Composition and dimensions of the cross section of the linear adhesive composite beam .....                                      | 244 |
| <b>Figure 7.3-</b> (a) Normal stress distribution in the steel profile and (b) Deflection according to the beam length .....                        | 246 |
| <b>Figure 7.4-</b> (a) Boundary conditions and load application on the model and (b) Vertical displacements of the steel beam .....                 | 246 |
| <b>Figure 7.5-</b> (a) Normal stress distribution in the non-connected assembly and (b) Deflection according to the beam length .....               | 247 |
| <b>Figure 7.6-</b> Sliding at the steel-glass interface in function of the length of the beam – Assembly with no connection .....                   | 247 |
| <b>Figure 7.7-</b> (a) Boundary conditions and load application on the unconnected model and (b) Vertical displacements .....                       | 247 |
| <b>Figure 7.8-</b> Procedure allowing evaluating the sliding at the steel-glass interface for the numerical simulations .....                       | 248 |
| <b>Figure 7.9-</b> (a) Normal stress distribution in the fully connected assembly and (b) Deflection according to the beam length .....             | 248 |
| <b>Figure 7.10-</b> (a) Normal stress distribution in the envisaged assembly (Fig. 7.2) and (b) Deflection according to the beam length .....       | 249 |
| <b>Figure 7.11-</b> Sliding at the steel-glass interface in function of the length of the beam – Envisaged assembly of Fig.7.2 .....                | 249 |
| <b>Figure 7.12-</b> (a) Vertical displacements and (b) sliding at the interface for the envisaged assembly of Fig. 7.2 .....                        | 250 |
| <b>Figure 7.13-</b> (a) Comparison of the deflection curves and (b) of the stress distribution for the three degrees of connection .....            | 250 |
| <b>Figure 7.14-</b> Local modifications of the steel beam at the support and load introduction positions to prevent instabilities .....             | 251 |
| <b>Figure 7.15-</b> Preparation of the glass plates and definition of the bonding thickness and area with Teflon plates .....                       | 252 |
| <b>Figure 7.16-</b> (a) Dead weight on the top of the assembly for constant adhesive thickness and (b) Silicone bonding example .....               | 253 |
| <b>Figure 7.17-</b> Test set-up for the large-scale beam tests and details of the complete load introduction system .....                           | 253 |
| <b>Figure 7.18-</b> Positions of the displacement sensors along the linear adhesive composite beam .....                                            | 254 |
| <b>Figure 7.19-</b> Positions of the six strain gauges along the linear adhesive composite beam .....                                               | 255 |
| <b>Figure 7.20-</b> Example of total force versus machine displacement ( $x=1100\text{mm}$ ) curve – linear adhesive composite beam .....           | 255 |
| <b>Figure 7.21-</b> Total applied force vs. deflection at (a) 550mm, (b) 1100mm and (c) 1650mm – linear adhesive composite beam .....               | 256 |
| <b>Figure 7.22-</b> Total applied force versus sliding at the interface for (a) LAC-1, (b) LAC-2, (c) LAC-3; (d) Sliding at the extremities .....   | 257 |
| <b>Figure 7.23-</b> Silicone net bonded area for (a) the first, (b) the central and (c) the last portions of the composite beam LAC-3 .....         | 257 |
| <b>Figure 7.24-</b> (a) Sliding along the beam length for a force of 60kN and (b) Relative displacement at the end of the beam .....                | 258 |
| <b>Figure 7.25-</b> (a) Force versus opening displacements for the 3 beams and (b) Force versus strains at the center of the glass .....            | 258 |
| <b>Figure 7.26-</b> Total applied force versus strains under the load position at (a) 150mm, (b) 300mm and (c) 420mm from the edge .....            | 259 |
| <b>Figure 7.27-</b> (a) Horizontal opening after the test; (b) Opening on the side after the test; (c) Too long cut for the plate positioning ..... | 260 |
| <b>Figure 7.28-</b> (a) Boundary conditions and load application on the holed beam system and (b) Vertical displacements .....                      | 260 |

|                                                                                                                                                           |     |
|-----------------------------------------------------------------------------------------------------------------------------------------------------------|-----|
| <b>Figure 7.29-</b> Total force versus deflections at (a) 1100mm and (b) 1650mm; (c) Sliding along the beam; (d) Force versus strains .....               | 261 |
| <b>Figure 8.0-</b> Organization chart of chapter 8 .....                                                                                                  | 263 |
| <b>Figure 8.1-</b> Description of the global system – Dimensions and position of the load – Mechanical adhesive connection .....                          | 264 |
| <b>Figure 8.2-</b> Composition and dimensions of the cross section of the mechanical-adhesive composite beam .....                                        | 264 |
| <b>Figure 8.3-</b> (a) simplification of the studied system; (b) Analytical solution of an infinite holed plate under uniaxial tensile loading .....      | 265 |
| <b>Figure 8.4-</b> (a) 2D analytical rigid fully fixed and (b) 3D deformable representation of the 3mm thick covering Teflon plate .....                  | 266 |
| <b>Table 8.1-</b> Different mesh sizes and orders for the numerical simulation of a glass plate loaded thorough a perfectly fitting pin .....             | 267 |
| <b>Figure 8.5-</b> (a) Maximum and (b) Minimum stress along the hole – Implicit – Glass plate loaded thorough a perfectly fitting pin .....               | 268 |
| <b>Figure 8.6-</b> Final displacement values of the silicone at the last valid increment for (a) Mesh 3 elts and (b) Mesh 10 elts .....                   | 270 |
| <b>Figure 8.7-</b> Total force versus silicone relative displacement diagram for (a) the 2D- and (b) the 3D-representation of the Teflon .....            | 270 |
| <b>Figure 8.8-</b> (a) Maximum and (b) Minimum principal stresses according to the position on the radius; (c) Silicone stress at $\theta=0^\circ$ .....  | 271 |
| <b>Figure 8.9-</b> (a) Maximum and (b) Minimum stress along the hole – Explicit – Glass plate loaded thorough a perfectly fitting pin .....               | 273 |
| <b>Figure 8.10-</b> Final displacement values of the silicone at the last valid increment for (a) classical and (b) ALE explicit resolution .....         | 274 |
| <b>Figure 8.11-</b> Total force versus silicone relative displacement diagrams – (a) classical, (b) Distortion control and (c) ALE .....                  | 274 |
| <b>Figure 8.12-</b> (a) Maximum and (b) Minimum principal stresses according to the position on the radius; (c) Silicone stress at $\theta=0^\circ$ ..... | 275 |
| <b>Figure 8.13-</b> Composition of the small-scale mechanical-adhesive connection (1 hole) and production details .....                                   | 276 |
| <b>Figure 8.14-</b> Details of the test set-up and final installed assembly with complete instrumentation – Small scale tests MAC .....                   | 277 |
| <b>Figure 8.15-</b> (a) Displacements in the Teflon and (b) Relative displacements in the silicone acc. to the time – Silicone 5mm thick .....            | 278 |
| <b>Figure 8.16-</b> Force versus relative displacements for (a) 5mm and (b) 10mm silicone thickness – Detail of the failure for 10mm .....                | 279 |
| <b>Figure 8.17-</b> Dimensions of the small-scale mechanical-adhesive connections (2 holes) and production details .....                                  | 280 |
| <b>Figure 8.18-</b> (a) Displacements in the Teflon and (b) Relative displacements in the silicone acc. to the time – 2 bolts system .....                | 281 |
| <b>Figure 8.19-</b> Force versus silicone relative displacements for (a) 5mm and (b) 10mm silicone thicknesses – 2 bolts system .....                     | 281 |
| <b>Figure 8.20-</b> Geometrical modifications to the numerical simulations for the case of one bolt with 5mm silicone thickness .....                     | 282 |
| <b>Figure 8.21-</b> Force versus relative disp. curves – Numerical simulations of the geometrical modifications presented on Fig. 8.20 .....              | 283 |
| <b>Figure 8.22-</b> (i) Linear elastic and (ii) Nonlinear elastic-perfectly plastic representations of the rigidity of the connection in FEA .....        | 284 |
| <b>Figure 8.23-</b> (a) Global model of the mechanical-adhesive composite beam and (b) Local definition of the connection behaviour .....                 | 285 |
| <b>Figure 8.24-</b> (a) Normal stress distribution in the composite section (Fig. 8.1); (b) Deflection and (c) Sliding acc. to the length .....           | 286 |
| <b>Figure 8.25-</b> Comparison of the deflection curves and (b) of the stress distributions for the four types of connection .....                        | 286 |
| <b>Figure 8.26-</b> (a) Chamber at the bolt, (b) Final welded and cleaned bolt and (c) Insertion of the fitting Teflon plate .....                        | 287 |
| <b>Figure 8.27-</b> Repartition of the three Teflon plates fitting the welded steel studs of the mechanical adhesive connection .....                     | 287 |
| <b>Figure 8.28-</b> Steps leading to the injection of the silicone and to the final assembly of the mechanical adhesive connection .....                  | 288 |
| <b>Figure 8.29-</b> Test set-up for the large-scale mechanical adhesive beam tests and details of the system under the load .....                         | 289 |
| <b>Figure 8.30-</b> Total applied force vs. deflection at (a) 550mm, (b) 1100mm and (c) 1650mm – Mechanical adhesive connection .....                     | 290 |
| <b>Figure 8.31-</b> (a) V-crack in the glass at (b) the bolt-glass contact; (c) Silicone failure under the load application point .....                   | 291 |
| <b>Figure 8.32-</b> Total force versus sliding at the interface for (a) MAC-1, (b) MAC-2 and (c) MAC-3; (d) Sliding at the extremities .....              | 291 |
| <b>Figure 8.33-</b> (a) Sliding along the beam length for a force of 60kN and (b) Relative displacement at the end of the beam .....                      | 292 |
| <b>Figure 8.34-</b> (a) Force versus opening displacements for the 3 beams and (b) Force versus strains at the center of the glass .....                  | 292 |
| <b>Figure 8.35-</b> Total applied force versus strains under the load position at (a) 150mm, (b) 300mm and (c) 420mm from the edge .....                  | 293 |

## NOMENCLATURE

|                           |                                   |                                                                                |
|---------------------------|-----------------------------------|--------------------------------------------------------------------------------|
| $\rho$                    | kg/m <sup>3</sup>                 | Density                                                                        |
| $E$                       | MPa                               | Young's Modulus                                                                |
| $\nu$                     | -                                 | Poisson's ratio                                                                |
| $HK_{0,1/20}$             | GPa                               | Glass knop hardness                                                            |
| $\alpha_T$                | 10 <sup>-6</sup> K <sup>-1</sup>  | Thermal expansion coefficient                                                  |
| $\lambda$                 | Wm <sup>-1</sup> K <sup>-1</sup>  | Thermal conductivity                                                           |
| $C_p$                     | Jkg <sup>-1</sup> K <sup>-1</sup> | Specific thermal capacity                                                      |
| $\epsilon$                | -                                 | Emissivity                                                                     |
| $n$                       | -                                 | Average refractive index for the visible spectrum                              |
| $\sigma$                  | MPa                               | Glass strength                                                                 |
| $r_0$                     | m                                 | Distance between two glass atoms                                               |
| $\gamma$                  | Jm <sup>-2</sup>                  | Glass fracture surface energy                                                  |
| $\sigma_{max}$            | MPa                               | Maximum stress                                                                 |
| $\sigma_{allowable}$      | MPa                               | Allowable stress                                                               |
| $w_{max}$                 | m                                 | Maximum deformation                                                            |
| $w_{allowable}$           | m                                 | Allowable deformation                                                          |
| $R_d$                     | MPa                               | Limit design value                                                             |
| $k_{mod}$                 | -                                 | Coefficient accounting for the load duration                                   |
| $k_c$                     | -                                 | Coefficient accounting for the construction type (DIN 18008)                   |
| $f_k$                     | MPa                               | Characteristic strength of the glass element (DIN 18008)                       |
| $\gamma_{M,FG}$           | -                                 | Safety factor for float glass according to the DIN 18008                       |
| $\gamma_M$                | -                                 | Safety factor for tempered glass according to the DIN 18008                    |
| $\gamma_{M,A}$            | -                                 | Safety factor for float glass according to the prEN 13474                      |
| $\gamma_{M,v}$            | -                                 | Safety factor accounting for the tempering according to the prEN 13474         |
| $k_{sp}$                  | -                                 | Coefficient accounting for the float glass process (prEN 13474)                |
| $f_{g,k}$                 | MPa                               | Float glass strength (prEN 13474)                                              |
| $k_v$                     | -                                 | Coefficient accounting for the tempering process (prEN 13474)                  |
| $f_{b,k}$                 | MPa                               | Tempered glass strength (prEN13474)                                            |
| $C_{ij}$                  | N/m <sup>2</sup>                  | Material parameters associated to W                                            |
| $N$                       | -                                 | Material parameter characterizing the highest degree of W                      |
| $W$                       | MPa                               | Strain energy function / Helmholtz free-energy function                        |
| $I_1$                     | -                                 | First invariant tensor of the left Cauchy-Green tensor defined in Eq. (2.11a)  |
| $I_2$                     | -                                 | Second invariant tensor of the left Cauchy-Green tensor defined in Eq. (2.11b) |
| $I_3$                     | -                                 | Third invariant tensor of the left Cauchy-Green tensor defined in Eq. (2.11c)  |
| $K$                       | MPa                               | Volumetric material parameter associated to W                                  |
| $\tau$                    | MPa                               | Shear stress                                                                   |
| $\gamma$                  | -                                 | Shear strain                                                                   |
| $a$                       | MPa                               | Isochoric material parameter associated to W                                   |
| $b$                       | MPa                               | Isochoric material parameter associated to W                                   |
| $c$                       | MPa                               | Isochoric material parameter associated to W                                   |
| $d$                       | MPa                               | Isochoric material parameter associated to W                                   |
| $e$                       | -                                 | Isochoric material parameter associated to W                                   |
| $\tau_{lin}$              | MPa                               | Linearized shear stress for adhesive peak stress                               |
| $\sigma_k$                | MPa                               | Tensile adhesive characteristic stress for an imposed strain of 138%           |
| $\vec{X}$                 |                                   | Vector                                                                         |
| $\overline{\overline{X}}$ |                                   | Tensor of second order                                                         |

|                       |                                                           |
|-----------------------|-----------------------------------------------------------|
| $\bar{\bar{X}}^{-1}$  | Inverse of the second order tensor                        |
| $\bar{\bar{X}}^T$     | Transpose of the second order tensor                      |
| $\dot{\bar{\bar{X}}}$ | Derivate of the second order tensor according to the time |
| Tr                    | Trace of the matrix                                       |
| det                   | Determinant of the matrix                                 |
| div                   | Divergence operator                                       |
| Grad                  | Gradient operator                                         |
| $DX/Dt$               | Partial derivate of X according to the time               |
| ln                    | Natural logarithm                                         |
| log                   | Logarithm                                                 |
| erf                   | Error function                                            |

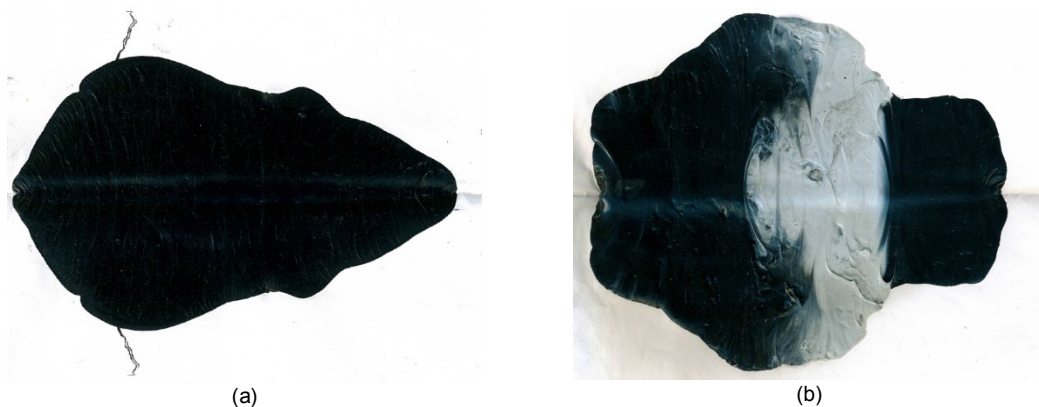


## APPENDIX A – Quality control of the adhesive samples

### A.1 Silicone mixing control

With the mold of the injection method, presented in section 4.2.1.1, three dog-bone samples can be produced each time. However, before injecting the adhesive in the three shapes, qualitative tests, allowing ensuring a correct mixing and evaluating the degree of curing, have to be made:

- i. The butterfly test, whose purpose is to check the mixing of the two components delivered separately by Dow Corning, represents the first test. Indeed, the first component is contained in cartridge of 600g and the second component in tubes of 30g each. Thus, regarding the imposed ratio of 10:1, two tubes of the second component have to be inserted in the large cartridge of 600g before proceeding to the mixing with the help of a coil inserted into a drilling machine. Even if the revolution speed and the duration of this operation are provided by the manufacturer, the butterfly tests must be realized. For these tests, a standard A4 piece of paper is fold in half and reopened to put a small bead of silicone. Then, the folded parts are closed again, pressed to obtain a thin film of adhesive and reopened for visual inspection. As the first component is white and the second component is black, the mixture and consequently the butterfly test result should be black with no trace of white or grey, see Fig. A.1.



**Figure A.1-** Butterfly tests with (a) correct and (b) incorrect mixing

This procedure is performed for each new cartridge and so each three adhesive dog-bone samples. If the butterfly test does not first succeed, the mixing operation is repeated and other butterfly tests have to be made until homogeneity.

- ii. The snap time test allows controlling the evolution of the curing process in prescribed environmental conditions, such as temperature and humidity. This action is carried out after the success of the butterfly test and stop only when the adhesive is completely cured. A simple container and a stick, e.g. a steel nail, are sufficient to proceed to this test. A small quantity of mixed silicone is poured inside the container, where the stick is then inserted. To check the condition of the adhesive, the stick is periodically pulled out and reinserted. At first, the silicone is liquid and progressively become stringier with the polymerization to finally break cohesively. When this last mode of failure is reached, the adhesive can be considered as cured. Hence, this qualitative test provides sufficient information on the state of the dog-bones and gives a reference to unmold them.

As 33 dog-bones samples were produced, these two operations were executed at least 11 times. All the data relative to the fabrication of the DC993 silicone dog-bone samples, such as the injecting date, the unmold date and the position of the dog-bone specimen in the mold are summarized in the Table A.1. As it can be noted, the samples were turned out maximum 5 days after injection.

## A.2 Silicone dog-bone samples - dimensions control

After a period of one month, in which the samples were stored at ambient temperature and humidity shielded from light, the dimensions of the tested zone were measured with the help of a calliper.

| N°   | Manuf. Date | Turn out   | Position | Dimensions of the tested zone |                |                |       |        |                |                |                |      |        |
|------|-------------|------------|----------|-------------------------------|----------------|----------------|-------|--------|----------------|----------------|----------------|------|--------|
|      |             |            |          | Width (mm)                    |                |                |       |        | Thickness (mm) |                |                |      |        |
|      |             |            |          | b <sub>1</sub>                | b <sub>2</sub> | b <sub>3</sub> | Aver  | σ      | t <sub>1</sub> | t <sub>2</sub> | t <sub>3</sub> | Aver | σ      |
| S-01 | 07/04/2011  | 11/04/2011 | 1        | 10,0                          | 10,0           | 10,0           | 10,00 | 0,0376 | 3,9            | 3,9            | 3,9            | 3,90 | 0,0284 |
| S-02 | 07/04/2011  | 11/04/2011 | 2        | 9,9                           | 10,0           | 10,0           | 9,97  |        | 3,9            | 3,9            | 3,9            | 3,90 |        |
| S-03 | 07/04/2011  | 11/04/2011 | 3        | 10,0                          | 10,0           | 10,0           | 10,00 |        | 3,9            | 3,9            | 3,9            | 3,90 |        |
| S-04 | 14/04/2011  | 15/04/2011 | 1        | 9,9                           | 9,9            | 9,9            | 9,90  |        | 3,9            | 3,9            | 3,9            | 3,90 |        |
| S-05 | 14/04/2011  | 15/04/2011 | 2        | 10,0                          | 9,9            | 10,0           | 9,97  |        | 3,9            | 3,9            | 3,9            | 3,90 |        |
| S-06 | 14/04/2011  | 15/04/2011 | 3        | 9,9                           | 9,9            | 9,9            | 9,90  |        | 3,9            | 3,9            | 3,9            | 3,90 |        |
| S-07 | 19/04/2011  | 20/04/2011 | 1        | 9,9                           | 9,9            | 9,9            | 9,90  |        | 3,9            | 3,9            | 3,9            | 3,90 |        |
| S-08 | 19/04/2011  | 20/04/2011 | 2        | 9,9                           | 10,0           | 10,0           | 9,97  |        | 3,9            | 3,9            | 3,9            | 3,90 |        |
| S-09 | 19/04/2011  | 20/04/2011 | 3        | 10,0                          | 9,9            | 10,0           | 9,97  |        | 3,9            | 3,9            | 3,9            | 3,90 |        |
| S-10 | 21/04/2011  | 26/04/2011 | 1        | 9,9                           | 9,9            | 9,9            | 9,90  |        | 3,9            | 3,9            | 3,9            | 3,90 |        |
| S-11 | 21/04/2011  | 26/04/2011 | 2        | 9,9                           | 10,0           | 10,0           | 9,97  |        | 3,9            | 3,8            | 3,9            | 3,87 |        |
| S-12 | 21/04/2011  | 26/04/2011 | 3        | 9,9                           | 10,0           | 10,0           | 9,97  |        | 3,9            | 3,9            | 3,9            | 3,90 |        |
| S-13 | 27/05/2011  | 30/05/2011 | 1        | 10,0                          | 9,9            | 10,0           | 9,97  |        | 3,9            | 3,9            | 3,9            | 3,90 |        |
| S-14 | 27/05/2011  | 30/05/2011 | 2        | 9,9                           | 9,9            | 9,9            | 9,90  |        | 3,9            | 3,9            | 3,9            | 3,90 |        |
| S-15 | 27/05/2011  | 30/05/2011 | 3        | 9,9                           | 9,9            | 9,9            | 9,90  |        | 3,9            | 3,9            | 3,9            | 3,90 |        |
| S-16 | 15/07/2011  | 18/07/2011 | 1        | 10,0                          | 10,0           | 10,0           | 10,00 |        | 3,9            | 3,9            | 3,9            | 3,92 |        |
| S-17 | 15/07/2011  | 18/07/2011 | 2        | 10,0                          | 10,0           | 10,0           | 9,99  |        | 3,9            | 3,9            | 3,9            | 3,92 |        |
| S-18 | 15/07/2011  | 18/07/2011 | 3        | 10,0                          | 10,0           | 10,0           | 9,96  |        | 3,9            | 3,9            | 3,9            | 3,93 |        |
| S-19 | 18/07/2011  | 19/07/2011 | 1        | 10,0                          | 10,0           | 10,0           | 10,00 |        | 4,0            | 4,0            | 4,0            | 3,96 |        |
| S-20 | 18/07/2011  | 19/07/2011 | 2        | 10,0                          | 10,0           | 10,0           | 10,00 |        | 3,9            | 3,9            | 3,9            | 3,94 |        |
| S-21 | 18/07/2011  | 19/07/2011 | 3        | 10,0                          | 10,0           | 10,0           | 10,01 |        | 3,9            | 3,9            | 3,9            | 3,93 |        |
| S-22 | 20/07/2011  | 21/07/2011 | 1        | 9,9                           | 9,9            | 9,9            | 9,93  |        | 3,9            | 3,9            | 4,0            | 3,94 |        |
| S-23 | 20/07/2011  | 21/07/2011 | 2        | 9,9                           | 9,9            | 9,9            | 9,92  |        | 4,0            | 4,0            | 4,0            | 3,97 |        |
| S-24 | 20/07/2011  | 21/07/2011 | 3        | 10,0                          | 10,0           | 10,0           | 9,96  |        | 4,0            | 4,0            | 4,0            | 3,96 |        |
| S-25 | 28/07/2011  | 29/07/2011 | 1        | 10,0                          | 10,0           | 10,0           | 9,96  |        | 4,0            | 4,0            | 4,0            | 3,97 |        |
| S-26 | 28/07/2011  | 29/07/2011 | 2        | 10,0                          | 10,0           | 10,0           | 9,97  |        | 3,9            | 3,9            | 3,9            | 3,94 |        |
| S-27 | 28/07/2011  | 29/07/2011 | 3        | 10,0                          | 10,0           | 10,0           | 9,98  |        | 3,9            | 3,9            | 3,9            | 3,93 |        |
| S-28 | 14/09/2011  | 15/09/2011 | 3        | 9,9                           | 9,9            | 9,9            | 9,90  |        | 3,9            | 3,9            | 3,9            | 3,90 |        |
| S-29 | 14/09/2011  | 15/09/2011 | 2        | 10,0                          | 9,9            | 9,9            | 9,93  |        | 4,0            | 4,0            | 4,0            | 4,00 |        |
| S-30 | 14/09/2011  | 15/09/2011 | 1        | 10,0                          | 10,0           | 10,0           | 10,00 |        | 3,9            | 3,9            | 3,9            | 3,90 |        |
| S-31 | 11/01/2012  | 12/01/2012 | 3        | 10,0                          | 10,0           | 10,0           | 10,00 |        | 3,9            | 3,9            | 3,9            | 3,90 |        |
| S-32 | 11/01/2012  | 12/01/2012 | 2        | 10,0                          | 9,9            | 10,0           | 9,97  |        | 3,9            | 3,9            | 3,9            | 3,90 |        |
| S-33 | 11/01/2012  | 12/01/2012 | 1        | 10,0                          | 10,0           | 10,0           | 10,00 |        | 3,9            | 3,9            | 3,9            | 3,90 |        |

**Table A.1-** Dimensions of the dog-bone samples for DC993

The positions, distinguishing the dog-bone specimens and the locations of the measured dimensions are presented in Fig. A.2. The “Aver” values are obtained by averaging either the width or the thickness for the three locations “1”, “2” and “3” and the standard deviations are calculated based on these “Aver” values. As it can be seen, the standard deviations of the width and the thickness are very low, which allows to conclude on the good reproducibility of the injection system.

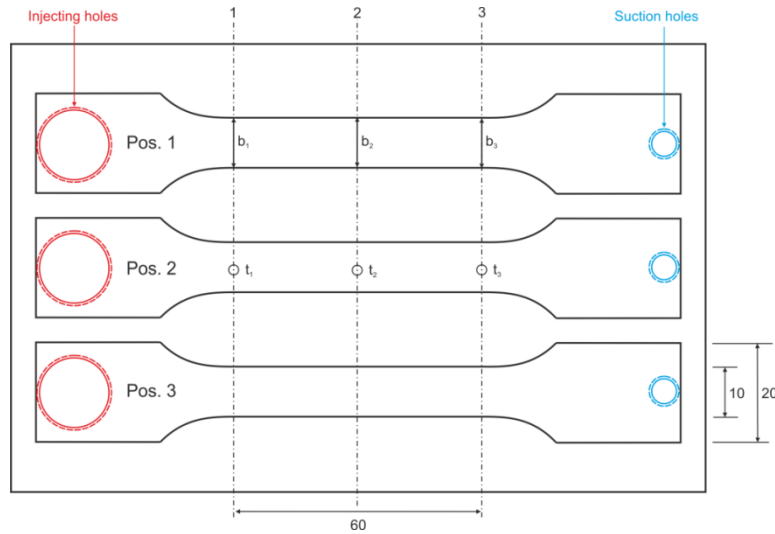
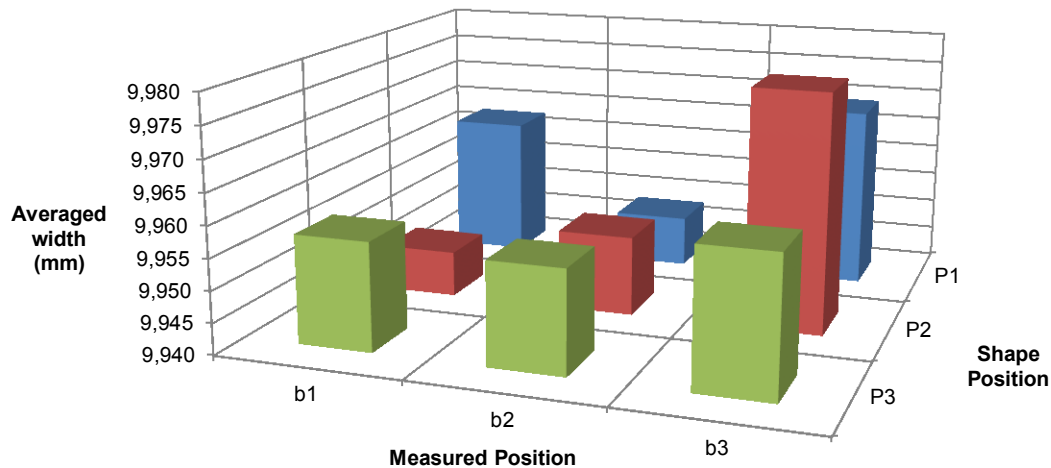
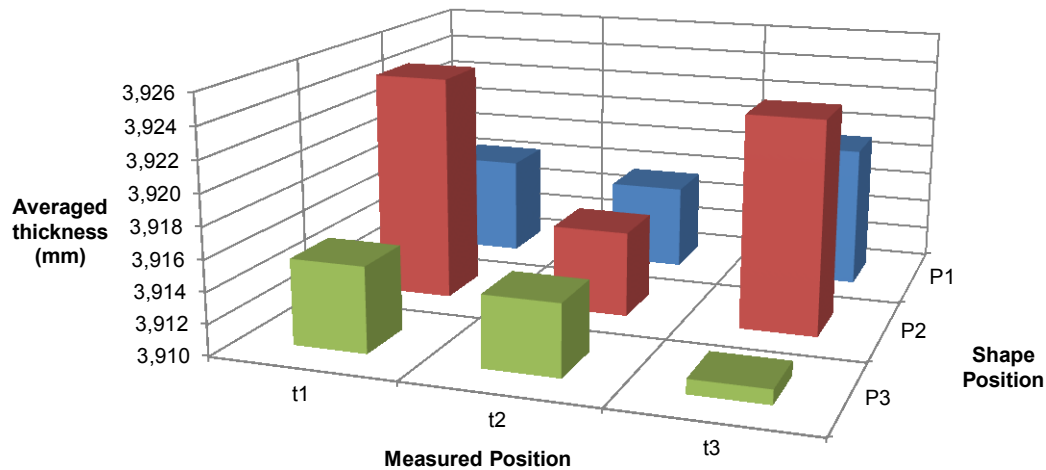


Figure A.2- Details of the measured positions –silicone dog-bone samples



(a)



(b)

Figure A.3- (a) Width and (b) Thickness function of the position in the mold

Nevertheless, to evaluate the possible influence of the mold on the dimensions of the manufactured dog-bone specimens, the averaged widths and thicknesses were plotted versus the shape position and the measured position, see Fig. A.3. For the width, the maximum dispersion of about 0,04mm is observed in the shape P2 between the position  $b_1$  and  $b_3$ . This value is very low compared to the desired width of 10mm and could also due to the lack of precision in the measuring phase. For the thickness, the maximum dispersion of about 0.015mm is found between the position  $t_3$  of shape  $p_3$  and the position  $t_1$  of shape  $p_2$ . Again, this dispersion is sufficiently small to be neglected.

### A.3 Silicone compressive samples - dimensions control

As for the dog-bone samples, the dimensions of the 35 cylindrical compressive samples, mentioned in section 4.2.2.1, were measured with a caliper and recorded in Table A.2.

| N°    | Manuf. Date | Turn out   | Dimensions    |        |          |             |        |          | Weight (g) |        |          |
|-------|-------------|------------|---------------|--------|----------|-------------|--------|----------|------------|--------|----------|
|       |             |            | Diameter (mm) |        |          | Height (mm) |        |          | w          | Aver.  | $\sigma$ |
|       |             |            | d             | Aver.  | $\sigma$ | h           | Aver.  | $\sigma$ |            |        |          |
| SC-01 | 22/12/2010  | 23/12/2010 | 45,7          | 45,631 | 0,191    | 20,8        | 20,769 | 0,345    | 43,3       | 43,437 | 0,724    |
| SC-02 | 07/04/2011  | 11/04/2011 | 45,7          |        |          | 20,8        |        |          | 43,7       |        |          |
| SC-03 | 14/04/2011  | 19/04/2011 | 45,7          |        |          | 21,2        |        |          | 44,5       |        |          |
| SC-04 | 14/04/2011  | 19/04/2011 | 45,4          |        |          | 21,1        |        |          | 44         |        |          |
| SC-05 | 19/04/2011  | 20/04/2011 | 45,3          |        |          | 21,3        |        |          | 44,4       |        |          |
| SC-06 | 21/04/2011  | 26/04/2011 | 45,5          |        |          | 20,3        |        |          | 42,9       |        |          |
| SC-07 | 21/04/2011  | 26/04/2011 | 45,4          |        |          | 20,7        |        |          | 43,2       |        |          |
| SC-08 | 21/04/2011  | 26/04/2011 | 45,2          |        |          | 21,1        |        |          | 44,3       |        |          |
| SC-09 | 27/05/2011  | 30/05/2011 | 45,2          |        |          | 20          |        |          | 41,4       |        |          |
| SC-10 | 27/05/2011  | 30/05/2011 | 45,6          |        |          | 20,8        |        |          | 43,2       |        |          |
| SC-11 | 27/05/2011  | 30/05/2011 | 45,7          |        |          | 20,6        |        |          | 41,5       |        |          |
| SC-12 | 15/07/2011  | 18/07/2011 | 45,8          |        |          | 21,3        |        |          | 44,5       |        |          |
| SC-13 | 15/07/2011  | 18/07/2011 | 45,5          |        |          | 20,9        |        |          | 43,5       |        |          |
| SC-14 | 15/07/2011  | 18/07/2011 | 45,7          |        |          | 21,3        |        |          | 44,0       |        |          |
| SC-15 | 18/07/2011  | 19/07/2011 | 45,7          |        |          | 21          |        |          | 43,8       |        |          |
| SC-16 | 18/07/2011  | 19/07/2011 | 45,7          |        |          | 20,7        |        |          | 43,6       |        |          |
| SC-17 | 18/07/2011  | 19/07/2011 | 45,5          |        |          | 21,1        |        |          | 43,6       |        |          |
| SC-18 | 20/07/2011  | 21/07/2001 | 45,7          |        |          | 21          |        |          | 43,6       |        |          |
| SC-19 | 28/07/2011  | 29/07/2011 | 45,7          |        |          | 20,8        |        |          | 43,8       |        |          |
| SC-20 | 28/07/2011  | 29/07/2011 | 45,7          |        |          | 20,5        |        |          | 43,3       |        |          |
| SC-21 | 14/09/2011  | 15/08/2011 | 45,8          |        |          | 20,8        |        |          | 43,3       |        |          |
| SC-22 | 20/09/2011  | 21/09/2011 | 45,5          |        |          | 20,4        |        |          | 42,9       |        |          |
| SC-23 | 04/10/2011  | 05/10/2011 | 45,6          |        |          | 20,4        |        |          | 42,6       |        |          |
| SC-24 | 04/10/2011  | 05/10/2011 | 45,4          |        |          | 20,5        |        |          | 42,4       |        |          |
| SC-25 | 11/01/2012  | 12/01/2012 | 45,8          |        |          | 20          |        |          | 42,8       |        |          |
| SC-26 | 11/01/2012  | 12/01/2012 | 46            |        |          | 20,2        |        |          | 43,1       |        |          |
| SC-27 | 02/05/2012  | 03/05/2012 | 46            |        |          | 21          |        |          | 43,8       |        |          |

|       |            |            |      |  |  |      |  |  |      |  |  |
|-------|------------|------------|------|--|--|------|--|--|------|--|--|
| SC-28 | 02/05/2012 | 03/05/2012 | 45,7 |  |  | 21   |  |  | 44,4 |  |  |
| SC-29 | 02/05/2012 | 03/05/2012 | 45,8 |  |  | 21,1 |  |  | 44,1 |  |  |
| SC-30 | 02/05/2012 | 03/05/2012 | 45,5 |  |  | 20,8 |  |  | 43,4 |  |  |
| SC-31 | 16/05/2012 | 18/05/2012 | 45,6 |  |  | 20,7 |  |  | 43,7 |  |  |
| SC-32 | 16/05/2012 | 18/05/2012 | 45,7 |  |  | 20,7 |  |  | 43,9 |  |  |
| SC-33 | 16/05/2012 | 18/05/012  | 45,8 |  |  | 20,8 |  |  | 43,1 |  |  |
| SC-34 | 06/06/2012 | 07/06/2012 | 45,7 |  |  | 20,4 |  |  | 43,4 |  |  |
| SC-35 | 14/06/2012 | 15/06/2012 | 45,8 |  |  | 20,8 |  |  | 43,3 |  |  |

**Table A.2-** Dimensions of the compressive samples for DC993

The average value of the diameter was slightly higher than the desired one, but the standard deviation was relatively small. Idem for the analysis of the height of the samples, for which a low dispersion was observed. Finally the weight of the samples was of interest, to ensure that no important air bubbles were trapped in each specimen. As it can be remarked, the variations of the weight were less than 2%, which definitely validated the manufacturing process.

#### A.4 Silicone push-out shear samples - dimensions control

To manufacture double lap-joint shear tests, two outer glass plates were necessary for only one inner steel plate. The glass plates, whose dimensions were 240x200x12mm were fabricated and tempered by VITRUM LUX. Chamfers all along the edges were done in order to avoid unwanted stress peaks and possible failure of the glass. The steel plates of dimensions 200x200x12mm were also machined to straighten the upper and lower edges. This, in combination with the calibrated Teflon plates, allowed to ensure the parallelism of all the edges and so the uniformity of the applied load. No particular treatment was brought on the glued surfaces of the steel. Solvent was employed to degrease each surface, either glass or steel, before applying the primer recommended by Dow Corning.

All the glass plates were measured with the help of a digital caliper, i.e. the width, height and thickness were assessed. Furthermore, the weight was also recorded to later appraise the quantity of silicone needed for each specimen. All these data, related to the glass, are presented in the following table:

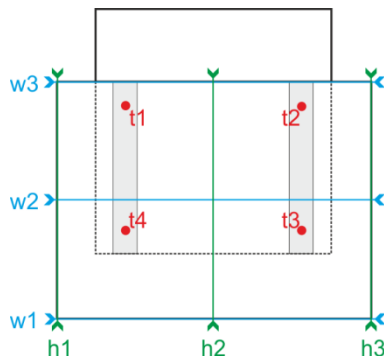
| N°       | Width (mm)     |                |                | Height (mm)    |                |                | Thickness (mm) |                |                |                | Weight (g) |
|----------|----------------|----------------|----------------|----------------|----------------|----------------|----------------|----------------|----------------|----------------|------------|
|          | w <sub>1</sub> | w <sub>2</sub> | w <sub>3</sub> | h <sub>1</sub> | h <sub>2</sub> | h <sub>3</sub> | t <sub>1</sub> | t <sub>2</sub> | t <sub>3</sub> | t <sub>4</sub> |            |
| GPO-01-1 | 241,5          | 241,5          | 241,4          | 200,5          | 200,1          | 200,3          | 12,08          | 12,10          | 12,05          | 12,07          | 1456,9     |
| GPO-01-2 | 241,6          | 241,3          | 241,3          | 200,1          | 200,2          | 200,1          | 12,06          | 12,05          | 12,10          | 12,10          | 1456,3     |
| GPO-02-1 | 241,1          | 241            | 241            | 200,3          | 200            | 200,1          | 12,06          | 12,07          | 12,06          | 12,04          | 1452,2     |
| GPO-02-2 | 241,5          | 241,4          | 241,2          | 200            | 200            | 200,2          | 12,07          | 12,06          | 12,10          | 12,10          | 1456,1     |
| GPO-03-1 | 241,5          | 241,2          | 241,3          | 200,3          | 200,6          | 200,7          | 12,10          | 12,11          | 12,06          | 12,05          | 1458,2     |
| GPO-03-2 | 241,5          | 241,5          | 241,3          | 200,5          | 200            | 200            | 12,09          | 12,10          | 12,05          | 12,06          | 1456,4     |
| GPO-04-1 | 241            | 241            | 241            | 200,5          | 200,3          | 200,3          | 12,06          | 12,06          | 12,06          | 12,06          | 1452,2     |
| GPO-04-2 | 241,4          | 241,3          | 241,1          | 200,6          | 200,2          | 200,2          | 12,09          | 12,09          | 12,09          | 12,09          | 1456,6     |
| GPO-05-1 | 241,5          | 241,2          | 241            | 200            | 200,1          | 200,3          | 12,06          | 12,07          | 12,07          | 12,06          | 1453,5     |
| GPO-05-2 | 239,9          | 241            | 240,9          | 200,1          | 200,1          | 200,2          | 12,05          | 12,06          | 12,06          | 12,05          | 1451,1     |
| GPO-06-1 | 241,1          | 240,7          | 240,5          | 200,5          | 200,5          | 200,2          | 12,04          | 12,09          | 12,09          | 12,05          | 1454,3     |
| GPO-06-2 | 241,1          | 241,1          | 241,1          | 200,1          | 200,1          | 200,1          | 12,07          | 12,05          | 12,05          | 12,05          | 1452       |

|          |       |        |       |       |       |       |       |       |       |       |        |
|----------|-------|--------|-------|-------|-------|-------|-------|-------|-------|-------|--------|
| GPO-07-1 | 241,4 | 241,2  | 241   | 200,5 | 200,8 | 200,4 | 12,09 | 12,10 | 12,07 | 12,07 | 1457,6 |
| GPO-07-2 | 241   | 240,6  | 240,4 | 200   | 200,2 | 200   | 12,03 | 12,03 | 12,04 | 12,04 | 1447,9 |
| GPO-08-1 | 241,2 | 241    | 241,2 | 200,1 | 200,3 | 200,6 | 12,03 | 12,06 | 12,05 | 12,03 | 1452,8 |
| GPO-08-2 | 241,6 | 241,4  | 241,6 | 200,1 | 200,1 | 200,3 | 12,07 | 12,04 | 12,09 | 12,07 | 1456,5 |
| GPO-09-1 | 240,6 | 240,9  | 240,6 | 200,4 | 200,4 | 200,5 | 12,07 | 12,07 | 12,07 | 12,07 | 1454,5 |
| GPO-09-2 | 241,2 | 240,9  | 240,6 | 200,2 | 200,2 | 200,3 | 12,10 | 12,08 | 12,06 | 12,06 | 1454,9 |
| GPO-10-1 | 241,6 | 241,4  | 241,6 | 200,1 | 200,1 | 200,6 | 12,05 | 12,06 | 12,10 | 12,10 | 1457,1 |
| GPO-10-2 | 204,8 | 240,7  | 240,5 | 200,2 | 200,2 | 200,1 | 12,03 | 12,03 | 12,03 | 12,03 | 1448,2 |
| GPO-11-1 | 241,3 | 241,2  | 240,6 | 200,1 | 200,3 | 200,4 | 12,07 | 12,07 | 12,10 | 12,09 | 1455,6 |
| GPO-11-2 | 241,4 | 241,4  | 241,4 | 200,5 | 200,1 | 200   | 12,07 | 12,06 | 12,10 | 12,10 | 1455,6 |
| GPO-12-1 | 241   | 240,9  | 240,8 | 200,2 | 200,2 | 200,9 | 12,03 | 12,04 | 12,04 | 12,03 | 1450,4 |
| GPO-12-2 | 241,5 | 241,4  | 241,5 | 200,4 | 200,5 | 200,5 | 12,10 | 12,10 | 12,06 | 12,07 | 1458,4 |
| GPO-13-1 | 240,6 | 240,6  | 240,6 | 204,4 | 204,3 | 204,4 | 12,07 | 12,07 | 12,07 | 12,08 | n      |
| GPO-13-2 | 240,7 | 240,6  | 240,6 | 204,3 | 204,3 | 204,4 | 12,04 | 12,05 | 12,05 | 12,05 | n      |
| GPO-14-1 | 240,7 | 240,7  | 240,7 | 204,4 | 204,3 | 204,3 | 12,04 | 12,05 | 12,05 | 12,04 | n      |
| GPO-14-2 | 240,6 | 240,6  | 240,6 | 204,3 | 204,3 | 204,3 | 12,06 | 12,06 | 12,06 | 12,06 | n      |
| GPO-15-1 | 240,7 | 240,7  | 240,7 | 204,4 | 204,4 | 204,4 | 12,02 | 12,01 | 12,09 | 12,1  | 1477,7 |
| GPO-15-2 | 240,7 | 240,7  | 240,6 | 204,4 | 204,3 | 204,4 | 12,09 | 12,1  | 12    | 12,01 | 1478   |
| GPO-16-1 | 240,7 | 2740,7 | 240,6 | 204,4 | 204,4 | 203,3 | 12,01 | 12,09 | 12    | 12    | 1477,1 |
| GPO-16-2 | 240,7 | 240,7  | 240,7 | 204,3 | 204,3 | 204,3 | 12,06 | 12,06 | 12,06 | 12,07 | 1477,4 |
| GPO-17-1 | 240,7 | 240,7  | 240,7 | 204,3 | 204,3 | 204,4 | 12,06 | 12,06 | 12,06 | 12,06 | 1477,5 |
| GPO-17-2 | 240,6 | 240,6  | 240,6 | 204,3 | 204,3 | 204,4 | 12,01 | 12    | 12,1  | 12,1  | 1477,4 |
| GPO-18-1 | 240,6 | 240,6  | 240,6 | 204,4 | 204,3 | 204,3 | 12,06 | 12,06 | 12,05 | 12,05 | 1477,5 |
| GPO-18-2 | 240,6 | 240,6  | 240,6 | 204,4 | 204,3 | 204,3 | 12,04 | 12,06 | 12,05 | 12,04 | 1476,4 |
| GPO-19-1 | 240,7 | 240,6  | 240,6 | 204,3 | 204,3 | 204,2 | 12,1  | 12,09 | 12    | 11,99 | 1476,3 |
| GPO-19-2 | 240,7 | 240,6  | 240,6 | 204,4 | 204,3 | 204,3 | 12,06 | 12,08 | 12,08 | 12,07 | 1479,5 |
| GPO-20-1 | 240,7 | 240,7  | 240,6 | 204,4 | 204,3 | 204,4 | 12,05 | 12,07 | 12,06 | 12,05 | 1477,7 |
| GPO-20-2 | 240,6 | 240,6  | 240,5 | 204,4 | 204,3 | 204,4 | 12,06 | 12,1  | 11,99 | 12    | 1477,4 |
| GPO-21-1 | 240,7 | 240,6  | 240,6 | 203   | 202,5 | 201,6 | 11,77 | 11,73 | 11,76 | 11,76 | 1420,5 |
| GPO-21-2 | 240,7 | 240,6  | 240,2 | 204,4 | 204,3 | 202,9 | 12,06 | 12,08 | 12,08 | 12,07 | 1473,5 |
| GPO-22-1 | 240,7 | 240,6  | 240,6 | 204,2 | 204,3 | 204,4 | 12,07 | 12,07 | 12,07 | 12,07 | 1477,9 |
| GPO-22-2 | 240,7 | 240,7  | 240,7 | 204,3 | 204,3 | 204,4 | 12,04 | 12,04 | 12,04 | 12,04 | 1475,2 |
| GPO-23-1 | 240,6 | 240,6  | 240,6 | 204,3 | 204,3 | 204,4 | 12,1  | 12,1  | 12    | 12    | 1478,2 |
| GPO-23-2 | 240,6 | 240,6  | 240,5 | 204,4 | 204,3 | 204,4 | 12,1  | 12,1  | 12    | 12    | 1478,1 |
| GPO-24-1 | 240,7 | 240,7  | 240,6 | 20,5  | 200,9 | 201,6 | 11,76 | 11,76 | 11,8  | 11,8  | 1416,1 |
| GPO-24-2 | 240,7 | 240,7  | 240,6 | 202,3 | 202,3 | 202,4 | 11,81 | 11,8  | 11,83 | 11,84 | 1432,5 |
| GPO-25-1 | 240,6 | 240,6  | 240,5 | 204,3 | 204,3 | 204,4 | 12,04 | 12,04 | 12,03 | 12,03 | 1474,8 |
| GPO-25-2 | 240,5 | 240,5  | 240,5 | 204,4 | 204,3 | 204,2 | 12,05 | 12,06 | 12,04 | 12,04 | 1476,5 |
| GPO-26-1 | 240,6 | 240,7  | 240,6 | 204,3 | 204,3 | 204,3 | 12,06 | 12,06 | 12,06 | 12,06 | 1478,2 |
| GPO-26-2 | 240,6 | 240,6  | 240,6 | 204,3 | 204,3 | 204,4 | 12    | 12,01 | 12,08 | 12,09 | 1477,6 |

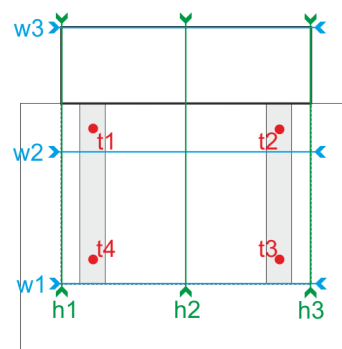
|          |       |       |       |       |       |       |       |       |       |       |        |
|----------|-------|-------|-------|-------|-------|-------|-------|-------|-------|-------|--------|
| GPO-27-1 | 240,6 | 240,6 | 240,6 | 204,3 | 204,3 | 204,3 | 12,04 | 12    | 11,97 | 12,03 | 1471,5 |
| GPO-27-2 | 240,6 | 240,5 | 204,4 | 204,4 | 204,3 | 204,4 | 12,04 | 12,03 | 12,04 | 12,04 | 1475,3 |
| GPO-28-1 | 240,6 | 240,6 | 240,5 | 204,4 | 204,4 | 204,3 | 12    | 11,98 | 12,09 | 12,09 | 1477,6 |
| GPO-28-2 | 240,5 | 240,5 | 240,5 | 204,2 | 204,2 | 204,3 | 12,03 | 11,99 | 11,99 | 12,04 | 1471,2 |
| GPO-29-1 | 240,7 | 240,7 | 240,6 | 204,4 | 204,4 | 204,5 | 12,06 | 12,06 | 12,05 | 12,06 | 1478   |
| GPO-29-2 | 240,7 | 240,7 | 240,7 | 204,4 | 204,3 | 204,4 | 12,1  | 12,09 | 12,01 | 12    | 1477,8 |
| GPO-30-1 | 240,7 | 240,7 | 240,7 | 204,4 | 204,4 | 204,4 | 12,09 | 12,1  | 12,09 | 12,09 | 1482,5 |
| GPO-30-2 | 240,7 | 240,7 | 240,6 | 204,4 | 204,4 | 204,4 | 12,07 | 12,05 | 12,05 | 12,07 | 1477,9 |
| GPO-31-1 | 204,7 | 240,7 | 240,7 | 204,4 | 204,3 | 204,4 | 12,04 | 12,03 | 12,03 | 12,04 | 1475,7 |
| GPO-31-2 | 240,7 | 240,7 | 240,7 | 204,4 | 204,3 | 204,3 | 12,07 | 12,06 | 12,06 | 12,07 | 1478,5 |
| GPO-32-1 | 240,7 | 240,6 | 240,6 | 204,4 | 204,3 | 204,4 | 12,07 | 12,06 | 12,05 | 12,06 | 1477,5 |
| GPO-32-2 | 240,7 | 240,7 | 240,6 | 204,4 | 204,4 | 204,3 | 12,1  | 12,09 | 12    | 12,01 | 1478,2 |
| GPO-33-1 | 240,6 | 240,7 | 240,6 | 204,4 | 204,3 | 204,4 | 12,09 | 12,09 | 12    | 11,98 | 1477,9 |
| GPO-33-2 | 240,6 | 240,6 | 240,6 | 204,4 | 204,3 | 204,4 | 12,01 | 12,01 | 12,1  | 12,1  | 1478,4 |
| GPO-34-1 | 240,6 | 240,6 | 240,6 | 204,4 | 204,3 | 204,3 | 12,07 | 12,06 | 12,06 | 12,06 | 1477,8 |
| GPO-34-2 | 240,7 | 240,7 | 240,7 | 204,3 | 204,3 | 204,4 | 12,06 | 12,06 | 12,06 | 12,05 | 1477,5 |
| GPO-35-1 | 240,7 | 240,7 | 240,6 | 204,4 | 204,3 | 204,4 | 12,1  | 12,1  | 12    | 12,03 | 1478,4 |
| GPO-35-2 | 240,7 | 240,7 | 240,7 | 204,4 | 204,3 | 204,4 | 12,08 | 12,07 | 12,07 | 12,09 | 1479,5 |
| GPO-36-1 | 240,7 | 240,7 | 240,7 | 204,4 | 204,3 | 204,3 | 12,05 | 12,04 | 12,04 | 12,05 | 1476,3 |
| GPO-36-2 | 240,7 | 240,7 | 240,6 | 204,3 | 204,3 | 204,3 | 12,04 | 12,04 | 12,04 | 12,04 | 1475,1 |
| GPO-37-1 | 240,6 | 240,6 | 240,6 | 204,4 | 204,3 | 204,5 | 12,08 | 12,06 | 12,07 | 12,08 | 1479,6 |
| GPO-37-2 | 240,6 | 240,6 | 240,5 | 204,4 | 204,3 | 204,3 | 12,06 | 12,06 | 12,05 | 12,06 | 1477,3 |
| GPO-38-1 | 240,6 | 240,6 | 240,6 | 204,3 | 204,3 | 204,4 | 12,01 | 11,99 | 12,09 | 12,09 | 1477,6 |
| GPO-38-2 | 240,6 | 240,6 | 240,5 | 204,4 | 204,4 | 204,4 | 12    | 12    | 12,1  | 12,1  | 1479,4 |
| GPO-39-1 | 240,6 | 240,6 | 240,6 | 204,3 | 204,3 | 204,4 | 12,1  | 12,1  | 12    | 12    | 1476,9 |
| GPO-39-2 | 240,7 | 240,7 | 240,7 | 204,4 | 204,4 | 204,4 | 12    | 12    | 12,09 | 12,09 | 1478,3 |
| GPO-40-1 | 240,6 | 240,6 | 240,6 | 204,4 | 204,4 | 204,4 | 12,1  | 12,1  | 12,03 | 12    | 1477,9 |
| GPO-40-2 | 240,7 | 240,7 | 240,7 | 204,3 | 204,3 | 204,3 | 12,04 | 12,06 | 12,05 | 12,04 | 1476,2 |

**Table A.3-** Dimensions and weights of the glass plates composing the push-out samples

The position of each glass measurement is shown in Fig. A.3. Moreover, the thickness positions were chosen according to the position of the silicone bands from the smaller bonded section.



**Figure A.4-** Positions of the glass measurements



**Figure 4.5-** Positions of the steel measurements

In addition, the dimensions and the weights of the steel plates were measured. The following table gathers all these data, whose positions were expressed as detailed in Fig. 4.5.

| Name   | Width (mm)     |                |                | Height (mm)    |                |                | Thickness (mm) |                |                |                | Weight (g) |
|--------|----------------|----------------|----------------|----------------|----------------|----------------|----------------|----------------|----------------|----------------|------------|
|        | w <sub>1</sub> | w <sub>2</sub> | w <sub>3</sub> | h <sub>1</sub> | h <sub>2</sub> | h <sub>3</sub> | t <sub>1</sub> | t <sub>2</sub> | t <sub>3</sub> | t <sub>4</sub> |            |
| SPO-01 | 200,8          | 200,6          | 200,6          | 197            | 197            | 197            | 12,12          | 12,18          | 12,08          | 12,14          | 3724,7     |
| SPO-02 | 200,8          | 201,4          | 200,9          | 196,9          | 196,9          | 196,9          | 12,06          | 12,01          | 12,06          | 12,13          | 3723,1     |
| SPO-03 | 201,2          | 201,9          | 201,4          | 196,9          | 196,9          | 196,9          | 12,05          | 12,09          | 12,06          | 12,01          | 3760,6     |
| SPO-04 | 200,6          | 201            | 201            | 196,9          | 196,9          | 196,9          | 12,2           | 12,19          | 12,22          | 12,21          | 3701,7     |
| SPO-05 | 201,2          | 201,5          | 201,5          | 196,9          | 196,9          | 196,9          | 12,08          | 12,11          | 12,13          | 12,16          | 3738,3     |
| SPO-06 | 200,4          | 200,8          | 201            | 196,9          | 196,9          | 196,9          | 12,19          | 12,15          | 12,07          | 12,12          | 3731,2     |
| SPO-07 | 200,4          | 200,7          | 200,9          | 196,9          | 196,9          | 196,9          | 12,1           | 12,09          | 12,1           | 12,14          | 3728,1     |
| SPO-08 | 200,9          | 201,9          | 201,2          | 196,9          | 196,9          | 196,9          | 12,05          | 12,08          | 12,11          | 12,06          | 3723,3     |
| SPO-09 | 200,5          | 201,1          | 200,9          | 196,9          | 196,9          | 196,9          | 12,14          | 12,21          | 12,18          | 12,14          | 3761,5     |
| SPO-10 | 200,1          | 200,7          | 200,7          | 196,9          | 196,9          | 196,9          | 12,14          | 12,2           | 12,16          | 12,08          | 3744,6     |
| SPO-11 | 199,3          | 199,2          | 199,2          | 196,9          | 196,9          | 196,9          | 12,2           | 12,17          | 12,14          | 12,21          | 3736       |
| SPO-12 | 199,7          | 199,5          | 199,5          | 196,9          | 196,9          | 196,9          | 12,11          | 12,06          | 12,04          | 12,16          | 3717,8     |
| SPO-13 | 200,5          | 201,1          | 201,6          | 197            | 197            | 197            | 12,18          | 12,14          | 12,18          | 12,21          | 3752,1     |
| SPO-14 | 201            | 201,3          | 201            | 196,8          | 196,8          | 196,8          | 12,18          | 12,14          | 12,08          | 12,16          | 3737,7     |
| SPO-15 | 201,4          | 201            | 201,3          | 197,2          | 197,2          | 197,2          | 12,1           | 12,16          | 12,17          | 12,16          | 3738,8     |
| SPO-16 | 199,7          | 199,8          | 200,3          | 197,2          | 197,2          | 197,2          | 12,02          | 12,15          | 12,1           | 12,04          | 3702,3     |
| SPO-17 | 200            | 199,4          | 199,4          | 197,2          | 197,2          | 197,2          | 12,18          | 12,11          | 12,15          | 12,1           | 3725,3     |
| SPO-18 | 201,2          | 201,5          | 200,9          | 197,2          | 197,2          | 197,2          | 12,2           | 12,14          | 12,14          | 12,15          | 3759,5     |
| SPO-19 | 201            | 201,5          | 201,6          | 196,8          | 196,8          | 196,8          | 12,18          | 12,24          | 12,14          | 12,16          | 3755,3     |
| SPO-20 | 201,8          | 201,9          | 210,2          | 196,8          | 196,8          | 196,8          | 12,18          | 12,16          | 12,14          | 12,12          | 3747,5     |
| SPO-21 | 200            | 199,8          | 200,3          | 196,8          | 196,8          | 196,8          | 12,19          | 12,15          | 12,19          | 12,18          | 3734,4     |
| SPO-22 | 199,9          | 199,8          | 201            | 196,8          | 196,8          | 196,8          | 12,19          | 12,11          | 12,05          | 12,19          | 3713,9     |
| SPO-23 | 201,6          | 201,5          | 201,5          | 197,2          | 197,2          | 197,2          | 12,21          | 12,23          | 12,18          | 12,2           | 3770,4     |
| SPO-24 | 200,9          | 200,9          | 201            | 197,2          | 197,2          | 197,2          | 12,09          | 12,08          | 12,12          | 12,18          | 3728,6     |

**Table A.4-** Dimensions and weight of the steel plates composing the push-out samples

The height of the steel was always slightly lower than the width, as it corresponded to the machined edges. As for the glass, very small dispersions were observed for this material, but they were sufficiently small to be tolerated.

The above data concerned each individual element, but were needed to determine the quantity of silicone applied on the final push-out assembly. The total thicknesses of all the fabricated specimens were again measured at the four specific points coinciding with the aforementioned thicknesses for the glass and steel plates. This allowed ensuring that the desired joint thicknesses were respected for each manufacturing procedure, i.e. for the pouring and injecting process. Furthermore, the weight of each realized push-out sample was also compared to the sum of the weights of the glass and steel plates composing it. With this information, it was possible to evaluate the total weight of used silicone. Any dispersion coming from thickness variation could also be visible by analyzing the total weight of silicone. These two points were investigated for all the 16 specimens of the Taguchi design of experiments presented in section 4.2.3.2.



The following table regroupes the repartition of the glass and steel plates, according to the design of experiments of the quasi-static shear tests, and the weights and thicknesses of each final specimen. The height, corresponding to the distance from the bottom of the assembly to the top of the inner steel plate, was measured in two distant points to also check the parallelism between the extreme edges in which will be transferred the load.

| N° | Composing plates      |        |                       | Weight (g) | Thickness (mm) |                |                |                | Height (mm) |       |
|----|-----------------------|--------|-----------------------|------------|----------------|----------------|----------------|----------------|-------------|-------|
|    | 1 <sup>st</sup> glass | steel  | 2 <sup>nd</sup> glass | w          | t <sub>1</sub> | t <sub>2</sub> | t <sub>3</sub> | t <sub>4</sub> | A           | B     |
| 1  | GPO-15-1              | SPO-14 | GPO-15-2              | 6778       | 42,9           | 42,7           | 42,7           | 43,0           | 237,9       | 237,9 |
| 2  | GPO-13-1              | SPO-11 | GPO-13-2              | 6769,2     | 42,6           | 42,7           | 42,4           | 42,3           | 238,4       | 238,4 |
| 3  | GPO-23-1              | SPO-09 | GPO-23-2              | 6875,8     | 48,3           | 48,7           | 48,7           | 48,4           | 238,6       | 239,3 |
| 4  | GPO-24-1              | SPO-10 | GPO-24-2              | 6757,2     | 48,1           | 47,9           | 47,6           | 47,7           | 238,3       | 238,4 |
| 5  | GPO-16-1              | SPO-13 | GPO-16-2              | 6980,6     | 45,0           | 43,5           | 42,5           | 44,0           | 237,4       | 237,4 |
| 6  | GPO-14-1              | SPO-12 | GPO-14-2              | 6971       | 44,9           | 45,4           | 44,0           | 43,4           | 237,8       | 237,8 |
| 7  | GPO-18-1              | SPO-15 | GPO-18-2              | 7150,6     | 48,9           | 48,4           | 48,9           | 49,5           | 237,3       | 237,3 |
| 8  | GPO-25-1              | SPO-07 | GPO-25-2              | 7161,9     | 48,1           | 48,1           | 47,9           | 48,5           | 237,3       | 237,3 |
| 9  | GPO-21-1              | SPO-14 | GPO-21-2              | 6709,8     | 42,4           | 42,4           | 42,3           | 42,4           | 238,6       | 239,9 |
| 10 | GPO-22-1              | SPO-13 | GPO-22-2              | 6785,7     | 42,7           | 42,3           | 42,3           | 42,7           | 237,9       | 237,9 |
| 11 | GPO-27-1              | SPO-09 | GPO-27-2              | 6866,7     | 48,3           | 48,3           | 48,9           | 49,1           | 239,0       | 239,1 |
| 12 | GPO-26-1              | SPO-11 | GPO-26-2              | 6842,1     | 48,3           | 48,4           | 48,7           | 48,4           | 240,0       | 239,3 |
| 13 | GPO-02-1              | SPO-02 | GPO-02-2              | 6862,7     | 43,0           | 43,0           | 43,1           | 43,2           | 236,7       | 236,7 |
| 14 | GPO-04-1              | SPO-04 | GPO-04-2              | 6903,2     | 43,6           | 43,1           | 43,1           | 43,5           | 236,6       | 236,6 |
| 15 | GPO-05-1              | SPO-05 | GPO-05-2              | 7061,5     | 48,5           | 48,5           | 48,7           | 48,7           | 237,0       | 237,0 |
| 16 | GPO-06-1              | SPO-06 | GPO-06-2              | 7068,8     | 48,8           | 48,6           | 48,5           | 48,8           | 236,6       | 236,7 |

**Table A.5-** Composition of the quasi-static shear push-out tests and characteristic weight and dimensions

By observing the total height of the specimens in the two extremities A and B, some minor deviations less than 1mm were found, which allowed to conclude on the parallelism of the edges. By crosslinking the previous three tables, it was possible to set up a new one comprising the total thickness and volume of the silicone for each sample, see Table A.6.

| N° | Silicone Weight (g) | Silicone ideal weight (g) | Difference (%) | 2 x thickness of silicone (mm) |                |                |                |         |       |           |
|----|---------------------|---------------------------|----------------|--------------------------------|----------------|----------------|----------------|---------|-------|-----------|
|    |                     |                           |                | t <sub>1</sub>                 | t <sub>2</sub> | t <sub>3</sub> | t <sub>4</sub> | Average | Ideal | Diff. (%) |
| 1  | 84,6                | 73,7                      | 14,8           | 6,6                            | 6,5            | 6,5            | 6,7            | 6,6     | 6     | 9,4       |
| 2  | -                   |                           | -              | 6,3                            | 6,4            | 6,1            | 6,0            | 6,2     | 6     | 3,1       |
| 3  | 158                 | 147,3                     | 7,2            | 12,0                           | 12,3           | 12,6           | 12,3           | 12,3    | 12    | 2,3       |
| 4  | 164                 |                           | 11,3           | 12,4                           | 12,1           | 11,8           | 12,0           | 12,1    | 12    | 0,7       |
| 5  | 274                 | 208,7                     | 31,3           | 8,8                            | 7,2            | 6,3            | 7,7            | 7,5     | 6     | 24,5      |
| 6  | -                   |                           | -              | 8,7                            | 9,3            | 7,9            | 7,1            | 8,2     | 6     | 37,4      |
| 7  | 457,9               | 417,4                     | 9,7            | 12,7                           | 12,1           | 12,6           | 13,3           | 12,7    | 12    | 5,6       |
| 8  | 482,5               |                           | 15,6           | 12,0                           | 11,9           | 11,7           | 12,3           | 12,0    | 12    | -0,4      |
| 9  | 78,1                | 73,7                      | 6,0            | 6,4                            | 6,4            | 6,4            | 6,4            | 6,4     | 6     | 6,7       |
| 10 | 80,5                |                           | 9,3            | 6,4                            | 6,0            | 6,0            | 6,4            | 6,2     | 6     | 3,4       |

|    |       |       |      |      |      |      |      |      |    |      |
|----|-------|-------|------|------|------|------|------|------|----|------|
| 11 | 158,4 | 147,3 | 7,5  | 12,1 | 12,1 | 12,8 | 12,9 | 12,5 | 12 | 3,9  |
| 12 | 150,3 |       | 2,0  | 12,0 | 12,1 | 12,4 | 12,0 | 12,1 | 12 | 1,1  |
| 13 | 231,3 | 208,7 | 15,3 | 6,8  | 6,8  | 6,9  | 6,9  | 6,9  | 6  | 14,2 |
| 14 | 292,7 |       | 57,0 | 7,3  | 6,8  | 6,7  | 7,2  | 7,0  | 6  | 16,3 |
| 15 | 418,6 | 417,4 | 0,3  | 12,3 | 12,2 | 12,4 | 12,4 | 12,3 | 12 | 2,9  |
| 16 | 431,3 |       | 3,3  | 12,5 | 12,3 | 12,3 | 12,6 | 12,4 | 12 | 3,4  |

**Table A.6-** Analysis of the weight and of the total silicone thickness

As it can be remarked, the largest variations in weight appeared for samples 5, 13 and 14, i.e. for the samples possessing a large glued area and a small thickness. For all the others, the estimated difference was about 10%, which was judged as correct. For the specimens exposing the biggest dispersions were associated the largest differences in total thickness. This implied that the data, weight and thickness, were correlated and were depending on the dimensions of the glued area. The pouring process was realized for these specimens and the compression applied to evacuate the surplus of silicone was consequently not enough. Nevertheless, compressing more could have led to a breakage of the glass plates.

## A.5 Acrylic dog-bone samples - dimensions control

As for the silicone dog-bone samples, the controls of the tested zone dimensions were realized for all the 34 manufactured acrylic specimens. As only two hours were needed to achieve a complete curing, the manufacturing date always corresponded to the unmolding date. The width and the thickness were measured with a digital caliper in three different locations, i.e. just after the radius and at the center, see Fig. A.6 and Table A.7.

| N°   | Manuf. Date | System | Dimensions of the tested zone |                |                |       |         |                |                |                |      |         |
|------|-------------|--------|-------------------------------|----------------|----------------|-------|---------|----------------|----------------|----------------|------|---------|
|      |             |        | Width (mm)                    |                |                |       |         | Thickness (mm) |                |                |      |         |
|      |             |        | b <sub>1</sub>                | b <sub>2</sub> | b <sub>3</sub> | Aver  | σ       | t <sub>1</sub> | t <sub>2</sub> | t <sub>3</sub> | Aver | σ       |
| A-00 | 01/07/2011  | 1      | 10                            | 10             | 9,9            | 9,97  | 0,00690 | 3              | 3              | 3              | 3,00 | 0,00081 |
| A-01 | 04/07/2011  | 1      | 10                            | 10             | 10             | 10,00 |         | 3              | 3,1            | 3              | 3,03 |         |
| A-02 | 04/07/2011  | 1      | 10,1                          | 10             | 10             | 10,03 |         | 3,1            | 3              | 3,1            | 3,07 |         |
| A-03 | 04/07/2011  | 2      | 9,9                           | 10             | 10             | 9,97  |         | 3              | 3,1            | 3              | 3,03 |         |
| A-04 | 05/07/2011  | 1      | 10,3                          | 10             | 10,1           | 10,13 |         | 3,1            | 3              | 3,1            | 3,07 |         |
| A-05 | 05/07/2011  | 2      | 10                            | 10             | 10             | 10,00 |         | 3              | 3              | 3              | 3,00 |         |
| A-06 | 05/07/2011  | 1      | 10,2                          | 10             | 10,2           | 10,13 |         | 3,1            | 3              | 3,1            | 3,07 |         |
| A-07 | 05/07/2011  | 2      | 10,3                          | 10,2           | 10             | 10,17 |         | 3              | 3,1            | 3              | 3,03 |         |
| A-08 | 06/07/2011  | 1      | 10,3                          | 10             | 10,2           | 10,17 |         | 3,1            | 3              | 3,1            | 3,07 |         |
| A-09 | 06/07/2011  | 2      | 10,3                          | 10             | 10             | 10,10 |         | 3              | 3,1            | 3              | 3,03 |         |
| A-10 | 06/07/2011  | 1      | 10,3                          | 9,9            | 10             | 10,07 |         | 3,1            | 3              | 3,1            | 3,07 |         |
| A-11 | 06/07/2011  | 2      | 10                            | 10             | 10             | 10,00 |         | 3              | 3              | 3              | 3,00 |         |
| A-12 | 06/07/2011  | 1      | 10,3                          | 10             | 10,1           | 10,13 |         | 3,1            | 3              | 3,1            | 3,07 |         |
| A-13 | 06/07/2011  | 2      | 10                            | 10             | 10             | 10,00 |         | 3              | 3              | 3              | 3,00 |         |
| A-14 | 07/07/2011  | 1      | 10,3                          | 10             | 10             | 10,10 |         | 3,1            | 3              | 3,1            | 3,07 |         |
| A-15 | 07/07/2011  | 2      | 10,3                          | 10,3           | 10,1           | 10,23 |         | 3              | 3,1            | 3              | 3,03 |         |
| A-16 | 07/07/2011  | 1      | 10,3                          | 10             | 10,1           | 10,13 |         | 3,1            | 3              | 3,1            | 3,07 |         |

|      |            |   |       |       |      |       |      |     |      |      |
|------|------------|---|-------|-------|------|-------|------|-----|------|------|
| A-17 | 07/07/2011 | 2 | 10,2  | 10,1  | 10   | 10,10 | 3    | 3   | 3    | 3,00 |
| A-18 | 07/07/2011 | 1 | 10,2  | 9,9   | 10   | 10,03 | 3,1  | 3   | 3,1  | 3,07 |
| A-19 | 07/07/2011 | 2 | 10,2  | 10,1  | 10,2 | 10,17 | 3    | 3   | 3    | 3,00 |
| A-20 | 08/07/2011 | 1 | 10,3  | 10    | 10,1 | 10,13 | 3,1  | 3   | 3,1  | 3,07 |
| A-21 | 08/07/2011 | 2 | 10,1  | 10    | 10   | 10,03 | 3    | 3   | 3    | 3,00 |
| A-22 | 08/07/2011 | 1 | 10,3  | 10    | 10,1 | 10,13 | 3,1  | 3   | 3    | 3,03 |
| A-23 | 08/07/2011 | 2 | 10,1  | 10,1  | 10   | 10,07 | 3    | 3   | 3    | 3,00 |
| A-24 | 08/07/2011 | 1 | 10,3  | 10    | 10,1 | 10,13 | 3,1  | 3   | 3,1  | 3,07 |
| A-25 | 08/07/2011 | 2 | 10,1  | 10,1  | 10   | 10,07 | 3    | 3   | 3    | 3,00 |
| A-26 | 02/05/2012 | 1 | 9,96  | 10,05 | 9,99 | 10,00 | 3,05 | 3,1 | 3,06 | 3,07 |
| A-27 | 02/05/2012 | 2 | 10,1  | 10,1  | 10,1 | 10,10 | 3,05 | 3,1 | 3,05 | 3,07 |
| A-28 | 03/05/2012 | 1 | 10,1  | 9,9   | 10,1 | 10,03 | 3,1  | 3   | 3,1  | 3,07 |
| A-29 | 03/05/2012 | 2 | 10,05 | 10,1  | 10,1 | 10,08 | 3,04 | 3,1 | 3,05 | 3,06 |
| A-30 | 03/05/2012 | 1 | 10,1  | 10,1  | 10,2 | 10,13 | 3,1  | 3   | 3,1  | 3,07 |
| A-31 | 04/05/2012 | 2 | 10,1  | 10    | 10,2 | 10,10 | 3,1  | 3   | 3,1  | 3,07 |
| A-32 | 04/05/2012 | 1 | 10    | 10,1  | 10,1 | 10,07 | 3    | 3,1 | 3    | 3,03 |
| A-33 | 04/05/2012 | 2 | 10    | 10,1  | 10,1 | 10,07 | 3    | 3,1 | 3,05 | 3,05 |
| A-34 | 04/05/2012 | 1 | 9,9   | 9,6   | 9,8  | 9,77  | 3,1  | 3   | 3,1  | 3,07 |

Table A.7- Dimensions of the dog-bone samples for the UV-acrylic MV 760

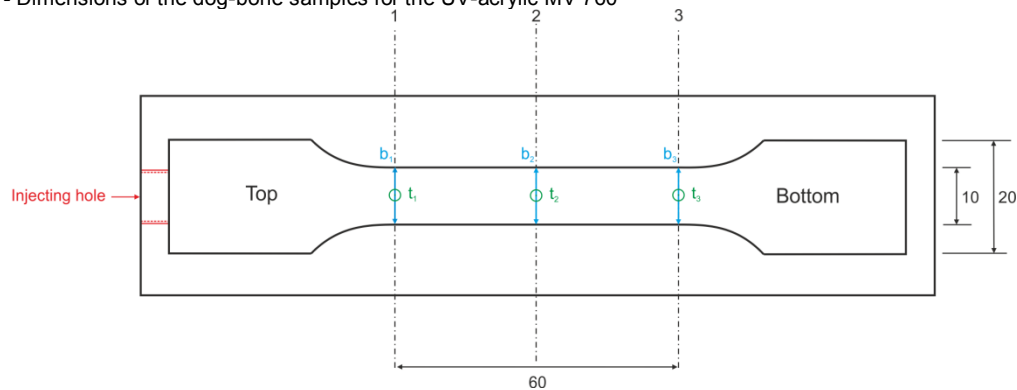


Figure A.6- Details of the measured positions –acrylic dog-bone samples

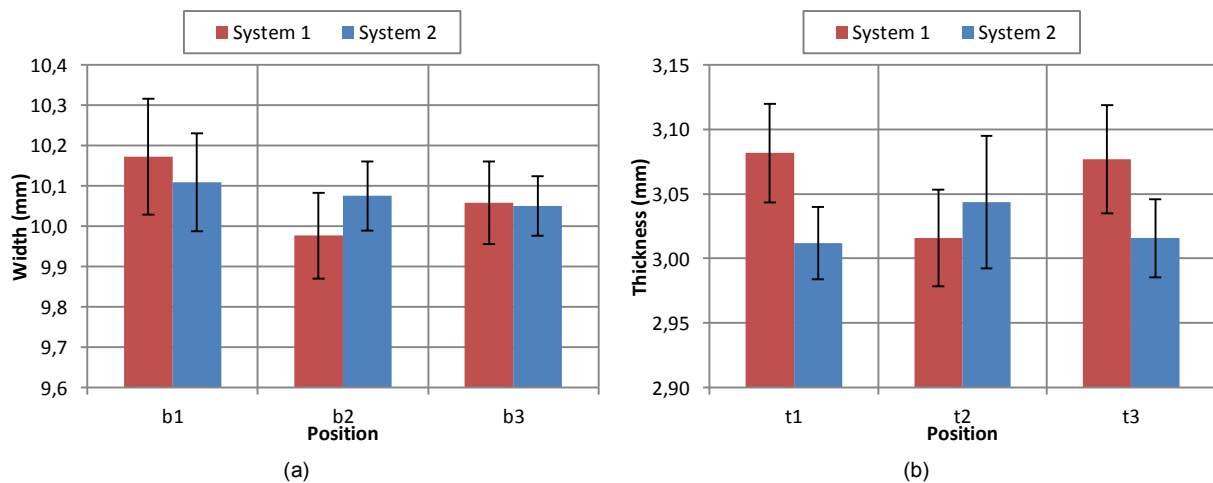


Figure A.7- Averages and deviations in (a) widths and (b) thicknesses according to the system and the positions

As it can be remarked, the global standard deviation in width was of 0,00690, representing the ideal width of 10mm divided by 1450, with no regard to the used system or the position. The dispersions in thickness were even lower as they corresponded to the ideal thickness divided by 3700. Thus, it could have been globally concluded that the dog-bone samples presented the same dimensions.

Nevertheless, to evaluate the possible influence of the system or some defects in the mold at a certain position, the total averages of width and thickness were evaluated in each case, see Fig. A.7. The standard deviations were superposed to these data. For system 1, the width was maximal at the upper position  $b_1$  and minimal in the center at  $b_2$ . For system 2, the width was also maximal at  $b_1$  but lowest at  $b_3$ . Nevertheless, for the two systems the standard deviation was close to 0,1, which represented one tenth of the measured value. The thicknesses were slightly higher than the desired thickness of 3mm. For system 1, the lowest thickness was found in the center, while it was the position presenting the highest value for system 2. Again the dispersions were less of 0,05mm, equivalent to the ideal thickness divided by 60.

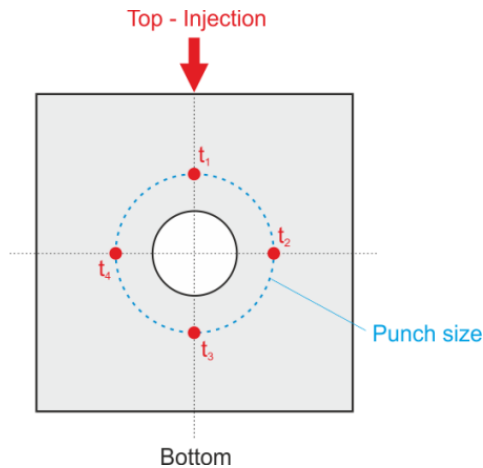
Consequently, it was conclude that both systems provided identical dog-bone specimens, whose dimensions, width and thickness, were independent of the regarded position, near the curvature radius or at the center.

## A.6 Acrylic shear samples - dimensions control

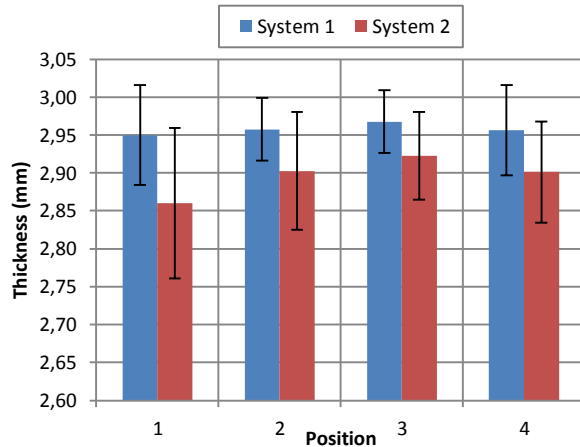
A control of the dimensions was operated on all the 16 produced acrylic samples destined to the shear tests on the adhesive alone in order to check the reproducibility of the fabrication method and evaluate the real dimensions for the later calculation of the stresses. As only two hours were needed to achieve a complete curing, the manufacturing date always corresponded to the unmolding date. The system employed for the production of the specimen was also recorded, as well as the thicknesses which were measured in four points around the shearing zone equivalent to the punch diameter of 25mm, see Fig. A.7. The averaged thickness was calculated for each sample and the standard deviation was evaluated for all these averaged results, see Table A.8.

| N°    | Manuf. Date | System | Thickness (mm) |                |                |                |       |       | σ |
|-------|-------------|--------|----------------|----------------|----------------|----------------|-------|-------|---|
|       |             |        | t <sub>1</sub> | t <sub>2</sub> | t <sub>3</sub> | t <sub>4</sub> | Aver  |       |   |
| AS-1  | 29/02/2012  | 1      | 2,9            | 2,92           | 2,95           | 2,95           | 2,930 | 0,069 |   |
| AS-2  | 01/03/2012  | 2      | 2,88           | 2,92           | 2,93           | 2,9            | 2,908 |       |   |
| AS-3  | 01/03/2012  | 1      | 2,97           | 2,97           | 2,96           | 2,95           | 2,963 |       |   |
| AS-4  | 26/04/2012  | 2      | 2,8            | 2,84           | 2,88           | 2,82           | 2,835 |       |   |
| AS-5  | 26/04/2012  | 1      | 2,81           | 2,87           | 2,88           | 2,82           | 2,845 |       |   |
| AS-6  | 05/03/2012  | 2      | 2,98           | 2,99           | 2,98           | 2,95           | 2,975 |       |   |
| AS-7  | 30/03/2012  | 1      | 2,98           | 2,98           | 2,99           | 2,98           | 2,983 |       |   |
| AS-8  | 30/04/2012  | 2      | 2,76           | 2,86           | 2,86           | 2,84           | 2,830 |       |   |
| AS-9  | 02/05/2012  | 1      | 3,02           | 2,99           | 3,02           | 3,02           | 3,013 |       |   |
| AS-10 | 30/04/2012  | 2      | 2,96           | 3,01           | 3,01           | 3              | 2,995 |       |   |
| AS-11 | 30/04/2012  | 1      | 2,97           | 2,97           | 2,97           | 2,97           | 2,970 |       |   |
| AS-12 | 01/03/2012  | 2      | 2,78           | 2,83           | 2,87           | 2,89           | 2,843 |       |   |
| AS-13 | 02/03/2012  | 1      | 2,98           | 2,99           | 2,99           | 2,99           | 2,988 |       |   |
| AS-14 | 27/04/2012  | 2      | 2,97           | 2,96           | 2,97           | 2,97           | 2,968 |       |   |
| AS-15 | 27/04/2012  | 1      | 2,97           | 2,97           | 2,98           | 2,97           | 2,973 |       |   |
| AS-16 | 27/04/2012  | 2      | 2,75           | 2,81           | 2,88           | 2,84           | 2,820 |       |   |

**Table A.8-** Dimensions of the shear UV-acrylic MV 760 samples



**Figure A.8-** Details of the measured positions – acrylic shear samples



**Figure A.9-** Averages and deviations in thicknesses according to the system and the positions

The global standard deviation of the thickness presented in Table A.8 was relatively low compared to the value of the thickness. Thus, globally it could have been concluded that almost no dispersion in thicknesses was found inducing a good reproducibility of the specimens and consequently of the tests. However, this global result did not account for the different systems for which some variations could exist. Therefore, for each system and each position, the average thicknesses and standard deviations were calculated and plotted in Fig. A.9. With this diagram, it was observed that the system 2 gave generally lower thicknesses for all the positions but with a difference of less than 0.1mm. Moreover, the standard deviations were also small in each case, which led to the indifference of the system and of the measured position. The samples were consequently judged as identical.

## A.7 Acrylic push-out shear samples - dimensions control

As for the silicone, push-out specimens were created to test the shear properties of the selected UV-acrylic adhesive. Three adherents were needed to manufacture these samples, i.e. two outer glass plates and an inner steel plate. The adhesive was symmetrically disposed between each layer of the assembly, see Fig. 4.100. The glass plates, measuring 100x100x10mm, were composed by annealed glass. Chamfers around the edges were made by VITRUM LUX in order to avoid unwanted stress peaks and possible failure of the glass. The steel element of 40x20x12mm was relatively small compared to the dimensions of the glass plates. These dimensions were designed by considering the adhesive viscosity and the capacity of the press combined with the shear modulus obtained from the previous modified shear tests on acrylic. No particular treatment was brought to the steel surfaces, only a decreasing with a solvent provided by the manufacturer, as operated for the glass plates.

To determine the final dimensions of the adhesive thicknesses, all the elements were first measured separately and then the thickness of the final assembly was evaluated. In the following table were recorded the name and number of each constituents of the push-out assembly:

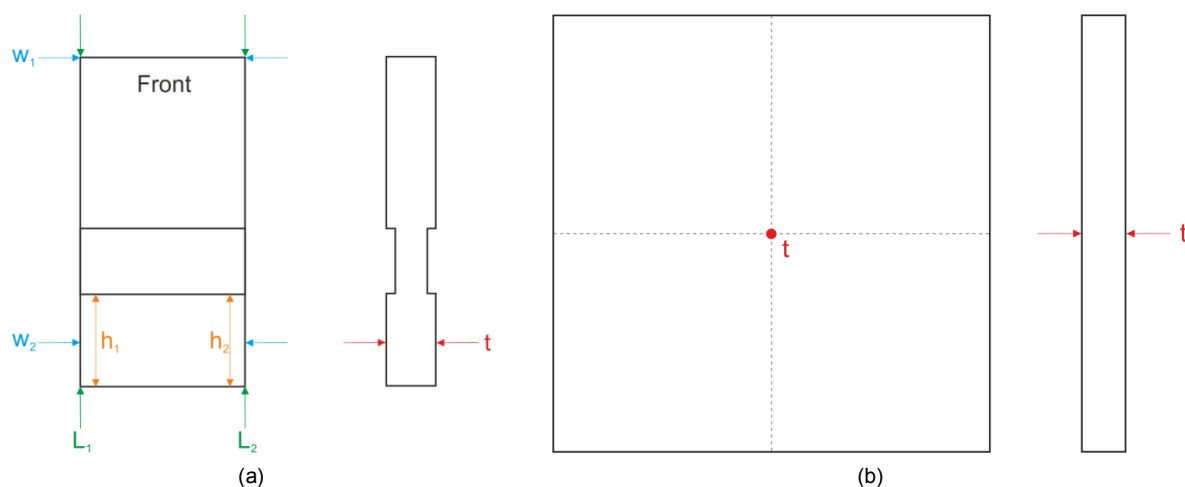
| Test N° | Final acrylic push-out constituents |         |            |
|---------|-------------------------------------|---------|------------|
|         | Glass front                         | Steel   | Glass back |
| 1       | GAPO-20                             | SAPO-01 | GAPO-19    |
| 2       | GAPO-18                             | SAPO-02 | GAPO-21    |
| 3       | GAPO-22                             | SAPO-03 | GAPO-23    |
| 4       | GAPO-24                             | SAPO-04 | GAPO-25    |
| 5       | GAPO-26                             | SAPO-05 | GAPO-27    |
| 6       | GAPO-28                             | SAPO-06 | GAPO-29    |
| 7       | GAPO-31                             | SAPO-07 | GAPO-30    |

|   |         |         |         |
|---|---------|---------|---------|
| 8 | FGPO-32 | SAPO-08 | GAPO-33 |
| 9 | FGPO-34 | SAPO-09 | GAPO-35 |

**Table A.9-** Composition of the acrylic push-out shear samples

The dimensions of the steel elements were measured in several positions, see Fig. A.10, with the help of a caliper and recorded in the following Table A.10 (a).

| Sample  | Position | Steel dimensions |       |            |       |                    |       |             |
|---------|----------|------------------|-------|------------|-------|--------------------|-------|-------------|
|         |          | Length (mm)      |       | Width (mm) |       | Bonded height (mm) |       | Thick. (mm) |
|         |          | $L_1$            | $L_2$ | $w_1$      | $w_2$ | $h_1$              | $h_2$ | $t$         |
| SAOP-01 | Front    | 40,15            | 40,18 | 20,08      | 20,08 | 10,43              | 10,38 | 12,14       |
| SAPO-01 | Back     |                  |       |            |       | 9,88               | 9,88  |             |
| SAPO-02 | Front    | 40,10            | 40,13 | 20,1       | 20,11 | 10,42              | 10,24 | 12,1        |
| SAPO-02 | Back     |                  |       |            |       | 9,88               | 10,1  |             |
| SAPO-03 | Front    | 40,19            | 40,18 | 20,23      | 20,17 | 10,68              | 10,54 | 12,09       |
| SAPO-03 | Back     |                  |       |            |       | 10,04              | 9,91  |             |
| SAPO-04 | Front    | 40,29            | 40,24 | 20,17      | 20,12 | 10,44              | 10,36 | 12,1        |
| SAPO-04 | Back     |                  |       |            |       | 9,87               | 9,86  |             |
| SAPO-05 | Front    | 40,10            | 40,11 | 20,07      | 20,06 | 10,25              | 9,93  | 12,24       |
| SAPO-05 | Back     |                  |       |            |       | 10,34              | 10,26 |             |
| SAPO-06 | Front    | 40,15            | 40,15 | 20,12      | 20,12 | 10                 | 10,5  | 12,13       |
| SAPO-06 | Back     |                  |       |            |       | 10,3               | 10,25 |             |
| SAPO-07 | Front    | 40,11            | 40,15 | 20,04      | 20,05 | 10,19              | 9,94  | 12,11       |
| SAPO-07 | Back     |                  |       |            |       | 10,49              | 10,41 |             |
| SAPO-08 | Front    | 40,23            | 40,17 | 20,17      | 20,16 | 10,41              | 10,3  | 12,1        |
| SAPO-08 | Back     |                  |       |            |       | 10,13              | 9,85  |             |
| SAPO-09 | Front    | 40,18            | 40,12 | 20,12      | 20,1  | 10,49              | 10,52 | 12,13       |
| SAPO-09 | Back     |                  |       |            |       | 10,12              | 9,85  |             |

**Table A.10-** Dimensions of the steel plates composing the acrylic push-out samples**Figure A.10-** Details of the measured positions of (a) the steel element and (b) the outer glass plate- Acrylic push-out shear

The thicknesses of the glass plates were also measured at the center of the element, see Fig A.10 (b), with a digital caliper and stored in Table A.11.

| Glass dimensions |         |         |         |         |         |         |         |         |         |
|------------------|---------|---------|---------|---------|---------|---------|---------|---------|---------|
| Sample           | GAPO-18 | GAPO-19 | GAPO-20 | GAPO-21 | GAPO-22 | GAPO-23 | GAPO-24 | GAPO-25 | GAPO-26 |
| Thick            | 9,84    | 9,75    | 9,85    | 9,83    | 9,81    | 9,83    | 9,84    | 9,82    | 9,83    |
| Sample           | GAPO-27 | GAPO-28 | GAPO-29 | GAPO-30 | GAPO-31 | GAPO-32 | GAPO-33 | GAPO-34 | GAPO-35 |
| Thick            | 9,83    | 9,84    | 9,84    | 9,83    | 9,82    | 9,81    | 9,83    | 9,83    | 9,83    |

**Table A.11-** Dimensions of the glass plates composing the acrylic push-out samples

By linking the measurements of the two previous tables, the total thickness of the adhesive for the two bonding areas was calculated by subtracting the total thickness of the manufactured assembly measured with a caliper to the sum of all the individual elements. Then, the assumption of an equal repartition of the adhesive thickness between the two bonded areas was conceded, which allowed evaluating the thickness of only one acrylic glued side, see Table A.12. With these last determined value was assessed the averaged thickness and the standard deviation.

| Test N° | Push-out thickness (mm) |                   | Adhesive thickness (mm) |                          |                |                   |
|---------|-------------------------|-------------------|-------------------------|--------------------------|----------------|-------------------|
|         | Final Assembly          | $\Sigma$ elements | Total                   | 1 side ( $\frac{1}{2}$ ) | Aver. (1 side) | $\sigma$ (1 side) |
| 1       | 32,03                   | 31,74             | 0,29                    | 0,145                    | 0,17           | 0,04              |
| 2       | 32,08                   | 31,77             | 0,31                    | 0,155                    |                |                   |
| 3       | 32                      | 31,75             | 0,25                    | 0,125                    |                |                   |
| 4       | 32                      | 31,76             | 0,24                    | 0,12                     |                |                   |
| 5       | 32,2                    | 31,9              | 0,3                     | 0,15                     |                |                   |
| 6       | 32,15                   | 31,81             | 0,34                    | 0,17                     |                |                   |
| 7       | 32,2                    | 31,76             | 0,44                    | 0,22                     |                |                   |
| 8       | 32,24                   | 31,74             | 0,5                     | 0,25                     |                |                   |
| 9       | 32,15                   | 31,79             | 0,36                    | 0,18                     |                |                   |

**Table A.12-** Evaluation of the acrylic adhesive thicknesses of the push-out specimens

As observed, all the adhesive dimensions were lower than the maximum thickness of 0.5mm advised by the adhesive manufacturer, which validated the production method. A very small variation existed between the samples, but could also be due to some uncertainties in the measurements, particularly to the hundredth of millimeter.

## A.8 Silicone push-out shear samples - peak stress - dimensions control

To evaluate the real occurrence of the stress peak, some small-scale push-out tests were prepared. The global geometry of the samples was identical to the one conducted in section 4.2.3, i.e. double lap joint assembly. The dimensions were lowered to only account for small overlap lengths whereby the stress scatterings and peaks occurred, i.e. 18mm, 12mm and 6mm, see Fig. 6.36. In this section, the compositions of the nine specimens, i.e. the two outer glass plates and the inner steel plates, were recorded, see Table A.13, in order to measure the real silicone thicknesses.

| Test N° | Final acrylic push-out constituents |        |            |
|---------|-------------------------------------|--------|------------|
|         | Glass front                         | Steel  | Glass back |
| 1       | GPO-13                              | SPO-01 | GPO-09     |
| 2       | GPO-14                              | SPO-02 | GPO-15     |

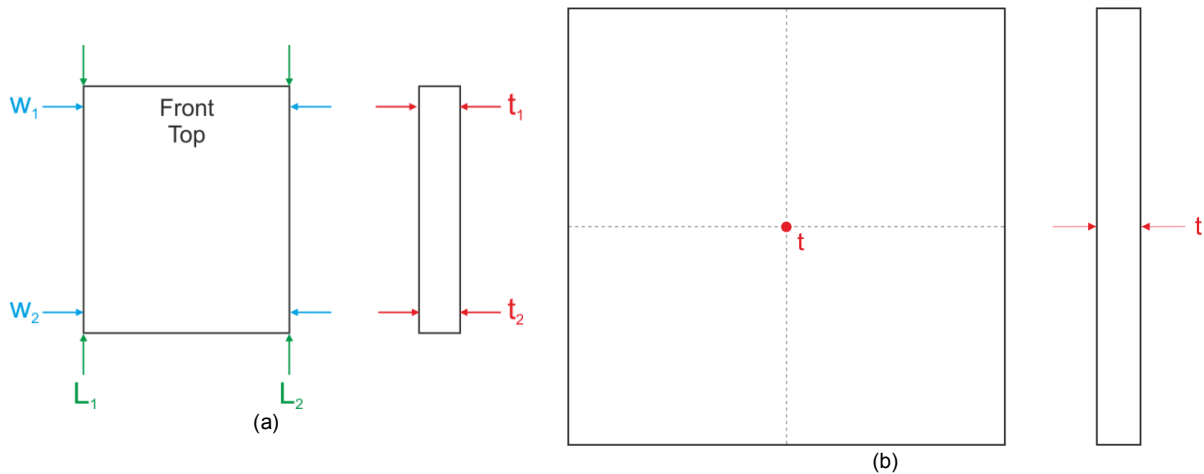
|   |        |        |          |
|---|--------|--------|----------|
| 3 | GPO-10 | SPO-03 | GPO-18-a |
| 4 | GPO-07 | SPO-04 | GPO-05   |
| 5 | GPO-12 | SPO-05 | GPO-11   |
| 6 | GPO-06 | SPO-06 | GPO-08   |
| 7 | GPO-17 | SPO-07 | GPO-16   |
| 8 | GPO-01 | SPO-08 | GPO-02   |

**Table A.13-** Composition of the small-scale push tests on silicone to assess the validity of the stress peak

As for the previous small-scale shear tests on acrylic adhesive, the dimensions of the steel part were measured in several positions with the help of a caliber, see Fig. A.11 (a), and recorded in Table A.14.

| Sample | Steel dimensions |       |            |       |                |       |
|--------|------------------|-------|------------|-------|----------------|-------|
|        | Length (mm)      |       | Width (mm) |       | Thickness (mm) |       |
|        | $L_1$            | $L_2$ | $w_1$      | $w_2$ | $t_1$          | $t_2$ |
| SPO-01 | 60,15            | 60,14 | 49,99      | 49,98 | 11,94          | 11,99 |
| SPO-02 | 59,95            | 59,96 | 50,20      | 50,20 | 12,00          | 12,02 |
| SPO-03 | 60,08            | 60,03 | 20,12      | 50,16 | 12,03          | 12,00 |
| SPO-04 | 60,03            | 60,07 | 20,19      | 50,19 | 12,00          | 12,00 |
| SPO-05 | 60,09            | 60,06 | 50,01      | 50,10 | 11,98          | 11,96 |
| SPO-06 | 60,02            | 60,05 | 50,06      | 50,12 | 11,96          | 12,00 |
| SPO-07 | 60,04            | 60,02 | 49,84      | 49,88 | 11,97          | 11,97 |
| SPO-08 | 60,07            | 60,10 | 50,16      | 50,21 | 12,05          | 12,05 |
| SPO-09 | 60,07            | 60,04 | 50,18      | 50,19 | 11,99          | 12,01 |

**Table A.14-** Dimensions of the steel plates composing the small-scale push tests on silicone



**Figure A.11-** Details of the measured positions of (a) the steel element and (b) the outer glass plate – Silicone push-out shear

The thicknesses of the glass plates were measured in the central part of these elements with a caliper, see Fig. A.11 (b), and stored in Table A.15.

| Glass dimensions |        |        |        |        |        |        |        |        |        |
|------------------|--------|--------|--------|--------|--------|--------|--------|--------|--------|
| Sample           | GPO-01 | GPO-02 | GPO-03 | GPO-04 | GPO-05 | GPO-06 | GPO-07 | GPO-08 | GPO-09 |
| Thick            | 9,77   | 9,79   | 9,79   | 9,84   | 9,84   | 9,85   | 9,84   | 9,83   | 9,83   |



| Sample | GPO-10 | GPO-11 | GPO-12 | GPO-13 | GPO-14 | GPO-15 | GPO-16 | GPO-17 | GPO-18-a |
|--------|--------|--------|--------|--------|--------|--------|--------|--------|----------|
| Thick  | 9,83   | 9,83   | 9,83   | 9,84   | 9,82   | 9,84   | 9,82   | 9,82   | 9,84     |

**Table A.15-** Dimensions of the glass plates composing the small-scale push tests on silicone

The three previous tables were cross-linked in order to determine the total thickness of the adhesive. By assuming an equal repartition of silicone between the two sides of the specimens, the half of the thickness was calculated, see Table A.16. As remarked, the averaged thickness on one side was of 3,1mm, which was relatively close to the expected one considering the small involved dimensions of the joint. Further, almost no deviation existed between the different values, which allowed concluding on the good reproducibility of the manufacturing method.

| Test N° | Push-out thickness (mm) |                   | Adhesive thickness (mm) |                          |                |                   |
|---------|-------------------------|-------------------|-------------------------|--------------------------|----------------|-------------------|
|         | Final Assembly          | $\Sigma$ elements | Total                   | 1 side ( $\frac{1}{2}$ ) | Aver. (1 side) | $\sigma$ (1 side) |
| 1       | 37,86                   | 31,66             | 6,20                    | 3,10                     | 3,10           | 0,038             |
| 2       | 37,95                   | 31,68             | 6,27                    | 3,14                     |                |                   |
| 3       | 37,87                   | 31,67             | 6,20                    | 3,10                     |                |                   |
| 4       | 37,78                   | 31,68             | 6,10                    | 3,05                     |                |                   |
| 5       | 37,81                   | 31,62             | 6,19                    | 3,10                     |                |                   |
| 6       | 37,85                   | 31,68             | 6,17                    | 3,09                     |                |                   |
| 7       | 37,75                   | 31,61             | 6,14                    | 3,07                     |                |                   |
| 8       | 37,85                   | 31,61             | 6,24                    | 3,12                     |                |                   |

**Table A.16-** Evaluation of the silicone adhesive thicknesses of the push-out specimens to assess the validity of the stress peak



## APPENDIX B – Choice of the Taguchi table

### B.1 General formulation

To implement a design of experiments, six steps have to be carried out, i.e. the proper definition of the objectives, the selection of the possible influent factors, the choice of the orthogonal table, the realization of the tests, their analyses and the final verification of all the results. The order of these steps cannot be inverted and only the first three steps are presented in this appendix.

Generally, for the first step a measurable quantity is selected, such as the strength of the material or elongation at break, and the final aim is to describe the evolution of this value according to influent factors. These factors are determined with the help of an Ishikawa diagram, listing all the possible causes of the changes, and can be of different natures:

- Continuous, such as the loading rate in a uniaxial test. The factor can take an infinity number of values within a defined range.
- Discreet, e.g. the different colors of a product, with a finite number of possibilities.
- Boolean, e.g. the presence or not of an artificial ageing, with only two values.

Then the choice of the orthogonal Taguchi table depends naturally on the number of envisaged factors (2, 3, 4, etc.), but also on their levels and the need to study their interactions. For Boolean factors, only two levels are possible, while for the continuous or discreet factors, two or more can be selected. Nevertheless, in order to carry a low number of tests, a limit of three levels is commonly considered. Hence the studied domain is correctly defined. For a design of experiments containing two factors at two levels, the studied domain is delimited by a rectangle represented in 2-dimensions, see Fig. B.1.

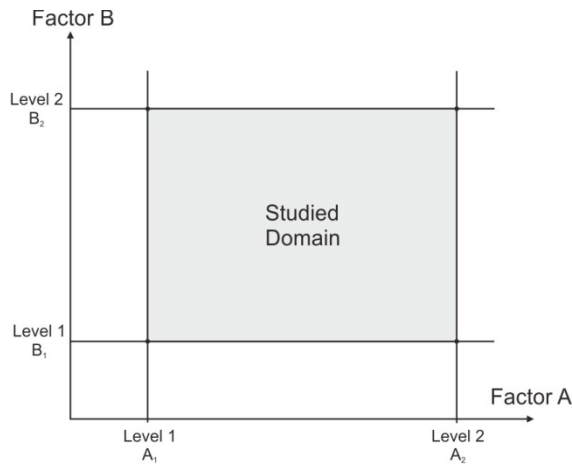


Figure B.1- Studied domain (2 factors – 2 levels)

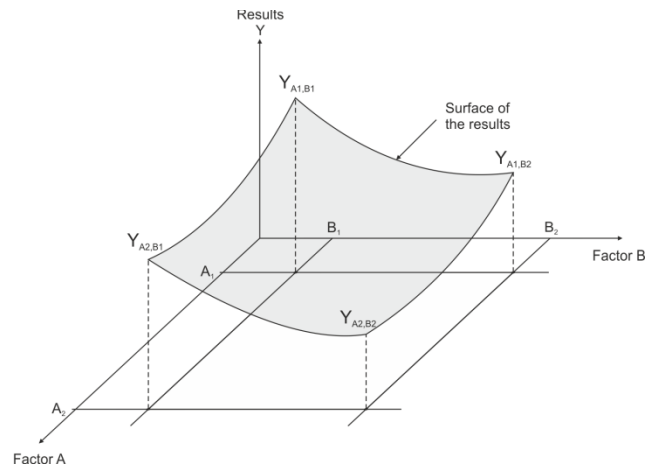


Figure B.2- Surface of the results (2 factors – 2 levels)

The tests provide the information for the vertices of the rectangular studied domain. However, to properly represent mathematically the surface of the results, see Fig. B.2, and evaluate the influence of each factor independently and their interaction, the formulation proposed by Vigier [B.1] is employed. The estimated response  $\hat{Y}$  can directly be expressed as the sum of the average of all results and the effect of the different factors, see Eq. (B.1).

$$\hat{Y} = I + A + B + AB \quad (\text{B.1})$$

With  $I$  the average of the total results,  
 $A$  the total effect of factor A (=Ageing),  
 $B$  the total effect of factor B (=Loading rate),  
 $AB$  the total effect of the interaction of factors A and B.

The total effect of a factor can be seen as the range between the averaged result at the highest level and the averaged result taken at the lowest level. For example, by concentrating on the factor A, the total effect is:

$$A = \text{Total effect of } A = \frac{Y_{A_2,B_1} + Y_{A_2,B_2}}{2} - \frac{Y_{A_1,B_1} + Y_{A_1,B_2}}{2} \quad (\text{B.2})$$

Furthermore, if all the factors possess two levels, the model of Eq. (B.1) including the interaction of the two factors can be rewritten with matrixes as follows:

$$\hat{Y} = I + [a_1 \ a_2] [A] + [b_1 \ b_2] [B] + \begin{bmatrix} ab_{11} & ab_{12} \\ ab_{21} & ab_{22} \end{bmatrix} [AB] \quad (\text{B.3})$$

$a_i$  the effect of the ageing A at level i,

$a_i = (\text{average of A results at level i}) - (\text{total average of results})$

With  $b_j$  the effect of the loading rate B at level j,

$b_j = (\text{average of B results at level j}) - (\text{total average of results})$

$ab_{ij}$  the effect of the interaction AB at level ij.

$ab_{ij} = (\text{results for A at level i and B at level j}) - (\text{estimation at ij})$

With the above definitions, the sum over all the levels of the effect of one factor is nil, e.g.  $a_1 + a_2 = 0$ . Hence the determination of the effect of one level of one factor allows obtaining the effect at the other level of the same factor. This property is also valid for the effect of the envisaged interaction. Consequently, one degree of liberty is associated to each factor, to the interaction and to the average of the total results. The total degree of liberty of a model of 2 factors at 2 levels is then 4 and the optimal Taguchi table to consider is denoted  $L_4(2)^3$ , see Table B.1.

| Test n° | 1 | 2 | 3 |
|---------|---|---|---|
| 1       | 1 | 1 | 1 |
| 2       | 1 | 2 | 2 |
| 3       | 2 | 1 | 2 |
| 4       | 2 | 2 | 1 |

**Table B.1-** Design Taguchi table  $L_4(2)^3$

| 1   | 2   | 3   | 4 |
|-----|-----|-----|---|
| (1) | 3   | 2   | 5 |
|     | (2) | 1   | 6 |
|     |     | (3) | 7 |

**Table B.2-** Interaction table for  $L_4(2)^3$

As it can be seen, the first column indicates the number of tests to be carried out and also corresponds to the index put side by side with the “L” in the notation of this table. The number in bracket indicates the levels of the factors and the exponent represents the maximum number of factors and interactions which can be evaluated. In the case of factors of level 2, the exponent is always equivalent to the number of tests minus one. In addition, it is not conceivable to have a number of tests inferior to the degree of liberties of the system. Therefore, the most important data leading to the choice of a design table are the levels of the factors and the degree of liberties of the envisaged model.

The next step is to associate each factor and each interaction to a column of the design Taguchi table. To do so the interactions between the different columns of table B.1 have to be analyzed in detail with the help of an interaction table, see Table B.2. The first column of the Taguchi table always corresponds to the most difficult factor to control because the level changes only one time. Then columns 2 and 3 remain for the choices of the second factor and the interaction. By attaching the second factor to the second column, the interaction AB is assimilated to the interaction between the first and second column of the Taguchi table. In Table B.2, this interaction is visualized by intersecting the line named (1) and the column 2. The result obtained points towards the third and only remaining column of Table B.1, which allows coming full circle.

This interaction between the columns and so between the factors can be represented by a simple linear, see Fig B.3.

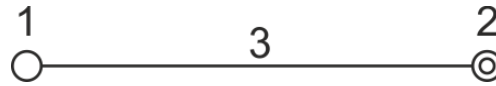


Figure B.3- Linear interaction graph for  $L_4(2)^3$

Finally, the complete test campaign to be investigated and corresponding of the study of two factors at two levels is defined by Table B.3. The columns of interactions between factors are conventionally not inserted in this table.

| Standard Test n° | Factors |      | Results        |
|------------------|---------|------|----------------|
|                  | A       | B    |                |
| 1                | 1       | 1    | $Y_{A_1, B_1}$ |
| 2                | 1       | 2    | $Y_{A_1, B_2}$ |
| 3                | 2       | 1    | $Y_{A_2, B_1}$ |
| 4                | 2       | 2    | $Y_{A_2, B_2}$ |
| Level 1          | Low     | Low  |                |
| Level 2          | High    | High |                |

Table B.3- Complete design of experiments (2 factors – 2 levels)

This table was achieved for the simple case of two factors at two levels and only one interaction. For more complex cases, involving more factors or several levels, a limitation of the number of studied interactions can be envisaged and the distribution of the columns of the Taguchi table to the factors becomes less obvious. Thus the linear interaction diagrams are as important as the Taguchi table.

## B.2 Existing Taguchi tables

In this paragraph are represented the most widely employed Taguchi tables and the associate linear diagrams. The interactions of third order, such as ABC, ABD or BCD, are not considered by this formulation.

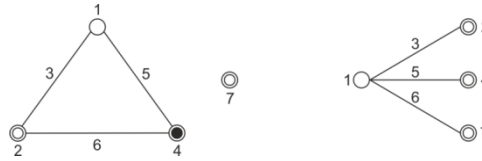
### a. Table $L_8(2)^7$

According to this table at least 8 tests have to be performed and 7 [factors level 2 + interactions] can be evaluated. This corresponds generally to the study of 3 factors and all the interactions of second order, or of 4 factors with 3 interactions.

| Test n° | 1 | 2 | 3 | 4 | 5 | 6 | 7 |
|---------|---|---|---|---|---|---|---|
| 1       | 1 | 1 | 1 | 1 | 1 | 1 | 1 |
| 2       | 1 | 1 | 1 | 2 | 2 | 2 | 2 |
| 3       | 1 | 2 | 2 | 1 | 1 | 2 | 2 |
| 4       | 1 | 2 | 2 | 2 | 2 | 1 | 1 |
| 5       | 2 | 1 | 2 | 1 | 2 | 1 | 2 |
| 6       | 2 | 1 | 2 | 2 | 1 | 2 | 1 |
| 7       | 2 | 2 | 1 | 1 | 2 | 2 | 1 |
| 8       | 2 | 2 | 1 | 2 | 1 | 1 | 2 |

Table B.4- Design Taguchi table  $L_8(2)^7$

The two linear graphs associated to this table are the following ones:

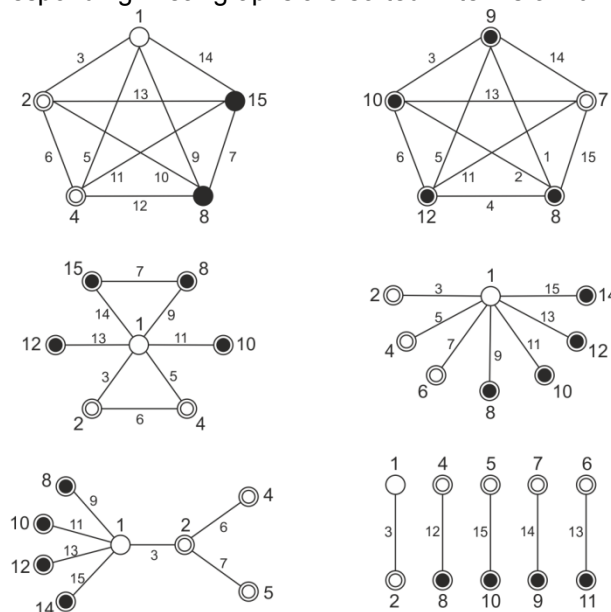
Figure B.4- Linear interaction graphs for  $L_8(2)^7$ **b. Table  $L_{16}(2)^{15}$** 

According to this table at least 16 tests have to be carried out and 15 [factors level 2+ interactions] can be analyzed.

| Test n° | 1 | 2 | 3 | 4 | 5 | 6 | 7 | 8 | 9 | 10 | 11 | 12 | 13 | 14 | 15 |
|---------|---|---|---|---|---|---|---|---|---|----|----|----|----|----|----|
| 1       | 1 | 1 | 1 | 1 | 1 | 1 | 1 | 1 | 1 | 1  | 1  | 1  | 1  | 1  | 1  |
| 2       | 1 | 1 | 1 | 1 | 1 | 1 | 1 | 2 | 2 | 2  | 2  | 2  | 2  | 2  | 2  |
| 3       | 1 | 1 | 1 | 2 | 2 | 2 | 2 | 1 | 1 | 1  | 1  | 2  | 2  | 2  | 2  |
| 4       | 1 | 1 | 1 | 2 | 2 | 2 | 2 | 2 | 2 | 2  | 2  | 1  | 1  | 1  | 1  |
| 5       | 1 | 2 | 2 | 1 | 1 | 2 | 2 | 1 | 1 | 2  | 2  | 1  | 1  | 2  | 2  |
| 6       | 1 | 2 | 2 | 1 | 1 | 2 | 2 | 2 | 2 | 1  | 1  | 2  | 2  | 1  | 1  |
| 7       | 1 | 2 | 2 | 2 | 2 | 1 | 1 | 1 | 1 | 2  | 2  | 2  | 2  | 1  | 1  |
| 8       | 1 | 2 | 2 | 2 | 2 | 1 | 1 | 2 | 2 | 1  | 1  | 1  | 1  | 2  | 2  |
| 9       | 2 | 1 | 2 | 1 | 2 | 1 | 2 | 1 | 2 | 1  | 2  | 1  | 2  | 1  | 2  |
| 10      | 2 | 1 | 2 | 1 | 2 | 1 | 2 | 2 | 1 | 2  | 1  | 2  | 1  | 2  | 1  |
| 11      | 2 | 1 | 2 | 2 | 1 | 2 | 1 | 1 | 2 | 1  | 2  | 2  | 1  | 2  | 1  |
| 12      | 2 | 1 | 2 | 2 | 1 | 2 | 1 | 2 | 1 | 2  | 1  | 1  | 2  | 1  | 2  |
| 13      | 2 | 2 | 1 | 1 | 2 | 2 | 1 | 1 | 2 | 2  | 1  | 1  | 2  | 2  | 1  |
| 14      | 2 | 2 | 1 | 1 | 2 | 2 | 1 | 2 | 1 | 1  | 2  | 2  | 1  | 1  | 2  |
| 15      | 2 | 2 | 1 | 2 | 1 | 1 | 2 | 1 | 2 | 2  | 1  | 2  | 1  | 1  | 2  |
| 16      | 2 | 2 | 1 | 2 | 1 | 1 | 2 | 2 | 1 | 1  | 2  | 1  | 2  | 2  | 1  |

Table B.5- Design Taguchi table  $L_{16}(2)^{15}$ 

And the most current corresponding linear graphs are sorted in terms of number of factors (5 to 10).

Figure B.5- Linear interaction graphs for  $L_{16}(2)^{15}$

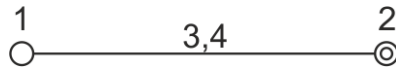
**c. Table  $L_9(3)^4$** 

According to this table 9 tests have to be performed and 4 [factors level 3+ interactions] appraised.

| Test n° | 1 | 2 | 3 | 4 |
|---------|---|---|---|---|
| 1       | 1 | 1 | 1 | 1 |
| 2       | 1 | 2 | 2 | 2 |
| 3       | 1 | 3 | 3 | 3 |
| 4       | 2 | 1 | 2 | 3 |
| 5       | 2 | 2 | 3 | 1 |
| 6       | 2 | 3 | 1 | 2 |
| 7       | 3 | 1 | 3 | 2 |
| 8       | 3 | 2 | 1 | 3 |
| 9       | 3 | 3 | 2 | 1 |

**Table B.6-** Design Taguchi table  $L_9(3)^4$

As for the Taguchi table  $L_4(2)^3$ , this one constitutes the minimal table for factors possessing three levels and therefore the number of interactions is limited to 2. The linear interaction graph associated is then:



**Figure B.6-** Linear interaction graph for  $L_9(3)^4$

### B.3 Case of the push-out shear tests

As mentioned in paragraph B.1, only the first three steps of the design of experiments methods will be presented for the more complicate case of the push-out shear tests.

#### i. Definition of the objectives

As for the dog-bone and compressive tests, the stress-strain diagrams are of importance to appraise the behaviour of silicone material and provide the optimum material law fitting the best the experimental data. The strength and elongation at break allow defining the limits and designing correctly this element in a more global system. And finally, evaluating the parameter influencing the stress-strain diagram and these limits is of high interest to predict the lifetime.

#### ii. Parameter of influence

For this study and with regards to the assembly of a push-out experiment, four distinctive parameters were selected:

- A. Ageing, which is a Boolean factor with only two levels.
- B. Bonding area, for which two different geometries were considered, i.e. either bonding all the surface or 2 strips each side. Thus, this factor possesses also two levels, a small bonding area (192cm<sup>2</sup>) or a large bonding area (544cm<sup>2</sup>).
- C. Bonding thickness, for which two dimensions were regarded, i.e. 3mm and the conventional 6mm proposed by standards and guidelines as the ETAG 002.
- D. Loading rate, whose influence is determined under two levels.

Thus the selected parameters of influence are among four and all possess two levels.

#### iii. Choice of the orthogonal table

The drawing up of a Taguchi table necessitates to define the number of interactions to latter calculate the degree of liberties of the model. In the present case, as the interactions between all the

parameters is not known, it is of interest to consider all the possibilities, even the interaction between the ageing and the loading rate. Consequently, with the formulation of Vigier and the limitation to second order interactions, the model can be mathematically written as:

$$\begin{aligned} \hat{Y} = & I + [a_1 \ a_2] [A] + [b_1 \ b_2] [B] + [c_1 \ c_2] [C] + [d_1 \ d_2] [D] + \\ & \begin{bmatrix} ab_{11} & ab_{12} \\ ab_{21} & ab_{22} \end{bmatrix} [AB] + \begin{bmatrix} ac_{11} & ac_{12} \\ ac_{21} & ac_{22} \end{bmatrix} [AC] + \begin{bmatrix} ad_{11} & ad_{12} \\ ad_{21} & ad_{22} \end{bmatrix} [AD] + \\ & \begin{bmatrix} bc_{11} & bc_{12} \\ bc_{21} & bc_{22} \end{bmatrix} [BC] + \begin{bmatrix} bd_{11} & bd_{12} \\ bd_{21} & bd_{22} \end{bmatrix} [BD] + \begin{bmatrix} cd_{11} & cd_{12} \\ cd_{21} & cd_{22} \end{bmatrix} [CD] \end{aligned} \quad (\text{B.4})$$

As described in paragraph B.1, each factor and each interaction present a degree of liberty equal to 1. Thus the total degree of liberty of the system is equivalent to 11 and the Taguchi table to work with is  $L_{16}(2)^{15}$ . Consequently to obtain all the desired information, at least 16 tests have to be carried out. As four individual factors are investigated, the linear graph to be chosen should exhibit the same or the closest number of factors. Therefore the first star linear graph of Fig. B.5 was selected to assign each factor to a column of the Taguchi table. The final design of experiment is then:

| Test n° | A<br>(= 1 Taguchi) | B<br>(=2 Taguchi) | C<br>(=4 Taguchi) | D<br>(=8 Taguchi) | Results  |
|---------|--------------------|-------------------|-------------------|-------------------|----------|
| 1       | 1                  | 1                 | 1                 | 1                 | $Y_1$    |
| 2       | 1                  | 1                 | 1                 | 2                 | $Y_2$    |
| 3       | 1                  | 1                 | 2                 | 1                 | $Y_3$    |
| 4       | 1                  | 1                 | 2                 | 2                 | $Y_4$    |
| 5       | 1                  | 2                 | 1                 | 1                 | $Y_5$    |
| 6       | 1                  | 2                 | 1                 | 2                 | $Y_6$    |
| 7       | 1                  | 2                 | 2                 | 1                 | $Y_7$    |
| 8       | 1                  | 2                 | 2                 | 2                 | $Y_8$    |
| 9       | 2                  | 1                 | 1                 | 1                 | $Y_9$    |
| 10      | 2                  | 1                 | 1                 | 2                 | $Y_{10}$ |
| 11      | 2                  | 1                 | 2                 | 1                 | $Y_{11}$ |
| 12      | 2                  | 1                 | 2                 | 2                 | $Y_{12}$ |
| 13      | 2                  | 2                 | 1                 | 1                 | $Y_{13}$ |
| 14      | 2                  | 2                 | 1                 | 2                 | $Y_{14}$ |
| 15      | 2                  | 2                 | 2                 | 1                 | $Y_{15}$ |
| 16      | 2                  | 2                 | 2                 | 2                 | $Y_{16}$ |

**Table B.7-** Design of experiments for the shear push-out tests

According to the linear graph, the interactions AB corresponds to column 3 of the Taguchi table, AC to column 5, AD to column 9, BC to column 6, BD to column 10 and CD to column 12. So the possible influence of all the interactions can be evaluated.



## APPENDIX C – ANAVAR method

To apprehend the effect of the factors or of the interactions, realizing a graphical analysis where the results are plotted for each factor constitutes the basis, but do not provide sufficient information and confidence. Therefore a mathematical analysis based on the analysis of the variance, named ANAVAR, is generally carried out. In this method, the influence of a factor is evaluated by comparing the variance of the factor over the variance of the residual to the tabulated F value of Fisher.

While the complete procedure is detailed in the first paragraph, only the important results will be exposed for the other paragraphs.

### C.1 Maximum stress of the first DOE – Silicone tension quasi-static

The first ANAVAR method was conducted to evaluate the influence of the loading rate and of the artificial ageing, i.e. elevated temperature, humidity and UV-radiation, on the maximum stress for tension silicone dog-bone samples subjected to quasi-static loading. The complete design of experiments table containing all the results is the following one.

| Test n° | A      | B            | $\sigma_{138\%}$ (MPa) |                |               | Average (MPa) |
|---------|--------|--------------|------------------------|----------------|---------------|---------------|
|         | Ageing | Loading rate | Test series 1          | Tests series 2 | Test series 3 |               |
| 1       | No     | 50mm/min     | 0,915                  | 0,948          | 0,916         | 0,926         |
| 2       | Yes    | 50mm/min     | 0,901                  | 0,892          | 0,896         | 0,896         |
| 3       | No     | 500mm/min    | 1,062                  | 0,918          | -             | 0,990         |
| 4       | Yes    | 500mm/min    | 0,941                  | 0,914          | -             | 0,927         |

**Table C.1-** Stress results for the 1<sup>st</sup> DOE of silicone dog-bone under quasi-static loading

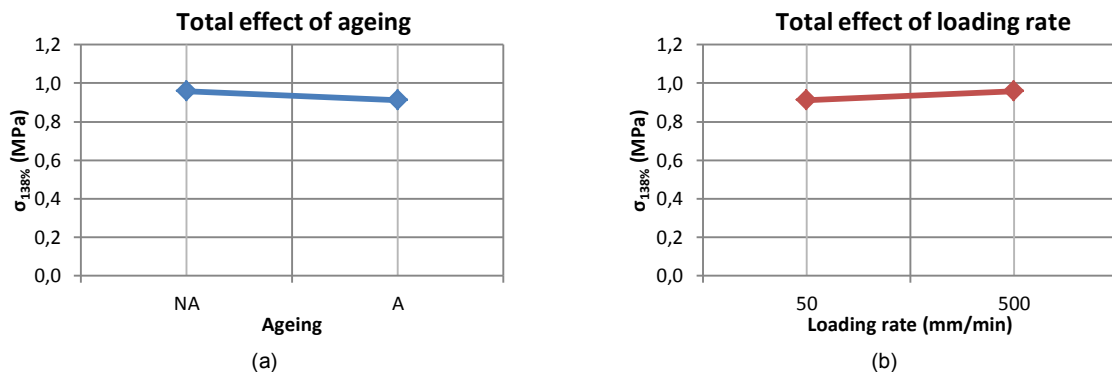
Then the determination of the total effect of each factor can be realized, by simply calculating the difference between the average results of level 2 and level 1, see Eq. (B.2) from Appendix B. For factor A (=ageing), the total effect of this factor is equal to:

$$\text{Total effect of A} = \frac{0,927 + 0,896}{2} - \frac{0,990 + 0,926}{2} = -0,046 \text{ MPa} \quad (\text{C.1})$$

And the total effect of factor B (=loading rate) is equal to:

$$\text{Total effect of B} = \frac{0,927 + 0,990}{2} - \frac{0,896 + 0,926}{2} = 0,047 \text{ MPa} \quad (\text{C.2})$$

Graphically, these values can be observed on the following curves representing the results for each specific factor, see Fig. C.1. They correspond to the difference, read on the vertical axis, between the two extreme values of the horizontal axis defining the studied domain.



**Figure C.1-** Total effect of the (a) ageing and (b) loading rate factors on the stress of the 1<sup>st</sup> DOE for silicone under tension

As it can be observed on the previous diagrams, the maximum stress decreases slightly (less than 5%) with the presence of ageing and increase with elevated loading rate. However, these observations cannot allow concluding properly on the effect of the factor, as the variations are very low, or on the effect of the interaction. Therefore the mathematical formulation for the surface of the results proposed by Vigier [B.1] and presented in Appendix B Eq. (B.3) has to be employed, as it presents the advantages to quantify the effect of each factor and of the expected interaction. To determine the different coefficient, the last column of Table C.1 can be rewritten as:

| No interaction |          | B        |           | Average (MPa) |
|----------------|----------|----------|-----------|---------------|
|                |          | 50mm/min | 500mm/min |               |
| A              | Non-aged | 0,926    | 0,990     | 0,958         |
|                | Aged     | 0,896    | 0,927     | 0,912         |
| Average (MPa)  |          | 0,911    | 0,958     | 0,935         |

**Table C.2-** Coefficients, interaction excluded, of the mathematical formulation for the maximum stress of the 1<sup>st</sup> DOE on silicone

Thus, with Table C.2, it is possible to establish the first part of the estimated response  $\hat{Y}$  without considering the interaction, see Eq. C.3.

$$\hat{Y} = 0,935 + [0,958 - 0,935 \quad 0,912 - 0,935] [A] + [0,911 - 0,935 \quad 0,958 - 0,935] [B] \quad (C.3a)$$

$$\hat{Y} = 0,935 + [0,023 \quad -0,023] [A] + [-0,024 \quad 0,024] [B] \quad (C.3b)$$

This above model is incomplete if the interaction is not taken into account. As evoked in the previous Appendix, this interaction is obtained by calculating the gap existing between one selected level of each factor and the approximated response of Eq. (C.3b). For example, when the specimen is non-aged and subjected to 500mm/min, the interaction coefficient  $ab_{12}$  is equal to:

$$ab_{12} = 0,990 - (0,935 + 0,023 + 0,024) = 0,008 \quad (C.4)$$

Hence it is possible to set up Table C.3 only concerning the effect of the interaction.

| With interaction (ab) |          | B        |           |
|-----------------------|----------|----------|-----------|
|                       |          | 50mm/min | 500mm/min |
| A                     | Non-aged | -0,008   | 0,008     |
|                       | Aged     | 0,008    | -0,008    |

**Table C.3-** Interaction coefficients of the mathematical formulation for the maximum stress of the 1<sup>st</sup> DOE on silicone

Consequently, the final mathematical formulation, characterizing the surface of the response for the studied domain is the following one:

$$\hat{Y} = 0,935 + [0,023 \quad -0,023] [A] + [-0,024 \quad 0,024] [B] + \begin{bmatrix} -0,008 & 0,008 \\ 0,008 & -0,008 \end{bmatrix} [AB] \quad (C.5)$$

This analysis was based on the averaged maximum stress for each test number, but it remains to calculate the residual associated to each sample tested. These values are determined by comparing the test result to the final mathematical model of Eq. (C.5). As example, for tests series 2, non-aged sample subjected to the highest loading rate, the residual is equal to:

$$r_{12}^{series\ 2} = 0,918 - (0,935 + 0,023 + 0,024 + 0,008) = -0,072\ MPa \quad (C.6)$$

All the estimated residuals corresponding to each test are regrouped in Table C.4.

| A      | B            | Residual r (MPa) |               |               |
|--------|--------------|------------------|---------------|---------------|
| Ageing | Loading rate | Test series 1    | Test series 2 | Test series 3 |
| No     | 50mm/min     | -0,011           | 0,022         | -0,010        |
| Yes    | 50mm/min     | 0,004            | -0,004        | 0,000         |
| No     | 500mm/min    | 0,072            | -0,072        | -             |
| Yes    | 500mm/min    | 0,013            | -0,013        | -             |

**Table C.4-** Residual of the 1<sup>st</sup> DOE concerning the stress for silicone under tension

In total 10 tests were realized, which implies 10 available degree of liberties. The average, each factor and the interaction necessitate 1 degree of liberties and so 6 remains for the residuals. The final table, constituting the foundation of the ANAVAR method and allowing determining the influence of the factor or the interaction on the maximum stress is given as follows:

| Source   | Square sum $\Sigma$                               | DDL                      | Variance                                              | F                           | F <sub>0.05</sub> |
|----------|---------------------------------------------------|--------------------------|-------------------------------------------------------|-----------------------------|-------------------|
| A        | $S_A = \frac{N}{n_a} \sum a^2 = 0,0053$           | $n_a - 1 = 1$            | $V_A = \frac{S_A}{n_a - 1} = 0,0053$                  | $\frac{V_A}{V_r} = 2,79$    | 5,99              |
| B        | $S_B = \frac{N}{n_b} \sum b^2 = 0,0056$           | $n_b - 1 = 1$            | $V_B = \frac{S_B}{n_b - 1} = 0,0056$                  | $\frac{V_B}{V_r} = 2,94$    | 5,99              |
| AB       | $S_{AB} = \frac{N}{n_a n_b} \sum (ab)^2 = 0,0007$ | $(n_a - 1)(n_b - 1) = 1$ | $V_{AB} = \frac{S_{AB}}{(n_a - 1)(n_b - 1)} = 0,0007$ | $\frac{V_{AB}}{V_r} = 0,35$ | 5,99              |
| Residual | $S_r = \sum r^2 = 0,0114$                         | $n_r = 6$                | $V_r = \frac{S_r}{n_r} = 0,0019$                      |                             |                   |
| Total    | $S_T = \sum (Y - \hat{Y})^2$                      | $N - 1 = 9$              |                                                       |                             |                   |

**Table C.5-** Variance analysis ANAVAR on the maximum stress of the 1<sup>st</sup> DOE for silicone under quasi-static tension

With  $n_x$  the number of level of x factor and,  $N$  the total number of tests carried out.

As the calculated F of Snedecor for all the factors and the interaction is lower than the tabulated value  $F_{0.05}$  with a security factor equal to  $\alpha = 0,05$ , neither the loading rate, nor the ageing or the interaction have an effect on the maximum stress for quasi-static tensile dog-bone tests on silicone sample.

## C.2 Initial stiffness of the first DOE – Silicone tension quasi-static

The second ANAVAR method was conducted on the same samples than the previous paragraph (1<sup>st</sup> DOE on silicone dog-bone samples under quasi-static loading), but concerning the stiffness at the origin, calculated in accordance to the ETAG 002. The possible influent factors were the regrouping artificial ageing and the loading rate. The complete design of experiments table containing all the initial stiffnesses is the following one.

| Test n° | A      | B            | Initial stiffness K <sub>0</sub> (MPa) |                |               | Average (MPa) |
|---------|--------|--------------|----------------------------------------|----------------|---------------|---------------|
|         | Ageing | Loading rate | Test series 1                          | Tests series 2 | Test series 3 |               |
| 1       | No     | 50mm/min     | 2,457                                  | 2,599          | 4,592         | 3,216         |
| 2       | Yes    | 50mm/min     | 2,863                                  | 4,015          | 5,345         | 4,074         |
| 3       | No     | 500mm/min    | 4,727                                  | 5,027          | -             | 4,877         |
| 4       | Yes    | 500mm/min    | 3,516                                  | 3,913          | -             | 3,714         |

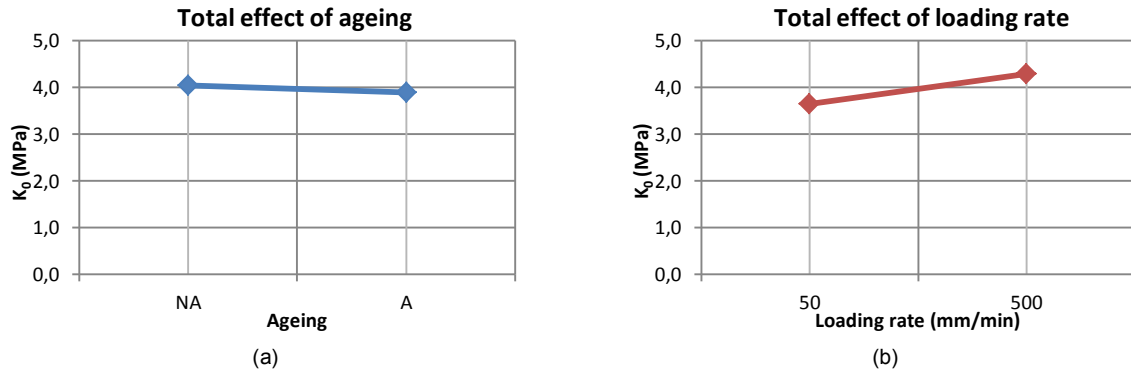
**Table C.6-** Initial stiffness results for the 1<sup>st</sup> DOE of silicone dog-bone under quasi-static loading

The total effects of the ageing factor A and the loading rate factor B are respectively equal to:

$$\text{Total effect of A} = \frac{3,714 + 4,074}{2} - \frac{4,877 + 3,216}{2} = -0,152 \text{ MPa} \quad (\text{C.7})$$

$$\text{Total effect of B} = \frac{3,714 + 4,877}{2} - \frac{4,074 + 3,216}{2} = 0,651 \text{ MPa} \quad (\text{C.8})$$

The graphical representation of the total effect of both factors is then given in Fig. C.2.



**Figure C.2-** Total effect of the (a) ageing and (b) loading rate factors on the initial stiffness - 1<sup>st</sup> DOE for silicone under tension

It can be noted that the initial stiffness decreases by applying an ageing on the sample and increase with the loading rate. To conclude on the influence of the factors and of the interaction on this recorded value, the mathematical formulation defining the surface of the results was again applied with a preliminary calculation of the coefficients without (Table C.7) and with interaction (Table C.8).

| No interaction |          | B        |           | Average (MPa) |
|----------------|----------|----------|-----------|---------------|
|                |          | 50mm/min | 500mm/min |               |
| A              | Non-aged | 3,216    | 4,877     | 4,047         |
|                | Aged     | 4,074    | 3,714     | 3,894         |
| Average (MPa)  |          | 3,645    | 4,296     | 3,970         |

**Table C.7-** Coefficients, interaction excluded, of the mathematical formulation for the initial stiffness of the 1<sup>st</sup> DOE on silicone

| With interaction (ab) |          | B        |           |
|-----------------------|----------|----------|-----------|
|                       |          | 50mm/min | 500mm/min |
| A                     | Non-aged | -0,505   | 0,505     |
|                       | Aged     | 0,505    | -0,505    |

**Table C.8-** Interaction coefficients of the mathematical formulation for the initial stiffness of the 1<sup>st</sup> DOE on silicone

Thus the complete mathematical formulation of the studied domain is the following one:

$$\hat{Y} = 3,970 + [0,076 \quad -0,076] [A] + [-0,325 \quad 0,325] [B] + \begin{bmatrix} -0,505 & 0,505 \\ 0,505 & -0,505 \end{bmatrix} [AB] \quad (\text{C.9})$$

| A      | B            | Residual r (MPa) |               |               |
|--------|--------------|------------------|---------------|---------------|
| Ageing | Loading rate | Test series 1    | Test series 2 | Test series 3 |
| No     | 50mm/min     | -0,759           | -0,617        | 1,376         |
| Yes    | 50mm/min     | -1,211           | -0,059        | 1,270         |
| No     | 500mm/min    | -0,150           | 0,150         | -             |
| Yes    | 500mm/min    | -0,199           | 0,199         | -             |

**Table C.9-** Residual of the 1<sup>st</sup> DOE concerning the initial stiffness for silicone under tension

With the final mathematical model, the residuals of each test were assessed and recorded in Table C.9. The variance analysis, concluding the ANAVAR procedure and allowing checking if the factors and the interaction influence the initial stiffness, is presented in Table C.10.

| Source   | Square sum $\Sigma$ | DDL | Variance | F     | F <sub>0.05</sub> |
|----------|---------------------|-----|----------|-------|-------------------|
| A        | 0,058               | 1   | 0,058    | 0,057 | 5,99              |
| B        | 1,059               | 1   | 1,059    | 1,049 | 5,99              |
| AB       | 2,555               | 1   | 2,555    | 2,530 | 5,99              |
| Residual | 6,058               | 6   | 1,010    |       |                   |
| Total    |                     | 9   |          |       |                   |

**Table C.10-** Variance analysis ANAVAR on the initial stiffness of the 1<sup>st</sup> DOE for silicone under quasi-static tension

From the comparison of the calculated Snedecor F value to the tabulated F<sub>0.05</sub> for each factor and for the interaction, it can be postulated that neither the artificial ageing of the loading rate or a combination of both affect the initial stiffness of the silicone under tension quasi-static tests.

### C.3 Stress ratio – Silicone tension long-term

For the case of long-term relaxation tests, an ANAVAR analysis was carried out to evaluate the stress decrease, symbolized by a reduction coefficient corresponding to the ratio of the stress measured at the instant “t” over the stress of reference at 60s. The aim of this study is to verify that the loss of stiffness is independent of the artificial ageing (elevated temperature, humidity and UV-radiation) and of the imposed displacement after these first 60s. Therefore, the ratio of the stress measured after the maximum test duration, i.e. 1200s, to the reference stress was considered. The complete design of experiments table containing all the results is the following one.

| Test n° | A      | B            | $\sigma_{t=1200s}/\sigma_{t=60s}$ (-) |               | Average (-) |
|---------|--------|--------------|---------------------------------------|---------------|-------------|
|         | Ageing | Loading rate | Test series 1                         | Test series 1 |             |
| 1       | No     | 30mm         | 0,829                                 | 0,933         | 0,881       |
| 2       | Yes    | 30mm         | 0,965                                 | 0,948         | 0,956       |
| 3       | No     | 72mm         | 0,940                                 | 0,918         | 0,929       |
| 4       | Yes    | 72mm         | 0,902                                 | 0,944         | 0,923       |

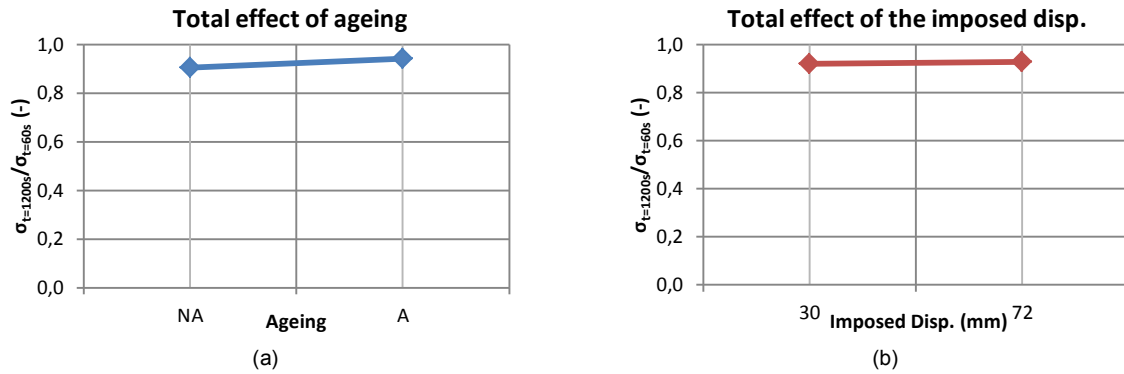
**Table C.11-** Stress ratio results for the DOE of silicone dog-bone under long-term loading

The total effects of the ageing factor A and the imposed displacement factor B are equal to:

$$\text{Total effect of A} = \frac{0,923 + 0,956}{2} - \frac{0,929 + 0,881}{2} = 0,035 \quad (\text{C.10})$$

$$\text{Total effect of B} = \frac{0,923 + 0,929}{2} - \frac{0,956 + 0,881}{2} = 0,0073 \quad (\text{C.11})$$

The graphical representation of the total effect of both factors is then given in Fig. C.3. As it can be remarked, the variation of the stresses ratio does not vary importantly. For the total effect of ageing, non-aged samples presents a lower stress ratio and consequently a higher stress reduction factor than aged samples. For the total effect of the imposed displacement, it can be noted that the stress ratio is almost constant for the two deformations. Thus, it would signify that both the ageing and the imposed displacement have no consequence on the stress decrease at a time of 1200s compared to the reference stress at 60s. To ensure this hypothesis, the mathematical formulation, defining the surface of the results, was established. A first calculation was conducted to determine the coefficients without interaction, see Table C.12, and then the coefficients accounting for the interaction, see Table C.13.



**Figure C.3-** Total effect of the (a) ageing and (b) imposed disp. factors on the stress ratio – silicone tensile long-term tests

| No interaction |          | B     |       | Average (-) |
|----------------|----------|-------|-------|-------------|
|                |          | 30mm  | 72mm  |             |
| A              | Non-aged | 0,881 | 0,929 | 0,905       |
|                | Aged     | 0,956 | 0,923 | 0,940       |
| Average (-)    |          | 0,919 | 0,926 | 0,922       |

**Table C.12-** Coefficients, interaction excluded, of the mathematical formulation for stress ratio – silicone tensile long-term tests

| With interaction (ab) |          | B      |        |
|-----------------------|----------|--------|--------|
|                       |          | 30mm   | 72mm   |
| A                     | Non-aged | -0,020 | 0,020  |
|                       | Aged     | 0,020  | -0,020 |

**Table C.13-** Interaction coefficients of the mathematical formulation for stress ratio – silicone tensile long-term tests

Hence the complete mathematical formulation could be set up for the studied domain:

$$\hat{Y} = 0,922 + [-0,017 \quad 0,017] [A] + [-0,003 \quad 0,003] [B] + \begin{bmatrix} -0,020 & 0,020 \\ 0,020 & -0,020 \end{bmatrix} [AB] \quad (C.12)$$

All the estimated residuals corresponding to each test are finally regrouped in Table C.14.

| A      | B             | Residual r (-) |               |
|--------|---------------|----------------|---------------|
| Ageing | Imposed disp. | Test series 1  | Test series 2 |
| No     | 30mm          | -0,052         | 0,052         |
| Yes    | 30mm          | 0,009          | -0,009        |
| No     | 72mm          | 0,011          | -0,011        |
| Yes    | 72mm          | -0,021         | 0,021         |

**Table C.14-** Residual for the stress ratio results – silicone tensile long-term tests

Eight tests were performed for this design of experiments, generating 8 degrees of liberty in total for the model. The average value, each factor and the interaction consume one degree of liberty each, leaving consequently 4 degrees of liberty for the residual. The variance analysis, to check if the factors and the interaction influence the ratio of the stress and so the stress reduction factor, is presented in Table C.15.

For this analysis, the  $F_{0,05}$  of Snedecor was different than the one of the first analyses, as the total number of degrees of liberty was lower. The new value of  $F_{0,05}$  was determined with the help of normalized table.

| Source   | Square sum $\Sigma$ | DDL | Variance | F     | $F_{0.05}$ |
|----------|---------------------|-----|----------|-------|------------|
| A        | 0,0024              | 1   | 0,0024   | 1,432 | 7,71       |
| B        | 0,0001              | 1   | 0,0001   | 0,064 | 7,71       |
| AB       | 0,0033              | 1   | 0,0033   | 1,984 | 7,71       |
| Residual | 0,0067              | 4   | 0,0017   |       |            |
| Total    |                     | 7   |          |       |            |

**Table C.15-** Variance analysis ANAVAR on the stress ratio – silicone tensile long-term tests

For all the factors and the interaction, the calculated F values were lower than the tabulated value  $F_{0.05}$ . This allowed concluding on the non-influence of the studied factors, i.e. the artificial ageing and the imposed displacements, on the stress ratio for a time of 1200s compared to the reference value at 60s.

#### C.4 Initial stiffness – Silicone compression quasi-static

As for the tensile test, the influence of the artificial ageing, regrouping the elevated temperature, the humidity and the UV-radiation, and of the loading rate on the initial stiffness, established with the procedure of the ETAG 002, was investigated for the case of quasi-static compression tests on silicone. The complete design of experiments table containing all the calculated initial stiffnesses is the following one.

| Test n° | A      | B            | Initial stiffness $K_0$ (MPa) |                | Average (MPa) |
|---------|--------|--------------|-------------------------------|----------------|---------------|
|         | Ageing | Loading rate | Test series 1                 | Tests series 2 |               |
| 1       | No     | 5mm/min      | 1,932                         | 1,876          | 1,904         |
| 2       | Yes    | 5mm/min      | 2,067                         | 1,622          | 1,845         |
| 3       | No     | 50mm/min     | 2,025                         | 1,674          | 1,850         |
| 4       | Yes    | 50mm/min     | 1,912                         | 2,317          | 2,114         |

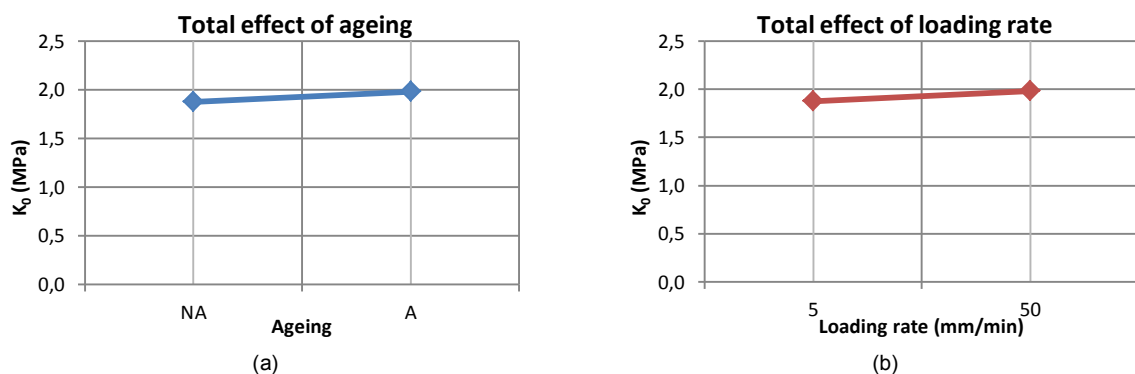
**Table C.16-** Initial stiffness results – DOE accounting for elevated temperatures – silicone quasi-static compression

The total effects of the ageing factor A and the loading rate factor B are respectively equal to:

$$\text{Total effect of A} = \frac{2,114 + 1,845}{2} - \frac{1,850 + 1,904}{2} = 0,103 \text{ MPa} \quad (\text{C.13})$$

$$\text{Total effect of B} = \frac{2,114 + 1,850}{2} - \frac{1,845 + 1,904}{2} = 0,108 \text{ MPa} \quad (\text{C.14})$$

The total effect of both factors is about 5% of the average values issued from tests, which suggests that their influences on the first portion of the curve, i.e. at low strains, are very low.



**Figure C.4-** Total effect of the (a) ageing and (b) loading rate factors on the initial stiffness – silicone quasi-static compression

The graphical representations of the total effect of these factors are given in the above Fig. C.4. The first remarks concerning the small dispersions of the total effects of both factors were confirmed by these representations. Indeed the slopes of the straight lines were relatively small. The mathematical formulation of the surface of response was established in two steps to confirm this postulate, with the calculation of the involved coefficients without interaction, Table C.17, and the other coefficients accounting for the interaction, Table C.18.

| No interaction |          | B       |          | Average (MPa) |
|----------------|----------|---------|----------|---------------|
|                |          | 5mm/min | 50mm/min |               |
| A              | Non-aged | 1,904   | 1,850    | 1,877         |
|                | Aged     | 1,845   | 2,114    | 1,980         |
| Average (MPa)  |          | 1,874   | 1,982    | 1,928         |

**Table C.17-** Coefficients, interaction excluded, of the mathematical formulation for initial stiffness – quasi-static compression

| With interaction (ab) |          | B       |          |
|-----------------------|----------|---------|----------|
|                       |          | 5mm/min | 50mm/min |
| A                     | Non-aged | 0,081   | -0,081   |
|                       | Aged     | -0,081  | 0,081    |

**Table C.18-** Interaction coefficients of the mathematical formulation for initial stiffness – quasi-static compression

With these two tables, the complete mathematical formulation could be established for the studied domain:

$$\hat{Y} = 1,928 + [-0,051 \quad 0,051] [A] + [-0,054 \quad 0,054] [B] + \begin{bmatrix} 0,081 & -0,081 \\ -0,081 & 0,081 \end{bmatrix} [AB] \quad (C.15)$$

All the estimated residuals corresponding to each test are finally regrouped in Table C.19.

| A      | B            | Residual r (-) |               |
|--------|--------------|----------------|---------------|
| Ageing | Loading rate | Test series 1  | Test series 2 |
| No     | 5mm/min      | 0,028          | -0,028        |
| Yes    | 5mm/min      | 0,223          | -0,223        |
| No     | 50mm/min     | 0,176          | -0,176        |
| Yes    | 50mm/min     | -0,202         | 0,202         |

**Table C.19-** Residual for the initial stiffness results – silicone quasi-static compression

Eight degrees of liberties, corresponding to the eight tests realized, were available. One dedicated to the average, one for each factor and one for the interaction, letting four degrees of liberties for the residual. The final variance analysis ANAVAR is presented in Table C.20

| Source   | Square sum $\Sigma$ | DDL | Variance | F      | $F_{0,05}$ |
|----------|---------------------|-----|----------|--------|------------|
| A        | 0,0211              | 1   | 0,0211   | 0,3454 | 7,71       |
| B        | 0,0231              | 1   | 0,0231   | 0,3788 | 7,71       |
| AB       | 0,0525              | 1   | 0,0525   | 0,8595 | 7,71       |
| Residual | 0,2443              | 4   | 0,0611   |        |            |
| Total    |                     | 7   |          |        |            |

**Table C.20-** Variance analysis ANAVAR on the initial stiffness – silicone quasi-static compression

All the estimated F of were inferior to the tabulated  $F_{0,05}$  values, demonstrating the invariance of the silicone properties towards ageing and loading rates, under small strain of quasi-static compression.



### C.5 Strains at a fixed stress – Silicone compression quasi-static

The influence of the ageing, centered on elevated temperature, and the loading rate on the strain at a fixed stress of 0,58MPa, corresponding to a compressive force of 9,5kN, was assessed with the help of the ANAVAR method. The results of the design of experiments were gathered in the following table.

| Test n° | A      | B            | $\varepsilon_{\sigma=0,58\text{MPa}} (-)$ |                | Average (MPa) |
|---------|--------|--------------|-------------------------------------------|----------------|---------------|
|         | Ageing | Loading rate | Test series 1                             | Tests series 2 |               |
| 1       | No     | 5mm/min      | 0,672                                     | 0,678          | 0,675         |
| 2       | Yes    | 5mm/min      | 0,661                                     | 0,705          | 0,683         |
| 3       | No     | 50mm/min     | 0,666                                     | 0,697          | 0,681         |
| 4       | Yes    | 50mm/min     | 0,673                                     | 0,640          | 0,657         |

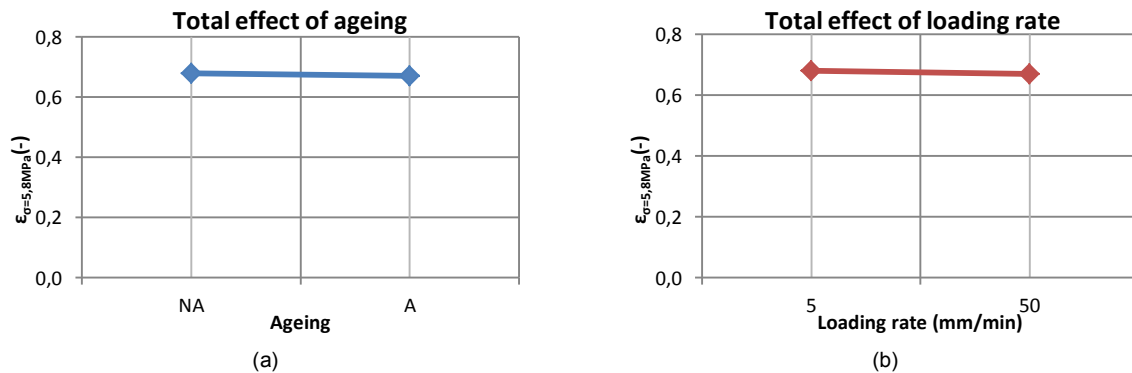
**Table C.21-** Strains at a fixed stress results – DOE accounting for elevated temperatures – silicone quasi-static compression

The total effects of the ageing factor A and the loading rate factor B are respectively equal to:

$$\text{Total effect of A} = \frac{0,657 + 0,683}{2} - \frac{0,681 + 0,675}{2} = -0,008 \text{ MPa} \quad (\text{C.16})$$

$$\text{Total effect of B} = \frac{0,657 + 0,681}{2} - \frac{0,683 + 0,675}{2} = -0,01 \text{ MPa} \quad (\text{C.17})$$

The effect of each factor could be considered as negligible. This observation is confirmed with the graphical representations of the total effect of these factors, see Fig. C.5.



**Figure C.5-** Total effect of the (a) ageing and (b) loading rate factors on the strains – silicone quasi-static compression

As it can be noted for both diagrams the variations of the strains are very low, which seems to induce a stability of the silicone properties at large deformations for the studied factors. To fully validate this observation, the mathematical equation of the surface of the response has to be established. A first determination of the coefficients without considering the interaction was effected, see Table C.22.

| No interaction |          | B       |          | Average (-) |
|----------------|----------|---------|----------|-------------|
|                |          | 5mm/min | 50mm/min |             |
| A              | Non-aged | 0,675   | 0,681    | 0,678       |
|                | Aged     | 0,683   | 0,657    | 0,670       |
| Average (-)    |          | 0,679   | 0,669    | 0,674       |

**Table C.22-** Coefficients, interaction excluded, of the mathematical formulation for the strains – quasi-static compression

Then the coefficients accounting only for the interaction were calculated, based on the principle of equation Eq. (C4), see Table C.23.

| With interaction (ab) |          | B       |          |
|-----------------------|----------|---------|----------|
|                       |          | 5mm/min | 50mm/min |
| A                     | Non-aged | -0,008  | 0,008    |
|                       | Aged     | 0,008   | -0,008   |

**Table C.23-** Interaction coefficients of the mathematical formulation for the strains – quasi-static compression

In consequence, the complete mathematical formulation could be established for the studied domain:

$$\hat{Y} = 0,674 + [0,004 \quad -0,004] [A] + [0,005 \quad -0,005] [B] + \begin{bmatrix} -0,008 & 0,008 \\ 0,008 & -0,008 \end{bmatrix} [AB] \quad (C.18)$$

All the estimated residuals corresponding to each test are finally regrouped in Table C.24.

| A      | B            | Residual r (-) |               |
|--------|--------------|----------------|---------------|
| Ageing | Loading rate | Test series 1  | Test series 2 |
| No     | 5mm/min      | -0,003         | 0,003         |
| Yes    | 5mm/min      | -0,022         | 0,022         |
| No     | 50mm/min     | -0,016         | 0,016         |
| Yes    | 50mm/min     | 0,017          | -0,017        |

**Table C.24-** Residual for the strains at a fixed stress results – silicone quasi-static compression

The distribution of the degrees of liberties is identical to the one of the previous analysis of section C.4, i.e. four degrees for the residual and one for the average, each factor and the interaction. Thus the complete ANAVAR is the following one:

| Source   | Square sum $\Sigma$ | DDL | Variance | F      | F <sub>0.05</sub> |
|----------|---------------------|-----|----------|--------|-------------------|
| A        | 0,0001              | 1   | 0,0001   | 0,2673 | 7,71              |
| B        | 0,0002              | 1   | 0,0002   | 0,3880 | 7,71              |
| AB       | 0,0005              | 1   | 0,0005   | 1,0406 | 7,71              |
| Residual | 0,0020              | 4   | 0,0005   |        |                   |
| Total    |                     | 7   |          |        |                   |

**Table C.25-** Variance analysis ANAVAR on strains at a fixed stress – silicone quasi-static compression

All the calculated F values are inferior to the tabulated F<sub>0.05</sub> values, meaning that neither the ageing or the loading rate or even a combination of these factors impact the behaviour at large strains of silicone elastomers under quasi-static compression.

## C.6 Stress ratio – Silicone compression long-term

Long-term relaxation tests were carried out on compressive samples to determine the influence of the artificial ageing, realized in accordance to the En 11431, and the imposed displacement. For this analysis, two levels for each factor were envisaged, i.e. non-aged/aged and 5mm/10mm. The results evaluated were the ratio of the stress at a time “t” over a reference stress at 60s. In the present study the stress ratio corresponding to the maximum test duration of 1200s was regarded. The complete design of experiments table containing all the results is the following one.

The total effects of the ageing A and the imposed displacement B factors are respectively equal to:

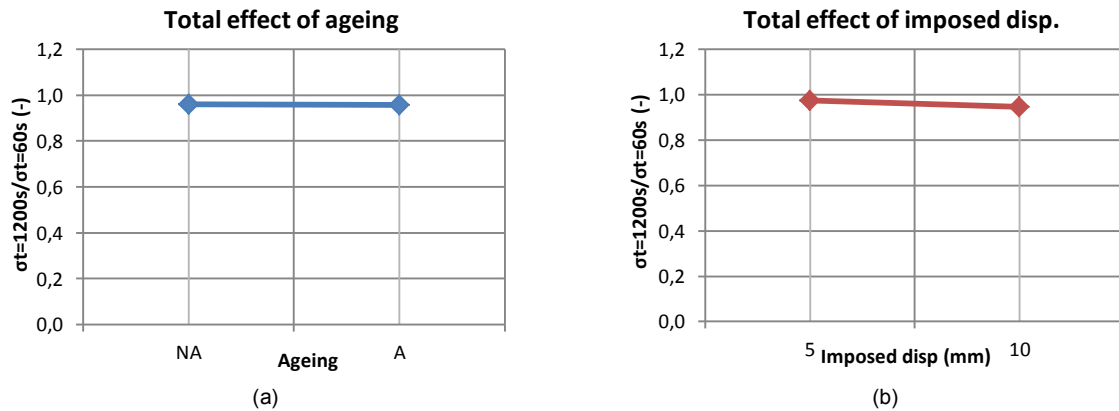
$$\text{Total effect of A} = \frac{0,943 + 0,974}{2} - \frac{0,947 + 0,972}{2} = -0,001 \quad (C.19)$$

$$\text{Total effect of B} = \frac{0,943 + 0,947}{2} - \frac{0,974 + 0,972}{2} = -0,028 \quad (\text{C.20})$$

| Test n° | A      | B             | $\sigma_{t=1200s}/\sigma_{t=60s}$ (-) |
|---------|--------|---------------|---------------------------------------|
|         | Ageing | Imposed disp. | Test series                           |
| 1       | No     | 5mm           | 0,972                                 |
| 2       | Yes    | 5mm           | 0,974                                 |
| 3       | No     | 10mm          | 0,947                                 |
| 4       | Yes    | 10mm          | 0,943                                 |

**Table C.26-** Stress ratio results – Taguchi DOE – silicone long-term compression

The total effect of the imposed displacement factor was 28 times higher than the effect of the ageing. However both values appeared negligible compared to the stress ratio. The graphical representations of the total effect of these factors confirmed this observation, see Fig. C.6.



**Figure C.6-** Total effect of the (a) ageing and (b) imposed disp. factors on the stress ratio – silicone long-term compression

Almost no variations were observed for the both diagrams, indicating a non-influence of the ageing and imposed displacement factors. To fully validate the non-influence of the two studied factors, the mathematical equation of the surface of the response had to be set up. For this analysis, the effect of the interaction could not be evaluated due to a lack of degrees of freedom from the non-repetition of the test series. Thus only the coefficients excluding the interaction had to be calculated, see Table C.27.

| No interaction |          | B     |       | Average (-) |
|----------------|----------|-------|-------|-------------|
|                |          | 5mm   | 10mm  |             |
| A              | Non-aged | 0,972 | 0,947 | 0,960       |
|                | Aged     | 0,974 | 0,943 | 0,958       |
| Average (MPa)  |          | 0,973 | 0,945 | 0,959       |

**Table C.27-** Coefficients, interaction excluded, of the mathematical formulation for the strains – long-term compression

In consequence, the complete mathematical formulation over the studied domain was the following:

$$\hat{Y} = 0,959 + [0,001 \quad -0,001] [A] + [0,014 \quad -0,014] [B] \quad (\text{C.21})$$

As no repetition of the test series was realized the table of the residual was identical to the table accounting for the interaction. All the estimated residuals, corresponding to each test, were finally regrouped in Table C.28.

| A      | B            | Residual r (-) |
|--------|--------------|----------------|
| Ageing | Loading rate | Test series    |
| No     | 5mm          | -0,016         |
| Yes    | 5mm          | 0,016          |
| No     | 10mm         | 0,016          |
| Yes    | 10mm         | -0,016         |

**Table C.28-** Residual for the stress ratio – silicone long-term compression

As four tests were performed, four degrees of liberties were available. One was automatically reserved for the average, one for each factor, letting only one degree of liberty for the residual. The final variance analysis, allowing checking if the factors influenced the stress ratio and consequently the stress reduction factor, is presented in Table C.29.

| Source   | Square sum $\Sigma$ | DDL | Variance | F    | F <sub>0.05</sub> |
|----------|---------------------|-----|----------|------|-------------------|
| A        | 0,000002            | 1   | 0,000002 | 0,2  | 161               |
| B        | 0,000802            | 1   | 0,000802 | 78,1 | 161               |
| Residual | 0,000010            | 1   | 0,000010 |      |                   |
| Total    |                     | 3   |          |      |                   |

**Table C.29-** Variance analysis ANAVAR on strains at a fixed stress – silicone quasi-static compression

Again the comparison of the F values demonstrated the non-influence of the ageing and the imposed displacement on the stress ratio for silicone subjected to long-term compression.

## C.7 Initial stiffness – Silicone shear short-term

To complete the basic range of actions affecting silicone joints during their façade-use, double-lap joint shear-short term experiments were realized. The possible influence of four factors at two levels, i.e. the artificial ageing, the bonding area, the joint thickness and the loading rate, on the behaviour of the adhesive under small strains was evaluated. To attain this objective, 16 tests in total had to be carried out. The calculated initial stiffness of each test corresponded to the slope of the stress-strain curve between two defined strains ( $\gamma=0,05$  and  $0,2$ ). All the initial stiffnesses of this design of experiments were gathered in the following table.

| Test n° | A      | B             | C         | D            | Initial stiffness<br>K <sub>0</sub> (MPa) |
|---------|--------|---------------|-----------|--------------|-------------------------------------------|
|         | Ageing | Area          | Thickness | Loading rate |                                           |
| 1       | No     | 4x(160x30mm)  | 3mm       | 3mm/min      | 0,825                                     |
| 2       | No     | 4x(160x30mm)  | 3mm       | 90mm/min     | 0,555                                     |
| 3       | No     | 4x(160x30mm)  | 6mm       | 3mm/min      | 0,600                                     |
| 4       | No     | 4x(160x30mm)  | 6mm       | 90mm/min     | 0,653                                     |
| 5       | No     | 2x(170x160mm) | 3mm       | 3mm/min      | 0,489                                     |
| 6       | No     | 2x(170x160mm) | 3mm       | 90mm/min     | 0,495                                     |
| 7       | No     | 2x(170x160mm) | 6mm       | 3mm/min      | 0,710                                     |
| 8       | No     | 2x(170x160mm) | 6mm       | 90mm/min     | 0,945                                     |
| 9       | Yes    | 4x(160x30mm)  | 3mm       | 3mm/min      | 0,604                                     |
| 10      | Yes    | 4x(160x30mm)  | 3mm       | 90mm/min     | 0,859                                     |
| 11      | Yes    | 4x(160x30mm)  | 6mm       | 3mm/min      | 0,755                                     |
| 12      | Yes    | 4x(160x30mm)  | 6mm       | 90mm/min     | 0,744                                     |
| 13      | Yes    | 2x(170x160mm) | 3mm       | 3mm/min      | 0,671                                     |
| 14      | Yes    | 2x(170x160mm) | 3mm       | 90mm/min     | 0,704                                     |

|    |     |               |     |          |       |
|----|-----|---------------|-----|----------|-------|
| 15 | Yes | 2x(170x160mm) | 6mm | 3mm/min  | 0,699 |
| 16 | Yes | 2x(170x160mm) | 6mm | 90mm/min | 0,267 |

**Table C.30-** Initial stiffness results – Taguchi DOE – silicone quasi-static shear

The total effects of the selected factors are respectively equal to:

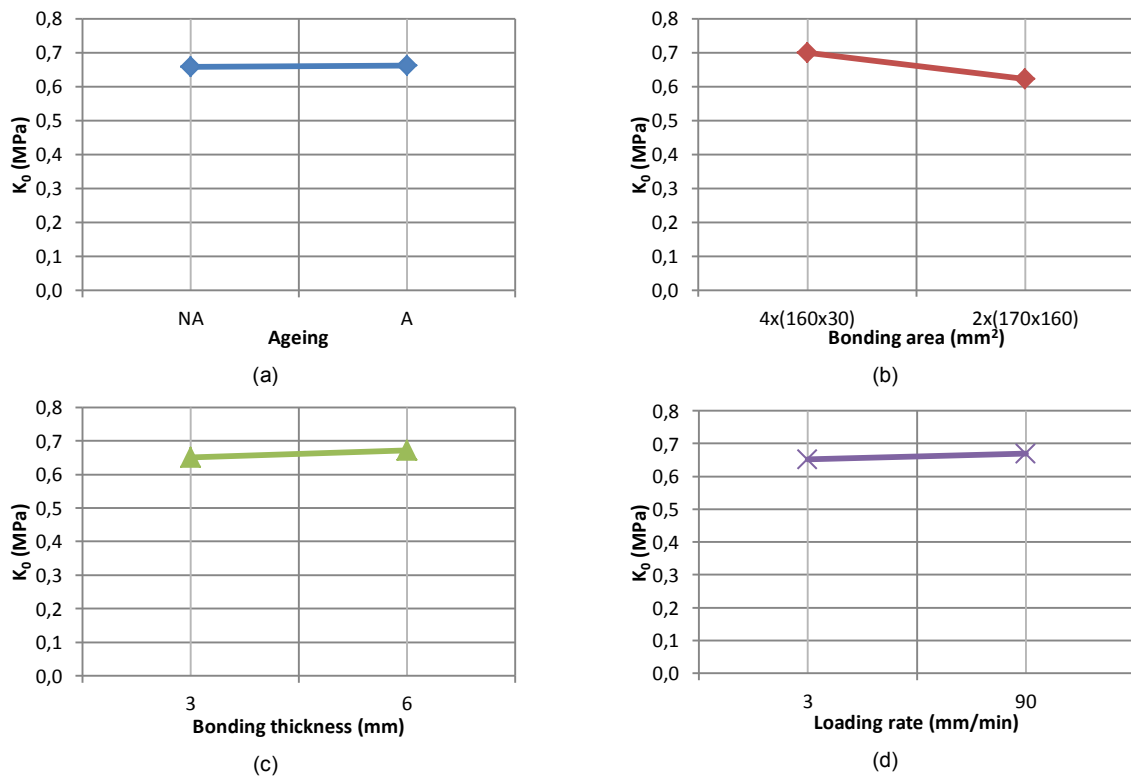
$$\text{Total effect of A} = \frac{\sum K_0^{\text{aged}}}{8} - \frac{\sum K_0^{\text{non-aged}}}{8} = 0,004 \text{ MPa} \quad (\text{C.22})$$

$$\text{Total effect of B} = \frac{\sum K_0^{2x(170x160\text{mm})}}{8} - \frac{\sum K_0^{4x(160x30\text{mm})}}{8} = -0,076 \text{ MPa} \quad (\text{C.23})$$

$$\text{Total effect of C} = \frac{\sum K_0^{6\text{mm}}}{8} - \frac{\sum K_0^{3\text{mm}}}{8} = 0,022 \text{ MPa} \quad (\text{C.24})$$

$$\text{Total effect of D} = \frac{\sum K_0^{90\text{mm/min}}}{8} - \frac{\sum K_0^{3\text{mm/min}}}{8} = -0,016 \text{ MPa} \quad (\text{C.25})$$

Thus, as it can be noticed, the total effect of the ageing and loading rate factors were inferior to the effect of the geometrical factors accounting for the bonding area and the thickness. This observation was confronted to the graphical diagrams representing these total effects of each factor, see Fig. C.7.

**Figure C.7-** Total effect of (a) ageing, (b) area, (c) thickness and (d) loading rate on initial stiffness – silicone quasi-static shear

Graphically, the bonding area and the thickness were the only two factors engendering some minor changes in initial stiffness, which corroborated the first analysis of Eq. (C.22) to (C.25). However to properly set conclusion on the influence of these factors on the shear behaviour at small strains, the complete ANAVAR method with the formulation proposed by Vigier had to be established. For this design of experiments, four factors were studied and therefore the previous representations for the case of only two factors at two levels could not be used anymore. Nevertheless, the same operations were conducted, with the first determination of the model's coefficient centered on each factor individually and then with the calculation of the coefficients belonging to the interactions.

The mathematical formulation of the surface of the response neglecting the interactions is the following one:

$$\hat{Y} = I + [a_1 \ a_2] [A] + [b_1 \ b_2] [B] + [c_1 \ c_2] [C] + [d_1 \ d_2] [D] \quad (C.26)$$

The coefficients  $a_1$  to  $d_2$  were simply calculated with the principle exposed in Appendix B and stored in Table C.31.

| A      |       | B     |        | C      |       | D     |        |
|--------|-------|-------|--------|--------|-------|-------|--------|
| $a_1$  | $a_2$ | $b_1$ | $b_2$  | $c_1$  | $c_2$ | $d_1$ | $d_2$  |
| -0,002 | 0,002 | 0,038 | -0,038 | -0,011 | 0,011 | 0,008 | -0,008 |

**Table C.31-** Coefficients, interaction excluded, of the mathematical formulation for the initial stiffness –quasi-static shear

To the mathematical model detailed in Eq. (C.26) were added the effects of the interactions of second order, see the following Table C.32.

| With 2 <sup>nd</sup> order interaction |       | D       |         | C       |         | B       |         |
|----------------------------------------|-------|---------|---------|---------|---------|---------|---------|
|                                        |       | $d_1$   | $d_2$   | $c_1$   | $c_2$   | $b_1$   | $b_2$   |
| A                                      | $a_1$ | -0,0113 | 0,0113  | -0,0573 | 0,0573  | -0,0392 | 0,0392  |
|                                        | $a_2$ | 0,0113  | -0,0113 | 0,0573  | -0,0573 | 0,0392  | -0,0392 |
| B                                      | $b_1$ | -0,0116 | 0,0116  | 0,0222  | -0,0222 |         |         |
|                                        | $b_2$ | 0,0116  | -0,0116 | -0,0222 | 0,0222  |         |         |
| C                                      | $c_1$ | -0,0112 | 0,0112  |         |         |         |         |
|                                        | $c_2$ | 0,0112  | -0,0112 |         |         |         |         |

**Table C.32-** Interaction coefficients of the mathematical formulation for the initial stiffness – quasi-static shear

In consequence, the complete mathematical formulation could be established for the studied domain:

$$\begin{aligned} \hat{Y} = & 0,661 + [-0,002 \ 0,002] [A] + [0,038 \ -0,038] [B] + \\ & [-0,011 \ 0,011] [C] + [0,008 \ -0,008] [D] + \\ & \begin{bmatrix} -0,039 & 0,039 \\ 0,039 & -0,039 \end{bmatrix} [AB] + \begin{bmatrix} -0,057 & 0,057 \\ 0,057 & -0,057 \end{bmatrix} [AC] + \begin{bmatrix} -0,011 & 0,011 \\ 0,011 & -0,011 \end{bmatrix} [AD] + \\ & \begin{bmatrix} 0,022 & -0,022 \\ -0,022 & 0,022 \end{bmatrix} [BC] + \begin{bmatrix} -0,012 & 0,012 \\ 0,012 & -0,012 \end{bmatrix} [BD] + \begin{bmatrix} -0,011 & 0,011 \\ 0,011 & -0,011 \end{bmatrix} [CD] \end{aligned} \quad (C.27)$$

As for the others analyses of the variances presented previously, the residual associated to each test were determined and recorded in Table C.33.

| A      | B             | C         | D            | Residual r (-) |
|--------|---------------|-----------|--------------|----------------|
| Ageing | Area          | Thickness | Loading rate |                |
| No     | 4x(160x30mm)  | 3mm       | 3mm/min      | 0,239          |
| No     | 4x(160x30mm)  | 3mm       | 90mm/min     | -0,084         |
| No     | 4x(160x30mm)  | 6mm       | 3mm/min      | -0,101         |
| No     | 4x(160x30mm)  | 6mm       | 90mm/min     | -0,054         |
| No     | 2x(170x160mm) | 3mm       | 3mm/min      | -0,078         |
| No     | 2x(170x160mm) | 3mm       | 90mm/min     | -0,077         |
| No     | 2x(170x160mm) | 6mm       | 3mm/min      | -0,060         |
| No     | 2x(170x160mm) | 6mm       | 90mm/min     | 0,215          |
| Yes    | 4x(160x30mm)  | 3mm       | 3mm/min      | -0,202         |
| Yes    | 4x(160x30mm)  | 3mm       | 90mm/min     | 0,047          |
| Yes    | 4x(160x30mm)  | 6mm       | 3mm/min      | 0,064          |
| Yes    | 4x(160x30mm)  | 6mm       | 90mm/min     | 0,091          |

|     |               |     |          |        |
|-----|---------------|-----|----------|--------|
| Yes | 2x(170x160mm) | 3mm | 3mm/min  | 0,041  |
| Yes | 2x(170x160mm) | 3mm | 90mm/min | 0,114  |
| Yes | 2x(170x160mm) | 6mm | 3mm/min  | 0,096  |
| Yes | 2x(170x160mm) | 6mm | 90mm/min | -0,252 |

**Table C.33-** Residual for the initial stiffness results – silicone quasi-static shear

In total 16 tests were realized generating 16 degrees of liberties. One degree was associated to the average value, one for each coefficient and each interaction, letting 5 degrees of liberties for the residual. Knowing this repartition, the complete ANAVAR method was conducted, see Table C.34.

| Source   | Square sum $\Sigma$ | DDL | Variance   | F      | F <sub>0.05</sub> |
|----------|---------------------|-----|------------|--------|-------------------|
| A        | 5,3297E-05          | 1   | 5,3297E-05 | 0,0009 | 6,61              |
| B        | 0,0236              | 1   | 0,0236     | 0,4181 | 6,61              |
| C        | 0,0018              | 1   | 0,0018     | 0,0327 | 6,61              |
| D        | 0,0011              | 1   | 0,0011     | 0,0188 | 6,61              |
| AB       | 0,0246              | 1   | 0,0246     | 0,4366 | 6,61              |
| AC       | 0,0526              | 1   | 0,0526     | 0,9327 | 6,61              |
| AD       | 0,0020              | 1   | 0,0020     | 0,0361 | 6,61              |
| BC       | 0,0079              | 1   | 0,0079     | 0,1394 | 6,61              |
| BD       | 0,0022              | 1   | 0,0022     | 0,0384 | 6,61              |
| CD       | 0,0020              | 1   | 0,0020     | 0,0358 | 6,61              |
| Residual | 0,282               | 5   | 0,0564     |        |                   |
| Total    |                     | 15  |            |        |                   |

**Table C.34-** Variance analysis ANAVAR on the initial stiffness – silicone quasi-static compression

By comparing the F values, it was found that the calculated F were each time lower than the tabulated F<sub>0.05</sub> values, which definitely proved the invariance of the silicone properties at small strains for quasi-static shear actions.

## C.8 Strength – Silicone shear short-term

The results obtained for the quasi-static shear experiments showed relatively well matched curves for strains between 0,2 and 0,8. In addition, the previous variance analysis demonstrated that the shear properties at small strains were completely invariant towards the environmental conditions or the geometrical dimensions. However, beyond the strain of 0,8, several different values of strength were found. To appraise the possible influence of the ageing, the bonding area, the joint thickness and the loading rate on these final values, the ANAVAR method had to be carried out. All the strengths of this design of experiments were gathered in the following table.

| Test n° | A      | B             | C         | D            | Strength $\tau_{\max}$<br>(MPa) |
|---------|--------|---------------|-----------|--------------|---------------------------------|
|         | Ageing | Area          | Thickness | Loading rate |                                 |
| 1       | No     | 4x(160x30mm)  | 3mm       | 3mm/min      | 1,302                           |
| 2       | No     | 4x(160x30mm)  | 3mm       | 90mm/min     | 1,583                           |
| 3       | No     | 4x(160x30mm)  | 6mm       | 3mm/min      | 0,919                           |
| 4       | No     | 4x(160x30mm)  | 6mm       | 90mm/min     | 1,302                           |
| 5       | No     | 2x(170x160mm) | 3mm       | 3mm/min      | 1,024                           |
| 6       | No     | 2x(170x160mm) | 3mm       | 90mm/min     | 1,185                           |
| 7       | No     | 2x(170x160mm) | 6mm       | 3mm/min      | 0,898                           |

|    |     |               |     |          |       |
|----|-----|---------------|-----|----------|-------|
| 8  | No  | 2x(170x160mm) | 6mm | 90mm/min | 0,931 |
| 9  | Yes | 4x(160x30mm)  | 3mm | 3mm/min  | 1,270 |
| 10 | Yes | 4x(160x30mm)  | 3mm | 90mm/min | 1,591 |
| 11 | Yes | 4x(160x30mm)  | 6mm | 3mm/min  | 0,729 |
| 12 | Yes | 4x(160x30mm)  | 6mm | 90mm/min | 1,252 |
| 13 | Yes | 2x(170x160mm) | 3mm | 3mm/min  | 1,220 |
| 14 | Yes | 2x(170x160mm) | 3mm | 90mm/min | 1,425 |
| 15 | Yes | 2x(170x160mm) | 6mm | 3mm/min  | 0,897 |
| 16 | Yes | 2x(170x160mm) | 6mm | 90mm/min | 0,514 |

**Table C.35-** Strength results – Taguchi DOE – silicone quasi-static shear

The total effects of the selected factors were respectively equal to:

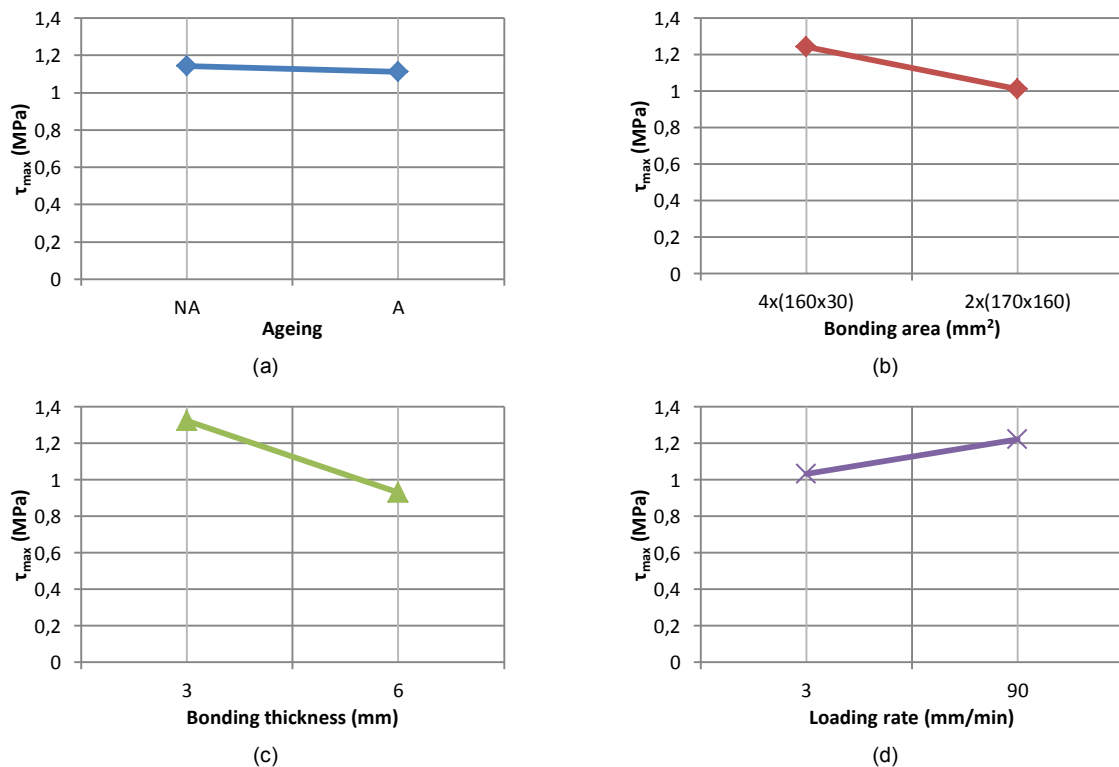
$$\text{Total effect of A} = \frac{\sum K_0^{\text{aged}}}{8} - \frac{\sum K_0^{\text{non-aged}}}{8} = -0,031 \text{ MPa} \quad (\text{C.28})$$

$$\text{Total effect of B} = \frac{\sum K_0^{2x(170x160\text{mm})}}{8} - \frac{\sum K_0^{4x(160x30\text{mm})}}{8} = -0,232 \text{ MPa} \quad (\text{C.29})$$

$$\text{Total effect of C} = \frac{\sum K_0^{6\text{mm}}}{8} - \frac{\sum K_0^{3\text{mm}}}{8} = -0,395 \text{ MPa} \quad (\text{C.30})$$

$$\text{Total effect of D} = \frac{\sum K_0^{90\text{mm/min}}}{8} - \frac{\sum K_0^{3\text{mm/min}}}{8} = 0,190 \text{ MPa} \quad (\text{C.31})$$

From these calculations, it could have directly been concluded that the ageing had no impact on the shear strength. This outcome was also observed on the diagrams of the total effect of each factor, as they represented the gap between the two extreme points. Only the diagram accounting for the total effect of the ageing presented a relatively small slope, while large variations were seen for the other factors, see Fig. C.8.



**Figure C.8-** Total effect of (a) ageing, (b) area, (c) thickness and (d) loading rate on the strength – silicone quasi-static shear



Further investigations had to be done to ensure of the influence of the three other factors. Thus, the coefficients of the mathematical formulation representing the surface of the response were estimated. At first, the interactions were neglected to determine, with the principle exposed in Appendix B, the coefficients of each parameter, see Table C.36.

| A     |        | B     |        | C     |        | D      |       |
|-------|--------|-------|--------|-------|--------|--------|-------|
| $a_1$ | $a_2$  | $b_1$ | $b_2$  | $c_1$ | $c_2$  | $d_1$  | $d_2$ |
| 0,015 | -0,015 | 0,116 | -0,116 | 0,198 | -0,198 | -0,095 | 0,095 |

**Table C.36-** Coefficients, interaction excluded, of the mathematical formulation for the strength –quasi-static shear

Then to complete the mathematical model, the effects of the second order interactions were included, see the following Table C.37 for the interaction coefficients.

| With 2 <sup>nd</sup> order interaction |       | D       |         | C       |         | B       |         |
|----------------------------------------|-------|---------|---------|---------|---------|---------|---------|
|                                        |       | $d_1$   | $d_2$   | $c_1$   | $c_2$   | $b_1$   | $b_2$   |
| A                                      | $a_1$ | -0,0121 | 0,0121  | -0,0669 | 0,0669  | 0,0176  | -0,0176 |
|                                        | $a_2$ | 0,0121  | -0,0121 | 0,0669  | -0,0669 | -0,0176 | 0,0176  |
| B                                      | $b_1$ | -0,0933 | 0,0933  | -0,0043 | 0,0043  |         |         |
|                                        | $b_2$ | 0,0933  | -0,0933 | 0,0043  | -0,0043 |         |         |
| C                                      | $c_1$ | -0,0258 | 0,0258  |         |         |         |         |
|                                        | $c_2$ | 0,0258  | -0,0258 |         |         |         |         |

**Table C.37-** Interaction coefficients of the mathematical formulation for the strength – quasi-static shear

Consequently, by regrouping the data of the two previous tables, the mathematical formulation describing the surface of the response was established for the studied domain:

$$\begin{aligned}
 \hat{Y} = & 1,128 + [0,015 \quad -0,015] [A] + [0,116 \quad -0,116] [B] + \\
 & [0,198 \quad -0,198] [C] + [-0,095 \quad 0,095] [D] + \\
 & \begin{bmatrix} 0,018 & -0,018 \\ -0,018 & 0,018 \end{bmatrix} [AB] + \begin{bmatrix} -0,067 & 0,067 \\ 0,067 & -0,067 \end{bmatrix} [AC] + \begin{bmatrix} -0,012 & 0,012 \\ 0,012 & -0,012 \end{bmatrix} [AD] + \\
 & \begin{bmatrix} -0,004 & 0,004 \\ 0,004 & -0,004 \end{bmatrix} [BC] + \begin{bmatrix} -0,093 & 0,093 \\ 0,093 & -0,093 \end{bmatrix} [BD] + \begin{bmatrix} -0,026 & 0,026 \\ 0,026 & -0,026 \end{bmatrix} [CD]
 \end{aligned} \quad (C.32)$$

With this complete model, the residuals of each experiment were determined and stored in the following Table C.38.

| A      | B             | C         | D            | Residual r (-) |
|--------|---------------|-----------|--------------|----------------|
| Ageing | Area          | Thickness | Loading rate |                |
| No     | 4x(160x30mm)  | 3mm       | 3mm/min      | 0,126          |
| No     | 4x(160x30mm)  | 3mm       | 90mm/min     | -0,046         |
| No     | 4x(160x30mm)  | 6mm       | 3mm/min      | -0,057         |
| No     | 4x(160x30mm)  | 6mm       | 90mm/min     | -0,023         |
| No     | 2x(170x160mm) | 3mm       | 3mm/min      | -0,081         |
| No     | 2x(170x160mm) | 3mm       | 90mm/min     | 0,001          |
| No     | 2x(170x160mm) | 6mm       | 3mm/min      | 0,012          |
| No     | 2x(170x160mm) | 6mm       | 90mm/min     | 0,068          |
| Yes    | 4x(160x30mm)  | 3mm       | 3mm/min      | 0,002          |
| Yes    | 4x(160x30mm)  | 3mm       | 90mm/min     | -0,082         |
| Yes    | 4x(160x30mm)  | 6mm       | 3mm/min      | -0,071         |
| Yes    | 4x(160x30mm)  | 6mm       | 90mm/min     | 0,151          |
| Yes    | 2x(170x160mm) | 3mm       | 3mm/min      | -0,047         |

|     |               |     |          |        |
|-----|---------------|-----|----------|--------|
| Yes | 2x(170x160mm) | 3mm | 90mm/min | 0,127  |
| Yes | 2x(170x160mm) | 6mm | 3mm/min  | 0,116  |
| Yes | 2x(170x160mm) | 6mm | 90mm/min | -0,196 |

**Table C.38-** Residual for the strength results – silicone quasi-static shear

The distribution of the degrees of liberty was equal to the one of the previous ANAVAR, with 15 degrees available. One was attributed to the average, one for each factor and each interaction, leaving four degrees for the residual. With this repartition, the complete variance analysis was realized, see Table C.39.

| Source   | Square sum $\Sigma$ | DDL | Variance | F       | F <sub>0,05</sub> |
|----------|---------------------|-----|----------|---------|-------------------|
| A        | 0,0038              | 1   | 0,0038   | 0,1373  | 6,61              |
| B        | 0,2150              | 1   | 0,2150   | 7,8255  | 6,61              |
| C        | 0,6241              | 1   | 0,6241   | 22,7118 | 6,61              |
| D        | 0,1449              | 1   | 0,1449   | 5,2741  | 6,61              |
| AB       | 0,0050              | 1   | 0,0050   | 0,1804  | 6,61              |
| AC       | 0,0715              | 1   | 0,0715   | 2,6031  | 6,61              |
| AD       | 0,0023              | 1   | 0,0023   | 0,0852  | 6,61              |
| BC       | 0,0003              | 1   | 0,0003   | 0,0108  | 6,61              |
| BD       | 0,1394              | 1   | 0,1394   | 5,0728  | 6,61              |
| CD       | 0,0107              | 1   | 0,0107   | 0,3881  | 6,61              |
| Residual | 0,1374              | 5   | 0,0275   |         |                   |
| Total    |                     | 15  |          |         |                   |

**Table C.39-** Variance analysis ANAVAR on the strength – silicone quasi-static compression

As it can be remarked, the calculated F values were superior to the tabulated values for the factor B and C, i.e. for the bonding area and for the thickness. Consequently, only these two factors considered individually have an influence on the shear strengths. Lower are the bonding area and the thickness and higher will be the silicone strength for quasi-static shear actions.

## C.9 Initial stiffness of the first DOE – Acrylic tension quasi-static

As for the silicone, quasi-static tensile tests on acrylic dog-bone samples were carried out in order to assess the influence of two parameters at two levels, i.e. the artificial ageing according to the ISO 11431 and the loading rate. In this section, only the first portion of the diagram was studied through the recorded chord modulus defined as the slope of the curve between two given strains, i.e. 0,05% and 0,25%. The complete design of experiments table containing all the results is the following one.

| Test n° | A      | B            | Chord modulus K <sub>0</sub> (MPa) |                |               | Average (MPa) |
|---------|--------|--------------|------------------------------------|----------------|---------------|---------------|
|         | Ageing | Loading rate | Test series 1                      | Tests series 2 | Test series 3 |               |
| 1       | No     | 50mm/min     | 1087,297                           | 980,461        | 1201,385      | 1089,714      |
| 2       | Yes    | 50mm/min     | 1209,374                           | 1154,144       | -             | 1181,759      |
| 3       | No     | 250mm/min    | 1495,163                           | 1331,919       | -             | 1413,541      |
| 4       | Yes    | 250mm/min    | 1416,507                           | 1350,156       | -             | 1383,332      |

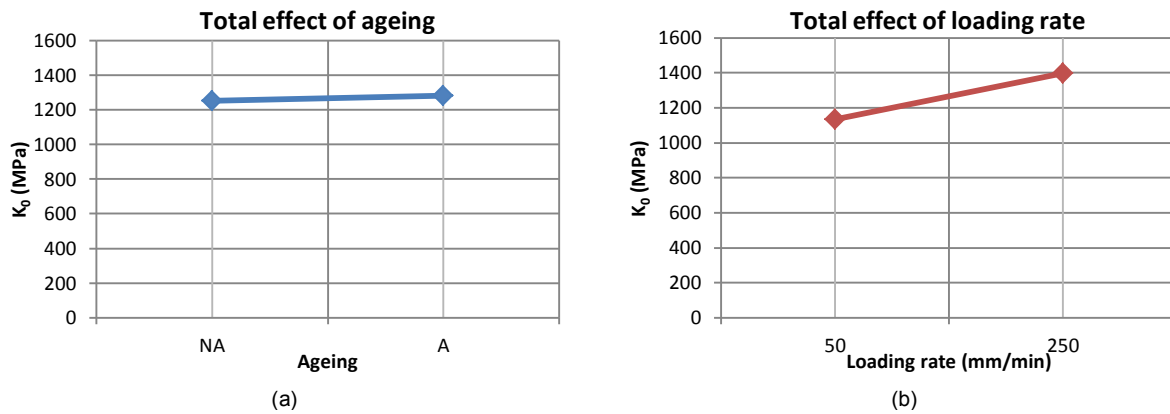
**Table C.40-** Initial stiffness results – DOE accounting for elevated temperatures – acrylic quasi-static tension

With the previous table, the total effects of the ageing factor A and the loading rate factor B were simply calculated:

$$\text{Total effect of A} = \frac{1383,332 + 1181,759}{2} - \frac{1413,541 + 1089,714}{2} = 30,918 \text{ MPa} \quad (\text{C.33})$$

$$\text{Total effect of B} = \frac{1383,332 + 1413,541}{2} - \frac{1181,759 + 1089,714}{2} = 262,7 \text{ MPa} \quad (\text{C.34})$$

Form these both values, a first hypothesis was set up, i.e. the effect of the loading rate was relatively consequent compared to the one of the artificial ageing. This postulate was simply correlated with the graphical representation of the total effect of both factors, see Fig. C.9.



**Figure C.9-** Total effect of the (a) ageing and (b) loading rate factors on the initial stiffness – acrylic quasi-static tension

Again the variation of the initial stiffness with the ageing was quasi-nil, inducing a negligible impact of the factor on the results at small strains. However, the effect of the loading rate was clearly observable with a strong increase of the Young's modulus with the loading rate. Nevertheless to conclude on the real influence of the two factors and also of the interaction, the complete ANAVAR based on the mathematical formulation of the surface of the results was again conducted with a first evaluation of the coefficients neglecting the interaction, see Table C.41.

| No interaction |          | B        |           | Average (MPa) |
|----------------|----------|----------|-----------|---------------|
|                |          | 50mm/min | 250mm/min |               |
| A              | Non-aged | 1089,714 | 1413,541  | 1251,628      |
|                | Aged     | 1181,759 | 1383,332  | 1282,545      |
| Average (MPa)  |          | 1135,737 | 1398,436  | 1267,086      |

**Table C.41-** Coefficients, interaction excluded, of the mathematical formulation for initial stiffness – acrylic quasi-static tension

The interaction coefficients were then determined according to the principle of equation C.4, see the Table C.42.

| With interaction (ab) |          | B        |           |
|-----------------------|----------|----------|-----------|
|                       |          | 50mm/min | 250mm/min |
| A                     | Non-aged | -30,563  | 30,563    |
|                       | Aged     | 30,563   | -30,563   |

**Table C.42-** Interaction coefficients of the mathematical formulation for initial stiffness – acrylic quasi-static tension

Thus the final mathematical formulation of the studied domain was equivalent to:

$$\hat{Y} = 1267,09 + [-15,46 \quad 15,46] [A] + [-131,35 \quad 131,35] [B] + \begin{bmatrix} -30,56 & 30,56 \\ 30,56 & -30,56 \end{bmatrix} [AB] \quad (\text{C.35})$$

All the estimated residuals corresponding to each test were then calculated and regrouped in the following Table C.43.

| A      | B            | Residual r (MPa) |               |               |
|--------|--------------|------------------|---------------|---------------|
| Ageing | Loading rate | Test series 1    | Test series 2 | Test series 3 |
| No     | 50mm/min     | -2,417           | -109,253      | 111,670       |
| Yes    | 50mm/min     | 27,615           | -27,615       | -             |
| No     | 250mm/min    | 81,622           | -81,622       | -             |
| Yes    | 250mm/min    | 33,175           | -33,175       | -             |

**Table C.43-** Residual for the initial stiffness results – DOE accounting for elevated temperatures – acrylic quasi-static tension

For the selected design of experiments, 9 tests were conducted. Thus, 9 degrees of liberties in total were available. As previously mentioned, one was attributed to the average, one for each factor and the interaction, letting 5 degrees of liberties for the variance. Knowing this repartition, the final table ending the ANAVAR method was set up, see Table C.44.

| Source   | Square sum $\Sigma$ | DDL | Variance   | F      | F <sub>0.05</sub> |
|----------|---------------------|-----|------------|--------|-------------------|
| A        | 2150,793            | 1   | 2150,793   | 0,259  | 6,61              |
| B        | 155274,841          | 1   | 155274,841 | 18,725 | 6,61              |
| AB       | 8407,105            | 1   | 8407,105   | 1,014  | 6,61              |
| Residual | 41463,035           | 5   | 8292,607   |        |                   |
| Total    |                     | 8   |            |        |                   |

**Table C.44-** ANAVAR on the initial stiffness – DOE accounting for elevated temperatures – acrylic quasi-static tension

The estimated F values of the ageing factor and of the interaction were both lower than the tabulated F<sub>0.05</sub> value, while it was not the case for the loading rate factor. Consequently, it was concluded that only the loading rate impacted the initial stiffness. Higher Young's moduli were reached for higher loading rates.

### C.10 Maximum stress of the first DOE – Acrylic tension quasi-static

To evaluate the influence of the artificial ageing, regrouping the elevated temperature, the humidity and the UV-radiation, on the last useful part of the stress-strain diagrams obtained for the quasi-static tension of acrylic adhesive, a variance analysis concerning the maximum stresses was conducted. The maximum stresses were the failure strength for the brittle curves and the yield stress for the ductile curves. Thus this analysis was performed independently of the found behaviour. The results associated to this design of experiments, containing 9 tests in total, are given in Table C.45.

| Test n° | A      | B            | Strength/Yield $\sigma_{\max}$ (MPa) |                |               | Average (MPa) |
|---------|--------|--------------|--------------------------------------|----------------|---------------|---------------|
|         | Ageing | Loading rate | Test series 1                        | Tests series 2 | Test series 3 |               |
| 1       | No     | 50mm/min     | 10,849                               | 9,971          | 10,930        | 10,583        |
| 2       | Yes    | 50mm/min     | 10,439                               | 10,742         | -             | 10,591        |
| 3       | No     | 250mm/min    | 13,672                               | 15,193         | -             | 14,433        |
| 4       | Yes    | 250mm/min    | 11,603                               | 14,618         | -             | 13,110        |

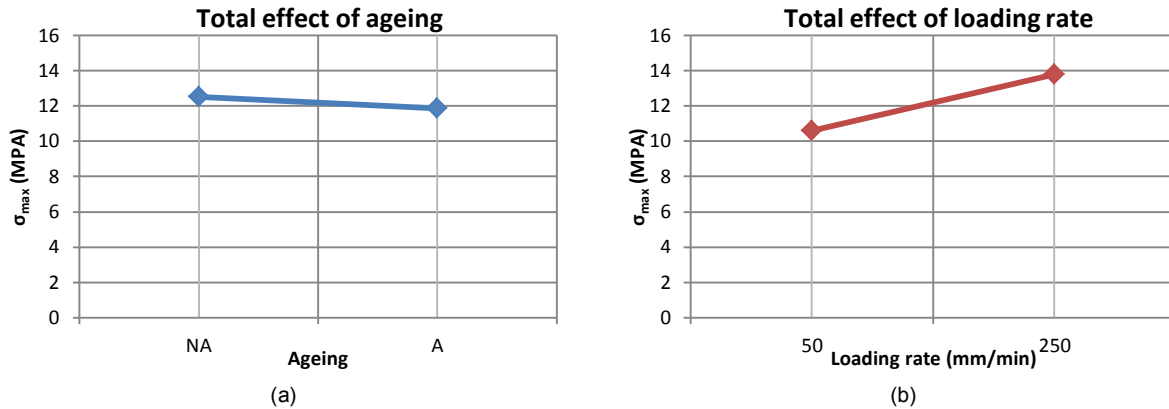
**Table C.45-** Maximum stress results – DOE accounting for elevated temperatures – acrylic quasi-static tension

The total effects of the ageing factor A and the loading rate factor B were then evaluated:

$$\text{Total effect of A} = \frac{13,110 + 10,591}{2} - \frac{14,433 + 10,583}{2} = -0,657 \text{ MPa} \quad (\text{C.36})$$

$$\text{Total effect of B} = \frac{13,110 + 14,433}{2} - \frac{10,591 + 10,583}{2} = 3,184 \text{ MPa} \quad (\text{C.37})$$

While the total effect of the ageing remained low, the total effect of the loading rate exhibited a higher value, indicating a possible influence of this last factor on the maximum stresses. This first observation was confirmed by the diagrams representing the total effect of each factor, see Fig. C.10.



**Figure C.10-** Total effect of the (a) ageing and (b) loading rate factors on the maximum stress – acrylic quasi-static tension

With the above diagrams, it was postulated that the effect of the loading rate was clearly consequent for the maximum stress, in contrary to the ageing for which the slope was small. To mathematically approve this postulate, the equation of the surface of the response was set up with a first calculation of the coefficients by neglecting the interaction, see Table C.46.

| No interaction |          | B        |           | Average (MPa) |
|----------------|----------|----------|-----------|---------------|
|                |          | 50mm/min | 250mm/min |               |
| A              | Non-aged | 14,433   | 12,508    | 10,583        |
|                | Aged     | 13,110   | 11,851    | 10,591        |
| Average (MPa)  |          | 10,587   | 13,771    | 12,179        |

**Table C.46-** Coefficients, interaction excluded, of the mathematical formulation for initial stiffness – acrylic quasi-static tension

The interactions coefficients were then determined with the help of the previous table, see Table C.47.

| With interaction (ab) |          | B        |           |
|-----------------------|----------|----------|-----------|
|                       |          | 50mm/min | 250mm/min |
| A                     | Non-aged | -0,332   | 0,332     |
|                       | Aged     | 0,332    | -0,332    |

**Table C.47-** Interaction coefficients of the mathematical formulation for the maximum stress – acrylic quasi-static tension

Consequently, the final mathematical formulation of the studied domain was equivalent to:

$$\hat{Y} = 12,179 + [0,329 \quad -0,329] [A] + [-1,592 \quad 1,592] [B] + \begin{bmatrix} -0,332 & 0,332 \\ 0,332 & -0,332 \end{bmatrix} [AB] \quad (\text{C.38})$$

With this equation, the residual associated to the 9 tests were evaluated, see Table C.48.

| A      | B            | Residual r (MPa) |               |               |
|--------|--------------|------------------|---------------|---------------|
| Ageing | Loading rate | Test series 1    | Test series 2 | Test series 3 |
| No     | 50mm/min     | 0,266            | -0,612        | 0,347         |
| Yes    | 50mm/min     | -0,151           | 0,151         | -             |

|     |           |        |       |   |
|-----|-----------|--------|-------|---|
| No  | 250mm/min | -0,760 | 0,760 | - |
| Yes | 250mm/min | -1,508 | 1,508 | - |

**Table C.48-** Residual for the maximum stress results – DOE accounting for elevated temperatures – acrylic quasi-static tension

The repartition of the degrees of liberties for this statistical analysis was the same than the previous one of section C.9, as the total number of tests conducted was the same. The complete table allowing appraising the influence of the two factors and of the interaction was the following one:

| Source   | Square sum $\Sigma$ | DDL | Variance | F      | F <sub>0.05</sub> |
|----------|---------------------|-----|----------|--------|-------------------|
| A        | 0,973               | 1   | 0,973    | 0,770  | 6,61              |
| B        | 22,815              | 1   | 22,815   | 18,070 | 6,61              |
| AB       | 0,994               | 1   | 0,994    | 0,788  | 6,61              |
| Residual | 6,313               | 5   | 1,263    |        |                   |
| Total    |                     | 8   |          |        |                   |

**Table C.49-** ANAVAR on the maxim stress – DOE accounting for elevated temperatures – acrylic quasi-static tension

Even if the studied values were not the same, this analysis on the maximum stress demonstrated, as for the analysis of the Young's modulus, the only impact of the loading rate. The effects of the artificial ageing according to the ISO 11431 and of the interaction were both negligible. Moreover, for a higher loading rate, the maximum stress was higher.

### C.11 Stress ratio – Acrylic tension long-term

As for the previous long-term tests on silicone, the evaluation of the stress decrease was realized by analyzing a stress ratio. This last ratio corresponded, for each resulting curve, to the stress at a defined time divided by a reference stress at 60s. The influences of the artificial ageing according to the ISO 11431 and the imposed displacement were determined with the ANAVAR method detailed below. These two factors possessed two levels and the complete results for the stresses at the maximum discretized time of 960s were considered, see Table C.50.

| Test n° | A      | B            | $\sigma_{t=960s}/\sigma_{t=60s}$ (-) |               | Average (-) |
|---------|--------|--------------|--------------------------------------|---------------|-------------|
|         | Ageing | Loading rate | Test series 1                        | Test series 2 |             |
| 1       | No     | 0,6mm        | 0,319                                | 0,370         | 0,345       |
| 2       | Yes    | 0,6mm        | 0,392                                | -             | 0,392       |
| 3       | No     | 1mm          | 0,458                                | 0,243         | 0,350       |
| 4       | Yes    | 1mm          | 0,514                                | 0,385         | 0,450       |

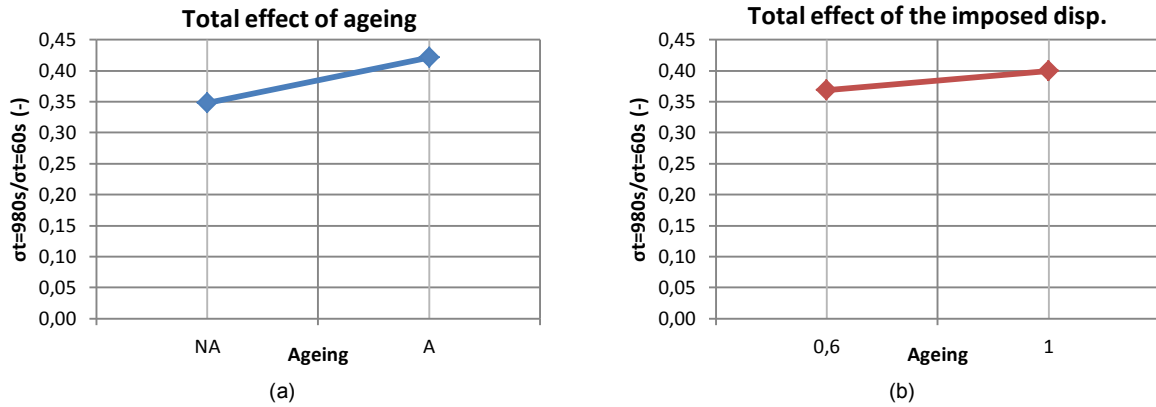
**Table C.50-** Stress ratio results for the maximum time of 960s – Taguchi DOE – acrylic long-term tension

With the average values of all configurations, the total effect of each factors were then calculated:

$$\text{Total effect of A} = \frac{0,450 + 0,392}{2} - \frac{0,350 + 0,345}{2} = 0,073 \quad (\text{C.39})$$

$$\text{Total effect of B} = \frac{0,450 + 0,350}{2} - \frac{0,392 + 0,345}{2} = 0,0316 \quad (\text{C.40})$$

These two values did not provide sufficient information to properly evaluate the influence of the factors. The total effect diagrams were consequently plotted to visually assess if, compared to the general stresses ratios, an impact on the studied value was observable, see Fig. C.11. From these two diagrams, it was seen that, for aged specimens and for the maximum imposed displacement of 1mm, the ratios were larger, indicating a smaller decrease of the stress compared to the reference.



**Figure C.11-** Total effect of (a) ageing and (b) imposed disp. on the stress ratio – acrylic long-term tension

However to properly conclude on the real influence, the mathematical formulation of the surface of the response proposed by Vigier had to be established. In a first step, the coefficient of the models neglecting the interaction were evaluated, see Table C.51.

| No interaction |          | B     |       | Average (-) |
|----------------|----------|-------|-------|-------------|
|                |          | 0,6mm | 1mm   |             |
| A              | Non-aged | 0,345 | 0,350 | 0,347       |
|                | Aged     | 0,392 | 0,450 | 0,421       |
| Average (-)    |          | 0,368 | 0,400 | 0,384       |

**Table C.51-** Coefficients, interaction excluded, of the mathematical formulation for the stress ratio – acrylic long-term tension

The interaction coefficients were then assessed with the previous table and the principle of equation C.4, see Table C.52.

| With interaction (ab) |          | B      |        |
|-----------------------|----------|--------|--------|
|                       |          | 0,6mm  | 1mm    |
| A                     | Non-aged | 0,013  | -0,013 |
|                       | Aged     | -0,013 | 0,013  |

**Table C.52-** Interaction coefficients of the mathematical formulation for the stress ratio – acrylic long-term tension

The complete mathematical formulation was set up by combining the results of the two tables:

$$\hat{Y} = 0,384 + [-0,037 \quad 0,037] [A] + [-0,016 \quad 0,016] [B] + \begin{bmatrix} 0,013 & -0,013 \\ -0,013 & 0,013 \end{bmatrix} [AB] \quad (C.41)$$

The next step corresponded to the calculation of the residuals with the above formulation. These residuals were regrouped in Table C.53.

| A      | B            | Residual r (-) |               |
|--------|--------------|----------------|---------------|
| Ageing | Loading rate | Test series 1  | Test series 2 |
| No     | 0,6mm        | -0,025         | 0,025         |
| Yes    | 0,6mm        | 0              | -             |
| No     | 1mm          | 0,107          | -0,107        |
| Yes    | 1mm          | 0,064          | -0,064        |

**Table C.53-** Residuals for the stress ratio for the maximum time of 960s – acrylic long-term tension

In total seven tests were carried out, offering consequently seven degrees of liberties. These last ones were allocated to the average, each factor and the interaction, letting only 3 degrees for the residuals.

The complete ANAVAR, ending this study and allowing evaluating the influence of the factors and their interaction, is presented in Table C.54.

| Source   | Square sum $\Sigma$ | DDL | Variance | F      | F <sub>0.05</sub> |
|----------|---------------------|-----|----------|--------|-------------------|
| A        | 0,0095              | 1   | 0,0095   | 0,8711 | 10,13             |
| B        | 0,0017              | 1   | 0,0017   | 0,1608 | 10,13             |
| AB       | 0,0012              | 1   | 0,0012   | 0,1070 | 10,13             |
| Residual | 0,0325              | 3   | 0,0108   |        |                   |
| Total    |                     | 6   |          |        |                   |

**Table C.54-** ANAVAR analysis on the stress ratio for the maximum time of 960s – acrylic long-term tension

The calculated F values were always found lower than the tabulated F<sub>0.05</sub> values. This indicated that none of the ageing or the imposed displacement factor or even their interaction changed the stress ratio decreased after 60s of constant strain.

## C.12 Stress ratio – quasi-static stress reference – Acrylic tension long-term

Long-term tensile tests results on acrylic adhesive showed an important decrease during the first 60s which could not be analyzed with the method of the previous section C.11 consisting in appraising the evolution of the stress ratio decrease with the stress reference at 60s. Therefore the reference was changed and considered as the averaged stress at 50mm/min issued from the quasi-static tensile study. Two references were consequently regarded, i.e. the quasi-static stress at the imposed displacement of 0,6mm ( $\epsilon=0,01$ ) and at the second imposed displacement of 1mm ( $\epsilon=0,0167$ ). The stress ratio results were stored in different tables and the variance analysis was simply conducted on the ratio presenting the maximum time of 960s, see Table C.55.

| Test n° | A      | B            | $\sigma_{t=960s}/\sigma_{quasi-static} (-)$ |               | Average (-) |
|---------|--------|--------------|---------------------------------------------|---------------|-------------|
|         | Ageing | Loading rate | Test series 1                               | Test series 2 |             |
| 1       | No     | 0,6mm        | 0,018                                       | 0,024         | 0,021       |
| 2       | Yes    | 0,6mm        | 0,047                                       | -             | 0,047       |
| 3       | No     | 1mm          | 0,053                                       | 0,017         | 0,035       |
| 4       | Yes    | 1mm          | 0,061                                       | 0,029         | 0,045       |

**Table C.55-** Stress ratio results for the maximum time of 960s – reference quasi-static stress – acrylic long-term tension

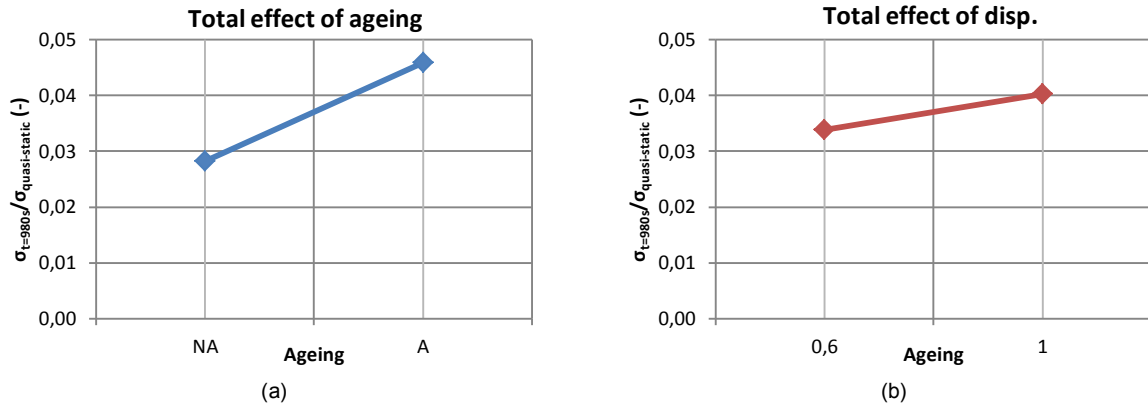
The total effects of each factors, i.e. the ageing A and the imposed displacement B, were quantified:

$$\text{Total effect of A} = \frac{0,045 + 0,047}{2} - \frac{0,035 + 0,021}{2} = 0,018 \quad (\text{C.42})$$

$$\text{Total effect of B} = \frac{0,045 + 0,035}{2} - \frac{0,047 + 0,021}{2} = 0,0065 \quad (\text{C.43})$$

Compared to the averaged stress ratios of Table C.55, the first value accounting for the influence of the ageing was relatively high, so as the second value representing the total effect of the imposed displacement. No conclusion could have been drawn from these only values. Thus, at first, the graphical models of these effects were plotted on Fig. C.12. The slopes were again significant and higher stress ratios were found for aged specimens and under an imposed displacement of 1mm. However, these variations could be due to one stress ratio lower than the others, e.g. for the aged specimen under 0,6mm presenting a value of 0,017. Therefore, the mathematical formulation of Vigier was employed in a second step to clarify and ensure of the real influence of the parameters. The coefficients of this model, neglecting the interaction of the factor, were determined, see Table C.56.





**Figure C.12-** Total effect of (a) ageing and (b) imposed disp. – stress ratio quasi-static reference – acrylic long-term tension

| No interaction |          | B     |       | Average (-) |
|----------------|----------|-------|-------|-------------|
|                |          | 0,6mm | 1mm   |             |
| A              | Non-aged | 0,021 | 0,035 | 0,028       |
|                | Aged     | 0,047 | 0,045 | 0,046       |
| Average (-)    |          | 0,034 | 0,040 | 0,037       |

**Table C.56-** Coefficients, interaction excluded, of the mathematical formulation – stress ratio quasi-static reference

With the above table, the interaction coefficients were calculated based on the principle of equation C.4, see Table C.57.

| With interaction (ab) |          | B      |        |
|-----------------------|----------|--------|--------|
|                       |          | 0,6mm  | 1mm    |
| A                     | Non-aged | -0,004 | 0,004  |
|                       | Aged     | 0,004  | -0,004 |

**Table C.57-** Interaction coefficients of the mathematical formulation – stress ratio quasi-static reference

The final mathematical formulation of the surface of the response and comprising the coefficients of each factors and of their interaction was then established:

$$\hat{Y} = 0,037 + [-0,009 \quad 0,009] [A] + [-0,003 \quad 0,003] [B] + \begin{bmatrix} -0,004 & 0,004 \\ 0,004 & -0,004 \end{bmatrix} [AB] \quad (C.44)$$

The residual associated to each stress ratio results were estimated with the above formulation and stored in Table C.58.

| A      | B            | Residual r (-) |               |
|--------|--------------|----------------|---------------|
| Ageing | Loading rate | Test series 1  | Test series 2 |
| No     | 0,6mm        | -0,003         | 0,003         |
| Yes    | 0,6mm        | 0              | -             |
| No     | 1mm          | 0,018          | -0,018        |
| Yes    | 1mm          | 0,016          | -0,016        |

**Table C.58-** Residuals for the stress ratio for the maximum time of 960s – quasi-static reference – acrylic long-term tension

The number of tests and consequently the repartition of the degrees of liberties were the same than for the previous section C.11, i.e. one ddl for the average, one for each factor, one for the interaction and 3 for the residual. The complete table ending the ANAVAR method and allowing evaluating the influence of the ageing and imposed displacement parameters is given in Table C.59.

| Source   | Square sum $\Sigma$ | DDL | Variance | F      | $F_{0.05}$ |
|----------|---------------------|-----|----------|--------|------------|
| A        | 0,0005              | 1   | 0,0005   | 1,3887 | 10,13      |
| B        | 0,0001              | 1   | 0,0001   | 0,1874 | 10,13      |
| AB       | 0,0001              | 1   | 0,0001   | 0,2773 | 10,13      |
| Residual | 0,0012              | 3   | 0,0004   |        |            |
| Total    |                     | 6   |          |        |            |

**Table C.59-** ANAVAR analysis on the stress ratio for the max. time of 960s – quasi-static reference – acrylic long-term tension

The calculated F values were again lower in each case than the  $F_{0.05}$  value, indicating that the ageing, the imposed displacement and their interaction had no impact on the stress-ratio with the quasi-static stress as reference.

### C.13 Initial stiffness – Acrylic shear quasi-static

The quasi-static shear properties of acrylic adhesive were first investigated on the only material without considering glass and steel adherents. Two different factors at two levels were studied, i.e. the artificial ageing and the loading rate. To assess the influence of these factors on the experimental stress-strain diagrams, a first analysis was realized at small strains by studying the shear modulus. This last was assimilated to a chord modulus between two defined strains of  $\gamma=0,01$  and  $\gamma=0,05$ . All the initial stiffnesses were evaluated and recorded in Table C.60.

| Test n° | A      | B            | $G_0$ (MPa)   |               | Average (MPa) |
|---------|--------|--------------|---------------|---------------|---------------|
|         | Ageing | Loading rate | Test series 1 | Test series 2 |               |
| 1       | No     | 1mm/min      | 12,458        | -             | 12,458        |
| 2       | Yes    | 1mm/min      | 4,616         | 8,869         | 6,743         |
| 3       | No     | 15mm/min     | 25,176        | 26,579        | 25,877        |
| 4       | Yes    | 15mm/min     | 19,091        | 28,160        | 23,626        |

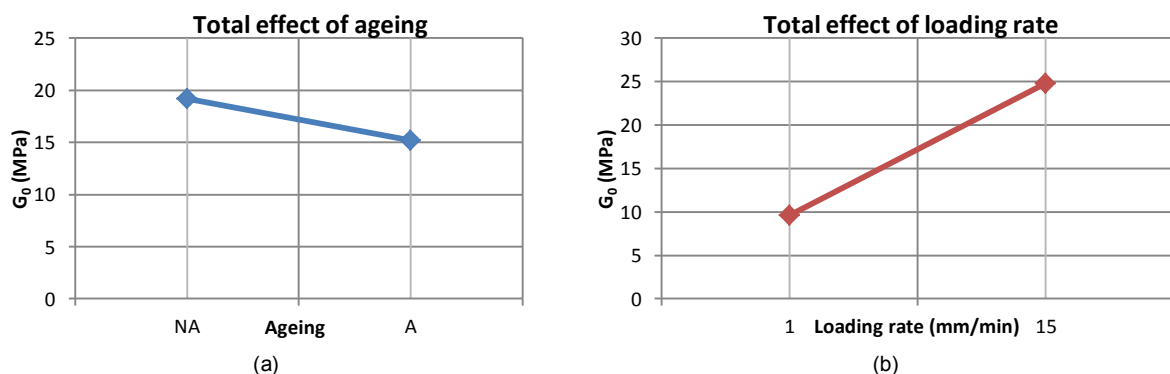
**Table C.60-** Initial stiffness results – Taguchi DOE – acrylic quasi-static shear

The total effects of the ageing factor A and of the loading rate factor B were both quantified:

$$\text{Total effect of A} = \frac{23,626 + 6,743}{2} - \frac{25,877 + 12,458}{2} = -3,984 \text{ MPa} \quad (\text{C.45})$$

$$\text{Total effect of B} = \frac{23,626 + 25,877}{2} - \frac{6,743 + 12,458}{2} = 15,151 \text{ MPa} \quad (\text{C.46})$$

The total effect value of the loading was about five times higher than the total effect value of the ageing. Unfortunately, no conclusion could have been drawn from these only data. Thus, the graphical representation of these effect were plotted for each factor, see Fig. C.13.



**Figure C.13-** Total effect of (a) ageing and (b) loading rate on the initial stiffness – acrylic short-term shear

As both factors seemed to affect the shear modulus of acrylic, the complete ANAVAR was conducted to verify this assumption. Therefore the mathematical formulation proposed by Vigier was established in order to fulfill this aim. The determination of the coefficients neglecting the interaction of factors was first achieved, see Table C.61.

| No interaction |          | B       |          | Average (MPa) |
|----------------|----------|---------|----------|---------------|
|                |          | 1mm/min | 15mm/min |               |
| A              | Non-aged | 12,458  | 25,877   | 19,168        |
|                | Aged     | 6,743   | 23,626   | 15,184        |
| Average (-)    |          | 9,600   | 24,751   | 17,176        |

**Table C.61-** Coefficients, interaction excluded, of the mathematical formulation – initial stiffness study – acrylic short-term shear

Based on the results of the above table, the coefficients of the interaction were then evaluated, see Table C.62.

| With interaction (ab) |          | B       |          |
|-----------------------|----------|---------|----------|
|                       |          | 1mm/min | 15mm/min |
| A                     | Non-aged | 0,866   | -0,866   |
|                       | Aged     | -0,866  | 0,866    |

**Table C.62-** Interaction coefficients of the mathematical formulation – initial stiffness study – acrylic short-term shear

The combination of the results of the two previous tables allowed formulating the mathematical equation representing the surface of the response on the studied domain.

$$\hat{Y} = 17,176 + [1,992 \quad -1,992] [A] + [-7,575 \quad 7,575] [B] + \begin{bmatrix} 0,866 & -0,886 \\ -0,886 & 0,886 \end{bmatrix} [AB] \quad (C.47)$$

The residuals were then assessed with the Eq. (C.47) and the principle of Eq. (C.6). This operation realized for each test allowed filling Table C.63.

| A      | B            | Residual r (MPa) |               |
|--------|--------------|------------------|---------------|
| Ageing | Loading rate | Test series 1    | Test series 2 |
| No     | 1mm/min      | 0                | -             |
| Yes    | 1mm/min      | -2,127           | 2,127         |
| No     | 15mm/min     | -0,702           | 0,702         |
| Yes    | 15mm/min     | -4,535           | 4,535         |

**Table C.63-** Residuals for the initial stiffness – acrylic short-term shear

The seven degrees of liberties, coming from the tests, were distributed to the average, each factor and the interaction to determine the degrees of liberties allocated to the residual. As for the design of experiment of section C.13, 3 degrees of liberties were associated to the variance. The final analysis ending the ANVAR method was detailed in Table C.64.

| Source   | Square sum $\Sigma$ | DDL | Variance | F       | F <sub>0.05</sub> |
|----------|---------------------|-----|----------|---------|-------------------|
| A        | 27,7699             | 1   | 27,7699  | 1,6284  | 10,13             |
| B        | 401,7090            | 1   | 401,7090 | 23,5561 | 10,13             |
| AB       | 5,2496              | 1   | 5,2496   | 0,3078  | 10,13             |
| Residual | 51,1598             | 3   | 17,0533  |         |                   |
| Total    |                     | 6   |          |         |                   |

**Table C.64-** ANAVAR analysis on the initial stiffness – acrylic short-term shear

The artificial ageing and interaction calculated F values were lower in both case to the tabulated  $F_{0.05}$  value, indicating that these two factors were non-influent on the shear modulus. However, the F value of the loading rate was clearly higher than the tabulated value, meaning that this factor impacted the studied results. For these shear quasi-static experiments, higher was the loading rate and higher was the generated initial stiffness. This result corresponded in all aspects to the one found for the tensile quasi-static tests on the same material.

### C.14 Maximum stress – Acrylic shear quasi-static

To complete the previous analysis evaluating the influence of the loading rate and of the artificial ageing on the shear modulus of acrylic adhesive, the ANAVAR was applied at large strains by studying the maximum stresses recorded during the testing phase. These stresses were all estimated at a constant strain of  $\gamma=1,10$ , see Table C.65.

| Test n° | A      | B            | $\sigma_{\gamma=1,10}$ (MPa) |               | Average (MPa) |
|---------|--------|--------------|------------------------------|---------------|---------------|
|         | Ageing | Loading rate | Test series 1                | Test series 2 |               |
| 1       | No     | 1mm/min      | 3,311                        | -             | 3,311         |
| 2       | Yes    | 1mm/min      | 3,091                        | 4,064         | 3,577         |
| 3       | No     | 15mm/min     | 6,277                        | 7,923         | 7,100         |
| 4       | Yes    | 15mm/min     | 6,703                        | 7,903         | 7,303         |

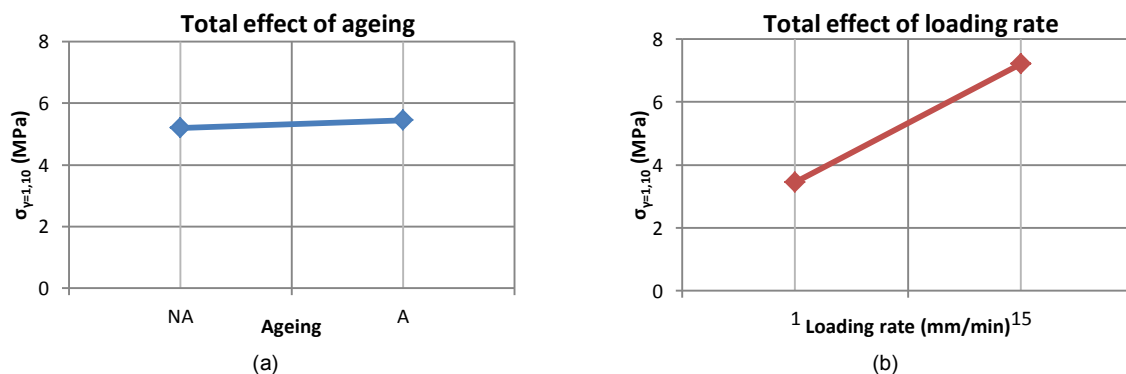
**Table C.65-** Maximum stress results – Taguchi DOE – acrylic quasi-static shear

The total effects of the artificial ageing factor A and of the loading rate factor B were simply calculated:

$$\text{Total effect of A} = \frac{7,303 + 3,577}{2} - \frac{7,100 + 3,311}{2} = 0,235 \text{ MPa} \quad (\text{C.48})$$

$$\text{Total effect of B} = \frac{7,303 + 7,100}{2} - \frac{3,557 + 3,311}{2} = 3,758 \text{ MPa} \quad (\text{C.49})$$

Again the value representing the total effect of the loading rate appeared clearly higher than the one representing the artificial ageing. Nevertheless, no conclusion could have been drawn from these only values, therefore the graphical diagrams of these total effects were first plotted, see Fig. C.14.



**Figure C.14-** Total effect of (a) ageing and (b) loading rate on the maximum stress – acrylic short-term shear

Strong similarities, identic lines orientations and slopes, existed with the total effect diagrams of the previous design of experiments concerning the shear modulus. While the loading rate seemed to impact the maximum stresses, the ageing was assumed as non-influent. For higher loading rates corresponded higher maximum stresses. To make sure of this graphical observations, the complete ANAVAR, based on the mathematical formulation propose by Vigier, was conducted. The first step consisted in the determination of the coefficient by neglecting the interaction, see Table C.66.

| No interaction |          | B       |          | Average (MPa) |
|----------------|----------|---------|----------|---------------|
|                |          | 1mm/min | 15mm/min |               |
| A              | Non-aged | 3,311   | 7,100    | 5,205         |
|                | Aged     | 3,577   | 7,303    | 5,440         |
| Average (-)    |          | 3,444   | 7,202    | 5,323         |

**Table C.66-** Coefficients, interaction excluded, of the mathematical formulation – maximum stress – acrylic short-term shear

With the above table and the principle of Eq. (C.4), the coefficients accounting for the interaction were evaluated, see Table C.67.

| With interaction (ab) |          | B       |          |
|-----------------------|----------|---------|----------|
|                       |          | 1mm/min | 15mm/min |
| A                     | Non-aged | -0,016  | 0,016    |
|                       | Aged     | 0,016   | -0,016   |

**Table C.67-** Interaction coefficients of the mathematical formulation – maximum stress – acrylic short-term shear

The final mathematical equation of the surface of the response was set up by combining the two previous tables:

$$\hat{Y} = 5,323 + [-0,117 \quad 0,117] [A] + [-1,879 \quad 1,879] [B] + \begin{bmatrix} -0,016 & 0,016 \\ 0,016 & -0,016 \end{bmatrix} [AB] \quad (C.50)$$

This equation allowed calculating the residuals corresponding to each conducted tests, see the following Table C.68.

| A      | B            | Residual r (MPa) |               |
|--------|--------------|------------------|---------------|
| Ageing | Loading rate | Test series 1    | Test series 2 |
| No     | 1mm/min      | 0                | -             |
| Yes    | 1mm/min      | -0,487           | 0,487         |
| No     | 15mm/min     | -0,823           | 0,823         |
| Yes    | 15mm/min     | -0,600           | 0,600         |

**Table C.68-** Residuals for the maximum stress – acrylic short-term shear

The repartition of the degrees of liberty was the same than from the previous design of experiments of section C.13, as the tested samples did not change. Thus one degree of liberty was associated to the average, one for each factor, one for the interaction and three for the residual. Knowing this repartition, the final table ending this analysis was established, see Table C.69.

| Source   | Square sum $\Sigma$ | DDL | Variance | F       | $F_{0.05}$ |
|----------|---------------------|-----|----------|---------|------------|
| A        | 0,0964              | 1   | 0,0964   | 0,1135  | 10,13      |
| B        | 24,7110             | 1   | 24,7110  | 29,0889 | 10,13      |
| AB       | 0,0018              | 1   | 0,0018   | 0,0021  | 10,13      |
| Residual | 2,5485              | 3   | 0,8495   |         |            |
| Total    |                     | 6   |          |         |            |

**Table C.69-** ANAVAR analysis on the maximum stress – acrylic short-term shear

While the two calculated F values for the ageing and the interaction were lower than the tabulated  $F_{0.05}$  value, the F value of the loading rate was largely higher. This indicated that the ageing had no impact on the maximum stress in contrary to the loading rate. As for the previous analysis of the shear modulus at small strains, higher was the loading rate and higher was the maximum shear stress.

### C.15 Discretized stress – Acrylic shear long-term

Long-term shear tests were carried out on acrylic samples to determine the possible influence of three factors at two levels each, i.e. the ageing, the loading rate and the imposed displacement. As three factors at two levels were investigated, the Taguchi table  $L_8(2)^7$  was selected. In total 8 tests were required and to conserve some degrees of liberties for the variance analysis, the interaction between these factors were neglected. The values studied corresponded to the stresses discretized at a certain time. In this section, two studies will be exposed, i.e. one for the stresses recorded at 60s and one for the stresses at 600s.

#### i. Stresses discretized at 60s

All the stresses were recorded for this defined time of 60s and stored in the following table:

| Test n° | A      | B            | C             | $\tau_{t=60s}$ (MPa) |
|---------|--------|--------------|---------------|----------------------|
|         | Ageing | Loading rate | Imposed disp. | Test series          |
| 1       | No     | 5mm/min      | 0,5mm         | 0,398                |
| 2       | Yes    | 5mm/min      | 0,5mm         | 0,260                |
| 3       | No     | 15mm/min     | 0,5mm         | 0,269                |
| 4       | Yes    | 15mm/min     | 0,5mm         | 0,276                |
| 5       | No     | 5mm/min      | 1,5mm         | 0,581                |
| 6       | Yes    | 5mm/min      | 1,5mm         | 0,501                |
| 7       | No     | 15mm/min     | 1,5mm         | 0,625                |
| 8       | Yes    | 15mm/min     | 1,5mm         | 0,453                |

**Table C.70-** Stresses discretized at 60s results – Taguchi DOE – acrylic long-term shear

The total effect values of all the three factors, ageing A, loading rate B and imposed displacement C were evaluated:

$$\text{Total effect of A} = \frac{0,45 + 0,50 + 0,28 + 0,26}{4} - \frac{0,63 + 0,58 + 0,27 + 0,40}{4} = -0,096 \text{ MPa} \quad (\text{C.51})$$

$$\text{Total effect of B} = \frac{0,45 + 0,63 + 0,28 + 0,27}{4} - \frac{0,50 + 0,58 + 0,26 + 0,40}{4} = -0,029 \text{ MPa} \quad (\text{C.52})$$

$$\text{Total effect of C} = \frac{0,45 + 0,63 + 0,50 + 0,58}{4} - \frac{0,28 + 0,27 + 0,26 + 0,40}{4} = 0,240 \text{ MPa} \quad (\text{C.53})$$

With these calculated values, the effect of the imposed displacement appeared clearly higher than the effects of the two other factors for the stress discretized at 60s. The graphical representations of these three factors, given in Fig. 4.96, confirmed this first assumption. Nevertheless, the mathematical formulation of Vigier was used to perform the complete ANAVAR method. As the interaction between factors were neglected, the only coefficients ignoring the interaction were evaluated with the principle exposed in Appendix B, see Table C.71.

| A     |        | B     |        | C      |       |
|-------|--------|-------|--------|--------|-------|
| $a_1$ | $a_2$  | $b_1$ | $b_2$  | $c_1$  | $c_2$ |
| 0,048 | -0,048 | 0,015 | -0,015 | -0,120 | 0,120 |

**Table C.71-** Coefficients, interaction excluded – Stresses discretized at 60s – acrylic long-term shear

The final mathematical equation representing the surface of the response on the studied domain was then built:

$$\hat{Y} = 0,420 + [0,048 \quad -0,048] [A] + [0,015 \quad -0,015] [B] + [-0,120 \quad 0,120] [C] \quad (C.54)$$

With the above mathematical formulation, the residuals of each configuration were then assessed, see Table C.72.

| Test n° | A      | B            | C             | Residual    |
|---------|--------|--------------|---------------|-------------|
|         | Ageing | Loading rate | Imposed disp. | Test series |
| 1       | No     | 5mm/min      | 0,5mm         | 0,035       |
| 2       | Yes    | 5mm/min      | 0,5mm         | -0,008      |
| 3       | No     | 15mm/min     | 0,5mm         | -0,065      |
| 4       | Yes    | 15mm/min     | 0,5mm         | 0,038       |
| 5       | No     | 5mm/min      | 1,5mm         | -0,022      |
| 6       | Yes    | 5mm/min      | 1,5mm         | -0,006      |
| 7       | No     | 15mm/min     | 1,5mm         | 0,051       |
| 8       | Yes    | 15mm/min     | 1,5mm         | -0,024      |

**Table C.72-** Residuals for the stresses discretized at 60s – acrylic long-term shear

No repetition of the test series was realized and so only 8 tests were conducted. The repartition of the 8 degrees of liberty was done as for the previous design of experiments, i.e. one was attributed to the average and one for each factor, letting 4 degrees of liberties for the residuals. This distribution allowed filling the table ending this analysis, see Table C.73.

| Source   | Square sum $\Sigma$ | DDL | Variance | F      | F <sub>0.05</sub> |
|----------|---------------------|-----|----------|--------|-------------------|
| A        | 0,01828             | 1   | 0,01828  | 6,875  | 7,71              |
| B        | 0,00174             | 1   | 0,00174  | 0,653  | 7,71              |
| C        | 0,11485             | 1   | 0,11485  | 43,202 | 7,71              |
| Residual | 0,01063             | 4   | 0,00266  |        |                   |
| Total    |                     | 7   |          |        |                   |

**Table C.73-** ANAVAR analysis on the stresses discretized at 60s – acrylic long-term shear

For the ageing and the loading rate factor, the calculated F values were inferior to the tabulated F<sub>0.05</sub> value, indicating a non-influence of these two factors on the stresses at 60s. However, the F values of the imposed displacement were higher than the tabulated value. This implied that this last factor was the only one impacting the stresses at 60s.

## ii. Stresses discretized at 600s

The same procedure was performed for the stress discretized at 600s. Table C.74 contains all the corresponding results.

| Test n° | A      | B            | C             | $\tau_{t=600s}$ (MPa) |
|---------|--------|--------------|---------------|-----------------------|
|         | Ageing | Loading rate | Imposed disp. | Test series           |
| 1       | No     | 5mm/min      | 0,5mm         | 0,172                 |
| 2       | Yes    | 5mm/min      | 0,5mm         | 0,169                 |
| 3       | No     | 15mm/min     | 0,5mm         | 0,143                 |
| 4       | Yes    | 15mm/min     | 0,5mm         | 0,177                 |
| 5       | No     | 5mm/min      | 1,5mm         | 0,314                 |
| 6       | Yes    | 5mm/min      | 1,5mm         | 0,355                 |

|   |     |          |       |       |
|---|-----|----------|-------|-------|
| 7 | No  | 15mm/min | 1,5mm | 0,396 |
| 8 | Yes | 15mm/min | 1,5mm | 0,333 |

**Table C.74-** Stresses discretized at 600s results – Taguchi DOE – acrylic long-term shear

As previously, the total effect values of the ageing A, the loading rate B and the imposed displacement C were calculated:

$$\text{Total effect of A} = \frac{0,33 + 0,36 + 0,18 + 0,17}{4} - \frac{0,40 + 0,31 + 0,14 + 0,17}{4} = 0,002 \text{ MPa} \quad (\text{C.55})$$

$$\text{Total effect of B} = \frac{0,33 + 0,40 + 0,18 + 0,14}{4} - \frac{0,36 + 0,31 + 0,17 + 0,17}{4} = 0,01 \text{ MPa} \quad (\text{C.56})$$

$$\text{Total effect of C} = \frac{0,33 + 0,40 + 0,36 + 0,31}{4} - \frac{0,18 + 0,14 + 0,17 + 0,17}{4} = 0,184 \text{ MPa} \quad (\text{C.57})$$

Similar results were identified for this stresses studied at 60s and 600s, i.e. the only factor exposing a relevant value was the imposed displacement. Furthermore, the signs of the results (C.57) and (C.53) were both positive confirming the tendency of higher stresses for higher imposed displacements. This phenomenon was corroborated graphically with the representation of the total effect diagrams of the three factors, see Fig. 4.92. Finally to properly conclude the study, the complete ANAVAR table, based on the mathematical formulation proposed by Vigier, was set-up. The coefficients of the models were simply determined with the principle presented in Appendix B, see Table C.75.

| A      |       | B      |       | C      |       |
|--------|-------|--------|-------|--------|-------|
| $a_1$  | $a_2$ | $b_1$  | $b_2$ | $c_1$  | $c_2$ |
| -0,001 | 0,001 | -0,005 | 0,005 | -0,092 | 0,092 |

**Table C.75-** Coefficients, interaction excluded – Stresses discretized at 600s – acrylic long-term shear

In the above table were directly contained the coefficients of the mathematical formulation which was written as:

$$\hat{Y} = 0,257 + [-0,001 \quad 0,001] [A] + [-0,005 \quad 0,005] [B] + [-0,092 \quad 0,092] [C] \quad (\text{C.58})$$

Then the residuals of each configuration were determined and regrouped in Table C.76.

| Test n° | A      | B            | C             | Residual    |
|---------|--------|--------------|---------------|-------------|
|         | Ageing | Loading rate | Imposed disp. | Test series |
| 1       | No     | 5mm/min      | 0,5mm         | 0,013       |
| 2       | Yes    | 5mm/min      | 0,5mm         | 0,007       |
| 3       | No     | 15mm/min     | 0,5mm         | -0,026      |
| 4       | Yes    | 15mm/min     | 0,5mm         | 0,006       |
| 5       | No     | 5mm/min      | 1,5mm         | -0,030      |
| 6       | Yes    | 5mm/min      | 1,5mm         | 0,010       |
| 7       | No     | 15mm/min     | 1,5mm         | 0,043       |
| 8       | Yes    | 15mm/min     | 1,5mm         | -0,023      |

**Table C.76-** Residuals for the stresses discretized at 600s – acrylic long-term shear

The distribution of the degrees of liberties was identical to the previous one with one for the average, one for each factor and four for the residuals. The final table ending the variance analysis was set-up, see Table C.77.



| Source   | Square sum $\Sigma$ | DDL | Variance | F      | $F_{0.05}$ |
|----------|---------------------|-----|----------|--------|------------|
| A        | 0,00001             | 1   | 0,00001  | 0,003  | 7,71       |
| B        | 0,00018             | 1   | 0,00018  | 0,069  | 7,71       |
| C        | 0,06797             | 1   | 0,06797  | 25,567 | 7,71       |
| Residual | 0,00428             | 1   | 0,00428  |        |            |
| Total    |                     | 7   |          |        |            |

**Table C.77-** ANAVAR analysis on the stresses discretized at 600s – acrylic long-term shear

The only decisive factor was again the imposed displacement, which exposed a calculated F value largely higher than the tabulated  $F_{0.05}$  value. Consequently, this factor impacted the results and for higher imposed displacements always corresponded higher stresses.

### C.16 Discretized stress – Imposed disp. of 3mm – Acrylic shear long-term

Two loading were imposed on the acrylic long-term shear specimens, i.e. a first one at 0,5mm or 1,5mm and a second one to 3mm directly applied on the already deformed samples. In this section, only the second loading results will be considered. The three factors studied for the first loading were conserved even if the meaning of the imposed displacement factor changed, i.e. it was viewed as a factor accounting for the loading path. Thus the Taguchi table  $L_8(2)^7$  remained unchanged with 8 tests in total. The interaction between the factors was again neglected to save some degrees of liberties for the variance analysis. The studied values were the new discretized stresses at 60s and 600s for the imposed displacement of 3mm, which were treated separately.

#### i. Stresses discretized at 60s

For this prescribed time of 60s, all the stresses of the design of experiments were recorded in the following table:

| Test n° | A      | B            | C             | $\tau_{t=60s}$ (MPa) |
|---------|--------|--------------|---------------|----------------------|
|         | Ageing | Loading rate | Imposed disp. | Test series          |
| 1       | No     | 5mm/min      | 0,5mm         | 1,025                |
| 2       | Yes    | 5mm/min      | 0,5mm         | 0,972                |
| 3       | No     | 15mm/min     | 0,5mm         | 0,876                |
| 4       | Yes    | 15mm/min     | 0,5mm         | 0,902                |
| 5       | No     | 5mm/min      | 1,5mm         | 0,857                |
| 6       | Yes    | 5mm/min      | 1,5mm         | 0,846                |
| 7       | No     | 15mm/min     | 15mm          | 0,943                |
| 8       | Yes    | 15mm/min     | 1,5mm         | 0,865                |

**Table C.78-** Stresses discretized at 60s results – Imposed disp. of 3mm – Taguchi DOE – acrylic long-term shear

The total effect values of all the three factors were evaluated with the above results:

$$\text{Total effect of A} = \frac{0,87 + 0,85 + 0,90 + 0,97}{4} - \frac{0,94 + 0,86 + 0,88 + 1,03}{4} = -0,03 \text{ MPa} \quad (\text{C.59})$$

$$\text{Total effect of B} = \frac{0,87 + 0,94 + 0,90 + 0,88}{4} - \frac{0,85 + 0,86 + 0,97 + 1,03}{4} = -0,03 \text{ MPa} \quad (\text{C.60})$$

$$\text{Total effect of C} = \frac{0,87 + 0,94 + 0,85 + 0,86}{4} - \frac{0,90 + 0,88 + 0,97 + 1,03}{4} = -0,066 \text{ MPa} \quad (\text{C.61})$$

In this case, all the total effect values remained relatively low, supposing that none of the factors impacted the stresses at 60s. This observation was then confirmed with the total effect diagrams exposed in Fig. 4.99. Nevertheless the complete ANAVAR was performed in order to properly assess the non-dependency of the stresses. To do so, the mathematical formulation representing the surface of the response was evaluated by neglecting the interaction of the factors. Consequently, only the coefficients of each factor were determined with the principle presented in Appendix B, see Table C.79.

| A     |        | B     |        | C     |        |
|-------|--------|-------|--------|-------|--------|
| $a_1$ | $a_2$  | $b_1$ | $b_2$  | $c_1$ | $c_2$  |
| 0,014 | -0,014 | 0,014 | -0,014 | 0,033 | -0,033 |

**Table C.79-** Coefficients, interaction excluded – Imposed disp. of 3mm – Stresses discretized at 60s – acrylic long-term shear

The final mathematical formulation of the surface of the response was based on the previous table:

$$\hat{Y} = 0,911 + [0,014 \quad -0,014] [A] + [0,014 \quad -0,014] [B] + [0,033 \quad -0,033] [C] \quad (\text{C.62})$$

All the residuals of each test were then evaluated with the previous equation and stored in Table C.80.

| Test n° | A      | B            | C             | Residual    |
|---------|--------|--------------|---------------|-------------|
|         | Ageing | Loading rate | Imposed disp. | Test series |
| 1       | No     | 5mm/min      | 0,5mm         | 0,053       |
| 2       | Yes    | 5mm/min      | 0,5mm         | 0,029       |
| 3       | No     | 15mm/min     | 0,5mm         | -0,068      |
| 4       | Yes    | 15mm/min     | 0,5mm         | -0,013      |
| 5       | No     | 5mm/min      | 1,5mm         | -0,050      |
| 6       | Yes    | 5mm/min      | 1,5mm         | -0,032      |
| 7       | No     | 15mm/min     | 1,5mm         | 0,065       |
| 8       | Yes    | 15mm/min     | 1,5mm         | 0,016       |

**Table C.80-** Residuals for the stresses discretized at 60s – Imposed disp. of 3mm – acrylic long-term shear

One degree of liberty was attributed to the average, one for each factor and four for the residuals. This repartition allowed establishing the table ending the ANAVAR analysis and appraising the effect of each factor, see Table C.81.

| Source   | Square sum $\Sigma$ | DDL | Variance | F     | $F_{0.05}$ |
|----------|---------------------|-----|----------|-------|------------|
| A        | 0,00165             | 1   | 0,00165  | 0,401 | 7,71       |
| B        | 0,00163             | 1   | 0,00163  | 0,396 | 7,71       |
| C        | 0,00870             | 1   | 0,00870  | 2,120 | 7,71       |
| Residual | 0,01641             | 4   | 0,00410  |       |            |
| Total    |                     | 7   |          |       |            |

**Table C.81-** ANAVAR analysis on the stresses discretized at 60s – Imposed disp. of 3mm – acrylic long-term shear

The calculated F value of each factor was inferior to the tabulated  $F_{0.05}$  value indicating that none of the factor affected the stresses at 60s.

ii. Stresses discretized at 600s

This protocol was repeated for the stresses discretized at 600s to cover all the test duration and make sure that the previous result was not due to a local effect. The stresses at this time were recorded for

each tests and stored in Table C.82.

| Test n° | A      | B            | C             | T <sub>t=600s</sub> (MPa) |
|---------|--------|--------------|---------------|---------------------------|
|         | Ageing | Loading rate | Imposed disp. | Test series               |
| 1       | No     | 5mm/min      | 0,5mm         | 0,605                     |
| 2       | Yes    | 5mm/min      | 0,5mm         | 0,531                     |
| 3       | No     | 15mm/min     | 0,5mm         | 0,592                     |
| 4       | Yes    | 15mm/min     | 0,5mm         | 0,581                     |
| 5       | No     | 5mm/min      | 1,5mm         | 0,517                     |
| 6       | Yes    | 5mm/min      | 1,5mm         | 0,578                     |
| 7       | No     | 15mm/min     | 1,5mm         | 0,634                     |
| 8       | Yes    | 15mm/min     | 1,5mm         | 0,614                     |

**Table C.82-** Stresses discretized at 600s results – Imposed disp. of 3mm – Taguchi DOE – acrylic long-term shear

The total effect values of all the three factors were evaluated with the above results:

$$\text{Total effect of A} = \frac{0,61 + 0,58 + 0,58 + 0,53}{4} - \frac{0,63 + 0,52 + 0,59 + 0,61}{4} = -0,011 \text{ MPa} \quad (\text{C.63})$$

$$\text{Total effect of B} = \frac{0,61 + 0,63 + 0,58 + 0,59}{4} - \frac{0,58 + 0,52 + 0,53 + 0,61}{4} = 0,047 \text{ MPa} \quad (\text{C.64})$$

$$\text{Total effect of C} = \frac{0,61 + 0,63 + 0,58 + 0,52}{4} - \frac{0,58 + 0,59 + 0,53 + 0,61}{4} = 0,009 \text{ MPa} \quad (\text{C.65})$$

As for the analysis concerning the stresses at 60s, none of the factors seemed to impact the stresses at 600s as the total effect values were relatively low. This was confirmed with the diagrams of the total effect of the three factors, see Fig. 4.99. The ANAVAR was carried out to corroborate this observation with the mathematical formulation of Vigier. The coefficients, neglecting the interaction of factors, were calculated, see Table C.83.

| A     |        | B      |       | C      |       |
|-------|--------|--------|-------|--------|-------|
| $a_1$ | $a_2$  | $b_1$  | $b_2$ | $c_1$  | $c_2$ |
| 0,005 | -0,005 | -0,024 | 0,024 | -0,004 | 0,004 |

**Table C.83-** Coefficients, interaction excluded – Imposed disp. of 3mm – Stresses discretized at 600s – acrylic long-term shear

The final mathematical formulation of the surface of the response was based on the previous table:

$$\hat{Y} = 0,581 + [0,005 \quad -0,005] [A] + [-0,024 \quad 0,024] [B] + [-0,004 \quad 0,004] [C] \quad (\text{C.66})$$

The residuals of each test were then determined with the above equation, see Table C.84.

| Test n° | A      | B            | C             | Residual    |
|---------|--------|--------------|---------------|-------------|
|         | Ageing | Loading rate | Imposed disp. | Test series |
| 1       | No     | 5mm/min      | 0,5mm         | 0,046       |
| 2       | Yes    | 5mm/min      | 0,5mm         | -0,017      |
| 3       | No     | 15mm/min     | 0,5mm         | -0,014      |
| 4       | Yes    | 15mm/min     | 0,5mm         | -0,015      |
| 5       | No     | 5mm/min      | 1,5mm         | -0,051      |
| 6       | Yes    | 5mm/min      | 1,5mm         | 0,022       |
| 7       | No     | 15mm/min     | 1,5mm         | 0,019       |

|   |     |          |       |       |
|---|-----|----------|-------|-------|
| 8 | Yes | 15mm/min | 1,5mm | 0,010 |
|---|-----|----------|-------|-------|

**Table C.84-** Residuals for the stresses discretized at 600s – Imposed disp. of 3mm – acrylic long-term shear

The repartition of degrees of liberty did not change compared to the previous analysis with one attributed to the average, one for each factor and four for the residual. This distribution allowed finishing the variance analysis with Table C.85.

| Source   | Square sum $\Sigma$ | DDL | Variance | F     | $F_{0.05}$ |
|----------|---------------------|-----|----------|-------|------------|
| A        | 0,00023             | 1   | 0,00023  | 0,057 | 7,71       |
| B        | 0,00449             | 1   | 0,00449  | 1,095 | 7,71       |
| C        | 0,00014             | 1   | 0,00014  | 0,035 | 7,71       |
| Residual | 0,00636             | 1   | 0,00636  |       |            |
| Total    |                     | 7   |          |       |            |

**Table C.85-** ANAVAR analysis on the stresses discretized at 600s – Imposed disp. of 3mm – acrylic long-term shear

The calculated F values were all lower than the tabulated  $F_{0.05}$  value. It was therefore concluded that no factor impacted the stresses discretized at 600s for an imposed displacement of 3mm. This result combined with the previous one attested of the invariance of the stress towards the ageing, the loading rate and the loading path.

## APPENDIX D – Evaluation of the distribution

Several normality tests exist to evaluate if a set of results follows a Gaussian distribution, i.e. the tests based on the empirical distribution function (e.g. Kolmogorov-Smirnov), the chi-squared test or the Shapiro-Wilk test. However, in most of the cases, a large number of data is necessary to be able to conduct these methods. Therefore, to determine the distribution of a small number of tests results of unknown normal distribution, i.e. average and standard deviation unknown, the Lilliefors test [4.6] is commonly employed. This test is based on the Kolmogorov-Smirnov method and so on the empirical distribution function. Three main steps have to be realized to carry out correctly the Lilliefors test:

- The calculation of the average and standard deviation for the tested samples.
- The evaluation of the cumulative distribution function with the estimated parameters obtained in the previous step.
- Then the difference between the empirical distribution function and the estimated distribution function in ii. is compared to tabulated limit values. If the maximum absolute value of the difference of the distribution functions is lower than the limit value, the normal distribution can be validated.

If no correspondence is found with the normal distribution, the Lilliefors method can be applied to test the null hypothesis of a log-normal distribution.

### D.1 Distribution of the maximum stress for the 1<sup>st</sup> tensile DOE on silicone

The Lilliefors method was first applied to evaluate if the maximum stress of the 1<sup>st</sup> DOE on quasi-static tensile tests on silicone followed the normal distribution.

| Null hypothesis  | H <sub>0</sub> "Normal distribution"                                                                                                                                                                      |
|------------------|-----------------------------------------------------------------------------------------------------------------------------------------------------------------------------------------------------------|
| Confidence level | 0,05                                                                                                                                                                                                      |
| Variable         | $\sigma_{138\%}$ (MPa) maximum stress from 1 <sup>st</sup> DOE tests                                                                                                                                      |
| Critical region  | H <sub>0</sub> accepted if and only if:<br>$D^N = \text{Max} \left\{ \left  F_n(\sigma_{138\%}) - \phi \left( \frac{\sigma_{138\%} - \hat{\mu}}{\hat{\sigma}} \right) \right  \right\} \leq D^N_{0.05,n}$ |

| Test designation | N° | Measured               | Estimated distribution function                   |                                                                                | Empirical distribution function |                                      | Tested values                         |                                         |
|------------------|----|------------------------|---------------------------------------------------|--------------------------------------------------------------------------------|---------------------------------|--------------------------------------|---------------------------------------|-----------------------------------------|
|                  | i  | $\sigma_{138\%}$ (MPa) | $\frac{\sigma_{138\%} - \hat{\mu}}{\hat{\sigma}}$ | $\phi \left( \frac{\sigma_{138\%} - \hat{\mu}}{\hat{\sigma}} \right) = \phi_i$ | $F_n(i) = \frac{i}{n}$          | $\frac{F_n(i-1)}{n} = \frac{i-1}{n}$ | $\left  \frac{i}{n} - \phi_i \right $ | $\left  \frac{i-1}{n} - \phi_i \right $ |
| S12 - 50 - A     | 1  | 0,892                  | -0,762                                            | 0,223                                                                          | 0,1                             | 0                                    | -0,123                                | <b>-0,223</b>                           |
| S13 - 50 - A     | 2  | 0,896                  | -0,690                                            | 0,245                                                                          | 0,2                             | 0,1                                  | -0,045                                | -0,145                                  |
| S02 - 50 - A     | 3  | 0,901                  | -0,595                                            | 0,276                                                                          | 0,3                             | 0,2                                  | 0,024                                 | -0,076                                  |
| S08 - 500 - A    | 4  | 0,914                  | -0,326                                            | 0,372                                                                          | 0,4                             | 0,3                                  | 0,028                                 | -0,072                                  |
| S04 - 50 - NA    | 5  | 0,915                  | -0,315                                            | 0,377                                                                          | 0,5                             | 0,4                                  | 0,123                                 | 0,023                                   |
| S19 - 50 - NA    | 6  | 0,916                  | -0,287                                            | 0,387                                                                          | 0,6                             | 0,5                                  | 0,213                                 | 0,113                                   |
| S16 - 500 - NA   | 7  | 0,918                  | -0,248                                            | 0,402                                                                          | 0,7                             | 0,6                                  | <b>0,298</b>                          | 0,198                                   |
| S06 - 500 - A    | 8  | 0,941                  | 0,212                                             | 0,584                                                                          | 0,8                             | 0,7                                  | 0,216                                 | 0,116                                   |
| S05 - 50 - NA    | 9  | 0,948                  | 0,353                                             | 0,638                                                                          | 0,9                             | 0,8                                  | 0,262                                 | 0,162                                   |
| S01 - 500 - NA   | 10 | 1,062                  | 2,659                                             | 0,996                                                                          | 1                               | 0,9                                  | 0,004                                 | -0,096                                  |

$$\hat{\mu} = 0,930 \quad \hat{\sigma} = 0,049$$

$$\text{Maximum } D^N$$

$$\mathbf{0,298}$$

$$\mathbf{0,223}$$

|            |                                                                       |
|------------|-----------------------------------------------------------------------|
| Conclusion | $D^N = 0,298 > D^N_{0.05,10} = 0,258$<br>Normal distribution rejected |
|------------|-----------------------------------------------------------------------|

**Table D.1-** Lilliefors normality tests concerning the maximum stress for the 1<sup>st</sup> DOE of tensile quasi-static tests on silicone

For this normality test, the limit value  $D_{0.05,10}^N$  is tabulated according to the confidence level and the number of tests. From this analysis, it is demonstrated that the maximum stress of the 1<sup>st</sup> DOE in quasi-static tension does not follow the normal distribution. Therefore it was decided to investigate the log-normal distribution with the help of a modified version of the Lilliefors test, see Table D.2.

| Null hypothesis  |  | H <sub>0</sub> "Log-normal distribution"                                                                                                                                                                       |  |  |  |  |  |  |
|------------------|--|----------------------------------------------------------------------------------------------------------------------------------------------------------------------------------------------------------------|--|--|--|--|--|--|
| Confidence level |  | 0,05                                                                                                                                                                                                           |  |  |  |  |  |  |
| Variable         |  | $\sigma_{138\%}$ (MPa) maximum stress from 1 <sup>st</sup> DOE tests                                                                                                                                           |  |  |  |  |  |  |
| Critical region  |  | H <sub>0</sub> accepted if and only if:<br>$D^{LN} = \max \left\{ \left  F_n(\sigma_{138\%}) - \phi \left( \frac{\ln(\sigma_{138\%}) - \hat{\mu}}{\hat{\sigma}} \right) \right  \right\} \leq D_{0.05,n}^{LN}$ |  |  |  |  |  |  |

| Test designation | N° | Measured               | Estimated distribution function                        |                                                                                     | Empirical distribution function |                            | Tested values                         |                                         |
|------------------|----|------------------------|--------------------------------------------------------|-------------------------------------------------------------------------------------|---------------------------------|----------------------------|---------------------------------------|-----------------------------------------|
|                  | i  | $\sigma_{138\%}$ (MPa) | $\frac{\ln(\sigma_{138\%}) - \hat{\mu}}{\hat{\sigma}}$ | $\phi \left( \frac{\ln(\sigma_{138\%}) - \hat{\mu}}{\hat{\sigma}} \right) = \phi_i$ | $F_n(i) = \frac{i}{n}$          | $F_n(i-1) = \frac{i-1}{n}$ | $\left  \frac{i}{n} - \phi_i \right $ | $\left  \frac{i-1}{n} - \phi_i \right $ |
| S12 - 50 - A     | 1  | 0,892                  | -0,794                                                 | 0,214                                                                               | 0,1                             | 0                          | -0,114                                | <b>-0,214</b>                           |
| S13 - 50 - A     | 2  | 0,896                  | -0,715                                                 | 0,237                                                                               | 0,2                             | 0,1                        | -0,037                                | -0,137                                  |
| S02 - 50 - A     | 3  | 0,901                  | -0,611                                                 | 0,271                                                                               | 0,3                             | 0,2                        | 0,029                                 | -0,071                                  |
| S08 - 500 - A    | 4  | 0,914                  | -0,322                                                 | 0,374                                                                               | 0,4                             | 0,3                        | 0,026                                 | -0,074                                  |
| S04 - 50 - NA    | 5  | 0,915                  | -0,309                                                 | 0,379                                                                               | 0,5                             | 0,4                        | 0,121                                 | 0,021                                   |
| S19 - 50 - NA    | 6  | 0,916                  | -0,280                                                 | 0,390                                                                               | 0,6                             | 0,5                        | 0,210                                 | 0,110                                   |
| S16 - 500 - NA   | 7  | 0,918                  | -0,239                                                 | 0,406                                                                               | 0,7                             | 0,6                        | <b>0,294</b>                          | 0,194                                   |
| S06 - 500 - A    | 8  | 0,941                  | 0,245                                                  | 0,597                                                                               | 0,8                             | 0,7                        | 0,203                                 | 0,103                                   |
| S05 - 50 - NA    | 9  | 0,948                  | 0,390                                                  | 0,652                                                                               | 0,9                             | 0,8                        | 0,248                                 | 0,148                                   |
| S01 - 500 - NA   | 10 | 1,062                  | 2,634                                                  | 0,996                                                                               | 1                               | 0,9                        | 0,004                                 | -0,096                                  |

|                      |                        |                  |              |              |
|----------------------|------------------------|------------------|--------------|--------------|
| $\hat{\mu} = -0,074$ | $\hat{\sigma} = 0,051$ | Maximum $D^{LN}$ | <b>0,294</b> | <b>0,214</b> |
|----------------------|------------------------|------------------|--------------|--------------|

|            |                                                                                 |
|------------|---------------------------------------------------------------------------------|
| Conclusion | $D^{LN} = 0,294 < D_{0.05,10}^{LN} = 0,296$<br>Log-normal distribution supposed |
|------------|---------------------------------------------------------------------------------|

**Table D.2.-** Lilliefors log-normal tests concerning the maximum stress for the 1<sup>st</sup> DOE of tensile quasi-static tests on silicone

The average  $\hat{\mu}$  and the standard deviation  $\hat{\sigma}$  are determined on the logarithmic value of the maximum stress. For the log-normal distribution, the limit value  $D_{0.05,10}^{LN}$  is calculated in accordance to the formula given in [4.6] for the specified confidence level and test number. As it can be noted, the null hypothesis of a log-normal distribution is accepted.

Then, considering this distribution, it becomes possible to calculate the characteristic maximum stress value defined in the EN 1990 [3.3], as:

$$X_k = \exp(m_y - k_n S_y) \quad (D.1)$$

$X_k = \sigma_{138\%,k}$  the characteristic maximum stress.

$m_y$  the mean value of the logarithmic stress, i.e.  $m_y = (1/10) \sum \ln(\sigma_{138\%}) = \hat{\mu}$

With

$S_y$  the standard deviation of the logarithmic stress, i.e.  $S_y = \left\{ (1/9) \sum [\ln(\sigma_{138\%}) - m_y]^2 \right\}^{1/2}$ .

$k_n$  coefficient accounting for the number of tests performed, for 10 tests  $k_n = 1,92$ .

By employing this formula, the 5% fractile stress value is equal to 0,843MPa, which is lower than the strength of 0,95MPa furnished by the manufacturer. This distinction provides from the definition of the

maximum stresses regarded in this analysis, i.e. stresses at defined elongation of 138% for which only one sample broke.

## D.2 Distribution of the maximum stress for all the tensile tests on silicone

The comparison of the two designs of experiments allowed proving the stability of the Dow Corning silicone properties towards the ageing, either at low or elevated temperatures, humidity and UV-radiation, and towards the loading rate. Hence regrouping all the data into one large class was possible. On this augmented set of results, the maximum stresses were considered to carry out the Lilliefors test with a log-normal distribution as null hypothesis. The complete analysis is detailed in Table D.3.

| Null hypothesis  | H <sub>0</sub> "Log-normal distribution"                                                                                                                                                                       |
|------------------|----------------------------------------------------------------------------------------------------------------------------------------------------------------------------------------------------------------|
| Confidence level | 0,05                                                                                                                                                                                                           |
| Variable         | $\sigma_{138\%}$ (MPa) maximum stress for all tests                                                                                                                                                            |
| Critical region  | H <sub>0</sub> accepted if and only if:<br>$D^{LN} = \max \left\{ \left  F_n(\sigma_{138\%}) - \phi \left( \frac{\ln(\sigma_{138\%}) - \hat{\mu}}{\hat{\sigma}} \right) \right  \right\} \leq D^{LN}_{0.05,n}$ |

| Test designation | N° | Measured               | Estimated distribution function                        |                                                                                     | Empirical distribution function |                            | Tested values                         |                                         |
|------------------|----|------------------------|--------------------------------------------------------|-------------------------------------------------------------------------------------|---------------------------------|----------------------------|---------------------------------------|-----------------------------------------|
|                  | i  | $\sigma_{138\%}$ (MPa) | $\frac{\ln(\sigma_{138\%}) - \hat{\mu}}{\hat{\sigma}}$ | $\phi \left( \frac{\ln(\sigma_{138\%}) - \hat{\mu}}{\hat{\sigma}} \right) = \phi_i$ | $F_n(i) = \frac{i}{n}$          | $F_n(i-1) = \frac{i-1}{n}$ | $\left  \frac{i}{n} - \phi_i \right $ | $\left  \frac{i-1}{n} - \phi_i \right $ |
| S07 - 500 - LT   | 1  | 0,836                  | -1,865                                                 | 0,031                                                                               | 0,067                           | 0,000                      | 0,036                                 | -0,031                                  |
| S15 - 50 - LT    | 2  | 0,873                  | -1,055                                                 | 0,146                                                                               | 0,133                           | 0,067                      | -0,012                                | -0,079                                  |
| S12 - 50 - A     | 3  | 0,892                  | -0,653                                                 | 0,257                                                                               | 0,200                           | 0,133                      | -0,057                                | <b>-0,124</b>                           |
| S13 - 50 - A     | 4  | 0,896                  | -0,579                                                 | 0,281                                                                               | 0,267                           | 0,200                      | -0,015                                | -0,081                                  |
| S02 - 50 - A     | 5  | 0,901                  | -0,482                                                 | 0,315                                                                               | 0,333                           | 0,267                      | 0,018                                 | -0,048                                  |
| S08 - 500 - A    | 6  | 0,914                  | -0,211                                                 | 0,416                                                                               | 0,400                           | 0,333                      | -0,016                                | -0,083                                  |
| S04 - 50 - NA    | 7  | 0,915                  | -0,200                                                 | 0,421                                                                               | 0,467                           | 0,400                      | 0,046                                 | -0,021                                  |
| S19 - 50 - NA    | 8  | 0,916                  | -0,172                                                 | 0,432                                                                               | 0,533                           | 0,467                      | 0,102                                 | 0,035                                   |
| S16 - 500 - NA   | 9  | 0,918                  | -0,134                                                 | 0,447                                                                               | 0,600                           | 0,533                      | <b>0,153</b>                          | 0,087                                   |
| S06 - 500 - A    | 10 | 0,941                  | 0,319                                                  | 0,625                                                                               | 0,667                           | 0,600                      | 0,042                                 | -0,025                                  |
| S05 - 50 - NA    | 11 | 0,948                  | 0,456                                                  | 0,676                                                                               | 0,733                           | 0,667                      | 0,058                                 | -0,009                                  |
| S10 - 500 - LT   | 12 | 0,951                  | 0,532                                                  | 0,703                                                                               | 0,800                           | 0,733                      | 0,097                                 | 0,031                                   |
| S14 - 50 - LT    | 13 | 0,954                  | 0,587                                                  | 0,721                                                                               | 0,867                           | 0,800                      | 0,145                                 | 0,079                                   |
| S09 - 50 - LT    | 14 | 0,971                  | 0,901                                                  | 0,816                                                                               | 0,933                           | 0,867                      | 0,117                                 | 0,050                                   |
| S01 - 500 - NA   | 15 | 1,062                  | 2,556                                                  | 0,995                                                                               | 1,000                           | 0,933                      | 0,005                                 | -0,061                                  |

$$\hat{\mu} = -0,078 \quad \hat{\sigma} = 0,054$$

|                  |              |              |
|------------------|--------------|--------------|
| Maximum $D^{LN}$ | <b>0,153</b> | <b>0,124</b> |
|------------------|--------------|--------------|

|            |                                                                                 |
|------------|---------------------------------------------------------------------------------|
| Conclusion | $D^{LN} = 0,153 < D^{LN}_{0.05,15} = 0,246$<br>Log-normal distribution supposed |
|------------|---------------------------------------------------------------------------------|

**Table D.3** Lilliefors log-normal tests concerning the maximum stress for all the tensile quasi-static tests on silicone

As for the Lilliefors test on the 1<sup>st</sup> design of experiments on a reduced number of samples, the log-normal distribution can be supposed with a better agreement for all the tensile tests. Thus the characteristic value, corresponding of the 5% fractile, was again calculated in accordance to the EN 1990 [3.3] and equation Eq. (D.1). Therefore the definitive characteristic maximum stress to be used for design is equal to 0,837 MPa.

### D.3 Distribution of the strain for all the compressive tests on silicone

As for the tensile tests, the properties of silicone in compression quasi-static were independent on the artificial ageing, either at low or at elevated temperatures, and on the loading rate for all the strain range. Thus all the data were regrouped in a large class, containing all the tested results. To analyze if the strain corresponding of a stress of 0,58MPa (i.e. force of 9,5kN) followed a normal distribution, the Lilliefors test was carried out over all the experimental estimated strains. The complete analysis is detailed in Table D.4.

| Null hypothesis  |  | H <sub>0</sub> "Normal distribution"                                                                                                                                                                                                          |  |  |  |  |  |  |
|------------------|--|-----------------------------------------------------------------------------------------------------------------------------------------------------------------------------------------------------------------------------------------------|--|--|--|--|--|--|
| Confidence level |  | 0,05                                                                                                                                                                                                                                          |  |  |  |  |  |  |
| Variable         |  | $\epsilon_{\sigma=0.58\text{MPa}}$ (-) strain at a stress of 0,58MPa – all results                                                                                                                                                            |  |  |  |  |  |  |
| Critical region  |  | H <sub>0</sub> accepted if and only if:<br>$D^N = \text{Max} \left\{ \left  F_n(\epsilon_{\sigma=0.58\text{MPa}}) - \phi \left( \frac{\epsilon_{\sigma=0.58\text{MPa}} - \hat{\mu}}{\hat{\sigma}} \right) \right  \right\} \leq D^N_{0.05,n}$ |  |  |  |  |  |  |

| Test designation | N° | Measured                               | Estimated distribution function                                     |                                                                                                  | Empirical distribution function |                            | Tested values                         |                                         |
|------------------|----|----------------------------------------|---------------------------------------------------------------------|--------------------------------------------------------------------------------------------------|---------------------------------|----------------------------|---------------------------------------|-----------------------------------------|
|                  | i  | $\epsilon_{\sigma=0.58\text{MPa}}$ (-) | $\frac{\epsilon_{\sigma=0.58\text{MPa}} - \hat{\mu}}{\hat{\sigma}}$ | $\phi \left( \frac{\epsilon_{\sigma=0.58\text{MPa}} - \hat{\mu}}{\hat{\sigma}} \right) = \phi_i$ | $F_n(i) = \frac{i}{n}$          | $F_n(i-1) = \frac{i-1}{n}$ | $\left  \frac{i}{n} - \phi_i \right $ | $\left  \frac{i-1}{n} - \phi_i \right $ |
| SC01 - 50 - A    | 1  | 0,640                                  | -1,870                                                              | 0,031                                                                                            | 0,1                             | 0                          | 0,069                                 | -0,031                                  |
| SC02 - 5 - A     | 2  | 0,661                                  | -0,718                                                              | 0,236                                                                                            | 0,2                             | 0,1                        | -0,036                                | <b>-0,136</b>                           |
| SC15 - 50 - NA   | 3  | 0,666                                  | -0,450                                                              | 0,326                                                                                            | 0,3                             | 0,2                        | -0,026                                | -0,126                                  |
| SC13 - 5 - LT    | 4  | 0,668                                  | -0,303                                                              | 0,381                                                                                            | 0,4                             | 0,3                        | 0,019                                 | -0,081                                  |
| SC05 - 5 - NA    | 5  | 0,672                                  | -0,116                                                              | 0,454                                                                                            | 0,5                             | 0,4                        | 0,046                                 | -0,054                                  |
| SC10 - 50 - A    | 6  | 0,673                                  | -0,023                                                              | 0,491                                                                                            | 0,6                             | 0,5                        | 0,109                                 | 0,009                                   |
| SC20 - 5 - NA    | 7  | 0,678                                  | 0,231                                                               | 0,591                                                                                            | 0,7                             | 0,6                        | 0,109                                 | 0,009                                   |
| SC16 - 50 - LT   | 8  | 0,679                                  | 0,267                                                               | 0,605                                                                                            | 0,8                             | 0,7                        | <b>0,195</b>                          | 0,095                                   |
| SC18 - 50 - NA   | 9  | 0,697                                  | 1,265                                                               | 0,897                                                                                            | 0,9                             | 0,8                        | 0,003                                 | -0,097                                  |
| SC06 - 5 - A     | 10 | 0,705                                  | 1,719                                                               | 0,957                                                                                            | 1                               | 0,9                        | 0,043                                 | -0,057                                  |

|                     |                        |               |              |              |
|---------------------|------------------------|---------------|--------------|--------------|
| $\hat{\mu} = 0,674$ | $\hat{\sigma} = 0,018$ | Maximum $D^N$ | <b>0,195</b> | <b>0,136</b> |
|---------------------|------------------------|---------------|--------------|--------------|

|            |                                                                       |
|------------|-----------------------------------------------------------------------|
| Conclusion | $D^N = 0,195 < D^N_{0.05,10} = 0,258$<br>Normal distribution supposed |
|------------|-----------------------------------------------------------------------|

**Table D.4-** Lilliefors normality tests concerning the strains at a stress of 0.58MPa – all compressive quasi-static tests on silicone

For this test, the null hypothesis of the normal distribution could be supposed, as the limit value  $D^N$  was inferior to the tabulated value  $D^N_{0.05,10}$ . In spite of the suitability to the normality, the log-normal distribution was also tested with the modified form of the Lilliefors procedure.

| Null hypothesis  |  | H <sub>0</sub> "Log-normal distribution"                                                                                                                                                                                                                 |  |  |  |  |  |  |
|------------------|--|----------------------------------------------------------------------------------------------------------------------------------------------------------------------------------------------------------------------------------------------------------|--|--|--|--|--|--|
| Confidence level |  | 0,05                                                                                                                                                                                                                                                     |  |  |  |  |  |  |
| Variable         |  | $\epsilon_{\sigma=0.58\text{MPa}}$ (-) strain at a stress of 0.58MPa – all results                                                                                                                                                                       |  |  |  |  |  |  |
| Critical region  |  | H <sub>0</sub> accepted if and only if:<br>$D^{LN} = \text{Max} \left\{ \left  F_n(\epsilon_{\sigma=0.58\text{MPa}}) - \phi \left( \frac{\ln(\epsilon_{\sigma=0.58\text{MPa}}) - \hat{\mu}}{\hat{\sigma}} \right) \right  \right\} \leq D^{LN}_{0.05,n}$ |  |  |  |  |  |  |

| Test designation | N° | Measured | Estimated distribution function | Empirical distribution function | Tested values |
|------------------|----|----------|---------------------------------|---------------------------------|---------------|
|------------------|----|----------|---------------------------------|---------------------------------|---------------|



|                | i  | $\epsilon_{\sigma=0.58MPa}$<br>(-) | $\frac{\ln(\epsilon_{\sigma=0.58MPa}) - \hat{\mu}}{\hat{\sigma}}$ | $\phi\left(\frac{\ln(\epsilon_{\sigma=0.58MPa}) - \hat{\mu}}{\hat{\sigma}}\right)$<br>$= \phi_i$ | $F_n(i)$<br>$= \frac{i}{n}$ | $F_n(i-1)$<br>$= \frac{i-1}{n}$ | $\left \frac{i}{n} - \phi_i\right $ | $\left \frac{i-1}{n} - \phi_i\right $ |
|----------------|----|------------------------------------|-------------------------------------------------------------------|--------------------------------------------------------------------------------------------------|-----------------------------|---------------------------------|-------------------------------------|---------------------------------------|
| SC01 - 50 - A  | 1  | 0,640                              | -1,906                                                            | 0,028                                                                                            | 0,1                         | 0                               | 0,072                               | -0,028                                |
| SC02 - 5 - A   | 2  | 0,661                              | -0,712                                                            | 0,238                                                                                            | 0,2                         | 0,1                             | -0,038                              | <b>-0,138</b>                         |
| SC15 - 50 - NA | 3  | 0,666                              | -0,441                                                            | 0,330                                                                                            | 0,3                         | 0,2                             | -0,030                              | -0,130                                |
| SC13 - 5 - LT  | 4  | 0,668                              | -0,292                                                            | 0,385                                                                                            | 0,4                         | 0,3                             | 0,015                               | -0,085                                |
| SC05 - 5 - NA  | 5  | 0,672                              | -0,104                                                            | 0,459                                                                                            | 0,5                         | 0,4                             | 0,041                               | -0,059                                |
| SC10 - 50 - A  | 6  | 0,673                              | -0,011                                                            | 0,496                                                                                            | 0,6                         | 0,5                             | 0,104                               | 0,004                                 |
| SC20 - 5 - NA  | 7  | 0,678                              | 0,242                                                             | 0,596                                                                                            | 0,7                         | 0,6                             | 0,104                               | 0,004                                 |
| SC16 - 50 - LT | 8  | 0,679                              | 0,278                                                             | 0,609                                                                                            | 0,8                         | 0,7                             | <b>0,191</b>                        | 0,091                                 |
| SC18 - 50 - NA | 9  | 0,697                              | 1,255                                                             | 0,895                                                                                            | 0,9                         | 0,8                             | 0,005                               | -0,095                                |
| SC06 - 5 - A   | 10 | 0,705                              | 1,691                                                             | 0,955                                                                                            | 1                           | 0,9                             | 0,045                               | -0,055                                |
|                |    | $\hat{\mu} = -0,395$               | $\hat{\sigma} = 0,027$                                            |                                                                                                  |                             | Maximum $D^{LN}$                | <b>0,191</b>                        | <b>0,138</b>                          |
| Conclusion     |    |                                    |                                                                   | $D^{LN} = 0,191 < D^{LN}_{0.05,10} = 0,296$<br>Log-normal distribution supposed                  |                             |                                 |                                     |                                       |

**Table D.5-** Lilliefors log-normal tests concerning the strains at a stress of 0.58MPa – all compressive quasi-static tests

Based on the log-normal distribution, the characteristic 5% fractile value was again calculated in accordance to the EN 1990 [3.3] and equation Eq. (D.1). The definitive characteristic strain to be used for design is equal to 0,640.

#### D.4 Distribution of the strength for all the shear tests on silicone

The ANAVAR method carried out on to determine the influence of four factors allowed demonstrating the effect of the bonding thickness and area on the shear strength of the silicone. As explained, the main dependencies to these factors were linked to the manufacturing procedures. Nevertheless, all the results were considered to evaluate if a log normal distribution could be assumed. Thus, as for the previous analysis, the Lilliefors test was employed. The complete analysis is detailed in Table D.6.

| Null hypothesis  | H <sub>0</sub> "Log-normal distribution"                                                                                                                                                   |
|------------------|--------------------------------------------------------------------------------------------------------------------------------------------------------------------------------------------|
| Confidence level | 0,05                                                                                                                                                                                       |
| Variable         | $\tau_{max}$ (MPa) strength for all tests                                                                                                                                                  |
| Critical region  | H <sub>0</sub> accepted if and only if:<br>$D^{LN} = \text{Max} \left\{ F_n(\tau_{max}) - \phi\left(\frac{\ln(\tau_{max}) - \hat{\mu}}{\hat{\sigma}}\right) \right\} \leq D^{LN}_{0.05,n}$ |

| Test designation | N° | Measured              | Estimated distribution function                    |                                                                                   | Empirical distribution function |                                 | Tested values                       |                                       |
|------------------|----|-----------------------|----------------------------------------------------|-----------------------------------------------------------------------------------|---------------------------------|---------------------------------|-------------------------------------|---------------------------------------|
|                  | i  | $\tau_{max}$<br>(MPa) | $\frac{\ln(\tau_{max}) - \hat{\mu}}{\hat{\sigma}}$ | $\phi\left(\frac{\ln(\tau_{max}) - \hat{\mu}}{\hat{\sigma}}\right)$<br>$= \phi_i$ | $F_n(i)$<br>$= \frac{i}{n}$     | $F_n(i-1)$<br>$= \frac{i-1}{n}$ | $\left \frac{i}{n} - \phi_i\right $ | $\left \frac{i-1}{n} - \phi_i\right $ |
| 06-1/06/06-2     | 1  | 0,514                 | -2,502                                             | 0,006                                                                             | 0,0625                          | 0                               | 0,056                               | -0,006                                |
| 27-1/09/27-2     | 2  | 0,729                 | -1,330                                             | 0,092                                                                             | 0,125                           | 0,0625                          | 0,033                               | -0,029                                |
| 05-1/05/05-2     | 3  | 0,897                 | -0,636                                             | 0,262                                                                             | 0,1875                          | 0,125                           | -0,075                              | -0,137                                |
| 18-1/15/18-2     | 4  | 0,898                 | -0,632                                             | 0,264                                                                             | 0,25                            | 0,1875                          | -0,014                              | -0,076                                |
| 23-1/09/23-2     | 5  | 0,919                 | -0,557                                             | 0,289                                                                             | 0,3125                          | 0,25                            | 0,024                               | -0,039                                |
| 25-1/07/25-2     | 6  | 0,931                 | -0,514                                             | 0,304                                                                             | 0,375                           | 0,3125                          | 0,071                               | 0,009                                 |

|              |    |       |        |       |        |        |              |               |
|--------------|----|-------|--------|-------|--------|--------|--------------|---------------|
| 16-1/13/16-2 | 7  | 1,024 | -0,195 | 0,423 | 0,4375 | 0,375  | 0,015        | -0,048        |
| 14-1/12/14-2 | 8  | 1,185 | 0,295  | 0,616 | 0,5    | 0,4375 | -0,116       | <b>-0,179</b> |
| 02-1/02/02-2 | 9  | 1,220 | 0,393  | 0,653 | 0,5625 | 0,5    | -0,090       | -0,153        |
| 26-1/11/26-2 | 10 | 1,252 | 0,478  | 0,684 | 0,625  | 0,5625 | -0,059       | -0,121        |
| 21-1/14/21-2 | 11 | 1,270 | 0,527  | 0,701 | 0,6875 | 0,625  | -0,013       | -0,076        |
| 24-1/10/24-2 | 12 | 1,302 | 0,609  | 0,729 | 0,75   | 0,6875 | 0,021        | -0,041        |
| 15-1/14/15-2 | 13 | 1,302 | 0,610  | 0,729 | 0,8125 | 0,75   | 0,083        | 0,021         |
| 04-1/04/04-2 | 14 | 1,425 | 0,910  | 0,819 | 0,875  | 0,8125 | 0,056        | -0,006        |
| 13-1/11/13-2 | 15 | 1,583 | 1,263  | 0,897 | 0,9375 | 0,875  | 0,041        | -0,022        |
| 22-1/13/22-2 | 16 | 1,591 | 1,280  | 0,900 | 1      | 0,9375 | <b>0,100</b> | 0,038         |

$$\hat{\mu} = 0,082$$

$$\hat{\sigma} = 0,299$$

Maximum  $D^{LN}$ **0,100****0,179**

Conclusion

$$D^{LN} = 0,179 < D^{LN}_{0,05,15} = 0,239$$

Log-normal distribution supposed

**Table D.6-** Lilliefors log-normal tests concerning the strength – all shear quasi-static tests

The log-normal distribution was again assumed for the silicone shear strength. Thus, based on this distribution, the 5% fractile value was evaluated with the help of the Eurocode EN 1990 [3.3]. The final characteristic value for design is equal to 0,630MPa.

## D.5 Distribution of the stress for all the oedometric tests on silicone

With the 6 experiments conducted on the oedometric specimens, the stress-strain curves were found more linear than for the other quasi-static results and independent of the loading rate. Thus, all the data were analyzed without considering this last factor. Furthermore, as none of the samples broke under the maximum authorized load by the machine, the stress examined in this study did not concern the maximum stress at failure but the stress at a fixed strain, corresponding to the maximum reached during the tests. The Lilliefors test was performed to assess if the data followed a log-normal distribution as it was the case in the previous sections. The complete analysis is detailed in Table D.7.

| Null hypothesis  | H <sub>0</sub> "Log-normal distribution"                                                                                                                                                                                         |
|------------------|----------------------------------------------------------------------------------------------------------------------------------------------------------------------------------------------------------------------------------|
| Confidence level | 0,05                                                                                                                                                                                                                             |
| Variable         | $\sigma_{\epsilon=0.035}$ (MPa) strength for all tests                                                                                                                                                                           |
| Critical region  | H <sub>0</sub> accepted if and only if:<br>$D^{LN} = \max \left\{ \left  F_n(\sigma_{\epsilon=0.035}) - \phi \left( \frac{\ln(\sigma_{\epsilon=0.035}) - \hat{\mu}}{\hat{\sigma}} \right) \right  \right\} \leq D^{LN}_{0,05,n}$ |

| Test designation | N° | Measured                        | Estimated distribution function                                 |                                                                                              | Empirical distribution function |                            | Tested values                         |                                         |
|------------------|----|---------------------------------|-----------------------------------------------------------------|----------------------------------------------------------------------------------------------|---------------------------------|----------------------------|---------------------------------------|-----------------------------------------|
|                  | i  | $\sigma_{\epsilon=0.035}$ (MPa) | $\frac{\ln(\sigma_{\epsilon=0.035}) - \hat{\mu}}{\hat{\sigma}}$ | $\phi \left( \frac{\ln(\sigma_{\epsilon=0.035}) - \hat{\mu}}{\hat{\sigma}} \right) = \phi_i$ | $F_n(i) = \frac{i}{n}$          | $F_n(i-1) = \frac{i-1}{n}$ | $\left  \frac{i}{n} - \phi_i \right $ | $\left  \frac{i-1}{n} - \phi_i \right $ |
| O8 - 0,1         | 1  | 12,277                          | -1,367                                                          | 0,086                                                                                        | 0,167                           | 0                          | 0,081                                 | -0,086                                  |
| O9 - 0,1         | 2  | 12,614                          | -0,822                                                          | 0,206                                                                                        | 0,333                           | 0,1667                     | 0,128                                 | -0,039                                  |
| O4 - 1           | 3  | 12,964                          | -0,270                                                          | 0,394                                                                                        | 0,5                             | 0,333                      | 0,106                                 | -0,060                                  |
| O6 - 1           | 4  | 13,500                          | 0,547                                                           | 0,708                                                                                        | 0,667                           | 0,5                        | -0,041                                | -0,208                                  |
| O7 - 0,1         | 5  | 13,535                          | 0,600                                                           | 0,726                                                                                        | 0,833                           | 0,667                      | 0,108                                 | -0,059                                  |
| O5 - 1           | 6  | 14,023                          | 1,313                                                           | 0,905                                                                                        | 1                               | 0,833                      | 0,095                                 | -0,072                                  |

|                     |                        |                                                                                 |              |              |
|---------------------|------------------------|---------------------------------------------------------------------------------|--------------|--------------|
| $\hat{\mu} = 2,576$ | $\hat{\sigma} = 0,050$ | Maximum $D^{LN}$                                                                | <b>0,128</b> | <b>0,208</b> |
| Conclusion          |                        | $D^{LN} = 0,208 < D^{LN}_{0.05,15} = 0,368$<br>Log-normal distribution supposed |              |              |

**Table 4.7-** Lilliefors log-normal tests concerning the stress at  $\varepsilon=0.035$  – oedometric quasi-static tests

In conclusion, the log-normal distribution was supposed for the stress at a fixed strain of 0,035. The characteristic 5% fractile value was again evaluated in accordance to the EN 1990 [3.3]. The final calculated characteristic stress was of 11,792MPa.



## APPENDIX E – Finite element procedures and subroutines

### E.1 Solving procedures

In all finite element software, the principle of virtual work applied to a discretized structure allowed obtaining the following equation:

$$[M][\ddot{u}] = [f^{ext}] - [f^{int}] \quad (E.1)$$

[M] the nodal mass matrix,  
With [f<sup>int</sup>] the nodal applied load matrix,  
[f<sup>ext</sup>] the nodal internal force matrix.

Based on this fundamental equation, two methods of resolutions were developed within the Abaqus finite element software, i.e. an iterative implicit method and an explicit method based on the kinematic state of the previous increment. The details of these two procedures are given in the following paragraphs.

#### a. Abaqus/Standard – implicit method

As aforementioned, the implicit method is an iterative procedure and requires the discretization of the total time in  $m$  increments. This method mainly consists in minimizing, for each increment, the residual assimilated to:

$$r(u^{n+1}, t^{n+1}) = [M]^{n+1}[\ddot{u}]^{n+1} + [f^{int}(u^{n+1}, t^{n+1})] - [f^{ext}(u^{n+1}, t^{n+1})] = 0 \quad (E.2)$$

Where  $t^n$  represents the time at the beginning of the increment  $n$ . Furthermore, even if the problem to be solved is independent of the time, a fictitious time is introduced to characterize the evolution of the applied loading. To determine the value of the displacements at a fix increment, a first approximation of their values is realized, mostly in connection with the results obtained from the previous increment, and some iterations are then carried out. The method of Newton-Raphson, necessitating a Taylor expansion at first order of Eq. (E.2), is applied to iterate the values and check the convergence, see Eq. (E.3), in which the bracket of the matrix were suppress to simply the expression.

$$r(u_{\alpha+1}^{n+1}, t^{n+1}) = r(u_{\alpha}^{n+1}, t^{n+1}) + \frac{\delta r(u_{\alpha}^{n+1}, t^{n+1})}{\delta u_{\alpha}^{n+1}} \Delta u_{\alpha}^{n+1} = 0 \quad (E.3)$$

With  $u_{\alpha+1}^{n+1}$  the displacements vector at increment  $n + 1$  for the iteration  $\alpha + 1$   
 $\Delta u_{\alpha}^{n+1} = u_{\alpha+1}^{n+1} - u_{\alpha}^{n+1}$  the displacements difference between consecutive iterations

By rearranging the above equation, the displacements for the following iteration could be written as follow:

$$u_{\alpha+1}^{n+1} = \left( \frac{\delta r(u_{\alpha}^{n+1}, t^{n+1})}{\delta u_{\alpha}^{n+1}} \right)^{-1} r(u_{\alpha}^{n+1}, t^{n+1}) + u_{\alpha}^{n+1} \quad (E.4)$$

The Eq. (E.4) should be repeated with  $u_{\alpha+1}^{n+1}$  until convergence is reached. Once achieve, the full operation has to be conducted for the following increments to finally attain the total time. Besides, to pass from one increment to another, a second Taylor expansion in relation to the Newmark- $\beta$  method should be used on the displacements, see Eq. (E.5.).

$$u^{n+1} = u^n + \Delta t \dot{u}^n + \Delta t^2 \left( \frac{1}{2} - \beta \right) \ddot{u}^n + \Delta t^2 \beta \ddot{u}^{n+1} = \tilde{u}^{n+1} + \Delta t^2 \beta \ddot{u}^{n+1} \quad (E.5)$$

With  $\beta$  constant,  $\Delta t = t^{n+1} - t^n$  and  $u^{n+1}$  an approximation of the displacements for increment  $n + 1$ . Thus, the acceleration, allowing calculating the new residual at the increment  $n + 1$ , becomes:

$$\ddot{u}^{n+1} = \frac{1}{\Delta t^2 \beta} (u^{n+1} - \tilde{u}^{n+1}) \quad (\text{E.6})$$

The above Eq. (E.6) is convenient, as it only depends on the displacements and their derivate of the previous increment and on the first approximation of the displacement at the investigated increment. Consequently, the combination and iteration of both Eq. (E.4) and (E.6) constitute the basis of the implicit method for the resolution of non-linear problems.

#### b. Abaqus/Explicit – explicit method

Even if the explicit method, implemented in Abaqus, is not based on an iterative method, the time is still discretized in several increments and Eq. (E.1) equal to:

$$[\ddot{u}]^n = [M]^{-1}([f^{ext}]^n - [f^{int}]^n) = [M]^{-1}[f]^n \quad (\text{E.7})$$

The central concept of this procedure being to advance the kinematic state from the previous increment, the explicit central difference integration rule is employed to define the displacement, the velocity and the acceleration at nodes, see the set of Eq. (E.8).

$$\Delta t^{n+1/2} = t^{n+1} - t^n \quad (\text{E.8 a})$$

$$t^{n+1/2} = \frac{1}{2}(t^{n+1} + t^n) \quad (\text{E.8 b})$$

$$v^{n+1/2} = \frac{u^{n+1} - u^n}{t^{n+1} - t^n} = \frac{u^{n+1} - u^n}{\Delta t^{n+1/2}} \quad (\text{E.8 c})$$

$$\ddot{u}^n = \frac{v^{n+1/2} - v^{n-1/2}}{t^{n+1/2} - t^{n-1/2}} = \frac{\Delta t^{n-1/2}(u^{n+1} - u^n) - \Delta t^{n+1/2}(u^n - u^{n-1})}{\Delta t^{n+1/2} \Delta t^{n-1/2}} \quad (\text{E.8 d})$$

Where  $t^n$  and  $v^n$  represent respectively the time and the velocity at the beginning of increment  $n$ . With the left member of the last equation Eq. (8.d), it then becomes possible to express the unknown  $v^{n+1/2}$  in relation to known functions:

$$v^{n+1/2} = v^{n-1/2} + \Delta t^n \ddot{u}^n \quad (\text{E.9})$$

Hence, going back to Eq. (E.8 c), a formulation of the displacement at the next increment could be proposed:

$$u^{n+1} = u^n + \Delta t^{n+1/2} v^{n+1/2} \quad (\text{E.10})$$

Eq. (E.9) and (E.10) constitute both fundamental equations of the algorithm of resolution of the explicit method. For the first increment, the time, the displacement and the velocity vectors are all initialized. The nodal acceleration vector for  $n = 0$  is calculated with the help of Eq. (E.7). The times are then actualized with Eq. (E.8. a) and (E.8 b) to later estimate the nodal velocities with Eq. (E.9) and the nodal displacements of the first increment with Eq. (E.10). With these last values, the nodal applied load matrix and the nodal internal force matrix can be updated for the first increment, which allows determining the acceleration vector for  $n = 1$ . As the total time cannot be achieved after the first increment due to the discretization principle, the equations Eq. (E.9), (E.10) and (E.7) have to be re-actualized with  $n \leftarrow n + 1$ . This complete procedure is conducted until the total time is attained.

In spite of the simplicity and robustness of the explicit method, some problems of convergence can occur and its stability is conditional. Indeed, a critical step time is defined as limit, see Eq. (E.11).

$$\Delta t < \Delta t_{critical} = \frac{2}{\omega_{max}} (\sqrt{1 + \xi^2} - \xi) \quad (E.10)$$

Where  $\omega_{max}$  is the maximum frequency of the linearized system and  $\xi$  a fraction of critical damping in the highest mode.

### c. Advantages of the 2 methods

While the explicit method requests less time of calculation than the iterative implicit method, it is also less stable. Therefore, these methods are antagonist and do not possess both rapidity and stability. The real advantages come however from the formulation of the problem. Indeed, only a Lagrangian representation is available with the implicit method, while the Eulerian is accessible for the explicit method. For the majority of non-linear problems, in which the hyperelastic material is subjected to large deformations, the mesh can distort excessively and the accuracy of the results drop due this effect, when the calculation did not abort. Thus, using adaptative meshing tools specific of the problem formulation becomes indispensable.

For Abaqus/Standard, two adaptivity techniques allow optimizing the mesh and avoiding distortions:

- Adaptative remeshing, which is based in an iterative process generating several meshes in order to determine the most appropriate one to be used for the full analysis. The user has to set some indicators related to the maximum error of discretization and the software will test and optimize the previous mesh to finally provide one unique mesh. This procedure is preferably used to simulate geometrical singularities with the aim to obtain the minimum number of elements required to obtain sufficient accuracy.
- Mesh-to-mesh solution mapping. With this second technique, when too many distortions are encountered, the analysis is stopped and the results are recorded according to the positions of the nodes. Then, the actual distorted mesh is erased and a new one is created on the studied deformed structure. The acquired results of the previous mesh are finally remapped on the new nodes to continue the calculation. Hence, this procedure requires performing several jobs in Abaqus. As the nodes of the old mesh do not necessarily correspond to the node of the new mesh some approximations are done and slight variations could be observed when the analysis is pursued. Therefore, several verifications have to be made after the rezoning of the results.

For Abaqus/Explicit, two other adaptivity techniques are available:

- Arbitrary Lagrangian Eulerian (ALE). This method combines the Lagrangian formulation, for which the nodes move with the material point and could thus be distorted, and the Eulerian formulation, for which the nodes are fixed while the material expand over the mesh. The repartitions of these two formulations over the material depend on the conditions, such as the boundary conditions, the load application and the contacts, imposed to it. In consequence, it appears possible to fix a certain region while letting evolve another. Hence, the only mesh needed progressively evolved and is smoothed within the analysis. This procedure is particularly effective to control the distortion.
- Control of the element distortion. For highly constrained material under large deformations, some elements can distort excessively and their volumes can then be negative, which directly abort the job. To prevent this effect, a constraint is applied on each element consisting in only authorizing a displacement offset of the nodes equal to the initial length of the element multiplied by a small ratio comprised between 0 and 1. This last ratio is specified by the user and could slightly stiffen its behaviour.

## E.2 Abaqus/Standard UHYPER-subroutine for silicone

To implement an hyperelastic user subroutine in Abaqus/Standard, the function UHYPER needs to be called. In the created file, the strain energy potential and its derivatives according to the invariants must be explicated. The complete UHYPER subroutine is given below:

---

C23456789012345678901234567890123456789012345678901234567890123456789

C

```

SUBROUTINE UHYPER (BI1,BI2,AJ,U,UI1,UI2,UI3,TEMP,NOEL,CMNAME,
1 INCMPFLAG,NUMSTATEV,STATEV,NUMFIELDV,FIELDV,FIELDVINC,
2 NUMPROPS,PROPS)

```

C

```

INCLUDE 'ABA_PARAM.INC'

```

C

```

CHARACTER*80 CMNAME

```

```

DIMENSION UI1(3),UI2(6),UI3(6),STATEV(*),FIELDV(*),

```

```

1 FIELDVINC(*),PROPS(*)

```

C

```

PARAMETER (ZERO=0.0D0,ONE=1.0D0,TWO=2.0D0,THREE=3.0D0)

```

C

```

A = PROPS(1)

```

```

B = PROPS(2)

```

```

C = PROPS(3)

```

```

D = PROPS(4)

```

```

E = PROPS(5)

```

```

F = PROPS(6)

```

C

```

U= A*(BI1-THREE)+B*(BI1-THREE)**2+C*(BI2-THREE)

```

```

1 -D/(BI2-THREE+E)+D/E+F*(AJ-1)**2

```

```

UI1(1)=A+2*B*(BI1-THREE)

```

```

UI1(2)=C+D/(BI2-THREE+E)**2

```

```

UI1(3)=2*F*(AJ-1)

```

```

UI2(1)=2*B

```

```

UI2(2)=-2*D/(BI2-THREE+E)**3

```

```

UI2(3)=2*F

```

```

UI2(4)=ZERO

```

```

UI2(5)=ZERO

```

```

UI2(6)=ZERO

```

```

UI3(1)=ZERO

```

```

UI3(2)=ZERO

```

```

UI3(3)=ZERO

```

```

UI3(4)=ZERO

```

```

UI3(5)=ZERO

```

```

UI3(6)=ZERO

```

```

RETURN

```

```

END

```

---

The definition of the different constants A to F= $K/2$ , whose values were regrouped in Table 5.21, must be done by the user in the finite element software interface Abaqus/CAE. Thus, the above subroutine could be as well employed for quasi-static numerical simulations as for the representation of the stress-strain behaviour at the end of the Mullin's effect.



### E.3 Abaqus/Explicit VUMAT-subroutine for silicone

In Abaqus/Explicit, no simple function similar to the previous UHYPER routine existed. Consequently, a general VUMAT subroutine, for which the Cauchy stress in a co-rotational framework had to be directly expressed, was created. The complete VUMAT subroutine is given below:

```

C23456789012345678901234567890123456789012345678901234567890
```

```
C-----
```

```
C SUBROUTINE VMAT FOR USER HYPERELASTIC MATERIAL PROPERTIES
```

```
C-----
```

```
 subroutine vumat(
```

```
C Read only (unmodifiable)variables -
```

```
1 nblock, ndir, nshr, nstatev, nfieldv, nprops, lanneal,
2 stepTime, totalTime, dt, cmname, coordMp, charLength,
3 props, density, strainInc, relSpinInc,
4 tempOld, stretchOld, defgradOld, fieldOld,
5 stressOld, stateOld, enerInternOld, enerInelasOld,
6 tempNew, stretchNew, defgradNew, fieldNew,
```

```
C Write only (modifiable) variables -
```

```
7 stressNew, stateNew, enerInternNew, enerInelasNew)
```

```
C
```

```
 include 'vaba_param.inc'
```

```
C
```

```
 dimension props(nprops), density(nblock), coordMp(nblock,*),
```

```
1 charLength(nblock), strainInc(nblock,ndir+nshr),
2 relSpinInc(nblock,nshr), tempOld(nblock),
3 stretchOld(nblock,ndir+nshr),
4 defgradOld(nblock,ndir+nshr+nshr),
5 fieldOld(nblock,nfieldv), stressOld(nblock,ndir+nshr),
6 stateOld(nblock,nstatev), enerInternOld(nblock),
7 enerInelasOld(nblock), tempNew(nblock),
8 stretchNew(nblock,ndir+nshr),
9 defgradNew(nblock,ndir+nshr+nshr),
1 fieldNew(nblock,nfieldv),
2 stressNew(nblock,ndir+nshr), stateNew(nblock,nstatev),
3 enerInternNew(nblock), enerInelasNew(nblock)
```

```
C
```

```
 character*80 cmname
```

```
C
```

```
C-----
```

```
C TENSOR DEFINITION
```

```
C
```

```
C SISO - Isochoric Part of the Cauchy Stress Tensor
```

```
C SVOL - Volumetric Part of the Cauchy Stress Tensor
```

```
C UBAR - Modified Stretch Tensor defined as FBAR=R.UBAR
```

```
C UBAR2 - Square of the Modified Stretch Tensor
```

```
C UBAR4 - Modified Stretch Tensor raised to the 4th Power
```

```
C-----
```

```
C
```

```
 dimension SISO(3,3),SVOL(3,3),UBAR(3,3),UBAR2(3,3),UBAR4(3,3)
```

```
C
```

```
parameter (ZERO=0.0D0,ONE=1.0D0,TWO=2.0D0,THREE=3.0D0,
1 FOUR=4.0D0,FIVE=5.0D0,SIX=6.0D0)
```

```
C
```

```
C-----
```

```
C USER LAW:
```

```
C
```

```
C U=A*(BI1-3)+B*(BI1-3)**2+C*(BI2-3)-D/(BI2-3+E)+D/E+I(AJ-1)**2
```

```
C A, B, C, D, E, K Constants
```

```
C-----
```

```
C
```

```
 A=PROPS(1)
```

```
 B=PROPS(2)
```

```
 C=PROPS(3)
```

```
 D=PROPS(4)
```

```
 E=PROPS(5)
```

```
 I=PROPS(6)
```

```
C
```

```
 do k = 1,nblock
```

```
C
```

```
C-----
```

```
C DETERMINANT AJ OF THE DEFORMATION TENSOR = DET STRETCH TENSOR
```

```
C-----
```

```
C
```

```
 DETU1=stretchNew(k,1)*(stretchNew(k,2)*stretchNew(k,3)-
```

```
1 stretchNew(k,5)**2)
```

```
 DETU2=stretchNew(k,4)*(stretchNew(k,6)*stretchNew(k,5)-
```

```
1 stretchNew(k,4)*stretchNew(k,3))
```

```
 DETU3=stretchNew(k,6)*(stretchNew(k,4)*stretchNew(k,5)-
```

```
1 stretchNew(k,2)*stretchNew(k,6))
```

```
 AJ=DETU1+DETU2+DETU3
```

```
C
```

```
C-----
```

```
C VOLUMETRIC PART OF THE CAUCHY STRESS TENSOR - SVOL
```

```
C-----
```

```
C
```

```
 SVOL(1,1)=TWO*I*(AJ-ONE)
```

```
 SVOL(2,2)=TWO*I*(AJ-ONE)
```

```
 SVOL(3,3)=TWO*I*(AJ-ONE)
```

```
 SVOL(1,2)=ZERO
```

```
 SVOL(2,3)=ZERO
```

```
 SVOL(1,3)=ZERO
```

```
C
```

```
C-----
```

```
C MODIFIED STRETCH TENSOR - UBAR
```

```
C-----
```

```
C
```

```
 UBAR(1,1)=AJ**(-ONE/THREE)*stretchNew(k,1)
```

```
 UBAR(2,2)=AJ**(-ONE/THREE)*stretchNew(k,2)
```

```
 UBAR(3,3)=AJ**(-ONE/THREE)*stretchNew(k,3)
```

```
 UBAR(1,2)=AJ**(-ONE/THREE)*stretchNew(k,4)
```

```
 UBAR(2,3)=AJ**(-ONE/THREE)*stretchNew(k,5)
```

```
 UBAR(1,3)=AJ**(-ONE/THREE)*stretchNew(k,6)
```

```
C
```

```

C-----
C SQUARE OF THE MODIFIED STRETCH TENSOR - UBAR2
C-----
C
UBAR2(1,1)=UBAR(1,1)**2+UBAR(1,2)**2+UBAR(1,3)**2
UBAR2(2,2)=UBAR(1,2)**2+UBAR(2,2)**2+UBAR(2,3)**2
UBAR2(3,3)=UBAR(1,3)**2+UBAR(2,3)**2+UBAR(3,3)**2
UBAR2(1,2)=UBAR(1,1)*UBAR(1,2)+UBAR(1,2)*UBAR(2,2)+UBAR(1,3)*
1 UBAR(2,3)
UBAR2(2,3)=UBAR(1,2)*UBAR(1,3)+UBAR(2,2)*UBAR(2,3)+UBAR(2,3)*
1 UBAR(3,3)
UBAR2(1,3)=UBAR(1,1)*UBAR(1,3)+UBAR(1,2)*UBAR(2,3)+UBAR(1,3)*
1 UBAR(3,3)
C
C-----
C TRACE OF UBAR2 - TRUBAR2
C-----
C
TRUBAR2=UBAR2(1,1)+UBAR2(2,2)+UBAR2(3,3)
C
C-----
C MODIFIED STRETCH TENSOR RAISED TO THE 4th POWER - UBAR4
C-----
C
UBAR4(1,1)=UBAR2(1,1)**2+UBAR2(1,2)**2+UBAR2(1,3)**2
UBAR4(2,2)=UBAR2(1,2)**2+UBAR2(2,2)**2+UBAR2(2,3)**2
UBAR4(3,3)=UBAR2(1,3)**2+UBAR2(2,3)**2+UBAR2(3,3)**2
UBAR4(1,2)=UBAR2(1,1)*UBAR2(1,2)+UBAR2(1,2)*UBAR2(2,2)+
1 UBAR2(1,3)*UBAR2(2,3)
UBAR4(2,3)=UBAR2(1,2)*UBAR2(1,3)+UBAR2(2,2)*UBAR2(2,3)+
1 UBAR2(2,3)*UBAR2(3,3)
UBAR4(1,3)=UBAR2(1,1)*UBAR2(1,3)+UBAR2(1,2)*UBAR2(2,3)+
1 UBAR2(1,3)*UBAR2(3,3)
C
C-----
C TRACE OF UBAR4 - TRUBAR4
C-----
C
TRUBAR4=UBAR4(1,1)+UBAR4(2,2)+UBAR4(3,3)
C
C-----
C DETERMINATION OF COEFFICIENTS - X,Y,Z
C-----
C
X=((ONE/TWO)*(TRUBAR2**2-TRUBAR4)-THREE+E)**2
Y=(TWO/AJ)*(A-SIX*B+(TWO*B+C+D/X)*TRUBAR2)
Z=(TWO/AJ)*(C+D/X)
C
C-----
C ISOCHORIC PART OF THE CAUCHY STRESS TENSOR
C-----
C
SISO(1,1)=Y*UBAR2(1,1)-Z*UBAR4(1,1)-(ONE/THREE)*(Y*TRUBAR2-

```

```

1 Z*TRUBAR4)
SISO(2,2)=Y*UBAR2(2,2)-Z*UBAR4(2,2)-(ONE/THREE)*(Y*TRUBAR2-
1 Z*TRUBAR4)
SISO(3,3)=Y*UBAR2(3,3)-Z*UBAR4(3,3)-(ONE/THREE)*(Y*TRUBAR2-
1 Z*TRUBAR4)
SISO(1,2)=Y*UBAR2(1,2)-Z*UBAR4(1,2)
SISO(2,3)=Y*UBAR2(2,3)-Z*UBAR4(2,3)
SISO(1,3)=Y*UBAR2(1,3)-Z*UBAR4(1,3)
C
C-----
C CAUCHY STRESS TENSOR
C-----
C
stressNew(k,1)=SISO(1,1)+SVOL(1,1)
stressNew(k,2)=SISO(2,2)+SVOL(2,2)
stressNew(k,3)=SISO(3,3)+SVOL(3,3)
stressNew(k,4)=SISO(1,2)+SVOL(1,2)
stressNew(k,5)=SISO(2,3)+SVOL(2,3)
stressNew(k,6)=SISO(1,3)+SVOL(1,3)
C
C open(15,file='C:\Temp\SVOL.txt',position='append')
C write(15,*) 'SVOL11=',SVOL(1,1),'for block',k
C write(15,*) 'SVOL22=',SVOL(2,2),'for block',k
C write(15,*) 'SVOL33=',SVOL(3,3),'for block',k
C write(15,*) 'SVOL12=',SVOL(1,2),'for block',k
C write(15,*) 'SVOL23=',SVOL(2,3),'for block',k
C write(15,*) 'SVOL13=',SVOL(1,3),'for block',k
C close(15)
C
end do
C
return
end

```

---

Nevertheless, as for the previous subroutine, the definition of the material coefficients A to I=K/2 of Table 5.21 must be done via the software interface Abaqus/CAE. This subroutine is valid for the quasi-static numerical simulations and for the consideration of the Mullin's effect. These differences are simply achieved by changing the values of the material coefficients.

Attention: the last coefficient "F=K/2", accounting for the volumetric effects had to be renamed "I" to avoid possible confusion with the deformation tensor F and the increment k. Therefore, it is highly recommended to keep the present notation!

## E.4 Abaqus/Standard UHYPER-subroutine for acrylic

As for the silicone material law implementation, an UHYPER subroutine had to be written. Further, as the acrylic 1D material model was issued from the one of the previous adhesive, the global structure remained the same. The strain energy potential and its derivatives according to the invariants were again calculated and combined in the following subroutine:

---

C23456789012345678901234567890123456789012345678901234567890123456789

C

```
1 SUBROUTINE UHYPER (BI1,BI2,AJ,U,UI1,UI2,UI3,TEMP,NOEL,CMNAME,
2 INCMPFLAG,NUMSTATEV,STATEV,NUMFIELDV,FIELDV,FIELDVINC,
 NUMPROPS,PROPS)
```

C

```
 INCLUDE 'ABA_PARAM.INC'
```

C

```
 CHARACTER*80 CMNAME
```

```
 DIMENSION UI1(3),UI2(6),UI3(6),STATEV(*),FIELDV(*),
```

```
1 FIELDVINC(*),PROPS(*)
```

C

```
 PARAMETER (ZERO=0.0D0,ONE=1.0D0,TWO=2.0D0,THREE=3.0D0)
```

C

```
 A = 2.59553
```

```
 B = -0.104569
```

```
 C = 0
```

```
 D = 0.399964
```

```
 E = 0.224742
```

C

```
 U= A*(BI1-THREE)+B*(BI1-THREE)**2+C*(BI2-THREE)
```

```
1 -D/(BI2-THREE+E)+D/E
```

```
 UI1(1)=A+2*B*(BI1-THREE)
```

```
 UI1(2)=C+D/(BI2-THREE+E)**2
```

```
 UI1(3)=ZERO
```

```
 UI2(1)=2*B
```

```
 UI2(2)=-2*D/(BI2-THREE+E)**3
```

```
 UI2(3)=ZERO
```

```
 UI2(4)=ZERO
```

```
 UI2(5)=ZERO
```

```
 UI2(6)=ZERO
```

```
 UI3(1)=ZERO
```

```
 UI3(2)=ZERO
```

```
 UI3(3)=ZERO
```

```
 UI3(4)=ZERO
```

```
 UI3(5)=ZERO
```

```
 UI3(6)=ZERO
```

```
 RETURN
```

```
 END
```

---

As it could have been remarked, the last coefficient F of the silicone subroutine was removed, as the acrylic was not quasi-incompressible. Further, the two coefficients A and C were redundant and one of them was arbitrarily set to zero. The other coefficients were dependent on the loading rate and the implemented behaviour was thus only valid for a specific rate. The proposed equations of Table 5.22

allowing calculating them could not be directly used in reason of the large deformation definition of the Abaqus software. The following procedure must be followed to evaluate the correct set of coefficients to be inserted in the software:

1. Selection of the loading rate and determination of the coefficients A,B,C and D of Table 5.22.
2. Establishment of the shear stress-strain diagram with the help of the self-developed material law also exposed in Table 5.22.
3. The stress-strain data assess within the previous point had to be fitted, with the help of the Levenberg-Marquardt presented in Fig. 5.7, to the following law:

$$\tau = 2A \tan(\gamma) + 4B \tan(\gamma)^3 + \frac{2C \tan(\gamma)}{[\tan(\gamma)^2 + D]^2} \quad (\text{E.11})$$

4. The acquired coefficients could then be injected in the UHYPER subroutine for numerical simulations.

For the three investigated loading rates, the coefficients to be used were gathered in Table E.1.

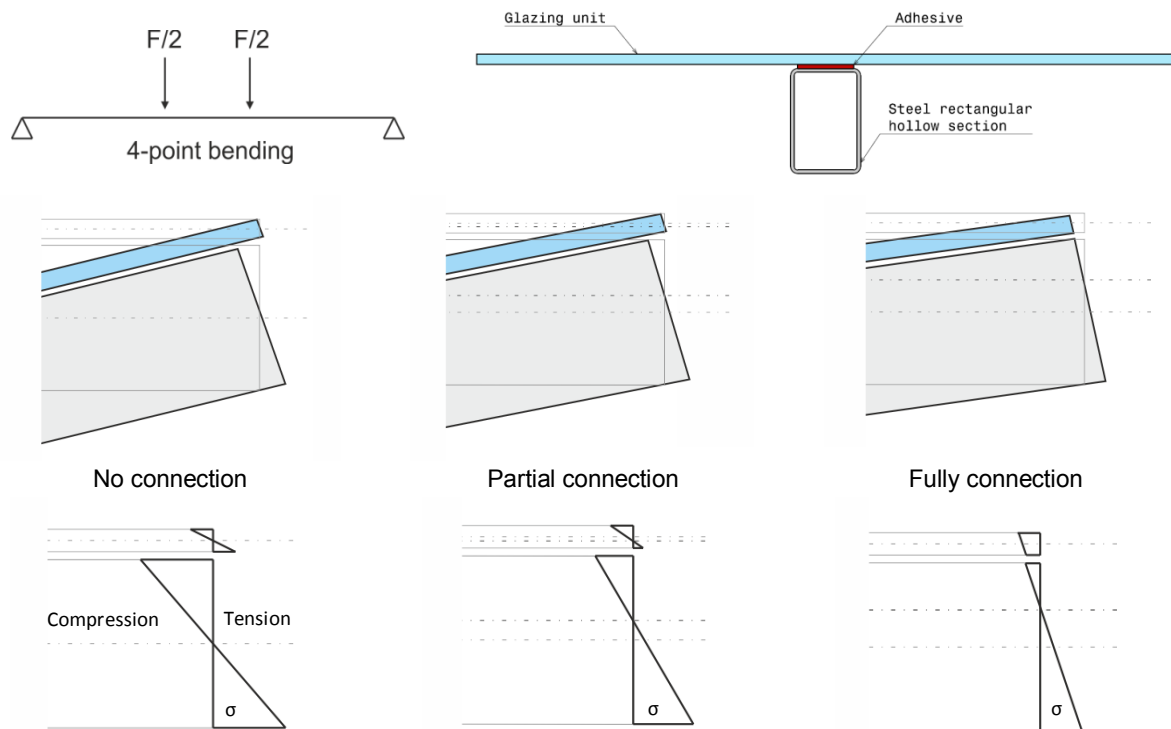
| Loading rate | Coefficients of the UHYPER subroutine |            |   |           |          |
|--------------|---------------------------------------|------------|---|-----------|----------|
|              | A                                     | B          | C | D         | E        |
| 15mm/min     | 2,59553                               | -0,104569  | 0 | 0,399964  | 0,224742 |
| 5mm/min      | 1,53048                               | -0,0481918 | 0 | 0,120153  | 0,146836 |
| 1mm/min      | 1,21907                               | -0,0433671 | 0 | 0,0413586 | 0,10248  |

**Table E.1-** Coefficients to be injected in the UHYPER material law for shear numerical simulations of acrylic adhesive

## APPENDIX F – Theoretical background of composite beams

### F.1 Fully vs. partial connections

As detailed in sections 3.3 and 3.4, the envisaged composite beams were composed by three main components, i.e. a steel rectangular hollow section, a monolithic thick glass plate and the adhesive. Two bonding materials were investigated, but due to the poor long-term properties of the acrylic, only the silicone elastomer was conserved for the manufacture of the linear adhesive and mechanical-adhesive composite beams. To evaluate the rigidity of such beams, a four point bending tests was set up, so that only a positive flexure moment was applied. While the silicone was mainly subjected to shear for the first continuous jointing method, it only acted in compression/tension for the second discontinuous type. The main role of this adhesive was to limit the sliding at the steel-glass interface for the both assemblies. Additionally, for the linear adhesive connection, it also prevented any vertical opening between the two adherends, i.e. the glass plate could not vertically dissociate from the steel beam. This function was guaranteed, for the mechanical-adhesive connection, by the covering steel plates preventing the squeezing out of the silicone. Nevertheless, a non-vertical separation was assumed in both case and for each theory presented below. The rigidity of the composite beam was directly dependent on the rigidity of the adhesive and three possible configurations could arise, i.e. a fully or a partial connection, see Fig. F.1.



**Figure F.1-** Deformation and stress distribution of three different rigidity of connections – steel to glass composite beam

When the connection is weak or inexistent between the glass and steel, the relative displacements at their interfaces can be large and each section subjected to important bending moments, especially for consequent loads and weak material cross sections. This generates large deflections in the center of the beam. Furthermore, compressive and tensile stresses develop in both sections, which could be harmful for the glass. At the opposite for a perfect connection, no sliding appears at the interface and the steel and glass parts are subjected to bending moments as well as longitudinal forces greatly reducing the deflection. With a correct design, the central axis of the section would be positioned in the steel web and only compressive stresses arise in the upper element, corresponding to an ideal case. However, with the envisaged elastomer connection, a partial interaction, for which some sliding occurs, is expected. The total deflection of the beam is lower than for non-connected elements but still

higher than the one of fully composite beam. In addition, and in contrary to the perfect connection, some tensile stress could develop in the glass element, depending on the rigidity of the jointing and also on the dimensions of the material cross sections.

As reference, the fully composite beam theory, centered on an elastic calculation, will be exposed in the next paragraph, as well as two partial connection theories proposed by Pischl and Lebet.

## F.2 Fully composite beam theory

To assess the stress distribution in the different elements composing a fully composite beam, two main assumptions have to be made:

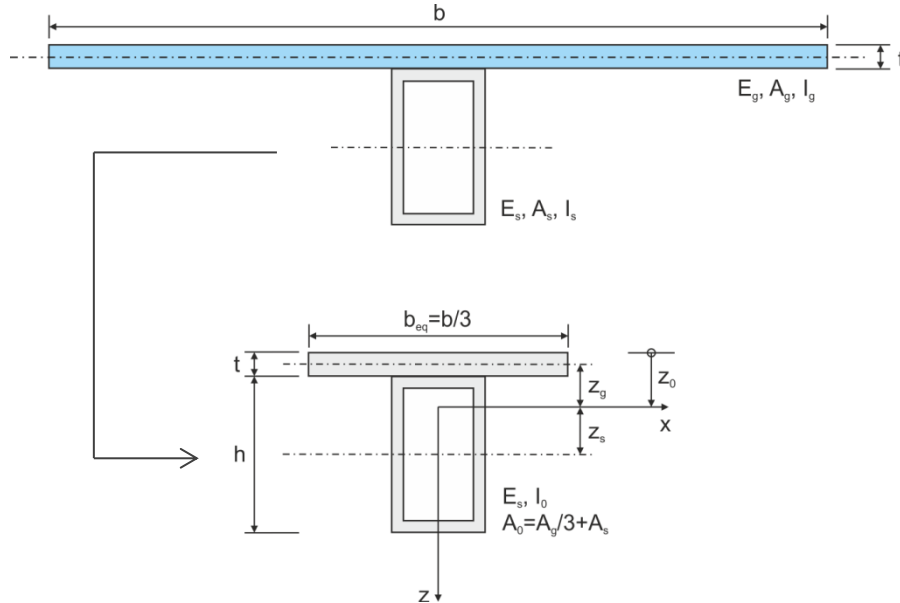
- The Bernoulli hypothesis is valid for the composite section, i.e. each straight section remains straight after deformation. Hence, the sliding at the interface steel-glass is non-existent and the displacements are continuous, see Fig. F.1.
- Only linear behaviours are considered for the steel and glass elements. While, this postulate is always true for the glass, it induces neglecting the large plasticity capacity of the steel.

For the calculation method presented below, the simplification, consisting in replacing the glass cross section by an equivalent steel section, is implemented.

The two above assumptions allows the calculation of an equivalence coefficient representing the ratio of the Young's modulus of the two materials, see Eq. (F.1). This coefficient is achieved by equalizing the deformations at the steel and glass interface.

$$n = \frac{E_s}{E_g} = \frac{210\,000\text{ MPa}}{70\,000\text{ MPa}} = 3 \quad (\text{F.1})$$

Where  $E_s$  correspond to the steel Young's modulus and  $E_g$  to the glass Young's modulus. Knowing this constant coefficient, the width of the glass plate is divided by three to form a steel equivalent cross section. As aforementioned, the optimum case for the glass element would be to have the neutral axis of the homogenized section in the steel flange, see Fig. F.2.



**Figure F.2-** Geometrical simplification for the calculation of fully connected steel to glass elements

The position of the neutral axis  $z_0$ , making reference to the upper face of the glass plate, is calculated with the following formula:

$$z_0 = \frac{A_g/3 \times t/2 + A_s \times (t + h/2)}{A_g/3 + A_s} \quad (\text{F.2})$$



The respective positions of the neutral axes of the glass and of the steel compared to the determined neutral axis of the composite beam were then assessed:

$$z_g = z_0 - \frac{t}{2} \quad (\text{F.3a})$$

$$z_s = t + \frac{h}{2} - z_0 \quad (\text{F.3b})$$

These last values were finally employed to evaluate the moment of inertia  $I_0$  of the whole composite beam:

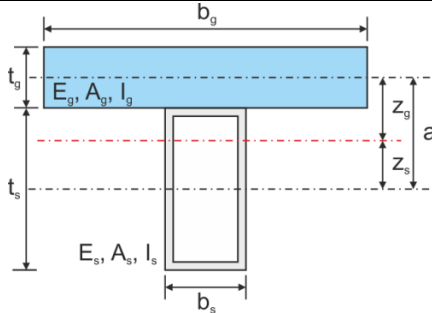
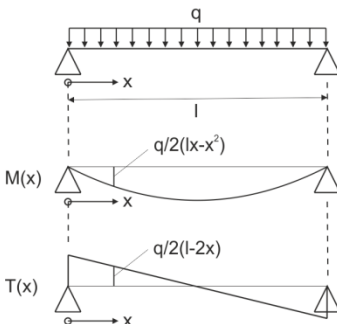
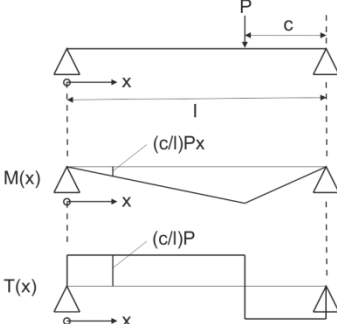
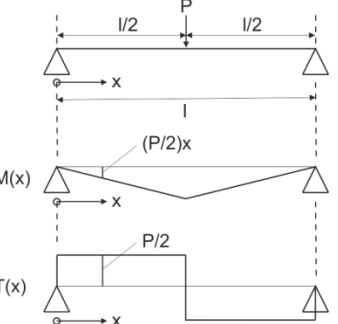
$$I_0 = \frac{I_g}{3} + \frac{A_g}{3} \times z_g^2 + I_s + A_s \times z_s^2 \quad (\text{F.4})$$

The normal stresses acting on the fibers of the composite beam subjected to a bending moment  $M$  can be obtained with the Navier formula, see Eq. (F.5). The bending moment  $M$  is dependent on the studied system and for a four point bending test, its maximum value appears between the two force application points.

$$\sigma = \frac{M}{I_0} z \quad (\text{F.5})$$

### F.3 Pischl formulation

One of the first partial connection theories was proposed by Richard Pischl in 1968 for the jointing of wood elements. In this theory, the relative displacement at the glass and steel interface was not considered as nil and the Bernoulli hypothesis was thus non valid. This method was based on the resolution of the differential equation linking the normal force and moment developing in the composite assembly. Knowing these data, the individual moment arising in each element could be obtained to later assess the stress distribution. These different steps were gathered in Table F.1 for three basic systems.

| Definition of the studied cross section                                                                                                                                                                                              |                                                                                                                                                                                                                                                                                      |                                                                                       |
|--------------------------------------------------------------------------------------------------------------------------------------------------------------------------------------------------------------------------------------|--------------------------------------------------------------------------------------------------------------------------------------------------------------------------------------------------------------------------------------------------------------------------------------|---------------------------------------------------------------------------------------|
|                                                                                                                                                   | <p>Geometrical characteristics definition:</p> $\begin{cases} A_0 = A_s + A_g \\ S_0 = a \frac{A_s A_g}{A_0} \\ I_0 = I_s + I_g + a \times S_0 \end{cases}$ <p>The rigidity K of the connection is defined by</p> $T = Ku$ <p>With u the relative displacement at the interface.</p> |                                                                                       |
| Differential equation of elastic partial connection                                                                                                                                                                                  |                                                                                                                                                                                                                                                                                      |                                                                                       |
| $\frac{d^2 N(x)}{dx^2} - \gamma^2 N(x) + \alpha M(x) = 0$ <p>With <math>\alpha = \frac{K}{E_s} \times \frac{a}{(I_s + I_g)}</math> and <math>\gamma^2 = \frac{K}{E_s} \times \frac{a}{(I_s + I_g)} \times \frac{I_0}{A_0}</math></p> |                                                                                                                                                                                                                                                                                      |                                                                                       |
| Loads repartitions and dimensions of the complete system                                                                                                                                                                             |                                                                                                                                                                                                                                                                                      |                                                                                       |
|                                                                                                                                                   |                                                                                                                                                                                                   |  |

|                                                                                                                                                                                                                    |                                                                                                                               |                                                                                                                                          |
|--------------------------------------------------------------------------------------------------------------------------------------------------------------------------------------------------------------------|-------------------------------------------------------------------------------------------------------------------------------|------------------------------------------------------------------------------------------------------------------------------------------|
| $N(x) = \frac{\alpha}{\gamma^2} M(x) \left[ 1 - 2 \frac{\cosh\left(\frac{\gamma l}{2}\right) - \cosh\left(\frac{\gamma l}{2} - \gamma x\right)}{\gamma^2 (lx - x^2) \cosh\left(\frac{\gamma l}{2}\right)} \right]$ | $N(x) = \frac{\alpha}{\gamma^2} M(x) \left[ 1 - \frac{l \sinh(\gamma c)}{\gamma c x \sinh(\gamma l)} \sinh(\gamma x) \right]$ | $N(x) = \frac{\alpha}{\gamma^2} M(x) \left[ 1 - \frac{1}{\gamma x} \frac{\sinh(\gamma x)}{\cosh\left(\frac{\gamma l}{2}\right)} \right]$ |
| $Q(x) = \frac{\alpha}{\gamma^2} T(x) \left[ 1 - 2 \frac{\sinh\left(\frac{\gamma l}{2} - \gamma x\right)}{\gamma (l - 2x) \cosh\left(\frac{\gamma l}{2}\right)} \right]$                                            | $Q(x) = \frac{\alpha}{\gamma^2} T(x) \left[ 1 - \frac{l \sinh(\gamma c)}{c \sinh(\gamma l)} \cosh(\gamma x) \right]$          | $Q(x) = \frac{\alpha}{\gamma^2} T(x) \left[ 1 - \frac{\cosh(\gamma x)}{\cosh\left(\frac{\gamma l}{2}\right)} \right]$                    |

**Table F.1-** Evaluation of the normal and shear forces in the composite section according to the Pischl theory

The bending moments developing in each steel and glass element could then be evaluated with the following formulas:

$$M_g(x) = (M(x) - N(x)a) \frac{I_g}{I_g + I_s} \quad (\text{F.6a})$$

$$M_s(x) = (M(x) - N(x)a) \frac{I_s}{I_g + I_s} \quad (\text{F.6b})$$

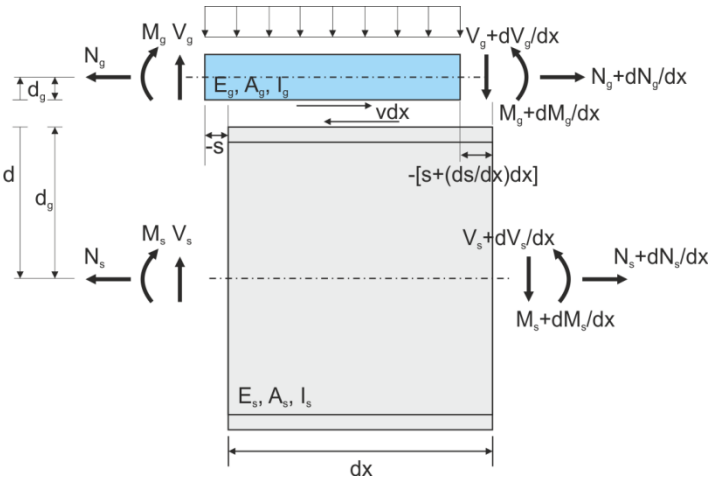
The final stress values could finally be expressed at the upper and lower fibers of the two materials with the equations Eq. (F.7a) and (F.7b).

$$\sigma_g = -\frac{N}{A_g} \pm \frac{M_g}{W_g} \quad (\text{F.7a})$$

$$\sigma_s = +\frac{N}{A_s} \pm \frac{M_s}{W_s} \quad (\text{F.7b})$$

#### F.4 Lebet formulation

Another elastic theory, accounting for partial connection, was also proposed by Lebet. While the Pischl theory was mainly based on the equilibrium equation of the internal force, the Lebet one was founded on the equilibrium equation of the sliding at the steel-glass interface. Nevertheless, the assumptions leading to the final expression of the differential equation were similar, i.e. both jointed materials were fully linear (without plasticity for the steel) and no vertical separation between the parts. The standard Bernoulli hypothesis was considered valid for the two elements accounted separately, so that their sections remain straight after deformation. The behaviour of the connection was once more fully linear with the only definition of the rigidity. The global system and fundamental equations were gathered in Table F.2.

| Definition of the studied cross section                                             | Fundamental equations                                                                                                                                                                                                                                                                                                                                                                                                                                                                                                                              |
|-------------------------------------------------------------------------------------|----------------------------------------------------------------------------------------------------------------------------------------------------------------------------------------------------------------------------------------------------------------------------------------------------------------------------------------------------------------------------------------------------------------------------------------------------------------------------------------------------------------------------------------------------|
|  | <p>The rigidity <math>K</math> of the connection is defined by</p> $V = Ks$ <p>With <math>s</math> the sliding at the interface and <math>V</math> the shear force. The shear force per unit of length is denoted.</p> <p>The sliding equilibrium equation is equal to:</p> $(1 + \varepsilon_g)dx + \phi dx d_g + s = (1 + \varepsilon_s)dx - \phi dx d_s + \left(s + \frac{ds}{dx} dx\right)$ <p>Where <math>\Phi</math> represents the curvature (equal for the two materials) and <math>\varepsilon_x</math> the strains of each material.</p> |

**Table F.2-** Definition of the studied composite beam and fundamental equilibrium equation according to Lebet theory

The equilibrium equations of the normal forces and bending moments of the steel and glass elements allow simplifying the fundamental equation of Table F.2 and ending up a differential one, see Eq. (F.8).

$$\frac{d^2 s}{dx^2} - \alpha^2 s = \alpha^2 \beta V \quad (\text{F.8})$$

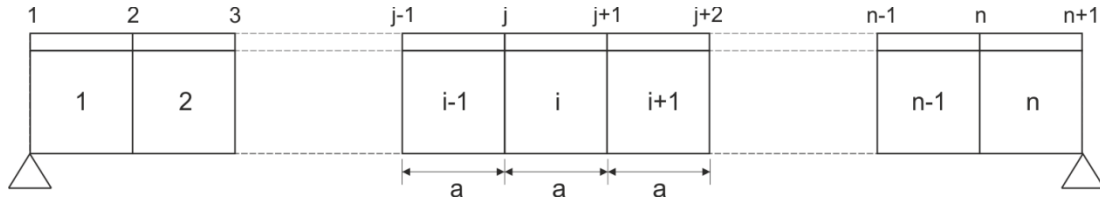
With  $\alpha^2 = \frac{KA_0}{eE_s I_0}$  ;  $\beta = \frac{ed}{KA_0}$  ;  $A_0 = d^2 + \frac{I_0}{A_s} + \frac{nI_0}{A_g}$  ;  $I_0 = I_s + \frac{I_g}{n}$  ;  $n = \frac{E_s}{E_g}$  (F.9)

The solution of the equation Eq. (F.8) for a constant section can be written in terms of hyperbolic functions depending on the position  $x$  and of shear force  $V$  as:

$$s = C_1 sh(\alpha x) + C_2 ch(\alpha x) - \beta V \quad (\text{F.10})$$

Where  $C_1$  and  $C_2$  are integration constants expressing the boundary conditions for one section. The determination of their values necessitates dividing the composite beam in  $n$  identical sections of length  $a$ , see Fig. F.3. By naming  $s_j$  and  $s_{j+1}$  the a priori unknown sliding at the position  $j$  and  $j+1$  of the section  $i$  and  $V_j$  and  $V_{j+1}$  the shear force at the same location, Eq. (F.10) can be rewritten as:

$$s_i(x) = \frac{(s_j + \beta V_j) sh[\alpha(a - x)] + (s_{j+1} + \beta V_{j+1}) sh(\alpha x)}{sh(\alpha a)} - \beta V_i(x) \quad (\text{F.11})$$



**Figure F.3-** Representation of the composite beam divided in several identical sections

With the above discretization,  $n+1$  sliding values at the extremities of the different sections have to be evaluated. Furthermore, with the continuity of the displacements at the junction of two consecutive sections, it becomes possible to write:

$$\frac{ds_{i-1}(x)}{dx} = \frac{ds_i(x)}{dx} \quad (\text{F.12})$$

By injecting the two expressions of Eq. (F.11) in the last equation, the following result is achieved:

$$s_{j-1} \frac{\alpha}{sh(\alpha a)} - s_j \frac{2\alpha ch(\alpha a)}{sh(\alpha a)} + s_{j+1} \frac{\alpha}{sh(\alpha a)} = \frac{\alpha \beta}{sh(\alpha a)} [-V_{j-1} + 2V_j - V_{j+1}] - \frac{\beta}{a} [V_{j-1} - 2V_j + V_{j+1}] \quad (\text{F.13})$$

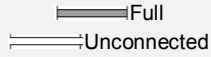
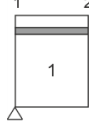
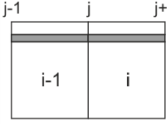
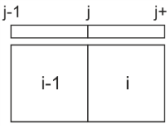
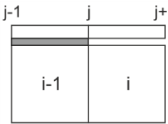
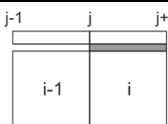
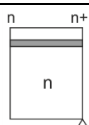
As it can be noticed with Eq. (F.13), the sliding at one position depends on the sliding at the previous and next positions. Thus, a matrix formulation can be used to express all the equations for each intersection:

$$[C]\{S\} = \{F\} \quad (\text{F.14})$$

With  $[C]$  a matrix filled with constant parameters and  $\{F\}$  a column vector depending on the shear forces. The final sliding values at the extremities of each section are appraised by inverting the  $[C]$  matrix and multiplying it by  $\{F\}$ .

In the establishment of the previous system of equations, the connection was regarded as effective and constant over the section. However, it could be decided to let free of connection some zones of the beam as the shear force could be neglected or inexistent, i.e. the central portion of an assembly subjected to a 4-point bending test. Hence, the previous set of equations should be modified to account for the possible transition of a connected and unconnected region. These changes were exposed in Table F.3.

$$\begin{bmatrix}
 c_{11} & c_{12} & 0 & & & & & & & & \\
 c_{21} & c_{22} & c_{23} & & & & & & & & \\
 0 & \dots & \dots & \dots & & & & & & & \\
 & & & c_{i-1,i-1} & c_{i-1,i} & 0 & & & & & \\
 & & & c_{i,i-1} & c_{i,i} & c_{i,i+1} & & & & & \\
 & & & 0 & c_{i+1,i} & c_{i+1,i+1} & & & & & \\
 & & & & \dots & \dots & \dots & \dots & & & \\
 & & & & & c_{n-2,n-2} & c_{n-2,n-1} & 0 & & & \\
 & & & & & c_{n-1,n-2} & c_{n-1,n-1} & c_{n-1,n} & & & \\
 & & & & & 0 & c_{n,n-1} & c_{n,n} & & & 
 \end{bmatrix}
 \begin{Bmatrix}
 s_1 \\
 s_2 \\
 \dots \\
 s_{j-1} \\
 s_j \\
 s_{j+1} \\
 \dots \\
 s_{n-1} \\
 s_n
 \end{Bmatrix}
 =
 \begin{Bmatrix}
 f_1 \\
 f_2 \\
 \dots \\
 f_{j-1} \\
 f_j \\
 f_{j+1} \\
 \dots \\
 f_{n-1} \\
 f_n
 \end{Bmatrix} \quad (F.15)$$

| Section<br> | $c_{i,i-1}$                                  | $c_{i,i}$                                                                                   | $c_{i,i+1}$                                  | $f_j$                                                                                                                                                                        |
|----------------------------------------------------------------------------------------------|----------------------------------------------|---------------------------------------------------------------------------------------------|----------------------------------------------|------------------------------------------------------------------------------------------------------------------------------------------------------------------------------|
|             | -                                            | $-\frac{\alpha \operatorname{ch}(\alpha a)}{\operatorname{sh}(\alpha a)}$                   | $\frac{\alpha}{\operatorname{sh}(\alpha a)}$ | $\frac{\alpha \beta}{\operatorname{sh}(\alpha a)} [V_1 \operatorname{ch}(\alpha a) - V_2] + \beta \frac{V_2 - V_1}{a}$                                                       |
|             | $\frac{\alpha}{\operatorname{sh}(\alpha a)}$ | $-\frac{2\alpha \operatorname{ch}(\alpha a)}{\operatorname{sh}(\alpha a)}$                  | $\frac{\alpha}{\operatorname{sh}(\alpha a)}$ | $\frac{\alpha \beta}{\operatorname{sh}(\alpha a)} [-V_{j-1} + 2V_j \operatorname{ch}(\alpha a) - V_{j+1}] + \frac{\beta}{a} [V_{j-1} - 2V_j + V_{j+1}]$                      |
|            | $\frac{1}{a}$                                | $-\frac{2}{a}$                                                                              | $\frac{1}{a}$                                | $\alpha^2 \beta a \frac{V_{j-1} + 4V_j + V_{j+1}}{6}$                                                                                                                        |
|           | $\frac{\alpha}{\operatorname{sh}(\alpha a)}$ | $-\frac{\alpha \operatorname{ch}(\alpha a)}{\operatorname{sh}(\alpha a)}$<br>$-\frac{1}{a}$ | $\frac{1}{a}$                                | $\frac{\alpha \beta}{\operatorname{sh}(\alpha a)} [V_j \operatorname{ch}(\alpha a) - V_{j-1}] - \frac{\beta}{a} [V_j - V_{j-1}] + \alpha^2 \beta a \frac{V_{j+1} + 2V_j}{6}$ |
|           | $\frac{1}{a}$                                | $-\frac{1}{a}$<br>$-\frac{\alpha \operatorname{ch}(\alpha a)}{\operatorname{sh}(\alpha a)}$ | $\frac{\alpha}{\operatorname{sh}(\alpha a)}$ | $\alpha^2 \beta a \frac{V_{j-1} + 2V_j}{6} + \frac{\alpha \beta}{\operatorname{sh}(\alpha a)} [V_j \operatorname{ch}(\alpha a) - V_{j+1}] + \frac{\beta}{a} [V_{j+1} - V_j]$ |
|           | $\frac{\alpha}{\operatorname{sh}(\alpha a)}$ | $-\frac{\alpha \operatorname{ch}(\alpha a)}{\operatorname{sh}(\alpha a)}$                   | -                                            | $\frac{\alpha \beta}{\operatorname{sh}(\alpha a)} [V_{n+1} \operatorname{ch}(\alpha a) - V_n] - \beta \frac{V_{n+1} - V_n}{a}$                                               |

**Table F.3-** Components of the two matrices [C] and {F} allowing the determination of the sliding under different junctions

With the complete determination of the sliding values, the normal forces and bending moments acting in the glass and steel elements can be calculated (equilibrium equations) with the following equations:

$$N_{s,j+1} = N_{s,j} - \frac{K}{e} \left\{ \frac{[\beta(V_j + V_{j+1}) + s_j + s_{j+1}](\operatorname{ch}(\alpha a) - 1)}{\alpha \operatorname{sh}(\alpha a)} - \beta a \frac{V_{j+1} - V_j}{2} \right\} \quad (F.16)$$

$$N_{g,j+1} = -N_{g,j+1} \quad (F.17)$$

$$M_{s,j} = \frac{(M_j - N_{s,j}d)I_s}{I_0} \quad (F.18)$$

$$M_{g,j} = \frac{(M_j - N_{s,j}d)I_g}{nI_0} \quad (F.19)$$

The normal stresses are then evaluated separately for each part at the junction of two sections by employing the results of the four previous equations:

$$\sigma_{s,j} = -\frac{N_{s,j}}{A_s} \pm \frac{M_{s,j}}{I_s} d_s \quad (\text{F.20})$$

$$\sigma_{g,j} = \frac{N_{g,j}}{A_g} \pm \frac{M_{g,j}}{I_g} d_g \quad (\text{F.21})$$

All these equations can be inserted in an Excel file to automatically compute the stresses along the length of the beam. A parametric study, in which the dimensions of all the elements would vary, could be conducted.



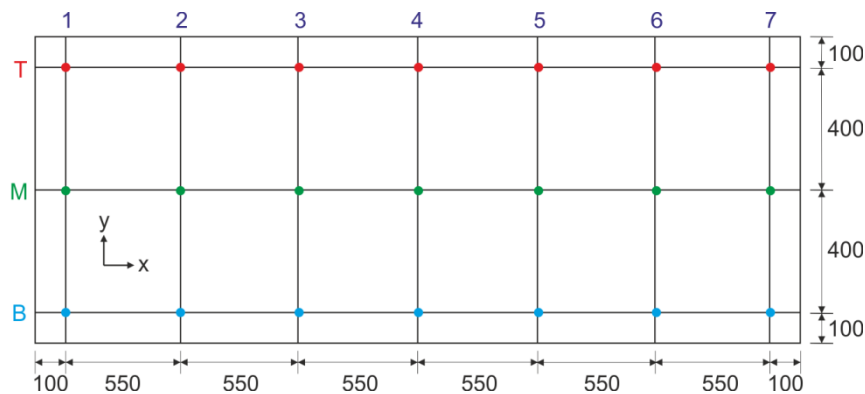
## APPENDIX G – Control quality of the large-scale beam tests

### G.1 Linear adhesive connection

While the modifications made on the steel profiles were operated within the University of Luxembourg, the fully tempered glass plates were externally fabricated by VITRUM LUX. The length of the latter matched the one of the steel total steel beam, i.e. 3500mm. The width of the monolithic glass panel was of 1000mm with a large thickness of 15mm. Except for the chamfers on the edges, no particular mechanical process was done on the three plates. A control of the length and width allowed ensuring of the proper dimensions with no variations. However, some differences in thicknesses were expected as the plates could not be issued from the same jumbo plate. Therefore, a control of the thickness was conducted in several points with the help of a digital caliper, see Table G.1 for the values and Fig. G.1 for the associated positions.

| Glass plate | Position along the width | Position along the length |       |       |       |       |       |       |        |       |
|-------------|--------------------------|---------------------------|-------|-------|-------|-------|-------|-------|--------|-------|
|             |                          | 1                         | 2     | 3     | 4     | 5     | 6     | 7     | Aver.  | σ     |
| GLAC-1      | Top (T)                  | 14,75                     | 14,74 | 14,73 | 14,72 | 14,74 | 14,7  | 14,72 | 14,805 | 0,081 |
|             | Middle (M)               | 14,8                      | -     | -     | -     | -     | -     | 14,75 |        |       |
|             | Bottom (B)               | 14,9                      | 14,91 | 14,9  | 14,9  | 14,89 | 14,88 | 14,85 |        |       |
| GLAC-2      | Top (T)                  | 14,92                     | 14,93 | 14,92 | 14,92 | 14,93 | 14,89 | 14,88 | 14,804 | 0,101 |
|             | Middle (M)               | 14,76                     | -     | -     | -     | -     | -     | 14,73 |        |       |
|             | Bottom (B)               | 14,73                     | 14,72 | 14,71 | 14,71 | 14,7  | 14,7  | 14,71 |        |       |
| GLAC-3      | Top (T)                  | 14,82                     | 14,81 | 14,81 | 14,81 | 14,82 | 14,81 | 14,82 | 14,890 | 0,085 |
|             | Middle (M)               | 14,87                     | -     | -     | -     | -     | -     | 14,8  |        |       |
|             | Bottom (B)               | 14,99                     | 14,99 | 14,96 | 14,98 | 14,98 | 14,99 | 14,98 |        |       |

**Table G.1-** Control of the thicknesses of the three glass plates acc.to the positions of Fig. G.1- linear adhesive connection

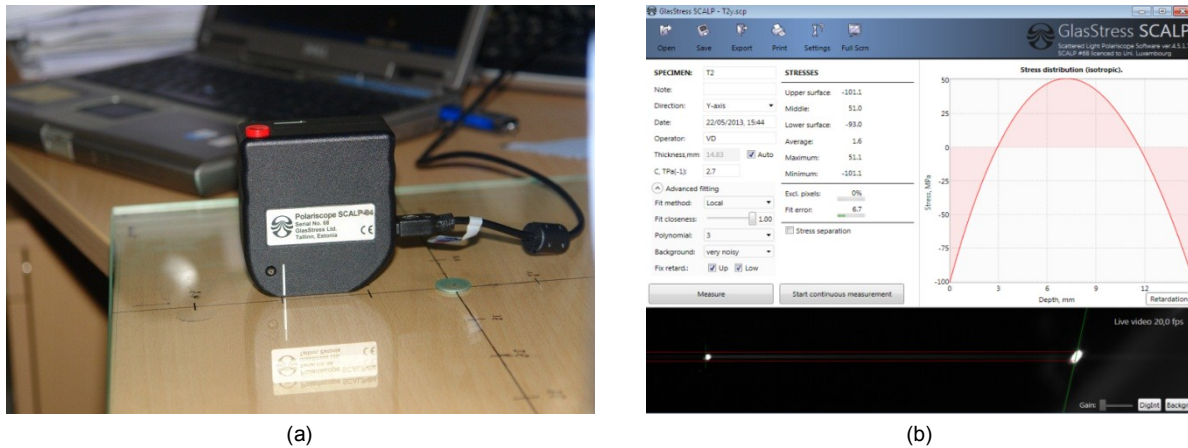


**Figure G.1-** Details of the measured positions – glass specimens of the linear adhesive connection

As it could have been remarked, one edge of the glass plates was always higher than the other one, even if these variations were small, i.e. of about 0,1mm. The first two glass plates possessed an average value identical with a low standard deviation. Only the averaged thickness of the third glass plate was slight higher, but with the same standard deviation. Consequently, the thickness variations could be neglected and a mean value considered.

Another control of the glass plate concerned the prestress induced by the tempering process. These data were evaluated in 21 points and in the x and y directions with the SCALP (Scattered Light Polariscope) system, measuring the compressive stress state on the outer part of the glass but also the tensile distribution in the core, see Fig. G.2. The definition of the tin side was of no importance with this device, even if it was placed directly on the steel side for the assembly, as it was more critical for the

glass plate. The prestresses at all the 21 points, referenced on Fig. G.1, were recorded in the following Table G.2.



**Figure G.2-** (a) Scattered Light Polariscope SCALP and (b) Example of stress distribution along the thickness of the glass

| Glass plate | Position along the width | Direction | Position along the length |        |        |        |        |        |        | Aver.   | $\sigma$ |
|-------------|--------------------------|-----------|---------------------------|--------|--------|--------|--------|--------|--------|---------|----------|
|             |                          |           | 1                         | 2      | 3      | 4      | 5      | 6      | 7      |         |          |
| GLAC-1      | Top                      | x         | -95,6                     | -99,6  | -96,4  | -93,5  | -92,5  | -100,4 | -106,3 | -96,338 | 5,753    |
|             |                          | y         | -92,4                     | -97,5  | -102,9 | -98,3  | -92    | -93,8  | -90    |         |          |
|             | Middle                   | x         | -90,8                     | -90,8  | -87,8  | -100   | -103,4 | -107,7 | -108,3 |         |          |
|             |                          | y         | -86,3                     | -86    | -87,8  | -92,4  | -90,4  | -88,7  | -95,4  |         |          |
|             | Bottom                   | x         | -102,6                    | -99,5  | -94    | -95    | -94    | -97,9  | -96,7  |         |          |
|             |                          | y         | -99,4                     | -102,6 | -97,1  | -105,5 | -99,5  | -95,9  | -99,5  |         |          |
| GLAC-2      | Top                      | x         | -111,9                    | -105,5 | -99,9  | -104,2 | -103,6 | -113,3 | -101,1 | -98,893 | 6,251    |
|             |                          | y         | -95                       | -101,1 | -92,5  | -92,4  | -99,2  | -92,4  | -97,9  |         |          |
|             | Middle                   | x         | -91,7                     | -95,8  | -88,6  | -98,1  | -98,7  | -97,2  | -110,2 |         |          |
|             |                          | y         | -96,6                     | -103,7 | -100,8 | -97,2  | -100,4 | -96,7  | -101,5 |         |          |
|             | Bottom                   | x         | -97,9                     | -105,1 | -103,2 | -104,7 | -102,9 | -102,2 | -98,6  |         |          |
|             |                          | y         | -102,7                    | -93,6  | -85,8  | -87,2  | -87    | -94,7  | -100,7 |         |          |
| GLAC-3      | Top                      | x         | -105,1                    | -108,8 | -108   | -103,1 | -98,5  | -106,7 | -102,2 | -96,055 | 8,312    |
|             |                          | y         | -96,7                     | -75,6  | -81,4  | -86,2  | -90,1  | -93,1  | -94,1  |         |          |
|             | Middle                   | x         | -91,6                     | -108,2 | -101,6 | -101,5 | -100   | -99,4  | -95,8  |         |          |
|             |                          | y         | -97,6                     | -91,8  | -97,3  | -92,3  | -92,2  | -106   | -95,4  |         |          |
|             | Bottom                   | x         | -92,3                     | -104,8 | -106,2 | -104,3 | -98,3  | -103,8 | -98,2  |         |          |
|             |                          | y         | -89,1                     | -85,4  | -89,1  | -79,2  | -88    | -84,2  | -91,1  |         |          |

**Table G.2-** Control of the prestress (maximum compression) of the three glass plates according to the positions of Fig. G.1

For a same glass plate and same position along the width, the measurements of the prestress in the x direction were slightly different to the ones of the y direction. Nevertheless, the relative deviations between the values were small, indicating that the prestress was isotropic, i.e. independent of the regarded direction. Furthermore, independently of the position along the width, i.e. in the center or at the edges, the prestress was identic, proving the uniformity of the prestress. Finally, all the glass plates presented close averaged values.

Due to the length of the beam, the control of the adhesive thickness could not be achieved in several positions, but only at the extremities were the Teflon spacers were inserted. Thus, no direct measure was possible. The only control was operated on the Teflon spacers under the load introduction points. The stillness of these elements demonstrated that the 3mm thickness was respected.

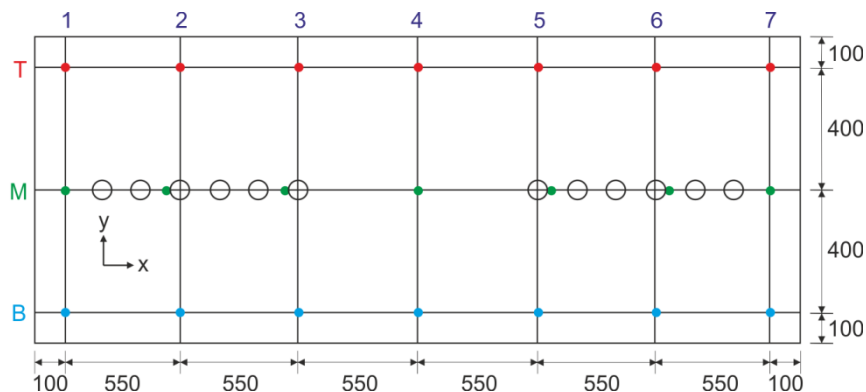


## G.2 Mechanical-adhesive connection

As for the previous type of connection, the steel beam modifications were made at the University of Luxembourg, while the glass manufacture operated by VITRUM LUX. The glass plates all measured 3500x1000x15mm and were chamfered around the edges. Holes of 40mm of diameter were cut each 200mm starting from the edges and within the first 1200mm, i.e. no change was made on the central zone of the glass between the two load application positions. These 12 holes were chamfered (1mm) to prevent possible stress concentrations. The length and width were simply checked as minor variations in these large dimensions could not affect the global behaviour of the composite assembly. Nevertheless, the recorded data were very close to the expected ones with about 1mm of deviation. Additionally the diameters of the holes were controlled with a digital caliper and were all alike with a size of 40,1mm, which allowed assessing the good reproducibility of the process. The thickness of the glass plate was inspected at several position of the glass, as it could vary with the producing method. The values recorded with a digital caliper were recorded in Table G.3 according to the positions drawn on Fig. G.3.

| Glass plate | Position along the width | Position along the length |       |       |       |       |       |       | Aver.  | $\sigma$ |
|-------------|--------------------------|---------------------------|-------|-------|-------|-------|-------|-------|--------|----------|
|             |                          | 1                         | 2     | 3     | 4     | 5     | 6     | 7     |        |          |
| GMAC-1      | Top                      | 14,71                     | 14,72 | 14,73 | 14,73 | 14,73 | 14,71 | 14,72 | 14,739 | 0,130    |
|             | Middle                   | 14,3                      | -     | -     | -     | -     | -     | 14,7  |        |          |
|             | Bottom                   | 14,8                      | 14,82 | 14,86 | 14,84 | 14,83 | 14,81 | 14,82 |        |          |
| GMAC-2      | Top                      | 14,89                     | 14,89 | 14,94 | 14,89 | 14,9  | 14,9  | 14,91 | 14,796 | 0,099    |
|             | Middle                   | 14,74                     | -     | -     | -     | -     | -     | 14,75 |        |          |
|             | Bottom                   | 14,7                      | 14,71 | 14,7  | 14,71 | 14,7  | 14,7  | 14,71 |        |          |
| GMAC-3      | Top                      | 14,71                     | 14,72 | 14,73 | 14,73 | 14,71 | 14,7  | 14,7  | 14,716 | 0,013    |
|             | Middle                   | 14,72                     | -     | -     | -     | -     | -     | 14,69 |        |          |
|             | Bottom                   | 14,72                     | 14,73 | 14,73 | 14,73 | 14,72 | 14,71 | 14,71 |        |          |

**Table G.3-** Control of the thicknesses of the three glass plates acc.to the positions of Fig. G.3- mechanical adhesive connection



**Figure G.3-** Details of the measured positions – glass specimens of the linear adhesive connection

Except for the last glass plate, one edge along the length presented again larger dimensions than the opposite one. However, these variations were sufficiently low to be neglected. This postulate was also confirmed by the control of the standard deviation of the measured data of one plate, which was of about 0,1mm, and the comparison of the averaged thickness values, which were similar in each case. In conclusion, only the averaged value, less than the expected 15mm, could be employed for further numerical investigations.

As the glass was fully tempered, the verifications of the prestress in several positions were made with the SCALP system presented on Fig. G.2. The 21 measurements were again done in both directions to ensure of the uniformity and of the isotropy of the prestresses. Even it had no importance on the

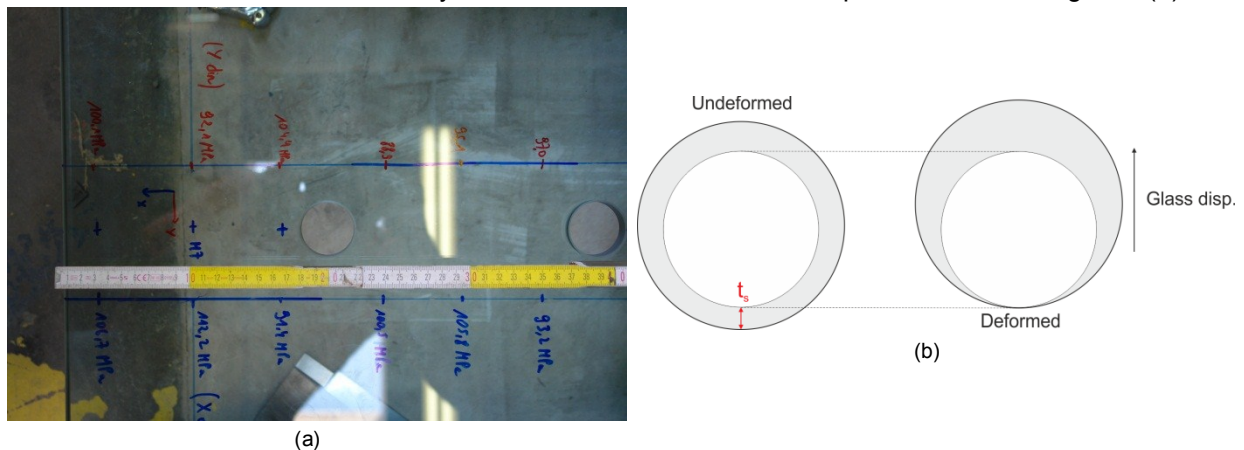
evaluation of the prestress, the tin side of the glass plate was always the face in relation with the steel flange and so not directly measured. As four holes (at 650 and 1200mm) coincided with the location of the prestress assessment, the data were retrieved as close as possible to the hole's edges. All the recorded values were stored in Table G.4 according to the positions described on Fig. G.3.

| Glass plate | Position along the width | Direction | Position along the length |        |        |        |        |        |        |         | Aver. | $\sigma$ |
|-------------|--------------------------|-----------|---------------------------|--------|--------|--------|--------|--------|--------|---------|-------|----------|
|             |                          |           | 1                         | 2      | 3      | 4      | 5      | 6      | 7      |         |       |          |
| GMAC-1      | Top                      | x         | -99,3                     | -97,6  | -92,2  | -96,1  | -92,8  | -92,2  | -95,4  | -97,579 | 5,965 |          |
|             |                          | y         | -95,6                     | -96,3  | -103,7 | -104,9 | -103,1 | -100,6 | -99,3  |         |       |          |
|             | Middle                   | x         | -106,4                    | -106,2 | -98    | -103,9 | -106,5 | -108,4 | -112,2 |         |       |          |
|             |                          | y         | -91,4                     | -92,3  | -97,4  | -92,7  | -93    | -90,5  | -92,1  |         |       |          |
|             | Bottom                   | x         | -99,7                     | -97,9  | -93,7  | -90,7  | -89,9  | -84,5  | -99,5  |         |       |          |
|             |                          | y         | -91,1                     | -94,5  | -94,7  | -105   | -102   | -97,3  | -97,7  |         |       |          |
| GMAC-2      | Top                      | x         | -102,1                    | -97,2  | -94,8  | -97,8  | -96,2  | -96,5  | -93,2  | -96,998 | 5,415 |          |
|             |                          | y         | -99,6                     | -96,7  | -101,4 | -92,8  | -103,6 | -102,9 | -100,9 |         |       |          |
|             | Middle                   | x         | -95,3                     | -104,2 | -100,4 | -99,7  | -94,8  | -102,4 | -106,3 |         |       |          |
|             |                          | y         | -96,3                     | -91,4  | -110,7 | -87    | -93,3  | -90    | -90,7  |         |       |          |
|             | Bottom                   | x         | -100,8                    | -94,2  | -93,1  | -89,3  | -84,1  | -91,7  | -101,2 |         |       |          |
|             |                          | y         | -90,6                     | -95,7  | -99,5  | -99,4  | -97,1  | -103,1 | -95,9  |         |       |          |
| GMAC-3      | Top                      | x         | -96,4                     | -93,6  | -91,7  | -92,6  | -91,4  | -95,5  | -103,4 | -96,555 | 4,983 |          |
|             |                          | y         | -93,1                     | -95,1  | -98,4  | -97,7  | -104,2 | -98    | -101,2 |         |       |          |
|             | Middle                   | x         | -107,4                    | -101,9 | -99,4  | -97,1  | -94,1  | -107,8 | -98,5  |         |       |          |
|             |                          | y         | -95,5                     | -80,1  | -96,1  | -93,4  | -89,6  | -93,6  | -94    |         |       |          |
|             | Bottom                   | x         | -96,7                     | -96,5  | -93    | -93,5  | -93,2  | -100,1 | -97    |         |       |          |
|             |                          | y         | -97,1                     | -94,9  | -102,2 | -104,4 | -95,9  | -92,7  | -97,3  |         |       |          |

**Table G.4-** Control of the prestress (maximum compression) of the three glass plates acc.to the positions of Fig. G.2

By isolating on position along the width of one glass plate, some minor variations could be observed between the two directions of the measurements. The x-values seemed to give a higher prestress than the y-value, but the differences were small and an isotropy state could be assumed. Between the different positions, no important deviation was noticed, indicating that the prestress was uniform over one glass plate. This was validated by the evaluation of the standard deviations, which represented only 1/20 of the averaged prestress. Finally, the averaged prestresses of the three plates were similar demonstrating the reproducibility of the process.

To ensure of the non-influence of the closeness to the hole or to the edge on the prestress value, several measurements in the x- and y- direction were done around the position M1, see Fig. G.4 (a).



**Figure G.4-** (a) Evaluation of the influence of the hole and edge on the prestress and (b) Silicone post-bonding measurement

After injection of the silicone, the distance between the steel bolt and the glass hole was measured in the compressive zone with a digital caliper, to exactly know the maximum sliding until steel to glass contact and thus glass failure. These values were recorded for the 12 holes of each plate according to Fig. G.4 (b) and regrouped in Table G.5.

| Pos.   | Silicone thickness in the compressive zone (mm) |            |     |     |      |      |      |      |      |      |            |      |
|--------|-------------------------------------------------|------------|-----|-----|------|------|------|------|------|------|------------|------|
|        | 1                                               | 2          | 3   | 4   | 5    | 6    | 7    | 8    | 9    | 10   | 11         | 12   |
| x (mm) | 200                                             | 400        | 600 | 800 | 1000 | 1200 | 2300 | 2500 | 2700 | 2900 | 3100       | 3300 |
| GMAC-1 | 4,7                                             | 4,7        | 5,6 | 5,7 | 6,3  | 5,3  | 4,6  | 4,4  | 4,4  | 5,7  | <b>4,2</b> | 4,9  |
| GMAC-2 | <b>4</b>                                        | 4,3        | 5,4 | 4,8 | 5    | 5,5  | 5,6  | 4,7  | 4,4  | 5,3  | 6,3        | 5,7  |
| GMAC-3 | 4,5                                             | <b>4,4</b> | 4,7 | 5   | 5,2  | 5    | 5,1  | 6,1  | 6,2  | 5,4  | 4,8        | 4,5  |

**Table G.5-** Silicone thickness measurement in the compressive zone - mechanical adhesive connection

As the silicone failed first in each case, the minimal distance between the glass hole and the steel bolt could correspond to the limiting sliding and had to be compared to the experimental data for the same location.

